6 Photon beamlines and scientific instruments

The high photon number per pulse, ultra-short pulse duration and high coherence of x-ray free-electron laser (FEL) radiation provide the opportunity to apply new x-ray experimental techniques, thereby enabling new areas of scientific investigation. In this chapter we will describe the x-ray instrumentation for the European X-Ray Free-Electron Laser (XFEL). This includes, in particular, a description of the various scientific domains and the main requirements for experiments in these areas.

The scientific case for an x-ray FEL was discussed previously in the context of the Linac Coherent Light Source (LCLS) project in Stanford, and reported in September 2000 (*LCLS: the first experiments* **[6-1]**); and also in the context of the Tera-Electronvolt Superconducting Linear Accelerator (TESLA) project (for a linear collider with integrated x-ray laser), and reported in the corresponding Technical Design Report (TDR) **[6-2]** in spring 2001. In preparing the present report, these previous efforts were of course taken into account as a starting point, but it was felt that enough time had passed and that sufficient new experience had been acquired with experiments and equipment at projects such as the Sub-Picosecond Pulse Source (SPPS) in Stanford, the “Free-electron LASer in Hamburg (FLASH)” vacuum ultraviolet (VUV)-FEL at Deutsches Elektronen Synchrotron Laboratory (DESY), and at other sources, to warrant an in-depth new consideration of the scientific perspectives and the accompanying requirements for instrumentation. In order to get as wide a European basis as possible, consultation of the scientific community was organised by holding four XFEL workshops at different locations in Europe:

- Diffraction, Crystallography and Imaging at the European XFEL, October 28/29, 2005, DESY, Hamburg, Germany.
- European XFEL Workshop on High Energy Density Science and Non-linear X-ray Processes, November 28/29, 2005 École de Chimie de Paris, Paris, France.
- Ultra-fast Time-Dependent X-ray Experiments at the European XFEL, January 20/21, 2006 Danish Academy of Sciences, Copenhagen, Denmark.
- Detectors for the European XFEL March 28/29, 2006, by the Rutherford Laboratory, Abingdon, UK.

The first three workshops concentrated on the validation of the radiation parameters chosen for the various undulator branches, on the scientific cases and the specific instrumentation requirements; the last workshop centred on the development of area detectors suitable for the XFEL. Most importantly, the workshops were very useful for identifying leading European scientists who became natural “spokespersons” for a given scientific field. These scientists have been editors of the majority of the material presented in this chapter, soliciting, coordinating and organising the contributions of many authors.

It is, therefore, fair to say that XFEL is the product of an international collaboration widely distributed across Europe.

Section 6.1 presents an overview of the x-ray installations that will be described in more detail in later sections. Section 6.2 describes the XFEL photon beam transport from the undulators to the experimental hall, including x-ray optical elements which are part of the scientific instruments. A possible layout of the photon beam transport of the five beamlines is presented. Section 6.3 describes the photon beam diagnostics to be installed in the beamlines and near the instruments, in order to allow the required measurement of the XFEL radiation parameters: most of these diagnostics will be provided on a pulse-by-pulse basis. Section 6.4 describes the various scientific domains and their experimental proposals. The latter have been analysed to define the requirements for the instruments to be installed at the European XFEL. A schematic of these instruments concludes each of the scientific areas. Section 6.5 describes instrumentation where specific developments are required for XFEL, in particular the areas of sample manipulation and environment, x-ray optics, optical lasers and x-ray detectors. Section 6.6 concludes the chapter with a summary of cost and manpower requirements.

6.1 Overview of the X-Ray systems

The European XFEL features five x-ray sources: Three long undulators, operated in the Self-Amplified Spontaneous Emission (SASE) mode, provide XFEL radiation in the photon energy range from 0.25 to 12.4 keV. Two further undulators provide spontaneously emitted synchrotron radiation at higher photon energies, from 20 to 100 keV. For each of these x-ray sources, a beamline guides the x-ray beam to the experimental hall, where the instruments for scientific experiments are located. The first installation phase of the European XFEL described in this report includes the installation of ten instruments (see Chapter 1). These instruments will be distributed on five photon beamlines. Since XFEL features a relatively small number of photon beamlines, each of them needs to serve more than one application or x-ray technique. This is in contrast to beamlines at storage ring sources and will lead to a more complex design of the beamlines. Another feature of European XFEL is that electron bunches can be prepared and distributed according to the needs of the experiment. The specific electron beam parameters could be the time pattern, the electron energy (and, therefore, the photon energy) or even more sophisticated parameters of the x-ray pulse. The flexibility of linear accelerators (linacs) is straightforward to exploit for an installation which features only one undulator, such as the FLASH facility at DESY. At the European XFEL it is envisioned that the five undulators and photon beamlines will operate quasi-simultaneously (see Section 5.1), so it is important that the electron beam parameter variation does not lead to a conflict in the operation of the various instruments.

One advantage of the European XFEL is its ability to accelerate a large number of electron bunches per second. The time pattern for fully loaded bunch trains is shown in Figure 6.1.1. Using fast switches in the beam distribution (compare Section 4.5.3.1) it will be possible to distribute a specific bunch pattern into the two electron beamlines, thus enabling operation with from 1 to 3,000 bunches per bunch train. The undulators located in the same electron beamline branch (two in beamline 1, three in beamline 2) will all receive the same electron bunch pattern. The instruments at these beamlines will operate more independently by the use of fast shutters upstream of the experimental stations, operating with a repetition rate of at least 10 Hz.

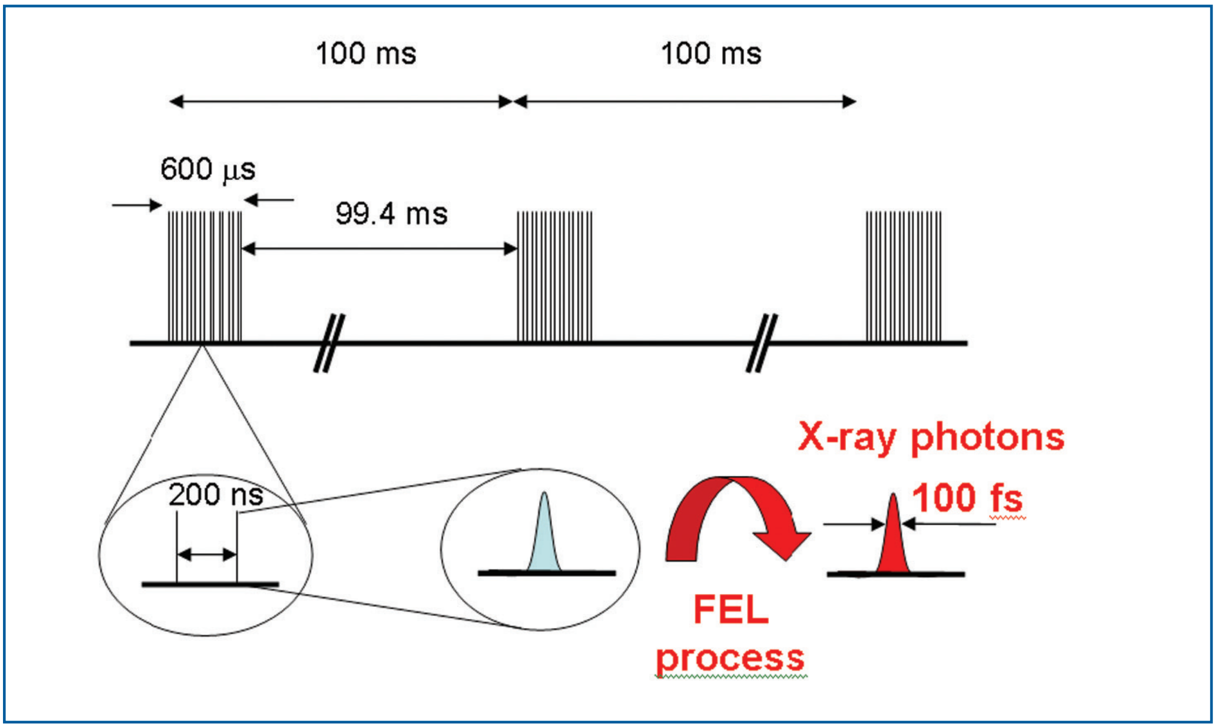

Figure 6.1.1 *Electron bunch time pattern with 10 Hz repetition rate and up to 3,000 bunches in a 0.6 ms long bunch train. The separation of electron bunches within a train is 200 ns for full loading. The duration of electron bunches is ~200 fs and the non-linear FEL process reduces the duration of the photon pulses to ~100 fs.*

Beamline	X-ray features	Proposed instruments
SASE 1	~12 keV High coherence High flux 3rd harmonic	PCS 1 – X-ray Photon Correlation Spectroscopy FDE 1 – Femtosecond Diffraction Experiments SPB 1 – Single Particles and Biomolecules
SASE 2	3.1 – 12.4 keV High coherence High flux	CXI 1 – Coherent X-ray Imaging HED 2 – High Energy Density XAS 2 – X-ray Absorption Spectroscopy
SASE 3	0.25 – 3.1 keV High coherence High flux 3rd harmonic	HED 1 – High Energy Density SQS 1 – Small Quantum Systems XAS 1 – X-ray Absorption Spectroscopy SQS 2 – Small Quantum Systems PCS 2 – X-ray Photon Correlation Spectroscopy CXI 2 – Coherent X-ray Imaging
U 1, U 2	15* – 90 keV	FDE 2 – Femtosecond Diffraction Experiments CXI 3 – Coherent X-ray Imaging RAD 1 – Research And Development

* This value of the lowest photon energy requires small modification of the U1 design presented in Chapter 5.

Table 6.1.1 *A possible distribution of scientific instruments discussed in Section 6.4 on the photon beamlines. Main x-ray features of the five beamlines are indicated.*

In the present stage of the European XFEL, a strong scientific case has been established. In Section 6.4, the requirement for instruments for scientific applications are discussed. However, no decision has been made yet on which ten out of the 15 instruments presented in Section 6.4 will be realised. This decision has to be prepared by the scientific advisory bodies of the European XFEL in the forthcoming 12 months. In order to give a proper description and costing of the facility in this report, we have evaluated all the proposed instruments and analysed their photon beamline requirements. The instruments have been allocated to the most appropriate beamline (see Table 6.1.1) leading to a beamline design described in Section 6.2.4. It is assumed that the overall concept of the photon beamlines will not change drastically if the final instrument configuration differs from the proposal presented here.

6.2 Photon beam transport

6.2.1 Photon beamline concept

The photon beam transport for the European XFEL is different from existing light sources due to the specific properties of FEL radiation. Most importantly, a large distance between undulator source and optical elements accepting the FEL beam is required. It allows the beam size to increase, thus reducing the enormous peak power. Also grazing incidence geometries are needed to spread out the beam footprint, requiring long drift paths to achieve sufficient beam separation. Due to the long distances involved, undulators, beam transport elements and instruments are located in different buildings. The undulators and beamlines will be located in tunnels which will impose transverse and longitudinal constraints (see Table 6.2.1). The limited number of beamlines requires a very flexible photon beam transport design since different instruments with different requirements may be installed on the beamlines. Needless to say, the beam transport between undulator and experiments hall must preserve the important XFEL photon beam parameters; namely time structure, flux, and coherence.

Although differences exist between the two hard x-ray FELs, the soft x-ray FEL, and the two x-ray-spontaneous synchrotron radiation beamlines, a modular design of the photon beamlines has been chosen. In the following we introduce the most important elements of this design. A more detailed discussion of each component is given later. For clarity we will focus our description mainly on the XFEL beamline SASE 1. A similar description (with slightly varying parameters) can be given for each of the beamlines (see Table 6.2.1 and Sections 6.2.4.1 – 6.2.4.5).

SASE 1 is equipped with a 200 m long undulator system and aims at the production of 12.4 keV FEL radiation. In the present design the undulator is followed by a 193 m long drift section preserved for future "undulator options". Several options have been discussed, but are not included in this first installation phase. Examples are self-seeding schemes, laser manipulation of the x-ray beam, two-colour insertion devices, or additional undulators segments for achieving lasing at higher photon energy than originally foreseen. After this section, the electron beam will be separated from the photon beam and will be deflected towards the next undulator. Where the separated electron beam comes close to the tunnel periphery, a shaft building is located from which two tunnels continue. In case of the terminating undulator (SASE 3, U2), the electron beam will be bent down into an electron beam dump located in an underground hall. Since it is expected that shafts and dump halls will exhibit slightly different ground motions than the neighbouring tunnels, beamline elements requiring exact positioning (e.g. position monitors, mirrors, or monochromators) cannot be located in or near these tunnel "interruptions". The layout with separate tunnel sections has the additional function of allowing access to some of the tunnels for work on beamline elements, while the facility is in operation.

	SASE 1	**SASE 2**	**SASE 3**	**U 1**	**U 2**
Electron beam separation	220	129	143	91	110
Intermediate shaft/dump building	385-415	215-245	155-180	195-225	135-160
Primary photon beam diagnostics	330-450	180-300	140-200	150-240	125-180
Bremsstrahlung beam stop	500	500	250	280	200
Monochromator	500	500	250-350	280	200
Experiments hall	960	910	400	590	295

Table 6.2.1 *Distances (in metres) of components from the end of the undulator for each of the five beamlines. Where appropriate, the start and end points of the units are indicated.*

The first beamline element is a combined unit of 10^4 gas attenuators and beam position monitors located in the vicinity of the shafts and dump halls. The gas absorber system will allow controlled adjustment of the photon flux over four orders of magnitude. Just before and behind the gas absorber, there are two non-invasive photon diagnostic tools: i) X-ray Gas Monitor Detectors (XGMDs) to measure the absolute photon flux; ii) Beam Position Monitors (BPMs), to image the transverse position and direction of the photon beam. These photon beam diagnostics systems will be described in Section 6.3. The following photon diagnostic station is primarily dedicated to photon beam-based alignment for the undulator segments (see Section 5.5). The next element in each of the beamlines is a *Bremsstrahlung* beam stop. A photon beam offset of 50 mm, followed by a collimator with an approximate opening of 10 mm, is required to prevent *Bremsstrahlung* radiation entering the experimental hall, both for radiation protection and signal background reduction. Two complementary schemes are envisaged: For experiments requiring maximum flux, a double-mirror fixed-exit system will be used to generate the offset, while experiments requiring an energy resolution better than the natural bandwidth of the SASE radiation, use crystal or grating monochromators. Perfect crystal monochromators are furthermore expected to preserve wavefronts better than mirrors and are, therefore, the preferred optical element to transport the beam in coherent beam or extreme focusing applications.

For beamlines requiring focused beams, optical elements will be needed at distances appropriate for the required demagnification. For moderate focusing (spot sizes ~100μm, demagnification near unity) focusing elements will be placed in the photon beam transport section. Further mirrors and crystal optics could be employed nearer to the experimental hall to guide the photon beams to separate instruments. The beamlines end at a safety shutter in front of the experimental hall.

6.2.2 X-ray optical elements

6.2.2.1 Mirrors

X-ray mirrors will be widely used for the XFEL. They provide high reflectivity and are achromatic tools to distribute the beams to the various experimental stations. In addition, they can be used to focus the x-ray beam and, by using the reflectivity cut-off for higher photon energies, allow reduction of higher harmonic radiation. The requirements for mirrors for XFEL radiation (discussed below) will apply to all kinds of mirrors used for beam distribution in flat geometry or, for focusing, in pre-shaped or dynamically bent geometries. A specific example is the double-mirror system to provide a fixed beam offset of 50 mm at the *Bremsstrahlung* beam stop. The distance (see Table 6.2.1) of these first mirrors to the undulator, of 500 m and 250 m in the cases of SASE 1, SASE 2 and SASE 3, respectively, is a compromise between reduction of photon fluence on the optical surface of the mirrors and available lengths of ultra-high precision mirrors, which in turn limits the acceptable photon beam size. The discussion of the resulting energy deposition on the mirror surfaces (see Section 6.2.2) gives confidence that mirrors in the chosen geometry will withstand the intense radiation safely.

The mirrors will be operated at angles below the critical angle (angle where total external reflection occurs), which depends both on the wavelength and the mirror surface material. For the 12 keV case, highly polished Silicon substrates with Carbon coating at a glancing angle of 2 mrad are proposed for the mirrors. The critical angle α_c of Carbon for this photon energy is 2.44 mrad generating an energy cut-off at ~15 keV. For the opening angle of FEL radiation of ~1 μrad (FWHM) and a distance of the mirror system of 500 m a 0.7 m long mirror could, thus, accept 6-σ of the beam, which will include the full coherent beam. For lower photon energies, the opening angle increases, leading to the requirement of larger mirror surfaces. This will be a problem in the case of SASE 2 where an opening of 3.4 μrad at 3.1 keV FEL radiation and assuming identical configuration of the mirror leads to a 6-σ mirror length of ~2.2 m. Mirrors of this length cannot be manufactured at the precision required for the XFEL (see below) and other solutions have to be found here.

Surface finish and figure errors

Since the mirrors are always in the beam (except when perfect crystals are used instead, see Section 6.2.2.2), they must preserve the wave front of the incident radiation to allow proper focusing and to maintain the coherence properties of the FEL sources. Estimates of the mirror requirements are generally based on models and ray-tracing codes for incoherent light sources. Since the FEL has a significant degree of coherence, one, in principle, needs to perform simulations of the effect of the mirror for the partially coherent beam. These could be either analytical simulations **[6-3]** or wave front propagation codes. The latter are routinely used for visible light propagation simulation, but are not yet available in full for x-ray radiation. Current understanding of the corresponding requirements on figure error and micro-roughness of mirror surfaces is, therefore, incomplete.

As a starting point for surface figure error, one can assume a value of 10% of the corresponding FEL radiation full angle (0.1 µrad at 12.4 keV). However, simulations indicate that if the maximum focal spot increase which can be tolerated is 10%, figure errors should be an order of magnitude smaller **[6-4]**. Ray-tracing seems to generate similar values. Figure 6.2.1 shows simulation results of focus and wave front deformation for two slope errors using the SHADOW code. The simulations neglect the influence of diffraction due to finite mirror lengths. For focusing experiments, where a beam divergence in the order of 1 mrad is acceptable, a Kirkpatrick Baez (KB)-mirror system in front of the sample could be used in addition to the upstream mirrors. In Figure 6.2.2 ray-tracing results for additional KB mirrors at 1 and 2 metres in front of the sample are shown. For a slope error of 0.01 µrad on all four mirrors, a sub-micron focus with an almost flat wave front is obtained. If the quality of the upstream double bounce mirrors is reduced to 0.1 µrad, but with the KB pair remaining at 0.01 µrad, a focus size in the sub-micron range can still be achieved, however, the wave front distortion will be in the Angstrom range. Recent measurements, however, show that the requirement on figure errors reduces strongly (~1 µrad) for a 20% spot size increase **[6-5]**, in a situation, similar to the XFEL, of long-source-to-mirror distances and strong focusing.

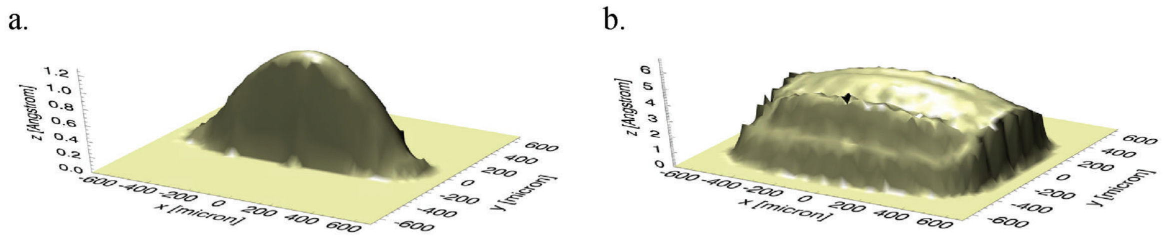

Figure 6.2.1 *Ray-tracing results for the double-mirror system at 500 m from the source. The x- and y-axes are the beam dimensions in horizontal and vertical direction. The z-axis shows the relative path lengths in Angstroms. With a slope error of 0.01 µrad rms (a) the beam essentially retains a undistorted spherical wave front and can be focused by bending one of the mirrors to about 70 µm FHWM in y-direction, very close to the source limited spot size. The unfocused direction is 750 µm FWHM. With a figure error of 0.1 µrad; (b), the wave front is distorted on the Angstrom level and the focusing in y-direction is much less effective (FWHM y: 400 µm, x: 820 µm).*

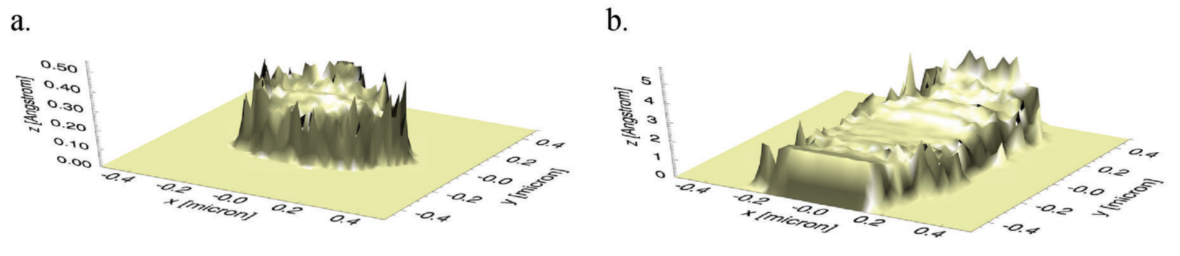

Figure 6.2.2 *Ray-tracing of focus and wave front deformation for the case of extreme focusing using KB-mirrors in front of the sample. 0.01 µrad (a) and 0.1 µrad (b) rms slope errors have been assumed for the double-mirror system at 500 m.*

At these accuracy levels the reduction of gravitational sag is important, but the symmetric beam of the FEL will allow horizontal reflection which essentially eliminates this problem. Given the XFEL output, heat deformation of the first mirror has to be expected which might be compensated for by operating the second mirror as an adaptive optic element. In a different application this mirror could be used to focus the beam in one direction. In addition to the figure error, the micro-roughness of the mirrors leads to scattering, thus, producing a wider, less collimated background in addition to the focal spot. Roughness in the order of 0.1 nm seems, at present, to be acceptable for most of the experiments.

State-of-the-art manufacturing achieves rms values of 0.09 nm micro-roughness and 0.3 µrad tangential slope errors for 0.5 m long mirrors (compare Figure 6.2.3). For plane mirrors, the radius was measured to be >240 km. Conventional metrology tools for verifying the optical surfaces, like long trace profilers and interferometers, are already close to their resolution limit because of the use of optical wavelengths. Therefore, the implementation of in-situ wave front sensors is required for improved characterisation of the performance of optical elements (see Section 6.3.1). It should be noted here that during recent years, a discussion started aimed at a better definition of mirror performance. The limiting process in mirror fabrication is metrology, measuring either local roughness or averaged slope errors. In a surface displacement power spectrum, these measurements make two non-overlapping areas. Specification of an x-ray mirror is usually done by values for roughness and slope error without correlating the two parameters. Furthermore, in x-ray applications it is not fully understood how the correlation of the two parameters influences the x-ray beam properties and therefore, the experimental observation. In this field more Research and Development (R&D) will be required in the forthcoming years to properly specify mirrors for XFEL applications.

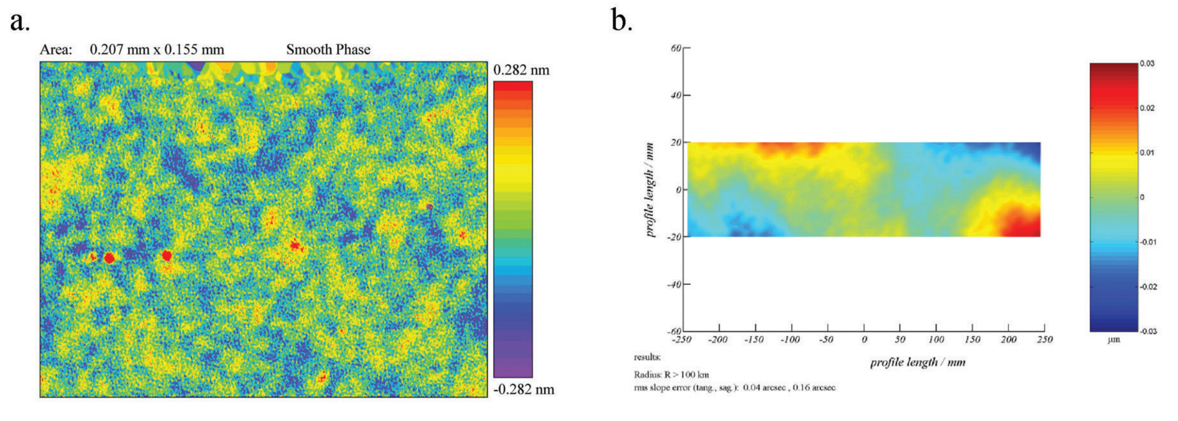

Figure 6.2.3 *Micro-interferometric measurement (a) and long trace profilometry (b) of a 0.5 m long plane mirror for a beamline at the Free-Electron LASer in Hamburg (FLASH) facility at DESY manufactured by Zeiss, Oberkochen. rms values of the surface roughness, tangential and sagittal slope errors are 0.09 nm, 0.3 and 0.6 µrad, respectively.*

Power dissipation

Due to the limited number of electron bunches per second, the average power load on the mirrors is very reasonable. In the case of SASE 1, with 72 W average power of the FEL radiation, and a reflectivity of 0.9, there is an average power density of ~50 mW/mm^2 at the mirror surface. The additional power due to spontaneous synchrotron radiation is estimated to be of the same order of magnitude. The particular time structure of the XFEL with up to 3,000 pulses within a period of 0.6 ms does, however, complicate the situation. The power density within this pulse train could be as high as ~8 W/mm^2. At third generation synchrotron sources, power densities up to several 100 W/mm^2 are currently handled by monochromator crystals with cryo-cooling schemes. Research and development is required to evaluate if these schemes can be equally applied to the long mirrors of the XFEL with their tight tolerances in figure error.

While the average power is still moderate, the peak power within a single pulse will be in the GW range. At these values, the principal problem may no longer be thermal distortion, but rather the possibility of ablation of the mirror surface, causing permanent damage. Ablation will depend on the radiation dose per pulse, which we will quantify as the energy absorbed per atom per pulse. To estimate the dose, we calculate the energy absorbed in the volume defined by the projected beam area A_{proj}. on the optical element and one attenuation length l_{att}, i.e. the depth into the material measured along the surface normal where the radiation intensity falls to 1/e of its value at the surface. Normalised to one atom, this energy corresponds to the atomic dose near the surface: $D_A = E_{pulse}(1-R)/A_{proj.} 1_{att} n_A$, where E_{pulse} is the energy in one radiation pulse, R is the reflectivity and n_A denotes the element specific density of atoms. In Table 6.2.2 we calculate the dose near the surface for some of the mirror configurations at the XFEL.

	Unit	SASE 1	SASE 1	SASE 3	SASE 3
Photon energy	keV	12.4	12.4	3.1	0.8
Pulse energy	mJ	2	2	8	13
Projected beam area	mm2	100	100	57	640
Mirror coating		Si	C	C	C
Grazing angle	mrad	2	2	10	10
Projected fluence	J/cm^2	2.0×10^{-3}	2.0×10^{-3}	1.4×10^{-2}	2.0×10^{-3}
n_A	cm^{-3}	5.0×10^{22}	1.1×10^{23}	1.1×10^{23}	1.1×10^{23}
(1-R)		2.57×10^{-2}	1.98×10^{-3}	0.54	7.46×10^{-2}
L_{att}	cm	5.30×10^{-7}	5.77×10^{-7}	1.06×10^{-5}	3.28×10^{-7}
Surface dose	eV/atom	1.2×10^{-2}	3.9×10^{-4}	4.0×10^{-2}	2.5×10^{-2}

Table 6.2.2 *Parameters for first mirrors and calculation of absorbed dose per XFEL pulse. The reflectivity and attenuation length data have been taken from the CXRO tables* **[6-6]**.

A surface dose of 0.01 eV/atom is a limiting dose below which no damage is expected **[6-7]**. The values of Table 6.2.2 indicate that for the XFEL in the SASE 1 and SASE 2 cases, the surface dose is about one order of magnitude below this limit, when using Carbon coatings. We, therefore, do not expect any damage mechanisms to be important. However, higher Z materials, such as Silicon, may already pose a problem. In the case of SASE 3, the calculated doses reach up to values of 0.01 eV/atom. There are experimental indications for the EUV regime that damage sets in only at significantly higher doses. However, further detailed studies to determine accurate damage threshold data are required **[6-8]**. Additionally, one will have to evaluate if there are cumulative effects that may cause damage over several thousands of pulses. The neglect of non-linear effects in the above considerations of potential damage by power load is, to some extent, supported by the absence of non-linear interaction during the operation of mirrors for FEL radiation at FLASH. Detailed investigations are underway to study the interaction of XFEL radiation with optical surfaces **[6-8]**.

6.2.2.2 Crystal monochromators

X-ray crystal monochromators will be required to reduce the 0.1% bandwidth of the FEL for various applications, in particular for spectroscopy. In addition, they can be used to match the radiation bandwidth to the one accepted by the sample in a diffraction experiment, which also reduces unwanted heating of the sample. The diffraction limited bandwidth is 1.4×10^{-4} for the Silicon (111)-reflection and 6×10^{-5} for the Diamond (111)-reflection. The energy resolution can be as small as a few 10^{-7} for high-order reflections but could be limited by time-dependent temperature gradients in the crystal. Diffraction by crystals creates relatively large deflection angles, which may be useful for distributing the beam to various instruments inside the experimental hall. Single crystals cannot deflect the full XFEL bandwidth at a particular Bragg angle.

In the following, Silicon and Diamond crystals will be described, as they have shown the highest prospect of fulfilling the requirements for XFEL sources. Whereas Silicon crystals can be grown to high perfection standards, Diamond has the advantages of higher heat conductivity and high damage threshold, thus, achieving good performance at high power loads. In this respect, isotopically enriched Silicon-28 (^{28}Si) could be an ideal material because of its enhanced thermal conductivity, see the heat load discussion below.

Silicon and Diamond crystals

Comparing Diamond and Silicon single crystals, one finds that the Diamond (111) reflection is similar to Silicon (220) except for the absorption thickness, which is more than one order of magnitude larger for Diamond **[6-9]**. Therefore, not only are the reflection properties of Diamond better, i.e. the peak reflectivity is (slightly) higher, but also less heat is absorbed. Beryllium, which is superior in this respect, cannot yet be grown as a dislocation-free crystal. In the best case it has a mosaic spread of 200 µrad. Silicon, on the other hand, is absolutely dislocation-free, while Diamond single crystals are only locally perfect **[6-10]**, although development of larger perfect Diamond crystal is showing promising progress. The Silicon (111) reflection provides a good matching (ω_H =22 µrad at 12.4 keV) for synchrotron beams, but only higher order reflections have a Darwin width small enough to match the XFEL beam divergence (1 µrad (FWHM) at 12.4 keV). This means that the reciprocal space element selected by a perfect crystal out of a spectrally wide, but well collimated beam will be anisotropic, typically with its long axis parallel to the beam direction. This situation is radically different from laboratory or even synchrotron radiation conditions. The choice between Silicon and Diamond will depend on the degree of crystal perfection that is needed, the actual heat loads and radiation damage considerations, as discussed below.

Heat load simulations

For Silicon crystal monochromators at third generation light sources, the average heat load limit is already reached in certain cases. For higher heat loads it is essential to develop schemes to maintain the monochromator performance. The thermal deformation of the crystal induced by heat load depends on the figure of merit α/k, where α and k are, respectively, the thermal expansion coefficient and the thermal conductivity. This ratio is strongly temperature dependent for Silicon and Diamond. At liquid Nitrogen temperature or even lower, α/k could be several orders of magnitude lower than at room temperature. Possible solutions to improve the performance of crystal monochromators are using crystals with lower α/k than Silicon, or using enhanced cooling techniques (higher cooling efficiency or lower temperature of the coolant). Diamond has lower α/k than natural Silicon in a wide temperature range, and is a good candidate. Presently, Silicon crystal monochromators are made of natural Silicon (^{nat}Si), which is composed of three stable isotopes: Silicon-28 (92% natural abundance), Silicon-29 (4.7% natural abundance), Silicon-30 (3.3% natural abundance). By purifying Silicon to 99.9% Silicon-28 (^{28}Si), the phonon mean free path increases, thereby significantly improving the thermal conductivity. The thermal conductivity is enhanced by 60% at room temperature, by a factor of 2.4 at liquid Nitrogen temperature (77K), and by a factor of 6 at 20 K. The maximum thermal conductivity (30 kW/m/K) of ^{28}Si at 20 K is 2.5 times higher than that of Diamond. Silicon-28 (^{28}Si) cooled by liquid Helium could be an ideal crystal monochromator for both its perfect crystalline structure and thermal properties. Also, ^{28}Si is available from semiconductor industries where it is used to reduce the chip temperature. Figure 6.2.4 shows k, α and the specific heat C_p versus temperature for Diamond IIa, and both ^{nat}Si and ^{28}Si **[6-11]**.

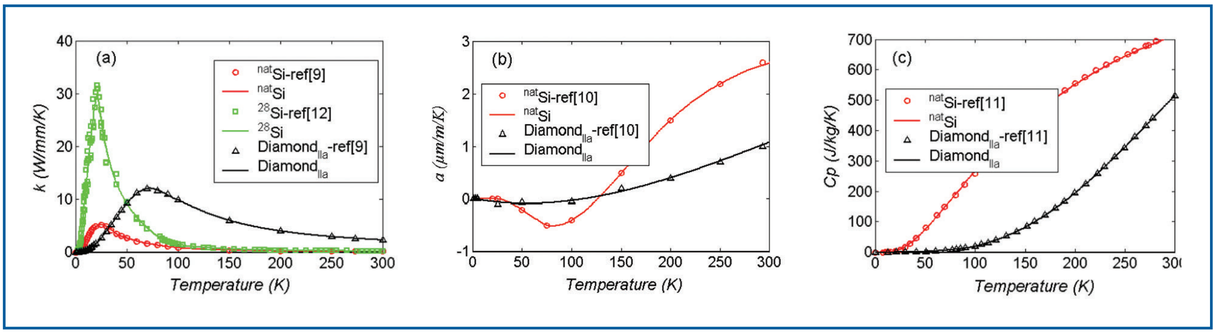

Figure 6.2.4 *Thermal conductivity (a) thermal expansion coefficient (b) and specific heat (c) of* ^{nat}*Si,* ^{28}*Si and Diamond IIa* **[6-11]**.

The response of cryogenically-cooled crystals to the heat deposition during a train of XFEL pulses has been studied by finite element modelling **[6-11]**. Results show the increase of crystal temperature during the pulse train, followed by a sharp decrease after the train. The repetition rate of 10 Hz does not lead to accumulated effects. For an energy Q = 2 J, deposited during the pulse train, the temperature variation at two locations of the crystal and the change in the slope errors are depicted in Figure 6.2.5. The geometry of the crystals studied here is a block of 120×60×60 mm^3 for ^{nat}Si, 20×20×20 mm^3 for both ^{28}Si and Diamond IIa. The crystals are cooled on five surfaces in order to maximise the cooling surface area. The Diamond crystal is cooled by liquid Nitrogen (h_{cv}=0.005 W/mm^2/K, T_f=77 K). The ^{nat}Si and ^{28}Si crystals are cooled by liquid Helium (h_{cv}=0.005 W/mm^2/K, T_f=8 K). X-ray beam size is 2×2 mm^2 with an incident angle of θ_{Bragg}=14°. The peak values of the thermal slope error and the maximum temperature are summarised in Table 6.2.3 for the three crystals as a function of deposited energy Q. In conclusion, ^{28}Si crystals cooled by liquid Helium offer thermal slope errors comparable to Diamond crystals for pulse train energies up to 2 J. Therefore, ^{28}Si crystal monochromators could be an interesting alternative to Diamond for applications where a perfect crystalline structure is needed. It is clear that liquid Helium cooling of crystals has not yet been established and needs a dedicated R&D effort.

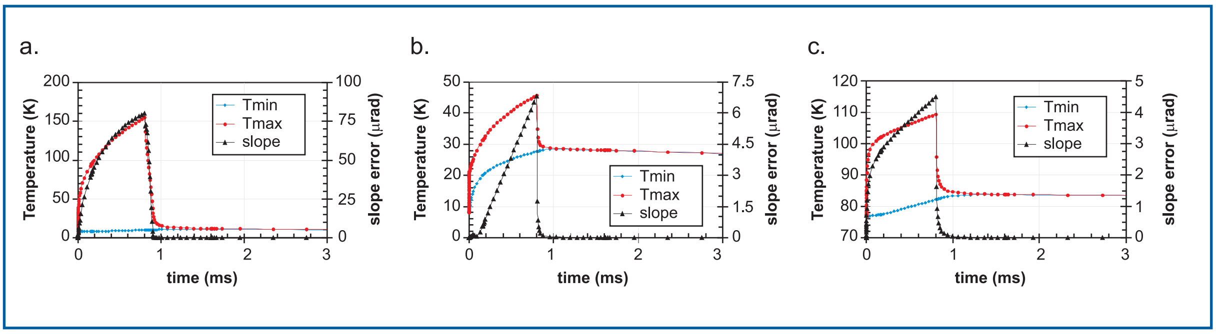

Figure 6.2.5 *Temperature and slope error variation during the course of a pulse train for (a)* ^{nat}*Si, (b)* ^{28}*Si, and (c) Diamond crystals (Q=2 J).*

Crystal	Cooling	Q [J]	P_{mean} [W]	T_{max} [K]	$slope_{PV}$ [µrad]
		2	20	109	4.5
Diamond IIa	Liquid Nitrogen	3	30	129	11
(20×20×20 mm^3)	(77 K)	5	50	178	41
		10	100	380	346
		2	20	46	6.8
Single-isotope ^{28}Si	Liquid Helium	3	30	69	26
(20×20×20 mm^3)	(8 K)	4	40	147	69
		5	50	360	346
		1	10	44	3
Natural Silicon	Liquid Helium	1.5	15	77	23
(120×60×60 mm^3)	(8 K)	2	20	155	80
		3	30	406	566

Table 6.2.3 *Calculated maximum temperature and peak-to-valley thermal slope error in three crystals at different pulse train energy values Q.*

Time structure after monochromatisation

Another point to be addressed is the effect of monochromatisation on the time structure of the XFEL pulse of 100 fs duration and its pulse substructure with coherent radiation bursts of ~0.3 fs duration. The x-ray pulse duration is in the order of the time needed for the pulse to traverse an extinction length (for perfect crystals) or an absorption length (for mosaic crystals). By definition of Bragg's law, the path difference of an x-ray beam is precisely one wavelength per lattice plane with respect to the beam reflected at the crystal surface. Thus, the time delay per lattice plane is λ/c where c is the speed of light. Consequently, pulse broadening might occur. Indeed, a simulation investigating the response of a Laue-case monochromator crystal in dynamical diffraction theory has shown a broadening of a δ-pulse **[6-12 – 6-14]**. The crystal reflection acts as a frequency filter and thus, has a broader response in the time domain. However, the simulation suggests that this broadening mainly changes the duration of the bursts to 2-3 fs, but leaves the overall pulse duration of 100 fs effectively unchanged. The simulation also shows that the amplitudes normalised to the average amplitude follow the same statistical law as the incident beam, namely the Rayleigh distribution. Further R&D is needed to implement dynamical diffraction into wave front propagation codes for complete description of time-dependent effects in diffraction.

6.2.2.3 Grating monochromators

For soft x-rays produced at SASE 3, grating monochromators have to be used in order to reduce the bandwidth of FEL radiation for spectroscopy applications. It is proposed to use a plane grating monochromator design originally conceived in 2001 for a soft x-ray beamline at the TESLA XFEL **[6-15]**. This monochromator operates in the photon energy range 0.5-3 keV, provides a resolution of 10^4 and is able to accept the high power levels of XFEL radiation. Its total length is in the order 120 m, thereby requiring integration of the monochromator in the photon beamline. Figure 6.2.6 shows the optical design which requires only minor modification.

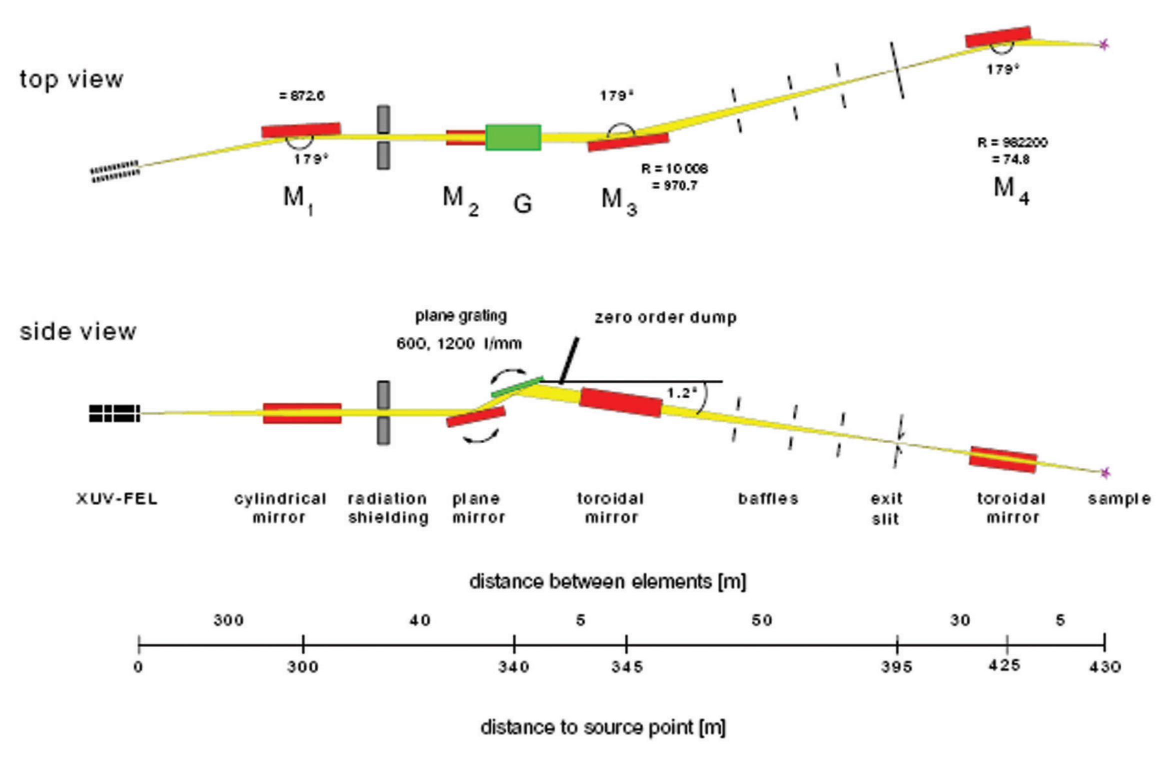

Figure 6.2.6 *Optical design for a high power XUV-plane grating monochromator* **[6-15]**.

6.2.2.4 Focusing optics

For a number of experiments, focusing the x-ray beam to a small spot is desirable to increase the photon density at the sample position. This means that the lens apertures should be as large as the beam to collect as many photons as possible. If the optics are illuminated with a fully coherent beam, the focused spot size will no longer depend on the source size or the demagnification factor. It will be diffraction-limited in the case of perfect optics and aberration-limited in the case of a non-perfect optics. Focusing x-ray optics can be divided in three classes; all have their advantages and drawbacks depending on the specific application, photon energy, achievable spot size, aperture, and robustness: (i) reflective, (ii) refractive, and (iii) diffractive. (Waveguides have also been used successfully to produce very small hard x-ray spot sizes **[6-16]**, but due to their small working distance and relative inefficiency compared to other focusing optics they are not likely to find widespread application at XFEL sources). A brief review on the present state-of-the-art for hard x-ray nano-focusing and the future potential with respect to the specific requirements in the context of the XFEL, will be given. This is summarised in Table 6.2.4.

	KB mirrors	**NFLs (refractive lenses)**	**KB mirrors**
Achieved focal spot [nm]	36×48 (15 keV, mirror **[6-17]**); 45 (24 keV, ML **[6-18]**)	47×55 (21 keV, **[6-19]**)	~150 (8 keV **[6-20]**; 12.7 keV **[6-21]**)
Aperture [µm]	100×100	30×40	50 - 300 (circular)
Efficiency	Close to 100%	20%	Typically 10%
Thermal stability	Good	Excellent	Poor (transmission) Good (reflection)
Diffraction limited	No	No	Yes
1 mm apertures	Difficult	Not applicable	Possible

Table 6.2.4 *Current performances of hard x-ray extreme focusing optics.*

Mirrors

High resolution x-ray mirrors are usually built in KB geometry. Significant progress has been made in the past year, the best spot sizes are on the order of 50 nm for single surface mirrors **[6-17]** and multilayer mirrors **[6-18]**. Typical apertures are 100 µm, which is matched to the transverse coherence lengths of third generation insertion device beamlines. The performance is still limited by the figure errors of the mirror surfaces. So far, no diffraction-limited resolution has been achieved, but metrology and surface machining are continuously improving, so that this may be possible in the near future. Damage by the high thermal loads of the XFEL seems unlikely, as the power is distributed over a large footprint of a bulk substrate, but even slight thermal deformations would deteriorate the focusing capabilities. A scaling up of the present apertures to collect the whole coherent flux of the source will be very difficult, especially when high (or even diffraction-limited) resolution is required, as the length of the mirror substrates has to increase. In this respect, using multilayer mirrors is probably the more promising approach as it requires much shorter lengths due to the higher reflection angles.

Refractive lenses

Refractive lenses are, in several respects, promising candidates for focusing hard x-rays at the XFEL. In comparison with mirrors they offer the advantage of a straight beam path. Additionally, the focus size is adjustable, because x-ray lenses are compound devices: single refractive lenses with long focal lengths can be arranged in a stack to form an effective lens with short focal length and therefore, a strong demagnification. A disadvantage of these systems is their chromaticity leading to different focal spots for different photon energies. The loss in coherence due to the passage through a large number of surfaces may also be an important consideration.

A. Moderate focusing by refractive lenses

Moderate focusing to beam spots the same size as the source or collimation of the beam can be achieved for the well collimated XFEL radiation by using one or several stacked Beryllium lenses. Since the lenses are chromatic, one has to foresee several lenses or stacks of lenses for the different photon energies. A high resolution table with the corresponding translations and rotations will be installed in the photon beamlines.

B. Extreme focusing by refractive lenses

The focal length of rotationally parabolic refractive lenses is currently limited to about 300 mm. This also limits the diffraction limited spot size of these optics, since it scales approximately with the square root of the focal length. Currently, small focal distances, i.e., $f<10$ mm, are realised by so-called nano-focusing lenses (NFLs) made of Silicon or Diamond (see Figure 6.2.7). For NFLs, focal spots as small as 15 nm are predicted **[6-19]**. Further reduction of the spot size using refractive optics requires the use of adiabatically focusing lenses that are predicted to focus about 10^8 photons per pulse to about 5 nm **[6-22]**, resulting in a gain of 8×10^6. In view of their application at an XFEL beamline, the following issues have to be addressed for refractive lenses.

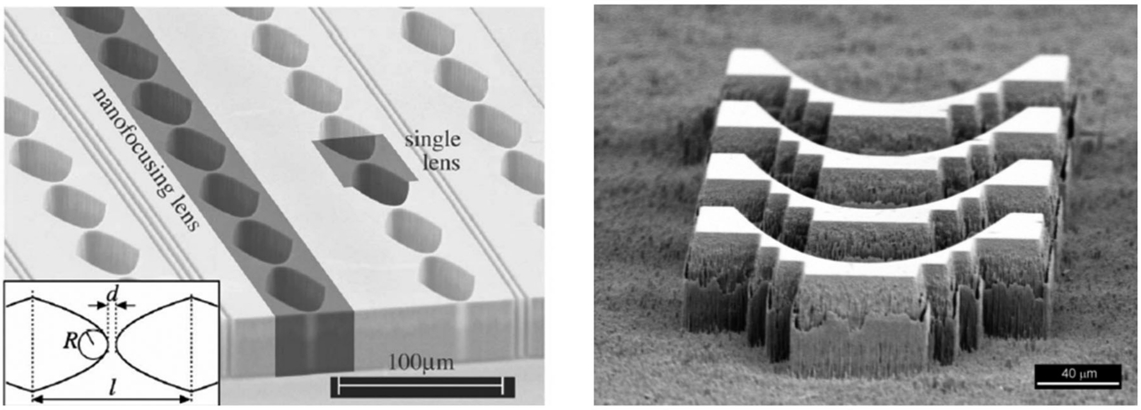

Figure 6.2.7 *Left: NFLs made by electron beam lithography and reactive ion etching of Silicon* **[6-19]***. Right: Diamond planar refractive lenses fabricated using a similar technique* **[6-23]***.*

Expected optical performance

To focus most of the monochromatic XFEL pulse to dimensions ~100 nm, rotationally parabolic refractive lenses made of Beryllium may be well suited. Table 6.2.5 summarises the expected focus properties for three different lens sets. Beryllium lenses are ideally suited for x-ray energies around $E=12.4$ keV (SASE 1), but can be operated down to about 5 keV (at SASE 2). For harder x-rays up to several 100 keV, refractive lenses made of different materials have been successfully used. This is of particular interest for focusing the spontaneous radiation from U 1 and U 2 **[6-24]**. For experiments requiring extremely small focal spot size, in general, the preservation of the wave front is of great importance. Experimental verifications of the wave front properties in the focus of a refractive lens are ongoing.

Radiation damage

Model calculations suggest that low-Z elements will be stable under irradiation with hard x-rays **[6-25]**. The maximal dose for Beryllium per pulse (assuming 10^{12} photons/pulse) at 12 keV gives ~10^{-5} eV/atom, well below the estimated surface dose of 0.01 eV/atom for damage (see Section 6.1.2.1). For Carbon (e.g., Diamond), the maximum dose is four times higher than for Beryllium, but following the above considerations, Diamond is expected to be stable in the XFEL beam, too.

Heat load

The average power expected for the SASE 1 undulator at the XFEL is about 72 W at 12.4 keV. Assuming a lateral beam size of 800 µm (FWHM) at the experiment, more than half of the radiation is expected to fall onto the aperture of a Beryllium lens. At this energy, about 3.6% of the incident power is absorbed in the first lens, corresponding to 2.3 W. Overall, 59 W are dissipated in the third set of lenses described in Table 6.2.5. On average, this corresponds to about 0.3 W per lens. Refractive lenses have been used in some synchrotron installations for years under very demanding conditions, e.g. for white beam collimation, without observing damage **[6-26]**.

Chromaticity

Due to the quadratic dependence of the refractive index for hard x-rays on the x-ray wavelength, refractive lenses are strongly chromatic. Optimal performance can only be reached for monochromatic x-rays, i. e. $\Delta E/E<10^{-4}$. The natural width of the SASE radiation ($\Delta E/E\sim10^{-3}$) will be focused to an interval along the optical axis that is about one order of magnitude larger than the depth of focus, effectively broadening the focus to several 100 nm. If this is not acceptable for a given experiment, a reduction of the bandwidth using a crystal monochromator may be required.

N	Unit	100	150	200
D_{eff}	µm	485	430	409
f	mm	480	345	289
N A		5.1×10^{-4}	6.2×10^{-4}	7.1×10^{-4}
Demagnification		1/2100	1/2900	1/3450
d_t	nm	73	60	53
Coherent spot size	nm²	732	602	532
Spontaneous spot size	nm²	852	652	572
σ_p	%	14.4	10.6	9.2
Photons/pulse in focus		7.0×10^{10}	5.3×10^{10}	4.6×10^{10}
Gain		1.7×10^{7}	2.0×10^{7}	2.3×10^{7}

Table 6.2.5 *Expected performance of Beryllium parabolic refractive x-ray lenses for focusing SASE 1 pulses at an energy of 12.4 keV. An undulator to experiment distance of 1000 m, a source size of 70×70 µm², a fluence of 10^{12} ph/pulse, and a beam size of 800 µm (FWHM) at the scientific instrument are assumed. For the Beryllium lenses, a radius of curvature of R = 200 µm, a geometric aperture $2R_0$ = 890 µm, and a minimum thickness d = 10 µm is chosen in accord with current technology. N is the number of single lenses, D_{eff} the effective aperture, f the focal length, NA the numerical aperture, d_t the diffraction limited spot size (FWHM), and σ_p the effective lens cross-section* **[6-27]**.

Diffractive optics

At present, the best resolution for x-ray focusing is obtained by using diffractive optics such as Fresnel or Multilayer-Laue Zone Plates (ZPs). Zone Plates have demonstrated a resolution beyond 30 nm **[6-28]**. The ultimate resolution of a ZP is in the order of the smallest, outermost zone width, meaning that nanolithography processes with sufficient resolution have to be applied. State-of-the-art electron-beam lithography and multilayer deposition tools are capable of placing the diffracting structures with lateral placement accuracies of a few nanometres, i.e. within a fraction of the outermost zone width. As a consequence, the wave front precision is controlled within a fraction of a wavelength, and diffraction-limited resolution is routinely achieved when sufficient transverse and longitudinal coherence is provided. Efficient focusing of hard x-rays by ZPs is more difficult because the zone structures must be sufficiently dense and thick to provide a phase-shift near π for best diffraction efficiency. The zone structures are typically made from heavy metals, and they must be on the order of 1 µm thick for hard x-ray focusing. Due to the difficulty in fabricating such high aspect ratio (10:1 or higher) structures, ZPs fabricated by electron beam lithography have been limited to a resolution of about 100 nm in the hard x-ray region **[6-20]**. Recent improvements in fabrication technology will soon allow reaching 50 nm or better **[6-29]** with commercially available devices. Increasing the aperture of these devices towards 1 mm is already possible. It should also be mentioned that diffractive optical elements with more complex functionality such as twin spot zone plates **[6-30]** or computer-generated holograms **[6-31]** can also be made. This unique feature can have very interesting applications in the context of holography and other assisted phase retrieval experiments. Multilayer-Laue ZPs offer the opportunity to reach a resolution beyond 10 nm with efficiency greater 30% **[6-28]**. Only 1-D focusing has been demonstrated so far by these devices, however, fabricating them with large zone aspect ratios is not difficult, thus they can have significant efficiency for hard x-rays.

One drawback of lithographic ZPs is that they are usually fabricated on thin transmitting substrates such as Silicon Nitride membranes, typically 100 nm in thickness. While these membranes only interact weakly with the incident beam, they have poor thermal conductivity. In addition, the heavy materials used to fabricate the zones, while thermally very stable, absorb a significant proportion of the incident beam. Consequently, the lifetime of ZPs may turn as short as a single x-ray pulse.

The possibility of combining the robustness of reflective optics with the diffraction-limited focusing of diffractive optics could be provided by using either multilayer based or crystal based Bragg-Fresnel lenses. They consist of a zone plate pattern etched into a reflecting surface. Although these elements are not used much at present, they can be made with small outermost zone width and large apertures **[6-32]**. A disadvantage of Bragg-Fresnel lenses is that both the focus location and angle depend on the photon energy. Nonetheless, these devices may turn out to be an attractive alternative to presently considered solutions.

6.2.2.5 *Transport of high harmonic radiation*

Several experiments require the use of higher harmonic radiation in pump-probe experiments using the fundamental radiation as the pump. According to Chapter 5, the intensities of third harmonic radiation are at the level of 1% of the fundamental line and fifth harmonic radiation is still at a level of 0.03% of the fundamental line intensity. In case of SASE 1, photon energies could be as high as 37 keV whereas for SASE 2, an energy range of 12 to 24 keV can easily be covered by the third harmonic. Even for SASE 3 it is possible to use the third harmonics of 3.1 keV in experiments combining soft and hard x-ray beams. The major difficulty to transport harmonic radiation to the experiments is the double-mirror system required to stop *Bremsstrahlung* and other background radiation. Due to the cut-off in photon energy at ~15 keV, these mirrors will not transport harmonic radiation in the standard configuration. By coating the mirrors with higher Z materials, one can shift the cut-off to higher photon energies, but the absorbed power is increased too. As an example, coating with Gold will shift the cut-off for 2 mrad grazing angle to >30 keV. At the same time, Gold has a very high reflectivity for photon energies up to ~12 keV at this grazing angle, thus, limiting the surface dose due to the fundamental FEL line to $\sim 3\times 10^{-4}$ eV/atom ($\sigma_s = 2.47\times 10^{-20}$ cm^2/atom at 11.8 keV).

Complete separation of fundamental and harmonic radiation can be achieved using a monochromator tuned to reflect harmonic radiation, while at the same time transmitting the fundamental order. For example, the third harmonic of SASE 1 at 0.033 nm is transported by the Diamond (111)-reflection with a Bragg angle $\theta_{Bragg} = 4.6°$, a Darwin width of 4.6 µrad and a corresponding energy resolution of $\Delta E/E \sim 6\times 10^{-5}$. In comparison to the normal operation (reflection of the fundamental with $\Delta E/E \sim 10^{-4}$), the heat load imposed on the crystal due to the full absorption of the fundamental is increased by only ~10%. Therefore, the discussion of heat load effects in Section 6.2.2.2 is also applicable for the transport of higher harmonic orders.

6.2.3 Other beam transport elements

In addition to the optical elements discussed in the previous section, the photon beam transport includes other elements required for control and diagnostics of the x-ray beam and for vacuum control purposes.

6.2.3.1 *Safety shutter*

Safety shutters are required to enable access to the downstream beamline area. They will be installed in the SASE 1, SASE 2 and U 1 beamlines to enable access to the photon beamline section between the access shafts and the experimental hall while continuing electron beam operation. The main purpose of the safety shutter is to block the x-ray radiation, including remaining *Bremsstrahlung* radiation propagating down the beamline. Usage of the safety shutter requires to fully open the undulator gap, as these shutters cannot be designed to withstand the average and peak power load of undulator or SASE operation. A second shutter of this type will be implemented in front of the experiments hall to enable access to the downstream experimental areas. The design of the safety shutter will include rigid as well as movable absorber elements to block the *Bremsstrahlung* at 17.5 GeV.

6.2.3.2 Slit system

In front of the first two mirrors a slit system will be implemented. The slit system will limit the power load on the mirrors by reducing the transmitted beam size and therefore, significantly reducing the transmission of unwanted spontaneous undulator emission. In Figure 6.2.8 the design of the high-power slit system designed for the PETRA-III facility is shown **[6-33]**. This design fulfils the requirements for an XFEL beamline and could be implemented with minor modifications.

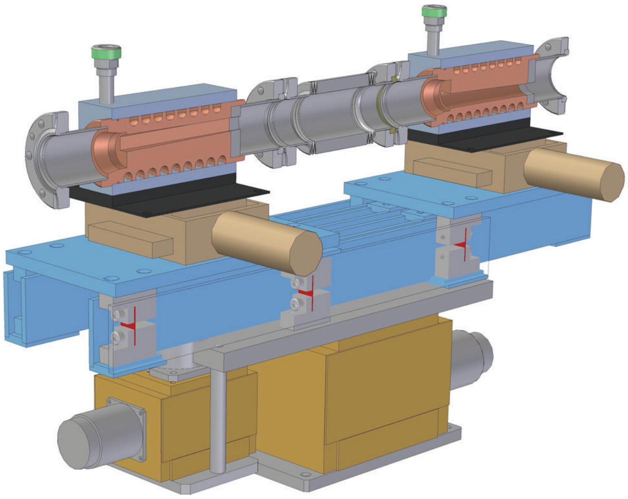

Figure 6.2.8 *High-power slit system designed for PETRA-III.*

6.2.3.3 Gas absorber system

At the FLASH facility, a gas absorber system based on single photon absorption in a gas, is in routine operation to attenuate the photon pulse intensity on user demand. Among other applications, the reduction of the photon intensity without changing the focusing geometry was found very useful in experiments investigating strong field phenomena. The absorber system consists mainly of a 15 m long gas-filled pipe, together with two differential pumping units (see Figure 6.2.9) to guarantee the ultra-high vacuum in the rest of the beamline. A similar set-up is foreseen to be implemented in all beamlines at the XFEL. In the hard x-ray regime the gas pipe needs to be elongated to 100 m and the maximum pressure will be in the mbar-range due to the reduced atomic cross-sections. As an instructive example, the transmission at 0.1 nm for four different pressures of Xenon is given in Figure 6.2.10(a.). It can be seen that in the range from 0.1-0.4 nm, an attenuation of 10^4 is always feasible by adjusting the pressure. The same holds for the soft x-ray regime (0.4-6 nm), where an absorption length of 30 m is sufficient, see Figure 6.2.10(b.). To reduce the consumption of Xenon gas, a recirculation scheme is envisaged.

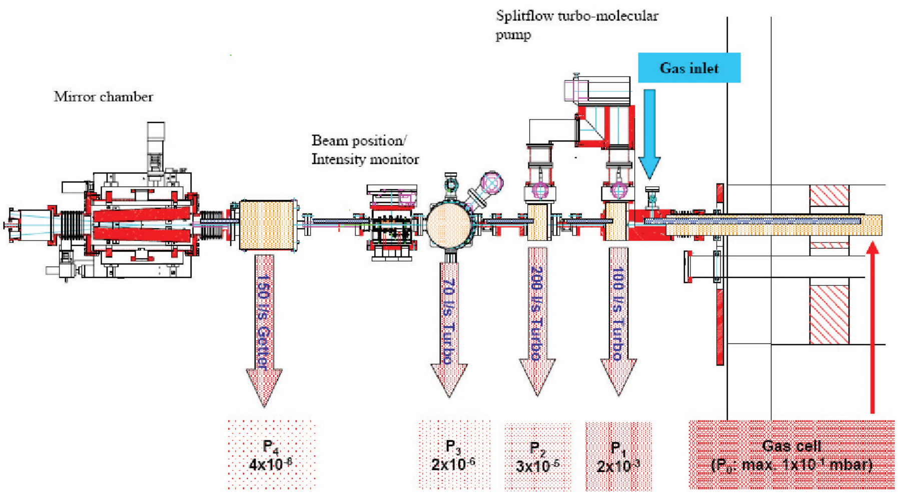

Figure 6.2.9 *Differential pumping unit used at FLASH for the transition from the gas-filled attenuator pipe to the ultra-high vacuum beam tube.*

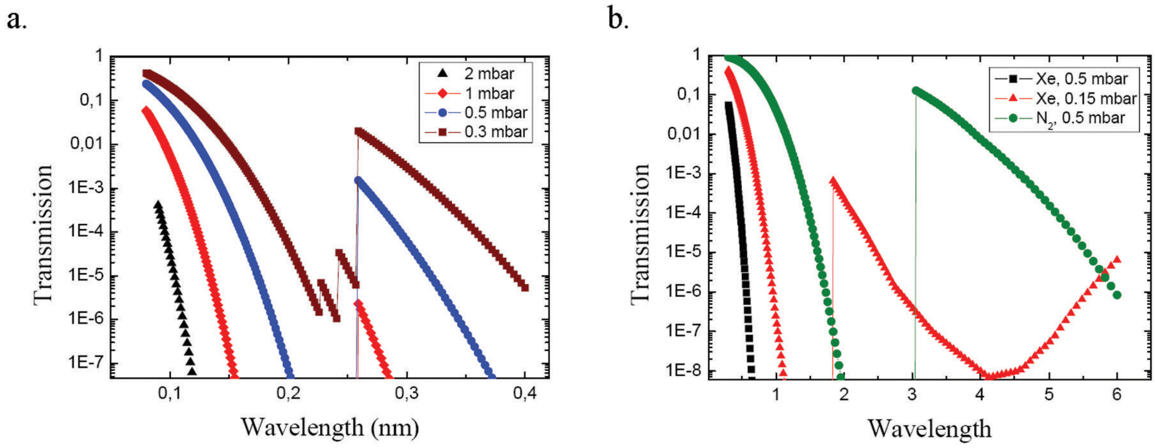

Figure 6.2.10 *Transmission of x-ray radiation through a gas-filled attenuator section. In (a.) results for the case of SASE 1 and SASE 2 and a 100 m long gas-absorber filled with Xenon gas at 4 pressures are shown. (b.) shows results for SASE 3 with a 30 m long attenuator at various pressures of Xenon and Nitrogen (N_2).*

6.2.3.4 Fast shutter for pulse selection

During the first experiments at the FLASH facility, a significant fraction of users needed to irradiate samples with only one FEL photon pulse at the repetition rate of the bunch train or even below that. Examples are experiments where the sample is significantly modified during the photon-sample interaction, but no continuous renewal of the sample is available, e.g. in solid target experiments. At FLASH this demand is met by a single shot shutter, see Figure 6.2.11. The XFEL will provide a bunch distribution scheme that allows sending only the bunch pattern requested by an experiment into one of the electron beamlines. However, if operating more than one experiment at this electron beamline, a fast shutter is considered useful for the selection of x-ray pulse trains to be accepted by a specific instrument. The operation of the user instruments, therefore, could significantly benefit from such a device. The XFEL version of such a fast shutter needs to operate at the pulse train repetition rate of 10 Hz with possibility for even faster repetition rates. Furthermore, the shutter will be designed to withstand full bunch trains.

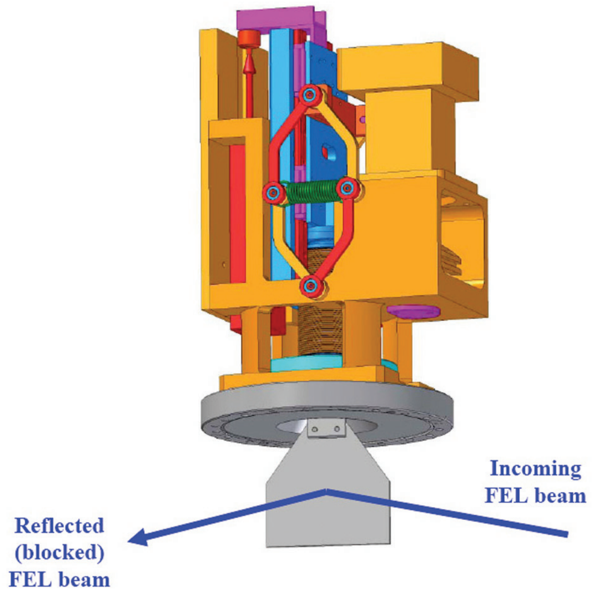

Figure 6.2.11 *Fast shutter at the FLASH facility.*

6.2.3.5 Beamline vacuum system

An average pressure of 10^{-7} mbar is targeted. This pressure range is determined by the acceptable absorption of the photon beam and by the operation and lifetime of ion-pumps. Differential pumping for a windowless operation of the beamline is mandatory. A vacuum system free of dust particles is necessary to avoid destructive effects on the coherence at the surfaces of mirrors and monochromators. This means all cleaning and mounting of devices has to be done in a class 100 clean room environment. The design and assembly of the beamline instruments have to take this requirement into account. To avoid contamination of surfaces, a Hydrocarbon-free vacuum (partial pressures of Hydrocarbons < 10^{-3} of the total pressure) is needed.

The layout of the vacuum structure distinguishes between SASE beamlines, which are longer and carry beams with high peak powers, and beamlines for spontaneous radiation. Typically, five vacuum sections are proposed, separated by valves: The first valve close to the particle beam should be an all-metal valve, while for the others, Viton sealed valves are preferred. This is because of simplicity, the particle-free operation, and the possible short closing times of these devices. The pressure demand for mirror and monochromator chambers will be in the 10^{-9} mbar range to minimise contamination. A beam pipe diameter of 100 mm is chosen to reduce the number of pumps along the beamline. Ion pumps with nominal pumping speed of 75 l/s installed at a distance of 30 m will result in an average pressure of $<10^{-7}$ mbar. The pressure difference at mirror and monochromator chambers will result from the differential pumping.

The first valve in the beamline (linac valve) has no protection against synchrotron radiation. This means it can only be closed when the related undulator is not radiating, e.g. the magnetic gap of all undulator elements is open or no electron beam is accelerated. All other section valves and the beam shutter are protected by the photon shutter. The two differential pumping stages of the absorption cell need a special operation and safety system. The accidental venting of large beamline parts with a long pumping time to restore the vacuum has to be prevented.

6.2.4 Description of the beamlines

6.2.4.1 SASE 1 – X-ray FEL radiation

This beamline is dedicated to the transport of hard x-ray radiation at photon energies near 12.4 keV. The undulator is not gap tuneable in that its length has been optimised for closed gap and photon energy of 12.4 keV at the nominal electron energy of 17.5 GeV. The SASE 1 beamline is most requested for ultrafast time-resolved diffraction experiments and for non-resonant x-ray photon correlation experiments, both operating at fixed photon energy. For diffraction on crystals, the XFEL bandwidth is too large and monochromatisation to $\Delta E/E \sim 10^{-4}$ will be required. The requirements are the same for correlation experiments, in this case to increase the longitudinal coherence length. Diffraction experiments on non-crystalline matter, single particles and bio-molecules can accept a much larger bandwidth. Therefore, these experiments do not require additional monochromatisation, and in addition, some of them, in particular those on single particles or molecules, will require the maximum achievable photon flux at the sample.

Therefore, two requirements exist and it is proposed to build the beamline with the capability to use either double-crystal or double-mirror optics, both in a fixed-exit geometry. Following these optical elements, a collimator with a 10 mm hole is required to stop *Bremsstrahlung* radiation. Moderate focusing with a demagnification near unity requires placing focusing elements near the first optical elements. Due to their high flexibility a stack of Beryllium lenses will be used here. A (compound) refractive lens has the advantage of being in-line and can be fast removed from or inserted into the beam. It can also be used for both bandwidth options, although the effect of focal length variation due to the chromaticity of the lens needs to be considered in the case of natural bandwidth ($\sim 10^{-3}$). For applications requiring the best possible preservation of wavefronts, e.g. in extreme focusing applications, no focusing will be used in the photon beam transport section and the lens is removed from the beam. In order to distribute the x-ray beam to spatially separated instruments inside the experimental hall, the photon transport is split into three lines. By means of two subsequent mirrors operating at a grazing angle of 2 mrad, a horizontal deflection angle of 8 mrad in relation to the direct beam is achieved. In this way, a horizontal separation of each of the three beams of 1.6 m at the entrance to the experimental hall can be achieved. Figure 6.2.12 shows a sketch of the photon beam transport system for the SASE 1 beamline. The figure shows the possibilitey of separating the XFEL beam to three beamlines by using mirrors to be inserted into the photon path. In Table 6.2.6 the main optical elements of the SASE 1 beamline are listed.

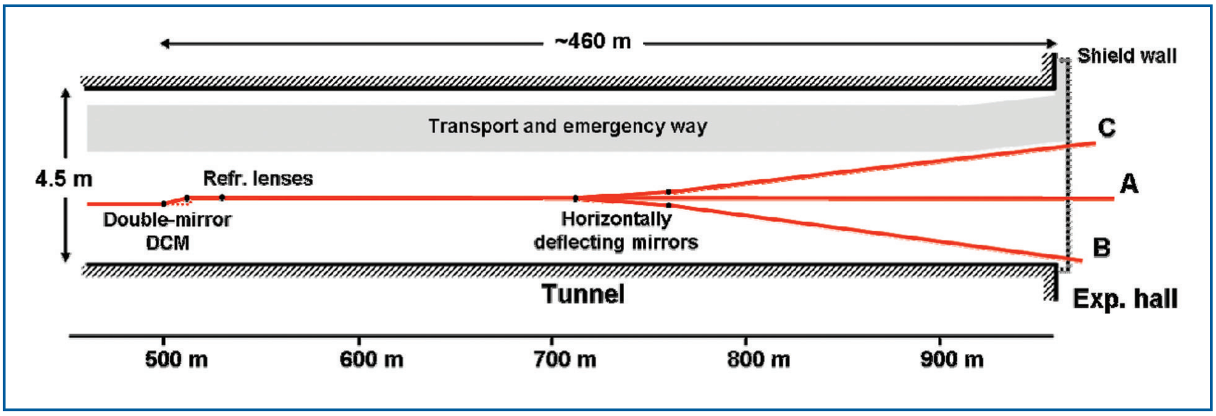

Figure 6.2.12 *Schematic layout of the SASE 1 beamline section from 500 m downstream to the end of the undulator at the experimental hall , including major optical elements.*

Name/ Line	Device	Distance [m]	Task
A1	Mirror	500	Plane mirror reflecting in horizontal geometry with a grazing angle of 2 mrad. Carbon coating reduces the surface dose for this mirror. Retraction is enabled for double-crystal monochromator operation.
A2	Mirror	512.5	Second mirror for back-reflecting beam to parallel orientation at an offset of 50 mm from the incident beam. This mirror could be built as an adaptive optics to either compensate for heat load deformation of the mirror A1 or focus the beam horizontally.
A3	DCM	515	Double-crystal monochromator to achieve the identical offset. Retraction is enabled for double-mirror operation. The monochromator allows operation at ~12 keV and for third harmonic radiation.
A	BS stop	520	Collimation against propagation of *Bremsstrahlung* radiation.
A4	Refractive lenses	530	For moderate focusing at the instruments and demagnification near unity refractive lenses will be used. They can be removed for transport of unfocused beam.
B1, C1	Mirrors	735	This is an assembly of two mirrors that can be placed alternatively in the FEL beam. They reflect, in horizontal geometry, the beam into two different directions for Lines B and C. Grazing angles are 2 mrad. In a third option, the beam passes without reflection for Line A.
B2, C2	Mirrors	785	To increase the horizontal offset a second set of mirrors is used in the two side lines. Grazing angles are 2 mrad. The location is chosen to achieve a maximum offset of 1.6 m
at			the end of the tunnel for each of the side lines with respect to the central line.
A, B, C		960	End of the tunnel and start of the experiments hall.
B		975	Instrument for diffraction experiments using side beam B.
C		980	Instrument for single particle diffraction at side beam C.
A		985	Instrument for photon correlation experiments using central beam A.

Table 6.2.6 *List of optical elements in the SASE 1 beamline. Components belong to the central line A or the side lines B and C. The longitudinal distances are given with respect to the end of the undulator.*

6.2.4.2 *SASE 2 – Tunable X-ray FEL radiation*

This beamline is dedicated to the transport of hard x-ray radiation in the photon energy range from 3 to 12 keV. The undulator is gap tunable in that its length has been optimised for a gap opening of 19 mm and photon energy of 12.4 keV at the nominal electron energy of 17.5 GeV. The SASE 2 beamline is requested for experiments carried out over a rather wide photon energy range. The interest is in specific absorption edges and resonances; one may also want to exploit the change of the absorption cross-section, e.g. in high energy density investigations. Tuning the photon energy in a small range is enabled by electron energy changing on short timescales. Monochromatisation to a bandwidth $\Delta E/E \sim 10^{-4}$ will be required in spectroscopy experiments. Also, coherent diffraction experiments, aimed at measuring large Q values, require monochromatisation of the XFEL beam in order to increase the longitudinal coherence length to the order of 1 µm. For coherent diffraction experiments the use of perfect crystals could provide the best solution to preserve the wave front properties of the XFEL beam as required for high resolution imaging (see Section 6.2.2). High energy density science experiments require the maximum achievable photon flux at the sample and usually do not need monochromatisation. Therefore, the situation resembles that of SASE 1 and a similar design of the first optics module including a double-mirror and a double-crystal monochromator is proposed. Following these optics, a collimator with a 10 mm hole is required to stop *Bremsstrahlung* radiation. To achieve moderate focusing with demagnification near unity focusing elements also need to be placed here. Refractive lenses are available for the upper part of the x-ray spectrum but will not work for photon energies <5 keV (see Section 6.2.2.4). For the photon energy range 3-5 keV, the second mirror of the double-mirror system will be replaced by a toroid. In order to distribute the x-ray beam to spatially separated instruments inside the experimental hall, the photon transport is split in to three lines. By means of two subsequent mirrors operating at a grazing angle of 2 mrad, a horizontal deflection angle of 8 mrad with respect to the direct beam is achieved for each of the side lines. In this way, a horizontal separation of the three beams by 1.6 m at the entrance to the experimental hall can be achieved. Figure 6.2.13 shows a sketch of the photon beam transport system for the SASE 2 beamline. The figure shows the possibility of distributing the XFEL beam to three beamlines by using mirrors to be inserted into the photon path. In Table 6.2.7 the main optical elements of the SASE 2 beamline are listed.

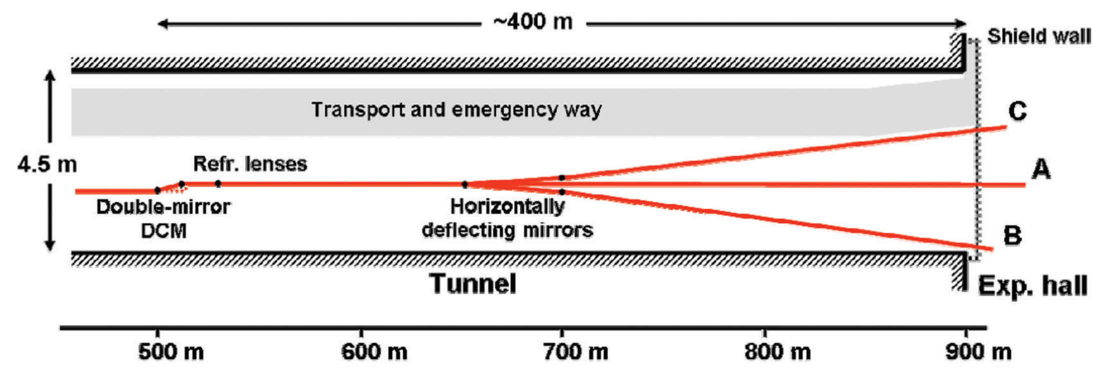

Figure 6.2.13 *Schematic layout of the SASE 2 beamline section from 500 m downstream to the end of the undulator at the experimental hall , including major optical elements.*

Name/ Line	Device	Distance [m]	Task
A1	Mirror	500	Plane mirror reflecting in horizontal geometry with a grazing angle of 2 mrad. Carbon coating reduces the surface dose for this mirror. Retraction is enabled for double-crystal monochromator operation.
A2	Mirror	512.5	Second mirror for back-reflecting beam to parallel orientation at an offset of 50 mm from the incident beam. This mirror could be build as an adaptive optics to either compensate for heat load deformation of the first mirror
A1			or focus the beam horizontally. In order to achieve focusing in both directions, a second, exchangeable mirror with toroidal shape is available.
A3	DCM	515	Double-crystal monochromator to achieve the identical offset. Retraction is enabled for double-mirror operation. The monochromator allows reflection at photon energies of 6-12 keV.
A	BS stop	520	Collimation against propagation of *Bremsstrahlung* radiation.
A4	Refractive lenses	530	For moderate focusing at the instruments and demagnification near unity refractive lenses will be used. Removable for transport of unfocused beam.
B1, C1	Mirrors	675	This is an assembly of two mirrors that can be placed alternatively in the FEL beam. They reflect, in horizontal geometry, the beam into two different directions for Lines
A			
			and C. Grazing angles are 2 mrad. In a third option, the beam passes without reflection for Line B.
B2, C2	Mirrors	725	To increase the horizontal offset a second set of mirrors is used in the two side lines. Grazing angles are 2 mrad. The location is chosen to achieve a maximum offset of 1.6 m at the end of the tunnel for each of the side lines with respect to the central line.
A, B, C		900	End of the tunnel and start of the experimental hall.
B		920	Instrument for high energy density experiments using side beam B.
C		915	Instrument for x-ray absorption using side beam C.
A		930	Instrument for coherent x-ray imaging experiments using central beam A.

Table 6.2.7 *List of optical elements in the SASE 2 beamline. Components belong to the central line A or the side lines B and C. The longitudinal distances are given with respect to the end of the undulator.*

6.2.4.3 SASE 3 – Tunable Soft X-ray FEL radiation

This beamline is dedicated to the transport of soft x-ray radiation in the photon energy range from 250 up to 3,100 eV. The extended tunability of this beamline is enabled by a combination of gap and energy tuning. For the nominal electron energy of 17.5 GeV, gap tuning provides access to a photon energy range of 775 to 3,100 eV. For a reduced electron energy of 10 GeV, the photon energy range of 250 to 1,000 eV is provided. Several of the scientific experiments proposed for this photon energy range have requested a monochromatisation better than the linewidth of the FEL radiation. A resolution of the order $\Delta E/E \sim 10^{-4}$ over the entire photon energy range fulfils most of the experiment requirements. To cope with the high power levels of the FEL radiation, all elements of the monochromator need to operate in very grazing geometry. The whole system, therefore, becomes rather long and can neither simply be integrated into the experimental station nor switched in and out of the beam. In Section 6.2.2.3 a plane grating monochromator designed for the specific radiation properties of the SASE 3 beamlines is presented. Its optical layout has been shown in Figure 6.2.6.

It is, therefore, proposed that the photon beam transport of the SASE 3 beamline includes two lines. Line A uses only mirrors to preserve the high photon flux. Some of these mirrors are curved to fulfil the requirements of the experiments with respect to focal spot sizes at the instruments. Line B includes a PGM, plane-grating monochromator using two or more gratings to cover the entire photon energy range. Figure 6.2.14 shows a sketch of the photon beam transport system for the SASE 3 beamline. The figure shows the possibility of distributing the two beams to two beamlines each by using mirrors to be inserted into the photon path. For the case of SASE 3, it is assumed that grazing angles of 10 mrad can be used. In Table 6.2.8 the main optical elements of the SASE 3 beamline are listed.

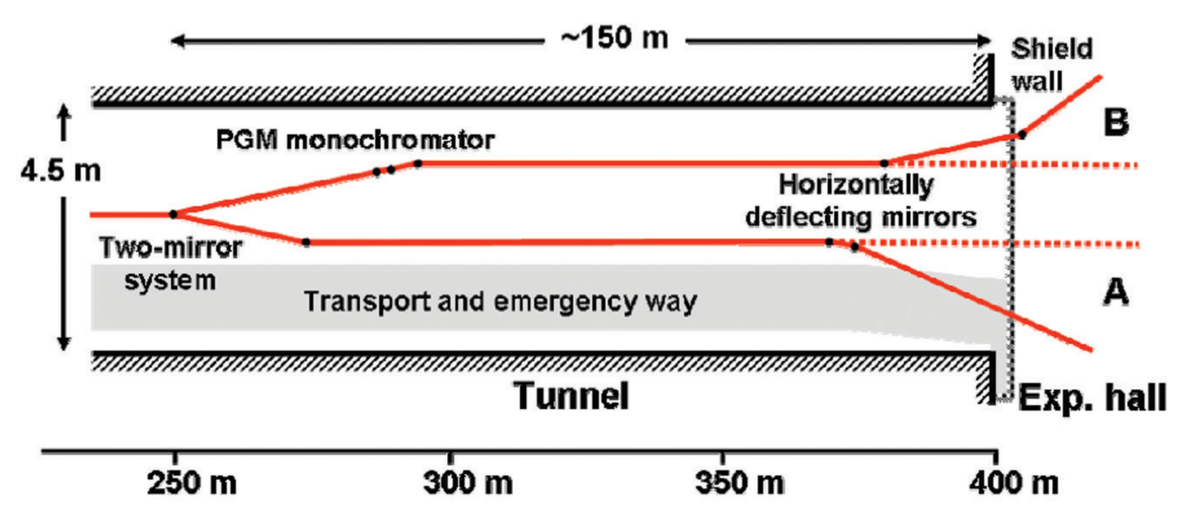

Figure 6.2.14 *Schematic layout of the SASE 3 beamline including major optical elements. The longitudinal scale has been increased by a factor of two compared to Figures 6.2.12 and 6.2.13.*

Name/ Line	Device	Distance [m]	Task
A1, B1	Mirror	250	Assembly of two mirrors to be placed alternatively in the FEL beam. They reflect the beam in horizontal geometry into the Lines A and B. Different mirrors will be used for this task: A1. plane mirror reflects towards the second mirror. B1. cylindrical mirror in order to adapt vertical divergence to the monochromator needs.
A2	Mirror	275	Back-reflecting beam to parallel orientation. This mirror would possibly be built as an adaptive optics to both, compensate heat load deformation of the mirror A1 or to focus the beam horizontally. In order to achieve focusing in both directions, this mirror needs to have toroidal shape.
A, B	BS stop	280	Collimation against propagation of *Bremsstrahlung* radiation.
B2	Mirror	290	A vertically reflecting plane mirror in front of the grating allows for a variable deflection angle so that the angles of incidence and diffraction at the grating can be set independently.
B	Grating	290	At least two gratings are required for the photon energy range 500-3100 eV. The grating operates in vertical reflection geometry.
B3	Mirror	295	Horizontally reflecting, toroidal mirror to focus virtual image onto exit slit.
B	Exit slit	345	Exit slit of the monochromator.
A3	Mirror	370	Distribution mirror that can be removed from the beam. Using a grazing angle of 10 mrad this mirror could achieve a displacement of the beam of 1,000 mm in the experimental hall.
A4	Mirror	375	This second mirror would generate an offset of 1,900 mm. Using focusing one aims for a demagnification near 1.
B4	Mirror	380	Toroidal mirror to refocus the exit slit at the sample position in a 1:1 geometry.
B5	Mirror	405	Flat mirror to achieve horizontal offset from straight beam. If placing here the toroidal mirror refocusing the exit slit increases the demagnification of ~6. In this case a flat mirror needs to be placed as mirror B4 in this line.
A, B		400	End of the tunnel and start of the experimental hall.
B		410, 425	Instruments for experiments using high spectral resolution.
A		420, 435	Instruments for experiments using high flux.

Table 6.2.8 *List of optical elements in the SASE 3 beamline. Components belong to line A, containing only mirrors, or to the monochromator line B. The longitudinal distances are given with respect to the end of the undulator.*

6.2.4.4 U 1 – Tunable and high energy x-ray synchrotron radiation

This beamline is very similar to U2, described next, with due consideration of the different distance to the experiment hall.

6.2.4.5 U 2 – Tunable and high energy x-ray synchrotron radiation

This beamline is dedicated to the transport of spontaneously emitted synchrotron radiation. The undulator can be tuned in the fundamental from ~20 up to 90 keV. Compared to the XFEL radiation, the intensity is reduced by ~10^3 in number of photons per pulse. This will ease all power considerations for x-ray optics, so that they need no further discussion. However, due to the small source size and the large distances, the spontaneous radiation is highly coherent. The coherent flux and the ultra-short duration of 200 fs need to be preserved by the beamline optics. Since the spontaneous radiation also has a larger angular opening than FEL radiation, the angular acceptance of the beamline, or the collimation of the x-ray beam, determines the intensity of the x-ray pulses. In Section 5.3 the intensity and spectral properties of spontaneous radiation are given for an angular aperture of 9×9 μrad^2. The scientific instruments to be located at this beamline will, in particular, make use of the high coherent flux at high photon energies and of the ultra-short pulse duration in combination with an increased bandwidth of $\Delta E/E \sim 10^{-2}$. Finally, for the x-ray optics R&D programme, this beamline will provide the highly brilliant radiation required to investigate particular aspects of optical elements, e.g. figure and roughness performance or temporal response of crystal monochromators.

These experimental requirements can be divided in to two groups: The first group needs perfect crystal optics to transport the coherent radiation to the corresponding instrument. The limitation in bandwidth will not be a disadvantage for these experiments, since the monochromatisation improves the longitudinal coherence. The second group are experiments requiring large bandwidth for diffraction and will require mirror optics to collect maximum flux and maintain the large bandwidth. For the relatively high photon energies, the grazing angles of mirrors, even if coated with high Z materials, are very small. For the reduced intensity at this beamline also multilayers optics is of interest, providing larger deflection angles. Similarly to the FEL beamlines, a *Bremsstrahlung* beam stop is required, and an arrangement similar to the one proposed for SASE 1 and SASE 2 is adopted. Using a double-mirror double-crystal arrangement in fixed-exit geometry allows placing a collimator for *Bremsstrahlung* radiation. Separation of the two lines for the two scientific instruments is achieved by a multilayer crystal followed by a refractive lens. The diffraction instrument is expected to operate at a fixed photon energy between 15 and 25 keV. The deflection angle and specific multilayer parameters, therefore, can be determined according to technical feasibility. Figure 6.2.15 shows a sketch of the photon beam transport system for the U2 beamline. For the case of U2 it is assumed that grazing angles of 2 mrad can be used. In Table 6.2.9 the main optical elements of the U2 beamline are listed.

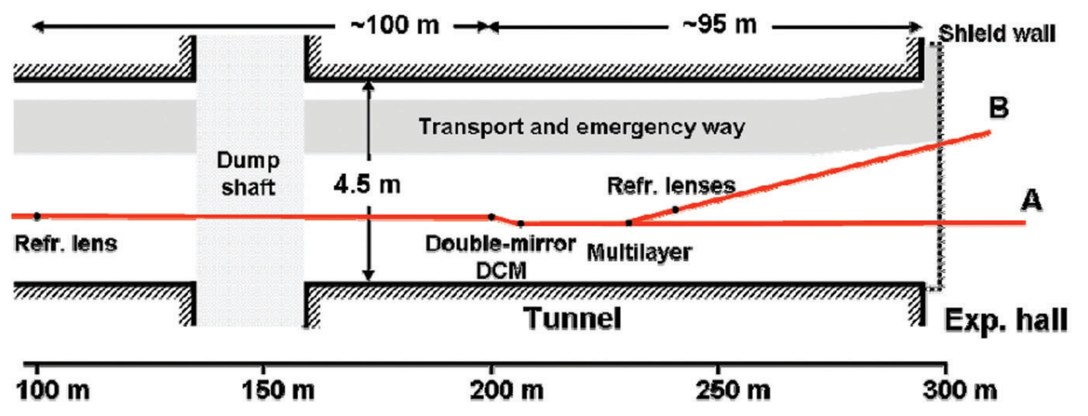

Figure 6.2.15 *Schematic layout of the U2 beamline including major optical elements. The location of the refractive lens for beam collimation is also shown.*

Name/ Line	Device	Distance [m]	Task
A1	Refractive lens	100	Collimation of the radiation cone to maintain high flux and large bandwidth. Retractable for transport of unfocused beam.
A1	Mirror	200	Plane mirror reflecting in horizontal geometry with a grazing angle of 2 mrad. High Z materials are required to achieve high reflectivity. Retraction is enabled for double-crystal monochromator operation.
A2	Mirror	212.5	Second mirror for back-reflecting beam to parallel orientation at an offset of 50 mm from the incident beam. This mirror could be built as an adaptive optics to either compensate heat load deformation of the first mirror A1 or focus the beam horizontally.
A3	DCM	215	Double-crystal monochromator to achieve the identical offset. Retraction is enabled for double-mirror operation. The monochromator allows reflection at photon energies of 15-100 keV using several crystals/reflections.
A	BS stop	220	Collimation against propagation of *Bremsstrahlung* radiation.
B1	Multilayer	230	Deflection of the beam towards Line B for diffraction studies. Retractable for straight transport in Line A.
B2	Refractive lenses	240	Moderate focusing at the instrument in a 4:1 focusing geometry. Removable for transport of unfocused beam.
A,B		295	End of the tunnel and start of experimental hall.
A A.		305	Instrument for x-ray optics development using central beam
A		315	Instrument for coherent x-ray imaging experiments using central beam A.
B		310	Instrument for large bandwidth diffraction using side beam B.

Table 6.2.9 *List of optical elements in the U2 beamline. Components belong to the central line A or the side line B. The longitudinal distances are relative to the end of the undulator.*

6.3 Photon beam diagnostics

Besides the photon-beam-based alignment of the undulators described in Section 5.5, photon beam diagnostics will be an essential tool for the commissioning and operation of the XFEL photon beamlines. Since photon diagnostics has successfully been used in the VUV wavelength range at the TESLA Test Facility (TTF) **[6-34]** and at FLASH **[6-35, 6-36]**, to a large extent the same concepts will be adapted for the x-ray regime. Ideal photon diagnostics techniques for the XFEL cover the full dynamic range of about seven orders of magnitude from spontaneous emission to SASE XFEL radiation in saturation, are suitable for single-pulse measurements (response time < minimum bunch spacing = 200ns), exhibit low degradation under radiation exposure in the x-ray regime, and must be ultra-high vacuum compatible. In the following sections two basic types of photon diagnostics will be described:

- diagnostics for the general characterisation and optimisation of SASE XFEL process and photon beam transport up to the scientific instruments;
- online (that is pulse-by-pulse) monitoring of crucial beam parameters like pulse intensity and pointing stability for user experiments and machine feedback.

6.3.1 Characterisation of beam properties

This section describes invasive diagnostics devices which cannot be used for online monitoring, but yield important information for the commissioning of the machine and photon beamlines. These devices will be located either in the primary photon beam diagnostic section (see Section 6.2.1) or will be integrated in the scientific instruments inside the experimental hall.

6.3.1.1 Intensity

Different kind of detectors such as gas-monitor-detector (see Section 6.3.2), micro-channel-plate (MCP)-based detector **[6-37]**, pin diode and calorimeter will be used to measure the intensity from spontaneous undulator emission when trying to achieve SASE gain or optimising saturation. Since the latter two detectors work within a limited dynamic range and not in parallel with user experiments, they will only be used for cross-calibration and during commissioning of the XFEL sources. MCP-based detectors cover a dynamical range of seven orders of magnitude and are in routine operation at the FLASH facility for optimisation of the FEL radiation. Figure 6.3.1 shows a schematic drawing of the device. The detector uses a thin Gold wire (50 µm diameter) or alternatively a Gold mesh with 65% transmission to reflect part of the FEL beam onto a calibrated MCP. Keeping the MCP in the low gain regime, one can determine the SASE gain with respect to spontaneous emission knowing the applied MCP voltage. By using an optimised geometry with small reflection angles and materials with higher reflectivity in the x-ray regime, one will be able to extend the capabilities of the MCP-based detector from the VUV wavelength range to x-rays. However, since the mesh or wire produces unwanted diffraction resulting in an inhomogeneous intensity distribution at the sample position, this device is not suitable for online monitoring of the intensity while operating user experiments.

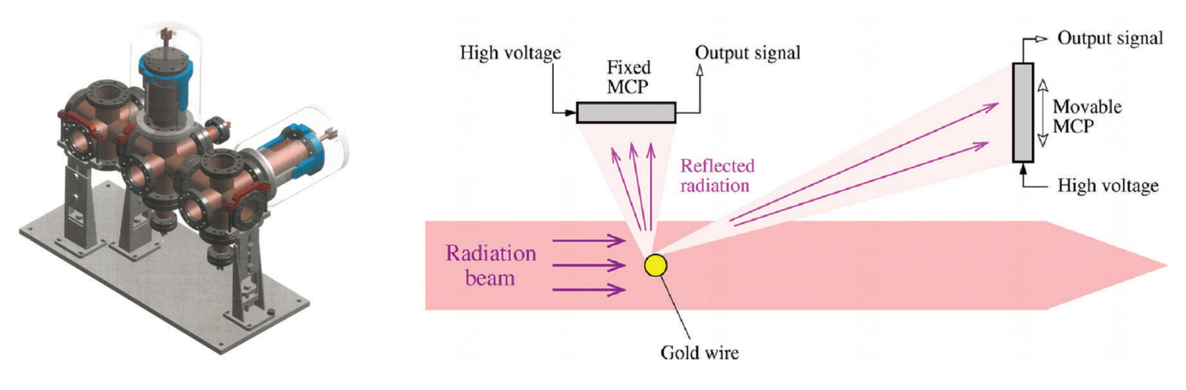

Figure 6.3.1 *Scheme of the MCP-based detector which is routinely operating at FLASH.*

6.3.1.3 Spectral characterisation

Spectral characterisation of the photon beam provides essential information for the optimisation of the SASE process and user experiments. Spectral beam properties can be used to cross-check the mean electron energy and determine the bandwidth of the FEL beam as well as the content of higher harmonics. Furthermore, the spectral distribution yields the number of modes in the pulse and can be used to estimate the pulse length **[6-38]**. Two techniques to determine the spectral distribution are proposed; an analyser based on a bent crystal scheme **[6-11]** will be able to disperse the collimated FEL beam and project the spectral distribution onto a linear array detector. This scheme has to be adapted to the bandwidth and towards single-shot use. Since this detection scheme is not transparent, we additionally propose a new non-invasive method based on photoelectron spectroscopy **[6-39]**.

6.3.1.4 Wave front measurement

The quality of the wave front of the coherent XFEL beam has a direct impact on the performance of several kinds of experiments. For example, a distorted wave front will lead to a loss in resolution for phase contrast imaging experiments or a degradation of the focusing and thereby, a loss in the available intensity for high field experiments. As discussed in Section 6.2.2, the requirements on slope error of optical elements for XFEL radiation are very demanding. The shape and slope error budgets of the reflecting elements surfaces required to preserve the wave front over a size of several millimetres are beyond what can be bought today. In fact, the metrology tools available are one of the most severe limitations in the mirror fabrication process. Moreover, even a perfect mirror or monochromator surface may be distorted in the beam either by thermal load or by the mounting itself. This is why it is necessary to develop techniques to measure the distortions of x-ray wave fronts in-situ. A precise knowledge of the wave fronts could then be a basis for learning about the properties of the source itself, to test and improve the optical components, and may even serve to compensate for errors in the illuminating x-ray wave.

A prototype Shack-Hartmann wave front sensor has already been successfully used to characterise the beam wave front and the focusing of beamline BL2 at FLASH **[6-40]**. Another approach to perform in-situ metrology in the hard x-ray regime has been developed at the Paul Scherrer Institute in Switzerland. The x-ray interferometer consists of a phase grating as a beam splitter and an absorption grating as a transmission mask for the detector. The device is able to measure wave front shape gradients corresponding to radii of curvature as large as several dozens of metres, with a lateral resolution of a few microns. This allows detection of wave front distortions of approximately 10^{-12} m or $\lambda/100$. The device was used with 12.4 keV x-rays to measure the slope error and height profile of multilayer mirrors **[6-41]** and Beryllium refractive lenses **[6-42]**. A similar setup could be used at the XFEL to investigate the quality of beamline optics under the extreme conditions of this machine.

6.3.1.4 Focus characterisation

A key point for the understanding and theoretical description of non-linear processes in the focused high intensity FEL beam is their dependence on irradiance. Therefore, among other quantities like pulse energy and duration, the determination of the spot size becomes essential. Conventional methods like knife-edge **[6-43]** and fluorescent screen technique **[6-44 – 6-47]** are limited to spatial resolution in the order of 1 to 2 µm and furthermore, will not withstand the irradiance level of the focused XFEL beam. Therefore, for the focus characterisation of the different XFEL beamlines, we intend to employ two techniques: The first based on wave front measurements (see above) and the second a novel method using atomic photoionisation **[6-48]**. Both methods have been successfully applied to determine the spot size of the microfocus beamline BL2 at FLASH. The latter one is based on a saturation effect upon photoionisation of rare gases and manifests itself by a sub-linear increase of the ion yield with increasing photon number per pulse (Figure 6.3.2). The effect is due to a considerable reduction of target atoms within the interaction zone by ionisation with single photon pulse and becomes stronger with decreasing beam cross-section. Since the cross-sections in the 10 keV range are many orders of magnitude lower compared to the VUV, this method will be of particular interest for spot sizes of 1 µm and below.

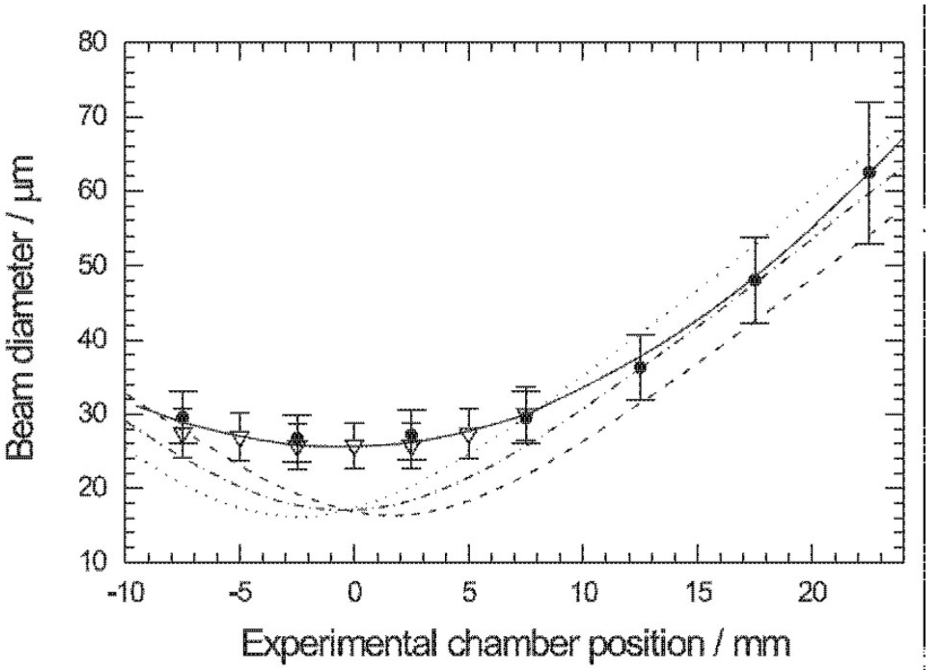

Figure 6.3.2 *Photon beam diameter measured at different positions around the focus position of BL2 at FLASH using a novel technique based on atomic photoionisation (taken from* **[6-48]***). The solid line represents a polynomial fit curve. The broken lines display ray-tracing simulations for horizontal (dashed line) and vertical direction (dotted line) and the mean of both (dashed-dotted line).*

6.3.2 Online diagnostics

Most user experiments need online information about important beam parameters, such as intensity and timing. This requires the use of diagnostic tools which operate in parallel and in a non-destructive way. Furthermore, due to the SASE-specific shot-to-shot fluctuations, it is mandatory to use pulse-resolved diagnostics. Since all detection schemes described in the following sections are based on the ionisation of gas, they will be placed in the differential pumping units in the gas attenuator section (see Section 6.2.3.3) to allow windowless operation at the required pressure level.

6.3.2.1 Online intensity monitors

Nearly all experiments require a determination of the photon flux, respectively the energy content in the radiation pulse. Thus, online monitoring of the pulse energy is mandatory for free-electron lasers. At FLASH a gas-monitor-detector (GMD) is in routine operation, measuring the photon flux of the highly intense and strongly-pulsed VUV radiation in absolute terms **[6-49, 6-50]** . The detector is based on the atomic photoionisation of a rare gas or Nitrogen at low particle density in the range of 10^{11} cm^{-3} which is about five orders lower than for classical ionisation chambers. The advantages are obvious: the detector is indestructible and almost transparent. Thus, the GMD can be used as a permanently operating device. Figure 6.3.3 shows visualisation of the pulse energy measurement over a sequence of pulses performed at FLASH at a wavelength of 32 nm.

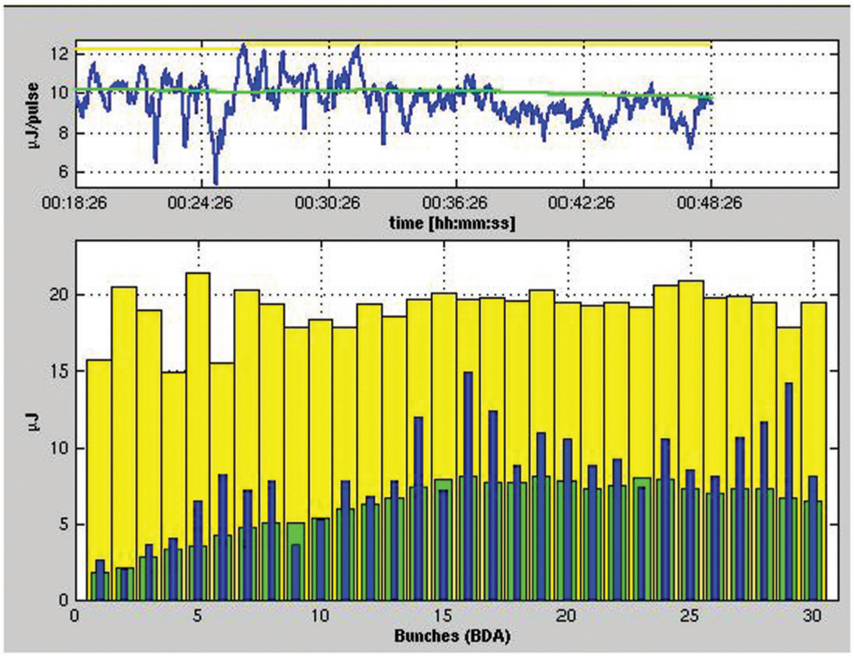

Figure 6.3.3 *Diagnostic panel in the control system of FLASH showing the yield of the gas-monitor detector. Top: Averaged ion signal. Bottom: Pulse-resolved electron signal for 30 FEL pulses at 1MHz repetition rate within one pulse train.*

Since the low photoionisation cross-sections in the x-ray regime are challenging for such a detector scheme, a prototype system for femtosecond x-ray pulses has been developed in close cooperation between DESY and the Physikalisch-Technische Bundesanstalt (PTB) in Berlin. After design and construction, the prototype has been successfully characterised and calibrated in the PTB laboratory at the electron storage ring BESSY II in Berlin **[6-51]**. In collaboration with the LCLS, first tests measurements **[6-52]** with femtosecond x-ray pulses at a photon energy of 9.4 keV have been performed at the Sub-Picosecond Pulse Source (SPPS) in Stanford.

A scheme of the XGMD and the responsivity as a function of photon energy is shown in Figure 6.3.4. Photoions are extracted by an electric field and, in contrast to former GMDs, detected by an amplifying open electron multiplier with a sensitive area of 2×2 cm^2 and a maximum gain in the order of 10^6. The system is optimised and tested for absolute ion collection/detection efficiency and linearity for up to 10^6 ions per pulse. For reliable operation of the multiplier, the target gas pressure measured by use of a calibrated spinning rotor vacuum gauge has to be below 10^{-1} Pa. Xenon is chosen as the target gas due to its comparably high photoionisation cross-section in the x-ray regime **[6-6]**. By applying an additional electric field distribution along the photon beam by means of an aperture system, the effective length of interaction volume can be extended to about 20 cm. The aim of the design is to detect 10 to 100 ions per pulse amplified to a pulse charge of about 10 pC and will allow for pulse-resolved measurements for x-ray pulses exceeding 10^7 photons.

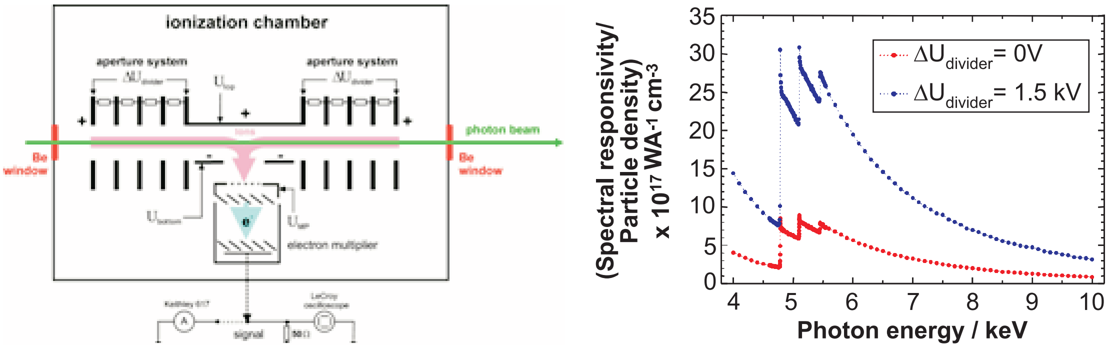

Figure 6.3.4 *Left: Schematics of the XGMD. Details are given in* **[6-52]**. *Right: Spectral responsivity of the XGMD normalised to the xenon particle density with (blue) and without (red) additional ion collection along the photon beam.*

The X-GMD based on the photoionisation of Xenon atoms is a reliable tool for the quantitative detection of femtosecond x-ray pulses with more than 10^7 (and up to 10^{15}) photons per pulse. Its time resolution (well below 100 ns) is dominated by the ion time-of-flight distribution of differently charged ionic fragments. The measurement uncertainties in absolute terms might be improved from currently 15% to 5%. Pulse-to-pulse instabilities are expected to be dominated by photoion signal statistics and are less than 1% for pulses of more than 10^{10} photons.

6.3.2.2 Time domain properties

An important target in the characterisation of the FEL radiation properties is the direct measurement of the x-ray pulse duration. Based on theoretical considerations the pulse length can be estimated by measuring the spectral distribution and the statistics of the pulse energies **[6-38]**. However, definitive measurements of the pulse length in the time domain are needed to prove the theoretical concepts. The proposed measurement methods are based on cross-correlation between optical laser and FEL pulses. To avoid systematic errors due to the jitter between laser and FEL, correlation experiments have to be designed in a way to deliver the pulse duration within a single shot. Experiments performed at SPPS have shown single-shot cross-correlation measurements using ultra-fast non-thermal melting of crystalline surfaces allow measuring pulse durations of the order 100 fs and relative timing of the two pulses **[6-54]**. Since the set-up is not transparent and distorts the x-ray pulse, it can not be used as an online diagnostic.

Two other single-shot laser/x-ray cross-correlation methods are currently being investigated to provide the same information without destroying the beam. Experimental validation in the x-ray regime is still missing. The first one uses the spectral broadening of photo-electrons, ionised by x-rays in the field of a strong laser of 800 nm wavelength **[6-55]**. The use of the extremely rapid photo-effect guarantees a temporal resolution of better than 1 fs. By realising different delays at different locations, temporal information is projected onto a spatial coordinate; thus, with an imaging electron spectrometer an arbitrary delay can be measured on a shot-to-shot basis. By evaluating the signal width on the detector the pulse duration can be determined as well. An instrument of this type has been installed at FLASH and has demonstrated the feasibility of the concept. An extension to the higher photon energies of the XFEL is straightforward because the correlation mechanism does not depend on specific atomic resonances but works with any photon energy exceeding the ionisation energy of an atomic shell. As the spectral broadening scales with the electron momentum, the cross-correlation becomes more efficient at higher photon energies. Figure 6.3.5 shows that the width of the spectral broadening is distinctively larger compared to the line width of the FEL and thus, easily detectable. Consequently, a laser intensity of 10^{12} W/cm^2, as currently used at FLASH, will suffice for the temporal characterisation of the XFEL pulses.

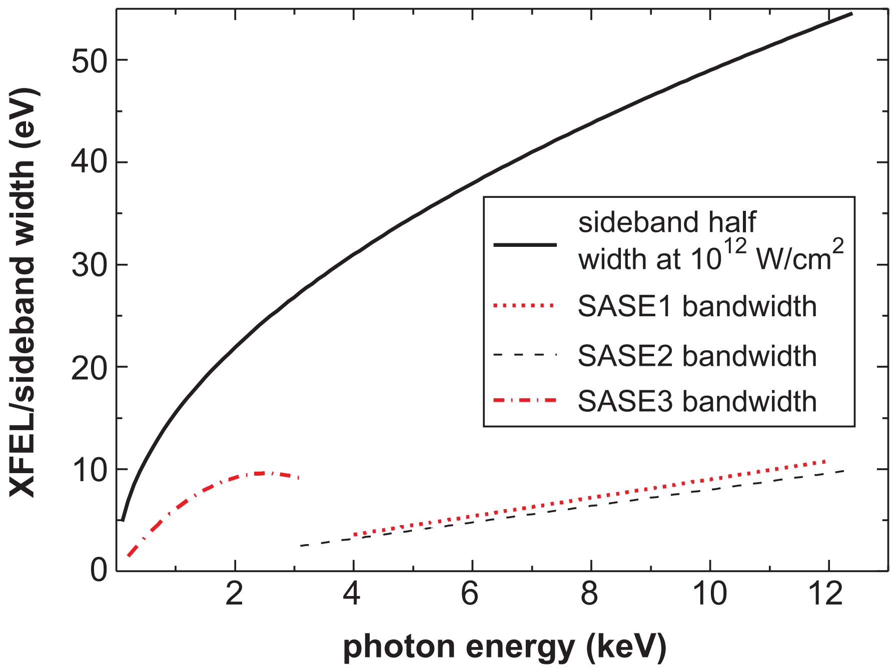

Figure 6.3.5 *Calculated spectral sideband half-width at 10^{12} W/cm^2 laser intensity in comparison with expected bandwidths of various XFEL branches.*

The second method measures an Auger line by detecting the Auger electrons by a time-of-flight (TOF) detector. An additional dressing field provided by a laser pulse will lead to the generation of sideband features due to *free-free transitions* (stimulated inverse *Bremsstrahlung*). The (first) sideband will be separated from the main Auger line by $E_L=h\omega=1.6$ eV at a laser central wavelength of $\lambda=780$ nm (Ti:Sa). The use of an Auger line is ideal as the features of the line are independent from the spectral properties of the exciting x-ray pulse, whereas a photoelectron line would mimic the broad spectrum of the x-ray pulse. The $KL_{23}L_3$ line in Argon, for example, has a width of ~1 eV at around ~800 eV. The temporal distribution of the Auger electrons carries the information about the duration of the x-ray pulse convoluted with the Auger decay time (which is known from literature to be around 1 fs so that it is significantly shorter than the x-ray pulse duration).

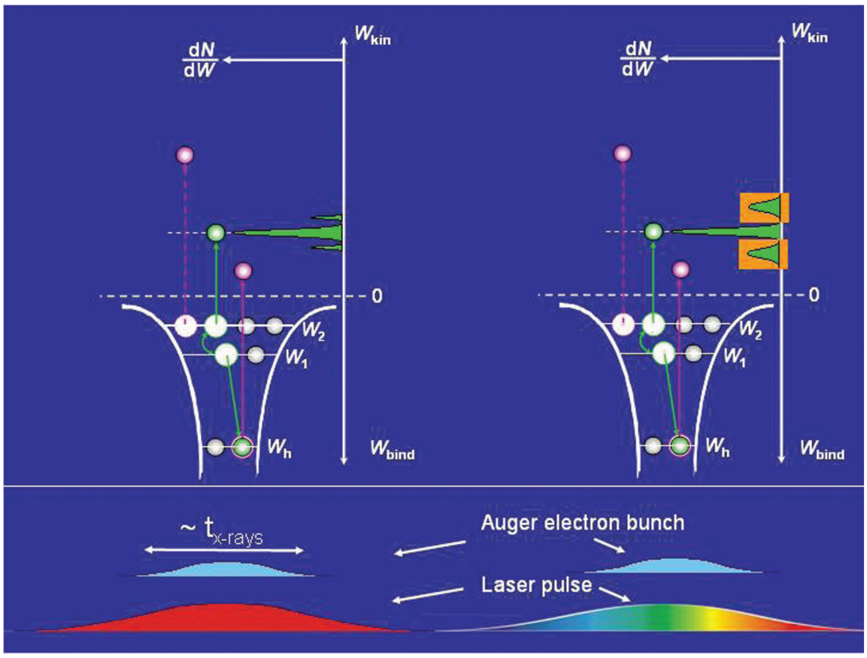

Figure 6.3.6 *Schematics of producing sidebands of Auger electron lines produced by the dressing field of a laser pulse with and without chirp, respectively.*

The idea is that the laser pulse providing the dressing field carries a significant linear chirp **[6-56]**. As different temporal portions of the Auger electron bunch interfere with different portions of the laser pulse, they will 'feel' different frequencies ω resulting in different energy shifts (EL). This leads to a broadening of the sideband which – in the case of a chirp-free electric field – would mimic the main band (see Figure 6.2.6). Given a linear chirp of 1 eV (λ=500-1,000 nm) in a laser pulse with $\Delta\tau$ = 300 fs this would lead to a 0.25 eV broadening of the Auger-sideband line for an x-ray pulse duration of 80 fs, which is detectable. Thus, the method can also provide the pulse duration on the 100 fs level as well as the jitter between the optical laser and the XFEL.

6.3.2.3 Beam position monitor

The spatial and angular stability of the XFEL radiation will be important for undulator alignment (see Section 5.5) as well as for photon beam transport to user end stations. In addition, the operation of the machine feedback system could be enhanced by the incorporation of x-ray beam position monitors (XBPM) along with the e-beam position monitors. Blade type XBPMs are current state-of-the-art for third generation synchrotron facilities and *white* beam. Blade XBPMs based on photoelectron emission from the blade material are capable to withstand the high power of undulator radiation. Since the information of the beam position is obtained from the halo of the undulator radiation, these detectors cannot be used without affecting the photon beam. Instead, XBPMs based on the detection of electrons/ions generated by the photon beam in the residual gas volume, are considered the best candidates for the XFEL. Residual gas XBPM (RGXBPM) will have no solid elements intersecting the beam. This indirect detection scheme yields a wide dynamic range and will directly detect the centre of gravity of the photon beam. Residual gas beam profile monitors were first developed to provide beam profile measurements at charged particle accelerators **[6-57]**.

An RGXBPM prototype (see Figure 6.3.7) has been developed and tested **[6-58]**. It consists of an ion chamber in which ions or electrons drift in an homogenous electrical field towards an MCP, which produces an image of the profile on a phosphor screen. This image is transferred by a fibre optic onto a directly coupled CCD camera. The prototype of the RGXBPM has been tested at FLASH and at the DORIS-III beamline BW3 to show the feasibility of the concept. In order to comply with the requirements at the XFEL, the resolution of the device has to be improved by one order of magnitude. Ongoing R&D efforts concentrate on the optimisation of the electrical field distribution inside the detector. At the XFEL, two position monitors will be installed in the differential pumping unit at both ends of the gas attenuator. With a distance of 100 m between the monitors, a spatial and angular resolution of 10 μm and 0.1 μrad, respectively, can be expected.

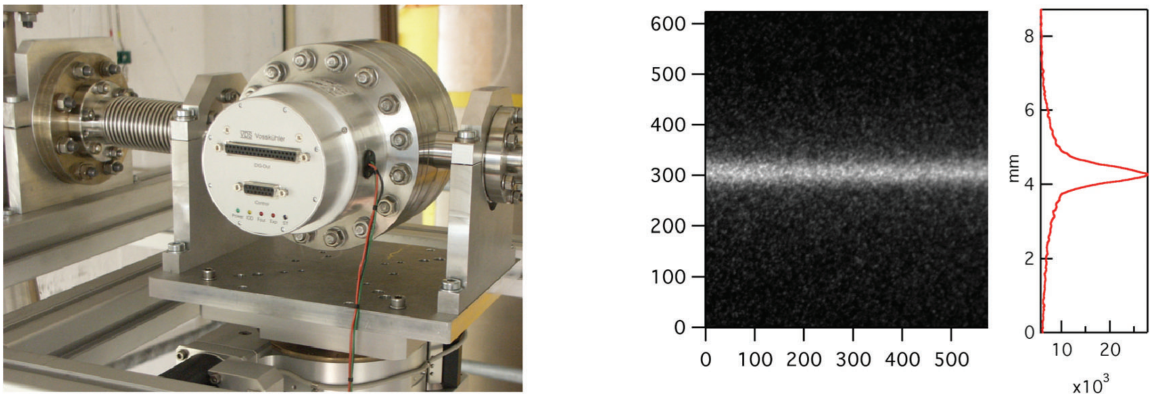

Figure 6.3.7 *Left: Prototype of the RGXBPM. Right: Image of the beam profile together with the corresponding integrated profile obtained at BW3, DESY, at a residual gas pressure of* 3×10^{-7} *mbar, an MCP gain of* 3×10^{4}*, and for a CCD exposure time of 300 ms.*

6.4 Scientific instruments

This section contains the experiment proposals and the instrumentation requirements of seven broad scientific domains or experimental techniques, and a programme for R&D on x-ray instrumentation. It is largely the result of a wide consultation of the scientific community. After outlining the new science which is made possible by the European XFEL and the corresponding requirements for the experimental stations, an attempt is made to condense these requirements in a proposal for a schematic beamline layout. The hope is that the common format of these layouts should help the comparison and the analysis of complementarities among the various instruments.

6.4.1 Small Quantum Systems

6.4.1.1 Scientific case

In the following sections we present the scientific case for XFEL experiments on Small Quantum Systems: atoms, molecules and clusters. These subjects were discussed at a workshop held in Paris in November 2005, and resulted in a number of concrete proposals for experiments to be performed at XFEL in the first few years of operation. The proposed experiments are divided into:

- linear processes, where there is only a single x-ray photon involved in the process, and, in some cases, a weak probe auxiliary field; and
- non-linear experiments, where there are two x-ray photons or an x-ray photon plus a photon from a strong pump laser field.

Linear processes

I. Inner shell ionisation in atomic ions

Multiply-charged ions determine the behaviour of hot media that exist both in astrophysical and technical environments. Especially under astrophysical conditions they are often exposed to x-ray radiation fields, so it is important to understand their interaction with high-energy photons. Modelling of absorption and emission spectra often lack sufficiently precise atomic data **[6-59]**. Apart from astrophysics, plasma physics requires precise photoionisation cross-sections for multi-electron ions in the x-ray range. Especially for heavier elements, these ions have a complicated multi-electron structure and are characterised by strong quantum-mechanical correlation effects; hence, the absorption processes frequently involve several interacting electrons. An example is given by the photoionisation resonances that determine the energy dependence of the photoionisation cross-section for many-electron species. The theoretical methods for predicting dynamical processes in systems with more than three electrons are presently undergoing intense development. For improving their reliability, experimental data are needed that probe the parameter spaces of both electron number and nuclear charge, as is possible in measurements on multi-charged ions.

The European XFEL offers new access to these studies as a radiation source strongly exceeding the spectral and temporal photon densities available so far. In addition, using the full pulse train capability of the European XFEL (compare Figure 6.1.1), the average photon flux will be considerably higher than at current soft x-ray sources. Thus, compared to standard neutral targets, ion storage techniques using trapped samples at rest or stored ion beams can be applied to perform single-event studies, even at the small densities to which these devices are limited. Typical densities in traps and beams are usually in the range 10^5 to $\sim 10^9$ cm^{-3}, at least six orders of magnitude smaller than for gas targets. Two types of experiments are planned for atomic ions: First, collinear merged beam experiments offer the opportunity of absolute cross-section measurements of x-ray single-ionisation processes for a wide range of ion charge states. Second, ion trap experiments offer the possibility of following the sequential ionisation, starting from lower charge states, in strong x-ray radiation fields.

The high brilliance of XFEL photon sources combined with efficiently trapped highly-charged ions, will facilitate selective photon excitation of states in few-electron ions for the first time. These excitations in highly charged few-electron ions will test the most advanced atomic structure calculations, including huge relativistic corrections and non-pertubative quantum electrodynamics in extremely strong fields. The compact electron beam ion trap (EBIT) can produce and trap 10^7 selected highly-charged ions in a volume of 100 $\mu m^2 \times 10$ mm which is a good match with the x-ray beam properties from the FEL. A scheme for experiments could be to direct the FEL beam of broad bandwidth directly into the EBIT and monitor the induced emission by x-ray spectrometers. Alternatively, fluorescence radiation can be monitored using a narrow-band monochromatic FEL x-ray beam that excites the trapped ions. Furthermore, two-photon excitation using counter-propagating XFEL beams might be implemented, which would result in a tremendous improvement of resolution by Doppler-free spectroscopy. For all these experiments, the opportunity to measure radiation from the trap itself is crucial.

We plan accurate spectroscopy of selected Lithium-like and Helium-like ions, such as Bi^{80+} and $U^{89,90+}$. In Lithium-like Uranium the $2s$-$2p_{1/2}$ splitting of around 280 eV should be measured to better than 0.01eV to determine higher order loops in the Lamb-shift correction. A resolution of 10^4 should be possible at these energies **[6-60]**. At much higher energy, the measurement of the 4.1 keV splitting of $2s$-$2p_{3/2}$ in U^{89+}, should be done where the accuracy so far is only 0.26 eV. The final aim would be a relative accuracy of 10^{-6} in these transition energies, but already, 10^{-5} would increase the level of precision considerably. To reach that, an extremely high spectral definition of the XFEL beam will be necessary and in addition, sympathetic/laser cooling of the trapped ions is required. A related application would be to very accurately measure the hyperfine splitting of inner-shell states in ions with nuclear spin, e.g. 1 eV in $2s_{1/2}$ of $^{235}U^{89+}$, in order to determine nuclear magnetisations of different isotopes. Note that the high spectral resolution will alter the temporal distribution of the x-ray pulse and lead to lengthening at the highest resolution. These effects are not expected to disturb the above proposed experiments.

We also propose to perform for the first time “optical pumping” experiments in the x-ray regime by using an EBIT and an FEL. This requires either a circular polarised XFEL beam or a highly monochromatic, linear polarised XFEL beam. Since the Zeeman sub-levels in the EBIT trapping field of 10T would be split by only 10^{-3} eV we propose to use circular polarised FEL radiation. In this case, the natural bandwidth of the XFEL of less than 1% should be sufficient to carry out the experiments. For example, with the positive circular polarised 280 eV XFEL photons (σ_+ light) interacting with the $^{238}U^{89+}$ trapped ions parallel to the magnetic field direction, only the 2s, m=+1/2 state would be populated. This experiment would allow, for the first time, polarisation of trapped, highly charged ions and to perform Zeeman spectroscopy on few-electron ions, e.g. to measure their g-factors. Using ions with nuclear spin, a polarisation of the nuclear magnetic moment can be reached via the hyperfine interaction.

II. X-ray photons scattered at trapped ion crystals

A unique state of matter that could be imaged with XFEL photons is strongly coupled ion plasmas (Coulomb crystals) in a Penning trap or Paul trap configuration. The equilibrium dynamics of Coulomb crystals could be studied, and, due to the low ion temperature, ultra-high resolution photon spectroscopy could be performed on transitions only accessible with XFEL photons.

At low temperature, a system of particles with the same charge (q) under the influence of an external confining force (One Component Plasma) liquefies or crystallises (forms Coulomb crystals). For a given harmonic external confining force, the interparticle distance in a Coulomb crystal becomes larger then the Wigner-Seitz radius r, which typically, is in the order of 15 µm, thus, giving densities of $n=3\times10^7$ ions/cm^3. A charged plasma of this type, unlike a neutral plasma, can exist at thermal equilibrium. The properties, in particular the equation of state, of infinite one-component Coulomb matter are well understood theoretically and the crystallisation point is known to be near $\gamma=170$, where the universal parameter $\gamma=q^2/rkT$ is the ratio of Coulomb to thermal energy kT. The fact that the parameter is universal also means that highly-charged ion plasmas can become strongly coupled and crystallise at higher temperatures than a singly charged ion plasma of comparable density, and that they are similar to high density plasmas at much higher temperature (e.g. in white dwarfs). Coulomb crystals of singly charged ions have been produced experimentally with laser cooling in electromagnetic ion traps (e.g. at the National Institute of Standards and Technology (NIST) and the Max-Planck-Institut (MPI) for Quantum Optics), and conditions for multiply-charged ion crystallisation have been established using a sympathetic cooling scheme at Lawrence Livermore National Laboratory (LLNL). The strongly coupled plasma condition will be achieved via sympathetic cooling with laser-cooled singly charged ions. In brief, first 9Be+ ions are caught and confined in the trap. These ions are electronically cooled, initially with a tuned circuit and then laser cooled using the resonance transition near 313 nm. Highly charged ions are then merged into the cold Be+ plasma, energy is exchanged by collisions and the kinetic energy of the highly charged ions is reduced to around 1 K. A value of γ of over 10^3 can thus, be reached with ions of q~50.

The highly charged ion crystalline phase can be imaged in fluorescence using transitions accessible with XFEL photons and a focusing element for x-rays. A synchronisation of XFEL photon pulses with the trap parameters and the image detector and with a probe laser to monitor the Be+ plasma temperature will cover the evolution from a non-equilibrium state, into a fully thermal equilibrated state as function of time (ms scale). The focusing condition of the XFEL photon beam will furthermore allow selective heating of, for example, the centrifugally separated highly charged ion cloud, thus creating a distortion of the equilibrium. Measurements of the line width of cooling transition in the Be+ ions as a function of time will allow conclusions about the phonon transport in the strongly coupled plasma components. Follow-up experiments could include high-energy XFEL photons capable of ionising an inner-shell selectively in the highly charged ions. Mixed plasmas with different Coulomb couplings can be created by using different ion components.

Results of this research will be beneficial to condensed matter physics, to the understanding of stellar interiors (for example, white dwarfs), and essential for high-resolution spectroscopy experiments. If one reaches an ion temperature of 10 K, the relative Doppler spread is down to 10^{-7}.

III. Molecular dynamics following x-ray photoionisation

Molecules are an important observatory tool for understanding colder astrophysical media and research on molecular regions close to strong radiation sources requires a good understanding of the cross-sections for x-ray induced processes and their products. For polyatomic molecules, several neutral products are often generated following electronic excitation or ionisation by x-ray absorption. The dynamics of the fragmentation process are best revealed by analysing the chemical nature of the final products and their relative momentum by counting techniques in event-based photoabsorption studies. For single-event fragmentation studies, the counting and imaging of neutral reaction products has been proven to be very efficient using fast-moving target systems, from which all break-up fragments are sent into a narrow cone in the forward direction with high offset kinetic energy. Using an energetic beam as the target, hence, allows universal and efficient detection of neutral fragments, in contrast to a target at rest where the fragments would have near-thermal energies and would be emitted in unpredictable directions. Fast-beam fragment imaging has been strongly developed over recent years for molecular ion beams. Beam storage techniques have been developed to control the vibrational and rotational excitation of the energetic molecular ion beam, thus, allowing studies with a well defined initial state distribution.

The high, pulsed photon intensities at the XFEL make it possible to perform x-ray photoabsorption experiments on molecular ion beams which are extremely dilute, but fast moving, target systems. These experiments, thus, produce single-event images of the fragmentation of polyatomic molecular systems following x-ray absorption and yield fragment branching ratios, fragment energies and momentum correlations between different fragments. As a particular field of study, one can consider the fragmentation of polyaromatic hydrocarbon (PAH) molecules that are observed in molecular clouds among others close to active galactic nuclei; such processes can be studied in fast-beam fragmentation studies with PAH cations. In addition, the analysis of neutral fragment channels following x-ray excitation and ionisation of smaller polyatomic molecules such as, for example, H_2O^+ and H_3O^+, is of great interest for fundamental dynamics in highly excited molecules, as such smaller systems lend themselves to direct comparisons between experimental and theoretical results. Simultaneous imaging and mass measurement of heavy fragments, as produced in interactions with PAH beams, is being intensely developed at present and will find new applications in these proposed XFEL experiments.

IV. Cluster experiments

Clusters represent an intermediate state of matter between large molecules and solids, having the same local density as a solid but the same average density as a gas. They offer a unique opportunity to study how the light-matter interaction evolves as the size of the target increases. The interactions of clusters with intense infrared laser pulses have been found to be extremely energetic. Ions with energies up to 1 MeV **[6-61]**, and multi-keV electron energies **[6-62 – 6-64]** have been observed. The ions are much more energetic and stripped to much higher charge states than would be obtained from atoms or small molecules irradiated at the same intensity.

However, the physics of the interaction changes dramatically at short wavelengths. Whereas in the infrared, the ponderomotive energy (i.e. the kinetic energy of the electron oscillations in the rapidly varying radiation field, $e^2E_0^2/4m\omega^2$) is considerable (600 eV at 10^{16} Wcm^{-2}) and electron motion in the field is large compared to the cluster size, at x-ray wavelengths, the ponderomotive energy is much less than 1 eV and electron motion is negligible. In the x-ray regime, single-photon ionisation of core electrons can occur, inner shell holes can be created and ionisation starts at much lower intensities than with infrared radiation, where tunnelling or multiphoton ionisation occur. In the infrared, the most heat is deposited in the cluster at three times the critical electron density of 10^{21} cm^{-3} (the critical electron density at a given frequency ω is the density n_c for which $\omega=[4\pi n_c e^2/m]^{1/2}$). In contrast, at x-ray wavelengths the critical electron densities of 10^{25}-10^{29} cm^{-3} will not be reached. This may lead one to expect that only weak coupling to clusters will occur. However, experiments with 100 nm radiation at DESY **[6-65]**, which measured 400 eV ions, as well as theoretical calculations, show that existing models for the optical region cannot simply be extrapolated down to x-ray wavelengths. Experimental tests of cluster fragmentation in XFEL beams of very high intensity are now needed.

To investigate the heating processes in clusters at short wavelengths, measurements will be made of ion and electron energies, ion charge states and x-ray spectra as a function of wavelength. Infrared laser radiation will then be used to probe the expansion following heating by the XFEL pulse. It was shown recently that ion energies and charge states can be maximised when the infrared probe pulse is timed to arrive when the electron density inside the cluster reaches a certain critical electron density after initiation of the heating by a pump pulse **[6-66]**. By measuring the optimum pump-probe delay for various target and pulse parameters, the expansion of the cluster can thus be mapped out.

XFEL radiation also offers a unique opportunity to investigate the structure-property relationship of reduced dimensional materials, in particular of size-selected atomic clusters. For these systems, typically containing less than 100 atoms, the cluster properties depend directly on the number of atoms in the structure. For example, the chemical reactivity can change by orders of magnitude with the addition or removal of individual atoms. Being very interesting material systems with a pronounced structure-property relationship, clusters and nanocrystals are bridging the gap between the atom and a bulk crystal. They are promising candidates for novel applications ranging from catalysis to magnetic storage and optoelectronic devices. Cluster research with the XFEL yields various opportunities of great importance.

The investigation of the electronic and geometric structure of size-selected atomic clusters has made significant progress over the last years. New experimental set-ups and powerful cluster sources as recently developed in the cluster consortium (lead by the University of Rostock) allowed first investigations of shallow core levels. The European XFEL will open the door to core level photoemission experiments on size-selected clusters in the gas phase. These experiments will be a unique possibility to unveil the electronic and geometric structure of clusters.

Non-linear processes

V. Multiphoton studies in the x-ray spectral region

The foreseen beam parameters at the European XFEL open up the perspective of non-linear optics in the x-ray spectral region. Here, we consider processes involving non-linear ionisation. Given that the photon energy ranges from 200 eV to 15 keV, even for extremely focused intensities up to 10^{18} W/cm^2, the ponderomotive energy $U_P=e^2E_0^2/4m\omega^2$ is much smaller than the photon energy and the ionisation potential. It follows that multiphoton (MP) (and not tunnelling) processes govern ionisation transitions. Because of the high photon energy, only inner-shells can be MP ionised (for outer shells, Above-Threshold Ionisation (ATI) can also be considered).

The K-shell two photon ionisation (TPI) cross-section scales as Z^{-6} (Figure 6.4.1). Reasonable intensities for the observation of K-shell TPI range from 10^{12} W/cm^2, for the light elements, to 10^{16} W/cm^2 for Z~35 (mean ionisation rate: ~10 ions/s). Saturation intensities range from 10^{17} W/cm^2 to 10^{21} W/cm^2, correspondingly. An unavoidable process is of course single photon outer-shell ionisation. For the 100 fs pulse duration of the XFEL, this will be the dominant ionisation process by several orders of magnitude, screening the TPI unless TPI is observed in highly stripped Hydrogen- or Helium-like ions.

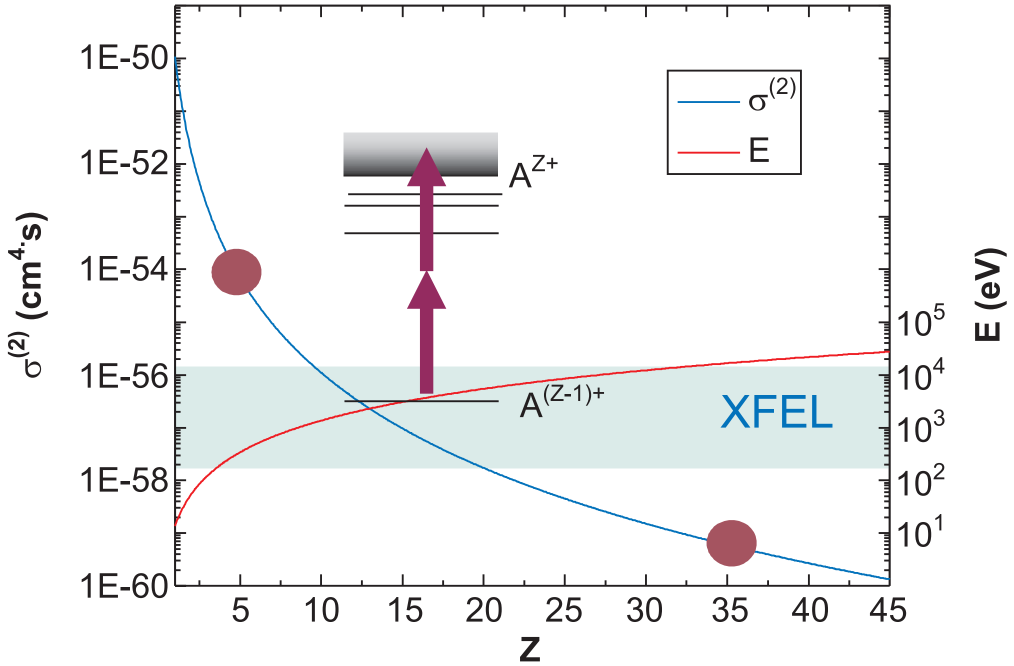

Figure 6.4.1 *Z dependence of the TPI cross-section and the binding energy in Hydrogenlike ions.*

Once x-ray multiphoton processes have been established, they can be used for several interesting applications. Two examples are mentioned below: Due to the non-linearity of the process, MPI provides 3-D spatial selectivity in the focused geometries required for its observation. Thus, it becomes appropriate for 3-D spatially resolved analytical applications, such as MP-XRF, MP-XPS and MP-Auger diagnostics. An even more important application is the use of MPI processes for the temporal characterisation of the XFEL radiation. It is well known that rigorous short pulse diagnostics require non-linear processes induced solely by the radiation to be characterised. Recent achievements in attosecond pulse metrology demonstrated the feasibility of approaches (based on non-linear autocorrelation) and instrumentation (autocorrelators) for the XUV spectral range (see, for example, **[6-67 – 6-70]**). These techniques are, in a straightforward way, extendable to shorter wavelengths for the benefit of XFEL beam diagnostics.

Alternatively, a “two-colour” version of this characterisation method can be envisaged, considering atomic systems submitted simultaneously to a strong pulse of x-ray radiation from the XFEL source and to an intense pulse of radiation from an optical (or infrared (IR)) laser; the atoms can experience radiative transitions involving continuum states that are “dressed” by the laser field. In the test-case of the single-photon ionisation of atomic species via the absorption of one x-ray photon from the XFEL, the photoelectron spectrum is significantly modified in the presence of the laser. It is expected that the photoelectron peak will be depleted and that a set of new peaks, termed “sidebands”, will appear. These peaks, equally spaced with interval $h\bar{\omega}_L$ where ω_L is the laser frequency, are located symmetrically on each side of the primary photoelectron line, as they result from the absorption or the stimulated emission of photons from the laser field. It turns out that, by monitoring the magnitude of the sidebands when varying the time delay between the XFEL and laser pulses, one can characterise the temporal properties of the XFEL pulse itself. We note that this implies that the temporal jitter in the SASE emission process is controlled, as well as the spatial overlap between the two beams. Using these experiments in a single-shot fashion enables measurement of the temporal properties of the XFEL pulses, such as, for example, measuring the jitter between optical laser and XFEL pulse or the duration of the XFEL pulse. Two proposals to carry out such measurements as a time domain diagnostic are discussed in Section 6.3.2.2.

Such spectra would represent a new type of ATI measurement, which continue to be thoroughly studied as they represent a paradigm for highly non-linear optical processes in atoms. The determination of the respective magnitudes and of the angular distributions of the associated photoelectron peaks, provide most useful data on the response of atoms to strong external fields. Until now, ATI was explored either in a single-colour scheme via the multiphoton absorption of IR laser radiation or in multi-colour schemes, with a comb of higher harmonics combined with the pump laser. Here, with the highly monochromatic XFEL radiation, the new possibility arises of observing the absorption of a single high frequency photon combined with the exchange of laser photons. This is in contrast with the case of harmonic sources in which it is difficult to single one frequency out of the comb. Again, measurements of the magnitudes and of angle-resolved cross-sections would provide new sets of data that will be relevant in the more general context of strong field atomic physics.

VI. Dynamics of aligned small molecules and molecular wave packet dynamics

As also will be discussed in Section 6.4.6, the time-resolved investigation of molecules in the gas phase becomes feasible using XFEL radiation. Here, we are proposing studies of laser-aligned small molecules in the gas phase. By laser aligning we can go from ensemble averaging to preferred orientation and can, thus, improve the information content of the measurable diffraction pattern. This can be seen as: (a) a stepping stone to single-molecule imaging of larger molecules as it will help address the timescales of x-ray induced Coulomb explosion; and (b) important fundamental molecular science, permitting us to follow the full dynamics of structural change in chemical reactions. Studies on gas-phase molecules in this range would require an ultra-short aligning laser pulse (e.g. Titanium-Sapphire pulse) followed at a variable delay by the XFEL pulse whose diffraction pattern is recorded in order to extract the structure of the molecular species. Different projections of the diffraction pattern or different polarisation axes of the X-pulse, as compared to that of the IR-laser pulse, could also be applied to retrieve 3-D diffraction patterns. The dynamics of molecular alignment or of other photo-induced reactions, possibly triggered by the IR-laser pulse, could be investigated. In addition to measuring the scattered x-ray photons, we propose that the momentum distribution of the x-ray produced photoelectrons should also be measured as this will carry the signature of the molecular structure due to the scattering of the outgoing electrons from other atomic centres in the molecule.

The spatial alignment of molecules can be regarded as a special case of population of coherent rotational states of the molecule. In a similar way one can also consider population of coherent vibration states, applying an IR short-pulse pump laser; and subsequently uses the XFEL radiation as the probe pulse (see Figure 6.4.2). The coherent mixing of vibrational states results in a non-stationary state or nuclear wave packet (WP) which evolves with time and depends on the phase, intensity and shape of the IR field. IR-x-ray pump-probe spectroscopy is a proper tool to study the dynamic of proton transfer in systems with Hydrogen bonding patterns (for example, water). Thus, the spatial confinement of the WP allows it to be selectively excited to the proton transfer well, thereby offering the possibility to map out of the molecular potential along the Hydrogen bond. Another topic of general and fundamental interest is the dynamics of the proton transfer in vibronically coupled core-hole states localised on different sites; this occurs for example in the Glyoxalmonoxime molecule. Through the crossing of the potentials, the proton transfer is accompanied by core-hole hopping. Moreover, x-ray photoionisation of laser-driven molecules offers a unique opportunity to study the electronic recoil effect, which is enhanced through the large size of the laser-induced nuclear WP. Finally, the WP revival caused by the anharmonicity allows the anharmonical shift to be resolved by making use of the one-to-one correspondence between the dynamics of the nuclear WP and the shape of the x-ray probe spectrum. In all these studies, the relative phase of the pump IR radiation strongly affects the x-ray probe spectra, as the WP trajectory is sensitive to this phase.

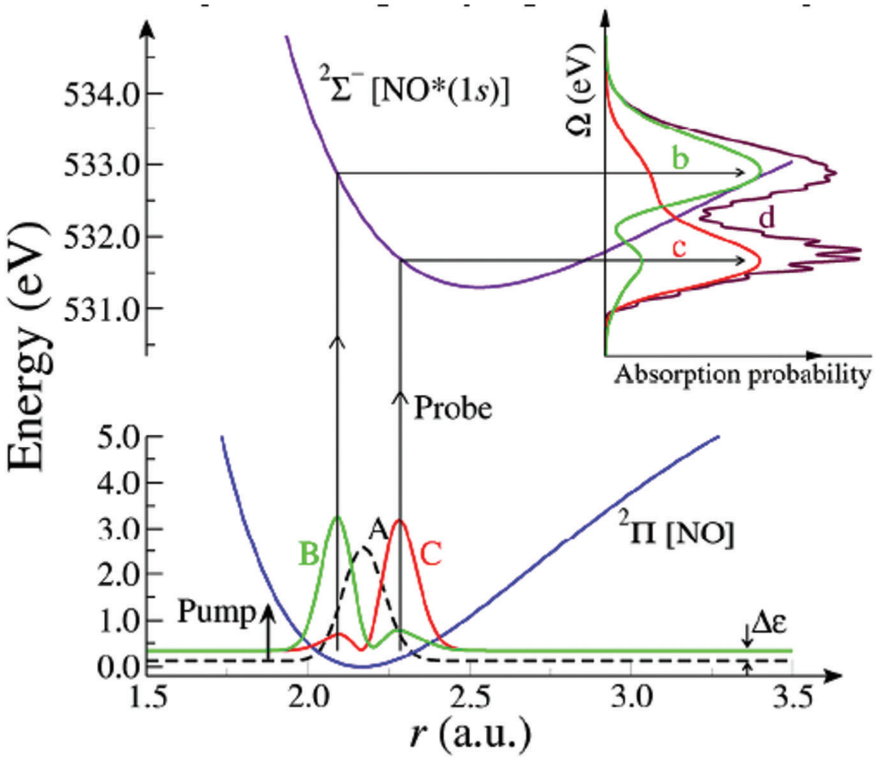

Figure 6.4.2 *Example showing how the shape of the vibrational wavepacket in the ground state of the NO molecule affects the lineshape of the O K-edge absorption.*

Regarding the general requirements in order to clock photochemical processes, time and spatial resolution of pump-probe measurements must be considered. The observation of motion in real systems needs rather high spatial resolution through a good localisation of the wave packet. Thus, the formation of the nuclear WP deserves special attention: the degree of localisation depends on the intensity, and on the shape of IR pulse. The localisation of the wave packet requires the coherent excitation of many vibrational levels; this makes it necessary to apply IR intensities of about 10^{12}-10^{14} W/cm^2. Moreover, the spread of the WP during its evolution must be rather small.

The key to achieving the necessary time resolution is a sufficiently short duration of less than 100 fs for the x-ray probe pulse. Slicing or compression techniques have already been proposed to shorten x-ray pulses to the desired region of 10-50 fs **[6-71 – 6-72]**. As the WP evolution depends on the phase of the IR field, the probe signal may become position sensitive and mixing would lead to de-phasing effects. To avoid such de-phasing, the spot size of the x-ray beam has to be kept at the size of the IR wavelength.

VII. Time-resolved photo-fragmentation of small molecules

Photo-fragmention studies using an IR pump pulse and a following x-ray probe pulse give access to new classes of experimental studies focused at the direct observation of spatial structures in molecular systems. Experiments are essentially based on the use of ultra-short (e.g. Titanium-Sapphire) laser pulses synchronised with femtosecond (fs) XFEL pulses. The following example applies one of the experimental methods available. A broad range of molecular species may be investigated using these techniques, however, in each case sufficiently specific and realistic quantities would need to be considered in order to outline the required experimental parameters in more detail.

By following an idea first reported by U. Becker et al. **[6-73]**, it would be interesting to investigate the breaking dynamics of molecular bonds such as NO in the N_2O molecule. In such a molecule, in fact, the Oxygen atom occupies a side position, which implies an asymmetry even in the inner shell binding energy of the two Nitrogen atoms, the central and terminal ones, respectively. In particular, the 1s binding energies of the two Nitrogen atoms are split by 3.93 eV, the central Nitrogen line being situated at about 409 eV and the terminal-atom line being centred at about 413 eV. The two lines are very well resolvable in spectroscopic experiments, having an FWHM of 0.7 eV and 0.54 eV, respectively. The N-line spectral splitting disappears once the NO bond is broken and the molecule is dissociated into an Oxygen atom and a N_2 molecule. We propose to use a pump-probe scheme in which an intense ultra-short pump beam induces multiphoton bond breaking in the molecule; and an ultra-short 400-420 eV XFEL pulse then photoionises the fragment at a variable delay. By means of photoelectron spectroscopy, the dynamics of bond breaking can be studied by monitoring the transition from the double to the single line associated to the N 1s shell as a function of the delay time.

6.4.1.2 Instrument requirements

From the specific needs of the experiments described above main requirements for the investigation of Small Quantum Systems (SQSs) can be derived. They concern the performance of the light source, the diagnostic equipment of the beamlines and their infrastructure. The needs for the experiments described in this section correspond most closely to the projected SASE 3 beamline for soft x-rays. The reason for using soft x-rays comes from the desire to study atomic or molecular excitations occurring in this photon energy range and from the perspective of studying non-linear multiphoton processes. Since the cross-section for these processes decreases strongly with increasing photon energy, the chances of carrying out such experiments are best for the soft x-ray regime. Furthermore, some users wish to study the interaction with circularly polarised x-ray radiation, again (naturally) available only from SASE 3.

Spectral radiation properties

Required photon energies vary from 250 eV to around 4100 eV. The lower edge is purely determined by the availability at the European XFEL. The XFEL experiments will, in a sense, be an x-ray continuation of work currently started at smaller photon energies (VUV and XUV). The upper edge corresponds to the L-shell fine structure in highly stripped U^{89+}. Most of the proposed experiments do not require a monochromator, but can accept the natural bandwidth of the FEL of 0.7% (250 eV) to 0.2% (3000 eV). Where spectroscopy at specific resonances or energy levels is proposed, an energy resolution of 10^{-4}-10^{-3} is required. Such resolution is possible because of the proposed monochromator of the SASE 3 beamline. In the case of the proposed investigation of highly stripped high-Z atoms (Experiment II. in Section 6.4.1.1), a resolution as good as 10^{-5}, in some cases even a near 10^{-5}, has been requested. This very high resolution monochromator will require a specific R&D effort, in particular in view of the high intensities. The temporal radiation properties will be affected by the use of high spectral resolution. A second reason to use a monochromator could be to reduce the higher harmonic contents. In particular, two-and-higher order multi-photon experiments are sensitive to photons at two or three times the energy and leading to single-photon ionisation events (Experiment V. in Section 6.4.1.1). For these experiments a reduction of higher harmonics of better than 10^6 seems to be required. Since calculations show that the natural radiation exhibits a ratio of 10^2-10^3, the realisation of far better suppression of higher order harmonics by means of optics and filters could be a real challenge.

Beam dimensions

The requested x-ray beam size is determined, in most cases, by the typical size of the sample of 100 µm which is the cross-section of the x-ray beam with an atomic, molecular or cluster jet. At this beam size the intensity will increase to ~10^{15} W/cm^2. For merged ion beam experiments (I. and III.) good overlap of x-ray and ion beams over ~0.5 m is required. For 100 µm spot size, the Rayleigh length will be sufficiently long to achieve this value. Experiments V. and VI. benefit from higher intensity and therefore need tighter focusing in order to reach intensities of ~10^{17} W/cm^2 and beyond. If one could reach spot sizes of 1 µm or even smaller diameters, intensities beyond 10^{19} W/cm^2 could be possible which may become important for the non-linear experiments.

Time domain requirements

Due to intrinsically small cross-sections, many of the experiments are luminosity limited. That means they require the maximum available photon flux and the highest achievable repetition rate. However, due to limitations in the detection channels (see the following discussion) the favourable bunch spacing for most of the experiments is in the regime 1 up to 20 µs. For Experiments I.-IV. investigating linear processes, the planned x-ray pulse duration of the order 100 fs will be largely sufficient. Beyond that the non-linear Experiments V.-VII. would greatly benefit from a reduced pulse duration down to <30 fs. All experiments investigating non-linear effects will suffer from the spike structure of the XFEL radiation. Simulations of the temporal distribution show that XFEL radiation at 250 eV still has many uncorrelated spikes (compare Figure 6.4.3). Monochromatisation will smooth this structure, therefore providing improved conditions.

Photon diagnostics requirements

All experiments will need diagnostic equipment regarding the measurement of the photon beam intensity on a pulse-to-pulse basis. In addition to the integrated photon number required by all experiments, those experiments investigating non-linear effects may require measurement of the temporal intensity distribution for each FEL pulse. This need arises from the dependence of the linear effects as a function of intensity (W/cm^2) and not of flux. The techniques to determine spectral and temporal information on a pulse-to-pulse basis are yet to be developed. In some cases the measurement intensity and some temporal properties for each pulse may already allow the identification of linear and non-linear contributions by using the dependence of measured process rates. Since most experiments will use optically thin samples, the transmitted beam can be used for various diagnostics. To achieve the small spot sizes, diagnostics of the beam spot location and spatial distribution at the sample location is required.

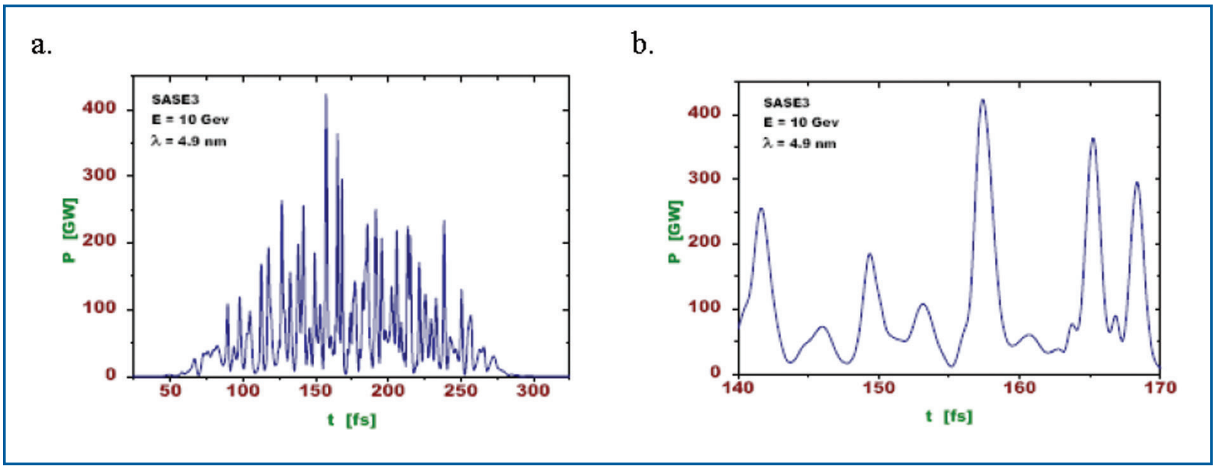

Figure 6.4.3 *Simulation of the temporal distribution of 4.9 nm radiation from SASE 3 at 10 GeV. (a) is the entire pulse and (b) shows a slice of 30 fs.*

Sample manipulation and environment

Many of the experiments will apply atomic, molecular or cluster beam techniques. Some of these sample injection systems operate at relatively high pressure (e.g. for rotational cooling of molecules or cluster formation) and as a consequence, the base pressure in experimental chamber may reach the 10^{-5} mbar level. Therefore, careful design of differential pumping stages for connection to the photon beamline needs to be considered. On the other hand, experiments may investigate extremely dilute samples, therefore, requiring partial pressure as low as 10^{-11} mbar. In these experiments, differential pumping is required to improve experiments vacuum against beamline vacuum.

Experiments in this scientific field will investigate ions over a large variety of masses (atoms, molecules and clusters) and charges (highly charged atomic ions). In addition to gas beam techniques, the use of ion storage techniques is proposed here. These could be ion trap techniques, such as EBIT or Penning trap, to store ion samples at rest or stored fast ion beams, which may be used in merged (collinear) or crossed beam geometry (see Figure 6.4.4). In order to efficiently carry out experiments using an ion trap or an electrostatic storage ring, it would be beneficial to make these infrastructures available at the XFEL. The footprint required for an ion trap set-up is of the order 5×5 m^2 and that of an ion storage ring is estimated to be in the order 15×15 m^2. It has to be noted that groups working in this field often operate their own, specific vacuum chambers. One should foresee the possibility of placing these chambers at a non-occupied vacuum port of the SQS instrument.

Detector requirements

Depending on the experiment, different detection techniques will be applied. Common to most experiments is particle detection, either electrons or ions. Time-of-flight techniques will be applied for energy measurement of the particles putting a constraint on the maximum repetition rate of the experiment. Typical flight times extend up to μs making

1 MHz operation desirable. To achieve very good energy resolution, retarding schemes will be used leading to particles flight times in the order 10 µs, thus, limiting the repetition rate to ~50 kHz. In combination with 2-D particle detectors, spatial and energy (3-D) resolving detectors can be applied for fragment imaging. In some cases, x-ray emission spectroscopy will be used and spectrometers, possibly even having high time-resolution by using ultrafast x-ray streak cameras (XSC), will be required. In addition, special detector arrangements like the COLTRIMS detector for multi-hit ion and electron coincidence detection will be used.

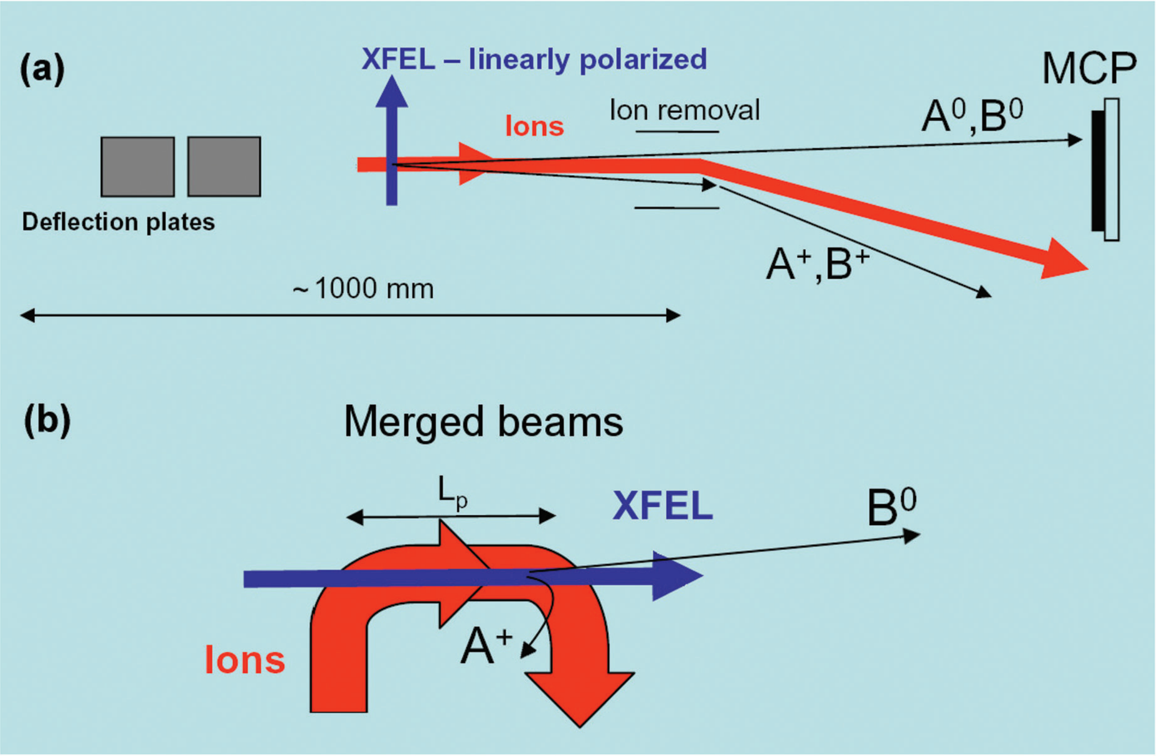

Figure 6.4.4 *Schematic arrangements for fast-beam molecular fragment imaging using (a) crossed ion and photon beams or (b) merged beams.*

Visible laser requirements

An important feature of many of the experiments in this field is the requirement for a synchronised high power ultra-fast IR or visible laser. Starting from a fundamental wavelength at ~800 nm (e.g. Titanium:Sapphire) it should provide wavelength from the fourth harmonic (200 nm) up to the deep infrared (10 µm; requires some R&D). High energy of 1-3 mJ should be provided for fundamental and harmonics, whereas Experiment VI. asks for large range tunability by optical parametric tuning. In this case, one will have to live with 10 µJ. A contrast ratio of larger than 10^5 is requested and the repetition rate should allow us to follow that of the FEL pulses. It is likely that a trade-off between laser pulse energy and repetition rate will have to be applied. For this class of experiments a pulse duration better then 50 fs and precise synchronisation with the FEL beam in the order of ~10 fs are required. If such synchronisation will not be possible, diagnostic tools to measure the time delay to similar accuracy are required.

6.4.1.3 *Realisation of the instruments*

According to their requirements, the SQS experiments need to be carried out at the SASE 3 beamline (see Section 6.2.4.3 for a description). SASE 3 enables photon energies from 250 up to 3,100 eV. For higher photon energies the saturation length of the FEL, at given project parameters, will exceed the undulator length. Those experiments requiring photon energies from 3,000 to 4,100 eV may have to be carried out at the SASE 2 beamline (see Section 6.2.4.2). The SASE 3 beamline could features two beam tubes: one for a monochromatic beam with a resolution of about 104 and one using only mirrors to guide the beam. Selection of the beam path is achieved by a set of two movable mirrors. The optics in both lines should not affect the polarisation of the XFEL radiation, thus, linear and circular polarisation can be selected by setting the undulator accordingly. It is not considered possible to bring the monochromatic and the mirror beam to the same location. The specific requirements of the SQS experiments, therefore, ask for two different instruments, described below.

SQS 1: Monochromatic beam

The proposed PGM monochromator design for the SASE 3 beamline (see Section 6.2.2.3) should provide a monochromaticity of the order 10^{-4} over the entire photon energy range from 500-3,000 eV. This resolution is required to carry out, for example, the inner-shell ionisation experiments of highly charged ions described in Section 6.4.1.1, Experiment II. Other spectroscopy-type experiments, investigating specific energy levels, will also use this instrument. The typical transmission of the monochromator is in the order of a few percent. Therefore, the SQS 1 instrument will not be suitable for experiments requiring the highest intensities. The requirement of a monochromaticity of 10^{-4} up to 10^{-5} cannot be fulfilled using the proposed, versatile monochromator design. For the SASE 3 photon energy range, such a resolution would require a specific R&D programme.

Two mirrors at a grazing angle in the order 10 mrad will be used to deflect the beam away from the forward beam direction. At the chosen sample location inside the experimental hall a focal spot size of the x-ray beam of ~100 μm will be available. This focus is achieved by using the mirrors within the monochromator design, i.e. by refocusing the exit slit onto the sample. If higher intensities will be required for the experiments, stronger demagnification of the monochromator exit slit will be needed. In this case the focusing mirror must move closer to the sample.

The following elements belong to the SQS 1 instrument inside the experimental hall. They are also depicted in the schematic layout of that instrument in Figure 6.4.5 and are listed in Table 6.4.1. Collimating apertures or a slit system will be placed in front of the experimental chamber to clean the beam from scattering. A gas photon flux monitor (see Section 6.3.2.1) will follow before a differential pumping section separates the beamline from the UHV vacuum chamber for experiments. For the energy range of this beamline, vacuum separation by means of windows is unlikely. The sample chamber will be equipped with systems for atom, molecule, or cluster beam production. We foresee sufficient pumping power to work at relatively high target densities of up to 10^{22}/cm^{-3}. Experiments to investigate electrons and/or particles and detectors operating in the TOF mode will be used. X-ray emission spectrometers could complement particle detection. Angular resolution may be used, at least in one direction. This vacuum chamber can be removed and space of 4×5 m^2 is foreseen to install specific sample manipulation schemes like ion traps or mass-selected cluster apparatus.

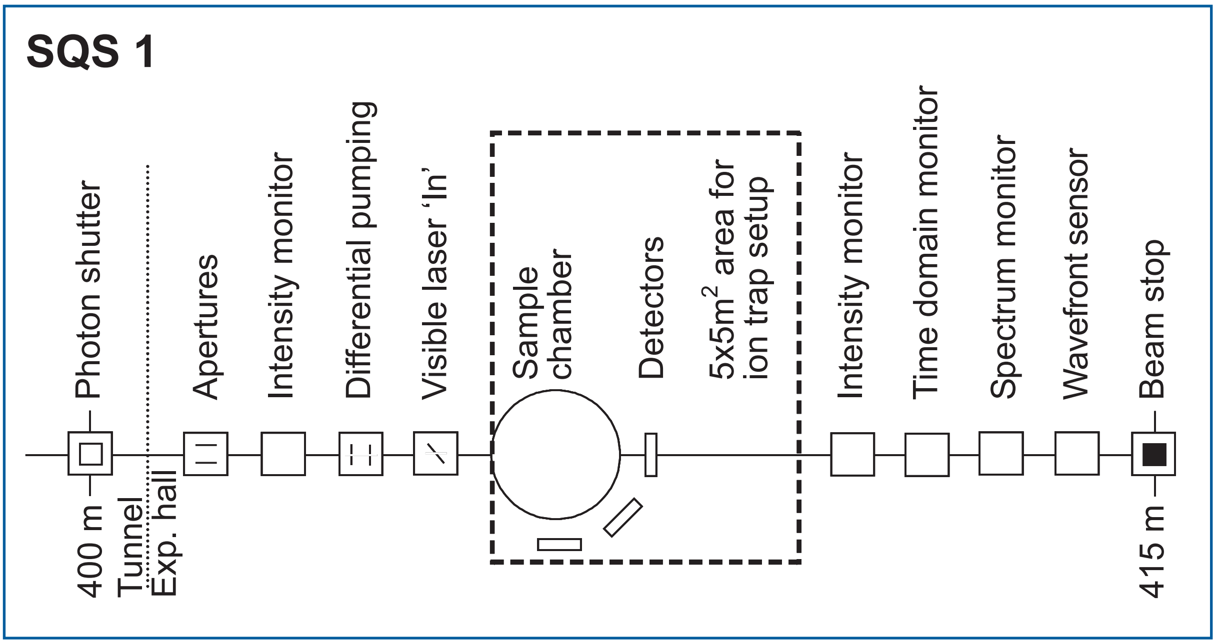

Figure 6.4.5 *Schematic layout of components of the SQS 1 station for monochromatic beam use. Distances are given in relation to the end of the undulator.*

Most of the experiments will absorb only a fraction of the incident beam intensity. It is, therefore, intended to use the transmitted beam for the purpose of diagnostics. A second gas monitor detector will be used to measure the transmission. At SQS 1 the spectral measurement is restricted to measurements of the higher harmonic content. Diagnostics of time-domain properties should deliver the arrival-time required for pump-probe experiments using the visible laser. Finally, spatial measurements are required to determine beam location and spatial distribution. Since these measurements are usually destructive they will be carried out in a dedicated set-up at the end of the line and before the beam stop.

The use of visible laser radiation at the SQS 1 instrument will be possible through distribution from the central laser room. The laser will be coupled into the vacuum in front of the sample chamber. Using mirrors with a central aperture, the laser beam can propagate collinear with the XFEL beam.

Item	Purpose	Specification
Slits/apertures	Beam definition, beam halo cleaning	1 µm accuracy, 0.25 µm repeatability
Intensity monitor	Measurement of incident photon flux	Transmissive (<5% absorption), single pulse measurement, relative accuracy $<10^{-3}$
Differential pumping	Separation of beamline and experiments vacuum	10^4 step for all elements
Laser inlet	Port-to-couple visible laser radiation into experimental chamber	Mirror with central hole, retractable
Sample chamber	Prepare and position samples, mounting of detectors, preparation for high gas loads	UHV, high pumping speed, x-y-z positioning
Detectors	Measurement of secondary particles, energy measurement, x-ray emission yields.	TOF for electrons/ions, imaging detector, x-ray spectrometer
Intensity monitor	Measurement of incident photon flux	Transmissive (<5% absorption), single pulse measurement, relative accuracy $<10^{-3}$
Spectral monitor	Measurement of harmonic content	single pulse measurement, relative accuracy $<10^{-3}$
Time monitor	Measurement time domain properties	Single pulse measurement
Spatial monitor	Measurement of spatial distribution, focus size	Single pulse measurement
Ion trap		5×5 m^2 area
Alignment unit	Positioning and position verification	Permanently operating, accuracy ~100 µm
Lead hutch	Radiation protection	$5\times10\times4$ m^3 (W×L×H), ± 1° thermal stability
Control hutch	Operation of the instrument	Working environment (Noise, temperature, light)

Table 6.4.1 *Elements and specifications of the SQS 1 instrument.*

SQS 2: High intensity beam

The SQS 2 instrument uses only mirrors for beam guiding. In this way much higher intensities can be achieved at the sample position to carry out e.g. the multiphoton studies in the x-ray spectral region described in Section 6.4.1.1, Experiment V. Other non-linear type experiments, investigating one- and two-colour phenomena will also use this instrument. The beam transport line for “mirror-only” of the SASE 3 beamline provides the options for unfocused and moderately focused beams (compare Figure 6.2.14). This beam is transported to a first vacuum port at this instrument, where micron, or even sub-microm, focusing will be possible. For a demagnification ratio of ~100, intensities as high as 10^{19} W/cm2 might be achievable. Sub-microm focusing requires dedicated optics near the sample and a beam transport which preserves the wavefront. This will be best achieved using flat mirrors. However, the unfocused beam of the SASE 3 beamline in the experimental hall has a size of 1.4-7.2 mm (FWHM) for photon energies of 3.1-0.25 keV, respectively. It is, therefore, considered very difficult building one focusing element that could be used for all photon energies. Since the instrument should feature only one single beam direction, using in-line optics, e.g. zone plates, is proposed. Using two deflecting mirrors a second port could be made available for experiments using the same instrument (compare Figure 6.4.6 and Table 6.4.2). Focusing to spot sizes ~100 μm will be achieved by using one of the offset mirrors.

Both ports will be equipped with similar instrumentation. Collimating apertures or a slit system will be placed in front of the experimental chamber to clean the beam from scattering. A gas photon flux monitor (see Section 6.3.2.1) will follow before a differential pumping section separates the beamline from the UHV system for the experiments. At the 100 μm port, the use of a dedicated vacuum chamber or an ion trap should be possible. In a more detailed layout of the instrument it has to be investigated if an ion beam storage ring can be accommodated at this station. It would require an area of ~15×15 m^2 and this is likely to exceed the available surface area. At the 1 μm port, a similar sample chamber as the one described for the SQS 1 station will be used. It will allow experiments using atom, molecule or cluster beams. This vacuum chamber can be removed and space of 2×3 m^2 is foreseen for sample environment installations. Most of the experiments will absorb only a fraction of the incident beam intensity. It is, therefore, intended to use the transmitted beam for the purpose of diagnostics. A second gas monitor detector will be used to measure the transmission. At SQS 2 the spectral diagnostics determines mean photon energy, bandwidth, and higher harmonic content of the radiation. Diagnostics of time-domain properties should deliver the arrival-time required for pump-probe experiments using the visible laser. Finally, spatial measurements are required to determine beam location and spatial distribution. Since these measurements are usually destructive, they will be carried out in a dedicated set-up at the end of the line and before the beam stop.

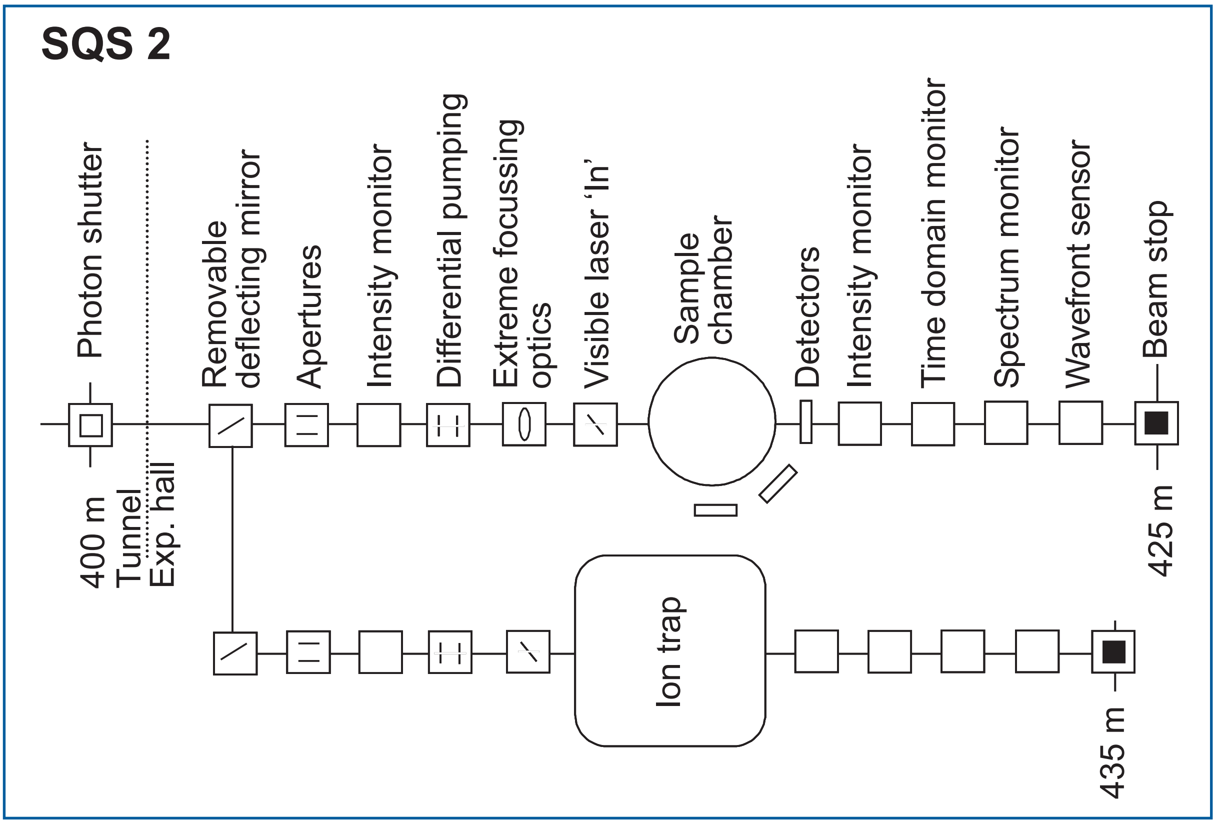

Figure 6.4.6 *Schematic layout of the SQS 2 station for "full" beam. The beam is directed either to the dedicated ion trap or a strong focusing optic, e.g. for studies of non-linear effects in atom, molecule or cluster beams.*

The use of visible laser radiation at both ports of the SQS 2 instrument will be possible through distribution from the independent laser room. The laser will be coupled into the vacuum in front of the sample chamber. Using mirrors with a central aperture the laser beam can propagate collinear with the XFEL beam.

Item	Purpose	Specification
Deflection mirror	Beam distribution to both ports, deflection angle 20 mrad	0.5 µrad angular stability, 0.2 µrad figure error, 0.1 nm surface roughness
Deflection mirror	Deflection angle 20 mrad	0.5 µrad angular stability, 0.2 µrad figure error, 0.1 nm surface roughness
Slits/Apertures	Beam definition, beam halo cleaning	1 µm accuracy, 0.25 µm repeatability
Intensity monitor	Measurement of incident photon flux	Transmissive (<5% absorption), single pulse measurement, relative accuracy $<10^{-3}$
Differential pumping	Separation of beamline and experiments vacuum	10^4 step for all elements
Focusing optics	~1 µm focusing for 0.25-3 keV	0.1 µrad angular stability
Laser inlet	Port-to-couple visible laser radiation into experimental chamber	Mirror with central hole, retractable
Sample chamber	Prepare and position samples, mounting of detectors, preparation for high gas loads	UHV, high pumping speed, x-y-z positioning
Detectors	Measurement of secondary particles, energy measurement, x-ray emission yields.	TOF for electrons/ions, imaging detector, x-ray spectrometer
Intensity monitor	Measurement of incident photon flux	Transmissive (<5% absorption), single pulse measurement, relative accuracy $<10^{-3}$
Spectral monitor	Measurement of harmonic content	Single pulse measurement, relative accuracy $<10^{-3}$
Time monitor	Measurement time domain properties	Single pulse measurement
Spatial monitor	Measurement of spatial distribution, focus size	Single pulse measurement
Ion trap		5×5 m^2 area
Alignment unit	Positioning and position verification	Permanently operating, accuracy ~100 µm
Lead hutch	Radiation protection	$10\times15\times4$ m^3 (W×L×H), ± 1° thermal stability
Control hutch	Operation of the instrument	Working environment (Noise, temperature, light)

Table 6.4.2 *Elements and specifications of the SQS 2 instrument.*

6.4.2 High Energy Density matter experiments

6.4.2.1 Scientific case

In 2003, two reports **[6-74, 6-75]** by the US National Academy of Science highlighted the field of High Energy Density (HED) physics as an important area for future research. This regime of matter is defined so that the energy density exceeds ~ 10^{11} Jm^{-3} (equivalent to a pressure of ~100 GPa). The regime of interest can be seen on the left-hand side of Figure 6.4.7, where we show the temperature-density phase-space for Hydrogen. Here we see that, for example, a solid density foil heated to a temperature of several eV would qualify. There are a variety of reasons for the widespread interest in HED physics. Further, the figure illustrate that conditions considered in the warm dense matter (WDM) regime occur in the cores of giant planets; for example, Jupiter's core is believed to be at a pressure of ~8000 GPa and a temperature in excess of 16,000 K. Moreover, other astrophysical objects such as accretion disks and astrophysical jets are in the hot dense matter (HDM) part of the HED regime **[6-76]**. On Earth, an important example is an inertial fusion capsule, the conditions for which are indicated as spherical compressions in the figure.

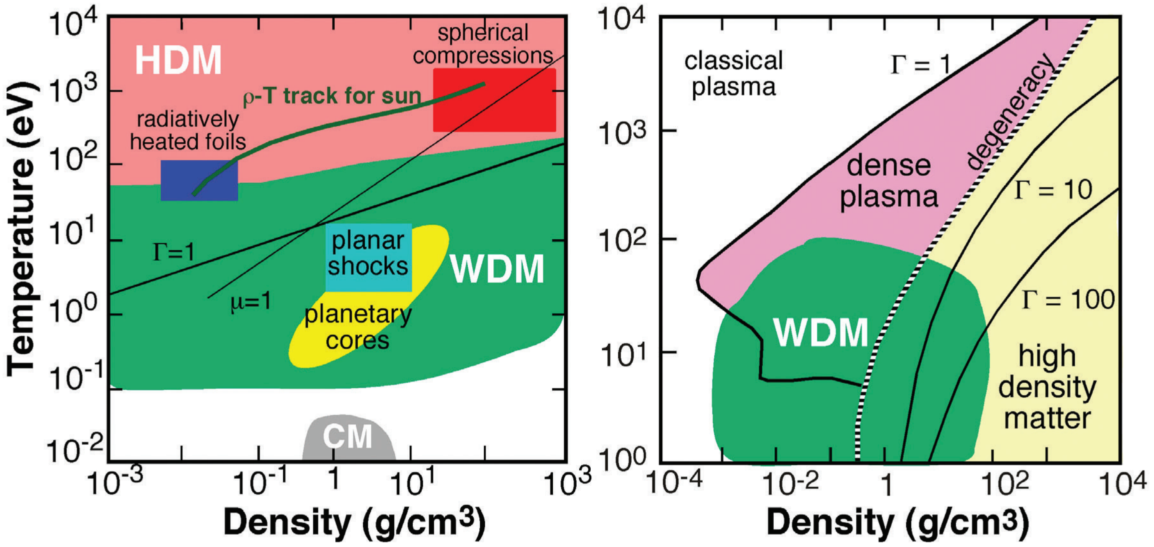

Figure 6.4.7 *Temperature-density phase-space diagrams for Hydrogen (left) and Aluminium (right) illustrating the various regions of matter relevant to the discussion of the HED regime. The hot dense matter and warm dense matter regions are indicated along with various examples of areas of application.*

Therefore, the HED regime, separated in HDM and WDM regions covers a vast part of phase-space, but importantly is not described by condensed matter approaches, a regime indicated by the "CM" at the bottom of the figure. In the right hand side of Figure 6.4.7 we show the temperature-density phase-space for Aluminium where it can be seen that there are some important physical characteristics to the WDM region. Firstly, the electrons are partially degenerate. The point at which degeneracy plays a role is indicated by the dashed line that cuts through the WDM region. As we see, for much of the WDM regime we cannot assume $kT<<E_F$ which is why condensed matter theoretical techniques are not suitable for describing this regime.

Note the Γ curves, where Γ is the ion-ion strong coupling parameter defined as $(Zxe)^2/R_i kT$ and represents the ratio of Coulomb energy between ions of average separation R_i and their thermal energy. When Γ_{ii} is of order unity, the ions are strongly correlated and perturbative plasma physics models are not applicable. Clearly this is a regime where theoretical modelling is not straightforward. It is also a regime where good experimental data is in short supply. The problem is illustrated in Figure 6.4.8, which shows the comparison between two models of the equation of state (EOS) which predict the pressure for a given density and temperature. The contours represent the percentage disagreement in the pressure for the two models of the EOS that are both as physically justified. Our full understanding of large planet formation and structure as well as the trajectory of inertial fusion capsule, depends on a better understanding of matter in the WDM and HDM regimes. There are currently experiments, using existing facilities, that can explore various aspects of the physics of HED matter **[6-76]**. These include Z-pinches, ion beams, short-pulse and high energy lasers. These all have their own advantages and limitations. Below, we discuss prospects for the XFEL, highlighting its own unique capabilities as both a creator and probe of HED matter. We shall see that, especially when combined with optical laser facilities, there is the prospect of a powerful and flexible research tool.

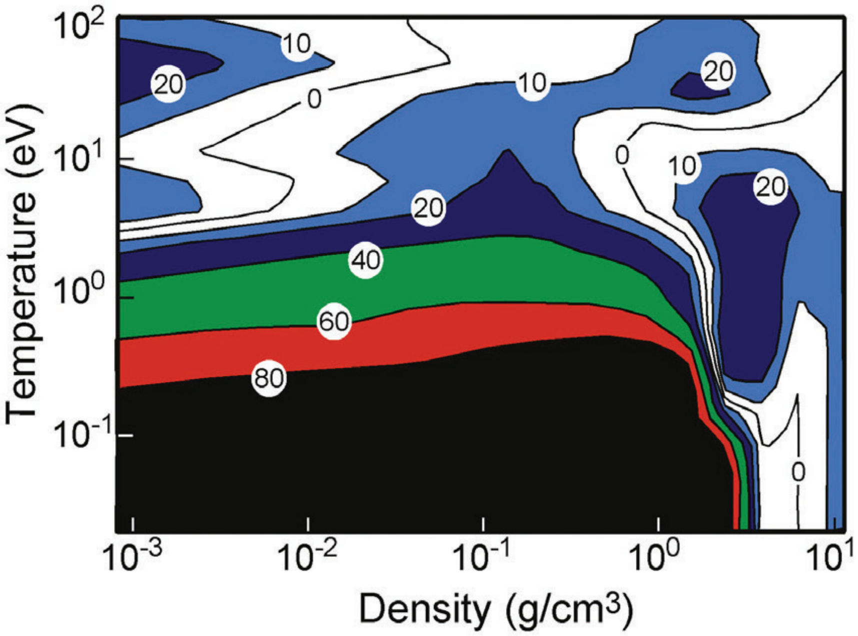

Figure 6.4.8 *Contour map of discrepancies in percent between models of the EOS for Aluminium.*

Prospects for XFEL radiation

The XFEL radiation will be above the plasma frequency of all possible densities that can be created and can penetrate a sample, heating it uniformly to create well-defined conditions that in many cases have not previously been available. As an example we show in Figure 6.4.9 the heating of an Aluminium sample with the proposed SASE 3 beam at 3.1 keV. In this example we assumed a focal spot of 60 µm, and it is envisaged that much tighter focusing and thus, higher temperatures will be available. We can see that the conditions across the foil are very uniform, with the temperature of ~6-10 eV corresponding to a deposited energy density of 7×10^{11} Jm^{-3}. As we will note later on, even higher energy densities (above 10^{14} Jm^{-3}) can, in fact, be created with the proposed XFEL beam parameters. The beam will be able to probe the internal structure of a sample in, for example, x-ray Thomson scatter experiments, giving unprecedented access to detailed physics at high density, where physics issues such as degeneracy and strong coupling come into play. Both as a creator and probe of HED samples, the XFEL has properties that will allow many detailed and previously impossible experiments. An initial list of proposed experiments and their technical requirements follows in the next sections.

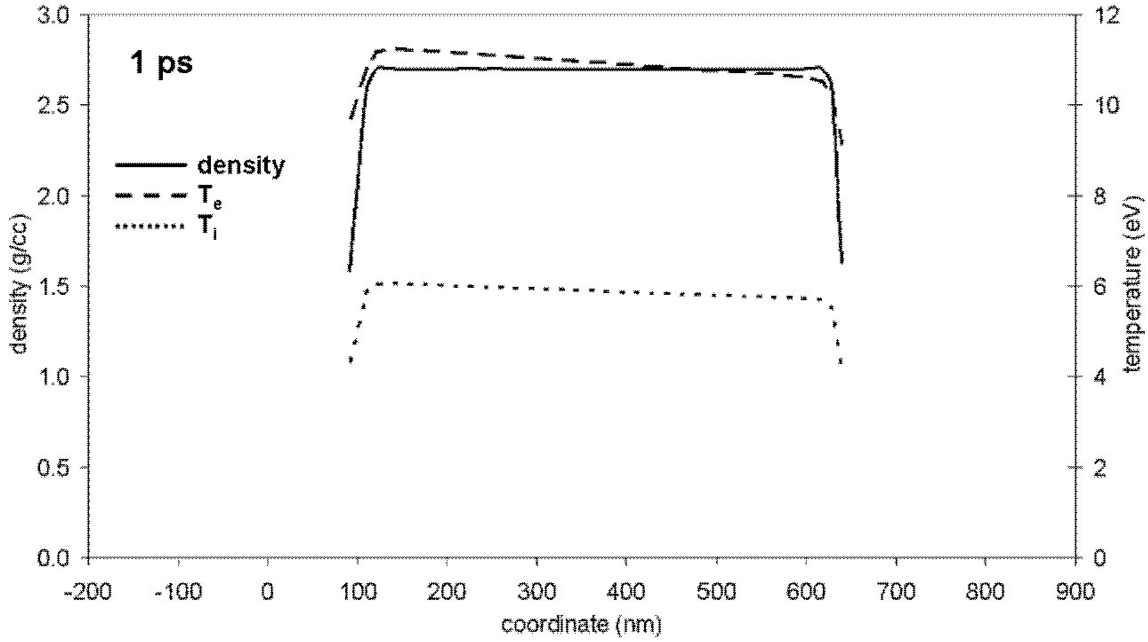

Figure 6.4.9 *Density and temperature of an XFEL heated Aluminium foil, 1 ps after heating. The foil is 0.55 µm thick and is heated by 3.1 keV radiation.*

Proposed experiments

The working group discussed several experimental proposals that would form the core of the initial experimental campaign classified into four broad categories:

- production and diagnosis of WDM;
- High Pressure States (HPS);
- production and diagnosis of HED Matter;
- plasma Spectroscopy (PS).

In the following sections we discuss these proposals. This is not an exhaustive list, giving only a reasonable flavour of the work discussed and proposed.

I. Warm dense matter experiments

As we saw, in Figure 6.4.9, it will be possible to create samples in the WDM regime, away from the shock Hugoniot. More importantly, they will be uniform well-defined samples. With monitoring of the incident, scattered and transmitted energy, we will obtain a measure of the absorbed energy density, so that meaningful comparison of theory and simulation can be made with experiment.

There will be several measurements that can be performed. If we heat a sample, such as the one depicted in Figure 6.4.9, with the XFEL, the timescale is short enough to give us essentially isochoric heating, depending on the intensity from ~1 eV to well over 100 eV. This will be followed by isentropic expansion, the trajectory for which will depend on the EOS. With a short pulse optical probe laser we can use techniques such as Fourier Domain Interferometry (FDI) **[6-77]** to get a very clear picture of the expansion velocity with time. Optical reflectivity measurements of the surface will be able to determine the conductivity of the sample. With the expansion well characterised and the knowledge that the sample is heated uniformly, the hydrodynamic conditions of density and temperature can be characterised and meaningful comparison to simulations performed.

A unique and productive class of experiment will use the XFEL as both pump and probe. We will separate a portion of the XFEL beam by use of grazing angle reflectors (~0.5° for C at 3keV), allowing us to use a portion of the XFEL beam as a time-delayed probe to measure the x-ray absorption for HDM where there are important effects on the energy level structure of the atoms and ions in the system. For dense plasmas where the strong coupling parameter between ions, Γ_{ii}, is much larger than unity, these effects are difficult to model theoretically **[6-78]**.

The XFEL is particularly suited to experiments on x-ray Thomson scattering. As the heating of the solid occurs, the electron density and temperature will evolve rapidly. This will affect the spectral signature of the scattering from the free and weakly bound electrons. Obtaining the scatter spectrum with, for example, intensity will be an important test of simulation. A more controlled approach will be to use a pump-probe technique, often by use of an optical laser to generate a preformed uniform sample from a thin foil. The point is well illustrated by Figure 6.4.10, which shows simulated x-ray scattering spectra for a WDM sample. The non-collective scatter is not model-dependent and by looking at both bound and free contributions, the electron density and temperature can be deduced. The forward, collective scatter does depend on whether local field corrections are applied to the free electron contributions. With such data we would be carrying out definitive experiments on fundamental issues in plasma physics, but good data will rely heavily on the availability of a very bright, narrow band x-ray scatter source with short duration, which is why the XFEL so neatly and uniquely fits the bill.

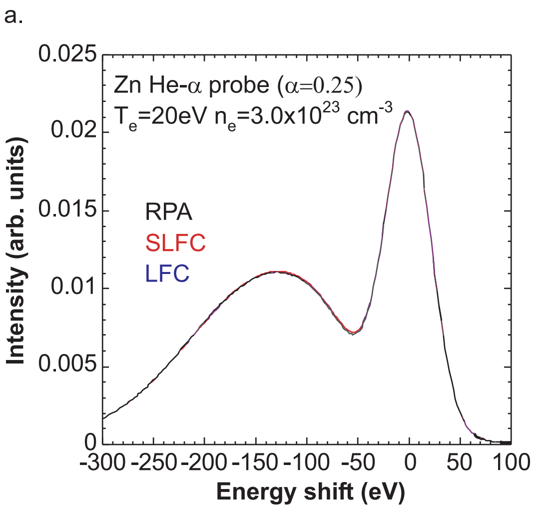

Figure 6.4.10: *Sample x-ray scattering structure factors. In (a) we see that the backscatter case (α<1) is not model dependent but can be used to diagnose temperature. The forward (collective regime, α>1) scatter (b) is model dependent.*

An important issue in the development of WDM experiments is equilibration **[6-79]**. As it is the electrons that are photo-excited by the absorption of x-rays these will be initially not described by a Maxwell-Boltzmann velocity distribution at a well-defined temperature. They transfer energy to ions via collisions in the matter; in Figure 6.4.9 we see the ions lag behind in temperature when the Spitzer-Brysk electron-ion collision rates are used. However, the use of a simple formulation for the electron-ion collision rate will be incorrect as the bound states of the ion will play a dominant role in the thermalisation process when the density is high and the temperature is low. For example, the sample starts as a solid with a lattice structure and the timescale for the ions to loosen their lattice-like arrangement may be several picoseconds.

One way in which we can probe the microscopic structure of the sample is to use angle-resolved x-ray scattering **[6-80]**. For example, we propose to use the SASE 3 beam at 3.1 keV to heat the sample. There are also second and third harmonics of the beam at about 10^{-3}-10^{-2} of fundamental intensity. By developing techniques for separating these, it should be possible to pump with the fundamental and probe with the harmonics. Although there are reduced photon numbers in the harmonics this will still be sufficient to provide accurate measurements. Further, the higher energy harmonics reduces absorption so that the scattered signal is not diminished nor does it perturb the sample. In this way, we propose to probe the evolution of the ion-ion structure of the sample as it is heated to WDM conditions **[6-81]**.

II. Bragg diffraction from surfaces

In particular, HED experiments aim to investigate the interaction of the intense XFEL radiation with the samples. The onset of plasma formation is of importance, however, to other techniques and an in-depth understanding of these processes is a key element in our ability to estimate the damage in optical components. The latest experiments at the FLASH facility at DESY have shown that a multilayer mirror can still function when irradiated at fluences far exceeding the conventional damage threshold, provided the pulses are short enough so that damage only occurs after the pulse has ended. However, this damage occurs on a single shot. Of particular importance is the investigation of processes by which matter is damaged in a cumulative manner. Recent molecular dynamics simulations by Mazevet et al. **[6-82]** have indicated that when the electrons in a solid are heated to a few eV, the timescale for the ions to move out of a lattice structure is several picoseconds. With the keV photon regime available at the XFEL, the principal mechanism of energy absorption will be inner shell photo-ionisation (the emission from the ions might be used as an observable). Some of the ions evolving from this single photon absorption process may lead to damage. An investigation of the structural processes following absorption of x-ray photons at much higher fluence will provide the necessary input for modelling such single photon damage processes. By comparing intense IR laser and XFEL radiation it will be possible to study the differences in energy transfer to the ions for both types of radiation.

In this proposal the instantaneous change of properties of solid samples irradiated by intense, femtosecond x-ray radiation will be investigated by Bragg diffraction. With sample crystals thinner than the extinction depth, diffraction will be observable, both in Bragg or Laue geometry and, indeed, furthermore, diffuse scattering could also be monitored. Measurements will be carried out as a function of XFEL radiation intensity and time-resolved using split-and-delay techniques of the XFEL beam.

III. Magnetic field generation and probing

This project is related to the idea of fast ignitor fusion, in which an ultra-high intensity laser pulse interacts with a compressed fusion pellet and the fast electrons generated ignite the core of the compressed fuel **[6-83]** to achieve ignition with much lower compression (and thus more hydrodynamic stability) than would be achieved with conventional laser-fusion. An important part of this concept is the generation of ultra-high magnetic fields, in the order of 100 T, in the interaction **[6-84]**. These fields are short-lived and exist over a small spatial scale and so are difficult to probe.

It is proposed that, with the XFEL synchronised to an ultra-short pulse (<100 fs) optical laser, capable of intensity $>10^{18}$ W/cm^2 on target, the XFEL can act as a probe of the high density plasma regime where the magnetic fields exist. By probing the laser-heated sample with an XFEL beam, the propagation of the electron beam into the solid can be observed. This can be carried out normal to the interaction direction of the optical beam by the use of narrow slab targets. As the electron beam propagates, the ionisation of the solid leads to changes in the refractive index leading to refraction effects that can be measured interferometrically.

With current technology, it is possible to build an interferometer that operates in the keV x-ray regime. Such an instrument would enable interferometric measurements of the electron density in the interaction region, in the same manner as has been achieved optically and in the soft x-ray regime. If a light beam is well polarised, then, on passing through the magnetic field generated, the plane of polarisation can be rotated by the

Faraday effect if the propagation is parallel/anti-parallel to the field direction or by the Cotton-Mouton effect if it is normal to the field. These techniques have previously been used to measure magnetic fields in laser-plasmas with optical probing. With an XFEL we can probe the high density regime well above the optical laser critical density. Further, it is possible that polarisation-dependent absorption changes will be easier to observe in the x-ray signal than a rotation of the polarisation. In this regime, the gradients in the plasma are high and, for example, the $\nabla N \times \nabla T$ magnetic field generation mechanism may lead to very high fields.

IV. High energy density experiments and plasma spectroscopy

Focusing the XFEL beam to less than 5 μm, will make it possible to reach intensities on target in excess of 10^{17} W/cm^2. This will make it possible to heat solid density samples to temperatures in excess of 300 eV with pressures in the 1 Gbar range. As for the WDM cases, we can use optical reflection spectroscopy, such as FDI, to diagnose the expansion of the plasma. At this temperature, the emission in the keV photon region can be detected with crystal spectroscopy and we expect to be able to observe some important spectroscopic effects such as line merging and continuum lowering effects on K-shell spectra at very high plasma densities in well defined samples – this latter criterion being most difficult to achieve in present-day laser-plasma experiments. One important type of experiment, not available with any other facility, will be to pump electronic transitions of ions in a dense plasma, making use of the tunable XFEL photon energy. This is illustrated schematically in Figure 6.4.11. and is a very important type of experiment as it will allow the investigation of the effect of plasma environment on transition rates between states. This is something that is expected to be important in the formation of emission spectra, but is, at present, very difficult to include in collisional-radiative models because there are no existing data. In Figure 6.4.12 we can see a simulation carried out assuming an Aluminium target is heated with an IR laser pulse to form a uniaxially constrained plume and at some later time a particular transition is pumped by the XFEL tuned to the transition energy. As the upper state is populated, collisions redistribute the electrons to other bound levels of the Helium-like ion and ionisation forms H-like ions. The rate at which this happens and hence, the resultant spectrum depends on the plasma electron density, which can be determined experimentally.

For this type of experiment to work, it is important that the pumping rate of the transitions during the pulse exceeds the rate of spontaneous decay and auto-ionisation of ~10^{12}-10^{14}s^{-1}. For the high brightness XFEL, radiation pump rates well in excess of this will be possible.

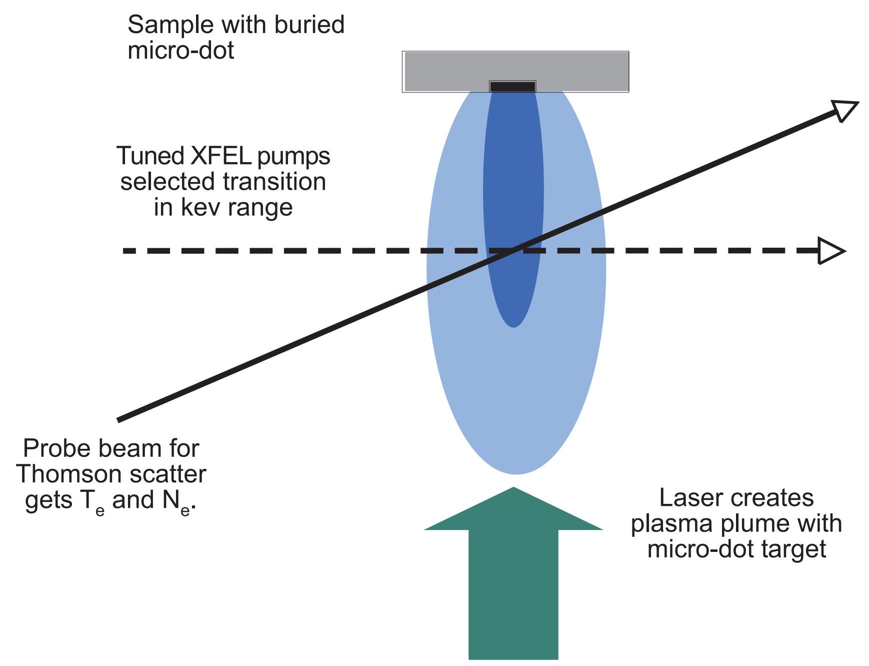

Figure 6.4.11 *Experimental arrangement for spectroscopy experiments. The burial of a microdot in a matrix helps to better define the plasma conditions at the time and place of excitation by the XFEL pump. Time- and space-resolved spectroscopy will be used to diagnose the emission.*

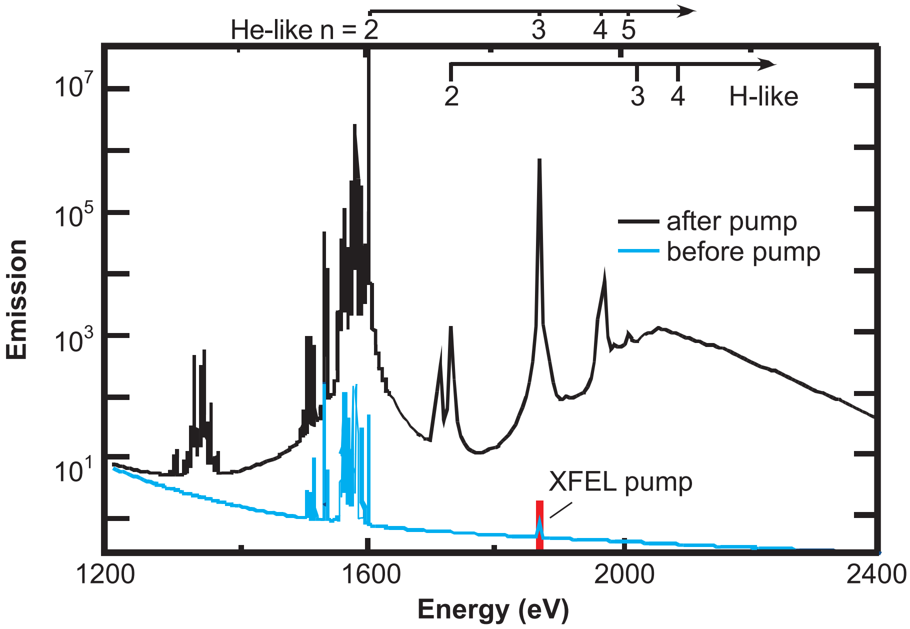

Figure 6.4.12 *Simulation of change to emission spectrum for an Aluminium plasma pumped with an XFEL tuned to 1,869 eV in order to pump the Helium-like $1s^2$-1s3p transition.*

V. Hollow ion emission

The XFEL radiation will enable the creation of hollow ion (HI) states, i.e., atoms/ions with vacancies in the inner core shells, in dense plasmas with atomic population densities more than 10 orders of magnitude higher than in traditional laser-produced plasma experiments. The subsequent x-ray emission, which will escape the extremely high-density plasmas without detrimental absorption, will allow new and innovative studies of atomic systems in intense Coulomb fields and importantly, can form the basis for a diagnostic of the local plasma conditions **[6-85]**.

The simulation of the emission from atoms and ions provides one of the most unambiguous and powerful methods for the understanding of basic phenomena in laboratory and astrophysical plasmas **[6-86 – 6-90]**. An important underlying assumption is that atomic physics is sufficiently well known to accurately predict the spectral signatures. In high-density plasmas, however, particle correlations will alter the statistical mechanics of the free and bound states so that the internal states of the system are dependent on the plasma parameters: Continuum lowering, energy level modification and altered spontaneous transition may occur **[6-91]**. In the extreme case of WDM **[6-92]**, the modifications of the outer bound electrons are so strong, that a perturbative approach for predicting the emission from these shells is not possible. Furthermore, there exists no theory to predict the modification of the internal structure that in the limit leads to complete disappearance, which is mandatory for calculating the corresponding spectroscopy for these extreme states. However, although these extreme states play a role in many high energy density experiments, creating WDM in a manner that can be quantified is not readily available.

X-ray transitions of HIs, i.e., $K^0L^n \rightarrow K^1L^{n-1}+h\nu^{\vec{Q}}$, connect the most strongly bound states in these systems **[6-93]**. WDM effects can, therefore, be studied as perturbations to these stable transitions. The basic scheme for a relevant pump-probe experiment is shown in Figure 6.4.11, where a visible laser creates a dense plasma on a picoseconds timescale that is then probed by the 100 fs duration XFEL pulse. The time-dependent simulation of the radiative properties using the MARIA-code **[6-94]** involves population kinetics together with radiation physics. Figure 6.4.13 shows the time-dependent line emission of Magnesium from this pump-probe experiment. Figure 6.4.13 (a) shows a simulation where all processes are included except photoionisation processes from and to the states K^0L^2, $K^0L^1M^1$, K^0L^3, $K^0L^2M^1$, while Figure 6.4.13 (b) contains all processes.

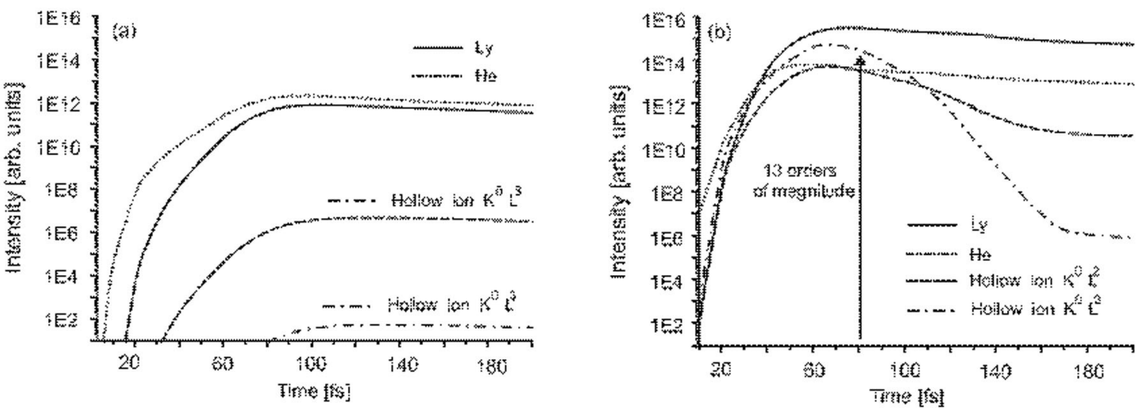

Figure 6.4.13 *Simulation of the transient line emission of magnesium ions in a pump-probe driven configuration using the MARIA code* **[6-25]**. *The transitions depicted are: Hydrogen-like 1s-2p (Ly_α), Helium-like 1s2-1s2p (He_α), and the HI transitions $K^0L^2 \rightarrow K^1L^1$, $K^0L^3 \rightarrow K^1L^2$. Parameters for the simulation were: $n_e=10^{21}$ cm^{-3}, $kT_e=30$ eV, $L_{eff}=30$ µm, $I=9.2x10^{16}$ W/cm^2, $\tau_{XFEL}=100$ fs, E=3.1 keV, $\Delta E=6.2$ eV. (a) without photoionisation channels from and to the states K^0L^2, $K^0L^1M^1$, K^0L^3, $K^0L^2M^1$, (b) with all photoionisation channels.*

The comparison illustrates the essential phenomena: inner-shell photoionisations from autoionising levels are the most important channels. Due to large autoionising rates – ~10^{12}-10^{15} s^{-1} – the HI states rapidly decay, however, the 100 fs x-ray pulse is sufficiently intense to initiate a chain reaction of inner-shell driven processes before destruction by autoionisation. As can be seen from the Figure 6.4.13 the x-ray pulse increases the HI emission by more than 13 orders of magnitude **[6-85]** to the level of the resonance line intensity (compare with Ly_α), which is well known to be observable **[6-95]**. That the x-ray pulse drives a sequence of photoionisation processes efficiently, can be seen from the intensity rise of Ly_α. That is, the dominant radiative process from the outer shell is photoionisation: $K^0L^2+h\nu \rightarrow K^0L^1+e$.

We now consider potential diagnostic applications of HI spectroscopy: First, we note that the standard application of Stark broadening for density diagnostics may be difficult as the interaction of intense radiation fields with the ions will result in a strong broadening of line transitions **[6-96]**. In low-density plasmas, this will limit the possible spectral resolution. Indeed, we find that for $I \approx 10^{13}$ W/cm^2 considerable broadening occurs, while an intensity of $I=10^{12}$ W/cm^2 the spectral resolution is radiation field limited to $\Delta\lambda/\lambda \sim 5\times10^{-4}$. However, it is important that the XFEL pulse initiates HI emissions where the relative intensity of the HI transitions $K^0L^n \rightarrow K^1L^{n-1}+h\nu$ provide information about the electron temperature and <Z> **[6-85]**. This in-situ diagnostic information for the weakly coupled regime also provides time-resolved information in the strongly coupled plasma regime. That the emission is strong only during the XFEL pulse and will have observable intensity indicates that we have a temperature-sensitive diagnostic of HED systems, with a 100 ps temporal resolution. Moreover, compared to usual optical femtosecond-laser pulses, which create hot electrons that effect the radiative properties employed for diagnostics, the XFEL pulse does not create hot electrons as it is in the classical regime with a small parameter $I\lambda^2$ **[6-97]**.

VI. Radiation hydrodynamics and "forest fire" experiments

Radiation hydrodynamics is a subject of extreme interest in astrophysics **[6-76]**. In recent years, there has been a concerted effort to test ideas about astrophysical plasmas **[6-98]** with experiments in the laboratory, so called laboratory astrophysics. It has been proposed that by focusing a high-power short-pulse optical laser into a gaseous cluster target **[6-99]**, a strong blast wave can be created in which radiation transport may play a key role. It was proposed that if such a target were to be produced, the XFEL beam would be used to modify the parameters by photo-ionisation of the region ahead of the blast wave. The effects on the propagation of the blast wave (for example, the production of various types of instability due to pre-ionisation) would then be a test of the simulations that are naturally complex as they involve hydrodynamics coupled to radiation transport. Such an experiment would require not only a high-power short-pulse for creation of the blast wave but an ancillary probe pulse for carrying optical interferometry of the blast region. Gas jet targets for the creation of cluster targets will also be needed, and the technology is readily available.

One type of experiment that may benefit from the short wavelength and duration of the XFEL is the investigation of so-called "forest fire" phenomena **[6-100]**. This is an effect that is predicted, but experimentally untested. It should occur when a dielectric is exposed to a high intensity optical pulse of only a few cycles duration – perhaps a 10 fs IR pulse. The usual avalanche mechanism of ionisation; where multi-photon ionisation free a few "seed" electrons, absorb energy by inverse *Bremsstrahlung* and then, when they are energetic enough, ionise further electrons across the band-gap, cannot occur on such a short timescale. Despite this, it is seen (**6-87**, and references cited therein) that the refractive index of dielectrics such as fused Silica, can be altered permanently by pulses of 30-50 fs at intensities well below the expected threshold.

The "forest fire" idea is that ionisation is enhanced locally when an electron is initially removed from a nucleus, for example, in a rare gas cluster under IR laser irradiation. What is predicted to happen is that, in the so called "tunneling regime" when the ionisation potential, I_p, is much smaller than the ponderomotive potential, U_p, the tunneling rate for electrons to escape is proportional to $\exp(1/E_0\cos\omega t)$, where E_0 is the amplitude of the electric field applied by the laser. If the electric field due to a "hole" created by initial removal of an electron is added, we see an exponential enhancement of the ionisation rate locally.

It is then predicted that small "islands" of ionisation will form and spread in a manner reminiscent of forest fires – hence the name. The spatial scale will be sub-micron and thus, it will be suitable to use the XFEL as a probe of the microscopic structure by, for example, angularly resolved Mie scattering from clusters.

VII. High pressure states of matter

Our current understanding of the fundamental physics of shock compression in condensed matter is still far from complete. Over the past few years there has been some progress made by using nanosecond sources of x-rays to probe crystals compressed using high-power optical lasers **[6-101]**, however the ultimate time-scales of the essential physics of interest – i.e. phase transformation, dislocation generation and flow, and plastic relaxation, occurs on the picosecond, or sub-picosecond level: a regime that can only be accessed by the XFEL. Thus, there is still a long way to go in developing this understanding. The XFEL provides a unique source for such experiments. With keV photons in a well collimated beam, it is ideally suited to probing shocks driven by optical lasers.

What we propose is that a nanosecond laser with ~100 J per pulse is used to generate shocks in single-crystal solid samples (e.g. single crystals of Copper to study plasticity (as there is no phase transition before shock-melt), Iron to study shock-induced Martensitic transitions, Lead to study shock-melting, etc). Optical reflection techniques such as Velocity Interferometry System for Any Reflector (VISAR) can be used to diagnose the shock speed and particle velocity on exit of the shock, thus providing traditional Hugoniot data. The XFEL beam will provide a means to probe the structure of the material after compression in the bulk of the sample. The excellent time resolution available will allow the observation of changes in structure due to phase changes to be recorded in unprecedented detail, and, importantly, on a timescale shorter than a phonon period. For example, the α-ε phase transition in Iron (body-centred cubic to hexagonal close-packed) has been observed in laser-shocked sample **[6-102]**. Molecular dynamics simulations suggest this occurs in ~1 ps timescale, longer than the XFEL pulse duration, but far shorter than the resolution that laser-plasma sources afford. The high flux of the XFEL beam will allow not only the traditional Bragg diffraction peaks to be observed, but the small angle and diffuse scattering (for example, from stacking faults) will be observable, adding more detail to our picture of materials under pressure and high strain rates. In particular, we believe it will be possible to directly measure stacking fault densities during shock compression, something that has hitherto been unobtainable, despite the fact that high transient dislocation densities are thought to be the means by which plastic deformation can occur on such short time-scales. In Figure 6.4.14(a) we see an example of an experiment that can be used to determine directly the compression profile in a shock wave. The spatial coherence of the source will be evident in features caused by refraction in the very steep gradients of the shock front. Some sample data using laser produced x-ray sources is seen in Figure 6.4.14(b.). With an XFEL, unprecedented temporal resolution will allow the compression, speed of the shock, and with VISAR, the particle velocity to be determined simultaneously. With pulse shaping capability added, it will be possible to investigate isentropic compressions as well as shock Hugoniots.

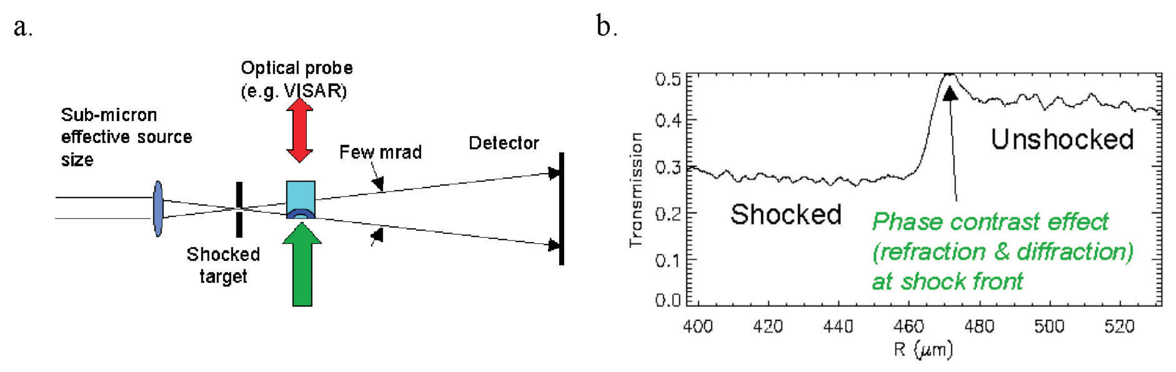

Figure 6.4.14 *Schematic of shock wave probing experiment (a). (b) shows a point projection profile of a shock front taken with a 10 micron x-ray source. Phase contrast effects are evident at the shock front. Using spatially coherent XFEL radiation, phase contrast effects will provide more information.*

6.4.2.2 Instrument requirements

From the specific needs of the experiments described above the main requirements for an instrument for investigation of HED matter can be derived. They concern the performance of the light source, the diagnostic equipment of the beamlines and their infrastructure. The experiments described in this section require tunable XFEL radiation of a relatively wide spectral range from ~0.6 to 12 keV. None of the European XFEL beamlines provides the entire photon energy range in the fundamental and the use of SASE 2 and SASE 3 beamlines is proposed instead.

Spectral radiation properties

Experiments in this field ask for nearly the entire photon energy range provided at the European XFEL Facility. Whereas the lower photon energies will mainly be used in experiments investigating the interaction of intense radiation with matter (Experiments I., III. and IV. above), the request for hard x-ray radiation follows from the needs in diffraction experiments to investigate structural properties of plasmas following laser heating or pressure shocks (Experiments IV. and V.). Also, plasma diagnostics using Thomson scattering techniques will benefit from higher photon energies (Experiments I. and IV). Real tunability is required in the plasma spectroscopy and hollow ion experiments where specific transitions will be investigated (Experiments VI. and V.). For these experiments, a range from 0.65 to 6.5 keV has been requested. In most experiments the natural bandwidth of XFEL radiation will be sufficient. Even for spectroscopy purposes this resolution should be sufficient, so that no monochromators are requested. Reduction or selection of higher order harmonics is a different topic that requires attention for these experiments. Higher harmonic content may be reduced to reasonable values using mirror cut-offs. Selection, however, requires spectral dispersion using gratings, i.e., for the soft x-ray regime, or very thin crystals in transmission geometry. Whereas the soft x-ray case has been investigated already, a separation of hard x-rays will require some R&D.

Beam dimensions

The requested x-ray beam size is determined, in most cases, by required intensity and the combination with visible laser beams. Typical beam sizes at the sample position are 1, 10, or 100 µm to reach the different intensity levels. If experiments use visible laser imaging or excitation, one has to take the spatial resolution of the visible laser beam of a few microns into account. Focusing below 1 µm will further enhance the available intensity, but diagnostics of such sub-micron plasmas will be extremely challenging.

Time domain requirements

These experiments will fully exploit the 100 fs time structure of XFEL radiation. It is, however, expected that the substructure of the pulses will not influence the excitation and probing processes. Since the HED experiments are usually destructive, such that the sample evaporates after being irradiated by the XFEL beam or the high-intensity visible laser beam, sample replacement is expected to be a time-determining parameter (see below). Synchronisation is generally linked to the use of visible lasers and will be discussed in the corresponding section. However, a synchronisation of ~100 fs will be required for the operation of x-ray streak cameras (XSC).

Photon diagnostics requirements

All experiments will need good diagnostic equipment to measure the photon beam intensity on a pulse-to-pulse basis. To estimate the intensity in W/cm^2 at the sample with a high degree of confidence, one must also consider the measurement of the pulse duration and of the spatial properties at the focus. The spectral diagnostics should provide the mean photon energy and the content of higher harmonic radiation. All measurement must be available on a pulse-to-pulse basis.

Sample manipulation and environment

Samples are thin foils of varying materials for the WDM experiments, thicker slab-like samples varying materials for the HDM and higher pressure experiments, and gas jets for the radiation hydrodynamics experiments. Many of the proposed experiments will require multiple shots to be taken, both to gather a scan of a particular parameter (for example, intensity on target) and to collect sufficient signal photons in experiments where the signal may be weak (for example, scattering). In the case of solids it will be necessary to move the sample to expose a fresh surface. Using the repetition rate of 1-10 Hz for the XFEL, we will need to be able to move the sample quickly but also maintain the alignment, in particular the focal spot size in the case where tight focusing onto target is required. It is possible to design automated systems that use a three-point triangulation in 3-D to define the plane in which a flat foil sits **[6-103]**. It can then move the foil automatically to maintain the exposed part at a fixed focal plane for the incident beam. The only constraint is that the system assumes that the surface is flat. It is clear that, depending on the nature of the experiment, some methods of moving targets into position and monitoring their position relative to the focal plane of the XFEL and/or the optical laser systems will need to be developed.

A capability for insertion of fresh targets without breaking vacuum will also be required. For some experiments, the presence of surface contaminants, such as oxide layers, will be undesirable as they may modify the interaction with the XFEL or the optical probe laser (as in FDI **[6-77]**). Since oxide layers can form very rapidly, some target preparation facilities close to the target area will be needed. Potentially target "cleaning" may need to be carried out in-situ, e.g. low fluence ablation of the top layers or RF cleaning (as sometimes used for compression gratings in laser systems **[6-104]**). In these experiments differential pumping is required to improve experiments vacuum against beamline vacuum.

Detector requirements

It is clear that x-ray spectroscopy plays a significant role in several experiments, i.e., in the class of experiments proposed above under Topics I., III., IV., and V., and it makes sense to have common facilities. High resolution x-ray spectrometers based on crystals are available with resolutions from ~10^3 to in excess of 10^4. In order to achieve high signal fluxes with single shot, one should employ either spherically or toroidally curved crystals **[6-105]** which will have a high flux gathering power and, in addition, can be used for imaging of the plasma where appropriate. These crystals should be coupled to CCD detection systems that are efficient in the keV x-ray region and have good pixel resolution of ~10 µm. Detectors with 2K×2K pixels are commercially available, but frame rates larger than 10 Hz for 16-bit dynamics should be targeted. In the keV photon region this gives single photon detection capability.

Furthermore, emission in the XUV regime will be of interest for the same group of experiments. There are high efficiency XUV spectrometers that operate with variable line-space gratings to give a flat field of spectral focusing suitable for use with a back-thinned CCD as detector **[6-106]**. These spectrometers can operate in the 300-2,000 eV regime and can achieve spectral resolutions up to ~10^3.

If small single-pulse signal levels are expected, integration over more than one pulse may be required. In these cases, the background noise of the CCD detectors will limit the signal-to-noise ratio if one does not cool the CCD chip. This can be done fairly routinely to 80°C. However, if the CCD sits inside the vacuum, as is often the case, cooling using water or cold gas is required. There is also a problem of condensation, of ice or hydrocarbon, onto the chip that may cause damage, so it is essential to prevent this. The use of "cold fingers" with liquid Nitrogen (N_2) as a coolant prior to cooling the chip, may serve to "clean" up the vacuum by causing condensation onto the "cold finger".

To allow time-resolved investigation of emission, e.g. in Experiments I., IV., and V., the use of streak cameras is proposed. Using these detectors it is important to improve the time-resolution, efficiency and stability of these systems. The required R&D work of ultrafast XSCs will be described in Section 6.5.4.

Visible laser requirements

Many of the experiments outlined in this section make use of optical laser pulses synchronised to the XFEL beam. In some experiments, the optical pulse is used either to generate a sample to be probed or pumped by the XFEL, e.g. in III., IV., V., VI. and VII.;

in others it is the optical pulse that probes the XFEL generated sample, e.g. in I. and IV. The required lasers can be distinguished by their energy. For probing XFEL-generated plasmas, ultra-short pulses (~30 fs) with energy of about 10 mJ are required. Operated at 1 to 10 kHz, this laser system can also be used for high-order harmonic generation (HHG) radiation. High contrast of ~10^{10} between the main pulse and ASE emission is required for "clean" interaction with the sample.

For experiments where the optical laser pumps the sample on ultra-short timescales, a sub-100 fs laser with energy capability of 10 J per pulse will be desirable. This is possible using the same laser front-end as for the above system, but with a much reduced repetition rate of ~10 Hz **[6-107]**. Basically, the difference would be additional amplifier stages. The beam size is likely to be 5-10 cm diameter and focusing off-axis parabolas will be required to focus to >10^{19} Wcm^{-2}. An important requirement will be suppression of pre-pulses, as ASE and non-linear chirp components would deposit energy onto the surface prior to the main pulse. A viable method to reach this suppression has been conversion to second harmonic requiring large area (5-10 cm diameter) second harmonic crystals with sub-mm thickness and high optical quality.

The third system would deliver up to 100 J sub-nanosecond pulses at 10 Hz repetition rate for generation of shocks in condensed matter as proposed in Section 6.4.2.1, Experiment VII. above. A fibre front-end is desirable to shape the pulse in order to optimise the pressure front. This technology currently exists and adaptive optics can be used to ensure a good quality of beam profile. This is important if uniform conditions are to be generated over a focal spot away from tight focus. To this end, beam relay optics and smoothing technology (eg phase ZPs) will be required. It may be possible that the requirements for sub-100 fs and sub-nanosecond can be fulfilled by a single laser system. Current chirped pulse amplification (CPA) technology, used to generate 30 fs pulses, requires the laser to generate a 'stretched' pulse of sub-nanosecond duration. If this is used as the long pulse option, all that is required subsequently is amplification to high energy. However, since versatility should be maintained and noting that, for some experiments, both types of beam will be required simultaneously, it is currently considered better to have the two systems independent of each other. In addition to the operational aspect, it is unlikely that two dedicated systems are more expensive than a single system capable of doing everything.

The optical lasers providing sub-100 fs pulses require precise synchronisation with the FEL beam in the order of ~10 fs. If such synchronisation will not be possible, diagnostic tools to measure the time delay to similar accuracy are required.

6.4.2.3 Realisation of the instrument

From their requirements, the HED experiments require two instruments: one at SASE 3 (HED 1 – Tunable soft x-rays) and the other at SASE 2 (HED 2 – Tunable hard x-rays). The SASE 3 beamline enables experiments at photon energies up to 3,100 eV. Those experiments requiring higher photon energies, i.e. 3.1 to 6.5 keV for HI spectroscopy and ~12.4 keV for diffraction measurements in proposals I., II., IV., and VII. will be best placed at the SASE 2 beamline. For both instruments additional monochromatisation is not necessary and beam transport using mirrors only will be considered. The corresponding beam transports in the SASE 2 and SASE 3 beamlines have been described in Section 6.2.4.2 and 6.2.4.3, respectively. Both instruments will require focusing the XFEL radiation. Moderate focusing to beam sizes in the order 100 µm is achieved by using a focusing element near the location of the off-set mirrors. Further focusing to 10 µm and smaller beam sizes will be integrated in the instruments and is described below. An important requirement of the design of the SASE 3 beamline is the ability to carry out pump-probe experiments using first and third harmonic radiation. This requires the transport of radiation with photon energies as high as 9.3 keV to the experimental hall. Due to the cut-off by the mirrors (operating at 10 mrad grazing angle at SASE 3), a set of different mirrors is likely to be required here. For SASE 2 this requirement applies only to the lowest photon energies of 3-4 keV.

HED 1: Tunable soft x-rays

Two mirrors at a grazing angle of the order 10 mrad will be used to deflect the beam away from the forward beam direction. At the chosen sample location inside the experimental hall, a focal spot size of the x-ray beam of ~100 µm will be available. This focus is achieved by using one of the offset mirrors. To enable focusing in the order 10 µm, it is proposed to use one of the beam deflection mirrors with a demagnification of 20. For micron or sub-micron focusing, special optics need to be employed that are positioned very close to the sample, providing a demagnification of 100 or higher. The HED 1 instrument will be required to carry out a large part of the experiments investigating the interaction of intense high energy radiation with matter described in Section 6.4.2.1, I., III., IV., and V. In addition to x-ray emission, many of these experiments use optical diagnostics.

The following elements belong to the HED 1 instrument inside the experimental hall. They are also depicted in the schematic layout of that instrument in Figure 6.4.15 and are listed in Table 6.4.3. Collimating apertures in front of the experimental chamber remove scattered radiation from the beam. A gas photon flux monitor (see Section 6.3.2.1) will follow before a differential pumping section separates the beamline from the UHV vacuum chamber for experiments. Given the energy range of this beamline, vacuum separation by means of windows is very unlikely.

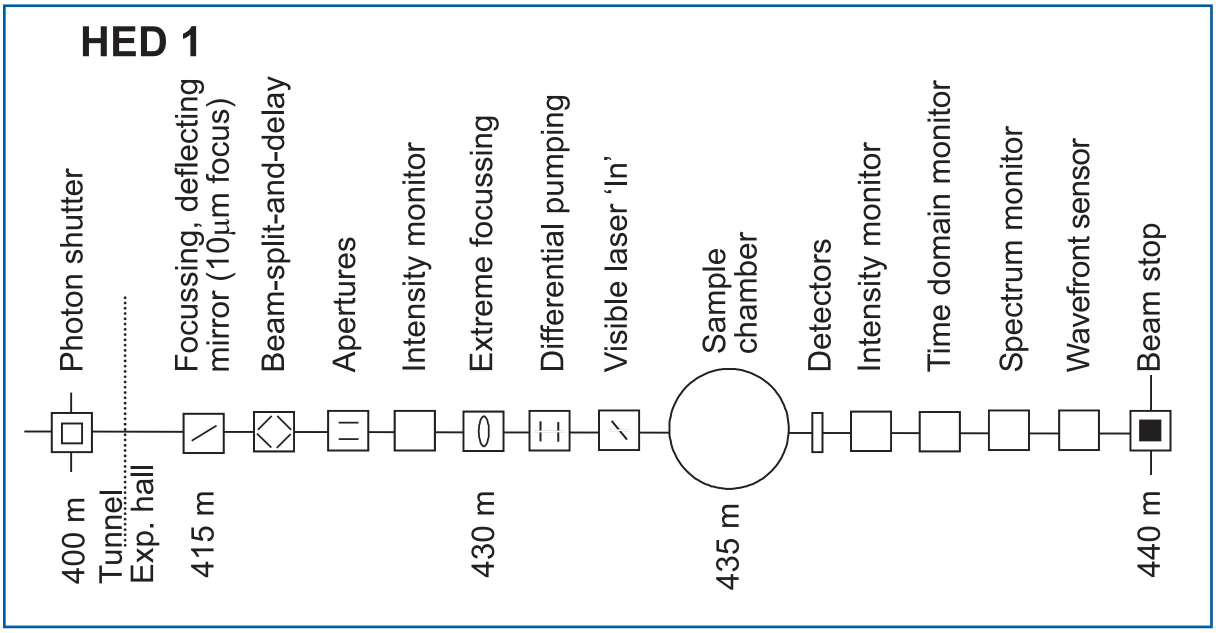

Figure 6.4.15 *Schematic layout of the HED 1 station, intended to be located at the SASE 3 beamline. The beam is directed straight to the sample chamber. Various focusing options will be available.*

The sample chamber will be equipped with a high-accuracy sample manipulator allowing x-y-z movements and rotation around two perpendicular axes. The chamber has to be capable of reaching 10^{-8} mbar for experiments sensitive to surface contamination. Sample loading from external chambers needs to be accommodated. For experiments using high target densities of up to 10^{22} cm^{-3} and high background pressure, sufficient vacuum pumping power will be necessary.

Most experiments will use photon detection by x-rays or visible light. However, particle detection using mass spectroscopy of neutral particles and electron TOF techniques should also be possible. The most important photon detection technique is x-ray emission. A variety of scattering angles should be realisable by the vacuum chamber design, in particular one needs to implement spectrometers that can observe in both a forward and backward direction, relative to the XFEL propagation, to perform detailed balance measurements. Due to the horizontal polarisation the vacuum chamber design should allow horizontal and vertical scattering.

Experiments can absorb significant fractions of the incident beam intensity. It is, however, intended to place most photon beam diagnostics in the transmitted beam. A second gas monitor detector will be used to measure the transmission. The spectral measurement should provide mean photon energy, bandwidth, and higher harmonic content on a pulse-by-pulse basis. Measurement of the detailed spectral, i.e. the width and distribution of spikes, is performed upon request only. Diagnostics of time domain properties should provide the arrival-times of the XFEL and the visible laser required for pump-probe experiments using the visible laser. Finally, spatial measurements must be made to determine the beam location and its spatial distribution. Since these spatial measurements are usually destructive, they will be carried out on a dedicated set-up at the end of the beamline and before the beam stop.

Item	Purpose	Specification
Deflection mirror	Beam separation from straight line, deflection angle 20 mrad, focusing to ~10 µm (optional)	0.1 µrad angular stability, 0.3 µrad figure error, 0.1 nm surface roughness
Beam-split-and-delay	Beam splitting (first/first; first/third), delay (first and third)	First harmonic in (un)equal parts, First/third separation, -10^2-10^6 fs adjustable delay
Focusing optics	≤1 µm focusing for 0.8-3.1 keV	0.1 µrad angular stability
Slits/apertures	Beam definition, beam halo cleaning	1 µm accuracy, 0.25 µm repeatability
Intensity monitor	Measurement of incident photon flux	Transmissive (<5% absorption), single pulse measurement, relative accuracy $<10^{-3}$
Differential pumping	Separation of beamline and experiments vacuum	10^4 step for all elements
Laser inlet	Port to couple visible laser radiation into experimental chamber	Mirror with central hole, retractable
Sample chamber	Sample positioning and orientation, systems to verify sample alignment, prevision of sample preparation, preparation for high gas loads, mounting of detectors	x-y-z move (0.25/1 µm), two rotations (0.25/1 mdeg), optical microscope, UHV conditions, high pumping speed
Detectors	Angle-, space-resolved x-ray emission	XUV – x-ray ranges, high efficiency, no scanning spectrometers
X-ray streak camera	Time-resolved detection	XUV – x-ray ranges, time resolution ~100 fs, stable, highly efficient
X-diffraction detector	Bragg diffraction and diffuse scattering from third harmonics (9.3 keV)	2-D detector, 1K×1K
Intensity monitor	Measurement of incident photon flux	Transmissive (<5% absorption), single pulse measurement, relative accuracy $<10^{-3}$
Spectral monitor	Measurement of mean energy, bandwidth and harmonic content	Single pulse measurement, relative accuracy $<10^{-3}$
Time monitor	Measurement time domain properties	Single pulse measurement
Spatial monitor	Measurement of spatial distribution, focus size	Single pulse measurement
Alignment unit	Positioning and position verification	Permanently operating, accuracy ~100 µm
Lead hutch	Radiation protection, temperature stabilisation, laser protection	$5\times12\times3$ m^3 (W×L×H), ± 1° thermal stability
Control hutch	Operation of the instrument	Working environment (Noise, temperature, light)

Table 6.4.3 *Elements and specifications of the HED 1 instrument.*

The availability of very intense visible laser radiation will form a critical boundary condition for HED 1. Receiving beam from the independent laser room the laser will be coupled into the vacuum in front of the sample chamber. Using mirrors with a central aperture the laser beam can propagate collinear with the XFEL beam. Further, input ports are needed for experiments where the visible laser is used as a diagnostics tool.

HED 2: Tunable hard x-rays

The HED 2 instrument will bear a strong resemblance to HED 1, the difference being that it is positioned at SASE 2 and is designed for hard x-rays. This instrument will be required for the part of the experimental programme to investigate the structural response of matter following deposition of energy and during the formation of plasmas described in Section 6.4.2.1, Experiments I., II., IV., VI. and VII. In addition, the investigation of HIs (Section 6.4.2.1, Experiment V.) extends into the hard x-ray range.

Since mirrors provide only shallow deflection angles in the order 4 mrad, a gallery of two mirrors is proposed to generate a reasonable offset from the straight beam. These are installed in the photon beam transport section inside the tunnels. Using the SASE 2 beamline lens system, a focal spot size of the x-ray beam of ~100 µm will be available in the experimental hall. Focusing in the order of 10 µm can be achieved by using a compound refractive lens about 100 m in front of the experiment. For micron or sub-micron focusing, special optics need to be employed positioned approximately 5-10 m upstream of the sample chamber, thus providing a demagnification of 100 and higher.

The following elements belong to the HED 2 instrument inside the experimental hall. They are also depicted in the schematic layout of that instrument in Figure 6.4.16 and are listed in Table 6.4.4. Collimating apertures or a slit system will be placed in front of the experimental chamber to remove scattered radiation from the beam.

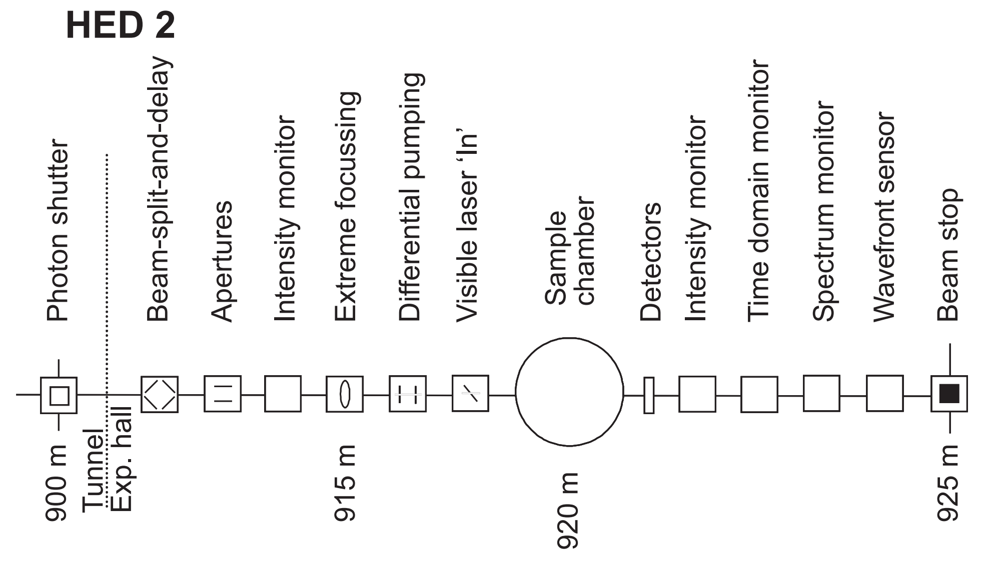

__Figure 6.4.16__ Schematic layout of the HED 2 station, proposed to be located at the SASE 2 beamline. The beam is directed straight to the sample chamber. Various focusing options will be available.

Item	Purpose	Specification
Deflection mirror	Beam separation from straight line, deflection angle 12 mrad achieved by 4-mirror gallery	0.1 µrad angular stability, 0.3 µrad figure error, 0.1 nm surface roughness
Beam-split-and-delay	Beam splitting (first/first; first/third), delay (first and third)	First harmonic in (un)equal parts, First/third separation, -10^2-10^6 fs adjustable delay
Focusing optics	≤1 µm focusing for 3.1-12.4 keV, (e.g. CRL system with variable lens number)	0.1 µrad angular stability
Slits/apertures	Beam definition,beam halo cleaning	1 µm accuracy, 0.25 µm repeatability
Intensity monitor	Measurement of incident photon flux	Transmissive (<5% absorption), single pulse measurement, relative accuracy $<10^{-3}$
Differential pumping	Separation of beamline and experiments vacuum	10^4 step for all elements
Laser inlet	Port to couple visible laser radiation into experimental chamber	mirror with central hole, retractable
Sample chamber	Sample positioning and orientation, systems to verify sample alignment, prevision of sample preparation, preparation for high gas loads, mounting of detectors	x-y-z move (0.25/1 µm), two rotations (0.25/1 mdeg), optical microscope, UHV conditions, high pumping speed
Detectors	Angle-, space-resolved x-ray emission	XUV – x-ray ranges, high efficiency, no scanning spectrometers
X-ray streak camera	Time-resolved detection	XUV – x-ray ranges, time resolution ~100 fs, stable, highly efficient
X-diffraction detector	Bragg diffraction and diffuse scattering (3.1-12.4 keV; possibly third harmonics)	2-D detector, 1K×1K
Intensity monitor	Measurement of incident photon flux	Transmissive (<5% absorption), single pulse measurement, relative accuracy $<10^{-3}$
Spectral monitor	Measurement of mean energy, bandwidth and harmonic content	single pulse measurement, relative accuracy $<10^{-3}$
Time monitor	Measurement time domain properties	Single pulse measurement
Spatial monitor	Measurement of spatial distribution, focus size	Single pulse measurement
Alignment unit	Positioning and position verification	Permanently operating, accuracy ~100 µm
Lead hutch	Radiation protection, temperature stabilisation, laser protection	$5\times12\times3$ m^3 (W×L×H), ± 1° thermal stability
Laser hutch	~100 J, sub-ns laser system	$5\times12\times3$ m^3 (W×L×H), ± 1° thermal stability
Control hutch	Operation of the instrument	Working environment (Noise, temperature, light)

Table 6.4.4 *Elements and specifications of the HED 2 instrument.*

An x-ray gas photon flux monitor (see Section 6.3.2.1) will follow before a differential pumping section separates the beamline from the UHV vacuum chamber for experiments. For the energy range of this beamline, vacuum separation by means of windows may be possible and needs to be investigated.

The sample chamber will be equipped with a high-accuracy sample manipulator allowing x-y-z movements and rotation around two perpendicular axes. Since hard x-rays probe the bulk, these experiments are intrinsically less sensitive to surface contamination than the ones at HED 1; however, the chamber should be capable of reaching 10^{-8} mbar. For experiments using high target densities of up to 10^{22} cm^{-3} and high background pressure, sufficient vacuum pumping power will be necessary. Most experiments will use photon detection by x-rays or visible light. The most important photon detection techniques are x-ray emission and diffraction in forward direction. For x-ray emission, a variety of scattering angles should be realisable by the vacuum chamber design, in particular, one needs to implement spectrometers that can observe in both a forward and backward direction, relative to the XFEL propagation, to perform detailed balance measurements. Due to the horizontal polarisation, the vacuum chamber design should allow horizontal and vertical scattering. For diffraction experiments, forward scattering will be most important and 2-D detectors will be particularly important for diffuse scattering experiments.

Experiments can absorb significant proportions of the incident beam photon flux. It is, however, intended to place most photon beam diagnostics in the transmitted beam. A second gas monitor detector will be used in transmission geometry upstream of the sample to measure the incident photon flux. The spectral measurement should provide mean photon energy, bandwidth, and higher harmonic content on a pulse-by-pulse basis. Measurement of the detailed spectral properties, i.e. the width and distribution of spikes, is performed upon request only.

Diagnostics of time domain properties should provide the arrival-times of the XFEL and the visible laser required for pump-probe experiments using the visible laser. Finally, spatial measurements must be made to determine the beam location and its spatial distribution. Since spatial measurements are usually destructive they will be carried out in a dedicated setup at the end of the line and before the beam stop.

The availability of very intense visible laser radiation will form a critical boundary condition for HED 2, as it does for HED 1. Receiving beam from the independent laser room the laser will be coupled into the vacuum in front of the sample chamber. Using mirrors with a central aperture the laser beam can propagate collinear with the XFEL beam. Further, input ports are needed for experiments where the visible laser is used as a diagnostics tool.

6.4.3 Coherent X-ray scattering and lensless imaging in materials science

Most of the material presented in this section is derived from the discussions in the working group "Imaging, Phase Retrieval and Image Reconstruction" at the Workshop on Diffraction, Crystallography and Imaging at the European XFEL, which took place on October 28 and 29, 2005 at DESY.

6.4.3.1 *Scientific case*

Coherent x-ray Diffraction Imaging (CXDI) is a rapidly advancing form of lensless microscopy that was opened up by the realisation that oversampled diffraction patterns can be inverted to obtain real-space images. The possibility was first pointed out by D. Sayre **[6-108]** but not demonstrated until 1999 by Miao et al. **[6-109]**. The phase information of the diffraction pattern, which is lost in its recording, is embedded in a sufficiently oversampled diffraction pattern, because this is intimately related to the Fourier transform of the object under investigation. The inversion of diffraction back to an image has been proven to be unique in two or higher dimensions, except for "pathological" cases of internal symmetry of the object or its diffraction pattern **[6-110, 6-111]**. Computational methods of performing the inversion, under very general constraints (for example, finite support of a sample, positivity of electron density, etc.) are an active area of development; they are often based on the iterative Hybrid Input-Output (HIO) method introduced in the 1980s by Fienup **[6-112]**.

Lensless imaging using coherent x-rays is an attractive alternative to electron microscopy because of better penetration of the electromagnetic waves in materials of interest; also, multiple scattering effects can be neglected, so that the first Born approximation can be safely used. In many cases, x-rays are less damaging to the sample than electrons and, in either case, the collection of a diffraction pattern is inherently more efficient than the use of lenses **[6-113]**. If the diffraction can be reliably inverted by computation, the method could be routinely used to reveal the structure of materials on the nanometre scale, far beyond the resolution of the traditional light microscope. The holographic method of combining a reference wave is an alternative way to perform the inversion **[6-114]**.

Lensless imaging is also well suited to the unique capabilities of the XFEL. According to recent theoretical calculations **[6-115]**, the incoming beam will have nearly full transverse coherence (80% transverse coherence, with a beam of a few mm^2 section; see also Section 5.2.2). Other unique properties of the XFEL, such as the high peak brilliance (we expect 10^{12} coherent photons in a single pulse) and ultra-short pulse time structure (100 fs pulses separated by 200 ns), allow us to consider applications of CXDI to structural analysis of nanometre-scale particles, inaccessible using third-generation undulator sources. The opportunity to study dynamics at such resolutions and on the sub-picosecond timescale with the XFEL, opens up entirely new research horizons.

In the last few years we have witnessed rapid development of CXDI techniques. Our experience is based, at the moment, on experiments that utilise the coherence properties of third generation synchrotron sources. The coherent scattering volume at these sources is mainly determined by the source size and distance from the source and is, typically, about 10 μm in the horizontal direction and 100 μm in the vertical direction for 10 keV x-ray energy and 50 m downstream from the source. The longitudinal coherence length is determined by the available monochromator and can reach ~1 μm. The coherent flux is determined by the brilliance of the storage ring and is typically 10^{12} ph/s in the pink beam. First, a very short overview of the results obtained using CXDI at these sources will be presented, and then some possible future experiments and the necessary technical requirements for the XFEL will be discussed.

Present status – Limitations at third generation sources

At the moment, the development of coherent x-ray scattering can be divided into two distinct parts: One is based on Bragg scattering of the incoming coherent beam on small crystals; the other is using the forward scattering geometry for non-crystalline objects. Both applications have their own advantages and limitations. In the case of Bragg diffraction, scattering angles are typically far away from the direct beam, so the whole diffraction pattern can be measured without the need of a beamstop, and there is no contribution from the beam-defining slits in the recorded diffraction pattern. On the other hand, scattering from non-periodic objects can be done only in the forward scattering geometry, making the use of a beamstop in front of the detector unavoidable. As a result, there is a certain amount of missing information in the reciprocal space for small q-values in this scattering geometry. Using the Bragg approach, it is easier to scan a sufficient region of reciprocal space with a 2-D detector to fully obtain 3-D information about the object. This can be done, for example, by fine angular scans near Bragg peak or by energy scans. In the case of scattering from non-crystalline objects, 3-D reconstruction is performed by measuring several diffraction patterns at different projection angles as in tomography and then reconstructing the object by iterative methods.

The following examples show that coherent x-ray diffraction of small crystals can provide us with information such as the crystal shape, internal structure and deformation field. Coherent x-ray diffraction imaging was applied to study 3-D structure of micrometre-sized Gold particles (see Figure 6.4.17) **[6-116, 6-117]**. The 3-D real-space density corresponding to the reconstructed phase and measured amplitude of the CXDI pattern is shown in Figure 6.4.17. The internal density contrast is in the form of bright and dark bands oriented parallel to both the [111] and [11-1] directions in the images. The [111] bands have a width of 50 nm, a period of 100 nm and a lateral extent of 600 nm, both within the section and between adjacent sections. The [11-1] bands have the same width and are slightly less extended. These features were interpreted to be deformation bands associated with sample preparation. The dark region of the band presumably corresponds to material with twinned stacking that would diffract in a direction different from the (11-1) imaging direction. Such bands are known to occur in soft fcc metals and are attributed to recrystallisation following slippage along [111] planes during deformation **[6-118]**.

In the above example, special care was taken to grow unstrained crystals. However, it can be shown, under very general conditions **[6-119]**, that if a coherent x-ray beam is scattered on a strained crystal, then the local symmetry around each Bragg peak is broken and the effect will be stronger at higher-order reflections. In the following example, equilibrium shapes of Lead nano-crystals were investigated **[6-120]**. First, the shape of the crystals was reconstructed from the measured coherent diffraction patterns (Figure 6.4.18) and, in addition, the projection of the strain field on the scattering vector Q was reconstructed (Figure 6.4.19).

The resolution obtained in this experiment was estimated to be 40 nm, and the main limiting factors were the incoming flux (the measurement time was 150 s per frame) and the detector sensitivity. We believe that the XFEL can substantially improve resolution by providing 10^{12} coherent photons in one pulse.

One of the most exciting applications of coherent XFEL beams in future will be the studies of quantum systems (quantum dots and quantum wires). This will be discussed in detail later in this chapter. Some initial experience and understanding of how coherent x-ray diffraction can be applied to quantum dot samples was obtained in **[6-121]** and **[6-122]**.

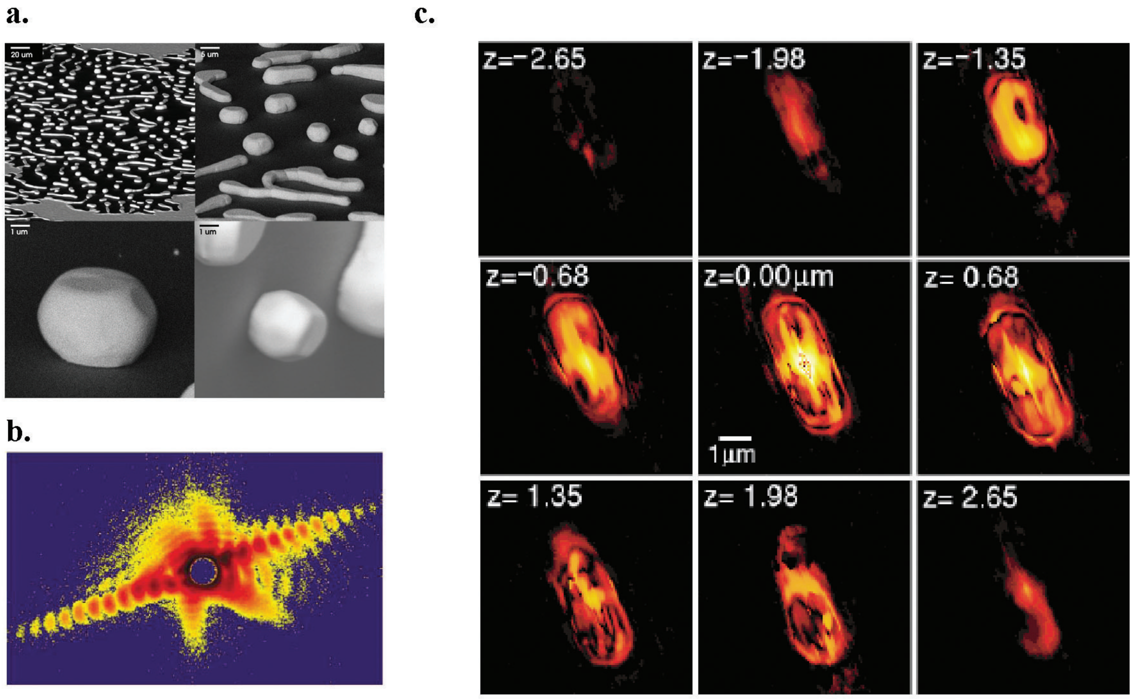

Figure 6.4.17 *(a) Scanning Electron Microscope (SEM) image of Gold particles that are obtained after annealing at 950°C for 70 hours; (b) coherent x-ray diffraction pattern from one of these crystals; (c) the 2-D slices through the best fit 3-D reconstructed density, separated as labelled.*

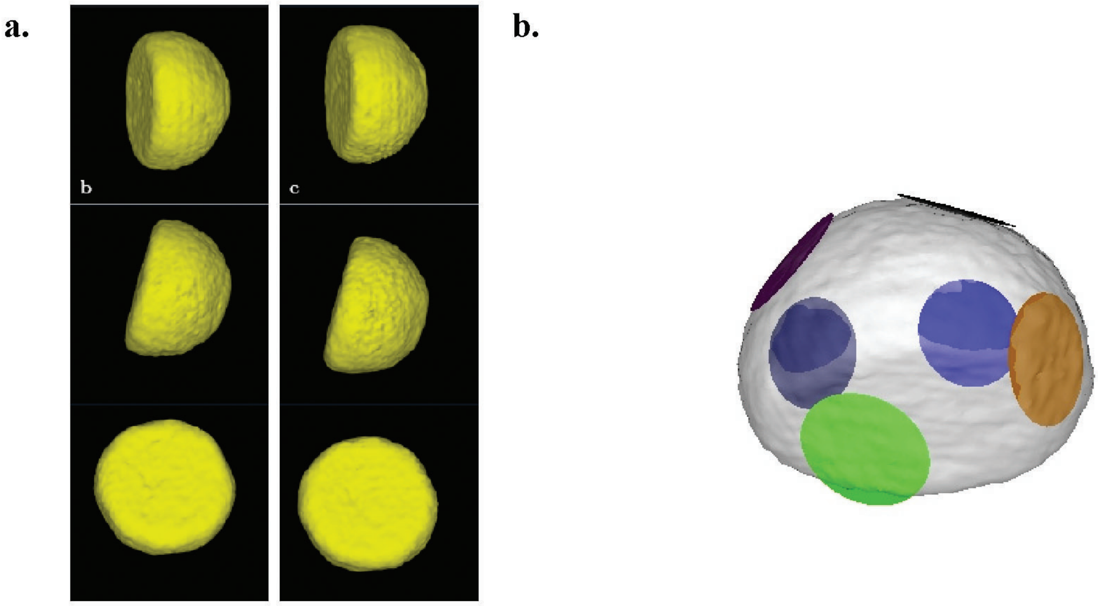

Figure 6.4.18 *(a) Surface plots of Lead reconstructed shapes. Left and right column corresponds to two best reconstructions; (b) 3-D view of (a) showing the fitted facet planes of the equilibrium crystal shape.*

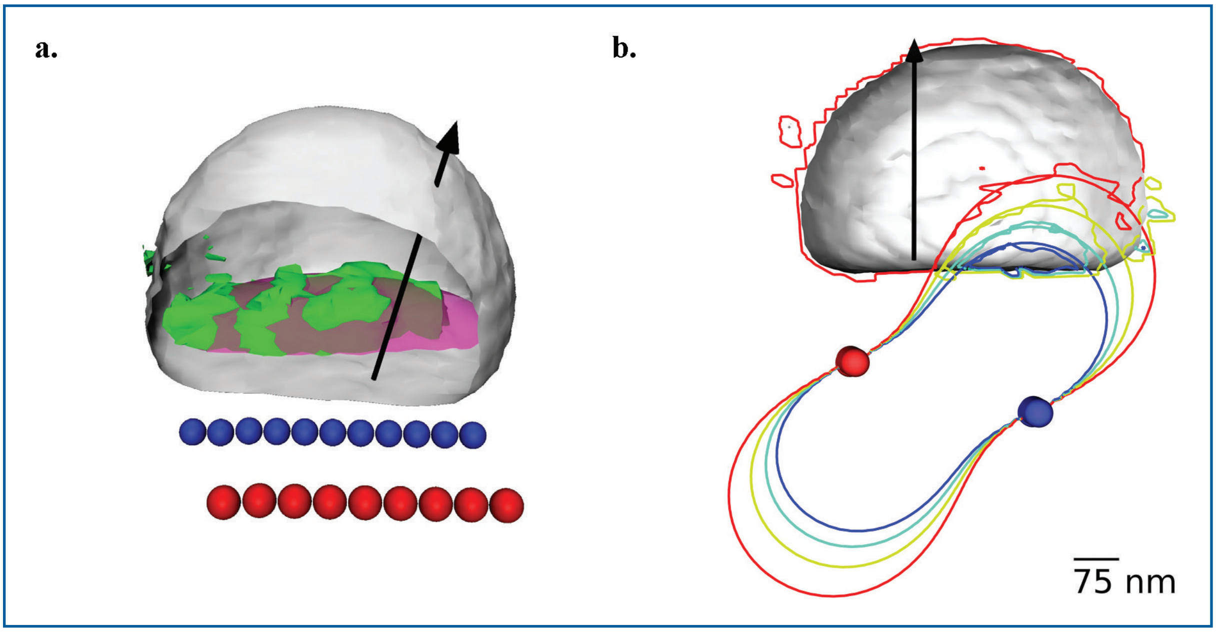

Figure 6.4.19   *(a) Single isosurface of the phase and the best fit superimposed on a cut-away image of the crystal density. The point defect lines used to generate the fit (dots) and the direction of Q (arrow) are also illustrated; (b) contour map of the cross section of the reconstructed phase of the complex density function on a plane passing through the middle of the nanocrystal. Smooth lines are the corresponding contours of the projection function* $\vec{Q}\cdot u(r)$*, where u(r) is the strain field calculated for two rows of point defects (balls) of opposite sign. Both sets of contours have spacing of 0.24 rad.*

In the experiment **[6-121]**, performed on a periodic array of Germanium islands on Silicon, the diffracted intensities show all the main features predicted **[6-122]**. However, it contains also a strong "diffuse" scattered intensity that, in a coherent beam, consists of the complicated speckle pattern due to inhomogenities of individual quantum dots. Here, measurements on single quantum dots are expected to provide a much "cleaner" diffraction pattern. We also think that 2-D periodic quantum dot structures could be an important step towards single molecule imaging.

It is clear that CXDI, especially with harder x-rays, is quite photon "hungry": the coherent flux per spatially and temporally coherent mode scales as the inverse third power of the photon energy. Moreover, pushing coherent scattering techniques to study nano-sized samples is even more demanding, as the number of elastically scattered photons decreases as the sample volume. The large coherent flux provided by XFEL will be crucial for the success of these experiments.

Coherent diffraction x-ray imaging experiments are also possible using the predominantly **forward scattering** by non-crystalline objects. The single molecule imaging experiment is the most challenging example of this. Scattering in the forward direction is determined by the electron density distribution of the sample. First results on 3-D reconstruction using coherently scattered diffraction patterns that were used for phasing were reported in 1999 in **[6-123]**. A 3-D reconstruction has been carried out on a specially prepared test Nickel sample using a series of 31 2-D diffraction patterns recorded from the sample with the rotation angles ranging from -75° to 75° in 5° increments. The resolution obtained in this experiment was estimated to reach 50 nm.

Recently, 3-D reconstruction with resolution 10 nm ×10 nm ×40 nm on a test sample using soft x-rays with energy 750 eV (1.65 nm wavelength) has been reported **[6-124]** (see also Section 6.4.7).

X-ray holography offers a complementary approach to iterative recovery of the object phase. Holography uses a well-defined reference wave mutually coherent with the scattered object wave to encode the phase in the coherent diffraction pattern from the object. The complex amplitude of the object wave is recovered from the recorded hologram, down to the sign of the phase, by a single (non-iterative) numerical calculation. Various optical geometries for holographic imaging have been demonstrated with soft x-ray lasers **[6-125, 6-126]**, undulator sources **[6-114, 6-127 – 6-130]**, and hard x-ray undulators **[6-131]**. The reference wave can be planar or curved; under appropriate conditions, a curved wave aids unique recovery of the phase **[6-132]**. As with CDXI, the recoverable object resolution is limited by the signal-to-noise ratio of the interference fringes recorded at the greatest momentum transfer Q in the coherent diffraction pattern. In holography experiments to date, this has been restricted to the maximum Q of the reference wave that can be produced by x-ray optics such as pinholes or ZP lenses. This currently corresponds to an object resolution of about 50 nm; this can be expected to improve to 15 nm **[6-133]** and possibly to as high as 1 nm as x-ray optics continue to improve **[6-134, 6-135]**. Figure 6.4.20 is an example of a reconstructed x-ray hologram showing magnetic contrast using a coplanar pinhole to form the reference wave.

Fortuitously, the experimental set-up and optics used for x-ray holography are readily shared with those used for CXDI in the forward-scattering direction. Consequently, it is practical to record holographic interference fringes (i.e. with a mutually coherent reference wave) out to the momentum transfer permitted by the optics, simultaneously with the reference-less coherent diffraction at higher momentum transfer than the hologram fringes. This two-pronged approach is promising because the phase provided directly by the reference wave can be used to improve the speed and accuracy of iterative phase retrieval of the reference-less coherent diffraction at high momentum transfer **[6-136]**. The recoverable resolution in this scheme, therefore, is not limited by the x-ray optics used to form the reference wave and thus, the hologram alone.

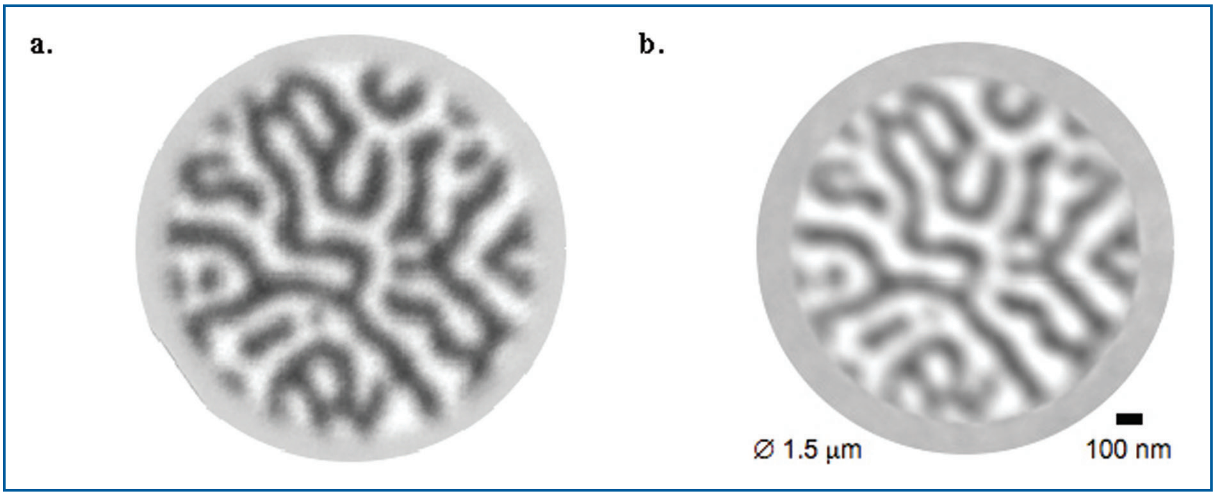

Figure 6.4.20 *(a) Scanning transmission x-ray microscope image of a CoPt multilayer containing labyrinthine magnetic domains; (b) reconstructed Fourier transform hologram of the sample, recorded at the BESSY UE56-SGM beamline. In both cases, the difference between opposite helicities of circularly polarised light is shown to reveal the magnetic domains* **[6-114]**.

Applications of the XFEL

I. Nanomaterials

Today's high technology industry demands increasing miniaturisation of device structures, mainly for integrated circuits in the semiconductor industry, but also of magnetic, optical and biological sensors. There has been a strong interest, recently, in the manufacturing and characterisation of structures on a nanometre scale, with the hope that the material properties of nanostructures can be tailored by changing their size, via quantum size effects. One important area is the development of next-generation magnetic storage media. Recent developments in this field are currently pushing the magnetic bit size below 100 nm. There has been considerable impact on our understanding of the growth and structural properties of nanostructures through the use of scanning microscopy techniques, which enable us to achieve atomic resolution in real-space structural determination. However, similar experimental techniques to obtain element specific electronic structure information on a nanometre scale are still lacking.

Despite the fact that many of the fascinating properties of nanoparticles can be exploited only for an ensemble of many particles, it may be of interest to study **properties of a single particle**. This would be of particular interest for in-situ studies of catalytic or magnetic behavior. Alternatively, investigating ensembles requires non-interacting particles with exactly the same size in order to obtain information about a single particle.

In the following, a possible application of the European XFEL for structural investigations of nanocrystalline compounds in the form of single particles are presented. Rough estimates show that single bunch exposures of nanocrystalline materials with diameters of 100 nm to the focused beam will produce a diffraction pattern with enough statistics for phase retrieval. The proposed XFEL Facility will, therefore, be of great interest for structural studies of two different classes of nanomaterials. The first class includes nanocrystals, i.e. materials with particle size in the range up to some 50 nm. Important groups of these materials are metal alloys and special ceramics based on oxides **[6-137]**. A common trend in modern material science is the adsorption of organic and metal-organic molecules onto the surface of nanocrystalline particles. The second class of materials comprises the extremely fine particles of clays and clay minerals. These materials usually do show translation periodicity; however, they are, in many cases, highly disordered.

Due to their small size, these materials cannot, at present, be investigated by single crystal x-ray diffraction techniques. For the detailed structural analysis of single crystals, it is important to obtain integral Bragg intensities with high reliability. Therefore, it is necessary to establish a highly precise monitoring system for photon flux, coherence and wavelength. An estimate of the sample sizes and exposure times that takes sample damage into account, based on a rough comparison to experiments at the European Synchrotron Radiation Facility (ESRF), shows that for a crystal of $100\times100\times100$ nm^3 size and the focused XFEL beam, diffracted intensities from a single bunch would provide a signal allowing the structure to be solved with sufficient accuracy. The information obtained from these data will be sufficient to determine the structure accurately (Bragg peaks) and the degree of disorder (continuous diffuse scattering). Ideally, if the whole crystal will be coherently illuminated, scattered intensity will produce a continuous diffraction pattern with high statistics that can be inverted and give the detailed structure of the defects in the crystal.

If sample degradation due to radiation-induced damage turns out to be tolerable, much smaller samples will be feasible, offering the exciting prospect of studying individual single nano-crystalline particles with x-ray diffraction techniques. With increasing sample size and respective beam diameter, the timescale is reduced correspondingly. If, for example, 1 μm resolution is considered sufficient for the determination of the local structure fluctuation, a thin needle or flat sample of larger overall dimensions can be sampled with a primary beam size of 1 μm diameter. In this case, an exposure of 600 ns is sufficient to record the diffuse scattering in a single orientation.

Particularly, for single crystal diffraction of crystals with strongly **fluctuating properties**, the sample stability is of crucial importance. Whether samples will be stable under the intense XFEL beam cannot, at present, be answered with any degree of certainty.

One of the important targets in this area of research are **quantum dot** structures. Progress in nanoscience and nanotechnology requires tools to investigate the structure of objects both on the mesoscopic and atomic levels. This is especially relevant in semiconductor devices based on heterostructures, where one big challenge is the investigation of individual nanostructures, which is important to quantify differences in self-assembled structures and to correlate these differences with the particular nanostructure location on the sample. This will be increasingly important for nanostructures embedded into electronic devices.

Using coherent nanometre-focused XFEL beams targeted on such samples could answer questions that cannot be solved with present levels of technology. Combining real-space mapping with nanometre resolution and coherent x-ray diffraction experiments could provide information about the size, shape, strain, and chemical composition of individual nanostructures after a single pulse exposure.

Spatially resolved CXDI from low-dimensional systems will play an important role in the understanding of the structure, fabrication, and functionality of many nanomaterials. The advancement of CXDI will have wide-ranging applications including the investigation of self-assembled and semiconductor nanostructures, surfaces and interfaces, extended defects, granular materials and many other systems.

An important field of semiconductor nanoscience research nowadays is investigation of single islands and few coupled islands to obtain their electronic properties. For this purpose, micro-photoluminescence (µ-PL) and photocurrent spectroscopy have been applied to measure transitions in neutral and charged single excitons **[6-138]**, mainly in InGaAs/GaAs quantum dot systems. For the interpretation of the results, model calculations based on the structure of the islands (size, shape, composition and strain profile and existence of facets) are performed **[6-138 – 6-140]**. Due to fluctuations in the quantum dot ensemble, which are difficult to quantify, these models usually contain free parameters, rendering the simulations ambiguous to a certain extent **[6-138]**. Being able to determine the structural parameters of a single island, and correlate the results to µ-PL and photocurrent results at **the same island** would considerably further this field. Transmission electron microscopy (TEM) and cross-section scanning tunnel microscopy (STM) cannot be used for this purpose, as these methods are destructive and do not allow preparation of a specific quantum dot for analysis. Using focused XFEL beams will make it feasible.

X-ray diffraction (XRD) has proven a powerful tool for the determination of composition and strain distribution in nanostructures. Several methods have been established, based on measuring the diffuse intensity distribution with high resolution in reciprocal space **[6-141 – 6-148]**. While conventional local probe techniques such as TEM typically reach lattice parameter resolutions about $\Delta a/a = 10^{-2}$, XRD experiments easily reach values of $\Delta a/a = 10^{-3}$ to 10^{-4}. So far, large ensembles of typically 10^5 to 10^6 nanostructures have been investigated by XRD, providing statistically well-averaged properties with a spatial resolution in the nanometre range for the **average object** under investigation. Focused XFEL beams, allowing high spatial resolution in addition to the high reciprocal space resolution, make the analysis for a **specific nanostructure** on the sample feasible. Considering the typical dimensions, an area with an extension of not more than about 100 nm has to be illuminated.

There has been considerable progress in recent years with x-ray focusing devices, and several groups have demonstrated focus sizes around, or even below, 100 nm **[6-149 – 6-155]**. Using XFEL beams will be beneficial because, due to the high degree of coherence, diffraction-limited focusing can be achieved, providing the smallest possible focus size and preserving full coherence across the beam.

One of the possible projects on XFEL can be the further development of the coherent x-ray diffraction imaging technique, with its application to single islands of semiconductors coherently grown on a substrate (like SiGe dots on Silicon). One of the most important outcomes of the whole project will be model-free determination of the anisotropic strain distribution in a single island (including buried ones), and in the substrate.

II. 3D structural characterisation of mesoscale systems

Investigating the meso- or nanoscale properties of hard materials has become a focus of the hard condensed matter community. In contrast to the atomic and macroscopic scale, our understanding of the structure on this scale is less mature. In particular, models tend to be based on average properties, despite the fact that the materials are often very heterogeneous on this scale. As an example, the macroscopic properties of metals such as strength or fatigue are governed by the properties of grains and dislocation structures and their interactions. The properties of the objects vary by orders of magnitude depending on factors such as size and crystallographic orientation. Present structural techniques cannot characterise this heterogeneity.

Neutron diffraction lacks the spatial resolution for observing the "building blocks". Electron microscopy, on the other hand, probes only the surface. As such, it can be used only for "post mortem" on sectioned samples. The dynamics cannot be probed, and interactions between objects cannot be observed directly. Also, heterogeneous structures tend to be truly three-dimensional, and sections can be misleading. Only recently, with third generation x-ray sources, has it become possible to get static information from each individual grain of micrometre size **[6-156]**. We believe that using CXDI and the power of XFEL we can investigate structural properties of mesoscale systems in three dimensions with nanometre resolution. Some applications to metal and ceramic systems are described in the following paragraphs.

Metals. Typical metal structures are presented in Figure 6.4.21, displaying the four inherent length scales: Grain structures in well annealed metals have typical sizes of 1 – 100 μm and are very homogeneous, as can be seen in Figure 6.4.21(a). Application of stress leads to deformation and the formation of individual dislocations at length scales 0.1 - 1 μm (Figure 6.4.21(b)). Increasing the deformation leads to dislocation structures at the few micrometer scale (Figure 6.4.21(c)). Upon annealing, new nuclei are formed which grow from the matrix and show no dislocations (Figure 6.4.21(d)). The processes of deformation and annealing are important in the "life" of every material, and it is evident that dynamic, e.g. time-resolved, data will help in understanding the underlying processes. Such data can only relate to the bulk of the material, as the surface is non-representative due to stress relaxation, dislocation migration, pinning on surface grooves, etc. The following specific questions of vital interest motivate such 3-D structural investigations to include:

- How do dislocation structures emerge from individual dislocations?
- How do grains and dislocation structures deform?
- Nucleation: Where in the deformed material do nuclei form, and what are the orientation relationships between nuclei and the sites at which they form? What is the nucleation mechanism?

- Growth: How do the nuclei grow – what is the kinetics as a function of the relative orientations of the nuclei and the surrounding dislocation structures? Does the morphology of the dislocation structure play a role? How are the various types of dislocation structures actually absorbed into the moving interface of the nuclei?

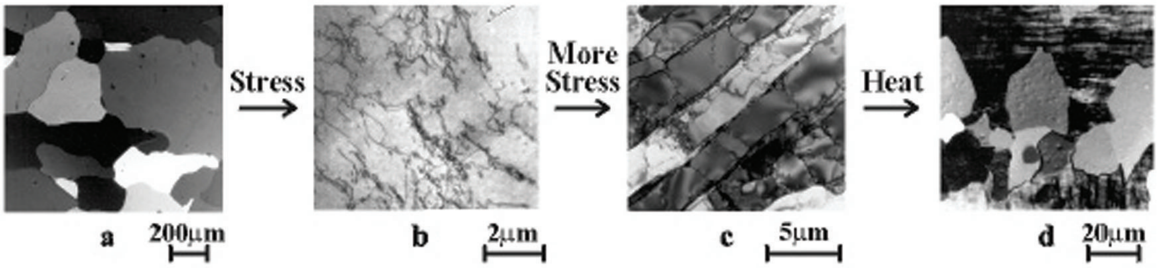

Figure 6.4.21 *Metal structures as observed by non-x-ray microscopy. The micrographs correspond to snapshots in time for random locations after exposure to stress and heat. No direct information about dynamics can, thus, be obtained using this method. (a) A well annealed grain structure shows evidence of tangled dislocations after some deformation (b) With more deformation these form into dislocation structures (c) Upon annealing, new nuclei form and grow from this deformed matrix (d) (from* **[6-2]***).*

These topics have been addressed in much detail by traditional means, but answers have been elusive. The XFEL combined with CXDI should be able to provide answers to some of these questions. Furthermore, combined dynamic investigations will be possible on three of the inherent length-scales: those of the sample, grain and dislocation structure. Hence, such data will be instrumental in the development of global models that bridge the length scales; in other words, in anchoring the macroscopic properties of interest to engineers to the mesoscale properties. The case for (industrial) alloys is similar, with the addition that the simultaneous use of tomography will be helpful in mapping and identifying secondary phases, inclusions, etc.

Ceramics. Modern ceramics tend to be heterogeneous partly because non-equilibrium parts of phase diagrams are used and partly because function/cost considerations dictate the use of several components (multilayers and inclusions). The kinetics of the reactions, phase transformations, etc. depend on the local environment of the grains, whether in the form of powders or sintered pellets. Again, surface studies are non-representative as the diffusion mechanisms are different. By providing local-scale information, ceramics processing will take a major step away from the present state of trial-and-error.

The study of grain dynamics with the XFEL source combined with CXDI, will allow the kinetics of the individual grains to be observed without locating the grains' exact positions. This will be a substitute for conventional in-situ powder diffraction. "Single crystal" structure refinements are applied here. In this way, a statistical study can be performed based on groups of grains with specific volume, orientation and/or stoichiometric properties. Furthermore, reactions between neighbouring grains can be observed directly by high-resolution mapping. The resolution of a few nanometres fits well with the grain size of many powders. The combination of diffraction and imaging is especially attractive in this case, since the structure and density of the various grains are often unknown.

III. Dynamic processes and time-resolved investigations of fluctuations

One potential of the XFEL lies in the ability to measure the **time-evolution** of transient structures on the 200 ns timescale of the XFEL pulse spacing. The 100 fs exposure time of a single bunch might catch a spontaneous fluctuation on that timescale. It is estimated that crystalline objects 10 nm across would give measurable diffraction patterns, and objects 100 nm across would be measurable during a single XFEL pulse. This type of application requires all the special properties of the XFEL: a coherent beam for the imaging, intensity because of the minute object size, and the short time structure for time-resolved experiments. In this regard, CXDI experiments could also take advantage of pump-probe methods being developed for other XFEL experiments such as X-ray Photon Correlation Spectroscopy (XPCS).

Another possible application of coherent femtosecond x-ray pulses will be for study of the surface dynamics. Consider a **crystal surface with an area** of only a few square micrometres. The coherent XFEL produces enough photons to fully characterise such an area in one bunch train, thus in < 1 ms. It will, thus, be possible to see step dynamics on the timescale of successive bunch trains (~100 ms). The dynamics can be caused either by statistical fluctuations or by growth or etching. This imaging would not only be faster than is currently possible, but could also be applied to systems under high gas pressure or at high temperature, or to surfaces buried under a solid or liquid, for which there are no alternative techniques. On a much slower time and larger length scale, a Silicon wafer has been imaged in this way during the etching of the native oxide **[6-157]**.

Of considerable scientific interest are the **spontaneously nucleated clusters of a crystalline solid** in an aqueous solution close to saturation. Time-resolved experiments with the XFEL would permit testing of the microscopic theory of classical nucleation, which has not been possible before. According to theory, solute molecules randomly associate into clusters with a thermodynamic equilibrium distribution, so that the largest clusters are the scarcest (Figure 6.4.22). Once a cluster exceeds the critical nucleus size, it becomes thermodynamically stable and grows into a macroscopic crystal. In standard nucleation theory, a smooth size distribution of small crystallites is assumed to be present up to the critical nucleus size. However, one can imagine that in reality, the size distribution is not smooth, but that certain sizes are preferred. In the case of 2-D nucleation on metal surfaces, such magic clusters have been observed using STM **[6-158]**. The sub-critical nuclei may also have a shape or structure that deviates substantially from that of the bulk crystals that eventually grow out of them. Since we are interested in atomic scale fluctuations upon a large background of parent material, it is advantageous to concentrate the beam onto a reasonably small sample volume in the order of a 1 μm^3 in order to improve statistics.

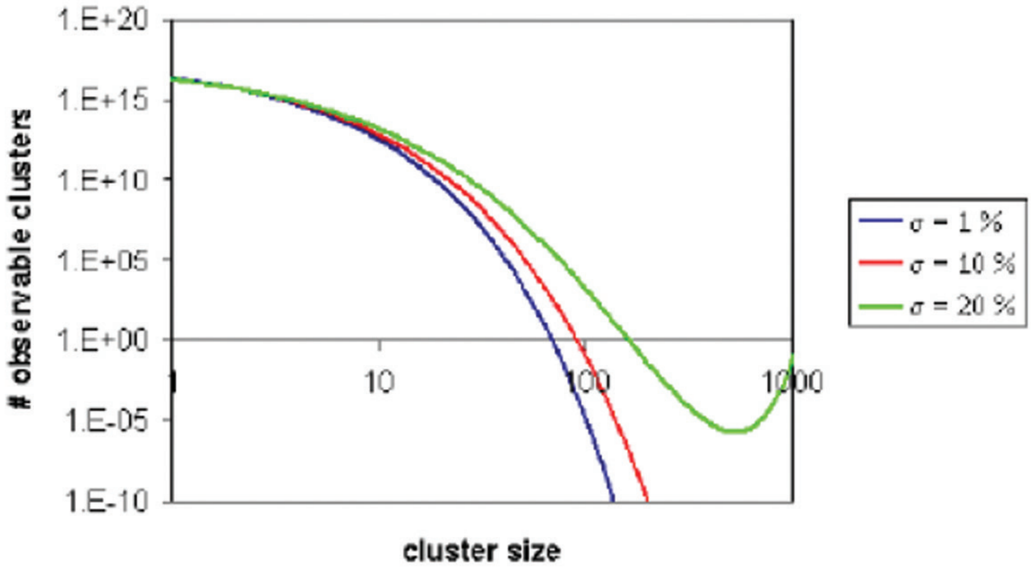

Figure 6.4.22 *An estimated cluster-size distribution as a function of supersaturation σ according to standard nucleation theory. Only a few clusters exist at an appreciable size.*

Possible systems for study, fall into the general category of **crystalline fluctuations in disordered matter**, induced by some excitation such as temperature. For metals research, suitable examples are the local ordering of a binary alloy above its critical temperature or composition fluctuations in amorphous metal alloys. Alexander and McTague **[6-159]** proposed there would be BCC phase fluctuations in liquid FCC metals. These have been confirmed by simulations by Shen and Oxtoby **[6-160]** and by Klein **[6-161]**.

Fluctuations in aqueous solution are also of interest. Concentrated salt solutions, close to saturation are expected to have critical fluctuations of the crystalline phase. When these “pre-critical” nuclei become sufficiently large, they nucleate into actual crystals. The expected timescale of the fluctuations will depend enormously on the degree of supersaturation, which can be controlled by temperature, for instance. The 100 fs pulse of the European XFEL will be easily short enough to obtain snapshots of them. There is also a large field of study of binary mixtures of fluids that show phase separation into ordered structures that could be detected by diffraction. Self-assembling molecular and biological systems might also be accessible if there is a characteristic length scale established that would lead to diffraction.

In some cases, the fluctuations will be rare events with a characteristic signature of a particular Bragg angle where the parent crystal structure diffracts. Here, the experiment would be run at the highest framing rate that the detector bank can achieve, with a corresponding rate of single XFEL pulses, synchronised to the readout. The data stream would be monitored for “trigger” events such as the appearance of speckles more intense than some threshold. This is analogous to the measurement strategy used in high-energy physics. Only the data immediately before and after such triggers would need to be saved for subsequent analysis. These measurements could also be performed with high-energy spontaneous radiation for sampling of a larger volume.

Other cases would produce a continuous stream of speckle snapshots, uncorrelated between frames because the fluctuations would be too fast. Statistical analysis of the distribution of speckles on each frame would be used to obtain the higher-order correlation functions of the nascent ordering under investigation. Presently, theoretical work **[6-162]** has started to extract the interesting higher-order correlations, e.g. three-point correlation functions. Theoretical considerations combined with conventional coherent diffraction data, obtained from amorphous alloys for example, could be used to anticipate the kinds of correlations that might be interesting in a given system. Very good statistical evaluation of these higher-order correlation functions could be obtained by automated processing of the data stream. The experiment would then consist of varying the sample temperature or composition systematically. Special detector readout schemes or streak camera methods might be introduced to observe the lifetime of these fluctuations.

To illustrate the kind of data that might be obtained with a snapshot experiment during a pre-crystallisation fluctuation, we calculated the diffraction pattern of a 10^3 atom cluster from a MD simulation of freezing, shown in Figure 6.4.23. The amplitude of its Fourier transform, shown in Figure 6.4.24, represents the square root of the intensity that would be measured with a single European XFEL pulse. Because this is oversampled, it should be directly phasable, and hence, invertible to (projection) images of the fluctuation. The size of the simulation represents a volume of less than $(10\ \text{nm})^3$, which is slightly less than can be achieved with focusing. A similar fluctuation within a larger volume will give the same signal, but more structured background.

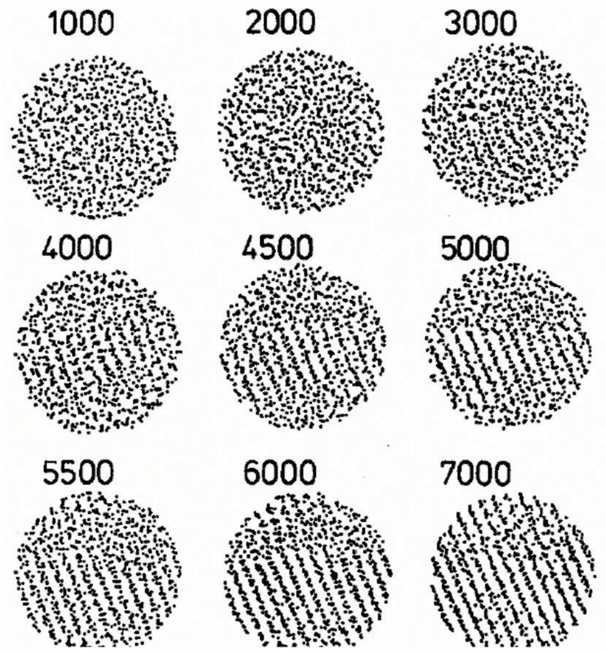

Figure 6.4.23 *Molecular dynamics simulation of freezing of a Lennard-Jones liquid of 864 atoms as a function of time steps after a temperature jump* **[6-162]**.

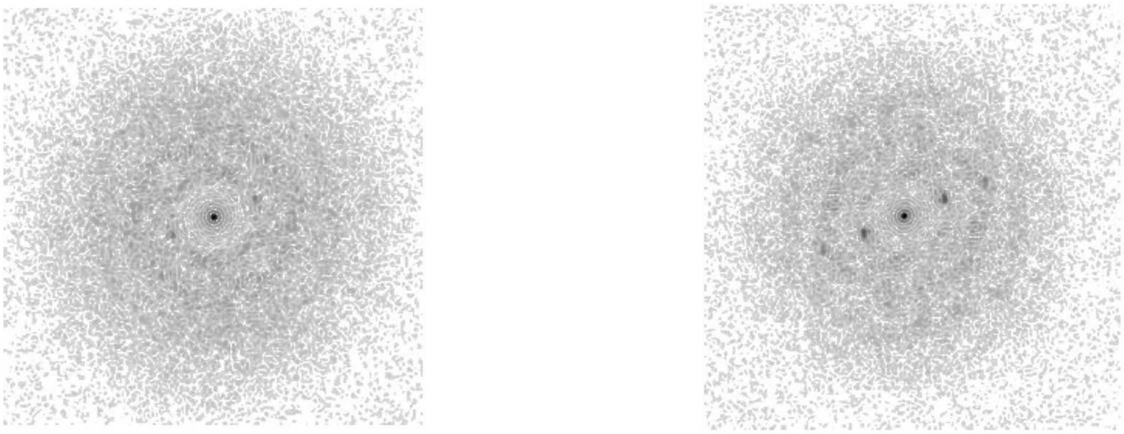

Figure 6.4.24 *Simulated diffraction patterns of the atomic distributions simulated in Figure 6.4.23, for the 1,000th (left) and 5,000th (right) time step.*

IV. Dynamics processes in metals and ceramics

The understanding of reactions during materials processing will have a new basis when experimental data and correspondingly refined modelling at spatial resolution below 1 µm and temporal resolution below 1 µs become available. Real-time small-angle x-ray scattering analysis may further be performed to analyse dissolution or coarsening of precipitates or pores with sizes smaller than ~1 µm, whereas the opening and closing of larger pores formed, for example, during creep, or close to a crack tip, may be measured using radiography under varying external load. Thus, comprehensive 3-D pictures of local microstructures may be derived with information content close to that obtained by the use of electron microscopy. A few examples from prominent areas have been selected below and indicate that time-resolved hard x-ray measurements at the XFEL can improve, to a great extent, the present-day knowledge of processing technologies. This applies equally well to techniques not mentioned yet, like extrusion, powder processing, sintering, cutting, carburising, rapid solidification, and joining. Even extremely fast processes like brittle cracking or fast deformation of materials by shock waves can be analysed.

Real-time investigation of welding. The high intensity and repetition rate of XFEL pulses will allow new and innovative real-time analysis of fast materials processing. For example, the in-situ study of fast formation and deformation of grains, as well as precipitation reactions during welding, will become feasible. This will greatly increase our basic understanding of the formation of microstructures in welds, which is regarded as an excellent basis for improving this joining technology. Time-resolved hard x-ray measurements at the XFEL laboratory are expected to greatly improve our knowledge of further processing technologies.

Precipitates and pores. The anticipated time resolution will allow the analysis of extremely fast growth and shrinkage of precipitates or pores. These effects may occur, for example, near crack tips, during melting, during solidification and fast cooling of droplets in powder processing, or during laser treatments of surfaces with local melting and fast cooling afterwards. Further novel analysis will be based on the extreme photon flux of beams with areas even less than 1 µm^2 which may allow tomographic small angle x-ray scattering investigations to be performed simultaneously with grain mapping so that spatial variations of sizes and number densities of precipitates and pores may be derived. Such analysis will, for example, significantly improve our basic understanding of failure mechanisms of materials around crack tips or the incoherent formation of creep pores in alloys and ceramics **[6-163]**.

Ultra-short pulse laser interactions with matter. The interactions of high power, short-pulse lasers with materials have recently aroused a lot of interest in both the scientific community **[6-164, 6-165]** and the technological arena **[6-166 – 6-169]**. On the one hand, understanding of the fundamental processes and basic mechanisms such as energy transfer from laser field to material, energy transport and subsequent athermal or thermal modifications in the material are largely lacking. On the other hand, technological processes such as laser drilling **[6-170]** and cutting, machining **[6-169]** and peening, and laser ablation for thin film deposition **[6-166]** have now been developed as alternative and replacing technologies for conventional processes. Laser damage in optical materials **[6-170]** presents a technological roadblock to high-tech processing of materials.

Given the femtosecond time structure and extremely high brilliance of XFEL sources, the dynamics of ultra-short pulse laser interaction with matter may now be explored experimentally by using a variety of time-resolved and spatially-resolved techniques. These include diffraction, imaging, and a whole host of spectroscopic methods to capture and record modifications in crystal structure, phase transformation **[6-171, 6-172]**, morphology and microstructure evolution, which occur during the time the material "sees" the laser light. Such dynamical data will in turn help to verify existing models and to construct new and better models of laser-matter interaction processes. These advances will further our basic understanding of laser-based technologies and help us to improve and develop them for future material processing and fabrication.

One of the possible applications can be a study of a short pulse laser ablation that is a promising process for nanoscience applications due to the low threshold for material removal from surfaces. In the laser-ablation process, solid material transforms into an unsteady phase initiated by a rapid deposition of energy. Different pathways for non-thermal excitation can be present for very short laser pulses **[6-166]**. In a recent paper **[6-173]**, an ablation of Gold particles of nanometre size induced by optical femtosecond excitation from a laser was studied. However, the time resolution for this study was limited by the pulse structure of the third generation synchrotron source ESRF in this case). One could extend these studies on the XFEL Facility when the ablation process can be studied with femtosecond resolution. In addition, if the analysis of the paper **[6-173]** was based on modelling of small angle scattering data collected from a large amount of particles, we could foresee a similar experiment using XFEL pulses focused on a single particle that will give enough diffracted intensity to reconstruct the shape of the nanoparticle before and after interaction with optical pulse.

6.4.3.2 *Instrument requirements*

The experiments described above lead to requirements for an instrument for scientific applications using Coherent x-ray Imaging (CXI). They concern the performance of the light source, of the optical elements and the diagnostic equipment, of the sample environment, and of detectors. The experiments described in this section require tunable XFEL radiation of a relatively wide spectral range from ~0.6 to 12 keV. Here, 12 keV radiation is requested due to its penetration in bulk investigations. Diffraction and imaging techniques will be applied at this photon energy. Investigations of magnetic systems or resonant scattering in the hard x-ray regime lead to the request for tunable radiation in the range ~3-11 keV. Full-field imaging experiments would employ 12 keV radiation in combination with a high-resolution in-line camera system. This in-line detector will need to be as large as possible an array (if possible, 4K×4K), optically coupled to an optimised fluorescent screen. The field of view is limited by the array size and the optical magnification and should not be compromised. Smaller photon energies around 1 keV will be used to investigate the structure and time evolution of nanostructures in the 20-50 nm range. For these particle sizes, 1 keV radiation provides sufficient penetration, but in general samples will not be isolated and surrounded by a vacuum. Otherwise, they would be studied using electron microscopy. Instead we want to be able to access objects growing in-situ, in contact with a liquid (e.g. water). We propose to use the Grazing Incidence Small Angle X-ray Scattering (GISAXS) Geometry, thus, avoiding the penetration problem. Another possibility is to use samples supported by very thin Silicon Nitride membranes and investigated in transmission geometry. Tunable beam energy around 0.5-1.0 keV will also be needed for the L-edges of 3d transition metals in very thin samples. Another application is the investigation of biological matter, preferably in the water window (0.28–0.5 keV), with enhanced contrast between water and organic materials. None of the European XFEL beamlines provides the entire photon energy range in the fundamental and the use of SASE 2 and SASE 3 beamlines is proposed instead. For materials science applications, such as those discussed in Section 6.4.3.1, Case III., the use of very hard x-rays at energies 60-90 keV is requested. The high photon energies are required to achieve sufficient penetration. Since, at these photon energies, the Ewald sphere of diffraction becomes almost flat, the experiments are well suited to investigations of diffuse scattering planes. These experiments will use the spontaneously emitted synchrotron radiation of U1 which also exhibits a very high degree of coherence.

The relative merits of x-ray microscopy methods suited to XFEL sources are compared in Table 6.4.5. Coherent full-field transmission x-ray imaging, x-ray holography, and CXDI, are described in the table. Holography provides the full complex amplitude of the object in one reconstruction step, whereas lensless CXDI is promising for obtaining the highest spatial resolution.

	Full-field	Holography	CXDI
Resolution limit	optics	reference	detector
Feasible resolution	~10 nm	~10 nm	~ 1 nm
Optics required	yes	yes	no
Coherence required	no	yes	yes
Focusing required	yes	no	no
Reference required	no	yes	no
Direct method	yes	no (one step)	no (iterative)
Phase retrieval needed	no (in focus)	yes (one step)	yes
Twin image problem	no (in focus)	no (unless inline)	no
Signal dynamic range	low	high	high
Compatible with CXDI	no	yes	

Table 6.4.5 *Relative merits and requirements of coherent full-field transmission x-ray imaging, x-ray holography, and CXDI.*

Spectral radiation properties

The degree of spatial coherence is often considered to be better using soft x-rays, but according to the design, the European XFEL will be fully coherent at all energies. The coherent flux is certainly higher for soft x-rays for a given source brilliance (cubic scaling, as mentioned above). It may be that lasing will be achieved faster for somewhat smaller photon energy, so there is interest in designing experiments operating at about 3 keV. In addition, energies in this range appear optimal for imaging of small biological specimens, based on a comparison of estimated radiation damage versus resolution in electron microscopy, x-ray microscopy, and x-ray crystallography data **[6-174]**. CXDI experiments designed to operate at intermediate, as well as hard x-ray, energies will have to take into account the impact on the optics and detector configuration. Many experiments can be carried out with the natural 0.08% bandwidth of the undulator because of the inherently small size of the diffracting object, but it will probably be worth having an optional Si(111) monochromator for the possible situations where the undulator is not up to specification or for large samples. It will be important to foresee a real-time diagnostics of the undulator performance.

X-ray optics requirements

In previous reports, the term **coherence preserving optics** had been used to describe the quality of optical elements when used with the almost fully coherent radiation of the XFEL. This term is somewhat misleading, as an optical element – no matter how strong its aberrations and distortions – cannot degrade the coherence of the radiation, meaning that it will not reduce the visibility of any diffraction or interference experiment. However, experiments aiming to retrieve amplitude and phase right after an object require a well-defined phase of the incoming wave front. While this phase is well known for a coherently illuminated, aberration-free, perfect optic, an imperfect optic will introduce wave front distortions which are usually unknown and thus, hard to correct for. Therefore, the term **wave front preserving** or **diffraction limited** seems to be more appropriate to describe optical elements, in particular with respect to the precision required for nanometre-scale CXDI. Results with diffraction-limited focusing by diffractive lenses at the 15 nm scale are promising in this case **[6-27]**. In fact, the condition to yield a well-defined "clean" wavefront may turn out to be more relevant for optics than the ability to achieve the smallest spot sizes. A situation, where the wave front illuminating the sample is unknown or, even worse, changes in time, must be avoided for the CXI experiments.

The requested beamsize in most experiments will be in the order of 0.1-1 µm. This is needed to limit the sample volume so that not too many fluctuations are sensed, and to concentrate the flux on the region of interest. The average heat load on the sample is not expected to be a serious problem because this is the same as at existing sources, but there will be considerable power levels over the duration of the pulse which could cause plasma formation. However, it seems unlikely that a crystalline nucleus would be completely disrupted on the timescale of the XFEL pulse duration. Further discussion on this topic and theoretical input on the "meaning" of temperature will certainly be needed.

Time domain requirements

These experiments do not make explicit use of the ultra-short pulse duration. However, to model the interaction of the intense radiation with the samples, the fluctuation of the pulse duration will need to be kept small compared to 100 fs timescale. Many experiments will require only single pulses at a 10-50 Hz repetition rate as the intense radiation leads to the requirements of sample exchange between exposures. Experiments investigating the time evolution of sample structure over a long period after initial excitation, envisage using the high repetition rate during the x-ray pulse trains. In this way, time information could be obtained in steps of ~200 ns over a period of 0.6 ms. Likely a logarithmic distribution of time steps is sufficient. These experiments require samples withstanding the energy dissipation over at least the period of the pulse train. This could be either specific 'radiation hard' materials or measurements where the incident photon flux is reduced, e.g. by introducing a monochromator or even an absorber. It is, therefore, the intention to use a variety of pulse patterns from single pulses up to several hundreds of x-ray pulses per electron bunch train.

Photon diagnostics requirements

All experiments will be in need of pulse-by-pulse diagnostic to determine photon flux, beam position and focus spot size at the sample position. Furthermore, it needs to be verified that the wavefront is stable in time. The spectral diagnostics should provide the mean photon energy and the content of higher harmonic radiation.

Sample manipulation and environment

In the experiments envisaged at the XFEL laboratory, the sample size of interest is envisaged to be below one micron. To collect diffraction data and to manipulate such small samples with extreme resolution, it will be necessary to set up high resolution microscopes integrated to the diffractometer. This could be a present-day optical, Scanning Electron Microscope (SEM) or Atomic Force Microscope (AFM) that will be useful for identifying and aligning the sample on the diffractometer. The sample stage will need a single high precision axis for tomography. Supporting samples on a membrane might work; if the membrane is blown away, the damage would be local and a second shot could be placed on an adjacent region. A square centimetre of sample will be enough for a million shots with ten microns spacing.

Injection of a jet of liquid into the vacuum of the beamline is a method that should work but will severely limit the range of samples available. It might be possible to design a windowless flow cell in which a liquid is held in place by capillary forces. This might be made to work in vacuum in some cases, but is certainly compatible with a Helium environment. Levitated samples, either electrostatically or magnetically, may be used. Using a sample in a gas stream is another option. One should consider the option of not preparing individual particles at all. The particles could be blown through the x-ray beam in a highly diluted gas stream. This could be similar to the sample environment planned for the single molecule station. New techniques will have to be developed to synchronise the movement of such small particles with the x-ray beam and the detection system. One would obtain a series of diffraction patterns at random orientation of different particles, each recorded with a fully transversely coherent x-ray beam. Analytical techniques that have been established for electron diffraction will have to be applied here to analyse the diffraction patterns in order to obtain structural information about the samples. It will be advantageous to have a system for aligning particles in the focus of the beam at least in one direction that will be an important factor for diffraction pattern sorting.

For most of the experiments proposed here, using windows around the sample in the focused beam should be avoided. The window material would become vaporised along with the sample. The use of windows could be possible for unfocused or attenuated beams but special care has to be taken for their quality. The possible restrictions could arise from the availability of x-ray windows. Ideally, a beamline should be windowless so as not to interfere with the coherent wavefront. However, for practical reasons, thin windows could be used in the unfocused beam, before the optics, for example, or in the detector system. Silicon nitride membranes can be fabricated as thin as 50 nm, are radiation-hard, amorphous, and contribute little undesired scattering (especially for hard x-rays). If kept under a few millimetres square, they can also support an air-vacuum interface such as a vacuum interface or a detector entrance window. Differential pumping could be viable, for example between a Helium sample environment and the machine vacuum. This might be relatively easy to achieve, given the very large distances involved.

Since for 12 keV radiation, windows can be allowed, user experiments could bring their own sample environment. Standard interchangeable sample environments (eg baby chambers) should be provided in addition. For experiments at magnetic resonances (3-12 keV), in-vacuum magnet- and cryosystems will be needed.

The 1 keV instrument will differ from the 12keV instrument in having a single vacuum system throughout, with no windows, including the detector chambers. A clever design of the vacuum system would allow plenty of in-vacuum motorised stages to mount optics at various distances. Perhaps there could be several sample stages at different distances from a fixed detector bank. Each one would have to have several translation stages packed close together to mount various optics. A good vacuum design needs to be flexible in allowing quick access for adjustments. Heating and cooling at the sample will be important as well as magnetic fields inside the vacuum.

Detector requirements

It is envisaged that the different experimental stations would correspond to the different detector configurations. Since the whole experiment is a snapshot (or series of snapshots), there will be no use for angular scanning using single-point detectors. Only a complete diffraction pattern or complete image would be useful, so the detectors will be parallel, possibly massively parallel ($>10^9$ pixels). The detectors will have to be optimised for a given class of samples that would define the experimental station. Ideally, the detectors should be able to distinguish each x-ray pulse of the XFEL. These experiments make high demands of two-dimensional x-ray detectors in terms of pixel number and size. The realisation of such detectors requires a specific R&D effort that will be described in Section 6.5.4. In Section 6.5.4.1 the specific detector requirements for the CXI instruments will be described. There will be a wide bank of parallel detectors at a few metres distance to see diffraction fringes from objects up to 10 µm in size (100 µm would be hard). A sophisticated system of (conical) collimators in front of the detector bank is needed for a clean scattered signal.

Imaging experiments at fixed photon energy, e.g. at 12 keV, require a high-resolution in-line camera system to record the images. The detector format will need to be as large as possible an array (4K×4K), optically coupled to an optimised fluorescent screen. The optical detector must be optimised for stability, linearity, reproducible background, but not so much for quantum efficiency.

Visible laser requirements

In this field of application no specific requirement for use of visible lasers for pump-probe experiments has yet been formulated. However, it is assumed that the experiments will need an ultra-fast laser to drive excitations of samples to be followed using the techniques described above. Visible ultra-fast lasers will be centrally provided for all instruments. The distribution of laser radiation to the instruments for CXI experiments can be designed at a later stage. The same applies to specific requirements, e.g. wavelength tunability. The instruments will foresee provision of these future options.

Other requirements

One important question is available computer power. On modern computers, 3-D Fast Fourier Transform (FFT) calculations for 1,024×1,024×1,024 data points can take about 10 seconds. Taking into account that for the full reconstruction several thousands iterations will be needed the time required for 3-D reconstruction of such a data set is ~14 hrs at present. Such durations could become a serious limitation for operating with big data sets. The hope is that in the coming years the data storage and processing time capabilities will improve considerably.

6.4.3.3 Realisation of the instrument

From their requirements, the CXI experiments ask for three instruments at SASE 3 (CXI 1 – Tunable soft x-rays), at SASE 2 (CXI 2 – Tunable hard x-rays) and at U 1 (CXI 3 – High energy x-ray spontaneous radiation). The SASE 3 beamline enables experiments in the range 0.28 to 1.0 keV and thus, covers the water window for investigation of biological specimen and the L-edges of the 3d transition metals for investigation of magnetic phenomena. At 1 keV, good conditions for investigation of nanocrystals are provided. Experiments requiring higher photon energies, i.e. 3-6 keV for M–edge investigations in actinides, 6-11 keV for L-edge investigations of rare earth elements and ~12.4 keV for bulk investigations, will be carried out at the SASE 2 beamline. Monochromatisation by using perfect crystals will be optional for the hard x-ray regime only. For beam transport, only mirrors will be used. The corresponding beam transports in the SASE 2, SASE 3 and U1 beamlines have been described in Sections. 6.2.4.2 to 6.2.4.4, respectively. All instruments will require focusing of the x-ray beam. Moderate focusing to beam sizes of the order 100 µm is achieved by using a focusing element near the location of the off-set mirrors. Extreme focusing to 0.1–1 µm beam size requires extremely short focal length and therefore needs to be integrated into the instruments.

CXI 1: Tunable soft x-rays

Since this experiment is most sensitive to alteration of the wave front by imperfect optics, it should be installed in the beam that comes directly from the offset mirrors, which have to be in the beamline for radiation protection reasons. Having 100 µm focusing provided through the second of these mirrors, the main focusing requirement of the instrument is to achieve much smaller spots.

The following elements belong to the CXI 1 instrument inside the experimental hall. They are depicted in the schematic layout of that instrument in Figure 6.4.25 and are described in Table 6.4.6. Collimating apertures or a slit system will be placed in front of the experimental chamber to define the beam size and to remove scattering from the incident x-ray beam. A gas photon flux monitor (see Section 6.3.2.1) will follow before a differential pumping section separates the beamline from the UHV vacuum chamber for experiments. For the energy range of this beamline, vacuum separation by means of windows is unlikely.

To achieve extreme focusing a special 0.1–1 µm focusing optics will integrated into the instrument. In this case the upstream beamline optics will use only flat mirrors in order to minimise wavefront errors. In-line optics that can be moved in and out will be an advantage. It will be integrated in the sample environment system so that the distance between optics and sample can be fitted to the proper focal distance of the optics. The sample chamber will be equipped with a high accuracy sample manipulator allowing x-y-z movements and rotation around two perpendicular axes. The chamber has to be capable of reaching 10^{-8} mbar for experiments requiring in-situ sample preparation and for samples sensitive to surface contamination. Sample loading from external chambers needs to be foreseen. Diffraction should be collected by a large 2-D area detector in the forward direction. It will be necessary to be able to vary the distance between sample and detector.

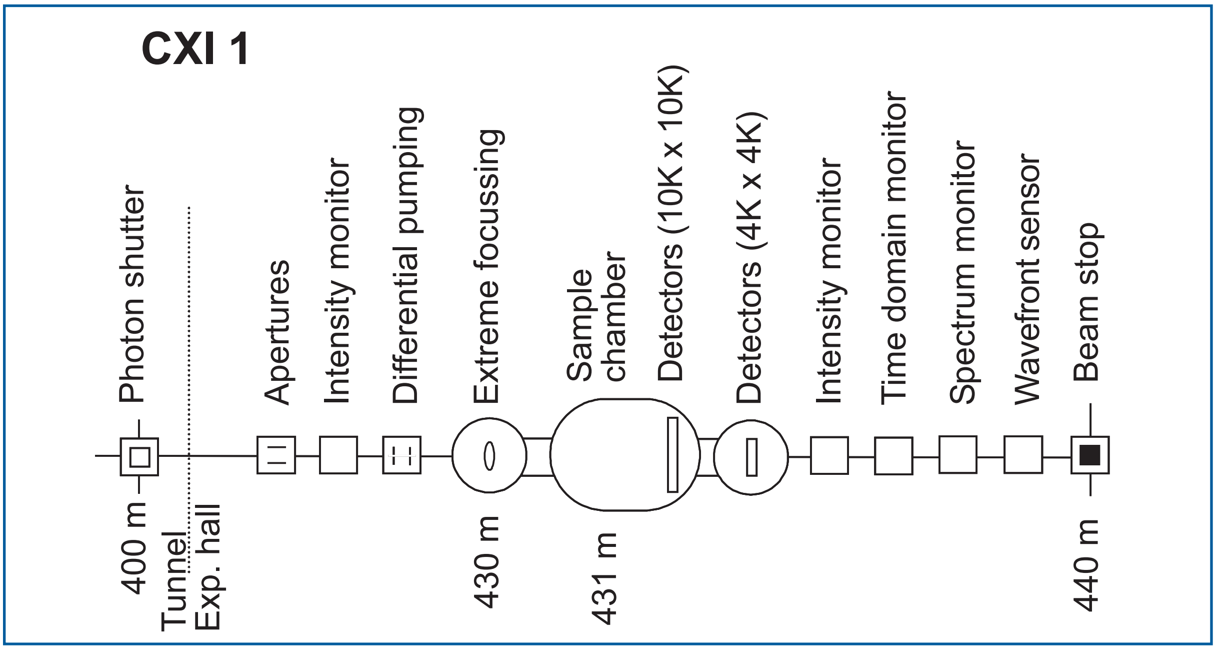

Figure 6.4.25 *Schematic layout of the CXI 1 instrument at the SASE 3 beamline. Variation in the distances between optics-sample-detector is foreseen.*

Experiments can absorb a significant proportion of the incident beam. It is, however, proposed to place most photon beam diagnostics in the transmitted beam. A second gas monitor detector will be used to measure the transmission. The spectral measurement should provide mean photon energy, bandwidth, and higher harmonic content on a pulse-by-pulse basis. Measurement of the detailed spectral properties, i.e. the width and distribution of spikes, is only performed upon request. Diagnostics of time domain properties should deliver the arrival-time required for pump-probe experiments using the visible laser. Finally, spatial measurements determine the beam location and its spatial distribution. Since these measurements are usually destructive they will be carried out in a dedicated setup at the end of the line and before the beam stop.

Item	Purpose	Specification
Slits/apertures	Beam definition, beam halo cleaning	0.25 µm accuracy, 1 µm repeatability
Intensity monitor	Measurement of incident photon flux	Transmissive (<5% absorption), single pulse measurement, relative accuracy $<10^{-3}$
Differential pumping	Separation of beamline and experiments vacuum	10^4 steps for all elements
Focusing optics	Extreme focusing for 0.28-1.0 keV	0.1 µrad angular stability
Sample chamber	Sample positioning and orientation, systems to verify sample alignment, provision of sample preparation	x-y-z move (0.25/1 µm), two rotations (0.25/1 mdeg), optical microscope, UHV conditions
Detector	Measurement of forward scatting in imaging experiments	2-D, 4K×4K pixels, 10×10 µm pixel size, central hole or beamstop
Detector	Measurement of diffraction for CXDI experiments	2-D, 10K×10K pixels, 0.1×0.1 mrad^2 pixel res.
Intensity monitor	Measurement of transmitted photon flux	Transmissive (<5% absorption), single pulse measurement, relative accuracy $<10^{-3}$
Spectral monitor	Measurement of mean energy, bandwidth, and harmonic content	Single pulse measurement, relative accuracy $<10^{-3}$
Spatial monitor	Measurement of spatial distribution, focus size	Single pulse measurement
Alignment unit	Positioning and position verification	Permanently operating, accuracy ~100 µm
Lead hutch	Radiation protection, temperature stabilisation, laser protection	4×10×3.5 m^3 (W×L×H), ±0.5° thermal stability
Control hutch	Operation of the instrument	Working environment (noise, temperature, light)

Table 6.4.6 *Elements and specifications of the CXI 1 instrument.*

CXI 2: Tunable hard x-rays

The CXI 2 instrument is designed for hard x-rays and could best be located at the SASE 2 beamline. Due to the coherence requirements, it should, again, be placed in the beam that comes directly from the offset mirrors. Having 100 µm focusing provided through the second of these mirrors, the main requirement of the instrument is to achieve much smaller spots. The use of a monochromatised beam with a bandwidth $\sim 10^{-4}$ is possible due to the double-crystal monochromator in the SASE 2 beamline.

The following elements belong to the CXI 2 instrument inside the experimental hall. They are depicted in the schematic layout of that instrument in Figure 6.4.26 and are described in Table 6.4.7. Collimating apertures or a slit system will be placed in front of the experimental chamber for beam definition and to reduce scattered radiation from the x-ray beam. A gas photon flux monitor (see Section 6.3.2.1) will follow before a differential pumping section separates the beamline from the UHV vacuum chamber for experiments.

For this energy range, vacuum separation by means of Beryllium or Diamond windows is another possibility. Great care has to be taken in the perfection of these windows is another possibility to preserve the wavefront properties.

To achieve extreme focusing, a special 0.1–1 µm focusing optics will be integrated into the instrument. In this case the upstream beamline optics will use only flat mirrors to minimise wavefront errors. In-line optics that can be moved in and out will be an advantage. The use of a pair of mirrors in KB geometry is another possibility. The optics are integrated in the sample environment system so that the distance between optics and sample can be fitted to the proper focal distance of the optics. The sample chamber will be equipped with a high accuracy sample manipulator allowing x-y-z movements and rotation around two perpendicular axes. The chamber has to be capable of reaching 10^{-8} mbar for experiments requiring in-situ sample preparation or being sensitive to surface contamination. Sample loading from external chambers needs to be foreseen. Diffraction in the forward direction should be collected by a large 2-D area detector. It will be necessary to be able to vary the distance between sample and detector. Again, Beryllium windows could become useful and the flight path may be realised in Helium to reduce absorption.

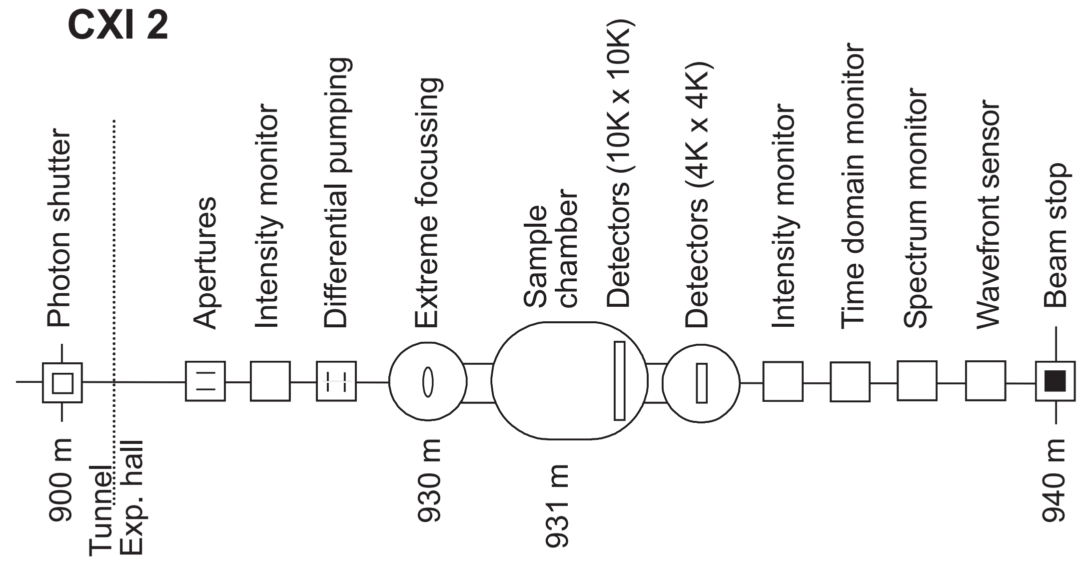

Figure 6.4.26 *Schematic layout of the CXI 2 instrument at the SASE 2 beamline. Variation in the distances between optics-sample-detector is foreseen.*

Item	Purpose	Specification
Slits/apertures	Beam definition, beam halo cleaning	0.25 µm accuracy, 1 µm repeatability
Intensity monitor	Measurement of incident photon flux	Transmissive (<5% absorption), single pulse measurement, relative accuracy <10^{-3}
Differential pumping	Separation of beamline and experiments vacuum	10^4 steps for all elements
Focusing optics	Extreme focusing for 3.1-12.0 keV	0.1 µrad angular stability
Sample chamber	Sample positioning and orientation, systems to verify sample alignment, provision of sample preparation	x-y-z move (0.25/1 µm), two rotations (0.25/1 mdeg), optical microscope, UHV conditions
Detector	Measurement of forward scatting in imaging experiments	2-D, 4K×4K pixels, 10×10 µm pixel size, central hole or beamstop
Detector	Measurement of diffraction for CXDI experiments	2-D, 10K×10K pixels, 0.1×0.1 mrad^2 pixel res.
Intensity monitor	Measurement of transmitted photon flux	transmissive (<5% absorption), single pulse measurement, relative accuracy <10^{-3}
Spectral monitor	Measurement of mean energy, bandwidth, and harmonic content	Single pulse measurement, relative accuracy <10^{-3}
Spatial monitor	Measurement of spatial distribution, focus size	Single pulse measurement
Alignment unit	Positioning and position verification	Permanently operating, accuracy ~100 µm
Lead hutch	Radiation protection, temperature stabilisation, laser protection	4´10´3.5 m^3 (W×L×H), ±0.5° thermal stability
Control hutch	Operation of the instrument	Working environment (noise, temperature, light)

Table 6.4.7 *Elements and specifications of the CXI 2 instrument.*

Experiments can absorb a significant proportion of the incident beam. It is, however, proposed to place most photon beam diagnostics in the transmitted beam. A second gas monitor detector will be used to measure the transmission. The spectral measurement should provide mean photon energy, bandwidth, and higher harmonic content on a pulse-by-pulse basis. Measurement of the detailed spectral properties, i.e. the width and distribution of spikes, is only performed upon request. Diagnostics of time domain properties should deliver the arrival-time required for pump-probe experiments using the visible laser. Finally, spatial measurements determine the beam location and its spatial distribution. Since these measurements are usually destructive they will be carried out in a dedicated setup at the end of the line and before the beam stop.

CXI 3: High energy x-ray spontaneous radiation

The CXI 3 instrument will be located at the spontaneous undulator beamline U 1, therefore, relaxed conditions with respect to the energy dissipation in the optics exist.

The instrument is optimised for operation with high energy photons in the range 50-90 keV. As the requirement for preservation of coherence equally applies to this instrument, it should be located in the beam that comes directly from the offset monochromator. The use of a monochromator instead of mirrors follows from the difficulty of obtaining high reflectivity at these photon energies. The collimating Beryllium lens in the beginning of the U 1 beamline will have some influence on the coherence properties and may need to be removed.

The following elements belong to the CXI 3 instrument inside the experimental hall. They are depicted in the schematic layout of that instrument in Figure 6.4.27 and are described in Table 6.4.8.

Collimating apertures or a slit system will be placed in front of the experimental chamber for beam definition and to reduce scattered radiation from the x-ray beam. A photon flux monitor (this could be a solid-state system in this case) follows. At these photon energies the beamline vacuum ends at the flux monitor. Polished Beryllium or Diamond can be used for vacuum window purposes.

To achieve extreme focusing, a special 0.1–1 µm focusing optics will be integrated into the instrument. One will have to investigate whether multilayer KB or refractive lens optics better preserve coherence and wavefront properties. The distance to the sample can be fitted to the proper focal distance of the optics. The sample will be mounted on a diffractometer including a detector arm for off-axis geometries. The diffractometer supports mounting of sample environments like cryogenic, heating or pressure cells.

Photon beam diagnostics of the transmitted beam provides photon flux and a wavefront sensor will be available for adjustment and verification of the micron focal spot.

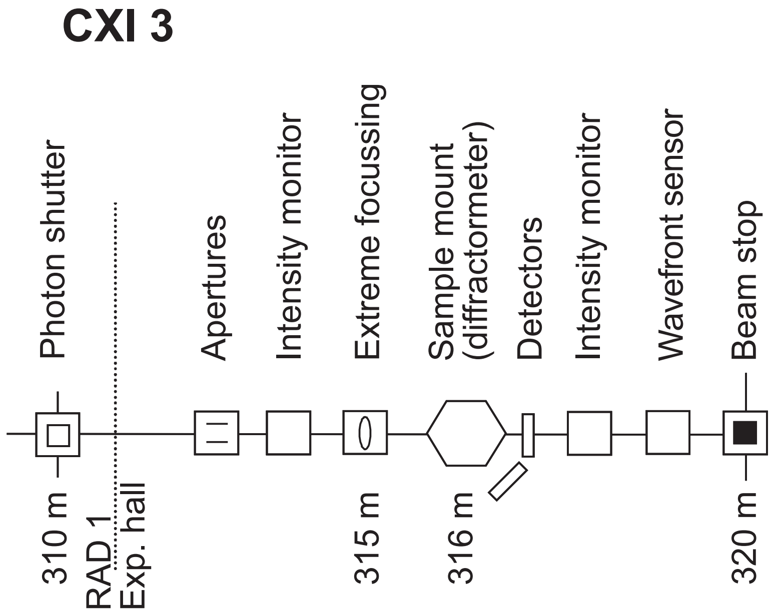

Figure 6.4.27 *Schematic layout of the CXI 3 instrument at the U 1 beamline. This instrument is located behind the RAD 1 instrument and distances are given in relation to the undulator end.*

Item	Purpose	Specification
Slits/apertures	Beam definition, beam halo cleaning	0.25 µm accuracy, 1 µm repeatability
Intensity monitor	Measurement of incident photon flux	Transmissive (<5% absorption), single pulse measurement, relative accuracy $<10^{-3}$
Focusing optics	Sub-µm focusing for 50-90 keV	0.1 µrad angular stability
Sample mount	Sample positioning and orientation, systems to verify sample alignment, provision of sample preparation	x-y-z move (0.25/1 µm), two rotations (0.25/1 mdeg), optical microscope
Detector	Measurement of forward scattering and diffraction	2-D, 4K×4K pixels, 10×10 µm pixel size, central hole or beamstop, mounted on diffract. arm
Intensity monitor	Measurement of transmitted photon flux	Transmissive (<5% absorption), single pulse measurement, relative accuracy $<10^{-3}$
Wavefront sensor	Verification of wavefront errors; Adjustment of sub-µm optics	
Alignment unit	Positioning and position verification	Permanently operating, accuracy ~100 µm
Lead hutch	Radiation protection, temperature stabilisation, laser protection	4×10×3.5 m^3 (W×L×H), ±1° thermal stability
Control hutch	Operation of the instrument	Working environment (noise, temperature, light)

Table 6.4.8 *Elements and specifications of the CXI 3 instrument.*

6.4.4 X-Ray Photon Correlation Spectroscopy

Coherent x-rays are particularly well suited for the study of nanoscale dynamics using x-ray photon correlation spectroscopy. The study of fast (t << 1 µs) dynamics (at large momentum transfers Q) was, up to now, restricted to the energy domain (inelastic) techniques. With the XFEL and its unprecedented peak brilliance and high degree of coherence one will be able to study fast dynamics in the time domain which is of outmost importance for a wide variety of phenomena **[6-175]**. Coherence preserving optics coupled with fast 2-D detectors will be essential to the success of this technique at the XFEL.

6.4.4.1 Scientific case

Complex nanoscale dynamics is an omnipresent phenomenon which is investigated at the frontier of condensed matter research. It comprises a multitude of collective processes such as the visco-elastic flow in liquids, polymer dynamics, protein folding, crystalline phase transitions or the switching of domains. The involved timescales range from femtoseconds to seconds. Slow processes (t >1 µs) are, in favourable cases, accessible via conventional XPCS at third generation synchrotron radiation sources **[6-176]**. The study of fast (t << 1 µs) dynamics (at large momentum transfers Q) is, however, restricted, up to now, to the energy domain (inelastic) techniques. This, however, will change with the new FEL sources providing extremely brilliant (B>10^{33} ph/s/mm^2/mrad^2/0.1% bw) and highly coherent x-ray beams. For the first time one will be able to study fast dynamics in the time domain, thus giving direct access to the dynamic response function S(Q,t), instead of S(Q,ω), which is of central importance for a variety of phenomena such as fast non-equilibrium dynamics initiated e.g. by a short pump pulse.

XPCS measures the temporal changes in speckle patterns produced when coherent light is scattered by a disordered system. Today's third generation synchrotron light sources can measure the low frequency dynamics (10^6 Hz to 10^{-3} Hz) in a Q range from, typically, 10^{-3} Å^{-1} up to several Å^{-1}. X-ray Photon Correlation Spectroscopy is, in particular, complementary to Dynamic Light Scattering (DLS) or Photon Correlation Spectroscopy (PCS) with visible coherent light which also probes slow dynamics ($\omega < 10^6$ Hz) but can cover only the long wavelength Q < 10^{-3} Å^{-1} regime. X-ray Photon Correlation Spectroscopy is furthermore, not subject to multiple scattering, a phenomenon frequently complicating the analysis of PCS data in optically opaque systems. Neutron-based techniques (inelastic and quasi-elastic neutron scattering, neutron spin-echo) or Inelastic X-ray Scattering (IXS) on the other hand, can access the same Q range as storage-ring based XPCS but probe the dynamic properties of matter at high frequencies from, typically, 10^{14} Hz down to about 10^8 Hz. The XFEL with its coherent flux increased by nine orders of magnitude, will allow, for the first time, coverage of dynamics up to about 10^{13} Hz at large Q. This is illustrated in Figure 6.4.28 showing frequency-wavevector space covered by a selection of relevant methods. There is a wide variety of problems to be addressed (see, for example, **[6-177, 6-178]**) and some prominent examples are summarised in the experimental programme.

Experimental programme

Coherence is one of the most prominent features of XFEL radiation. A comprehensive understanding of its coherence and correlation properties is not only of fundamental interest but a necessary condition for coherence-based experiments. A characterisation of the coherence properties is thus mandatory before proceeding to time domain experiments.

I. Coherence and correlations

The methodology of characterising coherence properties in terms of correlation functions is theoretically well developed and experimentally established by the optical laser community. We propose to setup and carry out an experimental programme aimed at studying first- and higher-order correlation functions, which allows one to determine not only the spatial and temporal coherence parameters (including the coherent flux) but also provides insight into the mode structure, photon statistics (bunching/antibunching) and possible non-Gaussian properties of the source. The programme will involve single (100 fs) shot Young's Double Slit experiments and (Hanbury-Brown Twiss type) intensity-intensity correlation experiments. The results will be fundamental to the tuning and upgrade programme of the facility since the results are directly comparable with FEL simulations that predict the mode structure and the degree of coherence. The expected high degree of coherence will also open a route to non-Gaussian dynamics (e.g. intermittent dynamics in complex fluids **[6-179]**) via higher order time correlation functions.

II. Study of glassy dynamics

Many liquids, when rapidly cooled below their freezing points, form metastable glassy or amorphous phases. This applies for a wide variety of materials including metallic alloys, oxides such as Silica, polymeric materials, and many others. Regardless of their importance, glassy materials are probably among the least understood materials at a fundamental level. Conventional equilibrium statistical mechanics does not predict the existence of the amorphous state, whereas it can explain most other states of matter, even quite exotic ones like superconductivity and superfluidity. Understanding visco-elastic effects in glassy materials is, thus, an important topic of fundamental research.

Glassy materials can be classified by the nature of their dynamics. In a typical glass-forming system, the viscosity increases exponentially by many orders of magnitude as temperature is lowered, until viscous flow processes are effectively frozen. Methods such as DLS or NMR have helped to characterise the relevant relaxation processes such as the primary (a) relaxation processes with timescales associated with viscosity. Other, faster (b) processes are also observed near the glass transition **[6-180]**. The nature and role of these processes are still under debate and discussed, for example, in the framework of mode coupling theory **[6-180, 6-181]**.

Experiments set up to study the transition require slow rates to look for the underlying thermodynamic phase transition but still need to be fast enough to avoid crystallisation. Light scattering, neutron scattering, and recently inelastic x-ray scattering **[6-182]** have examined phonon-like modes in these systems and have seen important changes near the glass transition. But measurement times are long, making the systems difficult and frequently even impossible to study with inelastic techniques in particular when the relevant timescales fall below the 1 MHz regime (see also Figure 6.4.28).

X-ray Photon Correlation Spectroscopy measures the time constants of a system as a function of wave vector and gives direct information on the dynamics. The region of Q and t covered by XPCS is very important for the understanding of the nature of the dynamics in glass forming systems both on the atomic and nanoscale. It is proposed to undertake studies spanning a very large range of timescales ($l0^{-12}$ to 10^{3} s) in order to observe the evolution of the dynamics from liquid to glassy behaviour as the temperature is lowered. There are many possible candidates for study, such as B_20_3. This is a random-network glass with well understood macroscopic properties **[6-183]**, and on which complementary Raman **[6-184]** and neutron scattering **[6-185]** studies have been performed. Its low electron density helps to minimise adiabatic heating by the beam. In order to cover the very large range in timescales different experimental set-ups (see below) will need to be applied.

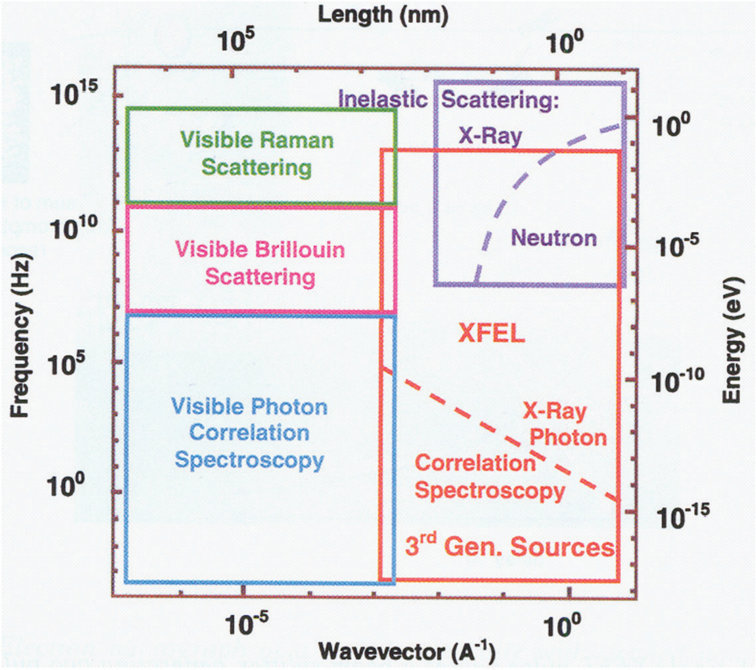

Figure 6.4.28 *Frequency-wavevector space covered by different experimental techniques. X-ray Photon Correlation Spectroscopy can operate at large Q and cover slow dynamics at third generation sources and fast dynamics at XFEL sources.*

III. Phonon spectroscopy

X-ray Photon Correlation Spectroscopy can access density fluctuations allowing experiments related to phonon spectroscopy that can be done today with inelastic x-ray and neutron scattering. However, since the dynamics is measured directly in the time domain, one can access the full timescale from picoseconds to nanoseconds and longer in a single experiment. Moreover, there is the opportunity to examine higher order correlation functions from a cross-correlation analysis of the speckle pattern. While traditional inelastic scattering experiments are limited to density-density correlations, picosecond-XPCS could shine new light on short time dynamics, where coordinated motions of several molecules become important, e.g. during a crystallisation process.

However, even with the extremely high brilliance of the XFEL, it will not be possible to observe equilibrium dynamics of phonons directly (maybe with the exception of extremely strong acoustic phonons very close to a Bragg peak) since the average scattered intensity per speckle will be much less than one count per pulse **[6-186]**. Therefore, one has to add many speckle patterns before a correlation analysis can be done. This will average out random thermal fluctuations. Instead, one will observe phonons that are coherently excited, e.g. by a first x-ray pulse. Typically, a first pulse will generate a hot spot in the sample in the order of the beam size and x-ray attenuation length. A delayed pulse will then reveal insights into the thermal transport processes. To generate a smaller hot spot, a focused laser beam can be also used as a pump. A way to introduce distortions on an even smaller length scale is the use of standing x-ray waves. One could either place the sample in the standing wave field of a Bragg reflection or use x-ray transient grating spectroscopy, where the coherent beam is split up and a standing x-ray pattern is generated by crossing these two beams.

IV. Surface XPCS with an XFEL

Surface XPCS experiments at third generation storage sources have been performed successfully in the past and surface dynamics has been investigated on a variety of systems such as membranes, polymer films or bulk liquids. Surface XPCS, in combination with the x-ray standing wave technique, allows, for example, the study of fluctuations of buried interfaces. However, the nanometer length scale of surface dynamics is not accessible due to the limited coherent photon flux. Here, the XFEL provides exciting new possibilities. We will give an estimate of the expected timescales and count rates of surface XPCS experiments at an XFEL for capillary wave dynamics on three model liquids: water, liquid Mercury and liquid Glycerol.

Water: At Q = 0.1 Å^{-1} the capillary waves on liquid water are overdamped waves with a correlation function $g_1(t) \sim \exp(-t/t_0)$. Continuum hydrodynamics yields a value of the relaxation time of $t_0 \approx 2.5 \times 10^{-11}$ s which is 100 times longer than the 100 fs pulse width and 10000 times shorter than the pulse separation of 200 ns. Therefore, a delay line unit (see below) is mandatory for measuring relaxation times in this time region.

Assuming a delay line efficiency of 1% one can operate with two pulses carrying about 10^{11} photons each. If the detector subtends a solid angle $\Delta\Omega$ the intensity scattered into the detector can be estimated via **[6-187]**:

$$I = \frac{\Delta\Omega}{A}\frac{d\sigma}{d\Omega} = I_0 \times \frac{\Delta\Omega}{A} \times L_x L_y \times \frac{\left|k_0^2(1-n^2)\right|^2}{16\pi^2} \times \left|T(k_1)\right|^2 \left|T(k_2)\right|^2 S(Q) \quad , \tag{6.2}$$

where A describes the beam area, I_0 the intensity of the incoming beam and $(d\sigma/d\Omega)$ the diffuse scattering cross section. $L_x L_y$ denotes the illuminated area, k_0 the x-ray wave number, n the index of refraction and $T(k_i)$ the transmission factors of the incident and exit beams, respectively. S(Q) is the capillary wave scattering function which can be approximated for grazing incidence geometry as $S(Q) \approx k_B T / 2\pi\gamma Q^2$ where γ denotes the surface tension. For incident angles below the critical angle of total external reflection, the number of photons scattered per (split) XFEL pulse at Q =0.1 Å^{-1} into a detector area of 50 × 50 µm^2 at 1 m distance is 4×10^{-4}. With 3,000 pulses and 10 Hz repetition rate, one will detect about 12 photons per second. Thus, within minutes sufficient statistics should be obtained. At Q = 1 Å^{-1} the count rate is 0.12 ph/s; at Q = 0.01 Å^{-1} one finds 1,200 ph/s.

In the energy domain the overdamped correlation function would yield a Lorentzian energy spectrum centred at $\omega = 0$ with a width ΔE of ca. 20 µeV for Q = 0.1 Å^{-1}. This energy broadening would be difficult to resolve with inelastic x-ray scattering.

Liquid Mercury: Liquid metals show interesting surface structures such as an atomic layering parallel to the free surface (liquid Mercury). Therefore, the capillary wave dynamics at small length scales is of special interest as the continuum hydrodynamics may be strongly affected by the layering properties of metal atoms at the surface. Up to $Q=0.2$ Å^{-1}, continuum hydrodynamics is predicting propagating capillary waves on a liquid Mercury surface. Capillary waves with larger Q values are overdamped. The combination of high surface tension, low viscosity and high density makes the capillary wave dynamics on liquid Mercury faster than that of water. Moreover, the large value of the surface tension decreases the x-ray scattering cross-section considerably. For $Q = 0.1$ Å^{-1} the expected relaxation time is 5×10^{-13} s ($\Delta E = 1.3$ meV) and the estimated countrate is about 0.18 ph/s.

Liquid Glycerol: Glycerol is a typical glass former and the viscosity strongly depends on temperature. At room temperature the viscosity of Glycerol is three orders of magnitude larger than that of water implying a considerably slower dynamics. Liquid Glycerol at -10°C has a viscosity of 35 Pa s. The capillary waves are overdamped and the relaxation time at $Q = 1$ Å^{-1} is 100 ns. One can, thus, operate in a time regime without need for a delay line unit and can use 10^{13} photons per pulse. As the surface tension of liquid Glycerol is similar to water, the scattering cross-section will be very similar. Just by inspecting the numbers it seems that nanometer scale surface dynamics should be observable at least with liquid Glycerol. For $Q = 0.1$ Å^{-1}, the relaxation time is 10^{-6} s ($\Delta E = 6.6$´10^{-7} meV) and the number of scattered photons into a 50×50 µm^2 aperture at 1 m distance is about 1,680 ph/s. We note that all these experiments are luminosity limited and the given estimates assume, in fact, the use of all 3,000 bunches in a 600 µs bunch train repeated at a 10 Hz repetition rate. Open questions to be investigated further are beam damage and the influence of bulk hydrodynamics **[6-188]** at large Q. The onset of non-classical behavior is a fundamental issue that is of interest for all liquids.

V. Time-resolved magnetic scattering

Magnetic x-ray speckle has been observed in a variety of systems **[6-189]**. More recently it has been shown that magnetic stripe domains can be imaged with a coherent soft x-ray beam **[6-190]**. Sensitivity to magnetism in the CoPt multilayer stemmed from tuning the beam energy to the Co L3 absorption edge at 778 eV (λ=1.6 nm). A reference aperture in the sample allowed retrieval of the real-space structure of the sample by simple Fourier transformation and a resolution of 50 nm was achieved. Provided there is enough intensity, the temporal fluctuations of spins and magnetic domains can be studied by recording the intensity changes at one given point (or Q value) in the scattering pattern as a function of time. Specific to magnetic scattering experiments is the necessity to tune the incident beam energy to distinct absorption edges in the material in order to achieve or increase the sensitivity to the magnetic states or bands. The best suited absorption edges ($M_{4,5}$) in rare-earth systems and in 3d transition metals ($L_{2,3}$) would require circularly polarised, soft x-rays as provided by the SASE 3 undulator. As the ultimate size resolution is set by the wavelength of the scattered radiation, XPCS in the soft energy domain will allow the study of domain dynamics down to domain sizes of several nm in 3d transition metals, exploiting 2p-3d scattering resonances, and in rare-earth compounds, exploiting the 3d-4f processes. As the coherent scattering is sensitive to the individual domain pattern (beyond statistical averages), critical dynamics can be probed on a nanometre length scale down to timescales in the nanosecond and sub-nanosecond range. This opens up new routes to the investigation of domain fluctuations in the vicinity of the (Curie or Neel) transition temperature. Whether or not thin film magnetic systems will be able to withstand the full

XFEL beam will need to be explored in detail. First estimates indicate that this will be a very serious issue.

VI. Non-equilibrium dynamics

When a disordered homogeneous material is rapidly brought to a new set of conditions, corresponding, for example, to the coexistence of two equilibrium phases, a spatial pattern of domains of the two phases develops. A change of conditions can, for example, be accomplished by a rapid quench from a high temperature to a low one below the miscibility gap. The result of such a quench is the creation of a microstructure of interconnecting domains. These domains grow in order to minimise the areas of the domain walls that separate the phases.

When the average domain size R(t) at time t is large compared to all other relevant length scales except for the dimension L of the system itself, the system looks invariant if all lengths are measured in units of that domain size. The time dependence of the average domain size can typically be described in terms of an exponent n, such that $R \sim t^n$. This scaling hypothesis applies to a large range of systems. For example, for systems described by a non-conserved scalar order parameter the growth exponent is found to be n=1/2. This applies, for example, Ising systems with spin-flip dynamics, binary alloys undergoing an order–disorder transformation or some magnetic materials. For other systems with conserved order parameter and with diffusion being the only growth parameter one finds n=1/3. This applies for the conserved Ising model and, for example, binary alloys undergoing phase separation. Information on the statistics of fluctuations about this average behaviour (which differs from classical fluctuation statistics) is, however, scarce because conventional methods are not easily applicable since (by the nature of the process) the absolute time matters. A time domain method, such as XPCS, can address such processes as has been shown in recent prototype experiments **[6-191, 6-192]**. Here, fluctuations about the average intensity can be quantified by means of a two time (t_1, t_2) intensity correlation function.

$$C(Q,t_1,t_2)=\frac{\langle I(t_1)I(t_2)\rangle-\langle I(t_1)\rangle\langle I(t_2)\rangle}{\left[\langle I^2(t_1)\rangle-\langle I(t_1)\rangle^2\right]^{1/2}\left[\langle I^2(t_2)\rangle-\langle I(t_2)\rangle^2\right]^{1/2}} \tag{6.3}$$

Figure 6.4.29 shows a contour plot of a two-time correlation function for the example discussed in **[6-17]**. Values of C for each contour and the directions of the alternative coordinates $t_{mean}=(t_1+t_2)/2$ and Δt are indicated. It is readily observed that the lagtime $\tau = \Delta t/2$ increases as a function of increasing absolute time t_{mean}, thus, showing that the dynamics is getting slower as a function of t_{mean}. It was shown in the experiment that the correlation times actually obey a scaling law in agreement with the model expectations. Similar experiments were carried out in phase-separating AlLi alloys and analysed successfully in terms of two-time correlation functions **[6-192]**. It is evident that the XFEL will allow the study of the early (short-time) stages of these processes. The XPCS pump-probe configuration will be ideally suited for any type, but in particular fast, non-equilibrium process. The pump or trigger source for reactions or transformations may comprise optical lasers, the XFEL, a Terahertz source, pulsed electric and magnetic fields and/or others.

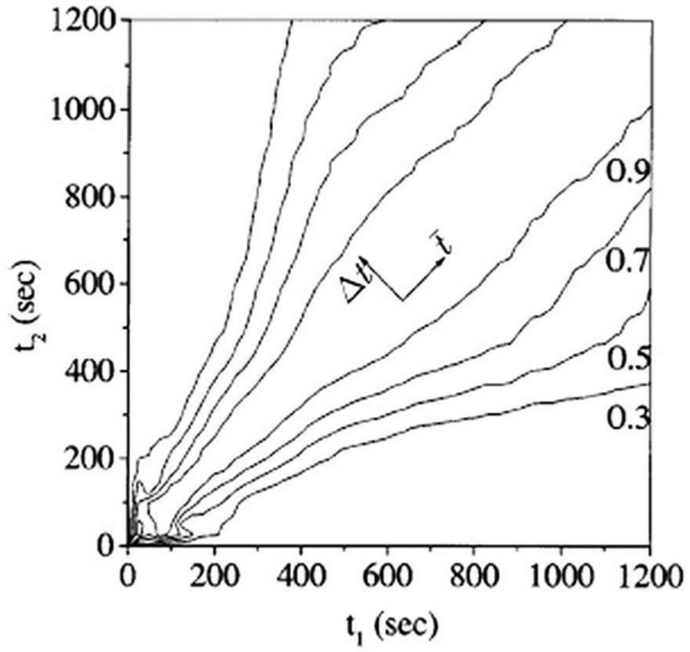

Figure 6.4.29 *Contour plot of two-time correlation function at Q=0.01 Å^{-1} in borsilicate glass after a quench to 963K.* Δt *refers to the lagtime and* $t = t_{mean} = (t_1+t_2)/2$ **[6-191]**.

XPCS technique

X-ray Photon Correlation Spectroscopy probes the dynamic properties of matter by analysing the temporal correlations between photons scattered by the material. Correlations of the scattered intensity can be quantified via the normalised time correlation function:

$$g(t) = \frac{\langle n(t)n(t+\tau)\rangle}{\langle n\rangle^2} \tag{6.4}$$

where n(t) is the number of detected photons at time t and the brackets denote the time average. X-ray Photon Correlation Spectroscopy requires the sample to be illuminated coherently. Thus an intense x-ray beam with sufficiently large transverse ξ_t and longitudinal ξ_l coherence length is required. The longitudinal coherence length $\xi_l = \lambda^2/\Delta\lambda$ depends on the monochromaticity of the beam. With an intrinsic bandwidth of ≈ 0.1% one finds $\xi_l = 100$ nm. Larger longitudinal coherence lengths can be achieved by monochromatisation. This estimate of the longitudinal coherence length agrees to within a factor of 2 with the results of simulations for the SASE process that yield a coherence time between 0.2 fs and 0.22 fs for $\lambda=0.1$ nm. The longitudinal coherence length must be larger or equal to the maximum path length difference in the sample under investigation. Thus, ξ_l sets a limit for the largest accessible momentum transfer Q. The transverse coherence length is usually determined by the source size σ, the wavelength λ and the distance to the source R via ξ_t » $(\lambda/2)\,(R/\sigma)$. For the XFEL, the beam can be expected to be largely spatially coherent, and ξ_t corresponds to the beam size. The flux of coherent x-rays is proportional to the source brilliance B via $F_c = (\lambda/2)^2 \times B$. The high coherent x-ray flux from the XFEL will allow XPCS measurements at higher frequency ω and on a greater variety of materials, overlapping with energy-domain measurements using neutron and x-ray inelastic scattering. Time-domain XPCS measurements will provide truly complementary information for understanding relaxational processes (e.g. often associated with the 'central peak' in inelastic scattering). The accessible time windows will naturally be influenced by the time structure of the XFEL (see also Figure 6.1.1). To exploit the unique features of the XFEL, we propose the development of an instrument with the capability for three types of XPCS techniques:

- Using the very high time-averaged coherent x-ray flux from the XFEL to carry out XPCS measurements over timescales from 10^{-1} to 10^{3} seconds or between 200 ns and 600 µs by recording a sequence of speckle patterns ('sequential' technique).
- Using the extremely high-peak coherent x-ray flux from the XFEL to carry out XPCS measurements over timescales from 10^{-12} to 10^{-8} seconds using a 'split-pulse' technique.
- The 'pump-probe' technique is based on a comparison of two speckle patterns. One taken before the pump pulse hits the sample and a second one taken at time Δt after the pump pulse has excited the sample.

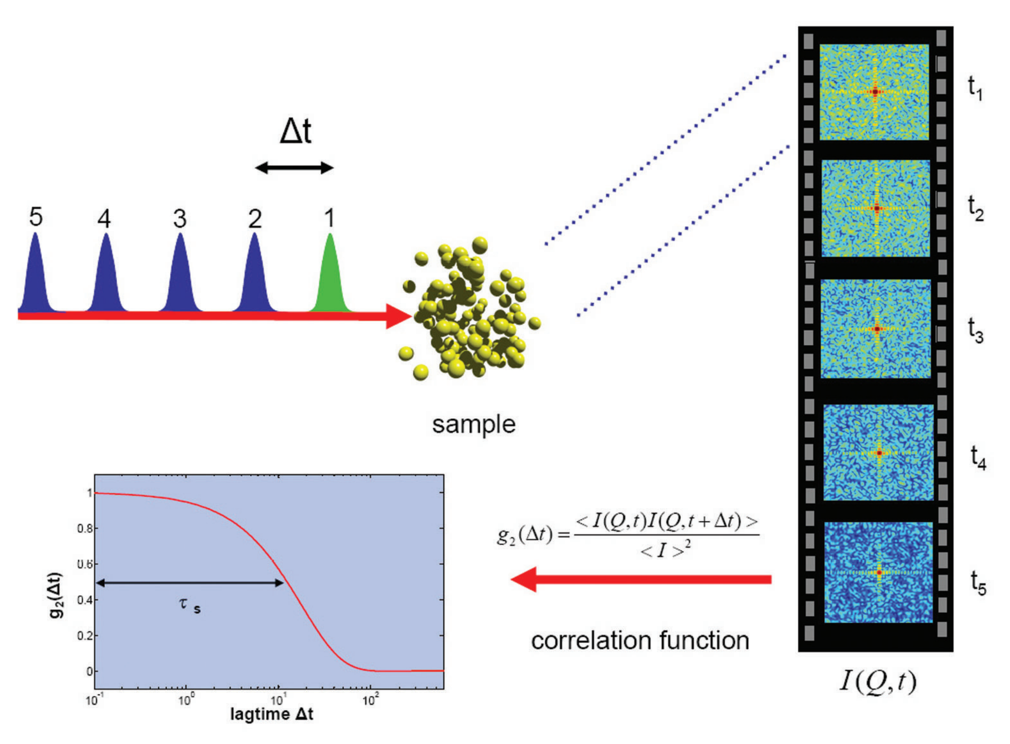

Figure 6.4.30 *Illustration of the XPCS sequential technique.*

Sequential technique: Important aspects of the microscopic dynamics of systems occur on relatively long timescales, e.g. longer than 0.1 s. This means that it will be possible to employ the very high time-averaged coherent x-ray flux from the XFEL, averaged over the 0.1 s bunch duration, to investigate the dynamics using XPCS data collection and analysis techniques that are similar to those used now. Such an experiment consists of collecting a sequence of speckle patterns on an area detector (see Figure 6.4.30). From an analysis of these sequences, correlation times from a few repetition times up to many minutes can be measured. The advantage of the XFEL will be in higher signal rates than currently available. The specific time structure of the XFEL will also allow the recording of dynamic data within the 600 µs long macro-bunches. The shortest time will be given by the micro-bunch separation of 200 ns. It might turn out to be favourable to divide up this time window in logarithmic time bins, thus, requiring a 2-D detector to operate at a 5 MHz frame rate but only with a limited number of frames to be stored.

Split-pulse technique: The short pulse duration of the XFEL will allow the extension of XPCS studies to much faster timescales than currently possible. For example, to understand the dynamics in glass-forming systems at the nanoscale, it will be important to carry out studies spanning a very large range of timescales (10^{-12} to 10^{3} s) in order to observe the evolution of the dynamics from liquid to glassy behavior as the temperature is lowered. In order to probe timescales between 10^{-12} and 10^{-8} s, we propose the development of a split-pulse technique (Figure 6.4.31), taking advantage of the instantaneous brilliance of the XFEL. The concept of the technique is to split each x-ray pulse into two equal-intensity pulses separated in time, but propagating along the same path. The scattering from the two pulses will then be collected during the same exposure of an area detector. If the sample is static on the timescale of the two pulses, the contrast in the summed speckle pattern will be the same as that from a single pulse. If the sample evolves on this timescale, the summed speckle pattern will have lower contrast. Thus, by analysing a set of such patterns, each for a different time delay, the correlation times of the system can be measured, on timescales down to the pulse duration. A pulse splitter with a path length difference variable from 3×10^{-4} to 3 m would give delay times from about 10^{-12} to 10^{-8} seconds. Longer time delays between pulses may be possible using two electron bunches in the FEL.

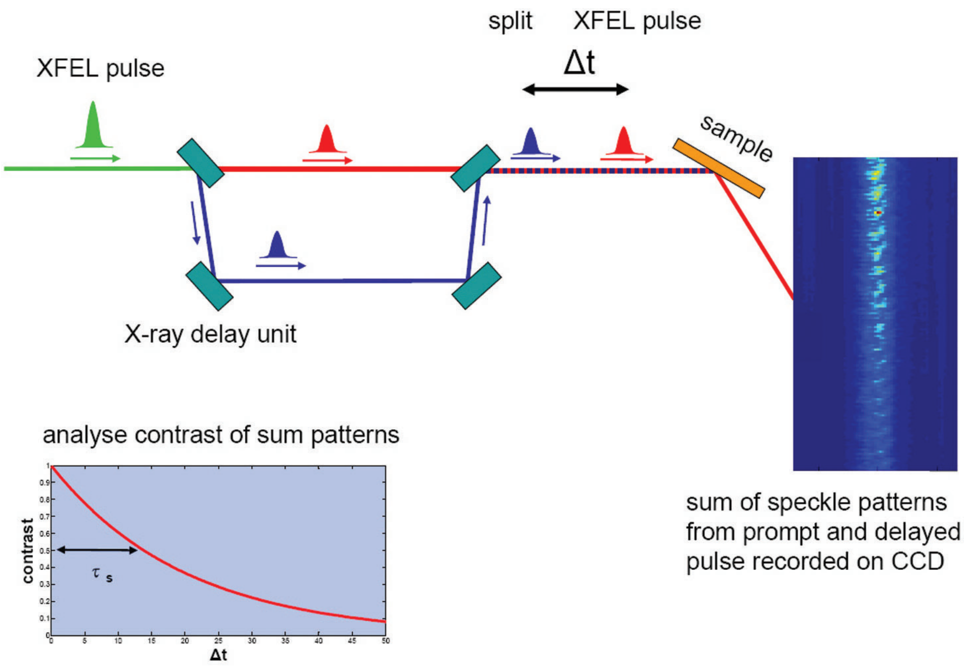

Figure 6.4.31 Illustration of the XPCS split-pulse technique.

Pump-probe technique: The XPCS pump-probe technique (Figure 6.4.32) compares two speckle patterns: one before exposing the sample to a pump pulse with a second pattern taken a time interval Δt after the pump pulse. The pump sources for reactions and transformations may comprise optical lasers, the XFEL, a Terahertz source, pulsed electric and magnetic fields, shock waves, and/or others. This allows us to address timescales between 100 fs and typically, 200 ns or longer. This configuration can be used to explore the timescales for magnetisation processes, phase transitions in ferroelectrics, surface dynamics and, for example, during pulsed laser deposition or internal motions in proteins. In principle one could also combine the pump pulse with the above described split-pulse technique.

Beam damage issues

The pulsed structure of the XFEL presents an important issue for the design of a beamline optimised for XPCS measurements, because of potential sample heating by the beam. For dynamics studies, one would like to avoid heating the sample by more than a few degrees during the measurement. For a pulsed source, two regimes must be considered: a) Adiabatic heating by each pulse, over timescales too small for significant heat flow, so that the temperature rise is determined by the heat capacity of the material; and b) steady-state heating by the time-averaged power in a train of pulses.

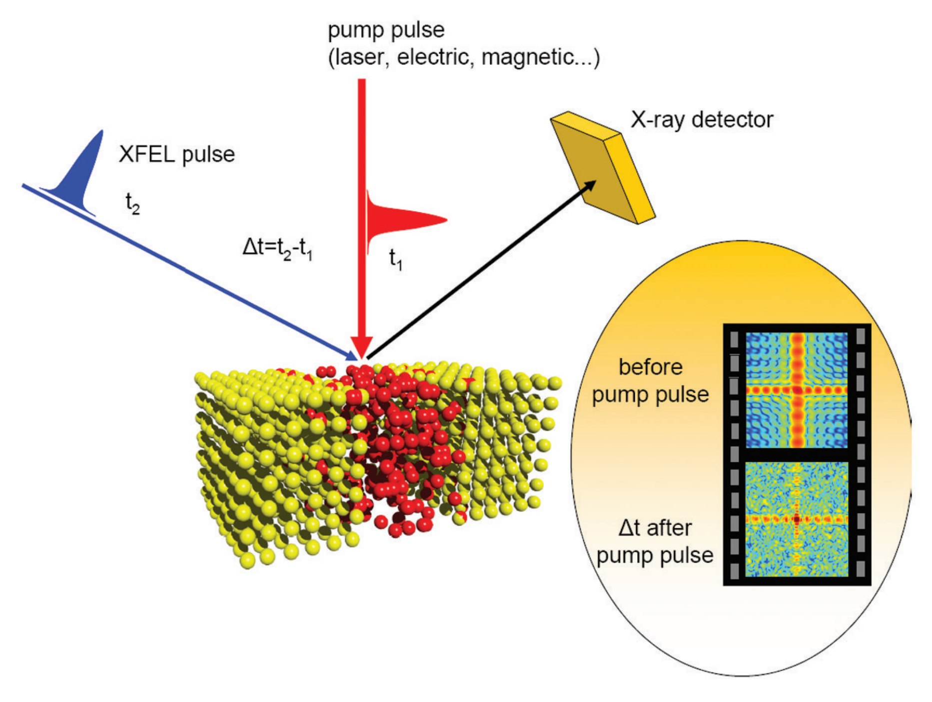

Figure 6.4.32 *Illustration of the XPCS pump-probe technique.*

In this second limit, the temperature rise is given by a balance of energy flow into and out of the sample volume. The ratio of the thermal time constant for heat dissipation to the pulse spacing determines whether the adiabatic or steady-state temperature rise is larger. Figure 6.4.33 illustrates the temperature response at the beginning of a pulse train in each of these limits.

The amount of sample heating in the adiabatic case can be evaluated using an analysis developed for the LCLS case **[6-179]**. Figure 6.4.34 shows a comparison of the quantities N_{MIN} (the minimum required number of photons per pulse to give sufficient signal per speckle), N_{MAX} (the maximum tolerable photons per pulse to avoid sample disturbance) and N_{AVAIL} (the available photons per pulse). These are plotted as a function of sample composition for two energies, using $\Delta T_{MAX} = 1$ K, a beam area of 10^{-4} cm^2, and two types of samples (having relatively narrow or broad scattering). The calculation predicts that XPCS will be feasible when the value of N_{MIN} is lower than both N_{MAX} and N_{AVAIL} (shaded areas). The result depends strongly on sample composition and photon energy. Because of the order-of-magnitude uncertainty in several quantities, these calculations do not provide exact limits, but do indicate that feasibility will depend upon photon energy, sample composition and scattering power.

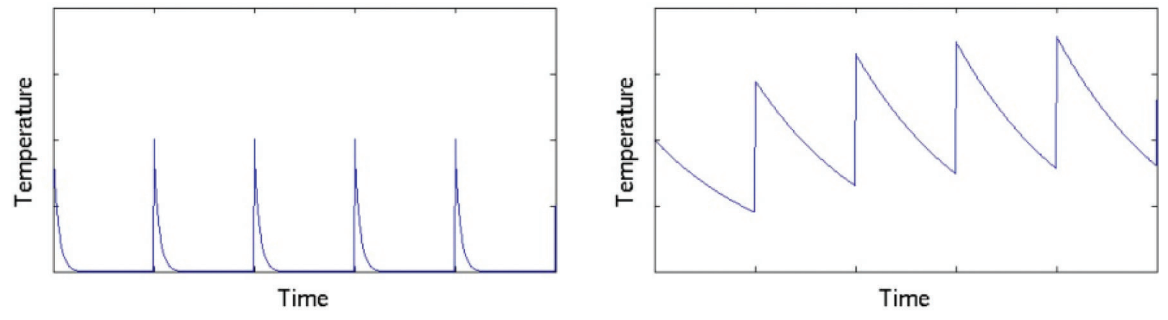

Figure 6.4.33 *Schematic temperature response to a pulse train, for samples with a thermal time constant that is a) smaller or b) larger than the pulse spacing.*

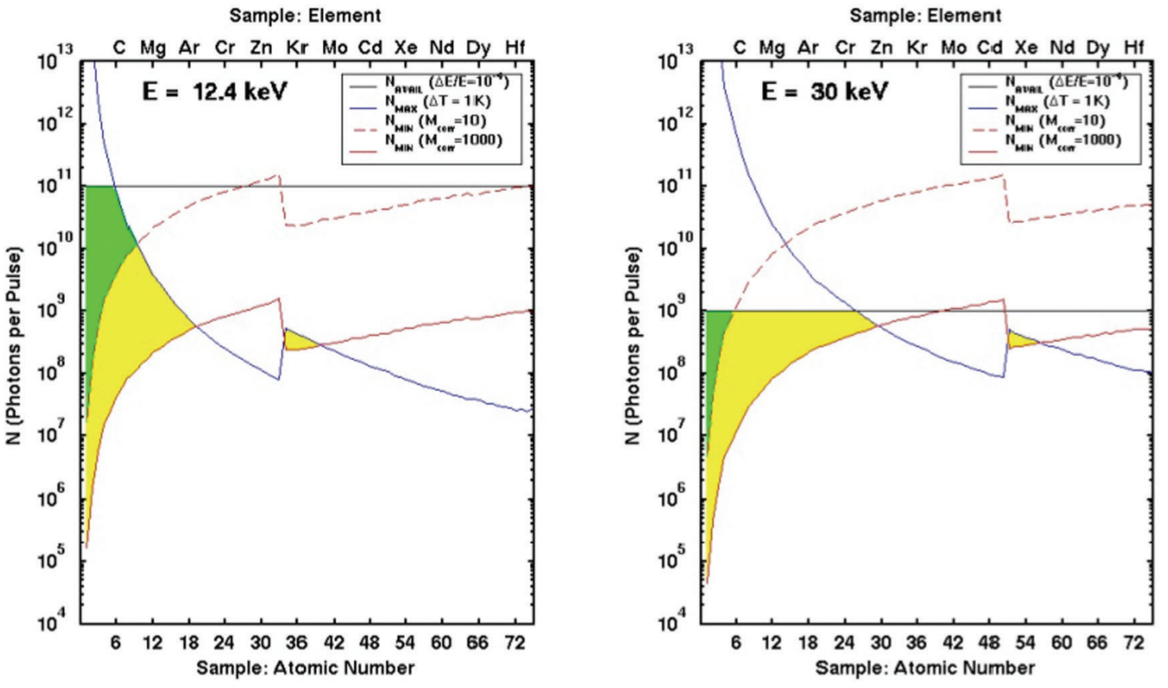

Figure 6.4.34 *Comparison of the calculated number of photons per pulse available from the XFEL (N_{AVAIL}), the number tolerable due to beam heating of the sample (N_{MAX}), and the number required for XPCS (N_{MIN}) for two types of samples, corresponding to a typical liquid or glass (M_{corr} = 10) or to nanoscale clusters in a polymer blend (M_{corr} = 1,000), as a function of sample composition, at 12.4 (left) and 30 (right) keV photon energies. Experiments are feasible in the shaded regions (see also* **[6-179]***).*

The relatively short time between pulses at the XFEL (200 ns) compared with LCLS (8 ms) means that steady-state sample heating must also be considered for the XFEL. Here. we present an analysis based on a simple transmission geometry, where the penetration depth of the x-rays is larger than the beam diameter. The illuminated sample volume is thus, a cylinder having the diameter of the beam, d.

We consider conduction transverse to the beam direction as the primary energy flow out of the sample. A thermal time constant can be calculated that is the ratio of the adiabatic temperature rise per unit deposited energy, to the steady-state temperature rise per unit deposited power. This is given by $\tau \approx d^2 \log(d_0/d)/8D_{th}$, where d_0 is the outer diameter of the thermal diffusion zone and D_{th} is the thermal diffusivity. Table 6.4.9 shows values of τ calculated for various sample materials, taking d_0 to be twice the absorption length at 12.4 keV. The time constant is smaller for smaller beam diameters. For highly conductive materials such as Gold or Copper, the thermal time constant can be less than the XFEL pulse spacing (200 ns). However, for most materials, the thermal time constant is larger than 200 ns, indicating that the steady-state temperature rise will be larger than the adiabatic temperature rise if the sample is exposed to every pulse.

Material	**D_{th} [cm^2/s]**	**τ (d=25 μm) [μs]**	**τ (d=10 μm) [μs]**
Au	1.32	0.40	0.063
Cu	1.12	0.46	0.074
Al	0.84	2.9	0.60
Al_2O_3	0.072	35	7.1
SiO_2 glass	0.003	890	180
H_2O liquid	0.0014	3200	590

Table 6.4.9 *Thermal time constants τ for various materials, taking d_0 twice the absorption length at 12.4 keV. Here d is the beam size and $D_{th}=k/C_p$ the thermal diffusivity.*

6.4.4.2 Instrument requirements

The experiments described above lead to requirements for an instrument for scientific applications using XPCS techniques. They concern the performance of the light source, the optical elements and the diagnostic equipment, the sample environment, and detectors. The experiments described in this section request mostly hard x-ray XFEL radiation at ~12 keV photon energy. For some experiments one wants to apply third harmonic radiation at considerably higher photon energy, thereby reducing the beam damage. In addition, for investigations of magnetism, tunable radiation around characteristic energies of magnetic materials are of interest. These are the $L_{2,3}$-edges of the transition metals (0.4 – 1.0 keV) and the $M_{4,5}$-edges of the rare-earth elements (0.9 – 1.5 keV). The full photon energy range of 0.4-12 keV in the fundamental FEL line and ~30 keV using higher harmonics will not be provided by any of the European XFEL beamlines solely. The use of SASE 1 and SASE 3 beamlines is proposed instead.

Spectral radiation properties

To improve the longitudinal coherence, and thereby, the accessible Q-range, monochromatisation of the incident radiation to the level $\Delta E/E \leq 10^{-4}$ needs to be achieved. Use of such a monochromator will at the same time increase the observable contrast in the scattering pattern and reduce the beam damage in the sample. For the hard x-ray case double-reflection fixed exit geometry will be used to maintain flexibility in the setup. The selection of third harmonic radiation will be achieved as well by this monochromator. For soft x-rays, the grating monochromator will have to be used to achieve the requested resolution. In selection of the optical elements of the monochromators great care has to be taken not to disturb the transverse coherence properties of the XFEL radiation.

X-ray optics requirements

Crucial for any coherence-based technique is the conservation of the x-ray wavefront by the first mirrors and the monochromator. It has been simulated for the hard x-ray case that a figure error in the range of 1 µrad would distort the beam at the instrument considerably. The target value for the figure error of the mirrors should be substantially better than 0.1 µrad. A similar stringent requirement holds for the monochromator crystals. The asymmetry angle between crystal planes and surface should be less than 0.1 µrad. To compensate figure errors resulting from heat load and gravitational sag, the second mirror should have a local active correction mechanism.

The most challenging request for optics comes from the proposed use of x-ray beam splitters for these experiments. A beam-splitter/delay-line unit will comprise up to eight perfect crystals providing a path length difference between the two split pulses between 1 ps and 10 ns.

The beamsize at the sample will be determined by the experiments, in particular the sample geometry. Therefore, focusing the XFEL beam to a spot size in the order 10-100 µm should be enabled.

Time domain requirements

These experiments probe dynamics on a huge timescale from 10^{-12} s up to several seconds. This can be achieved by exploiting the sequential and split-pulse techniques proposed in the previous section. The split-pulse and pump-probe techniques make use of the 100 fs pulse duration of the XFEL pulses. Whereas the split-pulse technique defines its own timescale by using one single pulse, the pump-probe technique uses two different sources and, therefore, requires synchronisation of the two sources. The synchronisation should be significantly better than the anticipated time resolution of ~100 fs. For the same reason the fluctuation of the pulse duration must be small compared to the 100 fs timescale. In addition, a synchronisation of 100 fs will be required for the operation of x-ray streak cameras.

It is anticipated that a variety of pulse patterns from single pulses at 10 Hz repetition rate up to several hundreds of x-ray pulses per electron bunch train will be used. A particular request comes from the sequential technique where it is possible to use the time pattern of the accelerator to probe timescales from 200 ns (shortest bunch distance) up to 600 µs (duration of bunch train).

Photon diagnostics requirements

All experiments will need good diagnostic equipment for the measurement of the photon beam intensity on a pulse-to-pulse basis. To further estimate the intensity in W/cm^2 at the sample with a high degree of confidence, the measurement of the pulse duration and of the spatial properties at the focus are important. Since monochromators are used the measurement of the mean photon energy is not required and spectral diagnostics should provide the content of higher harmonic radiation only. All measurements must be available on a pulse-to-pulse basis.

Sample manipulation and environment

Sample mounting and sample environments should allow for x-y-z linear movements (1µm repeatability and 0.25 µm resolution) and angular degrees of freedom (1/1,000 ° repeatability, 1/4,000 ° resolution.). The hard x-ray instrument could be placed in vacuum or even in air if windows are used as a vacuum interface. The windows should receive only the unfocused beam, meaning they should be mounted near the local optics. The soft x-ray instrument will differ from the other one in requiring a single vacuum system throughout, with no windows, including the detector chambers. A clever design of the vacuum system should allow variation of the distance to the detectors. For the soft x-ray experiments at magnetic resonances in-vacuum magnet- and cryosystems will be needed.

Detector requirements

These experiments make high demands on two-dimensional x-ray detectors in terms of frame rate, pixel number and pixel size. The realisation of such detectors requires a specific R&D effort that will be described in Section 6.5.4. The specific detector requirements for the XPCS instruments can be found in Section 6.5.4.1.

In addition, an ultrafast x-ray streak camera will be required for calibration of the x-ray beam split and delay line unit and point detectors for alignment and fixed-Q measurements.

Visible laser requirements

Visible lasers will be applied in pump-probe experiments. A wavelength tunable system providing pulse durations in the order of 30 fs and pulse energy up to 1 mJ at 800 nm will allow the carrying out of the experiments proposed in this area. Synchronisation to the x-ray beam in the order of the pulse duration or pulse-to-pulse measurements of the jitter is requested.

6.4.4.3 Realisation of the instrument

The XPCS experiments require two instruments at SASE 1 (PCS 1 – Hard x-rays) and at SASE 3 (PCS 2 – Tunable soft x-rays). For a description of the SASE 1 and SASE 3 beamlines see Sections 6.2.4.1 and 6.2.4.3, respectively. The bulk of experiments will be carried out at SASE 1 using hard x-rays at fixed photon energy. All experiments discussed in Section 6.4.4.1 under topics I.-IV. and VI. will use hard x-rays at fixed photon energy.

For some of these experiments it might be of interest to use third harmonic radiation; and PCS 1 foresees the possibility of using this photon energy for the sample location. The PCS 1 instrument will operate using a double-bounce fixed exit monochromator built into the SASE 1 beamline. Since this monochromator is positioned in front of the offset mirrors operation of the PCS 1 instrument without mirrors is enabled. The experiments investigating magnetism will be carried out at the PCS 2 instrument at the SASE 3 beamline using the built-in monochromator. The PGM monochromator of the SASE 3 beamline needs to be optimised in order not to disturb the wavefronts. Both instruments will require focusing the XFEL radiation.

Moderate focusing to beam sizes in the order of 100 µm is achieved by using a focusing element inside the corresponding beamlines. For the PCS 1 instrument this is likely to be compound refractive lenses (CRLs). By varying the location of the lenses, focal spots from 10-100 µm can be easily achieved. For the PCS 2 instrument refocusing of the monochromator exit slit is used to focus the beam at the sample location. Depending on the position of the focusing element, beam sizes from <10 to 100 µm can be achieved.

PCS 1: Hard x-rays

The following elements belong to the PCS 1 instrument inside the experimental hall. They are depicted in the schematic layout of that instrument in Figure 6.4.35 and are described in Table 6.4.10. The first part of the instrument includes specific optical elements for this instrument, like the beam-splitter-and-delay unit. This unit comprises up to eight perfect crystals providing a path length difference between the two split pulses between 1 ps and 10 ns. In addition, provision for additional focusing optics and/or a monochromator for $\Delta E/E <$ few 10^{-4} is made.

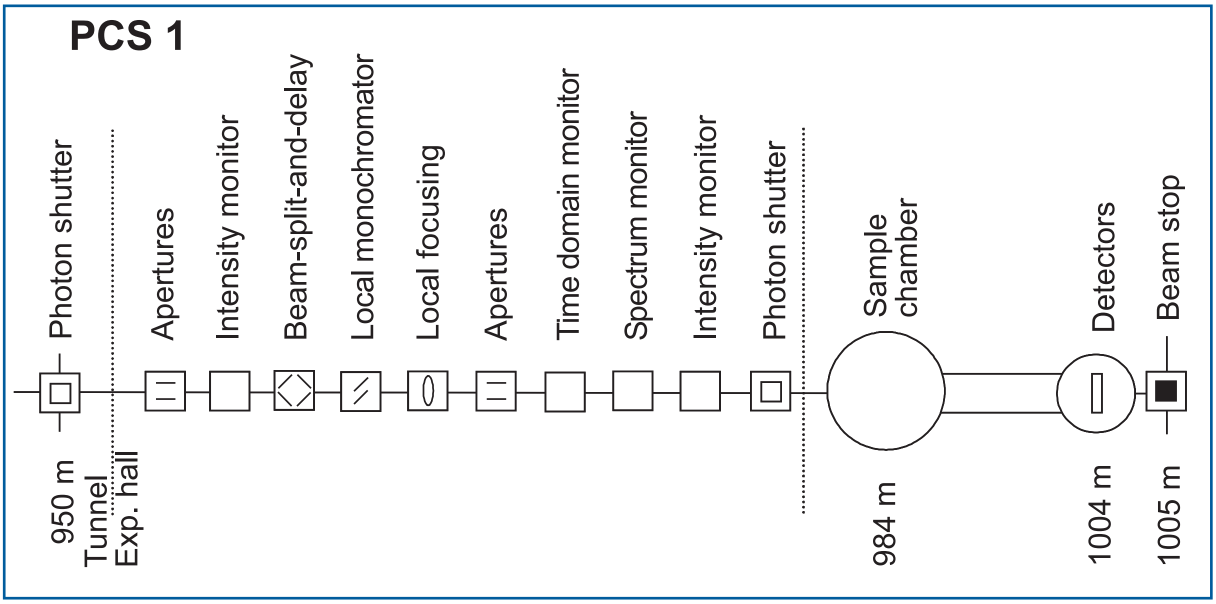

Figure 6.4.35 *Schematic layout of the PCS 1 instrument at the SASE 1 beamline. For this instrument diagnostics will be placed entirely upstream of the sample. The distance sample-detector can be varied.*

Item	Purpose	Specification
Slits/apertures	Beam definition, beam halo cleaning	0.25 µm accuracy, 1 µm repeatability
Intensity monitor	Measurement of incident photon flux	Transmissive (<5% absorption), single pulse measurement, relative accuracy $<10^{-3}$
Beam-split-and-delay	Splitting fund. line into equal parts, delay 1 ps to 10 ns	High optical accuracy to maintain wavefront and x-ray pulse duration
Monochromator	Optics: Bandwidth < few 10^{-5}	0.1 µrad angular stability, 0.1 mrad asymmetry error
Focusing optics	Optics: Extreme focusing (< 10 µm)	0.1 µrad angular stability
Slits/apertures	Beam definition,beam halo cleaning	0.25 µm accuracy, 1 µm repeatability
Time domain monitor	Measurements of x-ray arrival-time with respect to visible laser, x-ray streak camera	
Spectrum monitor	Measurement high harmonic content	Single pulse measurement, relative accuracy $<10^{-3}$
Intensity monitor	Measurement of incident photon flux	Transmissive (<5% absorption), single pulse measurement, relative accuracy $<10^{-3}$
Sample chamber	Sample positioning and orientation,	x-y-z move (0.25/1 µm), two rotations (0.25/1 mdeg)
Detector	Measurement of diffraction pattern	2-D, 5K×5K pixels, 80×80 µm^2 pixel size,
Alignment unit	Positioning and position verification	Permanently operating, accuracy ~100 µm
Lead hutch	Radiation protection optics unit, temperature stabilisation, laser protection	2×10×3.5 m^3 (W×L×H), ±0.5° thermal stability
Lead hutch	Radiation protection, temperature stabilisation, laser protection	4×22×3.5 m^3 (W×L×H), ±0.5° thermal stability
Control hutch	Operation of the instrument	Working environment (noise, temperature, light)

Table 6.4.10 **Elements and specifications of the PCS 1 instrument.**

The final slit/aperture module should provide tuneable collimation with 1µm repeatability and 0.25 µm resolution. These elements are bracketed by two diagnostics units and a beamshutter separates the optics section from the experiments hutch which is assumed to have a minimum length of 22 m. The sample environment allows for linear movements (1µm repeatability and 0.25 µm resolution) and angular degrees of freedom (1/1,000 ° repeatability, 1/4000 ° resolution.). The sample to detector distance should be as large as 20 m. The detector equipment comprises fast point detectors, a streak camera and fast 2-D detector(s). A laser system for pump-probe experiments will also be required.

PCS 2: Tunable soft x-rays

The following elements belong to the PCS 2 instrument inside the experimental hall. They are depicted in the schematic layout of that instrument in Figure 6.4.36 and are described in Table 6.4.11. The first element is a deflecting mirror that can be operated either as a flat mirror, using the focusing optics of the beamline, or as a focusing element, in order to achieve focusing of ~10 μm spot size. Next, the beam-splitter-and-delay unit is placed. For this photon energy it must be based on grating optics. A path length difference between the two split pulses between 1 ps and 10 ns is envisioned. Following an aperture and various diagnostics tools, including an x-ray streak camera for diagnostics of the beam-split-and-delay unit, a differential pumping section separates the beamline for the sample vacuum chamber. The use of windows will not be possible for this instrument. The sample environment allows for linear movements (1μm repeatability and 0.25 μm resolution) and angular degrees of freedom (1/1,000 ° repeatability, 1/4,000 ° resolution.). The sample to detector distance should be as large as 15 m. The detector equipment comprises fast point detectors and fast 2-D detector(s). A laser system for pump-probe experiments should be foreseen.

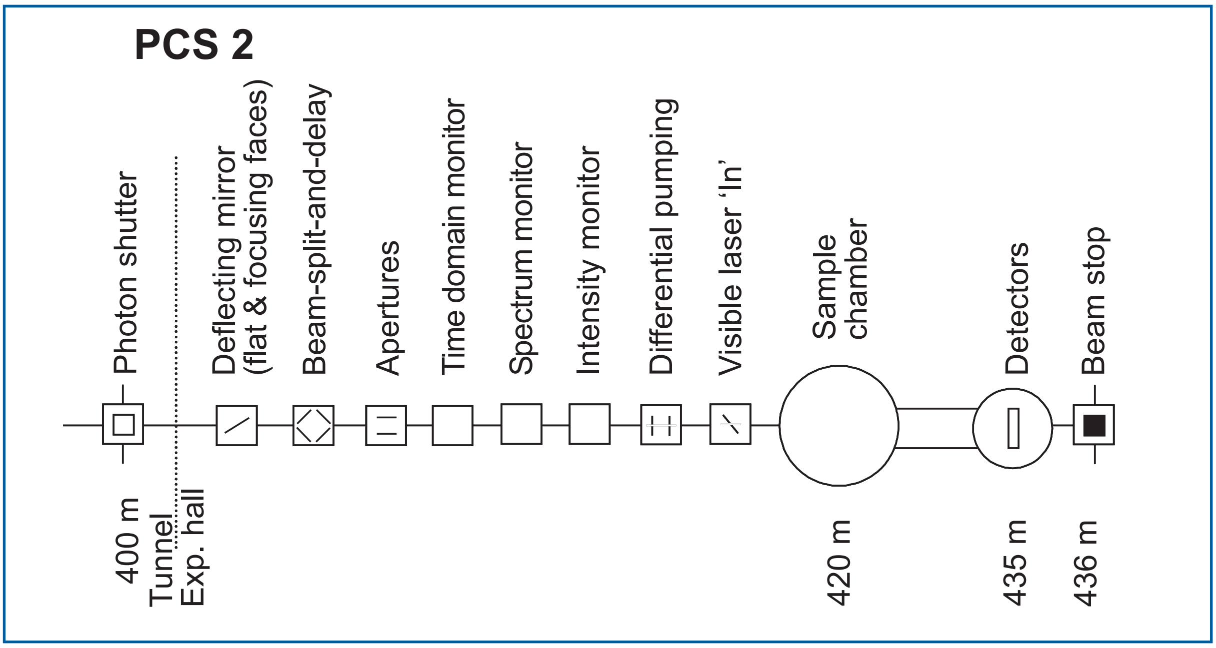

__Figure 6.4.36__ Schematic layout of the PCS 2 instrument at the SASE 3 beamline. For this instrument diagnostics will be placed entirely upstream of the sample. The distance sample-detector can be varied.

Item	Purpose	Specification
Deflecting mirror	Flat, if using beamline focusing optics, curved for ~10 µm focusing	0.1 µrad angular stability, 0.1 µrad figure error, 0.1 nm surface roughness
Beam-split-and-delay	Splitting fundamental line into equal parts, delay 1 ps to 10 ns	High optical accuracy to maintain wavefront and x-ray pulse duration
Slits/apertures	Beam definition, beam halo cleaning	0.25 µm accuracy, 1 µm repeatability
Time domain monitor	Measurements of x-ray arrival-time x-ray with respect to visible laser, x-ray streak camera	
Spectrum monitor	Measurement of high harmonic content	Single pulse measurement, relative accuracy $<10^{-3}$
Intensity monitor	Measurement of incident photon flux	Transmissive (<5% absorption), single pulse measurement, relative accuracy $<10^{-3}$
Sample chamber	Sample positioning and orientation	x-y-z move (0.25/1 µm), two rotations (0.25/1 mdeg)
Detector	Measurement of diffraction pattern	2-D, 5K×5K pixels, 80×80 µm^2 pixel size
Alignment unit	Positioning and position verification	Permanently operating, accuracy ~100 µm
Lead hutch	Radiation protection, temperature stabilisation, laser protection	$4\times22\times3.5$ m^3 (W×L×H), ±0.5° thermal stability
Control hutch	Operation of the instrument	Working environment (noise, temperature, light)

Table 6.4.11 *Elements and specifications of the PCS 2 instrument.*

6.4.5 X-ray absorption spectroscopy

6.4.5.1 Scientific case

The development of femtosecond lasers brought entirely new possibilities into the practice of time-resolved spectroscopy, both for the UV-VIS and IR-Raman spectroscopies **[6-193]**. In addition, it has boosted the capabilities of non-linear spectroscopies beyond what could be imagined before their advent. With the implementation of femtosecond laser spectroscopies, it became possible to conduct observations on timescales that are shorter than single nuclear oscillation periods in molecules, liquids, solids, surfaces, interfaces and proteins.

The pump-probe scheme has been a revolutionary tool for observing real-time motion of bound states of small diatomic molecules in the gas phase and of elementary chemical reactions taking place in their unbound states **[6-194]**. The realisation of these experimental possibilities requires not only adequate time resolution for probing vibrations, but also excitation mechanisms suitable for initiating molecular motion in a phase-coherent (i.e., synchronised) manner in order to “observe” the transient structures **[6-194, 6-195]**. This is the basis of **wave packet** dynamics that has brought about a description of the time evolution of systems in terms of **dynamics** rather than **kinetics**, which was, till then, the rule among chemists and biochemists. The implementation of pump-probe techniques and that of other ultrafast laser techniques to the study of systems of even greater complexity has occurred throughout the 1990's **[6-196 – 6-201]**, with the study of elementary reactions in gas phase organic molecules **[6-194]**, in liquids **[6-202]**, solids **[6-203 – 6-205]** and biological molecules **[6-198 – 6-201]**.

However, because of their wavelength, optical pulses cannot retrieve structural information. The structural information from femtosecond optical pump-probe experiments could only be obtained in the case of small diatomic or triatomic molecules in the gas phase, for which an **a-priori** knowledge of the potential energy surfaces is available **[6-194]**. This is usually not the case for larger assemblies of atoms (e.g. polyatomic molecules), and a further degree of complexity is added to the problem if we are dealing with condensed phases or biological samples, since intermolecular coordinates come into play.

In order to overcome these limitations, an extension of pump-probe techniques to the case where the probe pulse is in the x-ray domain has been considered and attempted by many since the mid-1990's **[6-206 – 6-212]**. Conceptually, the methods of ultrafast x-ray diffraction and x-ray absorption are similar to ultrafast optical pump-probe experiments, provided sufficiently short pulses of x-rays are available.

While the above stresses the possibility of **capturing transient structure**, it should also be underlined that any physical, chemical or biochemical transformation in matter (whether or not induced by light) is a consequence of a **redistribution of charges** (in particular, electrons) of the species constituting the system under study. Therefore, a technique is highly desired which, in addition to capturing **molecular or crystalline structures**, can also unravel the underlying **electronic structure changes** that drive the former ones. **X-ray absorption spectroscopy (XAS)** is such an approach, and with the advent of the XFEL, it will deliver an unsurpassed degree of insight into many physical and chemical phenomena.

Chapter V of the 2001 TDR **[6-213]** presented a very complete and comprehensive account of the scientific questions that could be dealt with the XFEL, in a broad range of systems: atoms, molecules and clusters, plasmas, condensed matter, materials, surfaces and interfaces, chemical systems, and biological systems, as well as in non-linear phenomena. The purpose of the present scientific case is to discuss technical issues related to x-ray absorption spectroscopy at the XFEL, in the light of recent scientific achievements with picosecond x-ray pulses at third generation synchrotrons **[6-211, 6-212, 6-214 – 6-225]**, and to present new scientific issues in chemistry, biology and condensed matter physics, which can only be addressed using x-ray spectroscopy as a method and an XFEL as a tool, and that were not covered in the TDR 2001. In this sense, the present study is an add-on to the 2001 TDR, and it can be updated whenever new scientific questions are raised.

Why x-ray absorption spectroscopy ?

The reasons that make XAS a particularly attractive technique for probing the electronic and geometric structure in a large class of systems are:

- It can be implemented in any type of media: gases, liquids, solids (amorphous or ordered), and biological samples. This allows, among other things, for a renewal of the sample, especially for time-resolved studies at the XFEL where sample damage may occur due to the high x-ray and/or optical laser flux.
- It is highly selective, since one studies one type of atom specifically, e.g., the physically, chemically or biochemically significant one, by simply tuning into its characteristic absorption edges.
- With X-ray Absorption Near Edge Spectroscopy (XANES) and Extended X-ray Absorption Fine Structure (EXAFS), one mainly probes the local structure in the immediate vicinity of the atom of interest. For time-resolved experiments in the femtosecond time domain, this is sufficient. Indeed, a typical timescale for the motion of matter is given by the velocity of sound: 0.03-0.1 nm/100 fs. This distance scale is exactly the one that is significant in chemical, biological and condensed matter physical phenomena. Since short timescales correspond to short distance scales, XANES and EXAFS are ideal structural tools in the femtosecond time regime of the XFEL.
- The precision of structural determination by EXAFS is on the order of 10^{-3} – 10^{-4} nm **[6-226 – 6-228]**, which is ideal for observing transient structures resulting from the photo-induced reaction.
- XANES looks at the valence orbitals of the atom of interest, which are precisely those involved in bond formation, bond breaking and bond transformation. Thus, one can detect the underlying electronic changes that drive the structural ones. In particular, the degree of oxidation of an atom and the occupancy of its valence orbitals are reported by XANES. In addition, for atoms embedded in an ordered atomic environment, the selection rules of core transitions can be altered by the local symmetry, so that structural information can also be retrieved.
- Using polarised x-ray pulses and laser-aligned samples permits the measurement of orientation-dependent spectra.
- It can detect optically silent species, which may result from a photoinduced process.
- Variants of x-ray absorption spectroscopy, such as linear and circular dichroism and spin-sensitive XAS, are now well established tools for the study of magnetic phenomena.

Why x-ray absorption spectroscopy at an XFEL?

The dramatic increase in flux and time resolution brought about by XFELs as compared to third generation synchrotron sources, will not merely be another breakthrough in technical achievement, but also allows us to truly envision new science. In terms of flux, we are on the verge of the revolution brought about by the discovery of lasers in the optical domain.

In the following the feasibility of time-resolved XAS experiments at an XFEL source are discussed.

Tunability and energy resolution

By definition, XAS requires a tuneable source. Furthermore, since one wants to resolve fine structure, an energy resolution of $\Delta E/E \approx 10^{-4}$ is desired. Apart from synchrotrons, that are limited in pulse duration to tens of picoseconds, there exist no sources of tuneable **femtosecond** x-ray pulses, in particular in the hard x-ray domain **[6-212]**. The XFEL is the only one that will be able to provide this tunability, as femtosecond lab-based sources cannot provide it, and seem far from reaching this regime. SASE 2 and SASE 3 cover the region between 1.6 and 0.1 nm, which is ideal for accessing the core excitations of most light and heavy elements. Considering energy resolution, the SASE 2 and SASE 3 will have an energy resolution of 8×10^{-4} to 1.8×10^{-3}, which is not sufficient for detailed XAS studies. This resolution can be improved by adding a monochromator. However, considerations of tunability and energy resolution cannot be disentangled from those of flux, which we now discuss.

Flux considerations

The calculation of the flux necessary to carry out a time resolved XAS experiment on transition metal compounds in a solution of first-row elements (e.g., water, hexane, and several other organic solvents), was already carried out in **[6-212]**. Figure 6.4.37 shows the required number of incident x-ray photons per data point to measure a transient EXAFS signal with unity signal-to-noise ratio. The calculations assume a 10% photolysis of the sample, and EXAFS changes are in the order of 1% relative to the absorption edge jump. Recent measurements of picosecond transient XAFS spectra of three different compounds **[6-223, 6-224, 6-229]** in aqueous solutions (consisting of three different elemental absorption edges) nicely confirm the results shown in Figure 6.4.37, when scaling the measured signal-to-noise (S/N) and excitation yields to the generic values used for the figure.

While these calculations indicate that a rather modest pulsed x-ray source is sufficient to measure transient structural changes via XAS, the need for more intense and shorter x-radiation to investigate new phenomena in the gas phase, in condensed phases and in biological systems (e.g., wavepacket dynamics) via XAS can only be underscored. One can evaluate the same parameter as in Figure 6.4.37, for the case of gas phase (with density 10^{11} cm^{-3}) and liquid phase samples (1mM aqueous solutions), and the results confirm that the corresponding experiments can be performed at the XFEL, some of them even with the spontaneous undulators sources.

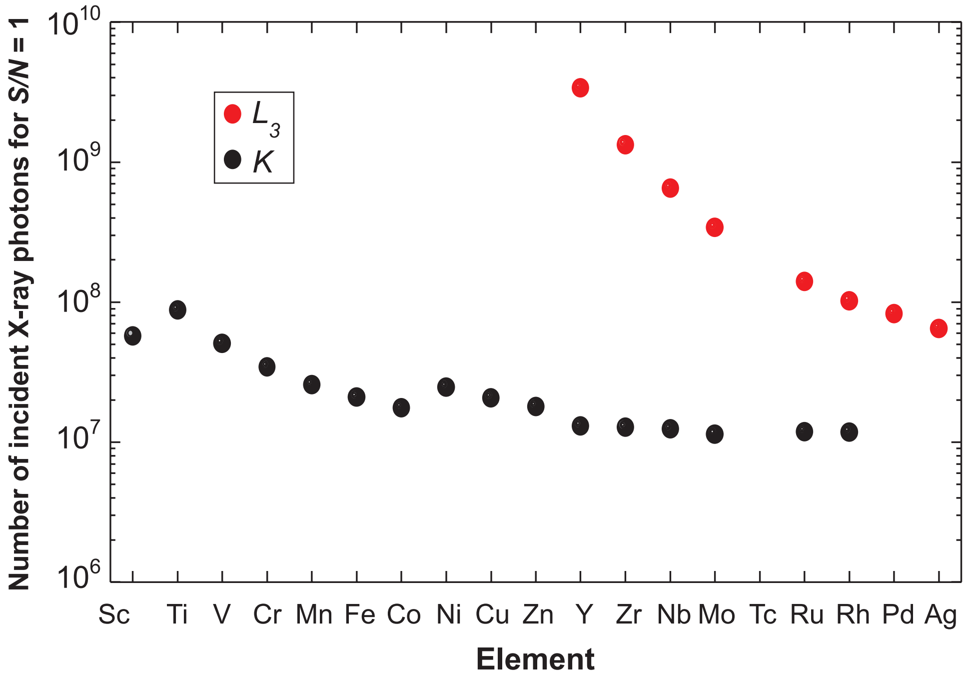

Figure 6.4.37 *Required number of incoming x-ray photons to observe time-resolved EXAFS of transition metal compounds in H_2O solution with a signal-to-noise ratio S/N = 1, assuming a laser photolysis yield of 10% and an EXAFS modulation change of 1 % relative to the absorption edge jump of the selected element. From* **[6-212]***.*

Time resolution

The achievement of femtosecond time resolution with lasers at the beginning of the 1980s allowed physicists and chemists to describe the behaviour of their systems in the language of **dynamics** (i.e. motion of bodies) rather than that of **kinetics** (evolution of populations), thus bringing an unprecedented level of insight into a host of phenomena (physical, chemical and biochemical) in a broad range of systems, from molecules to solids and proteins.

The 100 fs (and hopefully, even shorter) pulse width of the XFEL radiation, will provide us with the ability to detect molecular motion in general and molecular vibrations and phonons in a large class of systems, just as it is possible with femtosecond lasers by the observation of wave packet dynamics. However, the major difference with optical spectroscopy is that with x-rays, the actual structural details of the system can be captured in a **direct** fashion.

Just as in any pump-probe experiment, when the two laser pulses do not have the same colour, group velocity mismatch (GVM) introduces a temporal walk-off between the pulses, which in the case of ultrashort optical and x-ray pulses, is quite significant. Indeed, for a typical medium having an index of refraction of 1.5 in the optical domain, the GVM amounts to 1.6 fs/µm. For a sample thickness of 200 µm, this corresponds to 320 fs! It is, therefore, important to envision pump and probe geometries that overcome this limitation, in particular cross-beam geometries, eventually combined with specific sample geometries (e.g. line laser excitation of the sample, with x-ray probing along the excitation line).

Time structure

The bunch structure of the XFEL provides bunch trains at 10 Hz repetition rate, each consisting of up to 3,000 electron bunches at a repetition rate of 5 MHz (although, as explained in Chapter 4, one can deliver different time structures at the beamlines by a combination of slow and fast kickers in the beam distribution system). The commercial amplified femtosecond laser pulses run at either 1-5 kHz or at 50-300 kHz. Alternatively, unamplified oscillators run at 80 MHz or in cavity-dumped configuration at 1-5 MHz. The latter option seems quite suitable for a pump-probe experiment, but unamplified lasers have weaker energy/pulse than amplified ones. In addition, due to the 10 Hz repetition rate of the bunch trains, the laser pulses between bunch trains are lost, whichever laser repetition rate is used.

Finally, the choice of one or the other laser systems will be determined by the configuration of the experiment, and on the number of species that can be photolysed by the laser.

Experimental programme

What are the scientific issues which cannot be solved by present day technology, and require XAS at an XFEL? Several very exciting scientific issues were already presented in the TDR 2001**[6-213]**, but here we will be more specific and address issues that: a) concentrate on time-resolved studies; b) require XAS as an experimental method. The following examples are far from being exhaustive and mainly reflect the interest of the authors. It is obvious that entire fields are left out, that could later be added, if additional contributions are made to this text.

I. Atomic physics

Measurement of energy shifts of ionised atoms

Electrons in atoms and molecules are correlated, making the binding energy of an individual electron a function of its entire atomic environment. A change to this environment, such as the application of an external field or the removal of even a weakly bound valence electron, affects the entire system, including the deeply bound core-levels. This makes the energy levels within a single atom sensitive to the configuration, or simply the presence, of other electrons within the atom. Since the wavefunction of valence electrons partly extends deep into the ion core, their charge screening can even affect inner-shell electrons: Cubaynes et. al. **[6-230]** has shown that the binding energy of 2*p* (*L*-shell) electrons in Sodium changes by 2 eV, or about 5%, when the single 3*s* valence electron is excited to the 3*p* level. The influence of a valence electron extends even to the *K* shell: Comparison of measurements in Carbon ions from **[6-231, 6-232]** shows that the energy of transitions involving the *K* shell (1*s*-2*p* transition in C) differs by several electronvolts for differently charged ions.

While these effects have been known for a long time theoretically, their experimental observation only starts to appear now **[6-223, 6-224]**. Yet, with the development of time-resolved x-ray spectroscopy, they regain a special importance, since photoexcitation of an atom within a molecule, also affects the energetics of its core shells. This point was recognised in the recent picosecond XAS study of photoexcited coordination chemistry compounds **[6-223]**, and it calls for a careful examination of the core level shifts upon excitation of valence electrons. This needs to be investigated first in the case of atomic species, and the XFEL, with its high flux and short pulses, is an ideal tool in this respect. Furthermore, the option of using attosecond pulses may one day allow observation of the core level energetic shift in real-time.

Dynamics and evolution of plasmas

Plasma diagnosis will greatly benefit from the penetration power of x-rays, allowing the retrieval of information from the volume even for solid-density plasmas. Also, in order to obtain important plasma parameters, like temperature, density, charge state, and collective behaviour of dense, strongly-coupled plasmas, XAS is a very promising approach. It has already been implemented using a lab-based source of picosecond soft x-ray pulses to probe the evolution of an Aluminium plasma over the $L_{2,3}$ absorption edges **[6-233]**. However, the picosecond resolution of this experiment was not sufficient to capture the initial instants of the generation of the high energy density matter that is formed prior to the plasma. With the femtosecond pulses of the XFEL, it will be possible to map the full evolution of the plasma from its birth, by detecting the species in their various ionisation states, and how these change with time. Furthermore, the density distribution of different ionisation stages of atomic species can be determined by absorption contrast imaging. This possibility, based on the coherence of the x-ray beam, can be applied for imaging the plasma region, to obtain information about the density distribution for all plasmas one could produce.

X-ray diagnostic tools based on time-resolved XAS in the femtosecond regime would provide the first direct measurement of microscopic parameters of solid–density plasma, which could be used to properly interpret measurements of thermal and electrical conductivity, equation of state and opacity found in astrophysical environments as well as in virtually all plasma production devices.

II. Molecular and chemical physics

Just as with the advent of femtosecond lasers, chemistry is an area where some of the most spectacular achievements of the XFEL are anticipated, one of the major reasons being the importance of structural determination in the description of chemical reaction dynamics, but also the nature and vectorial properties of charge redistribution in chemical systems. Both types of information can be very well captured by ultrafast XAS. Here, we present a few cases where such studies can bring about important new insights into chemical dynamics, even in the case of small molecules.

Non-adiabatic dynamics of molecules

The first demonstrations of the power of ultrafast optical spectroscopy, which also marked the field of Femtochemistry, came from the study of gas phase small molecules **[6-194]**. The observation of intramolecular motion was possible by detecting their **wave packet** dynamics. Wave packets result from the coherent (synchronous) excitation of several molecular vibrational (but electronic, rotational, or phonon levels in solids are also possible) levels, while structural information was retrieved by relating the probe wavelengths to the difference potentials between the states involved in the probe transition. The demonstration of the observation of wave packet dynamics probed by soft x-ray femtosecond pulses from a high harmonic source was made by Leone and co-workers **[6-234, 6-235]**.

Aside from being ideal tools to establish techniques and concepts, there are still a number of pending issues in small (and large) molecules, related to the nature of **non-adiabatic couplings [6-236]**, which give rise to avoided crossing of potential curves. The non-adiabatic coupling matrix elements derive from the terms neglected in the Born-Oppenheimer description of electronic states of molecules.

They can arise from different types of coupling terms: spin-orbit, Coriolis, electrostatic, etc. Non-adiabatic couplings are the rule rather than the exception in molecular and condensed matter systems, and they are at the core of energy redistribution and chemical processes. Their full understanding in small molecules may help refine their description in larger molecules, and even in condensed phases, where they play a crucial role.

A particularly interesting example in this respect, is the case of NaI, which we believe is an ideal system for an experiment with the XFEL. Figure 6.4.38 shows its potential curves. The ground state has ionic Na^+I^- character, it crosses the first excited state, which has covalent character at an internuclear distance of ~0.69 nm, giving rise to an avoided crossing, which results in the upper and lower adiabatic potential curves shown in Figure 6.4.38.

Impulsive excitation of the upper state gives rise to formation of a wave packet (Gaussian on the left hand side of Figure 6.4.38), which evolves on the excited state adiabatic potential curve, with a period of 0.9-1.2 ps (black dots in Figure 6.4.39). In this evolution, as the Na-I distance stretches, the system goes from a covalent character to an ionic one, i.e. an electron transfer occurs from the Sodium atom to the Iodine atom, around the distance of the avoided crossing (dashed line in Figure 6.4.39). In addition, because of the coupling between the two potential curves, part of the wave packet crosses over from the bound excited state potential to the dissociative continuum of the ground state potential, resulting in a damping of the wave packet in the excited state adiabatic potential (black dots in Figure 6.4.39) and a bullet like generation of Sodium and Iodine atomic fragments on the ground state adiabatic potential (open squares in Figure 6.4.39).

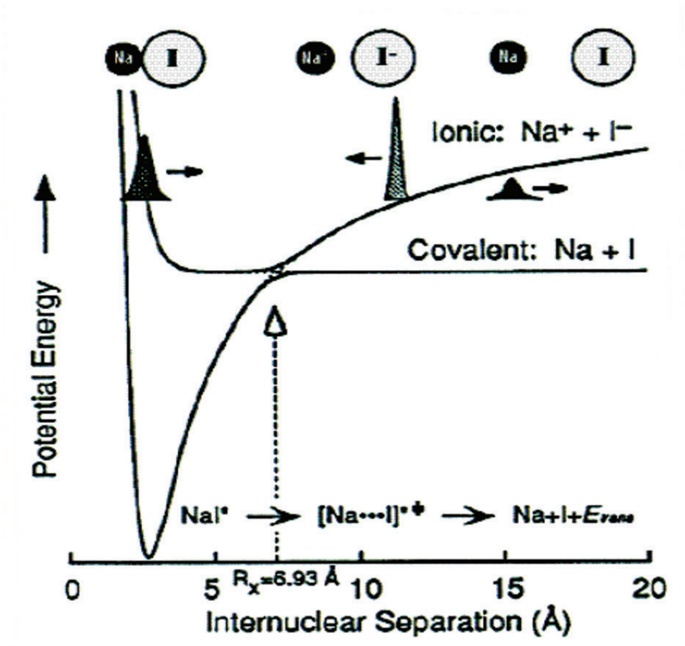

Figure 6.4.38 *Potential curves of the NaI molecule and principle of the pump-probe experiment. Femtosecond excitation creates a vibrational wave packet (Gaussian on the left) in the excited state, which will then evolve between the left and right turning points. In so doing, the wave packet passes by the point of crossing and part of it leaks via the dissociative channel giving Sodium and Iodine neutral fragments. After ref* **[6-194]**.

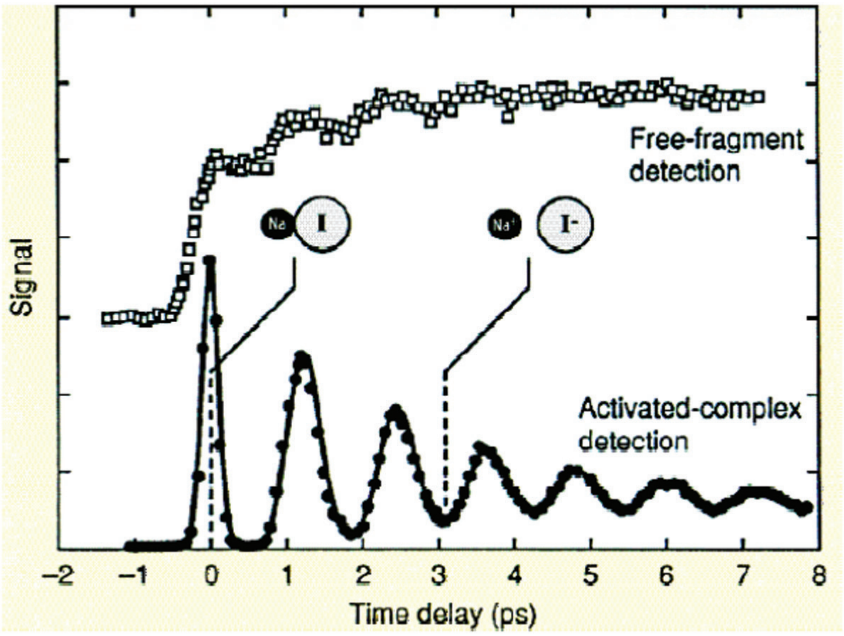

Figure 6.4.39 *Wave packet dynamics evolution on the excited state adiabatic potential of NaI (black dots), observed in a pump-probe experiment. Atomic Sodium fragments detected on the dissociative channel of the ground state adiabatic potential curve (Figure 6.4.38). After* **[6-194]**.

This molecule represents an ideal opportunity to understand the fundamentals of the coupling of nuclear and electron motion. Indeed, the time resolution of the XFEL is sufficient to resolve the vibrational coherences observed in the optical pump-probe experiment (Figure 6.4.39). In addition, by recording the time dependent EXAFS signal at the L edges of I near 4.5 keV, one can determine the internuclear distance with high precision, at each instant. More exciting is the fact that by recording the XANES of the Iodine and Sodium (in the soft x-ray domain) atoms, one can record the change of the ionisation state of these atoms, since for the Iodine atom a hole exists in the 5p valence orbital, which disappears in the I^- form, while for the Sodium atom, the 4s electron will disappear upon formation of the Na^+ ion. The exciting part of XANES at the XFEL is that it can also determine the degree of electron transfer and its distance (and time) range around the crossing point. These experiments at the XFEL will deliver an unprecedented degree of detail into the non-adiabatic processes, where electron and nuclear motion go together.

Solvation dynamics

Most chemical reactions and biological functions take place in solutions. This simple fact has galvanised a tremendous research effort aimed at elucidating the effects of the solvent on the chemical or biochemical reactivity. A complete understanding of liquid chemistry requires knowledge of the detailed molecular pathways that are involved in the reaction dynamics. The elucidation of a set of unifying principles describing chemical dynamics in liquids represents a challenge to both experimentalists and theoreticians **[6-196, 6-202, 6-237 – 6-243]**. The amorphous and dynamic nature of the liquid state leads to reaction systems of exceptional complexity.

Any chemical or photochemical reaction in the condensed phase starts off by a redistribution of charge in the chromophore. This, obviously, applies to photoinduced processes, with the advantage that light offers a clean way to selectively trigger reactions, both in energy and in time. While the redistribution of charge modifies the field of forces within the molecule and leads to its transformation (e.g. via bond breaking, isomerisation, etc.), it also changes the field of forces between the molecule and the solvent species, forcing the latter to rearrange on a timescale that may be shorter or concurrent with that of intramolecular reorganisation. The rearrangement of the solvent species is termed "**solvation dynamics**" (see Figure 6.4.40). It has been much studied by ultrafast laser techniques since the 1980s in a wide variety of solvents **[6-196, 6-202, 6-238 – 6-240, 6-244]**. The central role of solvation dynamics in chemistry and biology is obvious, since the solvent species are not just "spectator" species, but are part of the chemical or biological process. This concerns both steric and electrostatic effects **[6-237, 6-245 – 6-248]**. For example, it is well established that the structure of water around proteins plays a crucial role in their function, to the point that the layer of water around them is thought of as an integral part of the protein **[6-244]**.

Since the solute is excited instantaneously, the solvent species find themselves at time t=0 in a relatively high energy configuration due to the change of field of forces. Subsequently, they begin to move and rearrange to reach their new equilibrium configuration (Figure 6.4.40). This motion includes both translational and rotational rearrangements. The solvation process typically exhibits a multiexponential decay with timescales of <200 fs, several hundred femtoseconds and a few picoseconds to several tens of picosecond, depending on the solvent. This description, however, is already the source of some ambiguity.

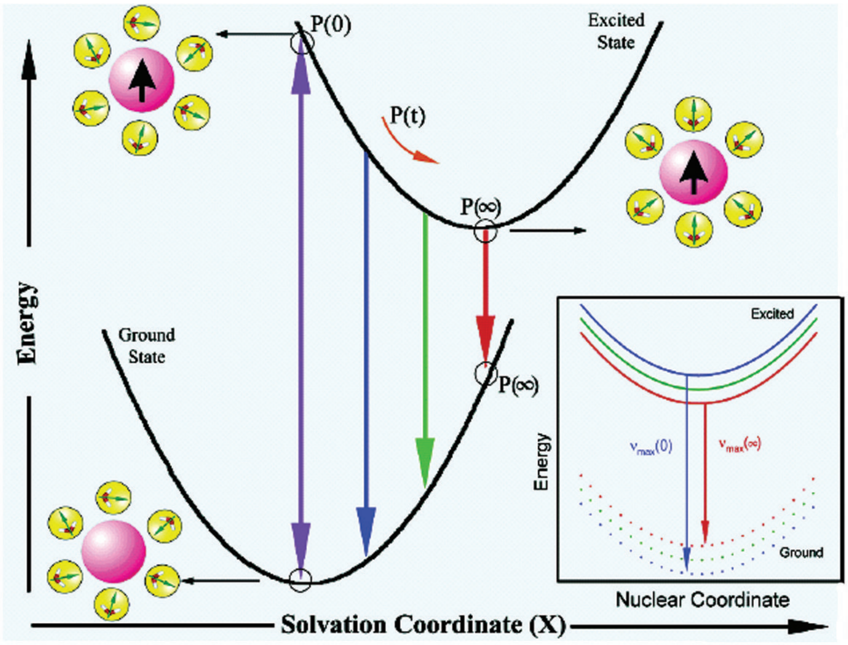

Figure 6.4.40 *Schematic illustration of the potential energy surfaces involved in solvation dynamics, showing the water orientational motions along the solvation coordinate together with instantaneous polarisation P. As an inset we show the change in potential energy along the intramolecular nuclear coordinate. As solvation proceeds, the energy of the solute decreases, giving rise to a red shift of the fluorescence spectrum.*

Indeed, so far, all the techniques that have been implemented to study solvation dynamics suffer from three shortcomings: a) they all rely on the use of dye molecules, which due to their shape, already form a specific solvent shell in their ground state. Therefore, the solvent response in the excited state is, to a certain extent, probe-molecule specific, since the dynamics that one observes on ultrashort timescales in the excited state reflect a departure from the initial structure; b) particularly at the shortest timescales, it is difficult to disentangle the high frequency intramolecular and intermolecular contributions; c) only optical methods have so far been used, which are unique in delivering time-domain information about the energetics of the system, but no visualisation of the solvent shell structure around the solute. This last point concerns not only the structural changes during the dynamics, but also after the rearrangement has taken place. The microscopic structural details are of importance, especially at short times, in part because they represent the most energy consuming part of the solvation process **[6-239]**, and correspond to the transition from an “inertial” regime to a “diffusive” one.

In order to visualise the solvation **structural** dynamics in real-time, femtosecond XAS is an ideal approach since it allows: a) a direct visualisation of solvent structures before, during and after the dynamics; b) the monitoring of the electronic structure changes (by

XANES) induced by the laser excitation and; c) the use of atomic ions as probe species, which are usually optically silent, but offer the great advantage of being free from internal modes, so only intermolecular changes are observed.

A successful experiment has already been carried out using the 100 ps pulses at the SLS **[6-229]**. The experiment consisted of exciting the I^- ion in water, to remove the electron and probing the electronic structure of the Iodine atom and the solvent structural changes around it by XANES and EXAFS, respectively. The data show entirely novel results, in that it was found that the solvent shell dramatically changes upon electron abstraction and transfers electron density back to the I^0 atom. However, this experiment only captured the **before** and **after** situations within hundreds of picoseconds. As mentioned above, crucial for a full description of solvation dynamics is the observation of the actual process of solvent rearrangement, and how it influences the charge redistribution within the solute. The time resolution of the XFEL of $\leq$100 fs should be sufficient to time-resolve the structural changes of the solvent shell in most solvents, including water **[6-240, 6-249]**.

Finally, any study that delivers the structural details of the solvent environment around a solute and its rearrangement as a function of time, establishes the use of the solute as a probe of solvent structure and dynamics in different physical and thermodynamical states: supercritical, supercooled, at interfaces, etc., for which a number of questions remain unanswered. In consequence, it opens a host of new opportunities for the study of liquid state dynamics in different media.

Chemical dynamics in liquids

The solvent shell also plays a crucial role in hindering or affecting the pathways of chemical channels of molecules, and in creating new ones. It is also a thermal contact, which removes energy from the excited species to the rest of the bath. A schematic representation of the processes that are induced in a solvated molecule by light excitation, is shown in Figure 6.4.41.

One of the most studied systems is the case of the I_2 molecule in liquids, and the various processes affecting it have been studied over the 1980s and 1990s in different media (liquids, rare gas matrices, high pressure gases and clusters) **[6-194, 6-250, 6-251]**. All of the ultrafast studies have so far been probing the intramolecular motion of the molecule and the way it is affected by the environment, but a clear understanding of the way the solvent cage affects the photochemical reaction dynamics goes by a direct visualisation of the cage response itself. Experimental studies and theoretical simulations **[6-251]** have shown that the first impact of the Iodine fragments on the solvent species occurs within 100-300 fs and takes up most of the energy involved in the reaction. It is followed by a rearrangement of the cage which occurs on the timescale of picoseconds and is affected by energy flow from the molecule to the bath. These processes can only be observed by XAS using the femtosecond x-ray pulses, which will be provided by the XFEL.

Coordination chemistry

Controlled electron transfer (ET) and charge separation in molecules are essential requirements for efficient storage and conversion of energy by chemical means, as well as for operation of nanoscale devices such as molecular conductors, rectifiers, transistors, memories, or non-linear optical materials **[6-252 – 6-255]**. Several approaches to molecular electronics use conceptually similar transmission of electronic effects, e.g. through coulombic interactions between mixed-valence complexes **[6-256]** or redox-induced valence tautomerism, whereby information is stored in distinct states of bistable molecules **[6-257, 6-258]**. Biological energy and information conversion provide further inspiration, since directional, long-range ET is the physical basis of photosynthesis, while charge-separation helps to drive retinal isomerisation in the process of vision **[6-259]**. Further progress towards molecular devices requires the development of systems capable of exact timing and switching of the rate and direction of the ET, and the underlying structural rearrangements involved within this. The rates of electron transfer are as important for efficient and error-free operation of molecular devices, as they are, for example, in plant photosynthesis. One of the purpose of XAS studies at the XFEL is to **obtain new and comprehensive understanding of electron transfer and charge separation** in metal-based molecular complexes and also, in multicomponent metal-based molecular assemblies (Donor Bridge Acceptor type), which can be envisioned as functional materials for specific applications.

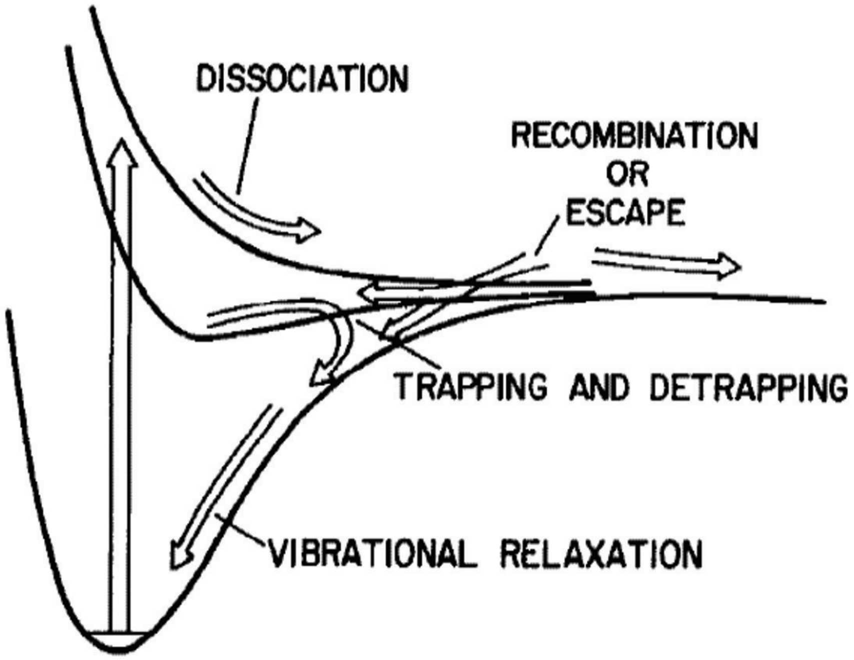

Figure 6.4.41 *Processes of photodissociation and geminate recombination of a molecule in solution. Typical timescales for dissociation are <1 ps, 1-10 ps for recombination or escape, 100-3,000 ps for trapping or detrapping, and 50-5,000 ps for vibrational relaxation The vertical arrow represents the initial light absorption. After* **[6-250]**.

Coordination chemistry compounds are among the most promising molecules for performing the above functions, and are the object of intense studies at present. In particular, ultrafast (femtosecond-picosecond) spectroscopy is used to investigate intra- and intermolecular ET, especially using UV-Vis transient absorption spectroscopy, UV pump/IR probe techniques, and time-resolved resonance Raman techniques. Vibrational spectroscopies (IR and Raman) provide a high degree of insight into the direction and nature of the electron transfer, by visualising the mode frequency changes of specific chromophores upon oxidation or reduction, but they are limited in time resolution, at best ~0.5 ps, and in their ability to detect low frequency modes, which often are the relevant ones. Optical pump-probe transient absorption spectroscopy easily reaches the few femtoseconds time-resolution, but it cannot detect the nature and direction of the ET. Finally, none of these ultrafast spectroscopic techniques deliver information about the excited state molecular structure, which is particularly important if one wants to analyse and rationalise ET, and eventually, design new compounds for optimal ET.

For the study of ET in metal-based molecular complexes, one needs a technique that: a) allows a direct visualisation of molecular structures both before, during and after the dynamics; b) allows monitoring of the electronic structure changes induced by the laser excitation; and c) can be implemented in disordered media, in particular, liquids. X-ray Absorption Spectroscopy is ideal in this respect and implementing it in a pump-probe configuration has recently been accomplished by Bressler, Chergui and their co-workers with 50-100 ps resolution on metal-based molecular complexes **[6-217, 6-223, 6-229, 6-260]**. Their results fully establish the technique on a routine basis for metal-based complexes in the picosecond time domain, and allow a systematic investigation of ET processes in this class of systems. However, the time resolution of tens of picosecond is not sufficient to fully resolve the dynamics of intramolecular ET processes, which occur on a timescale of $\leq$1 ps **[6-261, 6-262]**, nor to capture the details of the ultrafast energy relaxation cascade, which also occurs on hundreds of femtoseconds to a few picoseconds, and imply successive stages of structural rearrangement. This is where the utility of the femtosecond resolution at the XFEL comes in. Although seemingly paradoxical, the probing of transient structures in these (and other) molecular systems should be easier with femtosecond x-ray pulses than with picosecond ones, since the vibrational coherence imparted by the pump laser to the ensemble of molecules in the samples is preserved up to picoseconds in most systems.

An example of such potential functional materials are metal-diimine complexes, which are ideal for vectorial electron or energy transfer. In particular, M(II)-diimine square planar complexes (M=Pd, Pt) with a variety of anionic donor ligands, represent a perfect class of Donor-Bridge-Acceptor complexes, which may lead to long-lived separation of charge in the excited state of the metallo-organic chromophore **[6-263, 6-264]**. In order to reach this regime, the strategy is to avoid fast back-ET by introducing an energy barrier that results from facile structural reorganisation following the primary photoinduced ET.

In M(II) diimine bis-thiolate complexes (Figure 6.4.42), light-induced electron transfer from the donor thiolate part to the diimine part produces a charge-separated excited state. This process is accompanied by a structural reorganisation probably involving formation of a 3-electron S-Pt-S bond, which hinders back-ET, while the stability of the S-S bridge can be controlled by varying the nature of the R groups. Time-resolved optical studies and vibrational spectroscopies can only indirectly infer the decrease of electron density at the R-ligands and do not capture the ultrafast formation of the S-S bridge in the excited state. Both of these processes can be detected in a direct fashion by XAS of the photoexcited compound at the XFEL.

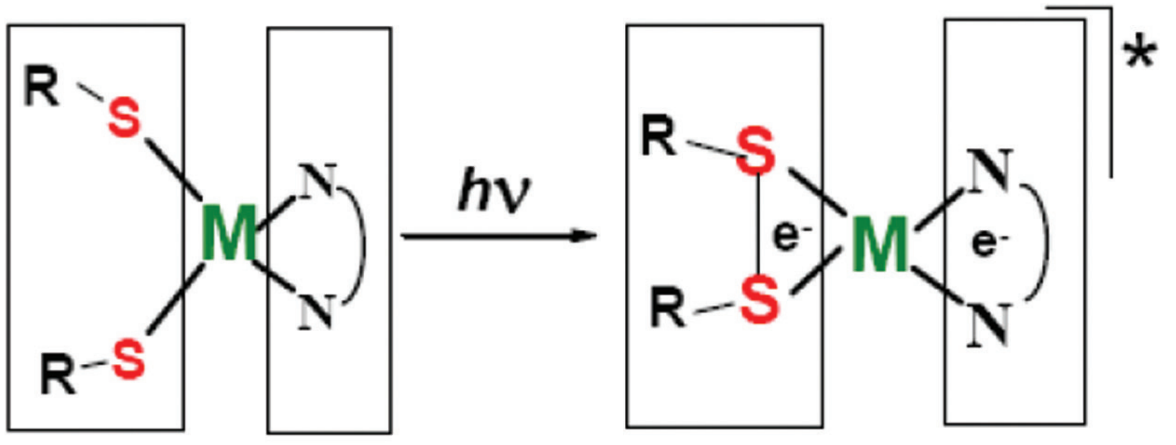

Figure 6.4.42 *Metal(II) diimine bis-thiolate complex: M = Pt, Pd or Ni, N)"N represents the diimine, and typical R groups are: H, -OCH_3, -$N(CH_3)_2$, NO_2.*

III. Biology

The importance of structure in biology is best expressed by this citation of F. Crick, the co-discoverer of the double helix structure of DNA: "If you want to understand function, study structure". The tremendous development of protein crystallography over the past 40 years is a result of the need to "understand function". But it is clear that observing the evolution of structure in biological systems, rather than just static structure, offers another dimension of insight. At the core of any biological function are chemical reactions, which at the molecular level, occur on the timescale of femtoseconds to picoseconds. There is another reason why studying biological systems at the shortest timescales is necessary: these systems perform their function with high efficiency and high selectivity, and unravelling the details of the underlying mechanisms at the molecular level, may help design biomimetic functional materials for various applications. The femtosecond resolution of the XFEL combined with XAS is an ideal tool in this respect. Model systems on which these concepts can best be demonstrated are heme proteins.

Heme proteins, such as hemo- and myoglobin, are involved in a variety of physiologically important biochemical reactions such as electron transfer, diatomic molecule storage and transport and catalysis. The heme group is a planar chromophore containing a coordination metal atom (in general, Iron), which is able to bind small diatomic and triatomic molecules such as NO, CO, O_2, CN, H_2O and H_2S. The investigation of heme proteins by time-resolved Laue diffraction is extensively described in Section 6.4.6. However, some of the scientific questions about the dynamics of these systems, in particular the electronic rearrangements in the metal d-orbitals that take place when the metal atom undergoes a spin transition upon ligand dissociation, can only be dealt with using XAS with the femtosecond resolution of the XFEL. Indeed, the ultrafast electronic structure changes in the metal d-orbitals **[6-265 – 6-269]** can be visualised by XANES, while the ultrafast structural changes associated with the multimode behaviour **[6-270, 6- 271]** can be visualised by EXAFS.

IV. Condensed matter physics and materials science

Luminescent materials

A wide variety of technologically important luminescent solids depend critically on the interaction between impurity ions and the surrounding local structure of a host material. Well known examples include ultrafast laser crystals such as Ti:Al_2O_3 or Ruby **[6-272]**. Thanks to this element specificity, femtosecond NEXAFS and EXAFS of the optically active impurity ion can offer a direct observation of the coupling between electronic and vibronic degrees of freedom in such systems, allowing us to gain a better understanding of the basic science underlying the luminescence process. Also interesting are "co-doped" luminescent crystals where energy transfer between different dopant species is important **[6-273]**.

Order-disorder phase transitions and data storage

Present-day multimedia strongly rely on rewritable phase-change optical memories. $Ge_2Sb_2Te_5$ (GST), the material of choice in DVD-RAM, has controversial structural properties and probably consists of well-defined rigid building blocks that are randomly oriented in space **[6-274]**. Laser-induced amorphisation results in drastic shortening of covalent bonds and a decrease in the mean-square relative displacement, demonstrating a substantial increase in the degree of short-range ordering, in sharp contrast to the amorphisation of typical covalently bonded solids. This novel order-disorder transition is due to a modification of the coordination geometry of Germanium atoms without rupture of strong covalent bonds, as schematically shown in Figure 6.4.43. It is this unique two-state nature of the transformation that ensures fast DVD performance and repeatable switching over ten million cycles.

The phenomenology of phase-change optical recording is simple. An initially amorphous as-deposited GST layer is crystallised by exposure to a laser beam of intensity sufficient to heat the material to a temperature slightly above the glass-transition temperature.

A subsequent exposure to an intense and short laser pulse melts the GST which is then converted into the amorphous state on quenching. A recorded bit is an amorphised mark against the crystalline background. The reversibility of the crystallisation-amorphisation process allows fabrication of rewritable memory.

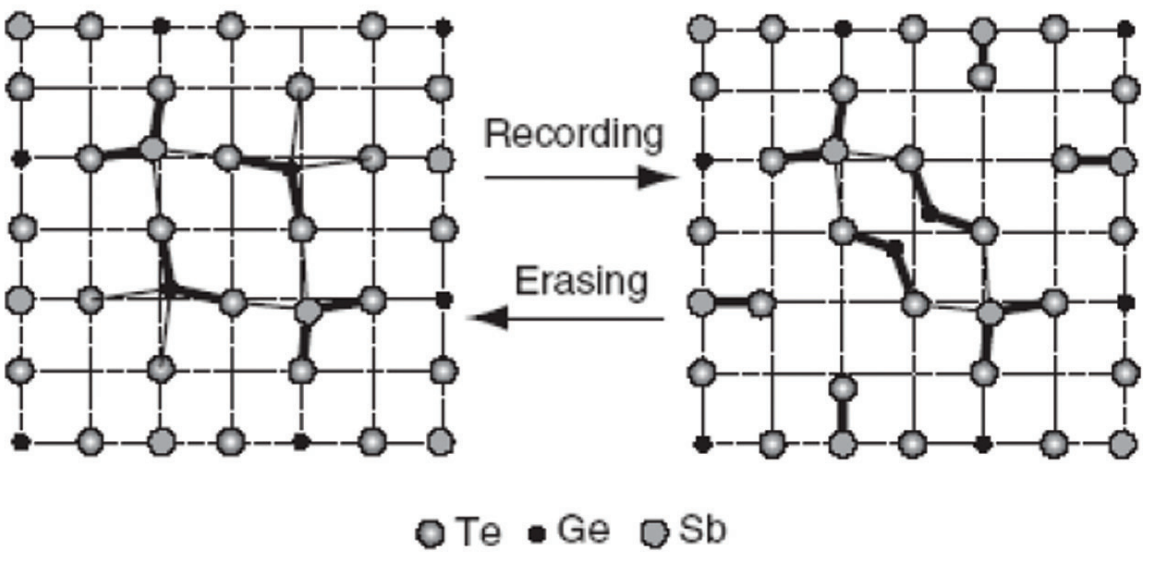

Figure 6.4.43 *Schematics of medium-range-order changes in the structure of GST upon reversible amorphisation-crystallisation. The umbrella-flip of Germanium atoms from the initially distorted rocksalt structure in the crystalline state (left) results in a shortening of Sb-Te bonds and subsequent distortions in the Te fcc sublattice (amorphisation) (right).*

An ideal tool for investigating the local structure of a material and its changes on the atomic scale independent of the state of the material (crystalline or amorphous) is XAS, which is already being used in a steady-state mode **[6-274 – 6-276]**. However, the timescales of the structural changes have never been measured. In addition, although it is generally assumed that the role of a laser pulse is to simply heat the material, it seems that electronic excitation creates non-equilibrium charge carriers that are crucial for the weakening and subsequent rupture of the subsystem of weaker Ge-Te bonds **[6-274]**. Such electronic structure changes occur on very short timescales (a few femtoseconds) and can be detected by XANES as done in non-thermal melting phenomena in solids **[6-219, 6-222]**.

The XFEL is an ideal tool to study the order-disorder phase transitions because: a) it provides the right time resolution to capture the atomic motion in real-time; b) for the same reasons as in the case of the luminescent materials, and since the sample is modified after each laser shot, the high flux per pulse at the XFEL makes these experiments feasible in a truly "single-shot" configuration, in which a narrow range of energies (set by the bandwidth of the source and a dispersive energy analyser) and times (set by the geometry of the experiment) can be probed with adequate statistics using a single XFEL pulse.

Magnetic phenomena

The study of magnetisation dynamics in thin films and nano/microstructures is motivated by applications in data storage and electronics, but also by the exciting fundamental physics that is involved. Magnetisation dynamics takes place over a large range of timescales, from some hundreds of femtoseconds up to years. At nanosecond timescales and above, magnetisation reversal in thin films takes place by nucleation of reversed domains and a subsequent propagation of domain walls. Below this regime, from some picoseconds up to nanoseconds, the dynamics is governed by the Landau-Lifshitz-Gilbert (LLG) equation which describes the precessional motion of the magnetisation around the direction of the effective field and the subsequent damping of this motion. This precessional motion can be used to obtain a coherent switching of the magnetisation direction of micron-sized magnetic structures in less than 200 ps **[6-277, 6-278]**, using magnetic pulses applied in the direction perpendicular to the easy axis of magnetisation. Even faster reversal, of the order of picoseconds or below, can be obtained using polarised lasers through the so-called inverse Faraday effect **[6-279, 6-280]**. At these very short timescales thermal effects induced by absorption of the photons, start to play a role and electron-electron and electron-phonon interactions **[6-281]** have to be taken into account.

Time-resolved studies of magnetisation dynamics have already been performed using the time-structure of synchrotron x-rays, with both space-integrated **[6-282]** and imaging techniques **[6-283 – 6-285]**. A pump-probe technique was used for these studies and the temporal resolution was limited to the sub-nanosecond time domain. Using the much shorter and intense x-ray pulses of the XFEL opens up the possibility of studying phenomena like the ones mentioned above, which until now are only accessible with laser beams. The advantage of x-rays over lasers is that they can provide element-selectivity through X-ray Magnetic Circular Dichroism in XAS **[6-284]**, and very high spatial resolution can be obtained if they are combined with x-ray microscopy techniques. This allows the ultrafast magnetisation dynamics in the different layers of multilayered magnetic systems (important for applications) to be studied separately. Also, the role of the spin and orbital magnetic moments of different elements in alloys and compounds on the magnetisation reversal can be studied separately.

Warm dense matter

Warm dense matter refers to the thermodynamic regime of matter at temperatures above ~1 eV with densities near that of solids (1-10 g/cm^3) (see also Section 6.4.2). Although such states of matter are fairly common in astrophysical bodies, their study on earth is limited by the experimental difficulty of making even basic quantitative measurements. Recently, some progress has been made in using ultrafast pump-probe soft x-ray absorption to study matter approaching this regime **[6-219, 6-222]**. In these experiments, the warm dense matter is created by a femtosecond laser that rapidly heats a thin foil target, generating, for a short time, very high temperatures in the inertially confined foil. A picosecond synchrotron x-ray pulse then probes the x-ray absorption in the vicinity of a characteristic edge, providing information on the electronic and structural condition of the foil as a function of time.

The high temporal resolution of the XFEL will allow the carrying out of such experiments in the femtosecond regime, opening up exciting opportunities to study the high-energy density non-equilibrium coupling between the laser-excited electrons and the initially very cold atomic lattice. This would manifest itself as very short (sub-picoseconds) dynamics in the near-edge spectral features, as the symmetry features of the solid are destroyed as energy is transferred to the ions, and the occupancy of valence orbitals is changed. In addition, the changes in bond distances and coordination numbers can be captured by ultrafast EXAFS.

One difficulty in these measurements is that the creation of warm dense matter is irreversible, meaning the sample must be replaced between each x-ray pulse. The high flux per pulse and short temporal duration of the SASE beamlines at the XFEL make these experiments feasible in a truly “single-shot” configuration, in which a narrow range of energies (set by the bandwidth of the source and a dispersive energy analyser) and times (set by the geometry of the experiment) can be probed with adequate statistics using a single pulse from the XFEL. As an example, consider a Chromium foil target. The Chromium K-edge is located at approximately 6 keV. Assuming a 0.08% bandwidth from one of the hard x-ray SASE beamlines, the bandwidth at the Chromium K-edge is approximately 5 eV, which is enough energy range to cover the edge shift from neutral Chromium to Cr^+, as well as the more dramatic pre-edge features of higher valence Chromium. X-rays from the undulator first encounter a bent crystal, set to both focus the beam in one dimension onto the sample and to disperse spectrally the x-rays transmitted through the sample. Thus, a detector placed behind the sample sees along one spatial dimension the transmission spectrum of the foil for each x-ray pulse. Temporal dispersion can be accomplished similarly, by using a large angle between the laser pump pulse and the x-ray probe pulse along the unfocused axis of the x-ray beam. The detector would then see a 2-D x-ray image behind the sample, with one spatial axis representing x-ray wavelength and the other pump-probe delay time, all in a single x-ray shot. Estimates using the XFEL performance goals yield a signal-to-noise ratio of approximately 10^3 per shot assuming ideal detectors and optics and a 1 ps time window. At the expense of photon number, the spontaneous emission beamlines can offer a wider spectral range.

Advanced implementation of XAS at the European XFEL facility

The possibility of the European XFEL tuning the photon energy very fast using an energy modulation of the electron beam invites an attractive solution for ultrafast studies. For less demanding samples, e.g., moderately concentrated liquid solutions, we can exploit a combination of Quick EXAFS (QEXAFS) with the time structure of the XFEL: a QEXAFS monochromator (Figure 6.4.44) synchronised to the sequence of x-ray pulses produced by the train of electron bunches with one RF pulse (every 200 ns for about 0.6 ms) could select a different energy for each single pulse, eventually covering an entire EXAFS scan (with $\Delta E = 0.1$-1 keV) in 0.2-1 eV steps at 10 Hz repetition rate.

Current QEXAFS monochromators can operate at 40 Hz and cover about 1-1.5° scan angle, which translates into about 1 keV tunability range at 10 keV photon energy. This translates into a 40 eV scan range per millisecond or about 24 eV over the sequence of x-ray pulses from one pulse train. By increasing the angular speed of the monochromator, one might be able to increase this range considerably, thus, enabling measurement of a full XAFS spectrum within 0.6 ms. Since the bandwidth of the FEL line alone is not sufficient to provide the complete XAFS spectrum, an energy chirp of the electrons within one bunch train is required. Synchronisation of the QEXAFS monochromator to the arrival of x-ray pulses to better than 100 μs is further required.

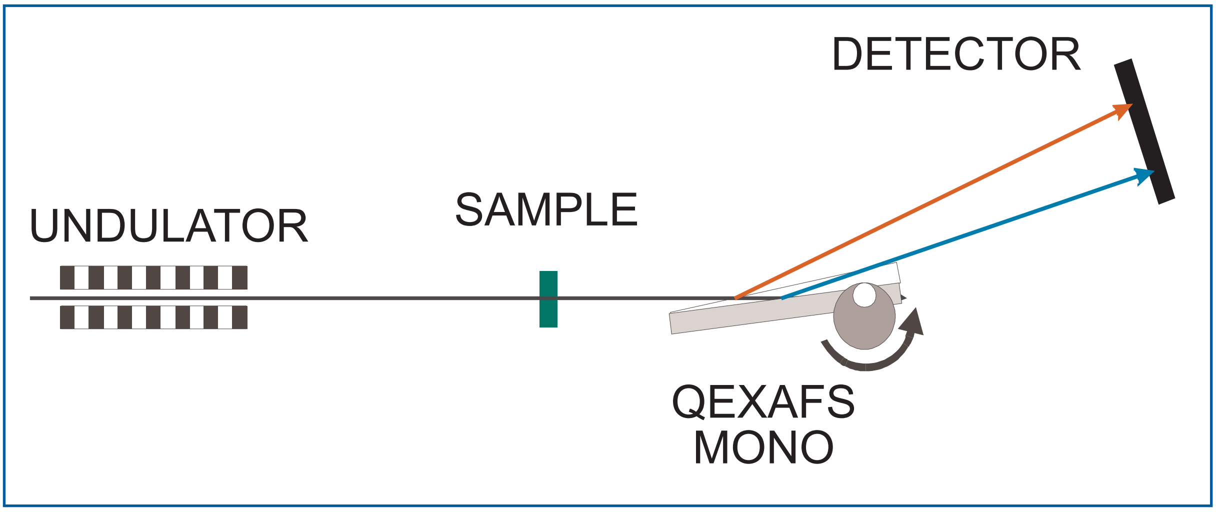

Figure 6.4.44 *Synchronising a QEXAFS monochromator with the pulse sequence of the XFEL could allow the measurement of an entire XAFS spectrum within one single train of x-ray pulses (lasting about 0.6 ms) in transmission mode. The rotating Bragg crystal will, thus, deflect different energies at different angles. The spectrum can be collected with a slow detector.*

Since the beam deflected by the QEXAFS monochromator would also point in a different direction, an imaging detector could record the signal from an entire bunch train reducing the requirement for fast readout to the bunch train repetition rate of 10 Hz. Since the incident signal varies it has to be measured pulse-by-pulse for normalisation purposes. A concern is the detector acceptance in terms of x-ray quanta. Starting from the high incident photon number of $10^9 – 10^{12}$ and a reduction of only $10^2 – 10^3$ due to bandwidth reduction and sample transmission, a large number of photons hit the detector. In a clever geometric arrangement one single pulse (for one single energy step) could cover about 1,000×10 pixels of the detector, thus entering a regime where detectors with maximised well-depth could work.

To circumvent this difficulty in a second setup, spectroscopy detection of fluorescent radiation is proposed (Figure 6.4.45). Here, the incident radiation is spectrally dispersed using the QEXAFS monochromator already in front of the homogenous sample. The pump laser could co-propagate with the x-ray beam using a mirror that rotates together with the Bragg crystal such that overlap in space and time can be perfectly maintained. X-ray fluorescence from the sample needs to be recorded using a spatially resolving spectrometer. In consequence, the spatial distribution of recorded fluorescence photons is a function of the incident x-ray energy, and can be converted into an XAS spectrum. As for the previous method normalisation of the incident photon flux for every single pulse is required. Another method could exploit the angular distribution of the incident rays using an array of Soller slits to distinguish between scattered light from different locations. In building the energy- and space-resolving spectrometer, it should be possible to determine the incident and emitted photon energy simultaneously, thus allowing measurement of shifts or broadening in the x-ray emission lines.

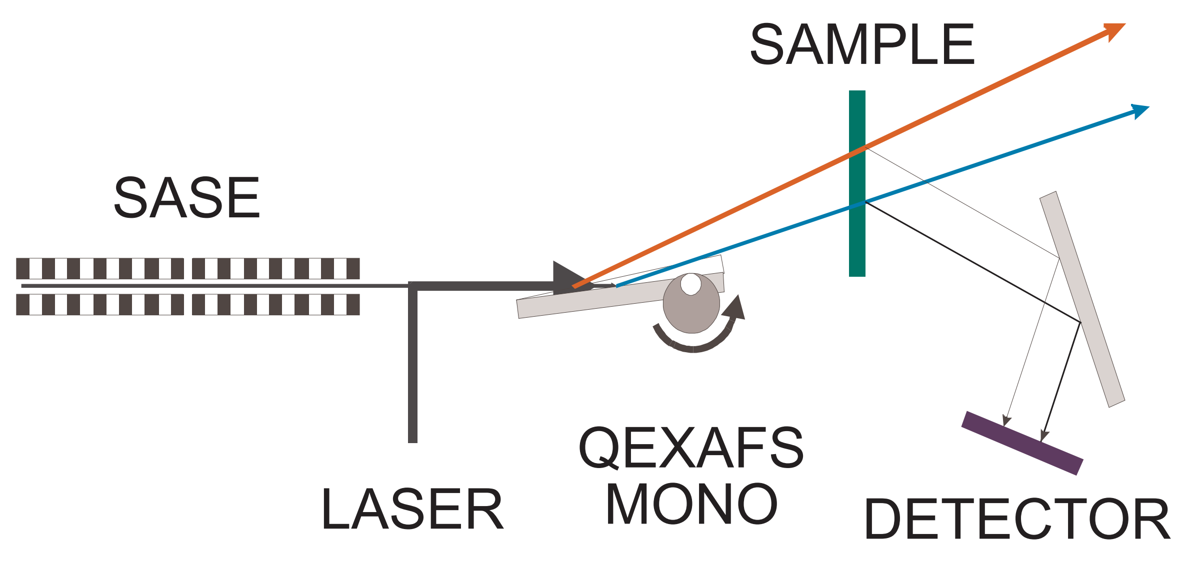

Figure. 6.4.45 *The rotating Bragg crystal deflects different energies at different angles, and a co-rotating laser mirror will ensure continued overlap between both laser and x-ray beams on the sample. X-ray fluorescence is collected spatially resolved using crystal spectrometers.*

6.4.5.2 Instrument requirements

The experiments described above lead to requirements of an instrument for scientific applications using XAS. They concern the performance of the light source, the optical elements and the diagnostic equipment, the sample environment, and the detectors. The scientific cases presented call for beamlines suitable to spectroscopy, thus, with a sufficient energy resolution and tunability range. For XANES investigations the intrinsic tunability of about 6% is certainly sufficient, this translates into about 50 eV near 0.8 keV and about 700 eV near 12 keV. EXAFS studies sometimes require a tunability range of about 1 keV, and both SASE 2 and SASE 3 will offer this capability. The SASE 2 and SASE 3 insertion devices will cover the energy range of 3-12 keV and 0.8 – 3 keV respectively. The dedicated beamlines have to concentrate on a specific energy range, given by the characteristics of the monochromating systems.

Spectral radiation properties

The measurements require an energy resolution in the order of $\Delta E/E \sim 10^{-4}$. This resolution is about 10-100 times better than the natural bandwidth of the XFEL radiation in the required photon energy range. The monochromatisation is usually achieved in the incident beam, but can, in principle, also be achieved using a dispersive element in the beam transmitted by the sample. However, the latter method increases the absorption of x-ray photons in the sample accordingly. The natural bandwidth in special cases provides enough of an energy range to investigate significant features in the XANES spectra using single x-ray pulses. For the entire XAFS information an energy range of 10% is required.

To implement advanced schemes to tune the photon energy very fast using the QEXAFS scheme (compare Section 6.4.5.1), the availability of the non-monochromatised beam has to be anticipated.

X-ray optics requirements

Although the technique does not require coherence, the coherence properties and wavefront errors of the x-ray beam can become crucial in these experiments. The reason is the required normalisation of the incident photon flux at the sample position. If coherence effects lead to variation of this photon flux in space or, even worse, in time, the normalisation will become very difficult. With respect to the monochromator crystals one needs to keep the error in asymmetry very small in order to avoid tilting the wavefront and thereby modifying the time pattern at the sample position.

The beamsize at the sample will be determined by the experiments, in particular the sample geometry. Therefore, focusing in the XFEL beam to spot sizes the order 100 µm should be enabled.

Time domain requirements

These experiments probe dynamics on the ultrafast timescale using pump-probe techniques. Pumping is usually achieved using an ultrafast visible laser. The synchronisation should be significantly better than the anticipated time resolution of ~100 fs. For the same reason the fluctuation of the pulse duration must be small compared to the 100 fs timescale.

It is anticipated that a variety of pulse patterns from single pulses at 10 Hz repetition rate up to several thousands of x-ray pulses per electron bunch train will be used.

Photon diagnostics requirements

The short- and long-term stability of the x-rays is of extreme importance for the quality of the experiments. The position stability of the emitted x-rays and even their spatial distribution should be monitored. Furthermore, all experiments will need diagnostic equipment for the measurement of the photon flux on a pulse-to-pulse basis. Since monochromators are used, the measurement of the mean photon energy is not required and spectral diagnostics should provide the content of higher harmonic radiation only. All measurements must be available on a pulse-to-pulse basis.

Sample manipulation and environment

The issue of sample handling under the high flux of the XFEL can be a serious problem, but it obviously depends on the type of experiments one is conducting. At this stage, we can say that concerning liquid samples (molecules or ions in solution, biological systems in solution, pure liquids, etc.), there are no serious challenges because the sample can be refreshed after each pair of laser-x-ray pulses (provided we have sufficient sample), as is already done in picosecond XAS experiments **[6-218]**.

For solid samples, the high XFEL flux may provide the solution since one can work in a single shot regime. Alternatively, given the relatively low repetition rate of the x-ray source, a shaker can be used to refresh the sample by moving another spot into the focus region.

It is clear that specific solutions have to be implemented for each type of experiment.

The hard x-ray instrument could be placed in a vacuum or even in air if windows are used as a vacuum interface. The windows should receive only the unfocused beam, meaning they should be mounted near the local optics. The soft x-ray instrument will differ from the hard x-ray one in requiring a single vacuum system throughout, with no windows, including the detector chambers. For the soft x-ray experiments at magnetic resonances, in-vacuum magnet- and cryosystems will be needed.

Detector requirements

The great advantage of XAS, as compared to other x-ray techniques, is that it does not rely on large area detectors, where read out time can be a serious problem for a high repetition rate experiment. In that sense, pump-probe experiments based on XAS are very similar to the analogue transient absorption experiments in the optical domain, and many of the detection methods can and have been implemented in time-resolved XAS experiments **[6-218, 6-286]**. The extension to XFEL-based experiments is, however, not straightforward, because one needs to detect in the order of $10^9 – 10^{11}$ photons of 10 keV energy within a 100 fs pulse, in any given experiment. We usually rely on the linearity of the detector for the given range of pulse intensities. For example, semiconductor photodiodes have proven their worth over a wide range of incident intensities, i.e., from single photon counting up to 10^5 photons within a 100 ps long x-ray pulse. The large carrier densities created in such a detector by an XFEL pulse will limit their use, although using large area photodiodes far away from the focus may relax these conditions considerably. Today, quasi white-light from Synchrotron Radiation (SR) Undulators achieves about 10^{10} photons within a 100 ps long pulse, and these sources may be used as a basis for assessing the utility of sensitive and linear detectors. In an alternative setup, x-ray fluorescence detection using spectroscopic techniques relaxes the detector requirements with respect to photons per time-interval considerably.

Visible laser requirements

Visible lasers will be applied in pump-probe experiments. A wavelength tunable system providing pulse durations in the order of 30 fs and pulse energy up to 1 mJ at 800 nm will allow the carrying out of the experiments proposed in this area. Using Optical Parametric Amplification (OPA) schemes a wavelength range of ~200 to 1500 nm should be available at the instrument. Synchronisation to the x-ray beam of the order of the pulse duration or pulse-to-pulse measurements of the jitter is requested.

6.4.5.3 Realisation of the instrument

For their realisation, the XAS experiments require two instruments at SASE 3 (XAS 1 – Tunable soft x-rays) and at SASE 2 (XAS 2 – Tunable hard x-rays). For a description of the SASE 2 and SASE 3 beamlines, see Sections 6.2.4.2 and 6.2.4.3, respectively. Experiments discussed in Section 6.4.5.1 under Topics I.-IV. will be carried out at these instruments depending on the element under investigation. As XAS is a local probe, the absorption edge of the corresponding element determines the photon energy to be used. Since all experiments require monochromatisation, one might use the monochromators installed in the SASE 3 and SASE 2 beamlines. However, advanced schemes also require receiving the full beam at the instrument and applying monochromatisation in the vicinity of the sample. Both instruments will require moderate focusing of the XFEL radiation to beam sizes in the order of 100 µm achieved by using a focusing element inside the corresponding beamlines. For the XAS 1 instrument refocusing of the monochromator exit slit is used to focus the beam at the sample location. For the XAS 2 instrument the focusing element will likely be Beryllium lenses.

XAS 1: Tunable soft x-rays

The following elements belong to the XAS 1 instrument inside the experimental hall. They are depicted in the schematic layout of that instrument in Figure 6.4.46 and are described in Table 6.4.12. A deflecting mirror provides the necessary beam offset for the instrument. Using a demagnification of 1 with respect to the exit slit of the monochromator, a beam spot of ~100 µm can be achieved. Following a slit/aperture unit, time and photon flux monitors follow. A differential pumping section separates the beamline from the sample. Also, the QEXAFS monochromator is installed after the differential pumping section. Between sample and monochromator an photon flux monitor is required to enable a pulse-to-pulse photon flux measurement. The sample environment includes the possibility of mounting spectrometers for fluorescent detection. Behind the sample chamber another photon flux and spectral monitor follows.

The sample environment allows for linear movements (1µm repeatability and 0.25 µm resolution) and angular degrees of freedom (1/1,000° repeatability, 1/4,000° resolution). The detector equipment comprises fast point detectors, space-resolved x-ray emission spectrometers and 2-D detector(s). A laser system including an OPA system for provision of widely tunable visible laser radiation is available.

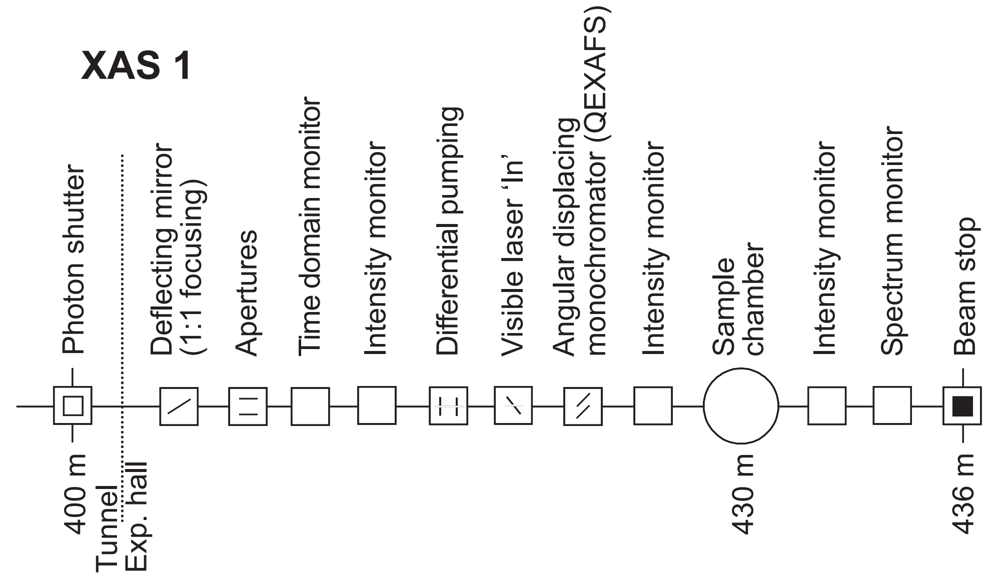

Figure 6.4.46 *Schematic layout of the XAS 1 instrument at the SASE 3 beamline. Distances are given in relation to the end of the undulator.*

Item	Purpose	Specification
Deflecting optics	Horizontal deflection by 20 mrad, 1:1 focusing of monochromator exit	0.1 µrad angular stability, 0.3 µrad figure error, 0.1 nm surface roughness
Slits/apertures	Beam definition, beam halo cleaning	0.25 µm accuracy, 1 µm repeatability
Time domain monitor	Measurements of x-ray arrival-time x-ray with respect to visible laser	
Intensity monitor	Measurement of incident photon flux	Transmissive (<5% absorption), single pulse measurement, relative accuracy $<10^{-3}$
Differential pumping	Separation of beamline and instrument	
Monochromator	Angular displacing monochromator (QEXAFS)	0.1 µrad angular stability, 0.1 mrad asymmetry error
Intensity monitor	Measurement of photon flux behind dispersive element	Transmissive (<5% absorption), single pulse measurement, relative accuracy $<10^{-3}$
Sample chamber	Sample positioning and orientation	x-y-z move (0.25/1 µm), two rotations (0.25/1 mdeg)
Detector	Measurement of transmitted radiation	2-D, 2K×2K, 10-30 Hz
XES spectrometer	Space-resolved detection of x-ray emission from the sample	In-vacuum, 10-30 Hz frame rate
Intensity monitor	Measurement of transmitted photon flux	Transmissive (<5% absorption), single pulse measurement, relative accuracy $<10^{-3}$
Spectrum monitor	Measurement of high harmonic content	Single pulse measurement, relative accuracy $<10^{-3}$
Alignment unit	Positioning and position verification	Permanently operating, accuracy ~100 µm
Lead hutch	Radiation protection, temperature stabilisation, laser protection	4×8×3.5 m^3 (W×L×H), ±1° thermal stability
Control hutch	Operation of the instrument	Working environment (noise, temperature, light)

Table 6.4.12 *Elements and specifications of the XAS 1 instrument.*

XAS 2: Tunable hard x-rays

For hard x-rays no significant offset can be achieved for short distances, thus, a deflecting mirror assembly inside the SASE 2 beamline tunnel and about 100 m upstream of the experimental hall is used for horizontal deflection. The XAS 2 instrument resembles XAS 1 very much. Only the first deflecting mirror inside the experimental hall can be avoided. The instrument is about 500 m further away from the end of the undulator. Due to the higher photon energies Beryllium windows might become usable. However, since the instrument is supposed to cover the entire photon energy range from 3-12 keV, a differential pumping section will be of advantage. Figure 6.4.47 depicts the principal setup of XAS 2 and a description of these elements can be found in Table 6.4.13. Further details are given in the section before on XAS 1.

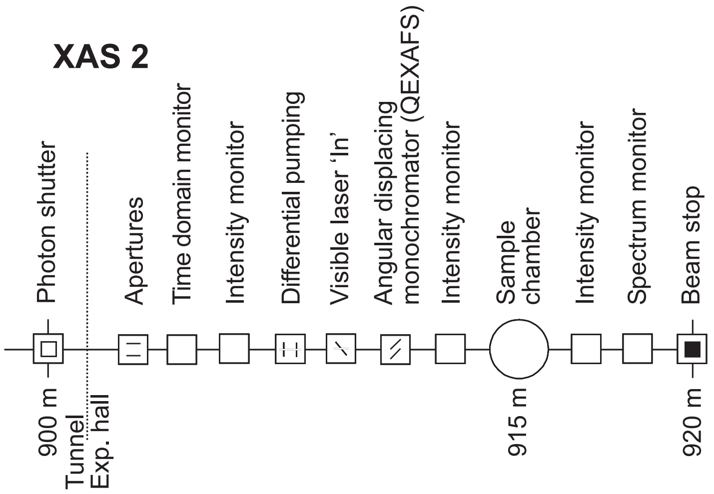

Figure 6.4.47 *Schematic layout of the XAS 2 instrument at the SASE 2 beamline. Distances are given with respect to the end of the undulator.*

Item	**Purpose**	**Specification**
Slits/apertures	Beam definition, beam halo cleaning	0.25 µm accuracy, 1 µm repeatability
Time domain monitor	Measurements of x-ray arrival-time x-ray with respect to visible laser	
Intensity monitor	Measurement of incident photon flux	Transmissive (<5% absorption), single pulse measurement, relative accuracy $<10^{-3}$
Differential pumping	Separation of beamline and instrument	
Monochromator	Angular displacing monochromator (QEXAFS)	0.1 µrad angular stability, 0.1 mrad asymmetry error
Intensity monitor	Measurement of photon flux behind dispersive element	Transmissive (<5% absorption), single pulse measurement, relative accuracy $<10^{-3}$
Sample chamber	Sample positioning and orientation,	x-y-z move (0.25/1 µm), two rotations (0.25/1 mdeg)
Detector	Measurement of transmitted radiation	2-D, 2K×2K, 10-30 Hz
XES spectrometer	Space-resolved detection of x-ray emission from the sample	In-vacuum, 10-30 Hz frame rate
Intensity monitor	Measurement of transmitted photon flux	Transmissive (<5% absorption), single pulse measurement, relative accuracy $<10^{-3}$
Spectrum monitor	Measurement of high harmonic content	Single pulse measurement, relative accuracy $<10^{-3}$
Alignment unit	Positioning and position verification	Permanently operating, accuracy ~100 µm
Lead hutch	Radiation protection, temperature stabilisation, laser protection	$4\times8\times3.5$ m^3 (W×L×H), ±1° thermal stability
Control hutch	Operation of the instrument	Working environment (noise, temperature, light)

Table 6.4.13 *Elements and specifications of the XAS 2 instrument.*

6.4.6 Femtosecond diffraction experiments

It has always been a dream of chemists and physicists to film the making of new molecules and structures to gain a deeper understanding of the parameters in the process. In fact how do atoms and molecules combine to form new molecules or structures? What is driving the transformation? How long does it take? Which atoms are involved? Does the environment catalyse the reaction? These questions are not easy to answer since the primary time steps in chemical and physical transformations are ultrashort, typically on the timescale of molecular vibrations. For example, in the symmetric stretch mode in water, the Hydrogen atoms vibrate along the O-H axis in 9.1 fs. And the heavier Iodine molecule oscillates with a 156 fs period. Femtosecond optical spectroscopy has provided a wealth of information about the timescales in femtochemistry but the long wavelength of light, 200-700 nm, precludes spatial information on the atomic length scale. Ultrafast electron diffraction (UED), on the other hand, can probe chemical reactions in the gas phase with 1 ps resolution, but the strong scattering of electrons makes is difficult to use UED in condensed matter, which is an important drawback since most biological and industrial processes take place in a condensed environment.

The European XFEL Facility will deliver extremely intense, 100 fs long pulses of x-rays that will become a fantastic new tool for studies in femtochemistry. The pulse is expected to contain 1×10^{12} photons in a 0.1% bandwidth at 12.4 keV. By comparison, beamline ID09 at ESRF produces 1×10^{10} photons in a 3% bandwidth at 15 keV in 100 ps. XFEL radiation is, thus, likely to revolutionise time-resolved studies: a 1,000-fold shorter pulse length, a 100-fold increase in single-pulse intensity and a 30-fold reduction in bandwidth. Simulations indicate that high-quality diffraction patterns from a protein and a liquid can be acquired in one single pulse. These exceptional parameters will lead to new experiments and groundbreaking discoveries.

6.4.6.1 Scientific case

The aim of pump-probe diffraction experiments with XFEL radiation is to visualise how matter rearranges during chemical or physical reactions with femtosecond resolution. One of the most striking pump-probe experiments with third-generation synchrotrons is Laue diffraction from myoglobin. Using single-pulse Laue diffraction at ESRF and the Advanced Photon Source (APS), it is possible to film, with 100 ps time resolution, the trajectories of CO molecules and the associated structural relaxations as they photodetach from the heme group and migrate towards the solvent. The advantage of working with crystals is substantial: if the non-excited structure is known, the Fourier difference maps determine the change in the electron density in three dimensions and without the need for a model. The maps probe, in principle, the induced changes in position for **all** atoms in the crystal, and this method is complementary to spectroscopy, that probes the local environment around a metal atom (Section 6.4.5(II.)). The unique feature required of the investigated proteins is that they retain their functionality in the crystalline state. This is due to the intrinsic softness of proteins and their large size, so that most residues are located far from the boundaries of the unit cell. There are limits, however, and hemoglobin is one of the best examples. Alternatively, such relaxations can be studied by small-angle-scattering SAXS but the information content is limited to one-dimensional maps that need interpretation. There is, however, great interest in SAXS since many systems, including membrane proteins, that cannot be crystallised, become accessible.

Further examples of application of ultrafast diffraction concern small molecules, whether in the gas or liquid phase, or in the solid state. In the solid state, detailed information on the structural evolution following excitation by a pump laser can be obtained by applying techniques such as time-resolved powder diffraction. With the short and intense x-ray pulses provided by the XFEL it will be possible to follow intra- and intermolecular structural relaxation processes which are connected to vibrational redistribution processes or to investigate the structure of ultrashort living intermediates (as excitonic states in organic dyes). Further opportunities are provided by resonant (anomalous) diffraction, which has a special sensitivity to electronic properties, and may be used to monitor electronic phase transitions on a fast timescale.

Experimental programme

I. Ultrafast diffraction from molecules in the gas phase

Molecular structural dynamics in the gas phase has already been studied by time-resolved electron diffraction with a temporal resolution approaching 1 ps and spatial resolution better than 0.001 nm **[6-287 – 6-289]**. Electrons are well suited for the gas phase due to its relatively high scattering intensity over x-rays. In general the scattering intensity of electrons is six orders of magnitude stronger than that of x-rays **[6-290, 6-291]**. Since the number of electrons per pulse used in a typical time-resolved electron diffraction is ~10^4 at 1 kHz operation **[6-288]**, one needs 10^{12} (= $10^4 \times 10^6 \times 10^2$) x-ray photons per pulse at 10 Hz operation to make up for the deficiency of the scattering intensity and the repetition rate. Therefore, once the XFEL comes on stage with its 10^{12} photons per pulse, it should be possible to study gas phase structural dynamics by time-resolved x-ray diffraction under similar conditions to time-resolved electron diffraction (a pressure of 1 – 10 torr in the scattering volume). What would be the advantages and disadvantages over time-resolved electron diffraction? Gas-phase time-resolved x-ray diffraction from an XFEL will have a time resolution limited by the x-ray pulse width, that is, about 100 fs. This time resolution is not only 10 times better than state-of-the-art electron diffraction, it also reaches the time window of molecular vibration. This means that the movement of atoms in a molecule can be filmed literally in real time. In addition, electrons are charged and hence, affected by small amounts of positive ions generated as by-products in most pump-and-probe experiments. This causes some baseline drift and complicates the data analysis **[6-292]**. X-rays do not suffer from this problem. The real disadvantage of x-ray diffraction, apart from the poor sensitivity to the lightest atomic species, is that inelastic scattering increases with the scattering angle whereas the situation is reversed in electron diffraction. This means that the usable q-range is inherently limited for x-ray diffraction even if a sufficient number of x-ray photons are provided. Typically, there is no usable elastic scattering for q values larger than 10 $Å^{-1}$. By contrast, the available q-range in electron diffraction is only limited by the electron flux. To summarise, time-resolved x-ray diffraction is feasible when we consider the photon-counting statistics. The diffraction signal from the gas phase dynamics is supposed to be much simpler than that from solutions, where solvent molecules also contribute. Therefore, gas-phase reactions should be studied prior to liquid-phase reactions for practical reasons.

Scientific applications

All molecular systems that have been studied by time-resolved electron diffraction can be revisited by time-resolved XFEL diffraction. Among the simplest molecular systems would be diatomic molecules such as NaI and I_2. These systems have been intensively studied by femtosecond optical spectroscopy, and they would be a natural first target for time-resolved x-ray diffraction in the gas phase. In addition, the electron diffraction signal in the femtosecond regime has been simulated for these systems **[6-293, 6-294]**. As shown in Figure 6.4.48, once a ground state Iodine molecule is excited to a repulsive excited state, the distance between the two atoms will expand and the Iodine molecule will eventually dissociate into two Iodine atoms. The wavepacket motion along the vibrational dissociation of the two atoms can be mapped out by x-ray diffraction in real time if sub-picosecond time resolution becomes available.

After acquiring full control of the relevant parameters for pump-probe experiments on diatomic molecules, more challenging targets could be considered: polyatomic molecules, e.g. the haloalkanes such as CF_2I_2, CH_2I_2, and $C_2F_4I_2$, organometallic such as $Fe(CO)_5$ and $(C_5H_5)Co(CO)_2$, and hydrocarbons such as pyridine (C_5H_5N) and cyclohexadiene (C_6H_8). It has been shown that a sufficient gas pressure can be easily obtained for these molecules. Due to the insufficient time resolution of electron diffraction, limited to a few picoseconds, the real-time movement of atoms could not be captured, but only the molecular structures of transient intermediates were obtained so far. For example, picosecond electron diffraction studies on ring-shaped molecules such as pyridine and cyclohexadiene showed that the ring is opened upon excitation at 267 nm, but it could not be determined whether the ring is broken in a symmetric or asymmetric fashion. If we can follow atomic motions in real time, this very initial movement can be captured. In addition, one can film intramolecular vibrational energy redistribution, which will affect the bond lengths and angles of an intermediate as a function of time. If the excitation pulse is linearly polarised, the excited molecules will tend to align their transition dipole moment along the polarisation. Femtosecond time resolution should readily observe this excitation anisotropy.

Clusters of atoms or molecules are even more challenging. These systems have been studied by time-resolved electron diffraction **[6-295]**, but only with microsecond time resolution determined by the flight time after a nozzle. Time-resolved x-ray diffraction should be able to follow the phase transition within a cluster and clarify the relationship between the structural parameters and the phase transition.

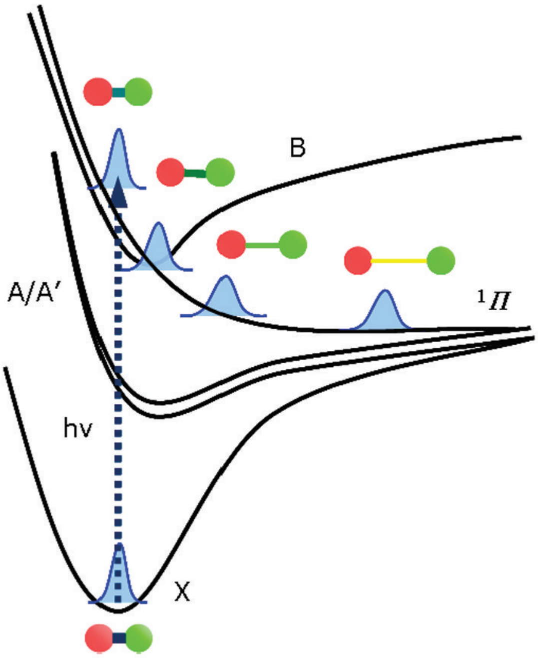

Figure 6.4.48 *Schematic view of the potential energy surfaces for ground and excited states of a diatomic molecule and the evolution of vibrational wavefunctions after photoexcitation.*

II. Liquid-phase photochemistry

The chemistry in solution phase is an important field of research as many biological and industrial reactions take place in solution. Time-resolved x-ray diffraction in liquid phase photochemistry has already been very successful in synchrotron-based experiments **[6-296 – 6-298]**, where it can determine molecular structures of intermediates in solution to a time resolution of 100 ps, limited by the x-ray pulse width from storage rings. In recent experiments, fairly complex reactions with up to six reaction channels in parallel were studied. Better time resolution has been demonstrated with laser-driven plasma sources **[6-299]** and at SPPS **[6-300]**, but the number of x-ray photons per pulse was not sufficient for liquid-phase dynamics, and only solid samples where the structural information is gathered from one or two reflections, were considered. In a typical time-resolved x-ray diffraction experiment, halide-containing solutes such as Br_2, I_2 $HgBr_2$, HgI_2, CH_2I_2 and $C_2H_4I_2$ are dissolved in liquids like methanol (CH_3OH) or tetrachloromethane (CCl_4). In the analysis of x-ray diffraction with 100 ps time resolution, the signal from a laser-excited solution could be decomposed into three principal components: the solute-only term, the solute-solvent cross term, and the solvent-only term; the analysis was aided by using Molecular Dynamics (MD) simulations for equilibrium. This approach was valid because the time resolution of 100 ps was much slower than the nuclear motions, and the system returns to equilibrium within 100 ps. With the femtosecond time resolution expected from the XFEL, the decomposition and the assumption of quasi-equilibrium are no longer valid, which actually means that the XFEL will open a completely new field of research.

Scientific applications

The solutes studied so far by 100-ps time-resolved x-ray diffraction in solution include diatomic molecules such as I_2 and Br_2, and haloalkanes such as CH_2I_2, $C_2H_4I_2$, and CHI_3. The heavy atoms such as Iodine increased the contrast against the solvent. Unlike a molecule in the gas phase, a solute in solution is surrounded by numerous solvent molecules. The presence of the solvent often alters the reaction pathways through the cage effect. Picosecond resolution allowed observation of these reaction pathways by tracking the structure of the transient intermediates during the course of the reaction, but the real interplay between the solute and solvent is beyond reach. As in the gas phase, femtosecond resolution in XFEL diffraction should allow the observation of the initial motions of the wavepacket once created in the excited state by a laser photon.

Once again, a diatomic molecule such as I_2 would be a good example. As shown in Figure 6.4.49, once an I_2 molecule is excited, the two Iodine atoms will start to separate, but will soon hit surrounding solvent molecules. Therefore, most of them geminately recombine to form a wavepacket either in the hot ground state or in the A/A' state. The lifetime of the A/A' state was long enough to be captured with picosecond time resolution, but the vibrational cooling of the hot ground state was marginally observed. The femtosecond resolution with the XFEL should allow the follow-up of the vibrational cooling. Vibrational cooling is one of two fundamental ways in which molecules in solution can induce the surrounding molecules to rearrange. The other way, which is also critical to solution chemistry, is through solvation.

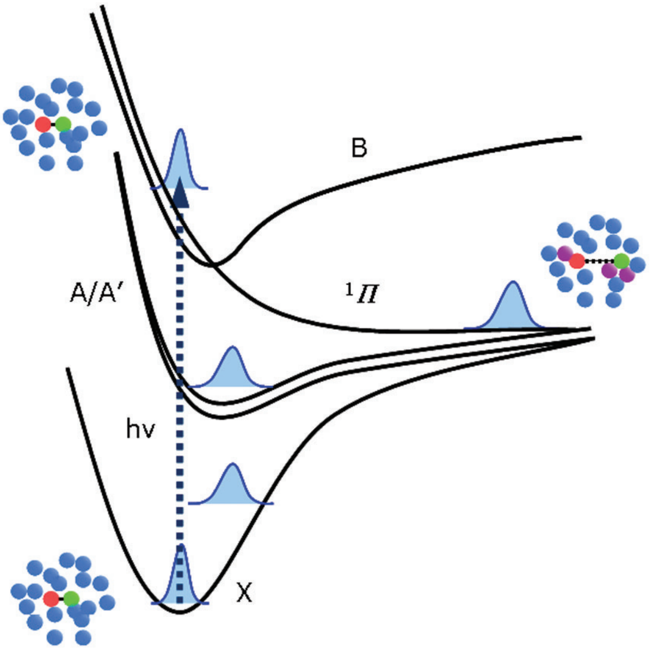

Figure 6.4.49 *Same diagram as Figure 6.4.48, but for I_2 molecules in solution.*

Molecular dynamics simulations of the photo-dissociation of I_2 in CCl_4 can define timescales for structural processes, as shown in Figure 6.4.50. Upon photon absorption, Iodine is put into the short-lived excited B-state that decays through a near conical intersection to a dissociative triplet p state. The Iodine can then dissociate completely or the two atoms are trapped by the solvent cage, which leads to geminate recombination. The photo-excitation of I_2 in liquid CCl_4 induced by a 100 fs laser pulse at 520 nm leads in the simulation to Iodine atoms hitting the cage in 320 fs at a separation of 0.7 nm and with a speed of 1,115 m/s.

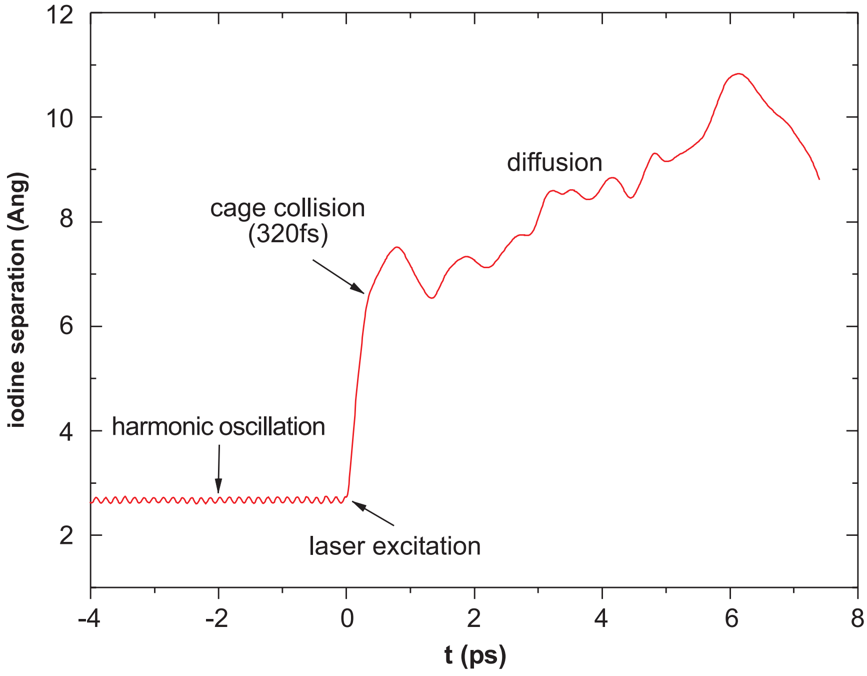

Figure 6.4.50 *MD simulation of the Iodine-Iodine distance for a dissociating Iodine pair.*

Turning to polyatomic molecules, a femtosecond laser pulse can initiate an electronic transition in a dye molecule such as Coumarin 153 dissolved in a polar solvent such as methanol (see Figure 6.4.51). The solute has zero dipole moment in its ground state (S_0), but a large dipole in its excited electronic state (S_1). This electronic transition is rapid as compared to nuclear motions in the solvent, the excited state is initially prepared with a solvation environment that is characteristic of equilibrium S_0, not S_1. Over time the solvent reorganises along the solvation coordinate in order to lower the solvation energy in the excited state **[6-301]**. This solvation dynamics can be followed by femtosecond x-ray diffraction.

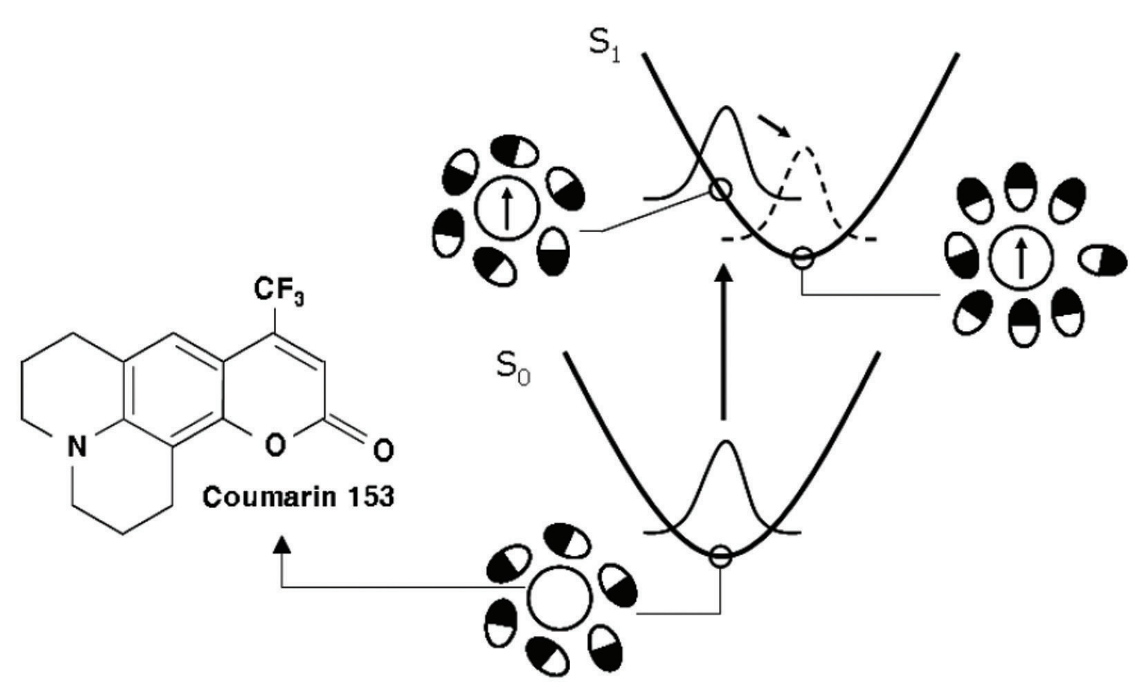

Figure 6.4.51 *Illustration of the role of dipoles in the solvation of Coumarin 153.*

Another interesting subject would be real-time observation of isomerisation in solution. For example, it is speculated that the angle between the two naphthyl groups of 1,1'-binaphthyl is changed by about 40° upon excitation from the ground to the first excited singlet state (see Figure 6.4.52). Since the surrounding solvent molecules have to be pushed out in the process, the time for this process is tens of picoseconds and depends on the viscosity of solvent, as demonstrated by time-resolved spectroscopy **[6-302]**. Femtosecond time resolution should be sufficient to follow this kinetics in real time.

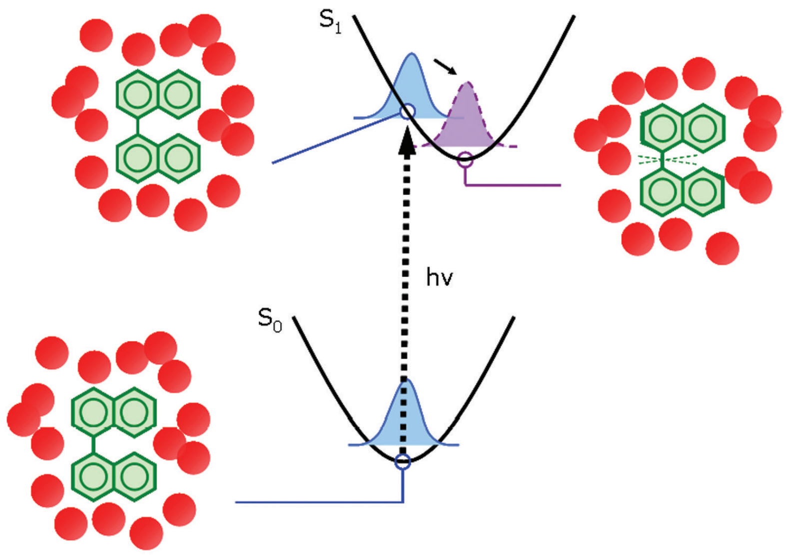

Figure 6.4.52 *Illustration of the solvent rearrangement around 1.1' - Binaphtyl.*

III. Femtosecond time-resolved Laue crystallography of proteins

A detailed mechanistic understanding of how proteins function requires knowledge not only of their static structures, but also of how their structures evolve as they execute their designed function. Recently, the technique of picosecond time-resolved x-ray crystallography was developed and used to visualise, with near-atomic resolution, structural changes in myoglobin as it evolved from the carboxy to the deoxy state **[6-303, 6-304]**. This transition was triggered with picosecond laser pulses and probed with picosecond x-ray pulses. This “pump-probe” approach recovered time-resolved diffraction “snapshots” whose corresponding structures were stitched together into movies that unveiled protein structure changes and ligand migration in real time. The driving force for this structural transition resides in a photolysis-induced displacement of the heme Iron, which moves 0.03 nm or 0.036 nm in the proximal direction. Correlated displacements of the heme, the protein backbone, and other side chains are evident throughout the protein at 100 ps, the earliest time accessible to synchrotron x-ray pulses. Figure 6.4.53 shows structural changes in wild-type MbCO determined 100 ps after photolysis. To enhance the visibility of weak features in the figure, the electron density was mapped non-linearly to color brightness. The most dramatic changes occur within the area enclosed by the white box, but smaller changes are evident over the entire dimensions of the protein. To witness how this piston-like Iron motion drives the structural changes observed in the 100-ps snapshot requires a significantly improved time resolution.

We know from time-resolved IR measurements that the fastest internal motion in photolysed MbCO is the rotation and trapping of CO in the primary docking site. Two trajectories were resolved with time constants of 200 and 500 fs, respectively. We would not expect to resolve the ligand orientation with x-ray crystallography, so around 200 fs time resolution should be more than sufficient to visualise the response of the protein to the ligand translocation event. The doming of the heme along with ligand translocation to the primary docking site triggers a so-called “protein quake” **[6-305]** whose propagation could be resolved for the first time. The biomechanical coupling of the heme doming to the tertiary conformation of Mb is presumably similar to that in hemoglobin, which undergoes a quaternary structure transition that leads to cooperative binding of Oxygen. Being able to explore these processes on the femtosecond timescale promises to help unveil the pistons, levers, wheels, and gears of biology.

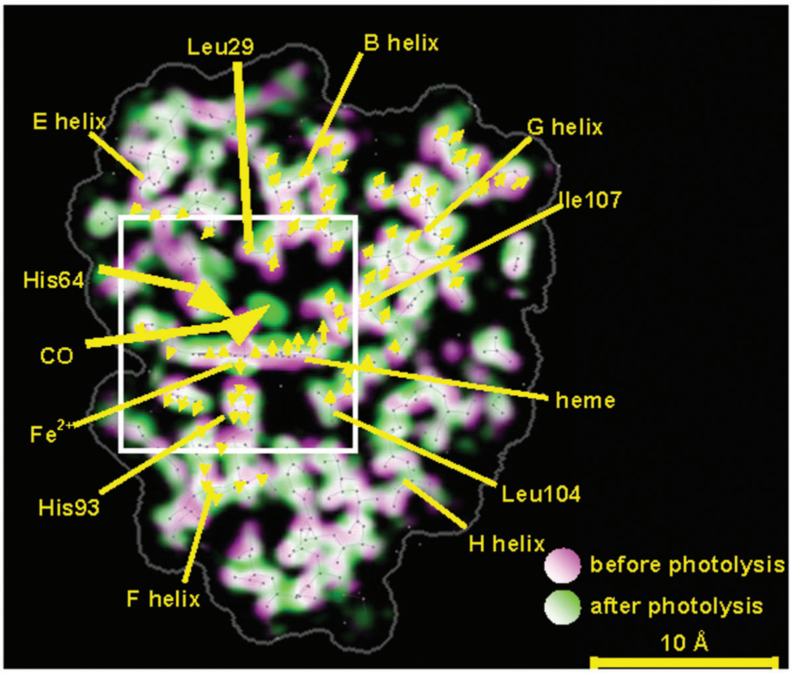

Figure 6.4.53 *Structural changes in wild-type MbCO determined 100 ps after photolysis. Electron density differences in wild-type MbCO presented as a colour-coded superposition of the density ascribed to the ground (magenta) and photolysed (green) states. Where magenta and green overlap, they blend to white. The direction of motion, as indicated by arrows, follows the magenta-to-green colour gradient.*

IV. Solid-phase photochemistry

The solid state is a rich arena of phenomena taking place on sub-picosecond timescales, and the XFEL is particularly suited for their investigation, as a complementary probe to ultrafast visible and IR lasers. In particular, photo-induced phase transitions provide a convenient way to set the zero of the timescale by triggering phenomena with a very short (~fs) laser pulse. The relatively high density of target atoms in solid matter allow the use of various techniques and examples of application of powder diffraction as well as resonant soft x-ray diffraction. These are described here.

Photo-induced effects in the solid state may start as local order-disorder processes (as a consequence of ultrafast structural relaxation pathways), and amplify to cooperative phenomena which can finally trigger structural reorganisation processes in the bulk. This behaviour has been found in the structural response function of pigments and dyes like organic molecular crystals or organic charge-transfer systems (1-D organic mixed stack compounds). They are also the underlying mechanism of other kinds of photo-induced solid state reactions (like photodimerisation and photopolymerisation). Detailed information on the structural evolution can be obtained by applying time-resolved x-ray diffraction both with single-crystal and powder-diffraction techniques. With the short and intense x-ray pulses provided by the XFEL it will be possible to follow intra- and intermolecular structural relaxation processes which are connected to vibrational redistribution processes or to investigate the structure of ultrashort-living intermediates (as excitonic states in organic dyes).

X-ray powder diffraction is a method for x-ray structure determination that has proven versatile and powerful in many applications, albeit having a reduced resolving power and efficiency. Applications from the areas of material sciences and chemistry take advantage of the fact that sample preparation for powder diffraction is much easier. There is no need to grow single crystals of considerable size and crystal quality. Furthermore, powder diffraction enables the investigation of several phases of the material at once using Rietveld refinement methods. With respect to the proposed experiments using FEL radiation, a further important advantage is that powder diffraction allows the collection of the entire structural information simultaneously, that is without the need to rotate or scan parts of the experimental setup. Therefore, single shot experiments become feasible. Figure 6.4.54 shows the radial distribution of a powder diffraction patter of bis-(methylammonium) manganese chloride (MAMC) before and following photoexcitation.

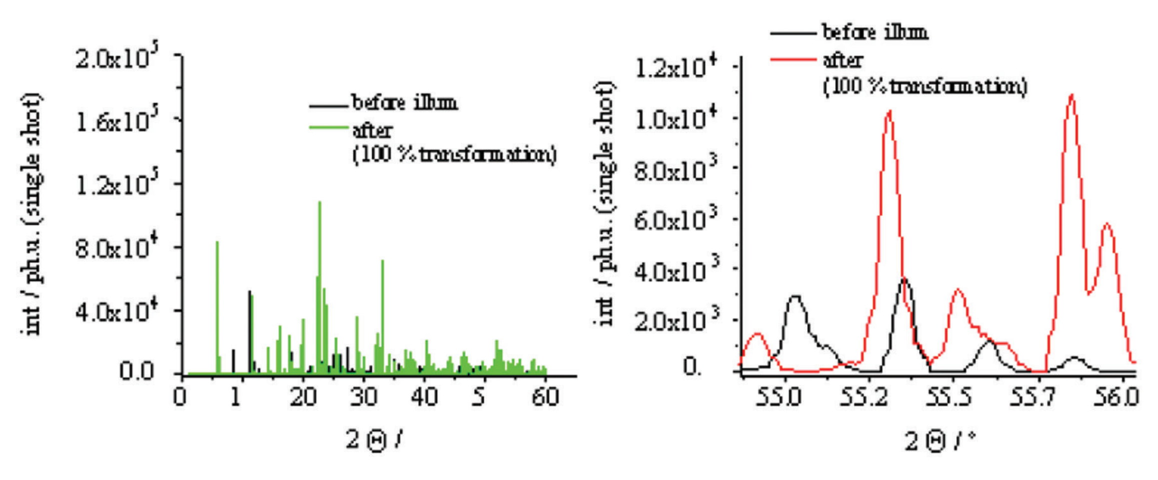

Figure 6.4.54 *Radial distribution function of powder diffraction of MAMC upon photo-excitation (assumed to be 100%) in the case of bulk transformation. The simulation shows the variation of the diffraction pattern before and after the photo excited phase transition.*

Another interesting possibility is the study of diffuse scattering induced by cooperative excitations. Cooperative interactions play a central role in many photoactive solids. The structural relaxation of the excited electronic states is not localised on individual molecules but entails many molecules in a “domino” or “cascading” effect. The first step is usually the formation of nano-domains which is followed by long-range order in 3-D. This gives rise to diffuse scattering that probes the deviation from the average periodic structure of the crystal. These deviations in structure appear on very short time-scales 0.1 to a few picoseconds and the signal amplitude is typically at least five orders of magnitude lower than Bragg reflections. It gives direct information about the nature (1-D - 3-D), the size and the dynamics of self-trapped excitations. The aim of these experiments is to see how these non-linear excitations form and propagate in the crystal.

Figure 6.4.55 shows a simulation of the time-evolution of a photo-induced plane in MAMC upon photo-excitation in the UV absorbing subunit of the molecule. The simulated angular intensity distribution of the diffusive scatter signal spans an angular range of

0.08 rad over which was integrated the angular intensity distribution. Applying classical simulations, the angular frequency of the photoexcited motion was calculated to be $2\pi\nu = 3.24\times10^{12}$ s^{-1} with a damping factor to about $\gamma = 3\times10^{11}$ s^{-1}. The displacement factor for this motion was determined to be about $\underline{u} = 10^{-4}$ nm in a potential which was calculated by density functional theory with a B3Lyp functional.

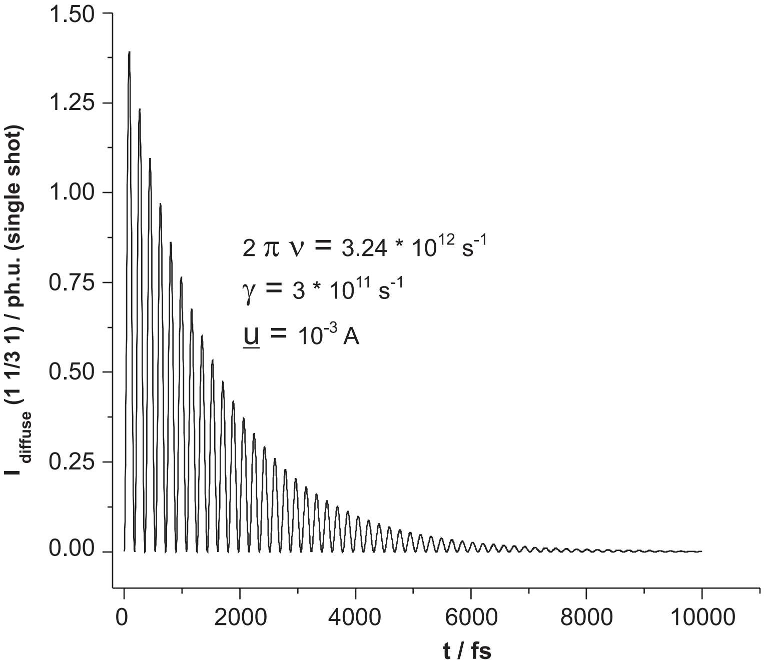

Figure 6.4.55 *Proposed time-evolution of a photo-induced plane [1 1/3 1] in MAMC upon photo-excitation in the UV absorbing sub-unit of the molecule.*

V. Photo-induced transitions in solid-state materials

Photo-induced phase transformations are a new way to manipulate matter by light, with the possibility of ultra-fast switching between two macroscopic states. In some unconventional photo-active materials, the structural distortions are not localised on one molecule, but involve a number of them that aggregate into nano-domains in 0.1- 1 ps. If a sufficient number of nanodomains is created by the laser, the crystal switches to a new phase in 1 100 ps. These cooperative phenomena take place in highly-correlated materials such as charge-transfer complexes (neutral to ionic transition), mixed-valence chains and oxides.

Charge-transfer materials

Recent investigation of the photo-induced neutral to ionic transformation in the charge transfer compound TTF-CA illustrate how the changes in the diffraction pattern indicate a macroscopic 3-D structural self-organisation on the 100 ps timescale **[6-306]**. Present results indicate that photo-induced disordering processes can occur at the sub picosecond timescale. Molecular crystals where the phase transitions are driven by coherent molecular motion are likely to be of great interest in the future. Such coherent phonons where investigated in Bismuth by 100 fs X- ray diffraction **[6-307]**. In the simple Bismuth structure, the intensity of one or two Bragg reflections makes it possible to observe the atomic reorganisation with laser driven plasma sources. However, for more complex materials such as molecular crystals where coherent oscillations are also observed **[6-308]**, the structure analysis will require a large number of Bragg reflections to be measured in real time, which is currently not possible. Ideally, it would be possible to observe the change in electronic structure before atomic reorganisation occurs (sub-picosecond), and then watch the evolving structural relaxation on longer timescales. This will make it possible to observe adiabatic compared to non-adiabatic processes, thus shedding light on the subtle coupling between electronic and structural degrees of freedom.

Diffuse scattering from the compound TTF-CA has been observed experimentally and is concentrated in planes resulting from the one-dimensional periodic nature of fluctuations **[6-308]**. The shape and intensity of the diffuse scattering signal depends on the correlation between molecules and there interaction range **[6-309]**: when the 1-D structure is formed, diffuse planes appear; with 3-D coupling setting in, this signal condenses onto the Bragg reflections and disappears. The time resolved change in shape and intensity will, thereby, provide information on the mechanism driving the transformation from localised excitation to the macroscopic domain.

Charge-orbital ordering

The phenomenon of charge/orbital-ordering in strongly correlated electron systems consists of the “crystallisation” of valence charges and/or sometimes orbital alignments **[6-310]**. Strong electron-electron repulsion gives rise to angstrom-scale charge super-lattices, which are not necessarily commensurate with the atomic lattice. Such CO/OO states are often observed in insulating phases of strongly correlated electron systems, which are sometimes in subtle competition with “hidden” metallic or superconducting states. Systems of particular interest include CMR manganites, High-Tc Cuprates, Nickelates and Cobaltates.

Charge ordering phenomena have been studied statically with a variety of scattering techniques, ranging from neutron to electron diffraction and, most recently, with resonant x-ray scattering **[6-311]**. Particularly interesting and controversial is the relationship that such electronic super-structure formation has with the atomic-structural degree of freedom (CDW formation, Jahn-Teller distortions and the like), and the extent to which atomic arrangements dictate the stability of charge-ordered insulators.

Resonant x-ray scattering to study CO states has been statistically shown to be most effective at the L-edges of the transition metal **[6-312]**, where: (1) the scattering cross section is enhanced; (2) important sensitivity to magnetically dichroic effects is observed; and (3) the final state of the x-ray transition coincides with the same 3d states of the transition metal that participate to the orbital ordering **[6-313]**. Yet, these static techniques become less insightful in the vicinity of critical points, where the rapid fluctuations that dominate the physics are averaged out, appearing only in weak inelastic reflections. The study of these phenomena in the time domain overcomes these problems, clarifying the nature of dynamic couplings between various degrees of freedom of the system.

To the extent that such ordered phases are sensitive to chemical doping, they are also susceptible to photo-doping and are found to undergo photo-induced phase transitions **[6-314, 6-315]**. The case of VO$_2$, a spin Peierls compound with a prominent insulator-metal transition, was recently studied. Ultrafast experiments combined mid-IR excitation and probing with femtosecond soft x-ray absorption **[6-316]** and femtosecond x-ray diffraction **[6-308]**. Most importantly for the type of experiments proposed here, it was shown how the analysis of the fundamental timescale for a photo-induced phase transition can help in establishing a hierarchy of events between electronic and structural degrees of freedom in a correlated electron system **[6-317]**.

To study these effects we propose optical pump, soft x-ray probe measurements of charge-ordering disordering dynamics (compare Figure 6.4.56). Improved sensitivity to the very weak signal from the valence charges can be obtained by measuring resonantly at the transition metal L-edges (0.5 – 0.9 keV), or at the Oxygen K-edge at 0.54 keV to study the rearrangement of Oxygen-containing molecules in the lattice. The proposal is to study two types of photo-induced excitation shown in Figure 6.4.56. First, impulsive excitation of electron-hole pairs across the bandgap using near-infrared light is an ultrafast analogue to the process of chemical doping. A second class of experiments is the coherent excitation of metal-Oxygen optic phonons with mid-infrared light. Experiments would actually cover a variety of techniques, like time-resolved diffraction, XAS or XPCS.

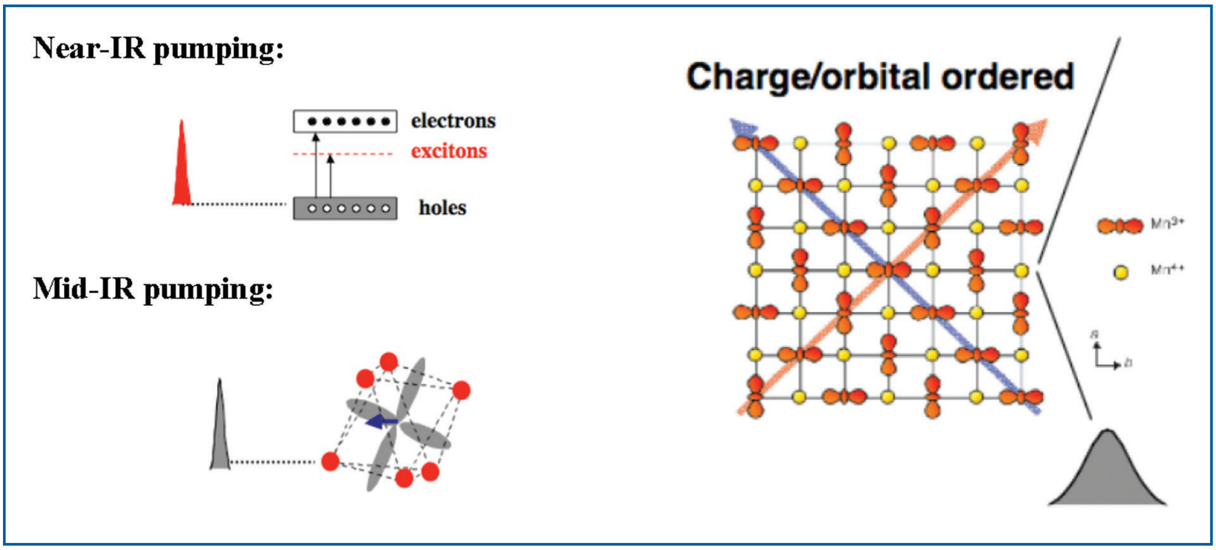

__Figure 6.4.56__ Pumping (left) and probing (right) charge/orbital ordered crystals using time-resolved techniques and resonant x-ray energies.

VI. Investigation of the solid-liquid phase transition and nanoscale materials

The transition from the crystalline to the liquid state, from order to disorder, has attracted great attention over the past 100 years, and has recently served as a testing ground for the development of ultrafast x-ray-based techniques. Much theoretical work has focused on the timescales and mechanisms by which this transition occurs. In some cases, one may view the melting process as an example of a chemical reaction occurring on a macroscopic length scale, in which light-induced changes in the potential energy surface of the solid lead to rapid atomic-scale movement. Many questions remain: What is the structure of the non-equilibrium liquid state? How does it evolve towards that of the equilibrium liquid (of higher density)? And how does the eventual recrystallisation process occur? These are important questions with respect to semiconductor processing and micro-machining. Ultrafast x-ray pulses produced by the XFEL would allow one to capture snapshots of the disordered liquid state and how it evolves. Measurements to date have focused on a limited number of high-Z materials. The European XFEL enables experiments in low-Z materials, for example, probing femtosecond dynamics in liquid Carbon, of important astrophysical interest, or the dynamics of the ice to liquid water transition following infrared vibrational excitation of the solid.

Recent measurements at the SPPS have probed optically induced liquid state dynamics in the semiconductor InSb **[6-300]**. Measurements have captured the first steps in the solid to liquid transition, during the first few hundred femtoseconds after excitation. Figure 6.4.57 shows two single-shot images of the x-ray diffracted intensity, conducted in a cross-beam geometry so that a range of times around t=0 are measured in a single shot. Time runs from left to right according to the temporal axis shown. In the top image, the x-rays probe the static material. In the lower image, a femtosecond laser pulse drives the transition from solid to liquid and one observes a rapid change in the diffracted x-ray intensity.

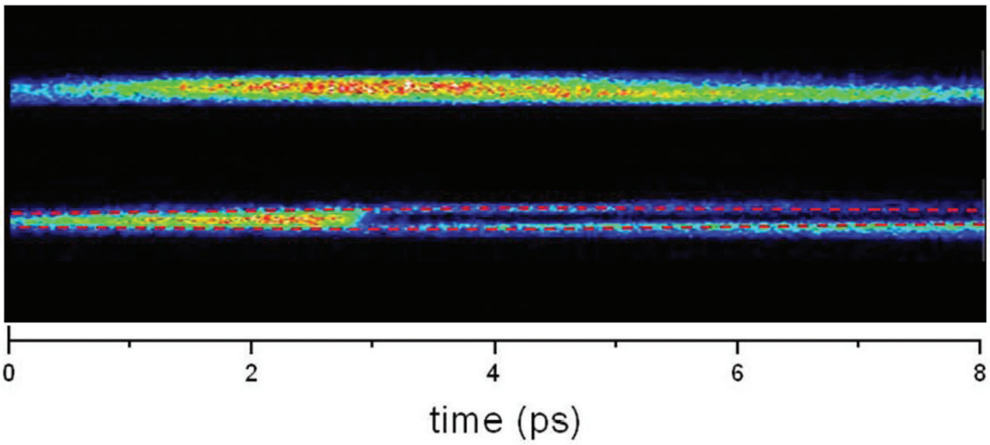

Figure 6.4.57 *X-ray diffraction images from InSb surface taken at SPPS. The timescale is determined by the cross-beam geometry of visible laser and x-rays. The top image is taken without a laser and the bottom shows the strong decrease in reflectivity at ~2.3 ps due to non-thermal melting following laser excitation.*

The melting dynamics and structural transformations discussed here are important to understand the functioning of nanoscale materials like semiconductor nanocrystals, known to exhibit important size-dependent properties of great technological interest. There is a natural interest in the structural dynamics of nanomaterials connected with applications in photoexcitation phenomena. Pulsed excitation is used in photonic materials to take advantage of ultrafast relaxations. On the other hand the understanding of static structure and interactions can also profit enormously from experiments, where the equilibrium structure is driven out of equilibrium, allowing to determine the dynamics and intermediate steps of structural and energetic relaxations. It has been observed that the ultrafast timescale for a phase transition in nanoparticles induces new channels of structure formation, such as a non-thermal ablation and strong near-field effects in plasmonic materials **[6-318]**. However, the investigation of structural dynamics of nanoscale materials is severely limited at present. XFEL radiation can provide the high excitation levels and the spatial and temporal resolution to investigate structural dynamics, in particular during primary steps of structure formation, at a much better accuracy than presently achieved.

Femtosecond diffraction techniques

Time-resolved x-ray diffraction experiments in the ultrafast timescale are performed in the pump-probe modus where a **reaction** is initiated by a pump pulse and the temporal evolution of this reaction is probed using an x-ray probe pulse. The timescale is established by the delay between pump and probe pulses and the use of (hard) x-rays allows the investigation of structural evolution (at atomic resolution). With the notable exception of the experiments on single particles or molecules, discussed in Section 6.4.7, given the weak scattering of x-rays from atoms, it is generally mandatory to work with ensembles of sample entities in order to enhance the signal and shorten the exposure time. The ultrafast initiation of a bulk sample will normally be done using femtosecond visible laser pulses, but one should keep in mind that the intensity levels achieved by XFEL radiation might allow triggering electronic reactions directly with x-rays. The laser pulse excites a subset of molecules in the sample, typically 1 in 1,000, and the diffraction from a delayed x-ray pulse probes the spatial evolution at that delay. If the reaction is reversible, the experiment can be repeated after a suitable delay, the delay depending on the reaction time and the time needed to cool the sample. In irreversible reactions, specific data acquisition methods have to be applied or the sample has to be exchanged between shots. By collecting structural information at many time delays, for example from 100 fs to 1 ms in nanosecond-steps, this sequence of spatial snapshots can be stitched together to make a movie of the structural processes following photoexcitation.

In ultrafast time-resolved experiments, the time resolution is usually determined by the convolution of the x-ray and visible laser pulse durations and their relative jitter. For the 100 fs XFEL pulses, 30 fs visible laser pulses, which are readily available commercially, and zero timing jitter, one obtains 104 fs as the time resolution, thereby insignificantly broadening the XFEL pulse duration. However, in this regime more subtle effects contribute to broadening of the time resolution. One contribution is the speed of optical light in condensed matter lower than the speed of x-rays. Considering a diffraction experiment in water with the x-rays transmitted through a thin sheet of water perpendicular to the beam. The speed of light is reduced from 3.0×10^8 m/s in air (vacuum) to 2.25×10^8 m/s in water ($n = 1.33$). Due to the different velocities the time resolution will, in general, reduce with increasing sample thickness. Let's consider a collinear beam experiment with 100 fs x-ray pulses and 30 fs laser pulses. Initially, the laser pulse is placed at the midpoint of the rising edge of the x-ray pulse. The nominal time delay is the time difference between the centres of the pulses, +50 fs. In the sample, the x-ray pulse will first catch up and finally overtake the laser pulse. After 400 fs, the visible laser pulse will be at the trailing edge of the x-ray pulse which means that the x-ray pulse is now 50 fs **ahead** of the laser pulse and no longer probing the excited state. 400 fs corresponds to a sample thickness of 120 µm. Time-resolved diffraction experiments in transmission, which is normally used with area detectors, aiming for a time resolution of the order of 100 fs will, therefore, require thin samples of ~ 25 µm. These thin samples limit the observable count rates.

Gas phase diffraction

A conventional pump and probe scheme can be used where a femtosecond laser pulse initiates the reaction and a femtosecond XFEL pulse probes the structural dynamics (see Figure 6.4.58). The diffraction pattern is recorded using a 2-D area detector. The laser and x-ray beam have to be co-linear to minimise the spatial and temporal mismatch between the pump and the probe. The gas vapour can be supplied through a nozzle connected to a heated sample reservoir **[6-287]**. Typically, the pressure just outside the nozzle is about 5 torr when the backing pressure is about 100 torr. In this condition, the ambient pressure inside the vacuum chamber can be as high as 10^{-3} torr. To maintain a good vacuum in adjacent chambers, differential pumping should be employed. For electron diffraction, the carrier gas that is normally used in time-resolved spectroscopic experiments cannot be used any more because the carrier gas also contributes to the diffraction, thereby increasing the background and hence, degrading the signal to noise. However, for x-ray diffraction, a low Z carrier gas such as Helium might be used because of its relative low scattering power against atoms with higher Z. Clusters of atoms or molecules can be obtained by using special nozzles and a sufficiently high backing pressure.

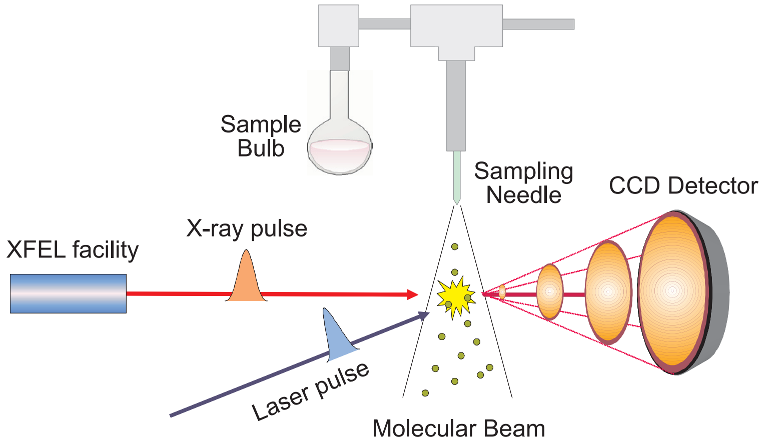

Figure 6.4.58 *Schematics of a gas phase diffraction experiment.*

Liquid scattering

The experimental setup used for picosecond liquid-phase x-ray diffraction used at present-day x-ray sources should be transferable to femtosecond x-ray diffraction with the XFEL. The pump-probe scheme is shown in Figure 6.4.59. The velocity mismatch between the pump laser and probe x-rays discussed above can be minimised by using a non-collinear geometry for x-rays and laser and restricting the probed sample volume. Concerning the sample cell system, two different setups have been used: a capillary-based system and an open-jet one. In the first system, the solution is circulated through a quartz capillary (0.3 mm diameter) to provide a stable flow. In the open-jet system, the capillary is removed and a stable jet is produced by a high-pressure slit nozzle (slit, 0.3 mm, Kyburz) at a speed ensuring the refreshment of probe volume for every laser pulse. The open jet system has the advantage over the capillary system that the scattering from the capillary materials is absent, which reduces the background substantially and increases the signal to noise ratio. The lower background also increases the accuracy of the normalisation process. If the whole setting can be housed in a Helium chamber or a vacuum chamber, the background from the air can be greatly reduced.

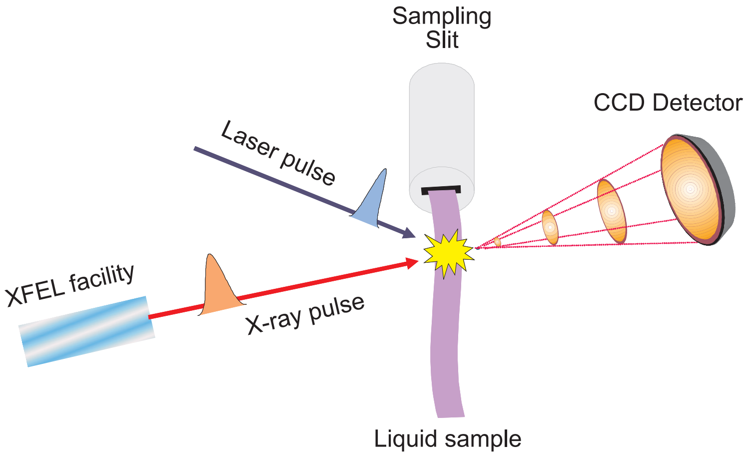

Figure 6.4.59 *Schematics of a liquid phase diffraction experiment.*

What is the prospect of filming chemical reactions in solution using single pulses of x-rays? What signal to noise ratio can one expect from having 10^{12} photons in one pulse? These questions are important as the technique requires high-quality images for time stamping where every image is recorded together with the actual laser/x-ray delay. In the following, the signal from a newly formed Iodine molecule surrounded by liquid CCl_4 will be calculated, taken 1 ps after recombination. Experience with liquid diffraction experiments on beamline ID09 at the ESRF enables calculations of the intensity distribution S(Q, t) for chemical reactions in liquids. The excess energy between the Frank-Condon state and the dissociation limit is 0.83 eV and this energy is transferred to the solvent in less than 1 ps. When the molecule is reformed at the dissociation energy 1.55 eV, the molecule is highly excited and oscillates between 0.23 and 0.4 nm. It is assumed that the excess energy decays exponentially with a 10 ps time constant. We can then determine the size of the molecule at its inner and outer turning points as a function of time. The turning points dominate the ensemble average and the molecular form factor can be approximated by the sum of these extreme states. The 0.1 mm^3 liquid CCl_4 contains 1.0×10^{16} molecules and we assume a ratio I_2* to CCl_4 molecules of 1: 1,000 after laser dissociation. The photon flux of the x-ray pulse is 10^{12} phts/pulse and the energy is 12.4 keV. The diffracted signal is recorded using an area detector. The ratio of scattered to incoming photons is 2.65×10^{-5} over the q-range 0-10 Å^{-1}. The calculated structure-factor difference (excited minus non-excited solution) is shown in Figure 6.4.60(a.) and (b.) for 1 ps and 25 ps, respectively. One observes that Iodine dominates the early signal while the solvent dominates the late signal. This effect comes from energy conservation in the x-ray volume on short timescales: when the Iodine signal decreases in the recombination process, the solvent becomes thermally excited. On the ultrafast timescale, this temperature rise takes place at constant volume (and density). For the liquid peak the detected signal shows photon flux of 12,000 photons/pixel/pulse (64×64 µm^2 pixel area). The distribution has axial symmetry and needs to be ring-integrated in order to obtain sufficient sensitivity for the difference signal. Figure 6.4.60(c.) shows the Iodine and solvent signals after integration. The situation changes when the axial symmetry of the image is used to ring-integrate the intensity. The counting noise from the solvent background is about sqrt (5×10^6) = 2,236, so for a signal level of ~ 4,000, the S/N ratio is ~2. The conclusion is that every single image can be recorded separately with a time stamp, at the frequency of the macro-bunch train, i.e. 10 Hz. The images can then be sorted in time bins and averaged to improve the S/N ratio. Finally, the simulation shows that the diffracted intensity is proportional to the flux density (ph/m^2/pulse) times the number of x-ray illuminated molecules in the sample. For a thin sheet of liquid, the scattered intensity is, thus, independent of the focal spot dimension. Given the extreme power density in the XFEL beam, it may be advantageous in some cases to work with the unfocused beam of 0.8-1 mm diameter.

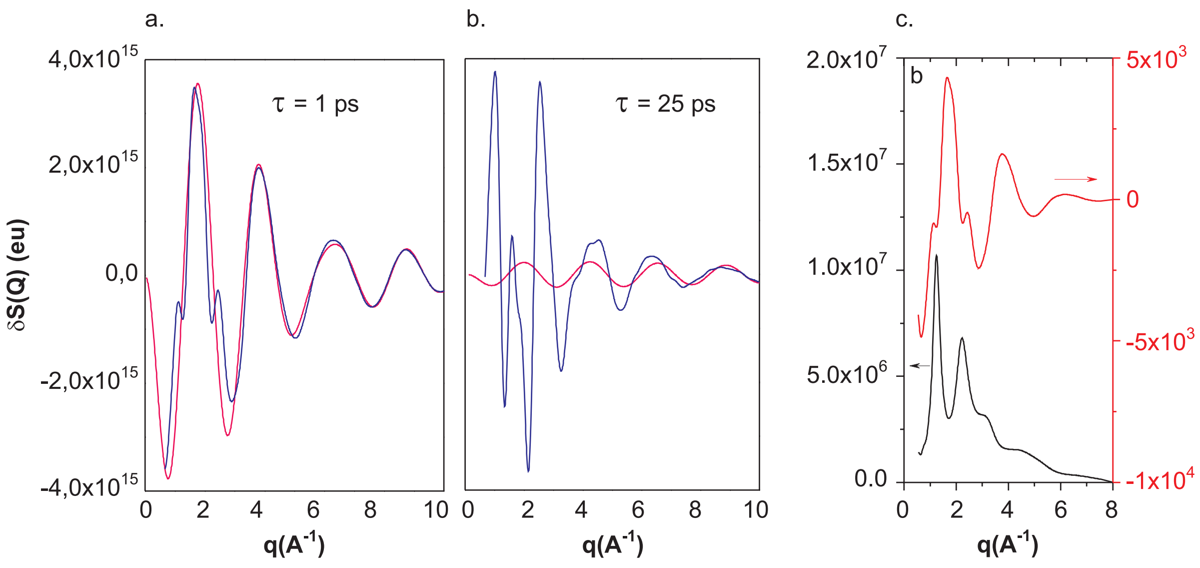

Figure 6.4.60 *Simulated difference oscillations from the recombination of I_2 for 1 ps (a.) and 25 ps (b.) time delay. The blue curves show the total signal, solute and solvent, the red curves show only Iodine. In (c.) the corresponding detector partial count rates for solution (black) and Iodine (red) for 1 ps delay after radial integration are given.*

Laue diffraction techniques

Hard x-ray pulses generated by an XFEL are expected to be about 1,000 times shorter and contain 100 times more photons than those generated by synchrotrons. Such pulse characteristics would provide an unprecedented opportunity to investigate protein function on the chemical timescale at near-atomic resolution. However, to effectively exploit x-ray pulses from an XFEL, there are numerous issues that require careful consideration.

X-ray heating: A single XFEL pulse delivered to a protein crystal would deposit sufficient energy to increase the temperature of the probed volume by about 10°C, if focused to a spot of 100 µm diameter. Since the energy is deposited in only 100 fs, a time far faster than that required for the crystal lattice to respond, the diffraction image would be minimally influenced by this T jump. On the other hand, how a crystal responds to this localised stress at longer times is not yet known. In any event, the cool-down period between successive x-ray pulses would have to be sufficient to dissipate this excess energy, and would probably restrict Laue experiments to repetition frequencies no higher than 3.3 Hz. The fact that the XFEL repetition frequency is limited to 10 Hz would not be a liability for Laue crystallography.

Shot-by-shot x-ray pulse characterisation: To take full advantage of ultrashort x-ray pulses, it is crucial that the laser be tightly synchronised with the XFEL pulse. The most advanced electronic phase-locked-loop cannot maintain synchronisation any better than a few hundred femtoseconds. Consequently, it is crucial to develop the ability to make single-shot measurements of the time difference so each diffraction image can be assigned an appropriate time stamp. That time stamp should be determined with sub-100 fs precision. Shot-to-shot intensity fluctuations of the primary beam can be tolerated, provided each diffraction pattern contains enough Bragg reflections to calculate a global scale factor. The number of reflections obtained with spontaneous undulator radiation is more than sufficient, but for XFEL radiation, the number of observed reflections will depend on sample mosaicity. Moreover, when using the SASE beam to record diffraction images, it will be crucial that the SASE spectrum either be reproducible on a shot-by-shot basis, or be measured on a shot-by-shot basis. (Changes in the spectral distribution lead to intensity changes of individual Bragg reflections that cannot be distinguished from structurally-induced changes.)

X-ray photon energy: The optimal x-ray energy for Laue crystallography would maximise the structural information achieved with the minimum amount of beam time. When the crystal lifetime is determined by x-ray radiation damage, the figure of merit is the number of photons detected, divided by the dose to the crystal. If laser radiation damage limits the crystal lifetime, the figure of merit is the number of photons detected, divided by the number of laser pulses required to collect the data. Using synchrotron radiation, it is the x-ray dose that limits the crystal lifetime, so the optimal x-ray energy is about 15 keV. When photolysing the protein crystal with 100 fs laser pulses, it is likely that the laser pulse will be more damaging to the crystal, so the optimal x-ray energy would be lower, where the diffraction efficiency is higher. Operating the XFEL at 12.4 keV is likely near the optimum for femtosecond time-resolved Laue crystallography.

Time-resolution limitations due to pump-probe geometry: Myoglobin crystals investigated at ESRF are optically very dense, and when photolysed near the peak of the Q-band absorption, the laser penetration depth is less than 100 microns. To address the severe mismatch between the x-ray and laser penetration depths, an orthogonal pump-probe geometry (see Figure 6.4.61) is adopted, in which the laser beam is focused from above and the x-ray beam probes the laser-illuminated edge of the crystal. This geometry requires precise positioning of the crystal surface at the intersection of the laser and x-ray pulses.

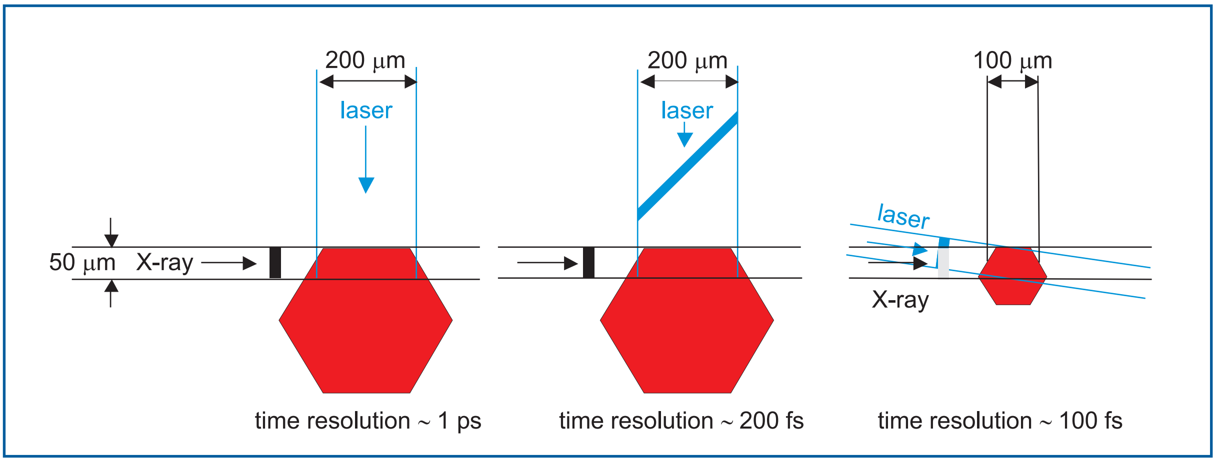

Figure 6.4.61 *Geometry considerations for the time resolution in different pump-probe geometries for a typically sized hexagonal myoglobin crystal. Orthogonal laser excitation significantly limits the time resolution, unless the wavefront of the laser beam is tilted by 45°. The best time resolution is obtained by collinear excitation limited by sample thickness due to velocity mismatch.*

The orthogonal pump-probe geometry optimises the spatial overlap between the pump and probe pulses, not their temporal overlap. For example, a 200 μm x-ray path length through a crystal photolysed from above would smear out the time resolution by nearly 700 fs. To mitigate this problem, it is possible to use dispersive or diffractive optics to incline the wave front of the laser beam so that the photons arrive at the surface of the crystal at the appropriate time. With this configuration, one still suffers smearing of the time resolution because the laser penetrates the crystal in a transverse dimension to the x-ray beam. If the vertical size of the x-ray beam was set to 50 μm using slits positioned near the sample, the time resolution could be improved to better than 200 fs. With these modifications, the orthogonal geometry can be employed with minimal sacrifice to the experimental time resolution.

Spontaneous compared to XFEL radiation: The spontaneous radiation provided at the European XFEL would be comparable in photon number to that achieved on ID09B at the ESRF. A bandwidth of ~1% is achieveable (see Section 5.3.) and if the electron bunch were in addition energy chirped, this bandwidth might even be broadened. With such a source, a complete set of data would require about 31 angular settings over a range of 60°. Because the spontaneous radiation is much more divergent than XFEL radiation, focusing optics would probably be needed to deliver the x-ray beam to the sample.

Using the monochromatic XFEL beam would require approximately 200 angular settings over a range of 60° (assuming 0.08% bandwidth and no mosaicity). The actual number of images required with XFEL radiation would depend on the degree of crystal mosaicity, with lower mosaicity requiring more images. With XFEL radiation, the dynamic range of the detector would have to be much higher than is currently available. Compared to synchrotron radiation, the XFEL radiation bandwidth is 30 times narrower and its photon flux is 100 times greater. Consequently, the brightness of the diffraction spots would be 3,000 times greater, and many spots would probably saturate the detector. If the XFEL beam had to be attenuated to avoid saturation, the data collection efficiency in this mode would be compromised.

The spontaneous radiation approach to Laue data collection would be relatively straightforward. However, the XFEL radiation approach, if done well, has the potential to provide higher quality diffraction data. At this stage, we would prefer to develop both methodologies, and assess experimentally which approach achieves the best results.

Detector characteristics: To maximise the signal-to-noise ratio of the diffraction images, it would be desirable to have a large area detector that can be read with 16-bit resolution at the pump-probe repetition frequency. Larger is better because the intensity of diffuse scattering decreases as the square of the distance, but the intensity of the diffraction spot remains essentially constant (provided the spot dimensions are determined by the point-spread function of the detector, not the mosaic spread of the crystal).

6.4.6.2 Instrument requirements

The experiments described above lead to requirements for an instrument for scientific applications using Femtosecond Diffraction Experiments (FDE). They concern the performance of the light source, the optical elements and the diagnostic equipment, the sample environment, and the detectors. The scientific cases presented request beamlines suitable for diffraction experiments at hard x-rays using 12.4 keV photon energy. Either intense XFEL radiation or spontaneously emitted synchrotron radiation is employed in these experiments and the incident bandwidth should be adapted to the sample system under investigation. Since the experiments do not require photon energy variation, the corresponding instruments should be located at the SASE 1 beamline for XFEL radiation and at the U 1 beamline for spontaneous radiation. A particular experiment (case V. in Section 6.4.6.1) has expressed an interest in using soft x-ray radiation for resonant experiments at the transition metal L-edges. This experiment requires use of the SASE 3 beamline and a reduced incident bandwidth of $\Delta E/E \sim 10^{-4}$. We propose that the XAS 1 instrument, described in Section 6.4.5.3, should provide the additional capability to carry out such studies. Due to the small signal changes to be observed the instruments require very good stabilisation and/or the tools to measure fluctuation of x-ray and visible laser parameters.

Spectral radiation properties

The gas phase and liquid experiments (Cases I. and II., Section 6.4.6.1) can perfectly accept the natural bandwidth of the XFEL or spontaneous radiation. Due to the small observable signal changes accuracy in the order of 10^{-4} is needed in mean energy or envelope of the energy distribution. Pulse-by-pulse measurement and single pulse data storage will ease this requirement slightly. However, high stabilisation is required for experiments on extremely dilute samples where the integration of scattering patterns is needed (e.g. gas phase molecules).

Laue diffraction experiments (Case III., Section 6.4.6.1) request photon energies around 12 keV and a bandwidth of 3% as ideal parameters. The large bandwidth can be achieved only by electron beam manipulation techniques like energy chirping, thus affecting other beamlines. Instead one could use more angular settings to cover the full reciprocal space. The energy distribution of the unmonochromatised XFEL radiation needs to be monitored for single pulses since changes in the spectral distribution lead to intensity changes of individual Bragg reflections that cannot be distinguished from structurally-induced changes.

For single-crystal and crystalline material investigations (Cases IV.-VI., Section 6.4.6.1) typically, a reduced bandwidth of 10^{-4} is requested. The reduced bandwidth raises the resolution of the measurement and reduces energy dissipation in the samples. The larger natural bandwidth has the advantage, however, that photo-induced variations of the lattice parameter can be observed over a larger range. Its use, therefore, should be enabled by the instrument design.

X-ray optics requirements

No specific requests have been made in this domain. A beam size of 30-100 microns is required in many of the crystalline samples in order to match the sample size or the volume with visible laser penetration. In the case of fluids one may envisage the use of the full unfocused beam. However, large x-ray beam areas require large visible laser spots and significantly raise the requirements of the visible laser beam with respect to homogeneity and parallelism.

For x-ray pump-x-ray probe experiments, a beam-split-and-delay optics is requested. This optical element should allow the XFEL beam to be split into equal parts, e.g. for auto-correlation measurements, and also with a high ratio of ~9:1, e.g. for pump-probe experiments. A path length difference between the two split pulses of between 100 fs and a few 100 ps is required.

Time domain requirements

These experiments probe dynamics on the ultrafast timescale using pump-probe techniques. Pumping is usually achieved using an ultrafast visible laser. The synchronisation should be significantly better than the anticipated time resolution of ~100 fs. For the same reason the fluctuation of the pulse duration must be small compared to the 100 fs timescale. It is anticipated that a variety of pulse patterns from single pulses at less than 10 Hz repetition rate (Case III., Section 6.4.6.1) up to several hundreds of x-ray pulses per electron bunch train will be used. The 600 µs long pulse train offers, in principle, the opportunity to follow the structural evolution of the sample time-resolved over a relatively long period with a resolution of 200 ns. Such experiments may require logarithmic distribution of pulses and rely on samples not sensitive to x-ray damage.

Photon diagnostics requirements

The short- and long-term stability of the x-rays is of extreme importance for the quality of the experiments. The position stability of the emitted x-rays and even their spatial distribution should be monitored. Furthermore, all experiments will need diagnostic equipment to measure the photon flux on a pulse-to-pulse basis. In cases where monochromators are used, the measurement of the mean photon energy is not required and spectral diagnostics should provide the content of higher harmonic radiation only. In many cases the samples are optically thin for x-rays and the transmitted radiation can be used for diagnostic purposes. All measurements must be available on a pulse-to-pulse basis.

Sample manipulation and environment

For gas phase and liquid scattering the sample is refreshed at the repetition rate of the x-ray pulses and no particular difficulties are expected. For crystalline samples, techniques for refreshing the probed sample volume at the repetition rate of the x-ray pulses have to be foreseen. When limiting the repetition rate for pump-probe experiments this is most easily achieved by using sample movement. Another possibility is to steer x-ray and visible laser beams together over the sample (see Section 6.4.5.1). The latter method needs a development programme to provide the required overlap and accuracy.

As a sample environment vacuum, air or Helium can be used. Vacuum chambers, connected via differential pumping will be required for the gas phase measurements. They should be able to reach 10^{-4} mbar. Open liquid jets operated in a vacuum or under a Helium atmosphere allow significant reduction of background with respect to an air environment. For solids investigation, a four-axes diffractometer with the possibility to mount samples in air, under Helium pressure, or in vacuum is required. The load capacity of the diffractometer must accept mounting of pressure- or cryosystems.

Detector requirements

The detector requirements for diffraction from disordered matter, e.g. gases or liquids and crystals, differs largely, leading to two different sets of parameters discussed in Section 6.5.4.1. Crucially important is the possibility of detecting a large number of x-ray photons per pixels and maintaining at the same time, the possibility of detecting very few photons. Simulations done for liquids indicate that 10^4 photons can easily hit one detector element using present-day geometries and commercially available pixel sizes. For crystalline samples, even higher photon numbers need to be expected. For crystals, the possibility of studying diffuse scattering at the same time leads to the request for a very large dynamic range. Significant scattering can be observed at larger Q, respectively at large angles. Therefore, the detector systems should allow coverage of an angular range up to 60°.

Visible laser requirements

Visible lasers will be applied in pump-probe experiments. A wavelength tunable system providing pulse durations in the order of 30 fs and pulse energy up to 1 mJ at 800 nm, will allow the experiments proposed in this area to be carried out. Using OPA schemes a wavelength range of ~200 to 1500 nm should be available at the instrument. Synchronisation to the x-ray beam of the order of the pulse duration or pulse-to-pulse measurements of the jitter is requested.

6.4.3.2 Realisation of the instrument

From their requirements, the FDE experiments ask for two instruments at SASE 1 (FDE 1 – Hard XFEL radiation) and at U 1 (FDE 2 – Hard x-ray spontaneous radiation). For a description of the SASE 1 and U 1 beamlines, see Sections 6.2.4.1 and 6.2.4.4, respectively. Experiments discussed in Section 6.4.6.1 under Topics I.-VI. will be carried out at these instruments. Most of the requirements and proposed implementations are identical for the two instruments. The major difference is the enhanced flux for the FDE 1 instrument by a factor of 10^3. For XFEL radiation, monochromatisation by use of crystal monochromators will be applied in the majority of experiments. However, some experiments will use the maximum available flux and therefore, omit monochromatisation. The SASE 1 beamline with its double-mirror double-crystal setup provides both kinds of radiation to the instruments. For FDE 2 using spontaneous radiation, no monochromatisation will be used since the experiments apply the full bandwidth. In order to collect the large angular cone a collimating optic, probably a refractive lens, needs to be installed as close as possible to the source in U 1.

Both instruments will require moderate focusing of the XFEL radiation to beam sizes in the order of 100 µm, achieved by using a focusing element inside the corresponding beamlines. Whereas, for the FDE 1 instrument a demagnification near unity can be applied, for FDE 2 one needs to take the collimating optics at ~100 m from the source into account.

FDE 1: Hard XFEL radiation

Since, for hard x-rays, no significant offset can be achieved for short distances, a deflecting mirror assembly inside the SASE 1 beamline tunnel, about 100 m upstream of the experimental hall, is used for horizontal deflection. The following elements belong to the FDE 1 instrument inside the experimental hall. They are depicted in the schematic layout of that instrument in Figure 6.4.62 and are described in Table 6.4.14.

The first part of the instrument includes specific optical elements for this instrument, most importantly the beam-splitter-and-delay unit. Next, defining apertures, a photon flux monitor and a differential pumping section come in front of the sample. The vacuum system of the beam transport can be intercepted here by a Beryllium window or can be connected to the sample vacuum chamber. The sample environment includes linear x-y-z movements (1µm repeatability and 0.25 µm resolution) and two angular degrees of freedom (1/1,000° repeatability, 1/4,000° resolution). Vertical scattering geometry is chosen for the diffractometer due to the horizontal polarisation of the radiation. Behind the chamber, a 2-D area detector with variable distance to the sample is mounted. On a circle segment, a 1-D detector is mounted covering a large angular range with high angular resolution and ~10^4 pixels. The forward direction is kept free and photon flux, spectral and time domain diagnostics follow. At the instrument a laser system is available, including the required diagnostics elements and an OPA system for provision of widely tunable visible laser radiation.

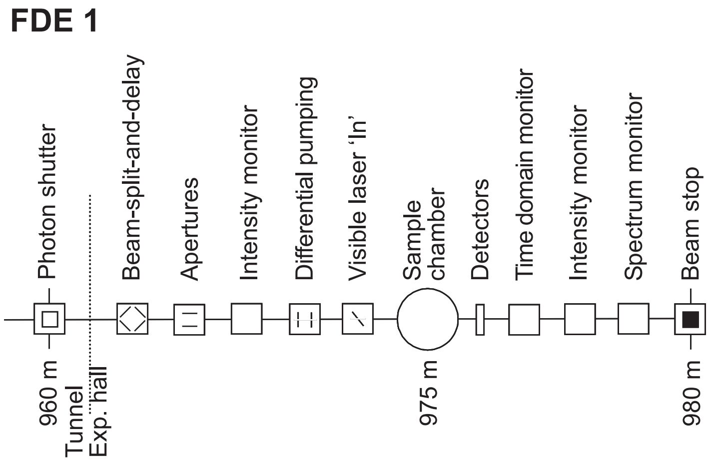

Figure 6.4.62 *Schematic layout of the FDE 1 instrument at the SASE 1 beamline. Distances are given in relation to the end of the undulator.*

Item	Purpose	Specification
Beam-split-and-delay	Splitting into equal or unequal parts, delay 100 fs to 300 ps	High optical accuracy to maintain x-ray duration
Slits/apertures	Beam definition, beam halo cleaning	0.25 µm accuracy, 1 µm repeatability
Intensity monitor	Measurement of incident photon flux	Transmissive (<5% absorption), single pulse measurement, relative accuracy $<10^{-3}$
Differential pumping	Separation of beamline and instrument	
Sample chamber	Sample positioning and orientation	x-y-z move (0.25/1 µm), two rotations (0.25/1 mdeg),
	Vacuum capability for gas phase	10 mbar
Detector	2-D patterns for gases and liquids, 1-D pattern for powders and crystals	2K×2K, 1 MHz,10K, 5 MHz
Intensity monitor	Measurement of transmitted photon flux	Transmissive (<5% absorption), single pulse measurement, relative accuracy $<10^{-3}$
Time domain monitor	Measurements of x-ray arrival-time x-ray with respect to visible laser	
Spectrum monitor	Measurement of distribution	Single pulse measurement, relative accuracy $<10^{-3}$
Alignment unit	Positioning and position verification	Permanently operating, Accuracy ~100 µm
Lead hutch	Radiation protection, temperature stabilisation, laser protection	4×10×3.5 m^3 (W×L×H), ±0.5° thermal stability
Control hutch	Operation of the instrument	Working environment (noise, temperature, light)

Table 6.4.14 *Elements and specifications of the FDE 1 instrument.*

FDE 2: Hard x-ray spontaneous radiation

Since spontaneous radiation is less intense, a multilayer is proposed to deflect the beam horizontally whilst maintaining the large bandwidth at the same time. The multilayer is located about 60 m upstream of the experimental hall. The following elements belong to the FDE 2 instrument inside the experimental hall. They are depicted in the schematic layout of that instrument in Figure 6.4.63 and are described in Table 6.4.15. The instrument includes defining apertures and a photon flux monitor in front of the sample. The vacuum system of the beam transport is ended by a Beryllium window. The sample mounting includes linear x-y-z movements (1µm repeatability and 0.25 µm resolution) and two angular degrees of freedom (1/1,000° repeatability, 1/4,000° resolution). Samples can be investigated in an air or Helium environment. The sample mount supports high loads for measurements in different environments, e.g. cryogenic, high pressure or high temperature. Vertical scattering geometry is chosen for the diffractometer due to the horizontal polarisation of the radiation. Behind the sample mount a CCD 2-D area detector with variable distance to the sample is mounted and a fast 1-D detector on a circle segment to cover the full space angle. The forward direction is kept free and photon flux, spectral and time domain diagnostics follows. At the instrument a laser system is available, including the required diagnostics elements and an OPA system for provision of widely tunable visible laser radiation.

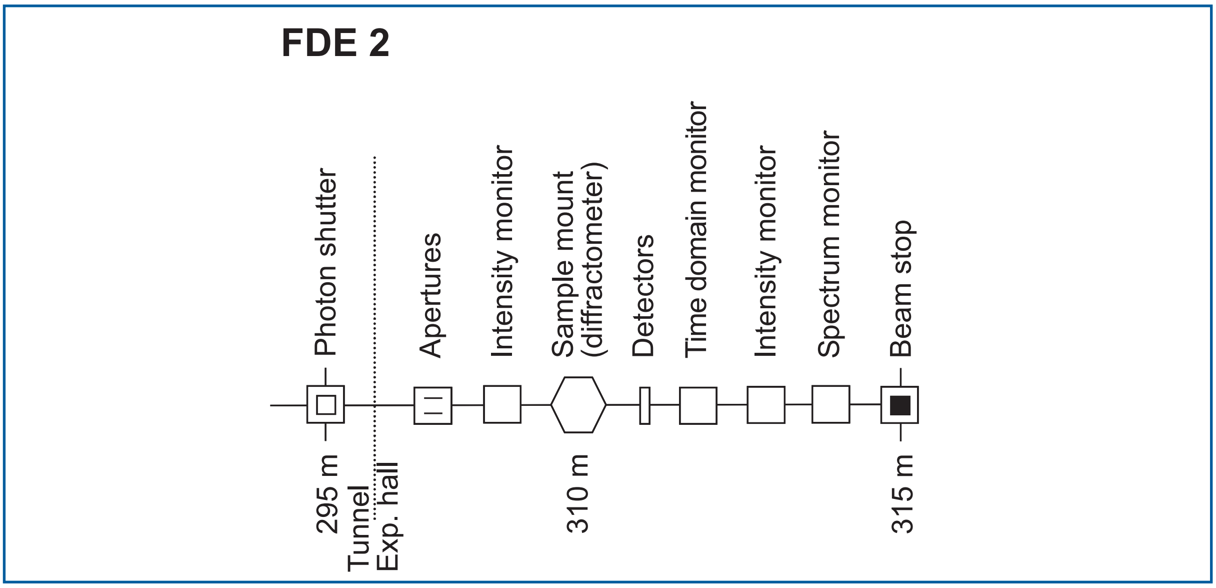

__Figure 6.4.63__ Schematic layout of the FDE 2 instrument at the U 1 beamline. Distances are given with respect to the end of the undulator.

Item	Purpose	Specification
Slits/apertures	Beam definition, beam halo cleaning	0.25 µm accuracy,1 µm repeatability
Intensity monitor	Measurement of incident photon flux	Transmissive (<5% absorption), single pulse measurement, relative accuracy $<10^{-3}$
Differential pumping	Separation of beamline and instrument	
Sample mount	Diffractometer, air or Helium environment	x-y-z move (0.25/1 µm), two rotations (0.25/1 mdeg), 100 kg load
Detector	2-D patterns 1-D pattern for powders and crystals	2K×2K, 10-30Hz, e.g. CCD 10K, 5 MHz
Intensity monitor	Measurement of transmitted photon flux	Transmissive (<5% absorption), single pulse measurement, relative accuracy $<10^{-3}$
Time domain monitor	Measurements of x-ray arrival-time x-ray with respect to visible laser	
Spectrum monitor	Measurement of distribution	Single pulse measurement, relative accuracy $<10^{-3}$
Alignment unit	Positioning and position verification	Permanently operating, accuracy ~100 µm
Lead hutch	Radiation protection, temperature stabilisation, laser protection	$4\times8\times3.5$ m^3 (W×L×H), ±1° thermal stability
Control hutch	Operation of the instrument	Working environment (noise, temperature, light)

Table 6.4.15 *Elements and specifications of the FDE 2 instrument.*

6.4.7 Ultra-fast coherent diffraction imaging of single particles, clusters and biomolecules

6.4.7.1 Scientific case

Summary

Theoretical studies and simulations predict that with a very short and very intense coherent x-ray pulse, a single diffraction pattern may be recorded from a large macromolecule, a virus, or a cell without the need for crystalline periodicity **[6-319 – 6-322]**. Measurement of the oversampled x-ray diffraction pattern permits phase retrieval and hence, structure determination **[6-323 – 6-330]**. Although individual samples will be destroyed by the very intense x-ray pulse, a three-dimensional data set could be assembled when copies of a reproducible sample are exposed to the beam one by one **[6-331]**. The challenges in carrying out such an experiment requires an interdisciplinary approach, drawing upon structural biology, atomic and plasma physics, mathematics, statistics, and XFEL physics. The potential for breakthrough science in this area is great with impact not only in the biological areas but in any other area of science and technology where structural information with very high spatial and temporal resolution is valuable.

Experimental programme

Much of what we know about the detailed structure of biomolecules, including proteins and DNA and RNA, has come through the use of x-ray diffraction. Conventional synchrotron radiation has revolutionised this field in the past two decades, enabling study of larger and more complex systems at increasingly high levels of resolution and on smaller (often micron-sized) samples. The key to this great success has been the use of Bragg diffraction from the multiple copies of molecules that are oriented and aligned in a single crystal. However, there are classes of proteins (as well as many other types of materials) that are difficult or impossible to crystallise, including membrane and many glycoproteins, for which a high resolution means of structure determination would be invaluable.

The development of XFELs promises to open up new areas in the life sciences by allowing diffraction imaging of virtually any macromolecule, protein complex, or virus without the need for crystallisation. The same technique can also be applied to study the structure of other nano-sized particles, for example, clusters. This technique, at present only simulated on a computer, represents a formidable scientific and technical challenge.

Before guiding the reader into a more detailed description of the experimental programme, we need to survey boundary conditions and the available parameter space within which these new developments are expected to take place.

Background for ultra-fast imaging

The scientific case for the ultra-fast imaging of single particles, cluster, and biomolecules is based on published theoretical studies and simulations **[6-319 – 6-322, 6-332, 6-333]**, and is supported by recent experimental results (discussed below) from the first soft x-ray free-electron laser, the FLASH facility at DESY.

Diffraction imaging is elegant in its experimental simplicity: a coherent x-ray beam illuminates the sample and the far-field diffraction pattern of the object is recorded on an area detector. However, radiation damage significantly limits the resolution of conventional imaging experiments. Damage is caused by energy deposited into the sample by the probes used for imaging (photons, electrons, neutrons, etc.). Cooling can slow down sample deterioration, but it cannot eliminate damage-induced sample movement **during** conventional measurements **[6-334, 6-335, 6-380]**. Ultra-short x-ray pulses from XFELs offer the possibility to extend the conventional damage limits, and will allow the imaging of non-crystalline biological (and other) materials. For proteins, simulations based on MD **[6-319, 6-320, 6-336]**, hydrodynamic **[6-337]**, and plasma models **[6-322]** indicate that if very short (100 fs or less) and very intense x-ray pulses are available ($\geq 10^4$ photons/nm^2 on the sample), then a single scattering pattern could be recorded from a single protein molecule in the gas phase before radiation damage manifests itself and ultimately destroys the sample (see Figure 6.4.64).

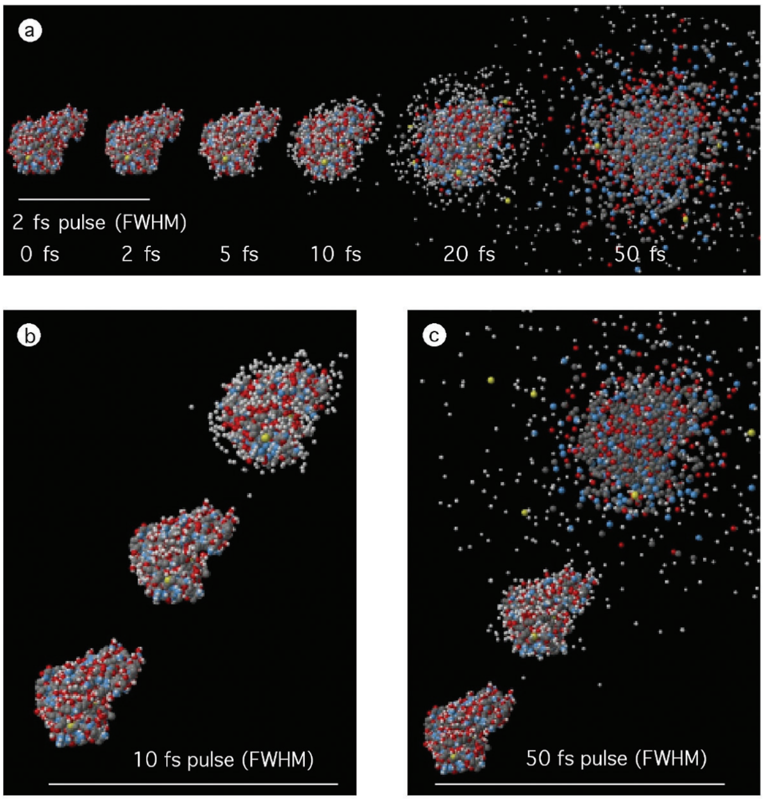

Figure 6.4.64 *MD simulation of radiation-induced Coulomb explosion of a small protein (lysozyme). White balls: H, Grey: C, Blue: N, Red: O, Yellow: S. Integrated x-ray intensity: 3×10^{12} (12 keV) photons/100 nm diameter spot (corresponding to 3.8×10^{8} photons/nm^2, or 3.8×10^{6} photons/Å^2 on the sample) in all cases. (a) Protein exposed to a 2 fs FWHM x-ray pulse, and disintegration followed in time. The atomic positions in the first two structures (before and after the pulse) are practically identical at this pulse length due to an inertial delay in the explosion. (b) Lysozyme exposed to the same number of photons as in (a) but the pulse FWHM is now 10 fs. The images show the structure at the beginning, in the middle and near the end of the x-ray pulse. (c) Behaviour of the protein during a 50 fs FWHM x-ray pulse. It is also apparent from the figure that during the Coulomb explosion, Hydrogen ions and highly ionised sulphurs are the first to escape the immediate vicinity of the protein (at 12 keV, the photoelectric cross-section for Sulphur is about 50 times larger than that for Carbon). Based on* **[6-319]**.

Only a small fraction of the x-rays that fall on the sample will actually interact with the molecule. The “useful” photons are those that scatter elastically and produce the diffraction pattern. However, the dominant interaction is K-shell photoionisation of the atoms in the molecule, which leads to damage. Photoionisation releases an electron with energy close to the incident photon energy (around 12 keV for 0.1 nm radiation). Several femtoseconds later, the K-shell holes of the non-Hydrogenic atoms (C, N, O, etc.) decay, mainly by emitting Auger electrons with relatively low energies 250 – 500 eV. In biologically relevant elements (C, N, O, S, P), a single absorbed x-ray photon leads to more than a single ionisation event in this way. The photoelectrons and the Auger electrons have different energies, and are released at different times. Early on in an exposure, most of these electrons escape the molecule. The escaping electrons leave behind a net positive charge. This charge can grow large enough during an exposure for the less energetic Auger electrons to become electrostatically trapped in the molecule. The more energetic photoelectrons become trapped later and only in larger molecules. Both escaping and trapped photoelectrons produce secondary electrons through collisional ionisation of atoms. The escaping photoelectrons produce, at most, a few secondaries, while trapped Auger and photoelectrons produce the majority of the secondaries. This has been modelled in detail for large (and cold) Carbon samples by Ziaja et al. **[6-338 – 6-341]**, and for water clusters by Timneanu et al. **[6-342]**. Figure 6.4.64 illustrates conditions near the physical limits for imaging **[6-319]**. For the two shorter x-ray pulses only very small changes in the atomic positions have had time to develop during the exposure (Figures 6.4.64(a.) and (b.)) although most of the atoms in the sample became photoionised. The life-times of K-shell core holes in biologically relevant elements (C, O, N) is long (around 10 fs), and as a consequence, very little Auger emission takes place in the sample during exposures that are shorter than about 10 fs (discussed below).

Resolution in these diffraction experiments does not depend on sample quality in the same way as in conventional crystallography, but is a function of radiation intensity, pulse duration, wavelength, and the extent of ionisation and sample movement during the exposure **[6-319 – 6-322, 6-336]**.

There is an additional component that will influence the final resolution of a 3-D diffraction data set. Each particle (macromolecule) is exposed to the beam only once, and disintegrates at the end of this process. The diffraction pattern, so recorded, encodes a two-dimensional projection image of the sample (and this may provide sufficient information for some applications). Three-dimensional imaging requires more than one view from the sample. In addition, the signal-to-noise ratio of raw diffraction images will probably be insufficient for a high-resolution reconstruction, and it will be necessary to obtain a redundant data set so that averaging can enhance the signal. Note that one could extend the depth of view from a single exposure by various holographic techniques based on external or internal reference beams, but a full 3-D reconstruction will most likely require **reproducible samples** exposed to the beam one-by one, and in different orientations. A "reproducible sample" (e.g. purified proteins) may contain heterogeneities, different subgroups of sample, and distinct conformers of the molecule. How reproducible a "reproducible sample" is and how well we can distinguish between similar and dissimilar structures will affect resolution through a B-factor-like component.

Conventional "single molecule" electron cryo-microscopy **[6-343, 6-344]** faces similar challenges as those described here. The basic requirement for reconstruction and/or signal averaging from many diffraction images is the ability to tell whether two noisy diffraction patterns represent the same view of the sample or two different views **[6-331]**. With this knowledge, averaging techniques can be used to enhance the signal and extend the resolution in a redundant data set. A 3-D diffraction reconstruction from a number of different exposures and views can take various routes. Techniques from "single molecule" electron cryo-microscopy **[6-344]** can be adapted here for determining the relative orientation of the images and for merging a large number of noisy 2-D diffraction patterns.

In the next stage, phases are derived from the 3-D diffraction pattern. In principle, there is a direct way to determine the phases required for the conversion using an approach called "oversampling" (for a recent review see **[6-345]**), and this has now been used successfully in a number of experiments **[6-327 – 6-329, 6-346 – 6-348]**. Practical algorithms exist **[6-328]** that are very robust and allow *ab initio* reconstruction of 3-D structures.

There is a need for "containerless packaging" so that only the sample of interest is imaged. We will also need sensitive detection of diffraction patterns with noise levels less than a single photon per pixel (discussed below), and the development of advanced reconstruction algorithms for orienting **[6-331]**, averaging, and inverting the diffraction images into the real-space molecule **[6-328, 6-329]**.

Photon-matter interactions on ultra-short timescales and at high x-ray intensities

Energy absorption is a subject of interest in practically all applications of XFELs, from biological imaging to creating astrophysical conditions in the laboratory. Imaging of single particles and biomolecules is based on the use of extremely intense and extremely short x-ray pulses to limit radiation-induced changes **during** the exposure so that high quality structural data is collected before significant changes take place in the sample (Figure 6.4.64). Single molecule imaging experiments at XFELs represent the high-end of today's high-energy density science. In a focused beam of an XFEL, more than 100 eV/atom will be deposited into the sample within a few femtoseconds, and this will turn the sample into a plasma at some point. The question is when and how?

Under extreme conditions in an intense photon field, electrons can be stripped rapidly from an atom. At optical frequencies, the corresponding high-field regime begins to occur at intensities of about $10^{14\text{-}15}$ W/cm^2, where some of the new atomic physics and plasma physics phenomena have been observed. At around 10^{18} W/cm^2, relativistic effects fully enter the dynamics of electrons in the optical frequency domain. The high-field regime in optical frequencies is well known but it is completely unexplored at x-ray frequencies (no experiments have so far been possible due to a lack of suitably intense x-ray sources). X-rays have three to four orders of magnitude higher frequencies than optical light, and as a consequence, the high-field limits for x-rays are expected to be much higher than those for the slower optical frequencies. Various estimates suggest that field ionisation becomes significant at around $10^{22\text{-}23}$ W/cm^2, and relativistic effects will dominate the picture at around 10^{26} W/cm^2. These numbers are very high compared to expected intensities of mildly focused pulses from an XFEL ($10^{16\text{-}17}$ W/cm^2). However, a highly focused x-ray beam (<100 nm focal spot) with more than 10^{12} photons in a pulse, and at pulse durations shorter than about 5 fs, will approach the high-field limits for x-rays. A quantum mechanical analysis of the electric field induced tunneling indicates that atoms may become stabilised against ionisation under these conditions in a high-frequency x-ray field **[6-349]**. There are no experimental data near this regime and expected stabilisation effects and other non-linear effects are not included in current damage models.

It is important to point out that other major components of the mechanism of damage formation are also different at optical and x-ray frequencies. At optical frequencies, outer shell processes dominate the ionisation of a sample; while at x-ray frequencies, inner shell processes take over (photoemission followed by Auger emission/x-ray fluorescence, shake-up and shake-off excitations, etc.). Inverse Bremsstrahlung absorption is significant at optical frequencies, while it is small at x-ray frequencies. These properties will affect the evolution of Coulomb explosions, and are responsible for differences in the heating of electrons, atoms and ions in the sample during (and after) a short exposure.

A. Physics of damage formation with x-rays

At 12 keV x-ray energy (~0.1 nm wavelength), the photoelectric cross-section of Carbon is about 10 times higher than its elastic scattering cross-section, making the **photoelectric effect** the primary source of damage. During this process a photon is absorbed and an electron is ejected usually from a low-lying orbital of the atom (about 95% of the photoelectric events remove K-shell electrons from Carbon, Nitrogen, Oxygen and Sulphur), producing a hollow ion with an unstable electronic configuration. Relaxation is achieved through a higher shell electron falling into the vacant orbital. In heavy elements, this usually gives rise to x-ray fluorescence, while in light elements, the electron falling into the lower orbital is more likely to give up its energy to another electron, which is then ejected in the **Auger process**. Auger emission is predominant in light elements like Carbon, Nitrogen, Oxygen and Sulphur (99-95%), thus, most photoelectric events ultimately remove two electrons from these elements. These two electrons have **different energies**, and are released at **different times**. Relevant K-hole lifetimes can be determined from Auger line-widths, and are 11.1 fs (Carbon), 9.3 fs (Nitrogen), 6.6 fs (Oxygen) and 1.3 fs (Sulphur). Note that the chemical environment of an atom will influence Auger life times to some degree. **Shake-up and shake-off excitations** (multiple ionisation following inner shell ionisation, see, for example **[6-350]**), initial- and final-state configuration interaction and interference between different decay channels will modulate this picture. Here again, the chemical environment of an atom will influence shake-effects to some degree. The release of the unbound electron “competes” with Auger electrons. When the first electron velocity is low (at low x-ray energies), the slow electron can interact with the other (valence) electrons on its way out and exchange energy. If the energy of the first electron is above some threshold, the sudden approximation is valid, and in general terms, less shake-up will happen. We expect this to be the case with primary photoelectrons of about 12 keV energies, and expect only a small shake-up fraction (about 10%, **[6-350]**). **Inelastic scattering** represents a direct momentum transfer from an x-ray photon to an electron, so that the x-ray photon is scattered with an altered energy. If the energy taken up by a bound electron is greater than its shell binding energy, the atom will be ionised. The inelastic cross-section of Carbon, Nitrogen and Oxygen is around 3% of the corresponding photoelectric cross-sections, whereas the inelastic cross section of Hydrogen is much higher than its photoelectric cross-section. Electrons ejected from atoms during exposure propagate through the sample, and cause further ionisation by eliciting **secondary electron cascades**. The extent of ionisation through this mechanism will depend on the size of the sample. Photoelectrons released by x-rays of 0.1 nm wavelength are fast (66 nm/fs), and they can escape from small samples early in an exposure. In contrast, Auger electrons are slow (9.5 nm/fs) for

Carbon and it is likely that they will thermalise even in a small sample. A detailed description of secondary electron cascades initiated by an electron with impact energies between 0.1 and 10 keV has been published **[6-338 – 6-341]**. In **late phases** of an exposure, a significant fraction of the emitted electrons will not be able to escape the increased positive potential of the sample. **Trapped electrons** will increase the kinetic energy of the sample through **thermal equilibration**; while at the same time, they will also slow down the Coulomb explosion of the sample by **partially screening** the positively charged protein core (all plasmas start cold and dense and become hot later). These opposing effects are explicitly incorporated into the damage models of Bergh et al. **[6-322]**, Hau-Riege at al. **[6-337]**, and Jurek et al. **[6-336]**, and are balanced by simplifying assumptions in the model of Neutze at al. **[6-319]**. Finally, a **transient radiation hardening of the sample** can be expected **during very short exposures**. The dominant interaction of hard x-rays with atoms is through K-shell photoionisation. This process creates hollow ions with one or both of the K-electrons expelled from the atom. The probability of photoionisation by x-rays in hollow ions is expected to be smaller than in relaxed ions or intact atoms. This short-lived "ionisation-resistance" lasts until outer shell electrons fill the vacant K-hole(s), and one may, thus, expect increased stability during short exposures (≤10-20 fs).

B. Modelling damage formation and sample dynamics

A number of damage models have been developed during the past few years **[6-319, 6-320, 6-322, 6-336 – 6-342, 6-350]**. Computer simulations using four different models are in general agreement with each other, and suggest that the structure of a molecule could be determined by judicious choice of FEL pulse length, intensity and wavelength before it is stripped by electrons, and is destroyed in a Coulomb explosion.

The MD model of Neutze et al. [6-319] describes x-ray induced damage stochastically based on the probability of a photoelectric or inelastic event. The force field incorporates Morse potentials for the description of chemical bonds, thereby enabling bonds with sufficiently high energy to break. For water, a simple point charge model was used and adapted in the same manner. The instantaneous probability of ionisation of atom *j* at time *t* is calculated as the product of its photoelectric cross section, and the time-dependent intensity of the x-ray pulse, I(*t*). Auger emission is modeled as a stochastic exponential decay to reproduce appropriate K-hole lifetimes. The direction of photo-emission is distributed according to a random deviate which follows a Gaussian distribution. A recoil velocity for the ionised atom due to inelastic scattering or the emission of a photo- or Auger electron is calculated from energy and momentum conservation. For inelastically scattered photons, the angle of deflection is determined by a random deviate following a Rayleigh distribution. For each inelastic scattering event, the electron's recoil energy is calculated, and in cases when this is greater than the binding energy of the electron, ionisation is modelled (this approximation was deemed sufficient for light elements with weakly bound electrons). An inventory is kept of all electrons in the sample, and changes in the photoelectric, elastic and inelastic scattering cross-sections are computed for all atoms, hollow ions and relaxed ions in 50 attosecond periods during exposure.

The hydrodynamic (HD) model of Hau-Riege et al. [6-337] includes the trapping of photoelectrons but does not treat atomicity explicitly. This model can be applied to both very small and very large samples (millimetres) while MD models are limited to macromolecules because of computing costs. The basic assumption of the HD model is that the sample can be described by a liquid-like continuum of matter rather than considering individual atoms. This gives a simplified description of the average effects of x-ray material interaction and atomic motion, which then permits calculations even on very big samples. The model further assumes that the particle is spherically symmetric, reducing the mathematical model to **one dimension plus time**. The model assumes that the motion of the atoms within the molecule is solely in the radial direction. The electrons and the atoms are treated as separate, structureless, fluids that interact through the Coulomb force and ionisation processes. The short-range electron-electron interactions are treated as a hydrodynamic pressure, and the long-range electron-electron and electron-ion Coulomb interactions are determined from the continuous net charge of the electrons and ions. In this model, all forces act radially. The model further assumes that the trapped electrons are thermalised among themselves, and that they are inertia-free, so that they quickly relax to a force-free spatial equilibrium. Finally, the x-ray matter interaction, atomic ionisation processes, and energy of the trapped electrons are described by time-dependent rate equations. The model shows that at later phases in an exposure, trapped electrons quickly relax in energy and position to form a cloud around the positive ions, leaving a neutral core and a positively charged outer shell (similar to Debye shielding). It is this positively charged outer shell that peels off first, and the Coulomb explosion then “burns” from the outside towards the inside (similar behaviour can be observed in the other models). In the inner core, there is hardly any ion motion but the high electron temperature leads to ionisation and blurring of the electron density. It is this latter effect that requires short pulse lengths to overcome damage.

Two further models have been published recently to include electron-electron, electron-atom, and electron-ion interactions:

MD with explicit electrons of Jurek et al. [6-336] – an MD/Monte Carlo (MDMC) model. This model extends the GROMACS-based MD model of Neutze et al. **[6-319]** by including explicit electrons in the simulations. Numerical modelling is based on the non-relativistic classical equation of motion. Quantum processes are taken into account by the respective cross-sections. Just like the first MD model, this model also includes photon-electron, photon-atom, and photon-ion cross-sections in addition to a description of the atom-atom, atom-ion, ion-ion, interactions. The MDMC model extends this by explicitly treating electron-atom, electron-ion, and electron-electron interactions. The model gives very detailed information on the movement of all atoms and electrons in and around the sample. A disadvantage of the model is that it is extremely demanding on computing power, and this limits its use to small samples only (a couple of thousand atoms).

MD with implicit electrons [6-322] – a MD/continuum electron (MDCE) model. This model uses a plasma approximation for the description of electrons released and trapped in the sample, and extends the GROMACS-based model of Neutze et al. **[6-319]** to include the effect of screening by free electrons through the inclusion of an electron gas. The electrons are approximated by a classical gas, and the electron distribution is calculated iteratively from the Poisson-Boltzmann equation. Simulations of water clusters reveal the details of the explosion dynamics, as well as the evolution of the free electron gas during the beam exposure. Inclusion of the electron gas in the model slows down the Coulomb explosion. Hydrogen atoms leave the sample faster than Oxygen atoms, leading to a double layer of positive ions. A considerable electron density is located between these two layers. The fact that protons leave much faster than the Oxygen means that the heavy part of the sample stays intact somewhat longer than the sample as a whole. A disadvantage of this model is its demand on computing power due to complex grid calculations when simulating larger samples.

While these models are significantly different from each other, they all come up with similar predictions.

C. Calculated scattering patterns for single molecules and particles

Radiation damage causes changes to atomic scattering factors (mainly through ionisations) and also to atomic positions. The creation of a large number of positive charges in close proximity within the sample results in a rise in the electrostatic energy of the sample, which drives its eventual explosion (Figure 6.4.64). The degree of conversion of potential energy into kinetic energy during the x-ray exposure is inertia limited, and as a consequence, strongly depends on the duration of the pulse and on the forces that develop. During the 2 fs pulse in Figure 6.4.64(a.), there was insufficient time for the kinetic energy to grow appreciably. In contrast, by the completion of the 50 fs pulse (Figure 6.4.64(c.)), the kinetic energy of the sample had surpassed its potential energy, and the explosion of the sample was already well underway during the exposure.

The effect of ionisation and ionisation-induced sample movement on the diffraction pattern can be calculated exactly at any point along the simulated trajectories. For unpolarised x-rays, the mean number of elastically scattered photons $I(\mathbf{u},\Omega)$ from a molecule illuminated by a plane wave, to be detected by an idealised detector pixel of a projected solid angle Ω centred at a positional vector $\mathbf{u}$, is given by

$$I(\mathbf{u},\Omega) = 1/2(1+\cos^2 2\theta)\Omega r_e^2 \int_{-\infty}^{\infty} I(t)\left|\sum_j f_j(t)\exp\{i\Delta\mathbf{k}(\mathbf{u})\cdot\mathbf{x}_j(t)\}\right|^2 dt \qquad (6.5)$$

where r_e is the classical electron radius; $I(t)$ is the intensity of the x-ray pulse; $f_j(t)$ is the atomic scattering factor for the j^{th} atom as a function of time; $\mathbf{x}_j(t)$ is the position of this atom as a function of time; and $\Delta\mathbf{k}$ is the change in the wave vector of the x-ray photon when scattered through 2θ radians towards the pixel centred at $\mathbf{u}$.

Radiation damage interferes with the atomic scattering factors $f_j(t)$ and the atomic positions $\mathbf{x}_j(t)$. Damage-induced changes in the scattering pattern, and the structural information, which can be recovered from the sample during an exposure can, thus, be quantified. Assessment of damage-induced changes in the diffraction pattern is based on the calculated differences between scattering from a sample that suffers radiation damage (I_{real}), and scattering from a hypothetical sample that suffers no radiation damage (I_{ideal}) over the same time period. The damage-induced error in the integrated diffraction pattern can thus be described by a weighted average agreement factor (R) between the two patterns as defined below:

$$R = \sum_{u} \left| \frac{K^{-1}\sqrt{I_{real}(u)} - \sqrt{I_{ideal}(u)}}{\sum_{u'} \sqrt{I_{ideal}(u')}} \right| , \qquad K = \frac{\sum_{u} \sqrt{I_{real}(u)}}{\sum_{u} \sqrt{I_{ideal}(u)}} . \tag{6.6}$$

$I_{\mathrm{real}}(\mathrm{u})$ is derived from the time-dependent atomic coordinates, $\mathbf{x}_{\mathrm{j}}(\mathrm{t})$, and scattering factors, $f_{\mathrm{j}}(\mathrm{t})$, of a sample exploding in the x-ray pulse, while $I_{\mathrm{ideal}}(\mathrm{u})$ is determined from a reference molecular dynamics simulation of an unexposed sample. R provides information on the extent to which the elastically scattered radiation is perturbed by x-ray-induced damage and provides a direct assessment of data quality ($R = 0$ is ideal, larger R means larger errors). Scaling factor K describes the relative scattering power of the sample. Macromolecular crystal structures in the Protein Data Bank have crystallographic R-factors of about 20%. Many of the structures, especially those collected earlier on photographic film, represent data sets with merging R-factors in the 5% to 15% range. Taking the latter value as an arbitrary upper limit, we regard damage as acceptable if $\mathrm{R} \leq 15\%$

D. The landscape of damage tolerance

The four published damage models are fairly different in what they include and what they neglect in their description of atoms, ions, electrons and their interactions with an intense x-ray pulse, but all models arrive at surprisingly similar results on pulse, fluence, and wavelength requirements for diffraction imaging. Here, we pick one of these models **[6-319]** to illustrate the available phase-space for high-resolution imaging of single macromolecules. Figures 6.4.65 and 6.4.66 show the landscape of damage tolerance in a broad parameter space around the expected pulse parameters of XFELs. Figure 6.4.65 gives calculated R-values for a protein molecule (lysozyme, see also Figure 6.4.64) exposed to 12 keV x-rays. Damage-induced error is plotted as a function of pulse length and intensity. Figure 6.4.66 shows that data quality improves with increasing x-ray energies. This is due to a favourable change with wavelength of the ratios of elastic, inelastic and photoelectric cross-sections in biologically relevant elements. Figure 6.4.67 illustrates the calculated scattering intensities for a large macromolecule, Rubisco **[6-351]**, at various points along the grey contour line (R = 15%) of Figure 6.4.65.

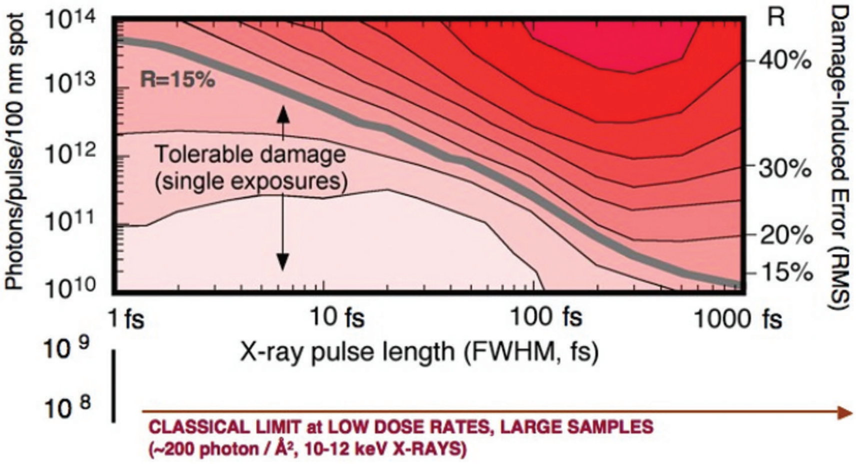

Figure 6.4.65 *The landscape of damage tolerance as a function of pulse length and intensity. The figure shows contour plots of the expected damage-induced errors (R) in integrated diffraction patterns as a function of pulse duration and photon intensity for 12 keV x-rays. The weighted average R-factor describes the extent to which the information content of elastically scattered x-rays is degraded due to radiation damage during the exposure (0% = no change in the structure, 67% = structure randomised). We regard damage as acceptable if R ≤ 15%, and this value is shown as a grey contour line in the figure.*

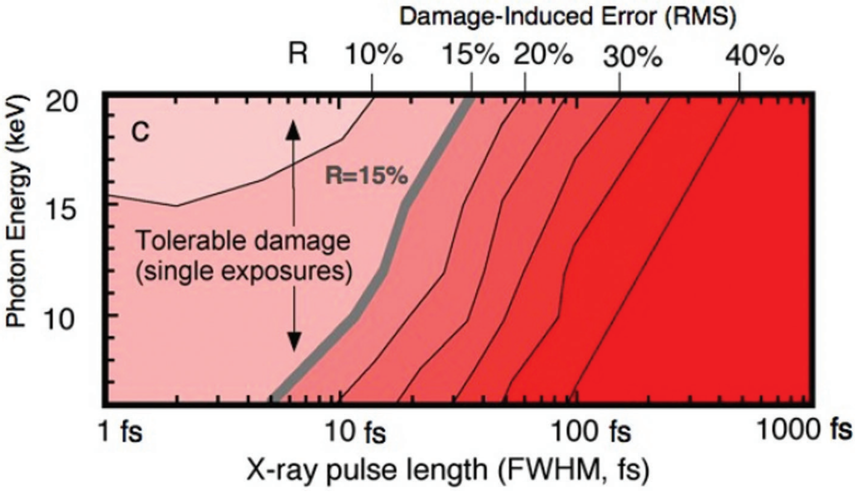

Figure 6.4.66 *The landscape of damage tolerance as a function of x-ray energy and pulse length. The figure shows contour plots of expected damage-induced errors (R) as a function of x-ray energy when the total number of elastic scattering events per Carbon atom is held constant (I_{tot} = 1.33×10^{12} for 6 keV; 1.85×10^{12} for 8 keV; 2.36×10^{12} for 10 keV; 3.0×10^{12} for 12 keV; 3.96×10^{12} for 15 keV; and 6.0×10^{12} for 20 keV x-ray photons/100 nm diameter). The weighted average R-factor describes the extent to which the information content of elastically scattered x-rays is degraded due to radiation damage during the exposure. We regard damage as acceptable if R ≤ 15%, and this value is shown as a grey contour line in the figure.*

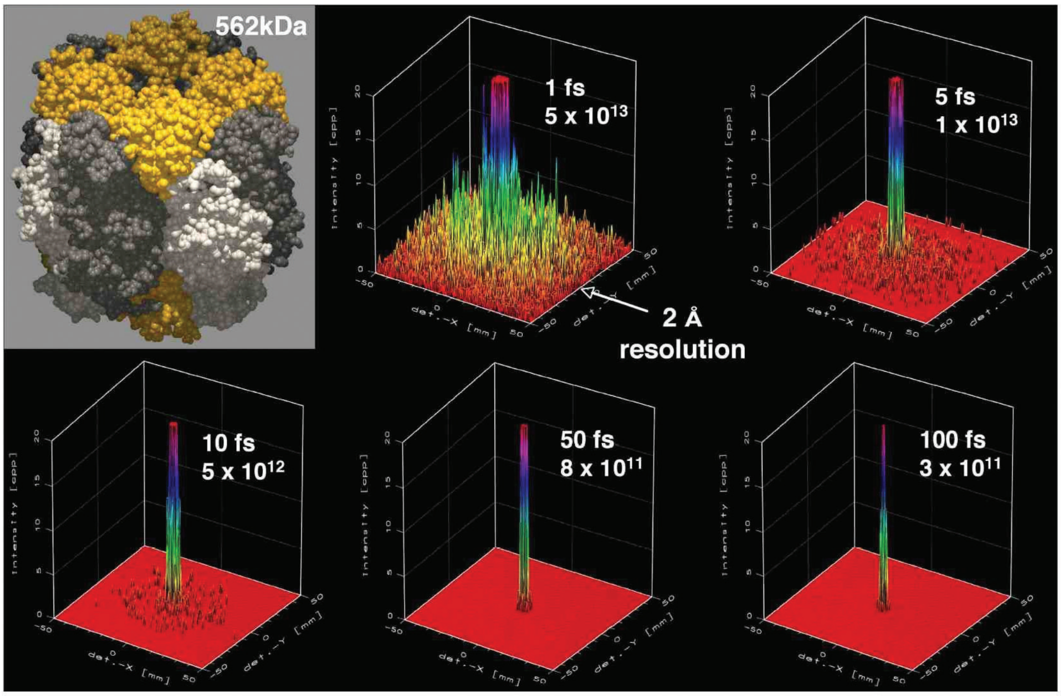

Figure 6.4.67 *Expected scattering patterns for a large macromolecule, Rubisco, with 15% damage-induced error. The figure shows calculated diffraction patterns with 1, 5, 10, 50 and 100 fs long pulses, at pulse intensities at the corresponding points along the grey contour line (R = 15%) of Figure 6.4.66.*

The data show that very short and very intense pulses may permit atomic resolution imaging of this macromolecule. During such short and intense pulses (1-10 fs), numerous K-holes may be present at any one time, reducing the photoelectric cross-sections of atoms in which they were produced, and thereby temporarily lowering the total number of primary ionisation events in the sample with x-rays. This effect can make the system radiation hardened to photoionisation during very short exposures. In addition, very short exposures can reduce Auger emission. If the pulse is shorter than the Auger decay time of the atom (i.e. shorter than around 10 fs for Carbon, Nitrogen, Oxygen), then significant Auger emission from these atoms will only happen after the passage of the x-ray pulse. This reduces damage during the exposure, as compared to longer pulses.

Achievable resolution as a function of pulse parameters and object size

A combination of results from the hydrodynamic continuum model **[6-337]** with the image classification model of Huldt et al. **[6-331]** allows one to map out the landscape of imaging resolution, molecule size and pulse requirements **[6-352]**. The results are shown in Figure 6.4.68, which show that it will be possible to image single molecules at very high resolutions with very short pulse durations (atomic resolution with pulses less than about 5-10 fs).

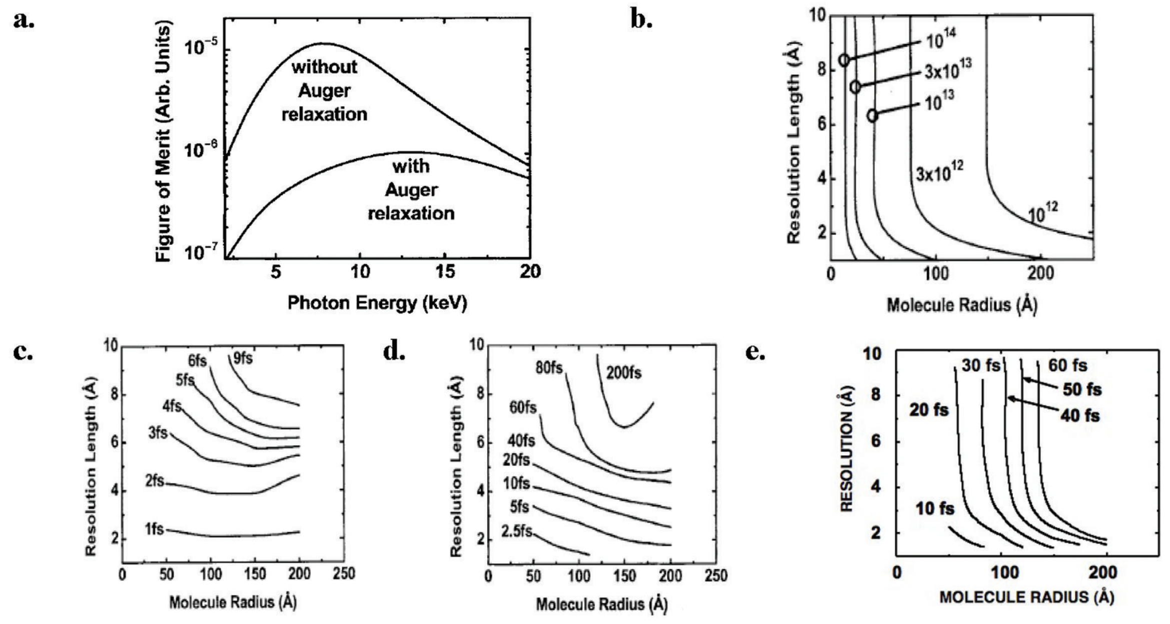

Figure 6.4.68 *Resolution compared to radius for different x-ray fluences: (a) Figure of merit (FOM) for imaging conditions as a function of photon energy; (b) x-ray fluence requirements to classify 2-D diffraction patterns of biological molecules according to their orientation with 90% certainty. The curves are labelled with the x-ray fluence in units of photons in a 100 nm spot; (c) plot of achievable resolution compared to molecule size for various pulse durations as limited by damage and classification. Atomic resolution imaging is achievable with pulse durations less than 5 fs and fluences greater than* 10^{12} *photons per 0.1 micron spot size; (d) pulse duration requirements are significantly relaxed for samples that give 10 times larger scattering signal (e.g. viruses or nanocrystals); (e) the use of a tamper and diffraction pattern repair can give similarly dramatic increases in pulse length for single particles.*

First, the optimal photon energy for diffraction imaging was estimated by maximising a FOM, defined as the ratio of signal minus noise to the radiation damage. As shown in Figure 6.4.68(a.), for pulses shorter than the Auger decay time (~10 fs for Carbon), the optimum photon energy is 8 keV, and for longer pulses it is 13 keV, although the peak FOM is much smaller.

Figure 6.4.68(b.) shows the required x-ray fluence versus image resolution length and particle radius, required to achieve a large enough diffraction signal to classify the patterns. Figure 6.4.68(c.) shows the pulse length requirements for x-ray imaging biological molecules with 12 keV photons, assuming no pre-orientation of the molecules. When the fluence requirements are relaxed by orienting molecules with laser fields, using nanocrystals containing only a small number of molecules, or helical molecules, or icosahedral virus particles, up to 10-20 times longer pulses can be tolerated, see Figure 6.4.68(d.).

The physical models of the interaction of a small particle with the XFEL beam have led to insights that offer additional ways to obtain high-resolution information with longer pulses. One such insight is that a tamper can be used to slow down the motion of atoms during the interaction with the pulse. The tamper may be a small water or Helium drop that surrounds the molecule, and which has a total mass comparable to that of the molecule. Modern electrospray techniques can precisely control the amount of solvent left around the molecule and can be used to select an optimum layer thickness.

Models show that as the molecule becomes charged by the ejection of photoelectrons, the positive charge is confined to the surface, by the ejection of photoelectrons, with a thickness of a Debye length. This layer is ejected first from the particle, and the Coulomb explosion proceeds from the outside in. A rarefaction wave propagates in from the surface at the sound speed, and hence, the centre of the particle undergoes destruction later. The tamper is, hence, a sacrificial layer that preserves the structure of the molecule it contains. However, even with a tamper, the atoms at the centre of the particle quickly become ionised and are surrounded by hot free electrons. Since the x-rays scatter from electrons, the diffraction pattern is substantially modified by this effect. A strict figure of merit, such as used above, does not allow us to tolerate this effect. But since most of the charge is still localised around atoms, structural information is still present. It has been found **[6-353]** that the diffraction pattern can be “repaired” to overcome the effects of ionisation.

The repair strategy assumes that the stoichiometry of the molecule is known and that the ionisation occurs randomly and homogeneously. The method essentially filters the diffraction pattern to correct for the change in atomic scattering factors due to ionisation. The cross-terms, or the effect of different atoms being ionised differently is not compensated for, but it is found in simulations that the simple filtering has a dramatic effect and can correct for 90% of the damage. When coupled with the tamper, this leads to pulse durations about 10 times longer (i.e. on the order of 50 fs), as shown in Figure 6.4.68(e). Experiments with XFEL pulses are required to test these concepts.

E. Finding image orientations, averaging, and building up a 3-D data set

Three-dimensional diffraction imaging will be performed by collecting a large number of noisy coherent x-ray diffraction patterns from a supply of identical particles. One diffraction pattern is collected per particle and the particles have random and unknown orientations. Image reconstruction requires: (1) image orientation and assembly of a 3-D data set; (2) signal averaging to reduce the effects of photon shot noise, radiation damage and any other experimental noise source; and (3) phase retrieval. The methods of reconstructing a 3-D image from a number of noisy diffraction patterns of random and unknown orientation are inspired by methods employed in single-particle electron cryo-microscopy **[6-343, 6-344]**.

The greatest challenge is likely to lie in the signal-to-noise ratio of the diffraction images. The inherent power spectral density of the spatial distributions of matter lead to a rapid decrease in intensity with scattering angle (corresponding to increasing resolution). Molecule variability and incoherent scattering increase the noise, particularly at high scattering angles. At the same time, the incident number of photons should be kept to a minimum in order to reduce radiation damage. Therefore, it is crucial that the data set be redundant, and that we locate and average those redundancies to increase the signal-to-noise ratio.

Statistical studies have shown that a signal of less than one photon per pixel would be sufficient to correlate diffraction images of identical particles presenting the same view, assuming photon noise only **6-[331]**. Correlation-based methods to average and orient large numbers of noisy, randomly oriented real-space images have been successfully developed in the electron microscopy community **[6-343, 6-344]**. Diffraction patterns are first classified into classes of like-orientation so that they can be averaged to increase the signal relative to noise **[6-331]**.

The average signal per diffraction pattern at the highest resolution, required for classification, is found to be much less than one photon per pixel, and an incident fluence of 10^8 ph/nm^2 is sufficient to achieve atomic resolution for particles greater than 15 nm radius **[6-331]**. Averaged diffraction patterns must be oriented in relation to each other in 3-D Fourier space, which may be achieved by the method of common lines (Figure 6.4.69), a technique widely used in electron microscopy, where the micrographs represent planar sections through the centre of the molecular transform. Diffraction images are different and represent spherical sections. Each pair of images will intersect with each other in an arc that also passes through the origin of the molecular transform (Figure 6.4.70).

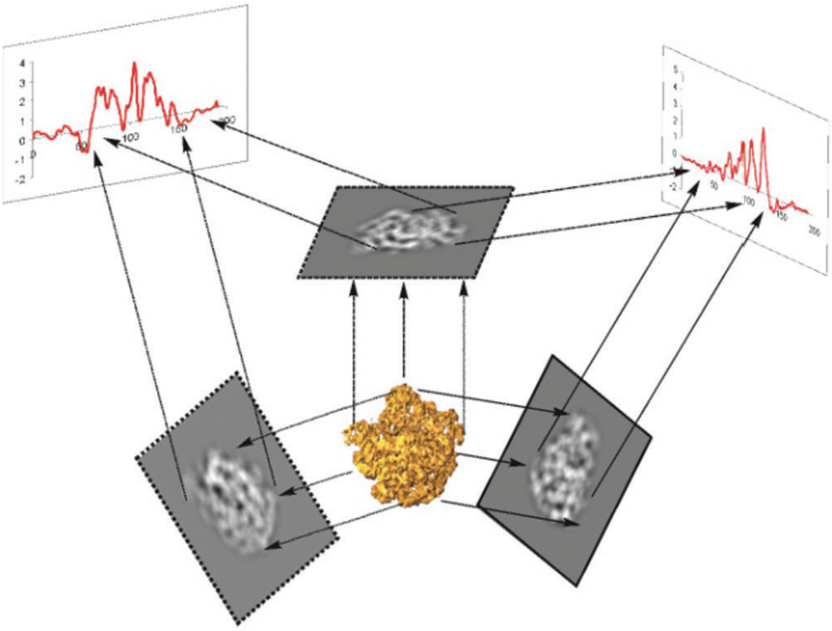

Figure 6.4.69 *Three-dimensional reconstruction in electron microscopy/tomography [26]. A 3-D data set can be assembled from individual images based on the common lines projection theorem. The common line is a hinge axis in tomography.*

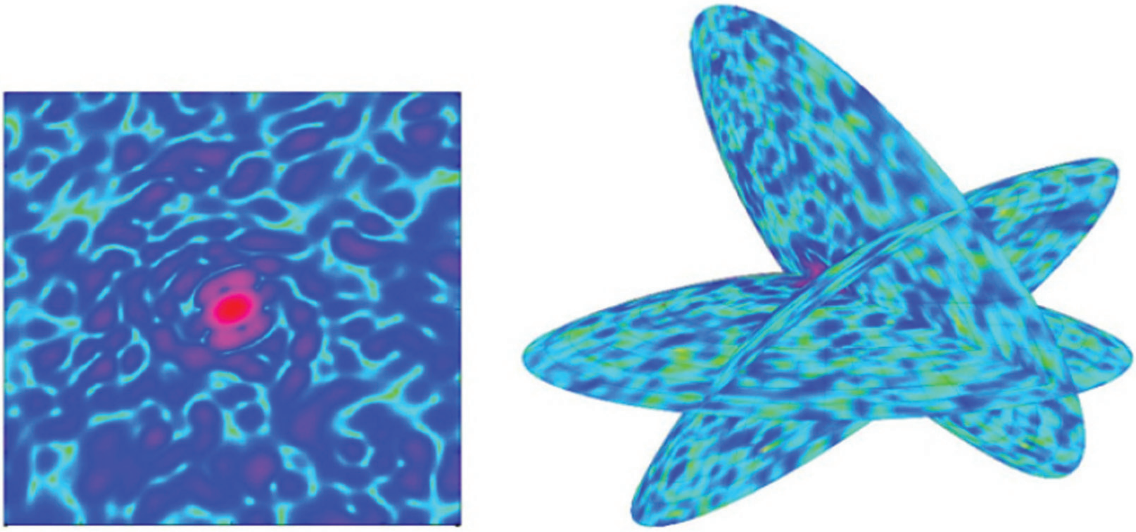

Figure 6.4.70 Intersection of diffraction images along common arcs in diffraction space. The figure on the left shows a predicted diffraction image for lysozyme. The figure on the right shows three different diffraction images of lysozyme intersecting along common arcs in diffraction space. Each arc gives a three-dimensional fix **[6-331]**.

If the signal is strong enough for the line of intersection to be found in two averaged images, it will then be possible to establish the relative orientation of these images. We note that due to the curvature of the sections (especially at x-ray wavelengths), the common arc will provide a 3-D fix rather than a hinge-axis. Moreover, the centric symmetry of the modulus of the molecular transform ensures that we obtain two independent repeats of the common lines in the two images. This feature provides redundancy for determining sample orientation, and is unique to diffraction images (Figure 6.4.71).

F. Laser alignment of molecules

As a further possibility, it may be feasible to record 3-D diffraction data sets of molecules using longer pulse durations and lower fluence by using a polarised laser to orient the molecule (or a number of molecules) and assist the data assembly. Diffraction data would be collected tomographically by rotating the polarisation of the laser once enough signal has been accommodated at a particular orientation. A linearly polarised AC laser field will induce a torque on a molecule that has an anisotropy in its polarisability (usually due to its non-spherical shape).

Without damping (as is the case of molecules in a vacuum) the molecule will oscillate with a period that depends on its moment of inertia, the polarisability anisotropy and laser intensity. This oscillation time is calculated to be 1 to 10 ns for small proteins to large complexes **[6-354]**. If the rise time of the intensity experienced by the passing molecule is sufficiently slower than the oscillation period, alignment will be induced adiabatically and the molecule will orient along the direction of the electric field vector without oscillating **[6-355]**.

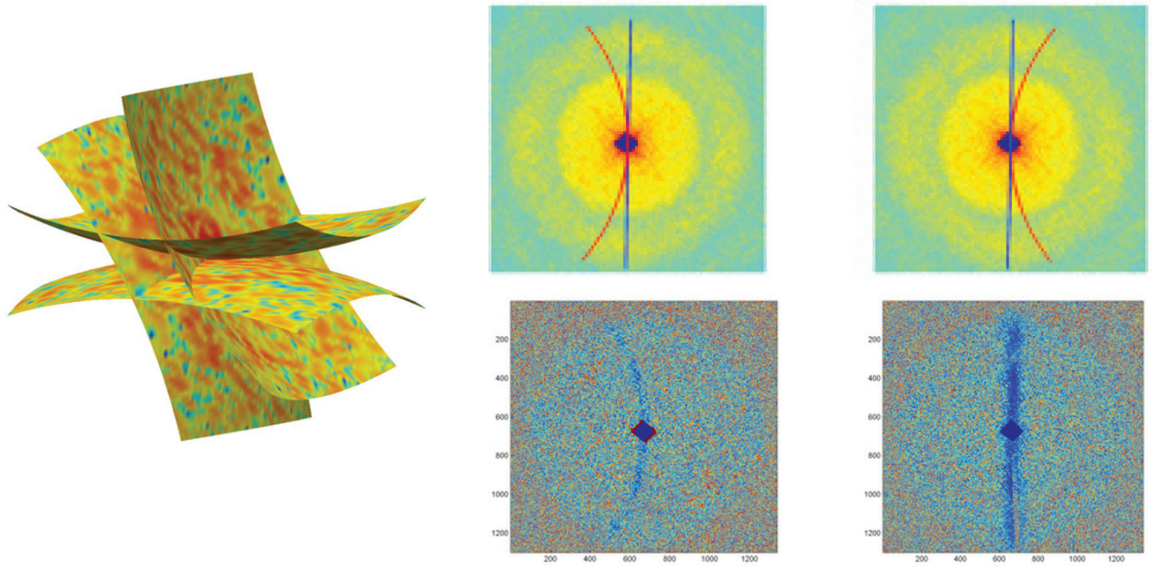

Figure 6.4.71 *Intersection of two Ewald spheres with their centrosymmetric opposites. Centrosymmetry gives an extra intersect as there are two common arcs of intersection in each diffraction pattern (upper row). The images in the middle show the expected arcs of intersections in two diffraction patterns from the experimental pyramid x-ray diffraction data set from Figure 6.4.68. Images in the bottom row show these very lines of intersections when the experimentally obtained patterns are subtracted from each other pair-wise* **[6-356]**.

The rise in intensity can be achieved simply by shaping the beam intensity (a Gaussian profile will suffice) with a length scale that depends on the particle velocity, to achieve rise times of about 100 ns. The degree of alignment depends on thermal fluctuations. The equipartition theorem applied to a harmonic oscillator results in the alignment error varying as the inverse of the square root of the laser power and molecule temperature.

The rotational temperature can be brought down to a few Kelvin by the supersonic expansion of the molecule into vacuum that occurs in the injection process, which should result in alignments of 1° to 10° for proteins such as lysozyme under adiabatic conditions **[6-354]**. This requires an intense laser field, on the order of 10^9 W/cm^2, which should be in the near infrared, far from vibrational resonances in the molecule.

The interaction energy of the molecule with the laser beam is the same for a molecule aligned parallel or antiparallel to the field axis and only a DC electrostatic field can break this symmetry. Nevertheless, recent work has shown that an image can be reconstructed from a diffraction pattern that is an average of these two directions **[6-357]**. Alignment of molecules along all three axes (with a sense ambiguity in each direction) has been achieved with high fields and simple inorganic molecules using elliptically polarised laser fields **[6-356]**.

The achievable image resolution will be limited by the degree of alignment, and in general for a length of the molecule of L and a standard deviation in the angle of orientation of $\Delta\theta$, the resolution will be about $L\,\Delta\theta\,/\,2$. For small proteins, such as lysozyme, which are only

$L = 4.5$ nm long, a misalignment of 10° gives a blurring of about 0.4 nm. More experimental studies are required to determine what degree of alignment is possible and the required laser parameters.

Larger particles require much less laser intensity due to their larger polarisabilities (tobacco mosaic virus particles can be aligned in water with static fields **[6-348]**). However, they must be aligned with far greater precision for a given image resolution, which is harder due to the rotational temperature. Thus, for large single particles, which will give large diffraction signals, laser alignment may be used **for reducing the number of classes needed to classify a pattern**. Laser alignment will provide a useful platform for developing techniques of single-particle diffraction imaging using the characteristics of pulses in the first stages of XFEL development, allowing us to achieve scientifically relevant results and to better validate models of the interaction of molecules with XFEL pulses.

G. Methods for phasing

A number of methods exist for recovering phases for objects that have a finite size, or "support". These include oversampling of continuous molecular transforms **[6-323, 6-324, 6-326, 6-359, 6-360]**, holographic imaging methods **[6-361 – 6-364]**, holographic data evaluation methods **[6-362, 6-365]**, classical methods of crystallography, and techniques for phase extension from lower resolution electron/x-ray cryo-microscopy images.

The past few years have seen the development of robust algorithms in solving the phase problem through oversampling the diffraction pattern, and this seems to be a most promising technique for the future. The 3-D diffraction transform of a non-periodic particle is continuous. Only the diffraction amplitudes are sampled at discrete points by the pixellated detector and the process of classification.

The measured diffraction intensities are proportional to the modulus squared of the Fourier transform of the wave exiting the object. On their own, these diffraction intensities are insufficient to back-transform to form an image in real space. That inversion requires knowledge of both the diffraction intensity and phase. If the diffraction pattern intensities are sampled finely enough, it is possible to solve this problem for the diffraction pattern phases **[6-323, 6-324, 6-326, 6-359, 6-360]**.

The solution to this non-linear inversion problem is usually obtained iteratively by sequentially enforcing known constraints in reciprocal space and in real space. Specifically, in real space we assert that the image has zero scattering strength outside the area of the object's boundary (called its "support") **[6-324]**, whilst in reciprocal space, the squared modulus of the Fourier transform of the image must equal the measured diffraction intensities. Such algorithms have now been used successfully for image reconstruction in x-ray diffraction experiments **[6-326, 6-329, 6-330, 6-348]**. An example of a reconstructed 3-D image is shown in Figure 6.4.72.

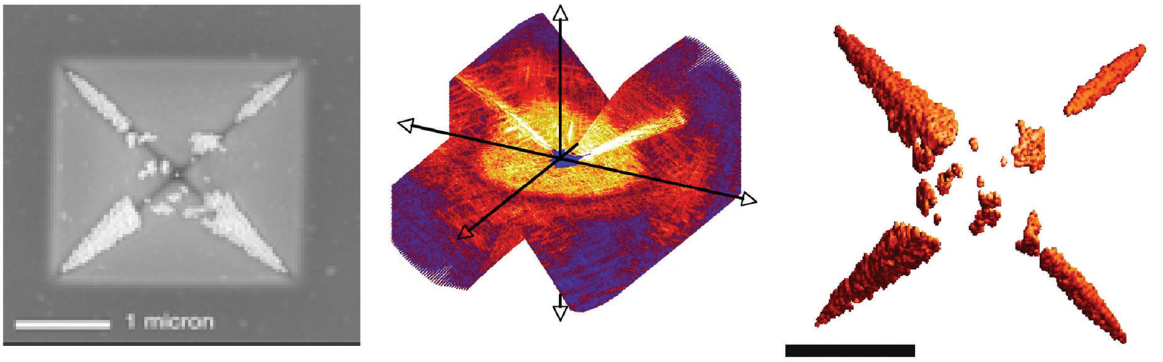

Figure 6.4.72 *Coherent diffraction imaging and image reconstruction* **[6-366]**. *Three-dimensional diffraction data (middle) recorded from a test object (left), consisting of 50-nm diameter Gold balls on a Silicon-Nitride pyramid-shaped membrane, at a wavelength of 1.6 nm, and a rendering of the ab initio 3-D image (right) reconstructed from the diffraction intensities to a resolution of 10 nm. The diffraction data were obtained by rotating the specimen in 1° increments from -70° to +70°, and then interpolated onto a 1,024*^{3}*-element array. A quadrant of the diffraction data set has been removed for visualisation in the central rendering of the 3-D diffraction intensities. The Gold balls seen in the rendering of the 3-D reconstructed image on the right fill the inside edges of the Silicon-Nitride pyramid. The scale bar is 1 micron.*

The algorithms usually require that the support of the object be known *a priori*, and the closer the support to the actual object boundary, the better the reconstruction. The algorithm called SHRINKWRAP successively refines an estimate of the support from a current estimate of the image **[6-328, 6-329]**. This algorithm does not require the support to be known and is remarkably robust at finding the smallest image support that contains the majority of the image intensity.

Another programme that has been used successfully to phase experimental data is SPEDEN **[6-321]**. This uses a constrained conjugate gradient solver to find the amplitudes of 3-D Gaussian blobs whose calculated diffraction intensities match the measurements while also minimising cost functions based on constraints (including a low-resolution target, 2-D projections or known phases). The algorithm finds the optimal image that fits all the constraints and, since it only ever performs calculations from real to Fourier space, it never needs to interpolate data onto a regular grid.

However, as a local optimiser, it does not have as large a volume of convergence as the iterative transform algorithms and it may be used in XFEL imaging as a way to refine images produced by SHRINKWRAP and avoid artifacts due to missing data.

Overview of the experimental programme

There is a general class of experiments that utilises the short time structure and the potential for very high intensities of the XFEL beam, and leads up to the exciting new regime in imaging outlined in the first sections.

It is immediately clear that small crystals, nanoclusters and 2-D crystals can already be studied at very high time resolution with low photon intensities from the beginning. In the following sections we will outline some exciting biological problems that become doable this way. Note that the saturation of the beam plays only a secondary role in these experiments, but will be important later.

It was emphasised in the introduction that damage by the incident radiation is the ultimate limit to the resolution of imaging techniques in biological molecules. It is ~ 2×10^4 photons/nm^2 at 10 keV incident photon energy. The primary damage is caused by the ~10 keV photoelectrons and the ~250 eV Auger electrons that are absorbed in the sample, causing secondary ionisation and, eventually, chemical damage. It is accepted wisdom that the damage in electron microscopy is about 1,000 times more benign with large samples than damage with x-rays.

This would imply that single particle imaging techniques would yield 10-fold lower resolution by x-ray scattering. There are, however, three mitigating factors in favour of x-rays: First, the scattering geometry of x-rays allows large angle data collection and the clean and simple geometry avoids distortions in the image. Second, if small particles can be used, the primary photoelectrons deposit only a small fraction of their energy and the damage should be ameliorated by ~20-40 fold. Third, time honoured techniques of attaching heavy atoms to clusters should increase the signal-to-noise ratio of single particle images.

In order to utilise the advantages outlined in the previous paragraph, two additional developments are needed: focusing of the beam to about 0.1 µm and the development of single particle injection techniques. The latter is well advanced in this partnership. We anticipate that very mildly ionised droplets will be injected into the focused beam just in time.

When mild focusing of the beam becomes available, e.g. the focusing of the projected 10^{12} photons in one pulse into a focal diameter of 0.5 µm, giving a flux of 2×10^6 photons/nm^2 at the focus, single particle images can be obtained using averaging techniques similar to those used in electron microscopy. This should open the door to virus structures, including their genomes, to the study of membrane proteins, to very high time resolution studies of other, known structures.

In summary, we will argue here that new and exciting biological problems will be open for investigation from the first day the beam becomes available. We foresee that our interim technical efforts in sample handling, attaching proteins to viruses and developing algorithms for single particle imaging will fully complement developments with the source. The experiments outlined represent major research lines far beyond the limits of currently available methodologies. We also hope that new research areas may emerge in a field as explosive as biology today by the time the XFEL becomes available. Shortening the pulse length would be a key improvement in all planned applications, including those described in the biological proposal. With shorter pulses, tighter focusing, very fast detectors and development of accurate injection techniques, biomolecular imaging should reach the extreme regime outlined in the theoretical part of this proposal.

I. Nanocrystals

These are open periodic structures with sub-micron dimensions. All macroscopic crystals start as nanocrystals. X-ray lasers may offer completely new avenues for structural studies on nanocrystalline samples. No such studies are currently possible. When a crystal is small, the Bragg peaks are broadened and the intensity between the Bragg peaks is not negligible. Both the Bragg peaks and the intensity between the peaks carries structural information. The oversampled diffraction pattern visible between Bragg peaks can directly provide phase information.

II. Two-dimensional crystals of macromolecules

Various estimates show that the number of different membrane proteins in various genomes is similar to the number of soluble proteins, yet there are only a small number of structures known today for integral membrane proteins as compared to well over 30,000 structures for soluble proteins. An understanding of the structure-function relationships in membrane proteins would make invaluable contributions to biochemistry, physiology and medicine, and would produce a substantial socio-economical impact (about 70% of all known drugs target membrane proteins).

Two-dimensional crystals of membrane proteins may be obtained from a number of membrane proteins, e.g. by epitaxial crystal growth methods. The intensity of the scattered x-rays, even from a small 2-D array, can be considerable with XFEL pulses. Integration of the diffraction rods requires images with different sample orientations to be recorded, and this could be achieved by merging data from several randomly oriented samples. This procedure could provide structural data on membrane proteins in bilayers.

III. Closed nanoclusters for structural studies

In contrast to nanocrystals (which are small but open periodic structures with translational symmetry), the nanoclusters we refer to here are closed structures, which may be periodic (like oligomeric proteins or the capsids of virus particles) but have no translational symmetry. Such nanoclusters come in very well defined sizes or can be made to make up well defined sizes and geometries.

We are developing procedures for assembling proteins of choice into regular nanoclusters for subsequent structural studies. Methods are available for the specific attachment of target proteins onto the surface of regular templates, e.g. icosahedral virus capsids. These methods will be applied to structural studies on soluble and membrane proteins at FELs. Assembling protein molecules into nanoclusters will increase the intensity of scattered radiation from otherwise small proteins. We wish to use modified viruses to construct well defined nanoclusters of a number of different proteins, including membrane proteins.

Expected outcome: structures for “uncrystallisable” proteins attached to the surface of regular templates.

IV. Virus structures and the structure of viral genomes

No high-resolution structure is available for any genome today. Small spherical viruses are among the simplest replicating systems in biology, yet the packing of the nucleic acid inside the capsid, and the factors affecting viral assembly, stability and disassembly are still not understood. Only a superficial picture is available today on the packing of the genetic material in intact viruses. This is due to the fact that in most viruses, the outer protein shell obeys the space group symmetry, while the inner material does not.

As a consequence, the image of the otherwise tightly packed nucleic acid inside the virion is rotationally averaged over some angular range. From images collected, we propose reconstruction to recover the structure of the inner part (the genome) of the virus. Further experiments will focus on the assembly/disassembly of the virus.

Of particular interest are viruses that cannot be crystallised (e.g. human immunodeficiency virus, herpes simplex virus, and many others). X-ray studies on viral particles in the gas phase (or in vitreous ice) could open up ways to capture elusive intermediates within the "life cycle" of a virus. An understanding of the functional dynamics of viruses may offer a means of interferring with infection. Experiments will capture dynamic events, e.g. steps in the assembly and disassembly of the virus, and studies on key initial steps in a viral infection.

V. Structural studies on single protein molecules

The need for crystals for high-resolution structural studies is a serious limitation today. Currently, this excludes a very large proportion (>60%) of proteins from detailed structural determination, and hinders progress in the area of structural genomics. Structures accessible today for analysis do not represent a random selection of proteins, and knowledge gained on "crystallisable" structures may not automatically translate into knowledge about "non-crystallisable" structures.

When sufficiently short pulses and a reasonable high pulse intensity become available in the focus, studies on large single individual molecules (probably with molecular masses in excess of 100,000 dalton) may become routinely possible.

VI. New horizons in time-resolved experiments

Biological function is a four-dimensional property. Time-resolved studies on structure, function and dynamics with x-ray lasers could cover catalysis, protein folding, nucleic acid folding, the assembly/disassembly of biomolecular complexes, viral uncoating, viral infections and so on. Such studies will first become possible on nanoclusters and nanocrystals as they require less stringent beam parameters than studies of single molecules. Later on, these experiments may be extended to individual biomolecules or cells.

Photochemical reactions

Marriage of femtosecond laser spectroscopy with femtosecond time-resolved structural studies will be possible.

Diffusion triggering, stop-flow studies

While certain key reactions in life are photochemical, most enzymes participate in diffusion-dominated processes with their reactants and partners. Time-resolved structural studies on diffusive processes in crystalline enzymes are difficult due to problems with mixing enzyme and reactant. Structural studies are only possible on intermediates which accumulate transiently in the crystal during a reaction. This requires a relatively fast binding followed by a relatively slow reaction. Due to the generally lower activity of crystalline enzymes, uniform catalysis can often be triggered by diffusing reagents (e.g. substrates) into crystals.

However, the speed of diffusion and ligand binding sets an upper limit to the speed of reactions which can be analysed this way. Past results show, that in an average-sized protein crystal, half saturation binding with small ligands can be reached within about a minute. One obvious possibility for lowering diffusion barriers is to reduce the sample size, get rid of the crystal, and use **stopped-flow** type mixing techniques for time-resolved experiments, where the sample can be sprayed into the beam after certain “aging” times following rapid mixing.

This can be done on purified proteins, nanoclusters or nanocrystalline slurries of enzymes instead of diffusing reactants into large single crystals. With very small samples, the vast majority of solution kinetic techniques and methodologies will suddenly become available for time-resolved structural investigations. We foresee that container-free sample handling methods based on spraying techniques, will open up new horizons here.

VII. Atomic clusters and nanocrystals

Another field of application is the investigation of atomic clusters’ and nanocrystals’ structures. Research on these systems has become a very important and active field of interdisciplinary interest in recent years **[6-367]**. They allow the study of how macroscopic properties of matter are formed through the assembly of their microscopic units. The transition from the atom to the solid is not a smooth transition at all but rather interesting variations can occur. The size of the clusters is a new parameter, which can be used to control their properties, namely geometrical and electronic structure, magnetic properties and chemical reactivity. A thorough understanding of these properties is also of fundamental interest for applications of clusters since they hold great promise in, for example, microelectronics and photocatalysis. The precise knowledge of the cluster geometry, i.e. the positions of the individual atoms, is essential for a detailed understand of many open questions in cluster research. X-ray scattering as a direct imaging technique would be an ideal tool for structure determination, since most of the present techniques are indirect tools. The application of time-resolved structure determination for these systems will immediately lead to new scientific applications, e.g. in photocatalysis.

Compared to biomolecules the situation is somewhat simpler: Many of these nanometre-size particles have some crystalline order which results in a concentration and enhancement of scattered light into Bragg-type peaks. Furthermore, the heavy elements in clusters scatter much more efficiently than light elements which are the basis of biomolecules. The prospects and limits are discussed in recent theoretical studies

[6-320, 6-336]. With 10 fs-long pulses it is possible to obtain scattering patterns for 200 atoms C clusters with sufficient quality before notable structure deformation sets in. A particle density of 1×10^7 cluster ions/cm^3 is needed in order to get one ion per interaction volume, if a volume of $0.3\times0.3\times10^4$ µm^3 is assumed. This is somewhat higher than what can be obtained with radio frequency traps with a rather large volume **[6-368]**. Further, and similar to the case of biomolecules, imaging of clusters and nanocrystals is directly linked to issues of radiation damage, plasma formation and laser cluster interaction. Recent experiments with FLASH unveil the complicated and interesting many-body dynamics of clusters **[6-369, 6-371]** irradiated by intense femtosecond-pulses. Initial experiments with the FLASH FEL at DESY operating at 32 nm, demonstrated the feasibility of single shot scattering measurements of nanometre-size clusters **[6-371]**. Some of this work on clusters can be regarded as model studies of radiation damage in bulk materials and biomolecules.

First results

Demonstration of flash-diffraction imaging using a soft XFEL

The first experimental verification of the principle of coherent flash-diffraction imaging has recently been performed at the FLASH facility **[6-330]**. The results show that an interpretable diffraction pattern can be obtained before the sample turns into plasma when exposed to an intense 25 fs-long photon pulse at 32 nm wavelength (Figure 6.4.73). In these experiments the beam was focused to a peak intensity of up to 10^{14} W/cm^2. We estimate that the absorbed energy density was approximately 20 eV/atom in the Silicon nitride and that the material **reached a temperature of about 6×10^4 K before vaporising**.

Significantly, the image obtained by phase retrieval and inversion of the diffraction pattern shows no discernible sign of damage, and the object can be reconstructed up to the resolution limit of the detector (62 nm with 32 nm photons). Damage occurs only after the pulse traverses the sample. A second exposure shows scattering from the hole that was created by the first pulse. These results provide the first experimental evidence for the basic principle of flash imaging, and this is the very technique we expect to lead to atomic resolution studies when hard XFELs become available.

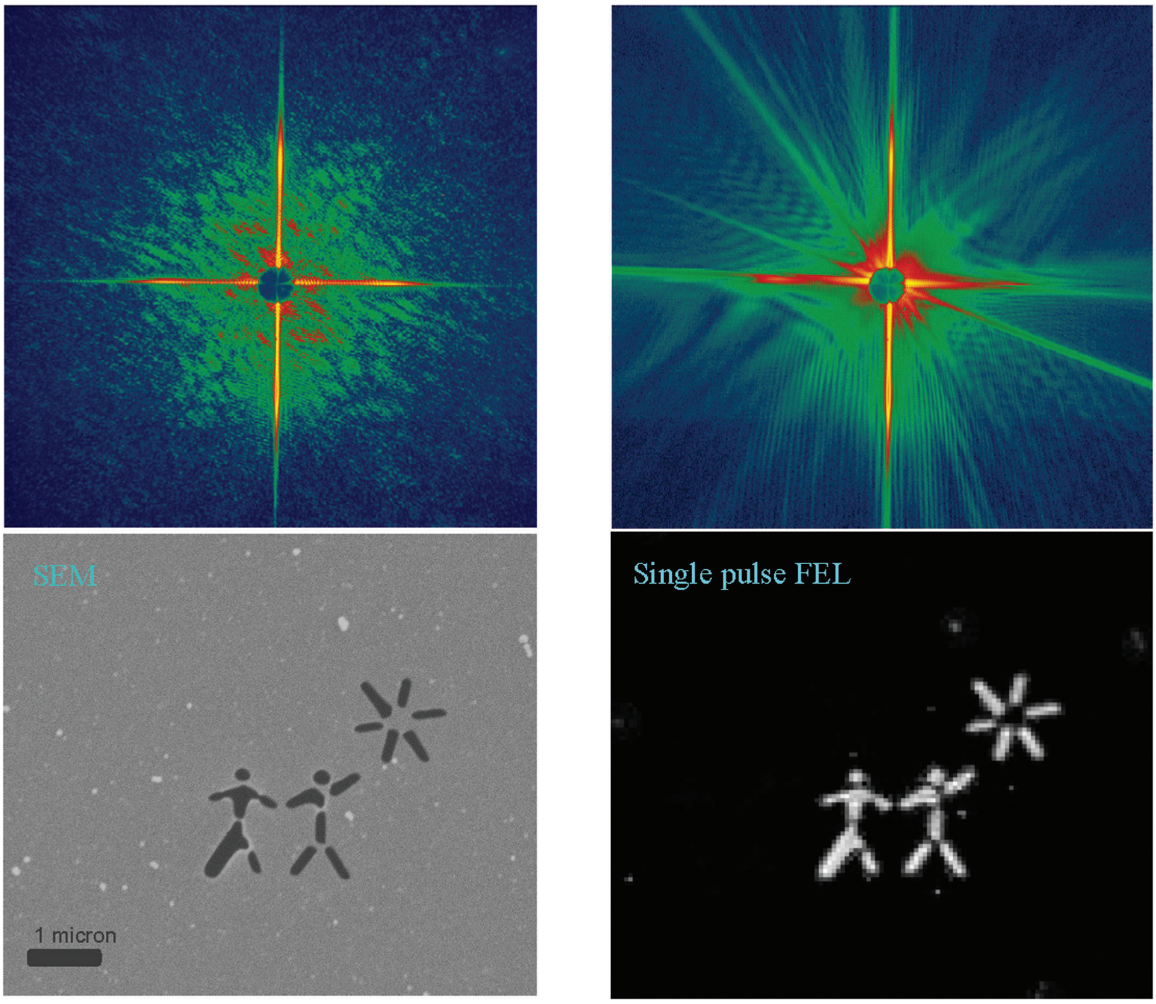

Figure 6.4.73 *Demonstration of single-pulse coherent diffraction imaging at 32 nm wavelength (February 2006). Top left: A diffraction pattern recorded with a single 25 fs-long FEL pulse at 32 nm wavelength from a test object placed in the 20 micron focus of BL2 at the FLASH facility of DESY (peak intensity: up to 10^{14} W/cm^2). We estimate that the absorbed energy density is approximately 20 eV/atom in the Silicon Nitride and that the material reached a temperature of about 6×10^4 K before vaporising. Top right: The diffraction pattern recorded on the second pulse some 20 seconds later, showing diffraction from the hole in the sample created by the first pulse. The sample was a pattern cut into a 20 nm thick Silicon Nitride membrane, shown at the bottom left from SEM. Bottom right: The image reconstructed to the resolution limit of the detector at 32 nm wavelength (corresponding to 62 nm resolution) from the single-shot diffraction pattern using the SHRINKWRAP phase retrieval algorithm. The algorithm only used the measured diffraction intensities and the knowledge that the diffraction pattern was over-sampled. We did not use the SEM image in the reconstruction.* **[6-330]**

Ultra-fast transmittance and reflectance data from FLASH

Other supporting data show that transmission and reflectance by solids remain **linear** up to 10^{14} W/cm^2 (the maximum that could be reached so far at the FLASH facility, absorbed energy in SiO_2: about 100 eV/atom), provided that this energy is deposited in the sample in a very short photon pulse (~30 femtoseconds at FLASH) **[6-372 – 6-374]**. The sample turns into a plasma, and it is destroyed **after** interaction with the intense photon pulse.

Similar studies show that the reflectivity of mirror surfaces (single component Silicon or Graphite, and multilayer mirrors made of Silicon and Carbon) remain constant over a very wide intensity range when interacting with a very short pulse from the soft XFEL of DESY. These mirrors work perfectly **once** near normal beam geometry even in a focused FEL pulse at 10^{14} W/cm^2 at 32 nm wavelength **[6-353, 6-372 – 6-374]**. Angularly resolved reflection data show that the period of the Si-C multilayer mirror changed as little as 0.3 nm **during the pulse [6-353]** but the surface was destroyed **after** interaction with the intense photon pulse (Figure 6.4.74), in line with our expectations.

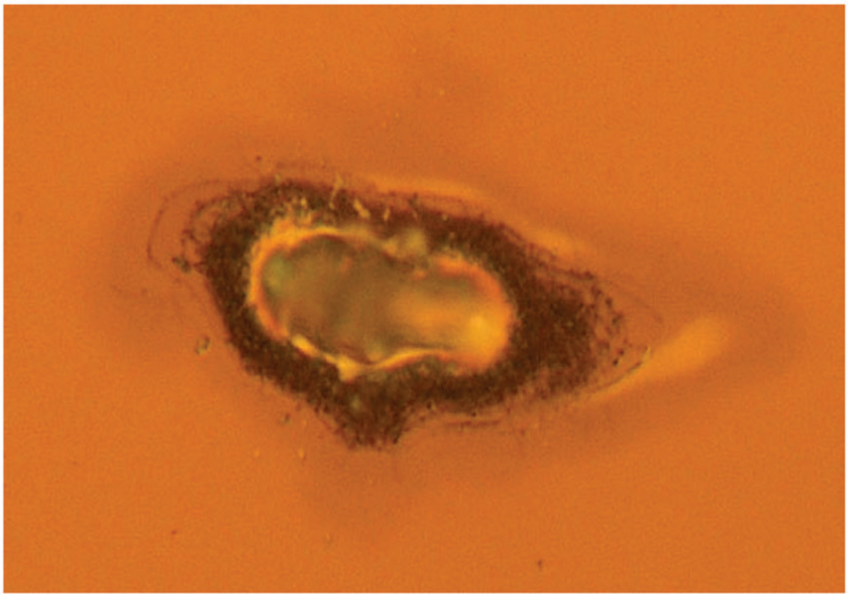

Figure 6.4.74 *Nomarski photograph of a Si-C multilayer mirror after interaction with an intense pulse of the FLASH soft x-ray laser at DESY. Wavelength: 32 nm, focal spot size: ~20 micrometer, energy density: ~10^{14} W/cm^2. The damage seen here developed after interaction with the intense photon pulse* **[6-353, 6-369 – 6-371]**.

6.4.3.2 Instrument requirements

The experiments described above lead to requirements for an instrument for scientific applications of imaging of Single Particle, clusters and Biomolecules (SPB). They concern the performance of the light source, the optical elements and the diagnostic equipment, the sample environment, and the detectors. The scientific cases presented required beamlines suitable for diffraction experiments at hard x-rays using 12.4 keV photon energy. Extremely intense XFEL radiation will be required in these experiments. Since the experiments do not require photon energy variation, the corresponding instruments should be located at the SASE 1 beamline for XFEL radiation.

The experiment consists of an apparatus to perform coherent x-ray diffraction imaging, and image reconstruction by phasing over-sampled diffraction patterns. The apparatus will include optics to focus the beam onto the sample to provide the necessary x-ray fluence together with pulse compression, as necessary. Samples will not survive the interaction with the focused XFEL beam, so we can consider three fundamental classes of experiment:

(i) 3-D diffraction imaging of reproducible structures;

(ii) 2-D imaging of single objects (like small living cells); and

(iii) 3-D diffraction imaging of single objects at low fluence.

Within these classes of experiment, we can consider variations, such as simultaneous (or time delayed) imaging of objects, imaging of reproducible structures in three-dimensions, imaging nanocrystals of different shapes, and imaging of two-dimensional (membrane protein) crystals. The third class listed above requires the unique coherence properties of the XFEL, and would be undertaken as a development step towards (ii) as well as providing learning that will be brought back to high-brightness third-generation sources.

Note that, while a single diffraction pattern as recorded in scheme (ii) is two-dimensional, this information exists on the Ewald sphere in reciprocal space **and indeed does contain information of spatial frequencies in the depth direction**. This is manifested by the ability to computationally focus through the object, by numerically propagating the complex-valued wavefield that is the retrieved image **[6-366]**. The depth resolution is simply the depth of field of the imaging system, given by λ/NA^2, where NA is the numerical aperture of the detector. For $\lambda = 0.15$ nm, NA = 0.3, the depth resolution is 1.6 nm, compared with a transverse resolution of 0.5 nm.

Spectral radiation properties

In most cases the experiments will exploit the natural bandwidth of XFEL radiation. In the case of large particles, i.e. 1 µm, the longitudinal coherence length needs to be increased to enable coherent diffraction at large Q values. Perfect crystal double-reflection fixed-exit monochromators providing a relative bandwidth of $0.5\text{-}1\times10^{-4}$ will be needed here. Such monochromators can be introduced in the beam path without interference with other beamline elements. Higher harmonic radiation at the level of 10^{-2}, compared to fundamental radiation, is not expected to cause a problem. For particular experiments third harmonic radiation may be useful since its use strongly reduces sample damage.

X-ray optics requirements

The beam from the XFEL will be focused to a variable spot diameter 0.1 to 10 microns (variable), depending on the overall sample size and desired x-ray fluence at the sample (some experiments can use larger diameter beams, including the unfocused beam). This requirement could be achieved by a Kirkpatrick-Baez mirror pair, or a grazing ellipsoidal mirror. No prefocusing optic would be used, and ideally, the number of beam-directing mirrors should be minimised. A given required spot size dictates a demagnification factor of the optic, which forms a demagnified image of the source. The optic-to-focal spot distance is equal to the source-to-optic distance multiplied by the demagnification, and so larger working distances can be achieved by placing the experiment further from the source. This has the added advantage of allowing larger aperture optics (since the unfocused beam is bigger) and hence, reduced fluence on the optical surfaces. For the small foci the stability of beam pointing becomes critical and needs to be minimised. A stability <10% spot size is wishful for the experiments using single shot on gases or solid samples. For the tomography experiments a stability clearly better than 10% is required.

The pulse duration will eventually need to be shortened, which could be achieved either by source modifications or by x-ray pulse compression, using, for example, strained crystal diffraction **[6-375]** or asymmetric multilayer gratings. Our current estimates are that pulses shorter than 50 fs with more than 10^{11} photons/pulse are required for realistic single-particle imaging.

Other optical elements include apertures placed in the beam to block unwanted scatter from the beamline. These apertures will be larger than the direct beam. Also called guard slits, these have to be positioned and manufactured very carefully to prevent rather than contribute to the problem. Slits with "soft" edges can be made from wedges of perfect Silicon crystals (as one particular option). The innermost edge is transparent, slowly becoming opaque. This apodises the diffraction pattern by removing high-spatial frequency from the slit structure. With coherent beams, several slits can be placed so that their edges are positioned in the node of the weak scattering pattern formed by the upstream edge.

Time domain requirements

The experiments will be performed in single shot operation mode, i.e. with single pulses and repetition rates of 10-50 Hz. The tomography experiments require conditions with very little sample damage (i.e. an attenuated beam) and could be performed using x-ray pulse repetition up to MHz employing pulse trains. Since no ultra fast pump-probe experiments are planned, an accuracy of x-ray arrival at the instrument in the order of a few picoseconds is completely sufficient.

Photon diagnostics requirements

All experiments will require shot-to-shot diagnostics on intensity fluctuations, spectral profiles, pulse shapes and pulse lengths. The strong focusing eases many of the requirements of x-ray beam diagnostics. Most important are the flux and the spatial distribution at the focus. For reaching the smallest (100 nm) foci, sophisticated diagnostics for adjustment and performance verification is required. The samples are optically thin for x-rays and the transmitted radiation can be used for diagnostic purposes. All measurements must be feasible on a pulse-to-pulse basis.

Sample manipulation and environment

Since the quantities of material in the sample under study will be minute, there should be very little other matter in the beam path, and therefore, the sample (and indeed the entire experimental apparatus) will be in ultra-high vacuum similar to conditions in conventional electron microscopy. The interaction chamber will house the sample manipulation and injection hardware, instrumentation for various diagnostics, and an in-vacuum area detector system to record the diffraction images (Figure 6.4.75).

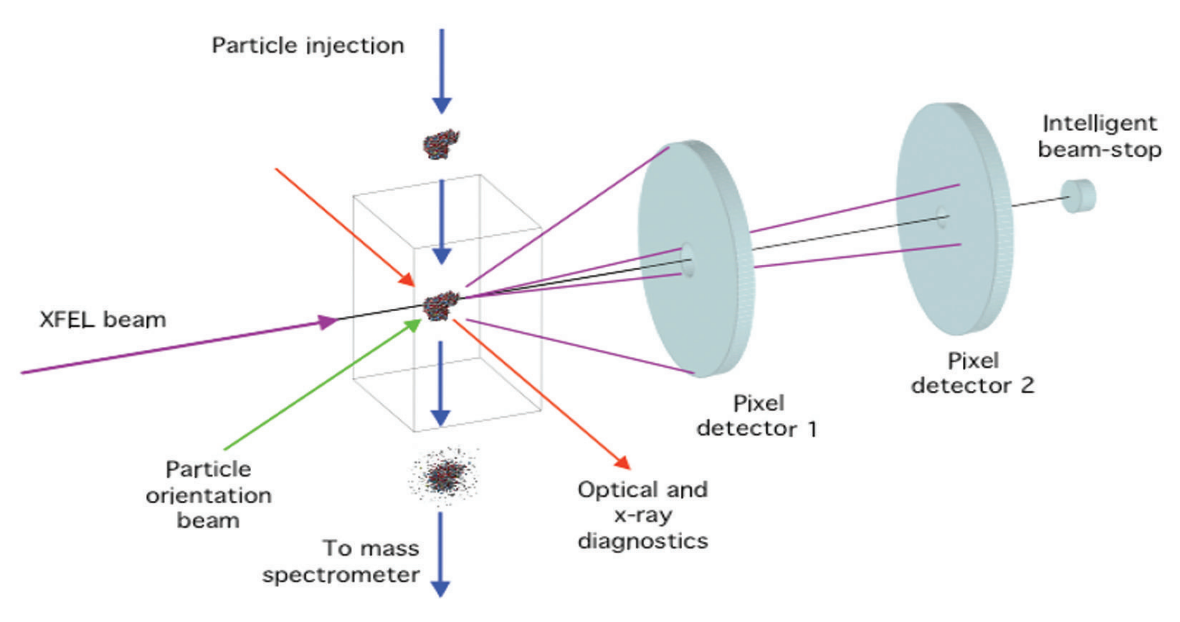

Figure 6.4.75 *Schematic diagram of the single-particle diffraction imaging experiment.*

We will use container-free methods based on spraying techniques to select and rapidly inject single hydrated molecules, nanoclusters of molecules, viruses and small living cells. Present sample injection and particle manipulation techniques will need to be improved significantly to achieve sufficient particle densities and injection precision. We will utilise electrospray ionisation (ESI) mass spectrometry and related ink-jet techniques as methods for introducing clusters, particles, viruses and cells with well controlled properties into the gas-phase **[6-376 – 6-380]**. We will explore techniques for trapping and aligning single particles in the focus, using optical, electrostatic, or electromagnetic methods. Sample diagnostics will be used to determine (a) if one or more of the particles were hit; (b) where the hits were along the beam path; and (c) how "good" were the individual hits. Such data can be obtained by measuring the UV-VIS light emission from the sample as it turns into a plasma, the electron and ion spectrum, and the fragmentation pattern at the end of the exposure. These data will be used in real time to veto bad shots.

In experiments on solid samples, the sample will be embedded into a thin layer of vitreous ice, positioned and manipulated in the beam using a cryogenic goniostat adopted from electron cryo-microscopy. Visual microscopy is used to manipulate the sample directly into the beam. The handling of these types of samples will be upgraded to be completely containerless by using a simple electrostatic system or special in-vacuum laser tweezers. This method would be ideal for diffraction imaging of membrane protein nanocrystals, but must be automated so that diffraction from thousands of individual crystals can be collected.

These two approaches require different detectors, and have different focusing requirements. Micron-sized objects will primarily be studied with the cryo-electromagnetic (EM) sample holder and experiments here will include studies on single cells, fibres (like Altzheimer fibres), organic and inorganic microstructures, micro- and nanocrystals, 2-D arrays, etc. Experiments using spraying techniques will be used to investigate nanometer-sized objects, including single virus particles, macromolecular complexes, and single biomolecules.

Initial experiments will use clouds of particles without stringent requirements, achievable with current methods, with and without alignment with a polarised laser. These will be improved upon, by first injecting short, concentrated bursts of particles into the beam focus area and relying on statistical positioning of individual particles. Such experiments require a focal spindle of about 5 mm length, shot-to-shot diagnostics to determine whether a particle was indeed hit by the x-ray beam and where the interaction happened along the focal spindle.

Detector requirements

The diffraction pattern will be recorded on a pixelated detector subtending a solid angle dependent on the desired resolution, with a hole in the middle to avoid the direct beam. There must be sufficient pixels in the detector to oversample the diffraction pattern, which depends on the sample size and desired resolution, as described below. The scattering from the sample covers a large dynamic range: it is strong very close to the central core, and at high angles there will be much less than one photon per pixel. Since the technique relies upon classifying and averaging a large number of patterns, the read noise must be considerably less than the photon count per pixel averaged over these patterns. Estimates of the noise level and dynamic range are given below, after first listing the requirements of pixel count and sampling. For larger structures, e.g. virus particles and single cells, a finer sampling will be needed than for smaller objects (Figure 6.4.76).

The detector size should not be larger than approximately 100×100 mm^2, in order to reduce the beam path from sample to detector. At better vacuum levels, this distance could be increased without increasing the background. Other desired parameters are a read-out speed per frame matching the pulse rate of the x-ray laser; a dynamic range of >10^6 for the entire pattern (for large single particles such as viruses); a dynamic range locally of ~1,000 (a dynamic range of 10^{6-8} could be achievable with two detectors, each with smaller range where the response of the second detector measuring the strong forward scattering component is reduced by appropriate means). Diffraction data may be supplemented by a lower-resolution image of the sample obtained with a **zone plate** or a **wave-front sensor** as it could prove valuable in enhancing the robustness of the oversampling phasing algorithms.

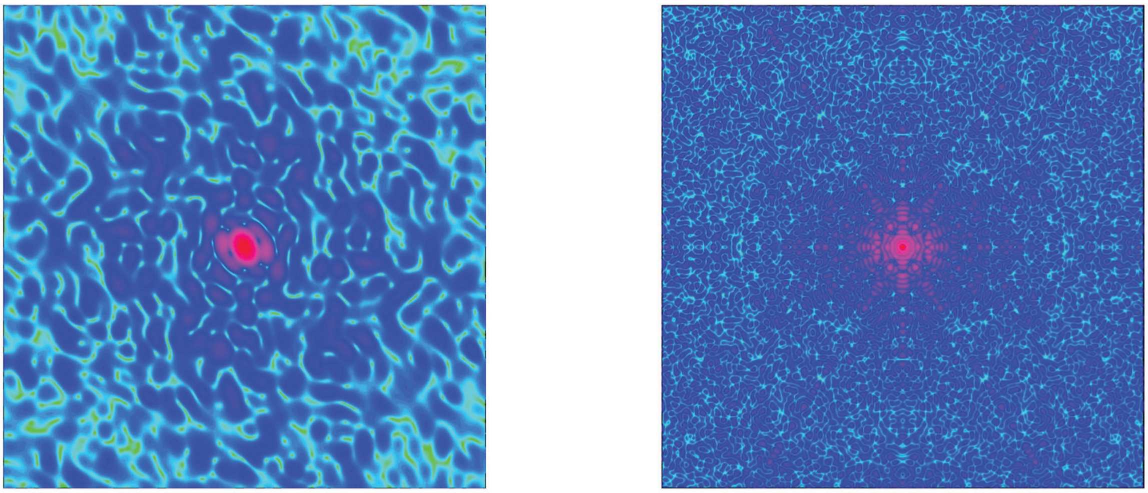

Figure 6.4.76 Planar section through the centre of the molecular transform of a small protein molecule (lysozyme, left) and of a larger virus capsid (tomato bushy stunt virus, right) at similar maximal resolutions. The level of detail is significantly different in the two pictures, and detectors should be able to resolve details in the patterns of even larger objects than a virus particle.

Pixel requirements

The pixel requirements simply depend on the number of resolution elements to sample the object of a given size at a given resolution, as described in Huldt et al. **[6-331]**, for example. To record to a resolution $f_{\text{max}} = 1/d$ requires a maximum scattering angle 2θ given by sin $\theta = \lambda f_{\text{max}}/2$. For an object of finite extent of width D, its molecular transform (in reciprocal space) is band limited. The Nyquist sampling rate of the transform is $1/D$ in each dimension. To measure this transform to a resolution $1/d$, in one dimension, requires samples from $-1/d$ to $+1/d$ or $2D/d$ samples. In real space this corresponds to samples at intervals $\Delta x = d/2$, which is the largest sufficient interval to measure periods larger than d. The detector measures the diffraction intensities, which are the modulus squared of the molecular transform, or equivalently, the Fourier transform of the object's autocorrelation function. For an object of extent D the extent of its autocorrelation is $2D$, which means that the diffraction intensities are band limited with a Nyquist rate of $1/(2D)$. The phase retrieval algorithms do not necessarily require sampling at this rate but experimental experience shows better results with higher sampling. Note that sampling at a higher rate than $1/(2D)$ does not add any information to the measurement, but may improve the signal-to-noise ratio of the measurement. However, pixelated detectors do not sample at points but integrate over the active area of the pixels. This corresponds to a Modulation Transfer Function (MTF) that may decrease to zero at spatial frequencies (at the detector) of period $2\,p$, where p is the pixel width. The effect of the MTF is to apply an envelope to the reconstructed real-space image, which should be no less than 0.7 at the largest radial extent of the object. As such, the detector's MTF influences the required pixel count. The number of pixels along the width of the detector is given by $N = 2\,D\,s\,/\,d$, where s is a sampling ratio per dimension (relative to the molecular transform Nyquist rate), with s

= 2 in the case of maximum required sampling (for which the 0.7 MTF level should occur for pixel frequencies no lower than $1/(4\,p)$).

We estimate the maximum requirement for number of pixels is $N = 2{,}000$, which corresponds to a particle size of 100 nm at a resolution of 1/(0.3 nm) and a sampling ratio of $s = 3$, or a particle size of 200 nm at the same resolution and a sampling ratio of $s = 1.5$. The larger sampling would be required if the detector MTF at $1/(2\,p)$ is about 50%. These are likely parameters for imaging nanoparticles, and for the imaging of arrays of biological particles. For the cow-pea mosaic virus (CPMV) test object described below, which has $D = 32$ nm, we require $N = 450$ pixels for $s=2$ and a resolution of 1/(0.3 nm). This reduced pixel count will be sufficient for most small biological samples, and a larger pixel count detector will be needed for larger objects (Figure 6.4.76).

Image reconstruction can be achieved with considerable missing data due to a "beamstop" or corresponding hole in the middle of the detector. However, the larger this region, the larger the uncertainty of various components of the image, and the less quantitative the image. If the central blank area covers no more than the central speckle, then the only missing data is essentially F_{000}. The speckle size for an object of width D is $1/D$ or $2s$ pixels in width. The dynamic range values given below were based on patterns with the central $2s \times 2s$ pixels excluded.

Simulations

Detector signals were computed for a test sample of a CPMV, with labelling of nanoclusters of Gold **[6-381]**. This may be an early test sample for LCLS and XFEL experiments. The atomic coordinates of the virus capsid (1NY7) were obtained from the EMBL-EBI Macromolecular Structure Database **[6-382]**. The capsid structure is hollow (since the DNA structure inside is unknown), and this was filled in with Carbon atoms in random locations and average density of 1.3 g/cm^3 (less mass than DNA). When the Gold labelling was applied, clusters were attached to the 65 symmetry sites (CYS 295) as described by Wang et al. **[6-380]**. Each Gold cluster was spherical with a diameter of 1.4 nm diameter, and contained 82 Gold atoms (density of 18.8 g/cm^3). The Gold increases the total scattered photons by less than 10%. The CPMV has a diameter of 32 nm, and a total molecular mass of 14.8 MDalton (13.7 MDalton without the Gold labelling). Larger sized samples have been simulated by arraying the CPMV structure in ordered and disordered groups of particles. The incident beam was modelled as a single-mode coherent Gaussian beam, with a waist diameter of 0.1 or 0.2 micron and a total flux of 10^{12} photons. The diffraction patterns were computed for a wavelength of 0.15 nm, with a programme that computes the scattered intensity from a collection of atoms illuminated by a focused single Gaussian mode, in the Born approximation (and no atom motion or ionisation):

$$I(\mathbf{k}_{out}) = \Omega r_e^2 I_0 \left| \sum_j f_j(\mathbf{q})\, u(\mathbf{x}_j) \exp\{i \mathbf{k}_{out} \cdot \mathbf{x}_j\} \right|^2 \tag{6.7}$$

where f_j is the structure factor for the j^{th} atom, r_e the electron radius, Ω the solid angle of a pixel, and an incident field described by Siegman **[6-383]**

$$u(\mathbf{x}) = u(\mathbf{r};z) = \sqrt{\frac{2}{\pi}}\,\frac{1}{w(z)}\exp\{-ikz + i\psi(z)\}\exp\left\{-r^2/w^2(z)\right\}\exp\left\{-ikr^2/(2R(z))\right\} \qquad (6.8)$$

with $w(z) = w_0\sqrt{1+(z/z_R)^2}$; $R(z) = z + z_R^2/z$; $\psi(z) = \tan^{-1}(z/z_R)$ (6.9)

The parameter w_0 is the waist radius (radius at which intensity is $1/e^2$), and is the $z_R = kw_0^2/2$ Rayleigh range. The length $R(z)$ is the radius of curvature of the wavefront at a distance z, along the propagation axis, from the waist. The wave-vector magnitude is defined as $k = 2\pi/\lambda$, and the momentum transfer $\mathbf{q}$ is given by $\mathbf{q} = \mathbf{k}_{out} - \mathbf{k}_{in}$ with:

$$\mathbf{k}_{in} = [\mathbf{x}_j, -R(z_j)]\,k/\sqrt{\mathbf{x}_j^2 + R^2(z_j)} \qquad (6.10)$$

Note that $\int_0^\infty 2\pi r\,u^2(r;z)\,dr = 1$, and thus the parameter I_0 is the total number of photons in the beam. In the simulations the intensity I is quantised and photon noise added (normally distributed with standard deviation $\sqrt{I}$).

Signal

Results of simulations are shown in Figure 6.4.77. For these calculations, the centre of the particle was always positioned in the centre of the beam, at the z location of minimum waist (z = 0). For the calculations shown here we used $I_0 = 10^{12}$ and w_0 = 0.1 μm (0.2 μm diameter waist) and w_0 = 0.05 μm (0.1 μm diameter waist). The calculations were carried out for an x-ray wavelength of 0.15 nm. The simulated array size was 422×422 pixels, with s = 2, corresponding to a resolution of 1/(0.3 nm). Most of the pixel values are zero or one photon, and the maximum and total photon counts (excluding the central 4×4 pixels) were 1,530 and 7.3×10^4, respectively, for the 0.2 μm diameter waist and 5,540 and 3.0×10^5, respectively, for the 0.1 μm diameter waist.

Note that larger samples do not necessarily give larger signals; there are a fixed number of photons per pulse and samples larger than the beam will require a proportionally larger beam and hence, lower fluence. Larger signals will be achieved with thicker objects and objects of higher-Z, and as such, the experiments of nanoscale inorganic samples will give stronger signals. Larger signals will also be achieved with arrays (2-D or 3-D) of particles, due to coherent addition in the Bragg directions.

Similarly, the imaging of large objects at low resolution (e.g. single-shot imaging of micrometre-sized cells beyond the radiation damage limit) will produce larger photons per pixel due to the coherent addition, in the forward direction, of scattering from atoms within a single resolution voxel **[6-384]**. For the case of crystals and arrays of identical unit cells, the photon count will increase in the Bragg peaks by a factor n^2, where n is equal to the total number of unit cells illuminated.

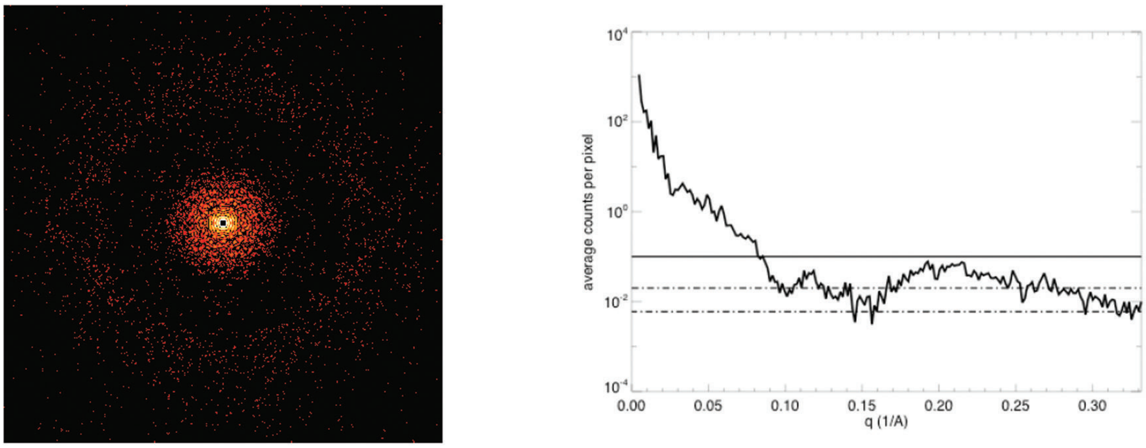

Figure 6.4.77 *Simulated diffraction data from the (CPMV test object, for a beam waist diameter of 0.2 μm. Total photon number in the incident beam was 10^{12}. The array is 422×422 pixels, corresponding to s=2, and a resolution of 1/(0.3 nm). The central 4×4 pixels were blocked. Total integrated photons are 7.3×10^4. The intensities are displayed on a logarithmic greyscale. Away from the centre most pixels have one or no photons. The maximum photon count is 1,530. The plot shows the radial average of the photon counts. The solid line is at 0.1 counts, the minimum counts needed to classify* **[6-331]**, *and the dotted lines denote the noise level for 10 and 100 averages, for a detector noise of 0.06.*

The signal between the Bragg peaks will only increase in proportion to n, but this signal can be built up by averaging, once classification has been achieved on the Bragg peaks. For a 2-D crystal with n unit cells, if the beam size matches the object size then the incident fluence will be proportional to $1/n$ and the Bragg peaks will increase in photon count by n, not n^2. For the simulations we have run on 2-D and 3-D crystals of 5×5 and 5×5×5 unit cells, we typically see a factor <10 increase in photon count. In all these cases, the pattern is strongest near the zero frequency and locally (within a 10×10 pixel patch) the intensity changes by a factor of about 1,000.

Noise

Data sets will be assembled by classifying patterns into classes of like-orientation and averaging patterns within each class. Huldt et al. **[6-331]** showed that accurate classification could be performed with as little as 0.1 photon counts, on average, per pixel, at the highest resolution of the pattern. For the CPMV particle simulation, this means we can classify out to the full resolution of the simulation, of 1/(0.3 nm), for the case of a 0.1 μm diameter waist (Figure 6.4.78). This means that when we sum together ten diffraction patterns the accumulated noise must still be less than one photon. Choosing a noise level of 0.2 photon (SNR = 5, Rose criterion) in the ten-frame sum, the noise per pixel for each pattern should be no larger than $0.2/\sqrt{10} \sim 0.06$ photons per pixel.

Many of these requirements are in line with general directions currently driving the development of x-ray area detectors for synchrotrons and other experiments planned for the x-ray lasers. The detectors needed for our studies are relatively small, and that alleviates some of the difficulties in developing faster detectors for our studies.

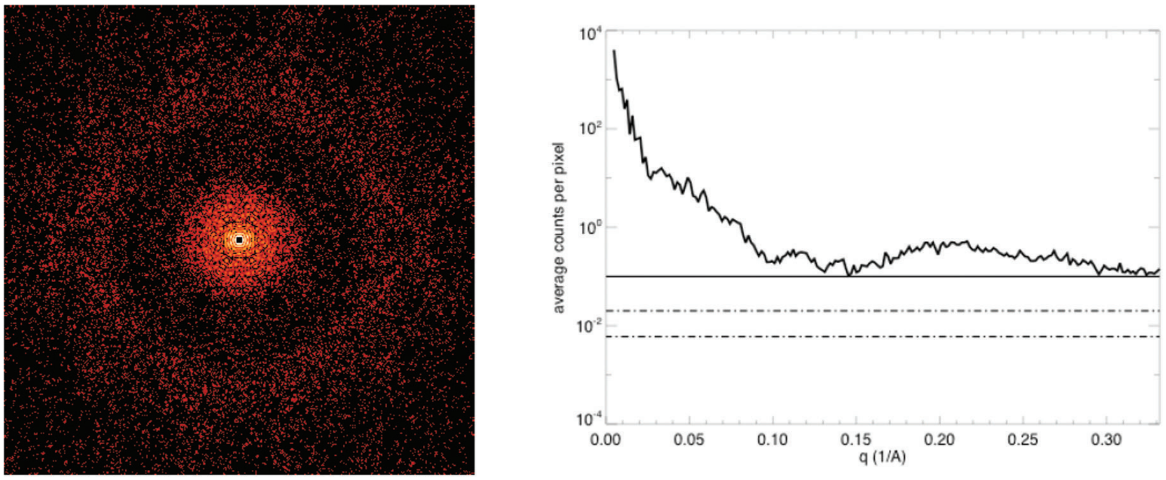

Figure 6.4.78 *Simulated diffraction data from the CPMV object, for a beam waist diameter of 0.1 μm, while all other parameters stayed the same as for Figure 6.4.77. The maximum photon count is 5,540, excluding the beamstop. The total integrated photons is 3.0×10*^{5}*. The plot shows the radial average of the photon counts. The solid line is at 0.1 counts, the minimum counts needed to classify, and the dotted lines denote the noise level for 10 and 100 averages, for a detector noise of 0.06 photons per pixel.*

Channel optics for detector shielding

We may find it necessary to shield the detector from scattering from gas or objects upstream from the sample, even with the judicious use of the apertures mentioned above. Ideally, the detector would only be sensitive to rays travelling in directions emanating from the sample position, so it would not detect scatter from any other object in the beam. Since downstream from the sample and off the axis of the direct beam, the x-ray intensity is very weak (the scattering from the sample) it may be feasible to use structures such as radial Soller slits (or, more precisely, square-pore capillary arrays) which accept only the diffracted light from a volume surrounding the sample (Figure 6.4.79).

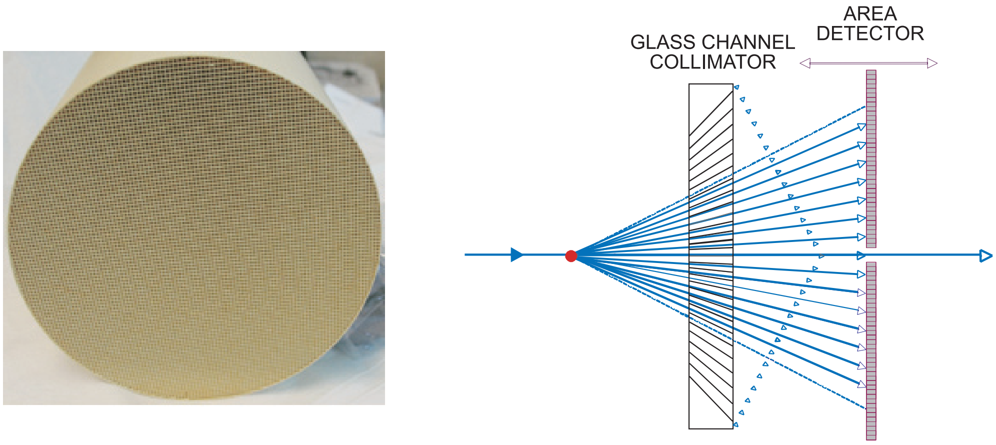

Figure 6.4.79 *Glass Soller collimator for filtering out stray light at the detector. These can be manufactured to conical shapes, and can have tapered channels with dimensions down to about 10×10 μm*^{2}*.*

Visible laser requirements

No short-pulse laser for time-resolved pump-probe experiments is required to begin with. However, such experiments are likely to be carried out in the future and the design of the instrument must allow access to a state-of-the-art ultrashort pulse laser for UV-IR radiation. As discussed in Section 6.4.7.1, alignment of single particles or clouds of particles will be performed using a polarised near-infrared laser, focused to an intensity of about 10^9 W/cm^2. For adiabatic alignment in the non-viscous environment of a pure vacuum, pulse durations longer than 100 ns are required. If the beam is focused down to 10 micron, this requires a laser with pulse energies of more than 100 µJ, or alternatively, a 1 kW continuous laser.

Computer hardware and software for data acquisition and data processing

Collecting, handling, and storing very large data sets

As in crystallography, the computer is a major component and algorithms are required to generate images from the measurements. Depending on the complexity of the molecule to be studied, the size of a diffraction pattern will be $N \times N$ pixels, with N = 100 to 1,000 (some applications may require N = 10,000). The need to build up a large enough signal to atomic resolution and to obtain full 3-D information may require about 10^5 - 10^6 diffraction patterns to be collected from a series of identical particles. This corresponds to about 40 Tb of data for N = 1,000. This volume of data could be collected in a day's operation and computing and data handling resources must be able to keep pace with this generation rate.

Data processing

The processing of the non-crystalline diffraction data, with reconstructed electron density as the end result, consists of two distinct stages. In the first, a large number of noisy 2-D diffraction patterns must be given orientations in 3-D reciprocal space and merged into a single 3-D diffraction pattern. In the second stage, phases are derived from the 3-D diffraction pattern based on iterative phase-retrieval methods from the over-sampled diffraction data set.

Image classification

The patterns will be collected from particles at random and of unknown orientation, so these patterns must be aligned with each other and assembled into a 3-D data set. Due to the large number of images required for an adequate signal-to-noise ratio in coherent x-ray setting, it may also be necessary to significantly advance the power of the basic algorithms used, e.g. in EM studies. The standard approach has been to divide the merging stage into two operations: classification and orientation. Classification corresponds to applying criteria to establish which 2-D diffraction patterns have similar orientations and can, therefore, be averaged to improve the signal-to-noise ratio. Image classification can be done successively, starting at low resolution and performing finer groupings as the resolution increases. The requisite algorithms are easily parallellised. Once the diffraction data is classified and averaged to achieve the required signal-to-noise ratio, it must be assembled into an N^3 array (now about 16 Gb).

Data reduction and merging

The relative orientation of the averaged images may be determined through the method of common lines, a technique widely used in electron microscopy, where the micrographs represent planar sections through the centre of the molecular transform. Diffraction images are different in that they represent spherical sections of centric objects. Each pair of images will intersect in an arc that also passes through the origin of the molecular transform. If the signal is strong enough for the line of intersection to be found in two diffraction images, it will then be possible to establish the relative orientation of these images.

We note that due to the curvature of the sections, the common arc will provide a 3-D fix rather than a hinge-axis. Moreover, the centric symmetry of the modulus of the molecular transform ensures that we obtain 2 x 2 independent repeats of the common lines in the two images. This feature makes for determining sample orientation redundant, and is unique to the diffraction geometry. It can lead to a complete determination of the relative angles of the diffraction patterns.

The standard approach to merging, i.e. classification followed by orientation, suffers from some arbitrariness that can be circumvented without compromising performance. Primary among these is the need to establish, at the outset, the number of orientations that will be averaged and to choose criteria to define membership in the orientation classes (e.g. closeness to representatives).

In an alternative approach, each 2-D diffraction pattern will automatically be assigned a unique set of Euler angles determined by a pseudo energy functional defined on an associated “adjacency graph,” which is a natural encoding of the likelihood that two patterns are close in orientation given the applicable model of noise (e.g. Poisson counting statistics). Based on preliminary studies by Elser **[6-357]**, it appears that computationally the most challenging step in this approach is not the minimisation of the pseudo energy functional but rather, the initialisation of the minimisation, which corresponds to embedding the adjacency graph into the space of orientations so that the topology is correct.

The solution to this problem, and in effect the rate-limiting step of the entire approach, is to obtain the four lowest eigenvectors of the adjacency matrix using the Lanczos sparse matrix algorithm. A particularly attractive feature of this initial embedding step is that it simultaneously serves as a diagnostic for data acquisition. From the spectrum of the lowest eigenvalues one can readily assess the degree to which the collected data forms a quasi-continuum in the space of orientations, and assembly of the 3-D diffraction pattern can proceed. This diagnostic is fast because it acts on a relatively raw form of the collected data (adjacency graph) and could perhaps be used in “real time” during data collection.

Phasing

The 3-D structure is related to the measured amplitudes through a 3-D Fourier transform. Since only the Fourier magnitudes are measured, phase retrieval methods must be employed to derive the phases and so determine the structure. The most promising approach is a method of generalised projections, in which known constraints are iteratively applied. This requires many thousands or tens of thousands of iterations, with two or more N^3 FFTs per iteration. The FFT is a demanding algorithm for parallel machines, and performance is usually limited by communication speeds. Efficient routines can be achieved when the number of nodes is equal to N, in which case two across-processor transposes are required. In general, the reconstruction problem requires $1{,}024^3$ FFTs to be performed in less than a second.

Hardware

A dedicated computer hardware configuration will be needed with large storage capacity. The primary objective will be to orient the patterns. Because the data rate in the experiments is very high (around 400 Tb/day near 100% hit rate), this will be a computing cluster where each node is responsible for either identifying members of particular orientation classes or establishing connectivity in the adjacency graph. A separate cluster will be used in the later steps of structure determination.

6.4.7.3 Realisation of the instrument

The experiment requires an instrument at SASE 1 (SPB 1 – Hard XFEL radiation). For a description of the SASE 1 beamline see Section 6.2.4.1. All studies discussed in Section 6.4.7.1 will be carried out using this instrument. The experiments require highest achievable intensities. For large particles (>100 nm) the use of a perfect crystal monochromator (optional) is required to reduce the bandwidth. The SASE 1 beamline provides a double-mirror double-crystal setup, allowing both direct beam and monochromatised radiation to the instruments. All optics needs to be flat and preserve incident wavefronts as good as possible. Strong focusing will be achieved near the samples. The monochromator provides the opportunity to use third harmonic radiation.

SPB 1: Hard XFEL radiation

Since the preservation of the wavefront is crucial in these experiments the number of optical elements needs to be kept small. Therefore, the instrument will best be located in the forward direction of the beam coming from the double-mirror/double-crystal unit. The following elements belong to the SPB 1 instrument inside the experimental hall. They are depicted in the schematic layout of that instrument in Figure 6.4.80 and are described in Table 6.4.16. First optical element will be optional x-ray pulse compression optics. Apertures define the beam profile in front of two focusing optics for focal spots 1-10 μm diameter and for extreme focusing in the order 100 nm.

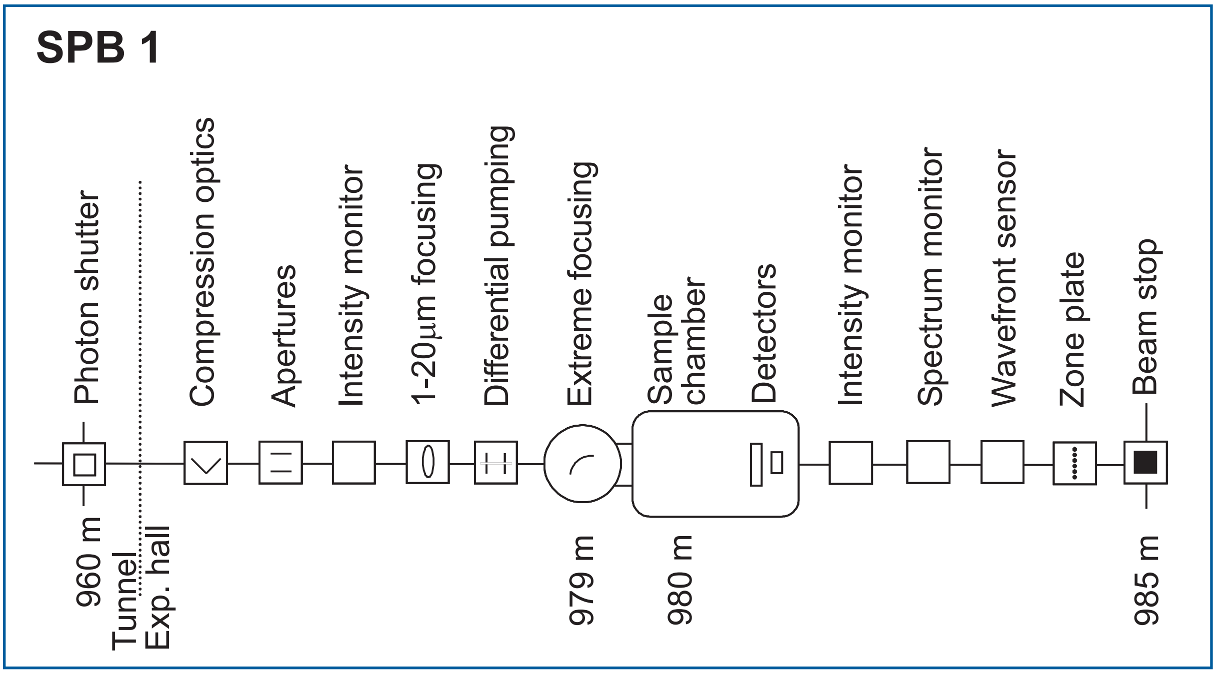

Figure 6.4.80 *Schematic layout of the SPB 1 instrument at the SASE 1 beamline. Distances are given in relation to the end of the undulator.*

For the larger focus, in-line optics would be ideal, but these are generally chromatic. Thus, the spatial performance at the focus is limited by chromatic blurring (compare Section 6.2.2). Reflecting optics, such as an ellipsoidal mirror, provide better performance but generate an angular deflection. For extreme focusing a pair of dynamically bent flat mirrors (K-B geometry) will be employed. This optic needs to be very close to the sample position. Apertures between the optics and the sample will both reduce background and provide shielding of the optics from debris. At the sample location the beam diameter is ~1 mm (FWHM; 12.4 keV) and mirrors need to operate at grazing angles of at least 4 mrad to accept 6σ of the beam. The resulting mirror length is ~600 mm.

The vacuum system of the beam transport will be connected to the sample chamber by means of a differential pumping section. The sample chamber assembly includes the extreme focusing optics, the interaction area with access for spraying techniques, cryo-sampleholder and for diagnostics systems, and the in-vacuum detector system. Sample environment diagnostics include fluorescence monitors to position hits along the x-ray beam path, mass spectrometer to analyse fragmentation, electron spectrometer and a visible light microscope including CCD camera. Behind the detector diagnostics for photon flux, spectral distribution ($\Delta E/E \sim 1\text{-}2\times10^{-4}$) and spatial profile or wavefront is required. All diagnostics need to operate in the single-pulse mode.

At the instrument a laser system is available. This system will be used for sample alignment techniques first. Provision for future installation of an ultrashort pulse laser for pump-probe experiments will be made.

Item	Purpose	Specification
Compression optics	Pulse compression to 5-10 fs with high reflectivity	Maintain x-ray duration, maintain wavefront
Slits/apertures	Beam definition, beam halo cleaning, apodising techniques to reduce scatter	0.25 µm accuracy, 1 µm repeatability
Intensity monitor	Measurement of incident photon flux	Transmissive (<5% absorption), single pulse measurement, relative accuracy $<10^{-3}$
Focusing optics	Generate 1-20 µm focus	Int. reflectivity ≥80%, stability 0.5 µm
Differential pumping	Separation of beamline and instrument	
Focusing optics	Generate 0.1 µm focus, K-B geometry	Int. reflectivity ≥80%, stability 0.1 µm
Sample chamber	Spraying techniques, cryo-sampleholder, sample diagnostics	UHV (10^{-8}-10^{-6} mbar)
Detector	Two 2D detectors for low and high count rate	Size minimum 1K×1K, dynamic range 10^3, in-vacuum opration, central hole maximum 4×4 pixel
Intensity monitor	Measurement of transmitted photon flux	Transmissive (<5% absorption), single pulse measurement, relative accuracy $<10^{-3}$
Spectrum monitor	Measurement of distribution	Single pulse measurement, relative accuracy $<10^{-3}$
Wavefront sensor	Measurement of spatial distribution at focal spot, adjustment of extreme focusing optics	$\lambda/10$ resolution
Zone plate	Beam profile measurement	
Alignment unit	Positioning and position verification	Permanently operating, accuracy ~100 µm
Lead hutch	Radiation protection, temperature stabilisation, laser protection	4×10×3.5 m^3 (W×L×H), ±0.5° thermal stability
Control hutch	Operation of the instrument	Working environment (noise, temperature, light)

Table 6.4.16 *Elements and specifications of the SPB 1 instrument.*

6.4.8 Research and development on x-ray instrumentation

Instrumentation for experiments using XFEL radiation creates new challenges in an area that has already witnessed an active development over the last decades driven by the synchrotron radiation community. To the already excellent properties of synchrotron radiation XFEL radiation adds the extremely high degree of transverse coherence, the thousand times shorter pulse duration and the high flux per pulse. Many measurements can be achieved in a single pulse exposure thus providing a tremendous advantage for time resolution. On the other side, single pulse measurements exclude averaging and will, thus, be determined by fluctuations.

The various experiments discussed before in this chapter are all based on the particular properties of XFEL radiation. The preservation and, eventually, the improvement of them is one of the challenges the new sources are facing. In this section a few fields are identified where the preservation and application of XFEL radiation properties will have a strong impact. Although current knowledge is advanced enough to design x-ray instrumentation for XFEL experiments, development will need to continue, once XFEL sources become available for experiments.

Obvious fields for continued development are the preservation of wavefronts using mirror or crystal optics and advanced optics schemes, e.g. for pulse compression, slicing or splitting. Also, the area of x-ray detection and diagnostics methods requires continued attention since the operation of XFEL sources is expected to lead to more sophisticated experiments with more challenging requirements. In the same direction, one expects that the particular properties of XFEL radiation lead to new advanced techniques, both for diagnostics and experimental schemes.

Although the properties of XFEL radiation and their application are the focus of interest, the following areas of research and development also require an experimental programme that, to a large extent, could use spontaneous synchrotron radiation. This radiation, albeit exhibiting less brilliance than the XFEL radiation, is still extremely well collimated, very intense per pulse and ultrashort in pulse duration. Parameters for spontaneous radiation, due to the high electron energy, do not vary significantly over a large photon energy range from ~10 keV up to ~100 keV (compare Section 5.3 and Table 5.3.2).

6.4.8.1 Scientific case

Experimental programme

In the following we describe four exemplary areas of research and development. These areas are directly related to the key properties of XFEL radiation and the requirements of experiments with XFEL radiation. Firstly, the high degree of coherence of XFEL radiation and the high brilliance poses a challenge for optics development. Diffraction-limited optics for 0.1 nm radiation are difficult to achieve, and the development of optics that preserve and exploit the wavefront, in relation to the coherence of the radiation is needed.

Secondly, the exciting properties of XFEL radiation such as pulse duration and photon number lead to a desire to apply new schemes for x-ray optics, only applied in the optical regime as yet. Thirdly, the requirement for sophisticated detection and pulse-by-pulse diagnostics methods for XFEL experiments makes a development programme necessary to improve current methods and develop of new ones. This involves the development of x-ray detectors. Finally, completely new schemes for x-ray experimental techniques have been proposed.

I. Wavefront preserving optics

The consequences of imperfection of optical surfaces on the properties of the x-ray pulse have been discussed in Section 6.2.2. Since current x-ray sources do not have a substantial coherent flux, the related issues cannot be solved yet and are of particular importance for XFEL instrumentation and research.

Mirrors

Surface roughness and slope error are important parameters affecting the performance of x-ray optics. The relation between both parameters and the consequences for the performance of x-ray optical elements is not yet understood **[6-386]**. Present metrology is near its resolution limit and new techniques need to be established or existing techniques reviewed to enhance the current understanding significantly.

Combining different laboratory metrology techniques in-situ with an x-ray beam of high coherence degree will provide new insights and lead to a better description of wavefront propagation by mirrors and other optical elements. In-depth understanding of the interplay between the shape function of an optical element and the variation in the propagation of a wavefront will lead to a new and better definition of these optics. This improved understanding might also lead to a reduction in some of the currently extremely challenging parameters.

Crystal optics

Perfect crystal optics is an important asset for the transport of radiation without disturbing wavefront properties. Single crystals with a high degree of perfection are available for Silicon. For reasons of energy dissipation and heat load, Diamond is an interesting alternative, however, its perfection is yet not high enough to reflect x-rays without damaging wavefront properties. The continued development and monitoring of newly grown Diamond crystals is, therefore, important.

In addition to the perfection of the crystal material, the preparation of the crystals must be very precise. Asymmetric orientation of reflecting planes leads to tilting wavefronts with respect to beam propagation which is important when trying to obtain the highest possible time resolution. Again, surface roughness of crystal needs to be considered in the full description. Investigation of wavefront properties after crystal reflection will firstly allow experimental validation of wavefront propagation codes and secondly, the measurement of crystal optics performance.

Heat load

Optical elements at the European XFEL undergo enormous heat load exposure in using the pulse train feature of electron acceleration. Temperature cycles of 50°C on surfaces in crystals or at mirror surfaces have been calculated. Several techniques have been proposed to solve this problem (see Section 6.2.2). Validation and further development will again require determining the performance of the optical system in terms of wavefront preservation.

II. Advanced x-ray optic schemes

Pulse compression

Generation of x-ray pulses shorter than the design value of 100 fs would lead to improved capabilities for several experiments. Amongst the methods that have been proposed are x-ray optics methods using multilayers or crystals. Manipulation of wavefront orientation and bandwidth chirping are techniques with a high potential in this area. Experiments investigating the spatial-temporal properties of reflections provide the necessary information to verify and improve the various concepts. The experiments will investigate properties of x-ray pulses before and after reflection by these optical elements spatially and temporally resolved. In particular, the time domain diagnostics will require significant improvement compared to current technology.

Beam-split-and-delay

The high number of x-ray photons in a single XFEL pulse raises the interest in x-ray experiments. Pump-probe techniques will be of interest and require splitting one XFEL pulse into intense pump and weak probe pulses. Other experiments, e.g. auto-correlation measurements, require equal splitting. Furthermore, the pulses need to have an adjustable time delay. Also, the selection of the other radiation properties, e.g. the photon energy, bandwidth or harmonic number will be of interest. First x-ray optics for splitting into two equally strong pulses used in XPCS techniques (see Section 6.4.4.1) are currently under development. Advanced x-ray techniques (see IV. below) will be based on these developments.

Phase modulation optics

Due to the high degree of coherence, the propagation and reflection of the x-ray pulse will strongly depend on wavefront properties. The importance of preserving the wavefront was stressed before. Similar to techniques applied in the visible light optics domain, coherent x-ray radiation also offers the possibility of building phase modulating optics. For focusing, this technique is already in place, but other domains are very attractive. An example is the development of slit systems that do not have singularities on the density modulation, thus, reducing coherent scattering.

III. X-ray detection and diagnostics methods

Photon flux and spatial distribution

Measurement of photon flux per pulse is an important diagnostic and will be required for XFEL experiments from the very beginning. It must allow operation in transmission and the simultaneous measurement of the spatial distribution of radiation will be a big asset. Currently proposed techniques use ionisation of gases. Although the current gas ionisation detectors provide the possibility of absolute calibration, a higher accuracy in the measurement of the photon number is desirable. Development of new monitors using gases or solids requires x-ray beams of well characterised properties that can be attenuated over a wide range.

Coherence

The degree of transverse and longitudinal coherence is crucial to many of the techniques and scientific applications. Many experimental methods determining coherence parameters have been proposed, but as yet, no real diagnostics monitors have been developed. In the long-term, monitoring of coherence properties should be possible on a pulse-by-pulse basis.

Time

Time domain diagnostics includes the measurement of the x-ray pulse arrival, its duration and eventually, its temporal distribution. For the optical domain these techniques are all well-established by now. However, for photon energies beyond the UV these techniques are not yet available. Many research projects are focusing on the different aspects of these measurements. Certainly, the measurement of the temporal distribution is very challenging, requiring for 12 keV x-rays a resolution of ~100 as to resolve the spike structure. Since this distribution is fluctuating for every pulse, the measurements need to be done pulse-resolved. Cross-correlation experiments using ultrashort pulse optical laser radiation (see below) are promising in this area.

Wavefront techniques

Using wavefront measurement techniques to diagnose the performance of the x-ray beam has been mentioned in Section 6.2.2 and before in this section. Many of the scientific experiments have further requested wavefront sensors in order to enable the alignment and characterisation of the focal spot at the sample location. Current developments have shown that wavefront sensors with high resolution in the order $\lambda/10$ at 0.1 nm can be realised. A major difficulty with the present designs is their limited dynamic range and the need to place the sensors into the direct beam. Therefore, in order to enhance the versatility and flexibility of these measurements, development of the sensors needs to be pursued.

X-ray detectors

The development programme for x-ray detectors for XFEL radiation is described in Section 6.5.4. It will include 0-D, 1-D and 2-D detectors. The response of the detectors to intense and ultrashort x-ray pulses needs to be analysed using lower intensity radiation of otherwise similar properties, and then XFEL radiation. Specific detector materials may also prove meaningful for diagnostics techniques for XFEL radiation, e.g. Diamond detectors are very promising for photon flux and beam profile measurements.

IV. Advanced techniques

Large solid-angle optics for single-shot experiments

For a signal to be meaningful for spectroscopy experiments investigating x-ray emission from atoms, plasma, liquids or solids, as much signal as possible for a single shot exposure will need to be collected. Typically, a spectroscopic resolution of 10^{-4} is required, thus, limiting the acceptance angles of standard spectrometers. Proposals for building systems with large acceptance angles using a series of crystals have been put forward and these will use either spherically or cylindrically curved analysers **[6-387]**.

Auto- and cross-correlation techniques

In particular for time domain studies and time domain diagnostics, the application of auto- and cross-correlation techniques will be required. While spontaneous radiation does have three orders of magnitude less flux then XFEL radiation, this flux will be rather similar to what can be used for diagnostics at the XFEL beamlines. Cross-correlation techniques using visible laser radiation are most promising due to the enhanced cross-sections compared to auto-correlation experiments. The latter experiments are feasible at full scale using XFEL radiation; spontaneous radiation will provide the possibility to do precursor studies.

X-ray photon pulse echo experiments

In investigating dynamics, inelastic scattering techniques probe the energy domain and direct techniques the time domain. While energy domain techniques benefit mainly from the increase in average brilliance of the European XFEL, time domain techniques will, in addition, profit from the ultra-short pulse duration. The development of a technique is proposed that makes use of the ultrashort pulse duration to study microscopic dynamics directly as a function of time. The idea is to transfer the scheme of the (resonant) neutron spin echo technique **[6-388]** to the x-ray case. Information on the sample dynamics is obtained by recombining two pulses which have been elastically scattered by the sample at an adjustable time delay and observing the interference pattern of the two pulses. As in the neutron case, information on the intermediate scattering function S(q,t) is obtained by a steady state experiment, without the need for fast detection.

The experiment consists of two x-ray delay lines located before and after the sample. The first part prepares two pulses, separated by an adjustable delay so that both pulses probe the sample structure at different times. The second delay line adds a second delay of exactly the same quantity so that the pulse delayed in the first optics and the one in the second optics overlap precisely. Consequently, three pulses arrive at the detector, where only the middle is the coherent sum of the two pulses with identical flight time. Only this pulse contains the information, whereas the pulses preceding and trailing provide only inherent background. The detector integrates all three pulses. Delay times from 100 fs up to the nanosecond regime are of interest here.

Possible applications of this technique will cover quasi-elastic scattering to probe diffusive motions or relaxation and inelastic measurements with high resolution. The wide time-interval offered by this technique is particularly valuable for systems showing non-exponential behaviour of the relaxation function, like glasses or bio-molecules. In the inelastic (short time, few picosecond) regime, the phonon density of states, in particular that of low-lying excitations, will be accessible.

X-Ray Transient Grating Spectroscopy (XTGS)

At an XFEL source the transient grating technique presently used for visible light studies **[6-389]** can be extended into the x-ray regime. With this technique the incoming beam is split into two transversely coherent beams which are crossed under an angle s to produce a standing wave field with periodicity $d=k_0 sin(s/2)$, where k_0 is the wavevector of the incident beams. The value of d can be in the range from one to several hundred nanometres.

If a sample is placed in the standing wave field it will produce a periodic density modulation in the sample which has the same periodicity as the standing wave. If an XFEL is used, this modulation is formed during a single laser pulse, and after the pulse, relaxation will occur. A second pulse with a delay to the first one forming the standing wave pulse, can now be used to probe the periodic modulations within the sample by means of x-ray scattering. If the modulations relax, the scattered intensity will increase. Therefore, if the measurement is repeated for different time delays, the time course of the relaxation can be followed. This can reveal valuable information about the local dynamics within the sample on a nanometre length scale.

6.4.8.2 Requirements of the instrument

The development projects for x-ray instrumentation require an instrument for R&D so that experiments needed to prepare specific projects and to validate the performance of XFEL-related x-ray instrumentation can be carried out. Once successful, the x-ray techniques will be available for all experiments at the European XFEL. Since many of the techniques use radiation much less intense than the XFEL radiation itself, the instrument could use the ultra-short and tunable spontaneous radiation from the U 1 undulator.

Spectral requirements

The experiments will require mirror-only and monochromatic radiation covering, in principle, all photon energies available at the European XFEL. However, we will restrict discussion in the following to the hard x-ray regime available at the U 1 beamline.

X-ray optics requirements

A versatile setup to insert various optical elements is requested. Since one of the main areas of work will be coherence properties, particular care has to be taken not to introduce wavefront errors by permanent optical elements. In-line optics will be used to focus the beam to approximately 100 µm spots.

Time domain requirements

Experiments will make use of single- and multi-pulse operations. The latter enhances the flux-per-pulse train considerably. In the timing experiment, the synchronisation between the x-ray pulse and optical laser needs to be accurate to well below the x-ray pulse duration.

Photon diagnostics requirements

Various detector systems for diagnostics of flux, spectral and temporal properties, and spatial distributions are needed. To begin with these will serve as references when developing new techniques and instrumentation.

Sample manipulation and environment

No particular samples will be investigated using this instrument. However, very precise x-y-z translation and three rotational degrees of freedom will be required. For the in-situ measurement of mirror performance, high performance metrology tools such as long-trace profilers and near-field microscopes need to be installed.

Detector requirements

Most experiments investigate intense reflection or diffraction spots. Therefore, point-like detectors can be applied in many of the experiments. These should be capable of reading at the 5 MHz repetition rate of the machine. A 1-D detector with sufficient spatial (10-50 µm) and/or angular resolution (10-50 µrad) in one direction is requested. Slow (10-50 Hz) 2-D detectors with CCD-like performance will be needed, too. Finally, for the performance of many optical systems an ultra-fast (~100 fs) x-ray streak camera will enable a lot of direct time domain measurements.

Visible laser requirements

For the cross-correlation experiments, access to the ultra-short pulse laser system with the possibility of using frequency multiplying is needed. Synchronisation of laser and x-ray pulses better than the pulse duration is required. Otherwise the measurement of the relative arrival-time is required.

6.4.8.3 Realisation of the instrument

The following describes an R&D instrument (RAD 1 – Hard tunable x-ray radiation) that will be located at the U 2 beamline. For a description of the U 2 beamline, see Section 6.2.4.5. This beamline cannot provide soft x-ray radiation, and experiments in these areas need to be carried out at other instruments. The instrument uses the double-mirror double-crystal system of beamline U 2. The collimating lens near the source increases flux and limits the beam size at the instrument. However, for experiments sensitive to coherence it has to be removed. A second, refocusing lens in 1:1 geometry provides a 100 µm focal spot at the instrument, thus, increasing intensity. The monochromator provides the opportunity to use third harmonic radiation.

RAD 1: Hard tunable XFEL radiation

The RAD 1 instrument should be located in the forward direction of the beam coming from the double-mirror/double-crystal unit in U 2 so that coherence studies, which benefit from minimising the number of optical elements disturbing the wavefront parameters, can be carried out. The following elements belong to the RAD 1 instrument inside the experimental hall. They are depicted in the schematic layout of that instrument in Figure 6.4.81 and are described in Table 6.4.17. Beam-defining apertures, followed by an intensity monitor and a spatial beam profile monitor will precede the first sample mount that includes metrology instrumentation. Behind, a mount for an optional strong focusing optic and a second intensity monitor follow. At less than a metre distance the sample diffractometer provides versatile mounting. The diffractometer can be removed from the beam.

The vacuum system of the beam transport will end in front of the sample mounts. Beryllium windows are used at this instrument. Subsequent intensity monitors, using gas ionisation techniques, can also be capsulated using thin Beryllium windows. Behind the detector, diagnostics for intensity, spectral distribution ($\Delta E/E \sim 1\text{-}2\times10^{-4}$), spatial profile and wavefront is required. Single-pulse mode operation of the diagnostics is preferred. At the instrument an ultra-short pulse laser for pump-probe experiments could be used.

A specialty of the RAD 1 instrument is that the beam will be transferred to a second instrument mounted behind. It is not anticipated that both instruments will be operated at the same time and all RAD 1 instrumentation must be mounted so that it can be moved out of the beam. The beam-defining apertures and the intensity and spatial beam profile monitors can be used for both instruments.

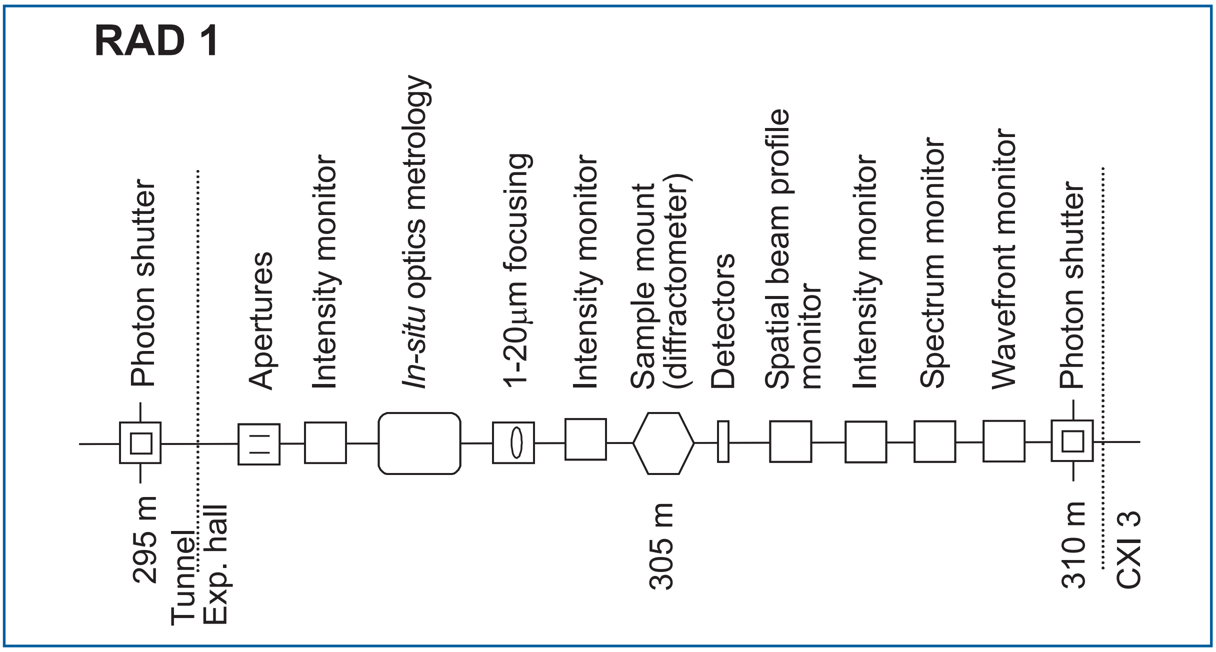

Figure 6.4.81 *Schematic layout of the RAD 1 instrument at the U 1 beamline. Distances are given in relation to the end of the undulator.*

Item	Purpose	Specification
Slits/apertures	Beam definition, beam halo cleaning, apodising techniques to reduce scatter	0.25 µm accuracy, 1 µm repeatability
Intensity monitor	Measurement of incident intensity	Transmissive (<5% absorption), single pulse measurement, relative accuracy $<10^{-3}$
Sample mount	In-situ measurement of mirror using ‘standard’ metrology	x-y-z translation, three rotations
Focusing optics	1-5 µm focus, refractive lenses or K-B system	Integrated reflectivity ≥80%, stability 0.1 µm
Intensity monitor	Measurement of incident intensity	Transmissive (<5% abs.), single pulse measurement, relative accuracy $<10^{-3}$
Sample mount	Diffractometer	
Detector	0-D, 1-D pixel detector (0.05×1mm2 pixel), 2-D CCD	5 MHz, 10K, 1 MHz, 10-50 Hz
Intensity monitor	Measurement of transmitted intensity	Transmissive (<5% absorption), single pulse measurement, relative accuracy $<10^{-3}$
Spatial beam profile monitor	Measurement of x-y distribution	Transmissive (<5% absorption), single pulse measurement
Spectrum monitor	Measurement of photon energy (mean, distribution, harmonics)	Single pulse measurement, relative accuracy $<10^{-3}$
Wavefront sensor	Measurement of spatial distribution at focal spot, Adjustment of extreme focusing optics	$\lambda/10$ resolution
Alignment unit	Positioning and position verification	Permanently operating, accuracy ~100 µm
Lead hutch	Radiation protection, temperature stabilisation, laser protection	5×10×3.5 m^3 (W×L×H), ±0.5° thermal stability
Control hutch	Operation of the instrument	Working environment (noise, temperature, light)

Table 6.4.17 *Elements and specifications of the RAD 1 instrument.*

6.5 Specific XFEL experiments instrumentation

Experiments using XFEL radiation will enter into domains of x-ray instrumentation where currently no experience exists. In addition, the proposed experimental programme (see Section 6.4) at the European XEL Facility and the operation of several beamlines and many scientific instruments (see Section 6.2) at this facility lead to specific requirements with respect to x-ray instrumentation. These require instrumentation of the soft and hard x-ray beamlines with specifications exceeding, in many cases, the existing technology, in particular the existing x-ray instrumentation at synchrotron radiation or laser facilities. Four specific areas of instrumentation have been identified and the R&D programme in these areas is described in the following sections.

Sample environment and manipulation

Instrumentation issues related to sample preparation, positioning and exchange of solid samples, sample injection systems for non-solid samples and specific sample environments fall into this category. Due to the high intensity of the x-ray pulses, in particular for focused radiation, the damage and beam modification of samples needs to be considered. Using continuous sample replacement has been proposed for this reason. Techniques vary from moving solids samples, using liquid or gas jets, or preparing single particles. Another issue is related to precise sample alignment required for experiments with spatial resolution in the 0.1-1 µm regime.

X-ray optics

The preservation of the x-ray beam properties using diffraction limited optics is important for all coherence applications and also for extreme focusing. The response of optical elements to the high peak power and to average power during pulse trains is a second obvious area of R&D in this category. Beam splitters and delay units are new optical elements in the x-ray domain to be employed by several of the instruments. In addition, specific optics using mirrors, crystals or grating will be required to provide the requested performance.

Optical laser

The proposed experiments require optical lasers for time-resolved experiments and also for diagnostics purposes. These lasers in general need to be synchronised with the x-ray beam. The requirements towards laser radiation in terms of pulse duration, repetition rate, pulse energy, tunability, and availability are more complex than commercially available laser systems. A dedicated instrumentation programme is, therefore, required.

Detectors and requirements

The specific needs of many of the instruments proposed in Section 6.4 lead to a requirement for 2-D x-ray detectors with specifications not available today. An R&D programme has to be implemented to develop, test, and install such detectors and a start has already been made by having had a dedicated workshop mentioned in the introduction to this chapter. Other specific detector developments, e.g. particle detectors and x-ray streak cameras, are considered too.

6.5.1 Sample environment and manipulation

6.5.1.1 Sample preparation

Experiments investigating nano-particles have been proposed in the fields of physics, material sciences, or structural biology. The preparation and characterisation of nano-particles before inserting them at the x-ray instrument is important for an efficient use of the available beam time at the XFEL. Whereas in material sciences the samples are relatively stable and also brought by the users, in biology one wants to study rather fragile systems including membrane nanocrystals, arrays of particles, virus templates, pure protein samples, viruses and cells. In many cases, particles and more complicated sample structures need to be prepared on specific sample holders that allow insertion into the instrument. The sample preparation includes the preparation of particles in dedicated laboratories, their characterisation by standard laboratory techniques, the preparation of samples on holders specific for insertion at the x-ray instruments and the pre-alignment and/or preparation for insertion. Since samples in many cases are sensitive to oxidation, the preparation and insertion under vacuum has to be possible.

Characterisation techniques such as high resolution microscopy, electron microscopy, atomic force microscopy, x-ray diffraction and small-angle scattering, visible laser spectroscopy are included here. Also, techniques for micromanipulation of nano-sized particles and inspection of samples after being used in the x-ray experiment are needed.

6.5.1.2 Sample positioning, exchange and alignment

After insertion at the x-ray instrument, the samples require exact positioning so that time is not wasted using XFEL radiation for alignment of samples. Having established a reference system for the sample area, the positioning occurs relative to this. The use of optical systems for online inspection is foreseen, in particular inside vacuum chambers. The accuracy of sample positioning is determined by the x-ray and visible laser beam sizes. Accuracy in the order 1 µm is required in all directions.

Experiments using solid samples will require concepts for exchanging samples at relatively high repetition. Sample exchange at the intra-bunchtrain repetition rate of ~1 MHz will require a sample speed of around 100 m/s (100 µm; 1 MHz) which is unlikely to be enabled for very complex structures. In focusing applications with extremely short depth of focus, one also needs to take into account that the sample remains in the same position along the x-ray beam after exchange.

An issue of specific interest to the XPCS experiments proposed is the stability of the samples in the x-ray beam. This needs to be known in order to prepare experiments. The issue of beam damage for different elements and materials as a function of intensity and photon energy, therefore, requires specific investigation.

In coherent diffraction experiments on intact cells and cell organelles using the unfocused, coherent beam of the XFEL, cryo-microscopic techniques could be suitable for tomography studies where a controlled sample rotation is necessary. Electron cryo-microscopy performs structural studies on hydrated samples at low temperatures in a high vacuum environment. Existing EM equipment can be adopted for similar studies in an x-ray beam. Sample molecules and particles may be embedded in a thin layer of vitreous ice of a few tens nanometres in thickness. Prior to an exposure, the sample(s) of interest may be located by UV/VIS fluorescence techniques, and once found, moved into the path of the x-ray pulse, using programmeable positioning devices. Such a technique requires excellent pointing stability from the XFEL, with minimal pulse-to-pulse creep. If this can be achieved, the complete repertoire of methods in electron cryo-microscopy will become available for x-ray experiments. Vitreous ice surrounding the sample will contribute to background. This method may, however, be the method of choice for large samples.

6.5.1.3 Sample injection systems

These systems usually work indeterministically in that gases or liquids are injected into the vacuum, disperse following thermodynamical laws and get pumped away or collected in the case of fluids. Characterisation of the spatial density distribution at the interaction point with the x-ray beam is generally required. In these cases, samples are exchanged continuously and the speed at which the exchange occurs determines the repetition rate of the x-ray pulses. More sophisticated methods have been proposed for XFEL experiments on ions and single particles, clusters or biomolecules.

In atomic physics applications, the use of traps or ion beams provides the opportunity to prepare highly ionised and, in laser-cooled systems, ordered states of ions that can be investigated using the XFEL beams. The use of traps allows investigation of the ions in the excitation state and also determines the sample volume of interactions. Thereby, the scattering probability raises and enables these experiments. In a related, and more ambitious, version of these experiments one would install an ion beam, operated in either cross- or merged-beam geometry (compare Figure 6.4.4).

In materials science and structural biology applications on single particles, their controlled injection is needed. Particles are injected from the outside into the x-ray beam in such a way that single particles intersect with the brief XFEL pulses. Ideally, one fresh, single particle is injected into every focused pulse at the pulse rate of the XFEL. To achieve this, the trajectories of the particles must be controlled both in space (< 1 µm) and time (< 10 ns), so that each one of them will be well aligned with the focused x-ray pulse. Present sample injection and particle manipulation techniques need to be significantly refined in order to position individual particles with sufficient precision. The related R&D programme cannot be driven by the European XFEL project. However, close collaboration with the scientific community is anticipated in the field in order to design the scientific instrument for these applications according to the ongoing research. The next paragraph briefly describes the current approach in this area of R&D.

Single particle injection

Initial experiments will use clouds of particles without stringent requirements, achievable with current methods, with and without alignment with a polarised laser. These will be improved upon, by first injecting short, concentrated bursts of particles into the beam focus area and relying on the statistical positioning of individual particles. Such experiments require a focal spindle of about 5 mm length, shot-to-shot diagnostics to determine whether a particle was indeed hit by the x-ray beam and where the interaction along the focal spindle took place.

More advanced techniques of particle introduction and manipulation include the injection of a few or even a single particle into the beam at the proper time with well-controlled velocity, or trapping single particles at the XFEL beam focus using optical, electrostatic, or electromagnetic methods. ESI and related ink-jet spraying techniques will be used for introducing samples (like molecules or single particles, such as viruses) into the gas phase.

Spraying techniques have been refined in recent years for use in mass spectrometry of large proteins, supramolecular complexes, such as intact ribosomes **[6-390]**, and even whole viruses **[6-391]**. The charge imparted onto a particle by the ESI process is convenient for manipulating the particles in the gas phase by electrostatic forces. If necessary, a charge-reduction scheme based on the charge-reduction electrospray method, can be used to reduce the charge on electrosprayed molecular ions or particles to one or a few elementary charges in a controlled way. For the particle introduction into ultra-high vacuum, it is proposed that aerodynamic lens or nozzle techniques used for single-particle mass spectrometry and bioaerosol mass spectrometry will be applied. Also, techniques based on reverse micelles or Helium droplets to provide a protective coat for the sample molecules if necessary, will be explored.

An area with a direct bearing on the experiments is a technique to orientate particles using visible laser radiation. This method, applied to small molecules, is also part of the SQS experimental programme. The scaling of present techniques to larger molecules, or even to entire particles needs to be addressed. Another important area is the control of sample debris after the interaction with the intense XFEL beam. These techniques will be used in many of the experiments aiming for highest intensity. Diagnostics tools for determining where the particle was actually hit by the x-ray beam will improve the data quality. A possibility would be spatially resolved fluorescence that is emitted by the particles during x-ray induced heating.

6.5.2 X-ray optics

6.5.2.1 Preservation of XFEL radiation properties

The high peak brilliance of the XFEL radiation follows from the ultra-short pulse duration and coherence of the x-ray beam. In particular, experiments applying time-resolved and coherence techniques make use of the properties. The x-ray transport to the scientific instruments must, therefore, preserve these properties. A particular challenge is the preservation of the wavefront here. The wavefront is important in many respects, as it governs the ability to focus to extremely small beam sizes, the possibility to retrieve structural data from coherent diffraction patterns and the time-smearing of the x-ray pulse. To fully understand and investigate the related phenomena, wavefront-propagation codes are required. Current codes must be extended to include x-ray diffraction theories in order to integrate time-dependent response of diffraction and must accept all kinds of x-ray optical elements.

Coherence

Most importantly, preservation of the coherence properties requires the specification of x-ray mirrors for the beam transport. At the European XFEL Facility mirrors have a central role in transporting the beam from the undulators to the experiments. The reason for using mirrors is that they are not chromatic and offer almost complete reflectivity. On the other hand for x-rays and low Z material, very small grazing angles are needed. In consequence, the mirrors become very long and the requirements to roughness and slope error are extremely high. The correlation of these two parameters and the consequences for x-ray diffraction are not fully understood yet and require further research. The soft x-ray optics requirements for wavefront preservation have to be formulated and the monochromator design has to be verified in this respect. Related to the degree of coherence of an x-ray beam is the acceptance by the optical elements. Currently, the beam transport is designed to accept 6σ beam size for the highest photon energy. For smaller photon energies the divergence increases (see Table 5.2.2) and less beam size is accepted.

Time domain

For time-resolved experiments it is important to maintain, or even shorten, the x-ray pulse duration. The various optical elements, therefore, need to be analysed with respect to their effect on the pulse duration and wavefront inclination. In particular, the asymmetry of single crystals can give a contribution here. The accuracy to cut single crystals needs to be determined and, if needed, an instrument for verification needs to be set up. It was shown earlier **[6-392]** that double-crystal monochromators in asymmetric Bragg reflection can contribute substantially to pulse duration broadening. In the other direction, it has been proposed that the x-ray pulse be shortened or sliced using crystals **[6-393]** or multilayers **[6-394]** in specific configurations.

Splitting the x-ray pulse into two parts and delaying one of the pulses with respect to the other is requested for XPCS experiments, as well as for time-resolved experiments using the x-ray beam to induce an ultrafast change of sample properties. In XPCS, typically, two equally strong pulses and delay times of 1 ps to 200 ns are required. For pump-probe experiments, the first pulse excites the sample and therefore, the required intensity distribution between the split pulses may be very asymmetric. Here the range of delay time goes from 100 fs to few hundred picoseconds.

6.5.2.2 Power dissipation in optical elements

The high photon number per x-ray pulse leads to very high peak power. Furthermore, the use of trains of x-ray pulses generates significant average power over the duration of the pulse train. An R&D programme must investigate the effect due to peak and average power dissipation to mirrors, monochromator crystals and beamline filters or windows. For peak power, the involved timescales are too short for thermal processes and the investigation of damage induced in the optics by single or accumulative effects needs to be investigated. First experiments have been carried out at the FLASH facility in the XUV regime and the scaling of the results towards the x-ray regime is of further interest.

In terms of average power, simulations have to be carried out to estimate the response of mirrors, crystals and window materials to the high average power during pulse trains. Specific schemes for preserving shape performance in mirrors include cryogenic cooling and active control mechanisms. For cryo-cooling of the long mirrors it has to be evaluated whether the extreme slope error tolerances can be preserved. Both schemes have to be integrated in the simulations in order to decide about the technology to be used.

6.5.2.3 *Specific optical elements*

In the following a few optical systems are listed which have been requested by the various experiments. Although quite specific at present they may turn out to be very important in the future for more general classes of experiments.

Focusing optics

In nearly all focusing applications different focal spot sizes are requested for one scientific instrument. Focusing stronger than required is a disadvantage due to the increased intensity (W/cm^2). A design for the optics must, therefore, be quite flexible to change between different configurations. However, the number of optical elements is limited and an optimised design for the focusing optics must be developed. Specific aspects of focusing optics are listed below:

- The question how to achieve the smallest foci and the x-ray beam properties at the focal spot has to be solved. This extreme focusing requires coherent radiation and the techniques discussed in Section 6.2.2.4 above will work differently and lead to different consequences for the x-ray beam properties at the focus. This, in turn, is expected to influence the data in single particle imaging experiments.
- How to obtain extreme focusing in the very soft x-ray regime from 250-500 eV, so that, at the same instrument, beamline SASE 3, higher photon energy extreme focusing experiments can also be carried out. Is it also possible to use a second optics to achieve 10-20 µm focal spot size for the same experiment?
- How to enable focusing in the 1 µm regime for a wide bandwidth, both at SASE 2 and at SASE 3. Can compound refractive lenses be used for this application and is it possible to keep the focus and the focusing optics positions fixed. What will be the effect on the focal spot properties?

Separation of first and third harmonics

In pump-probe applications using the x-ray beam to excite the sample, it is foreseeable that probing can also be done at a different wavelength. This can be advantageous if, in this way, the cross-section for the pumping and probing processes can be better matched. For the XFELs, the third harmonics is expected to have in the order of 1% intensity and would, therefore, provide an excellent, less intense probe pulse. To enable these experiments one needs to split the initial beam into two monochromatic beams and then transport both beams to the scientific instrument. For these experiments a specific solution for the first double-mirror has to be found. The current mirror layout does not reflect photon energies higher than 15 keV so a different solution has to be found.

Angular displacing monochromator

In the proposed x-ray absorption experiments fast rotation of a monochromator crystal to displace the x-ray beam on the sample is a key element of a technique that allows the measurement of entire absorption spectra in the course of a single pulse train of 0.6 ms. The technique of rotating crystals for QEXAFS applications has been developed to a certain standard **[6-395]** and it needs to be investigated to what extent the angular speed can be increased to match the requirements of this specific experiment. If successful, the technique will immediately be important in other experiments concerned with photon beam damage.

Ultra-high resolution soft x-ray monochromator

For precision spectroscopy on highly stripped ions, a bandwidth is required that is beyond the resolution a versatile monochromator, used by different applications, can provide. A resolution of 10^4 up to 10^5 will improve the precision of the proposed measurements significantly. The limitations of such a monochromator and whether it is possible to integrate it into the current beamline design for SASE 3 will be investigated.

X-ray emission spectrometers

For x-ray absorption spectroscopy, high energy density science and cluster research, the use of x-ray emission spectrometers has been proposed. For the XFEL experiments it is important to have efficient spectrometers covering a large solid angle. Such spectrometers have been proposed **[6-396]** and the effort required to build and the flexibility to operate such spectrometers need to be determined.

6.5.3 Optical lasers

To fully exploit the ultra-short pulse duration of the XFEL for time-resolved studies, synchronised ultra-short laser pulses in the optical regime are essential. Numerous optical/ x-ray pump-probe experiments have demonstrated that new insights in processes on the 0.1 nm length and femtosecond timescale can be explored **[6-397 – 6-400]** and many proposals to exploit XFEL envision scientific applications for these techniques (compare Section 6.4). Doubts whether two independent laser sources could be used for time-resolved experiments (due to the temporal jitter) with femtosecond time-resolution, were dispelled by groundbreaking progress in synchronising two lasers (e.g. **[6-401]**) and first experiments combining accelerator-generated femtosecond x-ray pulses with optical laser pulses at SPPS at Stanford **[6-402]**. By measuring the remaining temporal jitter precisely, the temporal resolution of the experiment was no longer determined by the timing jitter, but rather by the measurement precision itself.

Thus, an optical laser facility providing state-of-the-art laser technology (including synchronisation diagnostics) for all experimental end stations is strongly desired. The required specifications for such laser systems (see below) are extremely demanding, such that a permanent installation of the lasers, operated by experienced laser physicists, in the XFEL experimental area is absolutely necessary. For the vast majority of user groups it will not be possible to supply or support their own laser systems for these experiments.

Considering the user requirements and from general considerations, three different types of lasers for pump-probe experiments can be distinguished:

- lasers generating ultra-short pulses at medium to high pulse energy, 10 Hz;
- lasers generating ultra-short pulses at low pulse energy but high repetition rate;
- lasers generating highest possible pulse energy.

The following paragraph will outline the laser instrumentation programme for the European XFEL. The given specifications are meant to be available in the experimental chamber. Technical configurations to meet these specifications will be proposed in Section 6.5.3.2. Finally, auxiliary technical installations for the operation of the optical laser are described.

6.5.3.1 Types of lasers, technical specifications

Lasers generating ultra-short pulses at medium to high pulse energy

This type of laser predominantly meets the requirement for pulse duration equal to or even shorter than the duration of the XFEL pulses in order to achieve highest time resolution in pump-probe experiments. For this laser type a required pulse duration ≤ 30 fs (FWHM) will be adequate.

Experiments requiring very high field strength for the optical laser can also be carried out with this type of laser. For this purpose it is important to provide pulse energies ranging from the upper millijoule to joule range, as requested by the experiments (1 mJ – 10 J). Due to the high pulse energies, the repetition rate will be limited to 10 Hz (upgradeable to ~ 30 Hz), i. e. equal to the burst repetition rate of the XFEL pulses. It should be noted that state-of-the-art laser technology allows generation of pulses with 30 fs pulse duration and 10 mJ energy with kHz repetition rate. But considering the temporal pulse pattern of the XFEL (see also Figure 6.1.1) a kHz repetition rate would not give any advantage over a 10 Hz rate. On the contrary it will be easier to obtain high pulse energies at 10 Hz.

Lasers generating ultra-short pulses at high repetition rate and low pulse energy

This type of laser is intended for pump-probe experiments where it is essential to repeat the measurement as often as possible. For example, a high repetition rate is important for effects demanding large statistics (with single bunch detection, e.g. single photon counting, detection of rare events, etc). Due to the particular time structure of the XFEL a laser with 1 MHz repetition rate gains a factor of 600 compared to a 10 Hz operation.

Assuming the timing stability of the laser to FEL pulses within a bunch train is better than the pulse duration, with a high repetition rate laser the pump-probe data can be summed over the bunch train and signal-to-noise can be enhanced for single bunch laser operations. Another method to enhance the signal relative to background or drifts is the “lock in” technique: e.g. the laser operates at 1 MHz repetition rate while the FEL produces pulses at 2 MHz, thus, only each second x-ray pulse is combined with a laser pulse, allowing detection of the difference between laser on and off – despite noise. Further, a high repetition rate allows (with a specially designed synchronisation unit) fast scanning of the delay within a bunch train (complete pump-probe experiment within one bunch train).

The requested parameters are: pulse duration: ≤50 fs (FWHM), pulse energy 0.1 to 3 mJ for a repetition rate ≥100 kHz, preferentially 1 – 5 MHz.

6.5.3.2 Creation of the optical laser systems

General considerations

The laser systems should be based on commercially available solutions wherever possible. This provides reliable and well tested systems with the availability of fast assistance with severe hardware problems by service contracts with the vendor. Thus, downtimes can be minimised and the XFEL laser operating group can concentrate on the experiment support rather than laser repair. However, as shown below not all experimental requirements can be met by commercial laser systems. In particular, for the high repetition rate laser, an R&D project will be needed to enhance burst mode type lasers (as used at the FLASH facility, for example **[6-403]**).

Technical configuration of the short pulse oscillator

The front-end of the laser system will consist of an ultra-short-pulse laser oscillator meeting high synchronisation, stability (especially pointing stability) and reliability demands. The pulses from this oscillator will be used to seed two different amplifier chains (high repetition rate and high intensity). Since the demands on the synchronisation and stability require a considerable effort, it seems advisable to use only one well synchronised oscillator (for each laser laboratory, see below) to seed all amplifiers. It will be easier to tailor the oscillator parameters (bandwidth, beam diameter, etc.) to seed both amplifiers compared to the operation of two synchronised and stabilised oscillators.

The use of Titanium:Sapphire as laser material is a well established technique for the generation of ultra-short pulses – down to few-cycle pulses **[6-404]**. Using a piezo actuator in the cavity and appropriate feedback electronics, synchronisation to an RF-signal with a few femtoseconds accuracy can be achieved **[6-405]**. However, a Ti:Sapphire oscillator has several disadvantages: an expensive pump laser is needed and spatial drifts are observed since the cavity consists of many mechanical components. The upper level lifetime of Titanium:Sapphire is only 3 μs, thus, noise below 300 kHz will be amplified. However, the piezo control of the cavity length can only regulate up to several kHz. Therefore, in the frequency range from 10 to 200 kHz (currently) no control is possible.

The alternative to a Titanium:Sapphire oscillator is a fibre laser oscillator (e.g. Er-doped fibre) having several advantages over a Titanium:Sapphire oscillator: (i) high spatial stability (single mode fibre); (ii) no high quality pump laser needed; (iii) compact setup; (iv) long lifetime of upper laser level (Er: 8 ms), thus, it is less sensitive to noise. Using electro-optical modulators in the fibre laser oscillator, feedback frequencies up to 230 kHz were demonstrated **[6-406]**. Fibre lasers operating in the telecommunication band C have a wavelength in the range 1,530 – 1,560 nm. The second harmonic of such an oscillator can be directly used to seed a Titanium:Sapphire amplifier.

Currently, the bandwidth achieved with fibre lasers is not sufficient for the laser parameters demanded by the experiments, on the other hand, the development in the field is progressing extremely fast. Sub-50 fs oscillators can be purchased **[6-407]** and research is ongoing **[6-408]**. It is expected that in the next few years, fibre lasers with a pulse duration of well below 30 fs will be available. However, R&D is necessary to adapt this kind of laser as the front-end of the pump-probe laser system.

Technical configuration of ultra-fast medium high pulse energy amplifier

For 10 Hz, high power TW-class laser systems a number of commercial solutions are available. Typical parameters of these lasers are 30 - 50 fs pulse duration with pulse energies between tens of millijoules and several joules (maximum commercially available pulse energy at the moment: 5 J **[6-409]**). Such laser systems are based on the principle of chirped pulse amplification. The short pulses from the oscillator are chirped in a grating arrangement, amplified first in a regenerative Titanium:Sapphire amplifier to millijoule energy level and subsequently amplified with a multipass Titanium:Sapphire amplifier to joule energy level. Finally, the pulses are compressed in a second grating arrangement to nearly their original pulse duration. In order to avoid self-focusing in air and non-linear effects while coupling the intense beam through a window flange into the experimental chamber, for pulses with peak powers exceeding ~10 TW, the compressor (spatial extent: ~ $3 m^2$) will be located in vacuum close to the experimental chamber.

For the generation of pulses in the millijoule energy range, one can take advantage of the modular structure of the amplification chains and utilise pulses from the preamplifier stages. For that purpose it is recommended to have a separate, small compressor (in air). The modular construction of this kind of laser also permits the use of the uncompressed pulse which, in case of the 5 J/30 fs version, can provide up to 10 J with a pulse duration of roughly 1 ns (FWHM) for high energy density experiments.

Systems with the described architecture can provide pulse-to-pulse stabilities of 2% rms, pre-pulse contrast of $1:10^5$ and ASE $1:10^8$ for almost diffraction limited transversal beam profile (M2<1.5) **[6-409]**. For even better pre-pulse contrasts, OPCPA or SHG-stages might be added; however, these are no longer commercially available **[6-410]**.

Technical configuration of the high repetition rate amplifier

There is a strong user demand to use a highly repetitive laser system, capable of delivering more than one laser pulse during a bunch train. Commercial systems at repetition rates of up to 300 kHz providing 4 μJ pulses within 60 fs pulse duration are available **[6-411]**. However, the pulse energies as well as the repetition rate are rather far from the optimal specifications. It cannot be expected that the commercially available specifications will improve considerably in the next few years. Higher pulse energies are essential for many experiments. A system delivering 1 mJ pulse energies at 1 MHz repetition rate would result in 1 kW optical power which, even if technically feasible, causes tremendous operational expense; this is very hard to justify, since only 0.6% of the produced pulses can be used, as a result of the linac time structure. The problem can be elegantly approached using a laser system which operates in a pulsed burst mode. However, such a laser will not be commercially available. The pump-probe laser system at FLASH, designed and built by the Max-Born-Institute utilises an upgraded copy of the FLASH photocathode laser to pump two OPAs stages amplifying 100 fs pulses to pulse energies of 30 μJ at 1 MHz repetition rate (for a maximum of 800 pulses within 800 μs) **[6-403]**. The pulse energy can be significantly enhanced by reducing the repetition rate; thus, it is perfectly suitable for a large class of experiments.

Within an R&D project this type of laser could be redesigned and upgraded to provide sub-50 fs pulses with an energy of up to 1 mJ at 1 MHz. The pulse energy of the pump laser has to be increased (in comparison to the FLASH pump-probe (PP)-laser) and the amplified bandwidth has to be increased (e.g. by non-collinear OPA geometry **[6-412]**). Concepts utilising cavity-enhancement, relaxing the demands for pumping lasers, should also be pursued **[6-413]**.

Technical configuration of the 100 J class laser

A laser generating sub-nanosecond pulses with 100 J energy is not commercially available at the moment. However, lasers with similar specifications are in operation or in development in research laboratories. The architecture of such laser systems consists of a front-end, generating femtosecond or picosecond pulses followed by a stretcher that brings the pulse duration to nanoseconds. In a preamplifier (regenerative and multipass amplifier) the energy of the pulses is increased into the upper millijoule range. With several single pass amplifiers separated by vacuum spatial filters the energy is finally brought to the final value. The technical effort for the power amplifier is considerable because of thermal problems in the laser medium. For the same reason a repetition rate of only some 10 mHz is possible. Based on reports of existing laser systems with similar specifications the space, requirement can be estimated to be more than 50 m^2.

In comparison to the above laser systems, a 100 J-class laser must be regarded as rather special equipment for a limited group of experiments. It will likely be used only in connection with one of the XFEL beamlines. Therefore, the optimal technical solution is to arrange the laser system in close proximity to the scientific instrument. This also has the benefit of an easier beam transport. In consequence, this laser system should be regarded as part of the instrument using this laser. In view of the effort and the related cost, a close connection with the user community will be required for design, R&D and commissioning of this laser system.

Beam modification and frequency conversion modules

To widen the applicability of the laser for spectroscopic experiments, a wide spectral range will be offered. OPAs can provide a spectral range from 0.2 to 20 µm with pulse durations < 40 fs (FWHM) and conversion efficiencies of > 30% at incident 800 nm pulse energies of 2-3 mJ. To ease the laser beam transport (i.e. requirements on the mirrors and relay imaging), the 800 nm beam would be distributed to the experimental end station, generating the broad spectrum in the experimental area. The remote controllability via computers which is, therefore, needed is already included in commercial systems **[6-414]**.

With adaptive optics a spatial beam shaping can be performed to reach high optical beam quality in the experiment, e.g. focusing to diffraction-limited diameters. The module must be located before the power amplifier. Such a device, integrated in a laser system, is currently not commercially available so R&D efforts will be necessary.

To tailor the temporal shape of the laser pulses (e.g. for plasma physics or "femto-chemistry" **[6-415]**) the pulses can be shaped in the spectral domain using spatial light modulators.

Such a module must be located at a point with low pulse power, i. e. before the stretcher. All components are commercially available; however, its creation within an amplifier chain demands R&D efforts.

Laser installation

First experience at FLASH shows that it will not be sufficient to have only one laser system of each type (high repetition rate and 10 Hz medium to high pulse energy). In order to satisfy the requests for pump-probe experiments from five XFEL beamlines, two laser systems of each type will be necessary. To have at least two lasers of each type is also recommended to increase availability and as a security reserve in case of technical failure.

Arrangement of laser hutches relative to experimental stations

Two separate laser hutches are planned at the end of experimental areas corresponding to the SASE 1 and U 2 beamlines. Each laser hutch will deliver the laser beams to the three adjacent experimental areas. In addition, a beamline connection between both hutches will be required to increase flexibility of beam distribution and future upgrades. It is planned to equip each laser hutch with one high repetition rate system (0.1 - 1 MHz, 30 -50 fs, 0.1 to 3 mJ depending on repetition rate) and with one medium to high pulse energy system. For one laser hutch it is planned to provide highest pulse energies (20-100 TW e.g. 1-5 J, 30 fs) with a 10 Hz repetition rate, whereas in the second laser hutch a 1 TW laser system providing 30 mJ and 30 fs pulse duration seems sufficient. Due to the modular design of such systems a later upgrade for the second laser to several joules of pulse energy is feasible.

Space requirement

Laboratory space of between 80 to 90 m^2 is required for each laser room containing the ultrashort-pulse oscillator and two amplifier systems, including synchronisation, diagnostic, storage and spare capacity for future applications and/or lasers from users (for long-term experiments). Furthermore, about 20% of the area should be earmarked for future upgrades (e.g. few cycle-lasers, energy upgrades, etc.).

6.5.3.3 Synchronisation

The temporal resolution of pump-probe experiments using x-ray and laser pulses should be limited rather by the pulse duration of the x-ray pulse than by the jitter between the independent sources. Thus, a level of synchronisation in the order of a few tens of femtoseconds between laser and XFEL is required. The task is challenging but feasible according to current technology. Jitter below a few tens of femtoseconds would ensure stable temporal overlap (once found) between x-ray and optical pulses. This would tremendously ease the alignment of the pump-probe experiments, most of all processes occurring only during temporal overlap (e.g. sidebands in photoelectron spectroscopy as discussed in Section 6.3.2.2). However, it has been shown that even for large jitter (several hundred femtoseconds) it is possible to reach ~ 50 fs time resolution by measuring the jitter for each shot and sorting the measured pump-probe data after the experiment according to the jitter data **[6-402]**.

The distributed master-laser oscillator frequencies (available as optical pulse train and electronic RF signals) are stable within 10 fs (rms between 1 kHz and 10 MHz) (see Section 4.8). It has been shown that femtosecond laser oscillators (Titanium:Sapphire as well as fibre lasers) can be synchronised to an external (electronic RF) master frequency by controlling the cavity length by a piezo element driven by a phase-locked loop circuit, with an rms jitter better than 20 fs **[6-405, 6-406]**. Using the optically distributed femtosecond pulse from the master-laser oscillator, the synchronisation can be improved **[6-401]**. The schematics are shown in Figure 6.5.1. In principle, current technology can provide the desired stability. To simplify the synchronisation scheme and omit electronic circuits (potential sources for noise and drift) in the feedback, it may be worthwhile exploring techniques that are not well established, such as seeding amplifiers directly with the distributed master-laser oscillator pulses, or use these pulses to injection lock the local oscillators in the laser rooms. However, for future application (e.g. attosecond pulse options of the XFEL) pursuing alternative synchronisation schemes to further decrease remaining temporal jitter is strongly recommended. One approach is the use of a 5 fs laser pulse to create attosecond x-ray pulses due to energy modulation of the electron bunch **[6-416]**. Synchronising another few-cycle laser in the experimental area to the laser initiating the modulation, the jitter of the accelerator ceases and the synchronisation of the two few-cycle pulses defines the degree of synchronisation (see Section 4.8). Such an operation could eventually allow pump-probe measurements with a few femtosecond temporal resolution. Sweeping the delay between the two lasers within a bunch train (different delay for each micropulse in the bunch, so that a whole pump-probe experiment within a single bunch train is performed) even sub-femtosecond resolution might be possible (since mechanical vibrations are negligible during the 0.6 ms bunch train).

Other concepts such as the direct amplification of optical light produced by the accelerator (e.g. undulator transition radiation **[6-417]** dipole radiation or similar) will be tested at the FLASH facility (Proposal by M. Drescher, University of Hamburg). These experiments might well result in new ideas for alternative synchronisation methods for the XFEL as well.

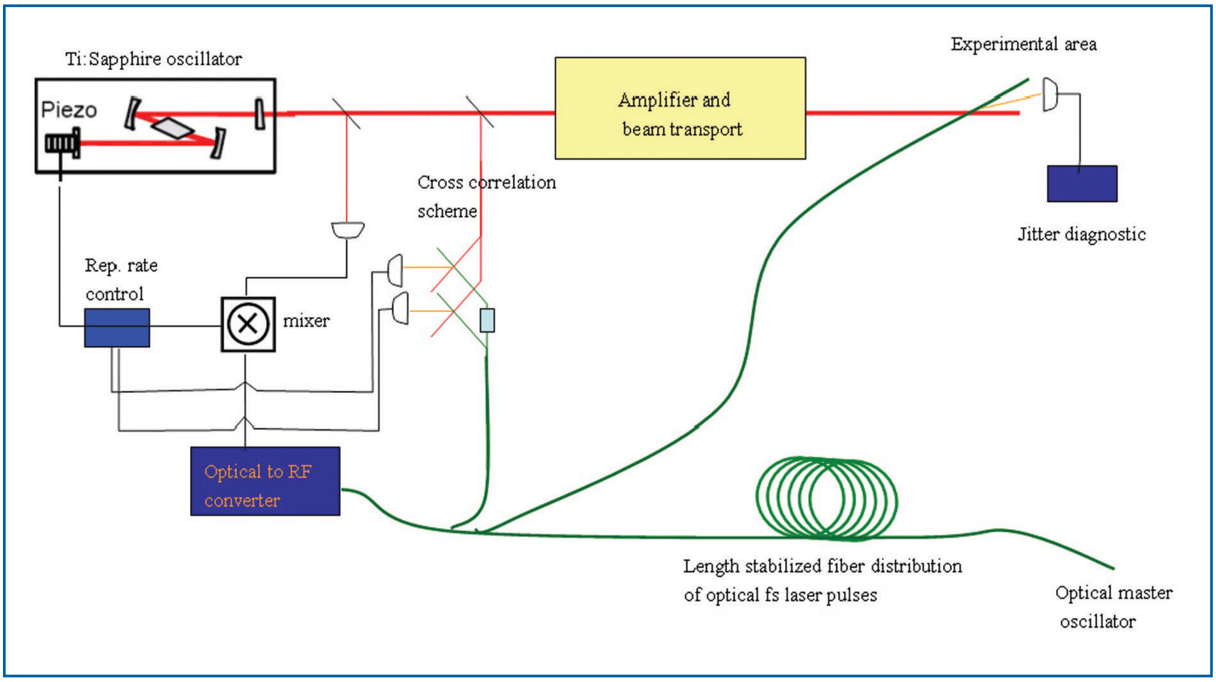

Figure 6.5.1 The synchronisation scheme for the femtosecond-oscillator is shown, including jitter measurement at the experiment. Besides the basic RF-based synchronisation loop (left) the balanced cross-correlation scheme (middle; adapted from **[6-401]***) is used to synchronise the repetition rate of the oscillator. The correlation setup in the experimental area (right) provides information about the jitter acquired by amplification and beam distribution.*

Measurement of synchronisation

As observed at the FLASH facility, even if the laser used for pump-probe measurements is well synchronised with the master oscillator, timing drifts and even picosecond jumps might occur. Applying slight changes to the accelerator settings (e.g. RF-phases) results in significant changes in the arrival-time (several picoseconds) of the electron bunch at the undulator. Furthermore, timing jitter and drifts may occur during the amplification process within the laser system **[6-418]**, and due to the beam transport system from the laser hutch to the experimental end stations, located several tens of metres away (see Figure 6.5.1). Therefore, an online timing monitor is indispensable. To determine the contribution to the jitter due to the laser amplification and the beam transport, a single-shot cross-correlation setup is needed at the experimental end station. Here, the timing jitter between the master-laser oscillator pulses (a fibre distribution station located in the experimental hutches is envisaged) and the amplified laser pulses can be directly measured in the experimental area.

To determine the jitter between the electron bunches (which is a good measure of the arrival-time of the x-ray pulse within tens of femtoseconds **[6-402]**), a well established technique like the electro-optical sampling, correlating optical laser pulses with the electric field of the electron pulse, can be utilised. Results at FLASH and at SPPS at Stanford Linear Accelerator Center (SLAC) **[6-402]** show a time resolution of about 50 fs for the arrival-time of the electrons with respect to the laser pulses. At the XFEL, an electro-optic sampling station in front of the undulators, driven by the optical femtosecond pulses from the master-laser oscillator will provide information on timing jitter between electron bunches and the master-laser oscillator. The timing difference between pump-probe laser and master-laser oscillator is continuously monitored and regulated as described above. In addition, phase pickup coils can provide timing information on the electron arrival-time with respect to the master-laser oscillator with a precision of ~20 fs (see Section 4.8.2.5) These two systems (electro-optical sampling and phase pickups) will provide timing information on a 50 fs level for the arrival-time of the electrons at the undulator in a non-invasive way for each electron bunch.

In addition, it is important to characterise the timing jitter of the pump-probe facility unambiguously between x-ray pulse and optical laser pulse in the experimental station for each pulse. A number of experiments can provide single-shot timing information between x-ray and optical pulses: non-thermal melting in single-shot geometry **[6-398]**, Auger electron sideband spectroscopy and spatially resolved photoelectron sideband spectroscopy (see Section 6.3.2.2). These experiments will be valuable tools in the commissioning and operation phases. Depending on the results, a permanent installation of such an experiment in the experimental area might be necessary.

6.5.3.4 Beam transport to instruments, characterisation and control

Laser beamlines

An evacuated system of beamlines is needed to deliver the laser pulses from the laser hutch to the experimental hutches. Using relay imaging techniques to reduce spatial jitter of the laser beam at the experiment, intermediate focusing of the beam is required. As focusing optics, mirrors should be preferred because of the smaller B-integral. Focusing the intense beams in air, non-linear spectral broadening and self-focusing might occur. Thus, the beamlines should be evacuated at least to backing pressure. To avoid too many optical components in the experimental area, the pulse compression for the “low power” lasers will take place in the laser hutches. In order to keep the beam size in reasonable diameters (~ 30 mm FWHM) the 20-100 TW beam will be transported temporally stretched. The compression to 30 fs pulse duration will take place in a vacuum compressor located in the experimental area.

The space requirements for vacuum pipes (63 mm diameter), switching mirrors, supports etc. from the laser hutch to the adjacent three experimental areas has to be included in the early planning of the layout. One additional beamline connecting the two laser laboratories is also foreseen.

Remote controllability

The experience at the pump-probe laser of the FLASH facility shows that a high degree of remote controllability is necessary to provide the user with all necessary variable parameters (delay, pulse energy, pulse duration, polarisation, etc.) to be changed without the attendance of a laser operator.

Diagnostics

A profound characterisation of the laser parameters at the instruments is mandatory to perform well defined experiments. Thus, besides the online measurement of the pulse energy, spectrum and beam profile and position, devices will be required to monitor the pulse duration and pulse front tilt (e.g. using a GRENOUILLE **[6-419]**) as well as the synchronisation (see above).

Safety installation

For automatic safety surveillance, two separate monitoring systems will be used. One system ensures the compliance with laser safety regulations (personnel interlock) and the second monitors critical conditions or dangerous states in the laser system (technical safety interlock). Both systems are based on the SPS-technology. The interlock systems must be characterised by the following main features:

Person interlock:

- double door entrance, independent emergency exit;
- main power of all laser units is switched off in case of breaking any safety condition;
- laser safety installation at the experimental places and in beam distribution.

Technical safety interlock:

- prevention of faulty operation;
- interlock SPS is connected with the computer-based remote control system of the laser.

6.5.3.5 Auxiliary requirements

According to the experiences with FLASH, the laser hutches should be air-conditioned within 1K, and furthermore, flow boxes producing filtered dust-free and temperature-regulated air flow at the laser tables are required, at least for the oscillator and the amplifiers. They allow temperature stabilisation to 0.1 K on the laser tables and will supply a clean environment for the amplifiers (avoiding optical damages due to dust). The regulation of the temperature to 0.1 K at the laser table is required since larger temperature fluctuations cause thermal expansion which in turn induces temporal drifts.

Since the laser hutches at the experimental area are devoted to user experiments, it will be necessary to provide additional laser laboratories for maintenance work and small scale R&D.

6.5.4 Detectors and requirements

6.5.4.1 Introduction

It is clear that optimum use of the unprecedented capabilities of the European XFEL calls for a dedicated and substantial detector development programme. This was acknowledged by the Scientific and Technical Issues working group in its interim report of January

2005 (see its Annex 5.1: "Dedicated detector development programme"). The detector development programme for the XFEL will pursue various approaches, including (but not limited to) sub-picosecond x-ray streak cameras combined with crystal spectrometers, particle detectors (for electrons, ions and clusters) and 0-D, 1-D and 2-D x-ray photon detectors. Each system will be constructed in a dedicated project, while at the same time being an integral part of the overall detector development programme as well as an integral part of the scientific application development programme. Such a matrix-like approach will guarantee that the developed detectors will fulfil the requirements of the scientific applications, that there is cross-fertilisation between the projects and unnecessary duplication is avoided. To achieve this, the European XFEL project will have a sufficiently large detector group that takes upon itself a central coordinating role. It will be assisted and steered by an International Detector Advisory Board. This Detector Advisory Board will be convened at the earliest possible date.

One of the reasons to push the SASE process to 12 keV (0.1nm), is to be able to determine the structure of samples down to atomic resolution. This means that for the imaging experiments, one has to sample very finely (up to 4k×4k sampling points as explained below), and for scattering experiments one has to go to high scattering angles (up to $2\theta= \pm60$ degrees). This means large detectors with many pixels. By using state-of-the technology art and dedicated, multi-national, development programmes, such detectors will be constructed over the next five years.

A number of further characteristics of the XFEL have direct consequences for the detectors to be used in the experiments. For example: the peak brilliance beyond 10^{33} ph/s/mrad^2/mm^2/0.1% BW will result in the fact that certain experiments are "single-shot" experiments. This means that all the data needed for the experiment has to be recorded for every pulse. A consequence is that "integrating" detectors is the only option (all photons arrive at once) and one cannot use "photon counting" nor "energy dispersive" detectors. Since one still needs "single photon sensitivity" (see below), special developments are called for. Furthermore, since every pulse is a new experiment, all the detectors involved in the experiment will have to be read out and the data stored before the next pulse arrives, very much like the mode of operation of High Energy Physics experiments. This means that to get the most from the high repetition rate enabled by the super-conducting technology of the linac, certain detectors will be constructed with sampling (framing) times down to 200 ns, and others with storage capacities of up to 3,000 samples (frames). It is clear that such detectors do not exist today. State of the art detector and micro-electronics technology will be used in dedicated detector development programmes, in order to construct such detectors within the next five years.

This section presents the requirements imposed by the experiments as well as an overview of the current detector technology that will be used to construct the detectors. It also contains the outcome of a two-day workshop on: "Detectors for the XFEL", held in Abingdon, UK on the 28th and 29th of March 2006, and organised jointly between the CCLRC and the XFEL project team. This detector workshop was the fourth and last in a series of workshops. The three previous meetings were focused on scientific applications at the European XFEL. The requirements for detectors provided by these applications workshops were then condensed into a document: "Draft Requirements for 2-D Detectors for the European XFEL". A first draft of this document was circulated amongst German detector laboratories and discussed during a one-day workshop on the 17th February 2006. As a result a modified draft was produced and circulated to the participants of the workshop in Abingdon two weeks ahead of the meeting. In the preparation phase, a delegation from CCLRC, including detector experts, visited Hamburg on the 20th of September and the 15th of December 2005.

Since the biggest demand for new types of detectors is in the field of 2-D hard x-ray photon detectors, this was chosen as the main focus during the starting phase. However, it is well understood that a similar start-up process will be initiated before the end of 2006 for other systems as well. In particular, there is a need for fast x-ray streak cameras, new kinds of particle detectors (electrons, ions and clusters), soft energy detectors as well as generic detectors for all stations such as photon beam intensity, position and timing detectors. Any detector development for this project will be more widely applicable to other sources, particularly FELs, but also storage ring sources (see also section: "Links to other FEL projects").

This section on detectors starts with a description of the detector requirements for each scientific application. Some of the requirements have already been mentioned in the specific sections on the applications. This is followed by an outline of the strategy foreseen for the developments, which consists of a two stage approach. The layout of phase one is then presented: the technology to be used for day-one operation and an outline of the research needed to reach optimum performance. At the end the preliminary programme for the start-up of phase-one and overall milestones are presented.

6.5.4.2 Experimental requirements

General

In what follows, an overview is given of the major detector systems required for each scientific area. The first two areas, SQS and HED, require particle detectors and x-ray streak cameras, respectively. The area of x-ray absorption spectroscopy needs either a 0-D or a 1-D x-ray photon detector (depending on the mode of operation). The other areas (coherent x-ray diffraction, single particle and bio-molecules, femtosecond diffraction experiments and XPCS) all need 2-D x-ray photon detectors as their main detector. It is clear that the optimum detector differs from application to application, and the individual requirements will be discussed in the next sections. A few requirements are common to all 2-D x-ray photon detectors. They all need "photon-counting-statistics" (Poisson) limited resolution. This is very important for the low intensity regions in the image where the difference between zero and one photon can be crucial for the successful interpretation of the data. They all have to be sufficiently radiation hard to withstand the fluxes generated (integrated dose) for a few years. It is, at this moment, not possible to give hard numbers of the required radiation tolerances, since it depends, crucially, on the mode of operation of the experiments, but integrated doses at the SASE stations can be expected to be comparable to integrated doses at current day storage rings. It is obvious that Detective Quantum Efficiencies (DQE) should be as high as possible. Again, giving hard numbers is not possible at the moment, since it depends on the details of the experiments. Some experiments will just take longer with a low DQE detector, whereas others become unfeasible. The x-ray photon energy range will be either between 8 and 12 keV for the hard x-ray SASE stations, or between 0.8 and 3 keV for the soft x-ray SASE station(s). Since the detectors will be operated in "integration mode", electronic pulse height analyses cannot be used to do harmonic rejection. If higher harmonic rejection is important, this has to be done by optical means, like mirrors or multi-layers.

An important issue for all detector systems is the number of frames per second and minimum framing time. The European XFEL will use superconducting linac technology, which allows for a high repetition rate, a characteristic that distinguishes the European XFEL from the other XFEL projects. For instance, the European XFEL will produce up to 30 000 pulses per second as compared to 120 for the LCLS. Therefore, for certain experiments, the crucial parameter will be to record as many images per second as possible, this would call for a "luminosity optimised" detector. For other experiments (for instance studies of exponentially decaying excited states) it is more important to be able to collect a limited number of frames, but with a minimum framing time of 200 ns (the minimum bunch spacing), at least at the beginning of the decay. Such experiments call for a "timing-optimised" detector. Ideally, the detector would record all 30,000 images per second.

A brief summary of the detector requirements per scientific application is given below. As stated above, in this first phase the focus is 2-D x-ray photon detectors. Subsequent phases will be needed to define in more detail the needs of other systems.

Small quantum systems

The area of "small quantum systems" studies the interaction between the x-ray pulses and atoms, molecules and small clusters. The x-ray pulse will create highly charged particles and/or result in photo-fragmentation. After the interaction, the resulting particles are detected and their state analysed. Therefore, the main requirement is for fast particle detectors with drastically increased detection rates. The requirements for the detectors as well as the limitations of the existing detectors during the XFEL operation are difficult to extrapolate from existing experiments. A lot of experience is currently being gained at FLASH and the weak points of existing systems analysed. Since the initial focus is on 2D-x-ray photon detectors, the requirements for the particle detectors as well as the need for new developments will be detailed and analysed in the fourth quarter of 2006.

High energy density

The HED community studies the plasmas produced through the interaction between a laser pulse (XFEL and/or visible light) and a specific target. The XFEL is used either as pump and probe via a beam-splitter or just as a probe. One of the main signals to detect is the time-dependent fluorescence of the plasma, which calls for the development of an ultra-fast XSC to be used in conjunction with an x-ray spectrometer. Such an XSC can also be used as a timing diagnostic tool of the XFEL beam itself. The XFEL will provide pulses with time durations of about 100 fs which would make it possible to study magnetisation dynamics. Therefore, one needs an XCS which has a time resolution of 100 fs or better.

Nowadays, XSCs only have a time resolution of ~300 fs or worse and in addition are limited in detection efficiency due to their design **[6-420]**.

XCSs are based on photon-electron conversion where electrons emitted by a photocathode are extracted, then synchronously deflected by sweep plates, and finally are imaged by a suitable electron detector system. In this way the temporal information is transformed into spatial information.

In order to get a reliable and highly efficient XSC with time resolution of ≤100 fs, R&D in the following fields will be preformed:

- First, one has to understand how the photocathode limits the time resolution and the efficiency and how one can improve and optimise both properties. The main problem is that the secondary electrons emitted by the cathode have a finite non-zero energy width **[6-421]**.
- The second field is the question of electron optics and how this is limiting the time resolution of the camera. There are suggestions for an isochronous design **[6-422]** but this needs further investigation and up to now, no such camera has been built because of the complicated design.
- The question of space charge has to be investigated because it is the fundamental limit to the temporal resolution of streak cameras, especially when operated at high electron densities.
- Another field is the design of the sweep plates and the electrical sweep pulse which has to match the velocity of the electron beam in order to get high sweep sensitivity.
- The question of synchronisation and the jitter problem associated with the GaAs photo switch, which is primarily caused by laser intensity fluctuations has to be addressed **[6-423, 6-424]**.
- Last but not least one has to find the optimal detection system to 2-D image the electron beam. All these questions need to be solved in order to get a reliable and highly efficient XSC with time resolution of ≤100 fs.

The XFEL project will benefit from the fact that the comparable project LCLS at Stanford, USA, has the same requirement and need for such a camera system. The results of ongoing programmes in the USA will show if this path results in a detector system that shows the required performance. The XFEL project will initiate a similar detector development programme in Europe and join the American efforts of developing an ultra-fast x-ray detector with high efficiency which has the time resolution of ≤100 fs.

Coherent x-ray diffraction imaging

In the experiment, the sample is illuminated by the coherent XFEL beam and diffraction images are recorded. The detector required to do this is a large 2-D x-ray photon detector.

In order to resolve structures down to an atomic resolution of 0.1 nm, using x-ray radiation of 0.1 nm, the detector has to span 120° (±60°). At the same time if one wants to study objects as large as 1,000 nm with a resolution of 0.2 nm we need 20,000 pixels in each direction (assuming a minimum over-sampling by a factor 2). This means an angular resolution of 120°/20,000 = 0.006°, or 0.1 mrad. An initial compromise could be a (movable) detector that only covers one quadrant of reciprocal space, giving a requirement of 10,000×10,000 pixels. Since the detector area will only be sparsely populated with diffraction spots, a desirable mode of operation is to have the option of on the fly reconfigurable regions of interests (ROIs).

Single photon sensitivity is needed for the low flux regions of the image, for high flux regions the limitation should be counting statistics. It is expected that up to 10^4 photons per pulse per pixel will be generated in the most intense parts, with an overall integrated count rate of 10^7 photons per pulse.

It is foreseeable that certain experiments want a “luminosity-optimised” detector (as many images per second as possible) and others a “timing-optimised” detector (200 ns framing time).

X-ray Photon Correlation Spectroscopy

Photon correlation spectroscopy analyses the temporal changes in a speckle pattern that are related to the sample’s equilibrium or non-equilibrium dynamics. The method operates in the far-field and takes advantage of the coherence properties of the beam. Data are taken in either sequential mode (with the accessible time windows determined by the time structure of the machine), in “split-pulse” mode giving access to fast (picosecond-nanosecond) dynamics (and requiring a delay-line device) or in “pump-probe” mode requiring a pump pulse. Experiments want to take advantage of as many bunches as possible.

The pixel size D_p must be equal or smaller than the speckle size D_s ($D_p \leq D_s$). The angular speckle size, θ_s, is given by:

$$\theta_s = \frac{\lambda}{D_b} \quad , \tag{6.11}$$

where λ is the wavelength, and D_b the size of the utilised (transversely coherent) beam. D_b can, in principle, be chosen as big as the transverse coherence length ξ_t and since the beam is expected to be spatially fully coherent, ξ_t can be as big as the full uncollimated beam. The usable beam size is, however, limited by the ability to resolve the speckle pattern within a reasonable sample-to-detector distance L. To resolve the speckle, the incident beam size D_b should not be larger than the speckle size at the detector. This yields:

$$D_b = \sqrt{\lambda L} \quad , \tag{6.12}$$

For λ=0.1 nm and L = 20 m the beam size should not exceed 45 µm. For these parameters the minimum speckle size is D_s = 45 µm, and the required pixel size $D_p \leq D_s$. Larger pixel sizes would lead to lower contrast in the speckle pattern.

We see that the smaller the incident beam size, the larger the speckles. However, heat load and sampling volume put a lower limit on the focal spot sizes to be used. A realistic lower limit to the beam size is 25 µm. Using an x-ray wavelength, λ=0.1 nm, we get:

$$\theta_s = \frac{1\times10^{-10}}{25\times10^{-6}} = 4\mu rad \quad , \tag{6.13}$$

For a detector distance of 20 m one finds a maximum pixel size of 80 µm. Taking this as an upper bound, one would require angular pixel sizes $(\lambda/L)^{1/2} \le \theta_p \le 4$ µrad. There are two types of experiments that have different requirements for the angular range of the detector: first, small angle scattering, looking at longer length scales, and second, single crystal diffraction, looking at the shorter length scales (down to atomic resolution).

In the case of single crystalline samples one gets distinct diffraction spots all the way out to a scattering angle of 60°. Since one might be interested in only a few diffraction spots one does not have to cover the full scattering range, which would mean 120 degrees at a distance of 20 m! However, one could move a smaller 2-D detector to the diffraction spots. It is foreseen that ten diffraction spots have to be covered simultaneously, thus, ten of these smaller area detectors are needed. The detector module defined for the small angle scattering experiment is then sufficient for the single crystal experiment.

The detector size needed for the small angle scattering experiment is determined by the minimum length scale we want to observe. If we want to see details down to 10 nm using 0.1 nm radiation, we need to go out to a scattering angle of 0.6 degrees, meaning 1.2° in total (21 mrad). With an angular resolution of 4 µrad, one would need 5,000 pixels in each direction.

However, if one does not use a monochromator to increase the monochromaticity and with that the longitudinal coherence length (see below) one will be limited in angular range by the fact that the Path Length Difference (PLD) of the various rays hitting a pixel has to be smaller than the longitudinal coherence length, which is given by:

$$\xi_l = \frac{\lambda^2}{\Delta\lambda} \quad . \tag{6.14}$$

The natural monochromaticity $\Delta\lambda=10^{-3}\times\lambda$, gives $\xi_l=10^3\times\lambda$ and for λ=0.1 nm radiation we get ξ_l=100 nm. It can be shown geometrically that the PLD is given by:

$$PLD = 2W\sin(\theta)^2 + D\sin(2\theta). \tag{6.15}$$

where W is the thickness of the sample and D is size of the beam. For typical values for sample thickness of 1 mm, beam size of 25 µm, longitudinal coherence length of 100 nm, maximum scattering angle of 0.10 degrees, corresponding to 0.2 degrees (3.5 mrad) detector coverage, with 4 µrad resolution leads to a requirement of 875 pixels. This means a 1K×1K detector, which should be the basic building block.

Tiling several of these 1K×1K detector modules together would allow one to cover SAXS pattern with length-scales down to 10 nm (in which case, one has to use a monochromator to increase the longitudinal coherence length). Therefore, a good strategy is to build a basic building block with 1K×1K pixels, to be tiled to a 5K×5K imager.

The maximum intensity per pixel per pulse is ≤1,000 photons. Single photon sensitivity is needed at low intensities; this means the counting statistics will be limited.

X-ray absorption spectroscopy

The fast pulse structure of the electron beam of the XFEL accelerator makes it ideally suited to performing time-resolved x-ray spectroscopy. There are two possible modes of operation.

Mode 1

Stepped energy scan. With a suitable variable gap undulator and crystal monochromator it is possible to make "conventional" stepped scan spectroscopy measurements. Obviously, the system under study would have to be capable of being reproduced in its starting configuration for each point in the scan, e.g. in a pump-probe experiment. In this mode the sample could be extremely dilute and the fluorescence signal measured by an energy-dispersive detector array. Time-resolved measurements in the 1 ms to 100 ms regime can be done purely using the bunch structure; however, this domain can also be accessed by other SR sources. Timing measurements using the 100 fs bunches can still be made in this configuration if single pulse macro bunches are selected, and then the 100 fs-100 ms regime can be explored. This will require ionisation chambers that can deal with the instantaneous flux without losing linearity. For dilute samples, fluorescence detection or Auger electron detectors are required. The main challenges here centre on the instantaneous flux: conventional energy dispersive detectors will suffer massive pile-up; therefore, new and special signal processing electronics will be built to overcome these limitations.

Mode 2

Energy dispersive. A bent crystal monochromator can be used to produce a focused, but angularly dispersed, beam at the sample. The beam is transmitted through the sample on to a position sensitive detector which now records the entire range of energies simultaneously. The position sensitive detector would need 1,000 channels, be charge integrating and capable of being read out in the time between the 100 fs pulses, i.e. at 5 MHz. Again, it would be possible to have the pulse train incompletely filled: if one 100 fs pulse per bunch was selected, this would allow the 100 fs to 100 ms regime to be accessed and relax the readout time requirement of the detector. The best detectors currently available based on Silicon microstrip technology only operate at speeds up to 10 µs. Considerable development will take place to increase their speed, if this mode of operation is retained.

The advantage of the dispersive configuration is that all points in the spectrum are recorded simultaneously and time slices can be recorded at the maximum framing rate of the detector. This is a much more efficient means of data collection than the step-scanning mode, but requires a higher concentration of the element whose absorption edge is being studied, as the sample absorption is measured in transmission rather than by an indirect process such as x-ray fluorescence or Auger emission.

Femtosecond diffraction experiments

From a detector perspective, this field can be separated into two domains which have very different requirements, especially concerning the spatial resolution: non-crystalline and crystalline samples.

Pump-probe scattering experiments on non-crystalline samples

A sample, typically in solution, is promoted to a "pumped" state by a pump pulse (e.g. a visible laser, magnetic or electric field, XFEL or other pulse) and analysed after time Δt with an XFEL bunch. Samples are in solution, which means that the scattered signal is (nearly) circularly symmetric, and the scattering intensity is slowly varying as a function of momentum transfer (scattering angle).

In this experiment, the form of the scattered signal is determined by the sample rather than by the source (except of course for the intensity). Therefore, we can base our requirements on existing experiments on storage ring sources.

In this pump-probe experiment one compares a pumped (excited) state with the un-pumped (ground) state. Simulations on for instance I_2 dissociation show that changes down to length scales of 0.065 nm are significant and can be measured. This means a scattering angle 2q=100° is needed (using 0.1 nm radiation) and the detector has to cover ±100°. In liquid scattering this is often expressed in a Q-range where, Q=4psin (q)/λ and the detector has to cover up to Q=10 Å^{-1}.

The experiments will look at the changes in only a few inter-atomic distances. One can show that for small changes in inter-atomic distance we get approximately five oscillations in the Q range between 0 and 10 Å^{-1}. For large changes (rupture of molecules) we get approximately 10 oscillations. Since we only probe a few changes, a sampling with 250 points over the entire Q range is sufficient, even if we get up to 20 oscillations. This gives 500 sampling points (positive and negative scattering angles) per direction. Corresponding to an angular resolution of 200/500=0.4° (=7 mrad).

We need to measure small changes in large signals. Therefore, counting statistics-limited resolution is needed. Based on the experience gained at the ESRF we can extrapolate to the European XFEL (which has 10^2 times the number of x-rays per bunch), giving a maximum of 10^4 photons per pixel per pulse, and an overall integrated flux of 10^7 photons per pulse.

It is conceivable that experiments requiring as many pulses per second as possible to be recorded and thus, need a "luminosity" optimised detector. Other experiments will want to sample the time evolution of the system with a "timing optimised" detector (200 ns time resolution, at least in the beginning).

Pump-probe scattering experiments on crystalline samples

Again, the sample, either a powder or a single crystal, is promoted to a "pumped" state and analysed after time Δt with an XFEL pulse. Samples will give Bragg peaks, meaning localised intense spots on a low intensity background in the case of single crystals, or "Bragg-rings" (powder rings) meaning spotty (intense) rings on a low intensity background.

The angular resolution required is defined by both the size of the Bragg spots and the number of spots we want to measure (separation between the Bragg spots). The first one is independent of the distance between sample and detector (parallel beam), the second one scales linearly with detector distance.

The size of the Bragg spots is defined by a convolution of the mosaicity of the sample, the monochromaticity and divergence of the beam, and the size of the focal spot (or the size of the sample, whichever is the smallest). Assuming a static sample (in 100 fs, macroscopic matter cannot move), and $\Delta E/E=10^{-3}$ the Bragg spot size is basically defined by the beam size on the sample (divergence of the beam is a few µrad). Assume an intermediate focal spot size of a 100 µm (FWHM), then the Bragg spots will also be 100 µm (FWHM) on the detector, no matter what the detector distance is. This gives approximately 300 µm FW1%M. We want to be able to resolve 1,000 diffraction spots across the detector, giving a detector size of 300 mm. For 0.1 nm radiation, and a resolving power down to 0.1 nm, we have to measure out to $2\theta=\pm 60°$, which defines the sample to detector distance to be: L = 150/tan(60) = 85 mm. In summary: we need 3K×3K pixels of 100 µm. It is no surprise that detectors of this type are currently used at storage rings for protein crystallography.

Single photon sensitivity is needed for low flux; for high flux the limitation should be counting statistics. Based on the experience at the ESRF (1.4×10^{10} photons per pulse), we can estimate a maximum of 10^5 photons per pulse per pixel at the European XFEL ($\sim10^{12}$ photons per pulse). The overall integrated intensity is expected to be in the order of 10^7 photons per pulse.

It is conceivable that experiments requiring as many pulses per second to be recorded, or that experiments want to sample the time evolution of the system (200 ns time resolution, at least in the beginning), although in this case sample heating will be a major obstacle.

Single particles and bio-molecules

The so-called "single molecule diffraction" involves the recording of speckle patterns in the far field. Phase retrieval by "oversampling" requires very fine detector resolution, where the achievable structural resolution is determined by the maximum accessible momentum transfer (requiring a large detector).

Again, the detector has to span 120° (±60°). In order to solve structures as large as 100 nm (a large virus for example) down to atomic resolution, we need 4,000 pixels in each direction (assuming a minimum oversampling by a factor of 2). This means an angular resolution of 120°/4,000 = 0.03°, or 0.5 mrad. The sample to detector distance should be minimised and should be evacuated, since anything between the sample and the detector (even the residual molecules in a vacuum) will increase the background.

Another important aspect is the ability to collect scattering of even the very small angles, close to the primary beam. This means that for a small sample to detector distance. the primary beam stop might create too much shadowing. Therefore, the option to have two detectors has been discussed. The first, close to the sample, collects large angle scattering and has a central hole to let the small angle part of the scattering pattern pass to the second detectors. This small angle part is then collected by a second detector at a much larger distance. The option of two detectors is also advantageous as it increases the dynamic range of the detector system.

Single photon sensitivity is needed for the low intensity regions of the image; for high intensity regions the limitation should be counting statistics. It is expected that up to 10^4 photons per pulse per pixel will be generated in the most intense part (small angles). An overall scattered flux of 10^7 photons per pulse is expected. Since the intense x-ray pulse will destroy the single particle (Coulomb explosion), time is needed for the residuals to be pumped away (“the smoke has to clear”), therefore, the foreseen repetition rate is 10 Hz. The detector has to be housed inside a vacuum chamber, although a thin entrance window could be considered for protection of the detector.

Hard x-ray by spontaneous radiation

The last field of applications is concerned with the use of hard x-rays up to 100 keV from spontaneous radiation. Two main advantages of this source over existing (SR) sources are the short pulse length and the low emittance. To fully exploit the potential of these sources, detectors with high efficiency at high energies will be constructed. It is clear that the main challenge will be in developing high-Z detector materials. Materials like GaAs and CdZnTe are promising candidates. Since the focus of the initial phase is one 2-D x-ray photon, detectors for the 8-12 keV range, the requirements and for the high energy detectors will be detailed in the first part of 2007.

6.5.4.3 Strategy

Two-phase approach

The detector requirements imposed by the experiments, and listed above, present a major challenge for detector builders. At the same time, several potential solutions exist by using today’s state-of-the-art technology, as will be shown further on. It is important to realise that Europe has a strong background and experience in building large scale detection systems, stimulated by high energy physics, space research as well as SR research. As a result, Europe holds a world leading position in many areas relevant to the detectors needed for the European XFEL, including, but not limited to, Silicon drift detectors, hybrid pixel detectors, monolithic active pixel sensors, high density inter-connects, and deep sub-micron chip design. There are various laboratories throughout Europe that have specialised in either specific detector components or complete detector systems. Also, there already exists a number of collaborations between laboratories providing complementary expertise. The European XFEL will stimulate the formation of consortia that will be able to supply detector systems on day one of the XFEL operation that meet most, if not all, of the requirements. Prototypes of such detectors will be ready when the LCLS is coming on-line. Besides starting the development and subsequent construction of the detectors for the first experiments using state-of-the-art technology as soon as possible, it is also crucial to initiate a research programme into detector technologies in order to arrive at uncompromised performances in the future.

Since the XFEL will produce SASE radiation in both the hard (8-12 keV) and the soft (0.8–3 keV) x-ray range, and since many applications intend to use both, it is mandatory that x-ray detectors are developed for both energy ranges. The situation is further complicated by the fact that the spontaneous emission undulators will produce very hard x-rays, well above 100 keV. An initial focus will be put on the 8-12 keV energy range, at the same time enough flexibility will be built into the detector systems, to make them applicable to the lower and higher x-ray energies as well, possibly with somewhat compromised performances. In a second phase, research will be initiated to optimise the detector systems for the lower and higher x-ray energies, this includes, but is not limited to, the development of detector materials different than Silicon, like GaAs and CdZnTe.

Experience has shown that both the planned experiments and the requirements quickly evolve in the first years of the project (new ideas, better defined ideas, etc.). We will, therefore, proceed in at least two phases (see also Table 6.5.1):

- **Phase 1:** Define, design and construct the detectors for day-one operation of the XFEL, using (optimised) current state-of-the-art technology, and based on the requirements imposed by the currently planned experiments.
- **Phase 2:** Define, design and construct the optimised ("ideal") detectors using the experience gained from the construction and operation of day-one systems, using new detector technologies, using the experience gained at other sources (like FLASH and the LCLS) and based on new and better defined requirements (new experiments).

Phase 1 will advance in various steps (partly in parallel):

- Step one: 2-D x-ray photon detectors;
- Step two: 0-D and 1-D x-ray photon detectors;
- Step three: x-ray streak cameras;
- Step four: particle detectors (electrons, ions, atoms and clusters);
- Step five: generic detector research.

This phase has already started with the dedicated workshop on "Detectors for the XFEL", following the three scientific application workshops. The first step of Phase 1 focuses on the requirement for 2-D x-ray detectors, judged to be the area requiring most efforts. As indicated at the end of this chapter, the requirements are currently being detailed via an interaction between detector builders and application scientists. A call for propositions to construct the required 2-D x-ray detectors will be launched before the summer of 2006. The exact format of the call (call for proposals, pre-proposals, letters of interest, etc.) is currently being decided upon. The deadline for replies will be 15 September 2006, after which a selection will be made before the end of 2006. The consortia retained in the selection will then be asked to prepare a detailed project plan. At this stage a strong interaction with the relevant application scientists will be needed. It is anticipated that the application scientists will be part of the consortium building the detector(s). To guide this process, a Detector Advisory Board will be convened as soon as possible.

Link to other FEL projects

Because the XFEL, operating at 5MHz, places the most severe demands on the detectors, the developed systems will naturally be applicable at many other FEL or SR x-ray sources. In addition, with appropriate modification, applications can be found for the XFEL detectors on other, lower energy XUV/VUV FELs, both existing and planned, elsewhere in the world.

It is important to consider the other major XFEL facility, LCLS, currently under development in the USA, which will be in operation before XFEL. The formal link already existing between the LCLS project and DESY will be extended to the XFEL GmbH once it comes into existence and starts detector activities. The European detector laboratories already have good informal links with the American project and access to this facility for detector testing will be available. Although LCLS will have a very different pulse structure, it will be an important test bed for XFEL detector systems. Appropriate detector technologies will be exchanged between the USA and Europe. It is worth pointing out that the ESRF running in 16-bunch mode produces 176 ns spaced x-ray pulses, close to the 200 ns of the XFEL. Therefore, access to the ESRF for timing issues-related studies will be very beneficial. Access to FLASH for testing components, in particular timing-related issues is foreseen at an early stage.

6.5.4.4 Design and construction of 2D-systems in Phase 1

In what follows an overview is given of the technologies that will be used to construct the Phase 1 2-D x-ray detectors. As stated before, there exists a lot of experience within the European detector community in constructing such systems for real experiments, be it synchrotron radiation, particle physics or space research. Examples will be given of systems that have been developed or are under development and their shortcomings for the XFEL applications will be discussed, indicating the fields where developments are needed. The examples given are by no means exhaustive, and the omission of certain projects and developments means neither a judgement about their importance nor about their applicability to the XFEL requirements. Also, the fact that a specific project is quoted here indicates neither any pre-selection nor preference for the XFEL project. The selection of the most suited technologies and competitive consortia will be made via a fair and open competition.

Hybrid pixel array detectors

One of the technologies very likely to be used for one or more of the 2D-detector systems is hybrid pixel array detectors (PADs). A hybrid PAD consists of a detector layer which is an array of photo diodes that converts the incoming x-ray to electrons and holes. This detector layer is then coupled, via bump-bonds, to a pixellated readout chip (application specific integrated circuit, or ASIC). Each pixel contains its own signal processing electronics as well as a buffer to store the data. The device is schematically given in Figure 6.5.2.

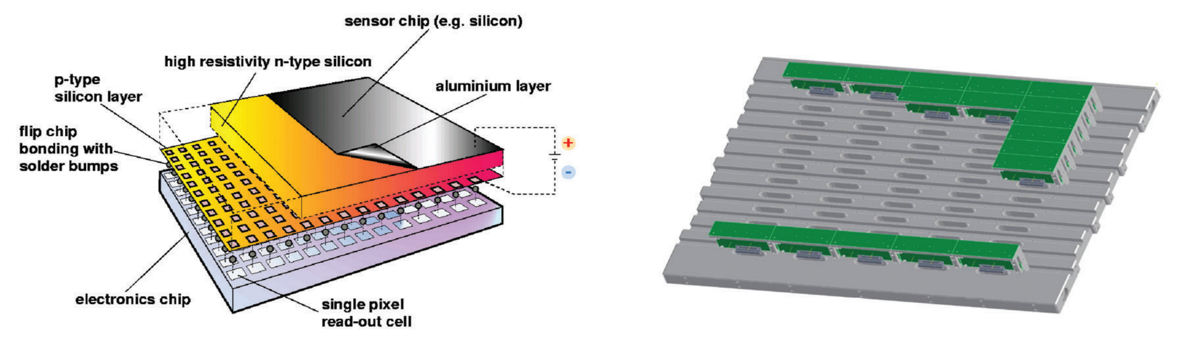

Figure 6.5.2 *Left: Schematic layout of a hybrid PAD (Courtesy: M. Campbell). Right: PILATUS 6M module containing 17 of total 60 modules. The total detector will have 6 million pixels, and will almost be 45×45 cm^2 (Courtesy of Ch. Broennimann* **[6-425]***).*

One of the advantages of hybrid PADs is that the sensor layer and the electronics chip can be optimised separately. In this way it is possible, for instance, to design a single electronic chip and to couple it to different sensor chips optimised for different x-ray energies, either by using different thicknesses of Silicon, or different materials like GaAs or CZT. A lot of experience for using these hybrid PADs has been gained over the past years through the various projects like: MEDIPIX, PILATUS, XPAD, APAD, etc. The first three are European projects and use photon counting. APAD is an American project (CHESS) using integrating chips. For the XFEL applications, new electronic chips will be designed, using very low-noise integrating electronics, with storage capacities of a few hundred frames or more. The APAD chip, for example, can store only eight consecutive frames. This will be done in the newest CMOS technologies (0.13 micron) and using radiation tolerant designs (like ring-gate transistors). The individual modules given in Figure 6.5.2 will then be assembled into large systems similar to the PILATUS project at SLS/PSI, (also shown).

Silicon drift detectors (SDDs)

The semi-conductor drift chamber invented in 1984 by Gatti and Rehak, uses a sideward drift principle, which allows for the use of small read-out anodes, having small capacitance, even for large area detectors. This small capacitance results in a very low-noise device, with excellent spectroscopic performance. Many devices have since been constructed based on this drift principle, and Fano-limited performance has been reached in multi-element devices **[6-426]**. The very low noise performance of these systems can be used to obtain single photon sensitivity, an important requirement for the imaging experiments at the XFEL. Since all photons arrive in 100 fs, energy discrimination (spectroscopy) inside the detector is not possible. However, the spectroscopic performance of the detector can be used to tell the number of monochromatic photons absorbed, giving counting statistics limited performance. Furthermore, by keeping drift lengths small, 5 MHz framing rates are technically possible. A very promising system is the controlled drift detector (CDD) with DEPFET readout and running in continuous readout mode (non-controlled mode). A schematic layout is given in the Figure 6.5.3.

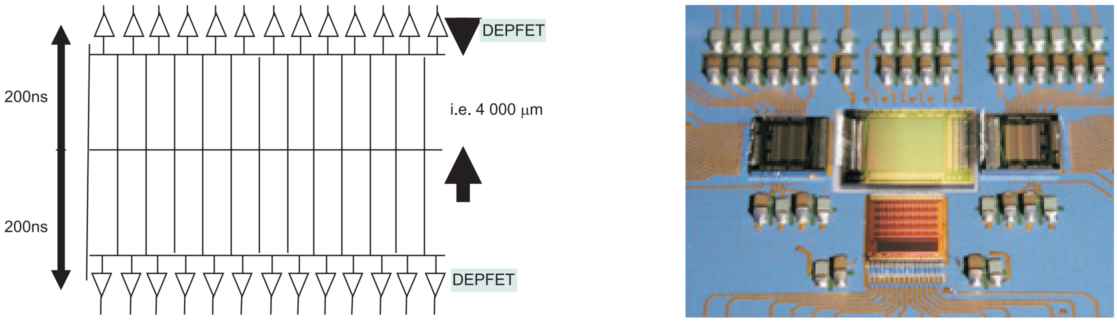

Figure 6.5.3 *Left: schematic layout of a CDD detector with DEPFET readout allowing 200 ns framing time. (Courtesy of L. Strüder). Right: operational CDD detector with front-end read-out electronics. (Courtesy of L. Strüder).*

Such detector modules will be coupled with ASICs for readout and frame storage. By using the most advanced CMOS technology (0.13 µm) and possible 3-D interconnects it looks possible to store ultimately 3,000 frames, although this might not be reachable for the day-one detectors. The drift detector principle described above has been used several times in detectors for high energy physics as well as for space research. A picture of an actually operational device is given in the right part of Figure 6.5.3.

Column parallel CCDs

Very fast CCDs are currently in development for particle physics applications such as the linear collider. There, customised CCDs are being developed that readout each column of the sensor in a parallel fashion, increasing the frame rate by orders of magnitude. Prototype custom CCDs have been built that bump-bond directly to high density readout ASICs down one readout edge of the CCD. This means that rather than read out the CCDs through one or more corner, each column has a dedicated output and is instrumented with its own amplifier and analogue to digital converters (ADC). In this arrangement charge is shifted from the CCD into the readout ASIC where it is measured and stored. The standard CMOS technology in the readout ASIC provides excellent matching and accurate charge-to-voltage conversion. Bump-bonding of the ASIC to the CCD means that the pitches of ~20 µm can easily be achieved and the low parasitic capacitance of the bonds minimises the noise performance penalty of interconnect load.

Figure 6.5.4 illustrates the concept. The picture on the left shows a schematic of the imaging surface of the CCD. Each column is clocked in parallel and samples converted at the bottom of each column. The image on the right shows a readout ASIC (in blue) bump-bonded to the CCD where the image is captured. These designs are currently highly optimised for the linear collider flavour identification (LCFI) application. If this concept is retained for one of the applications at the XFEL, they will be adapted to cope with increased dynamic range and modified to match the XFEL timing structure.

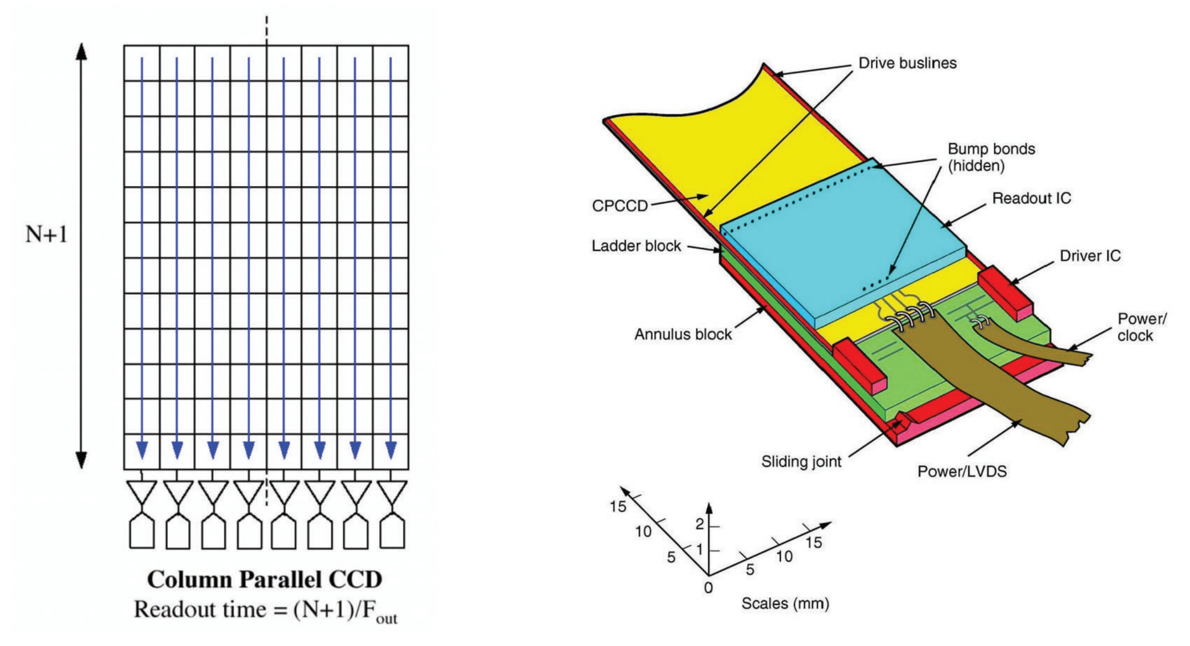

Figure 6.5.4 *Image showing a column parallel CCD (left) with bump-bonded readout (right) ASIC (courtesy of LCFI).*

MAPS

Monolithic active pixel sensors (MAPS) were proposed as imaging devices over 10 years ago **[6-427, 6-428]**. They are manufactured in a standard microelectronics technology (mainly CMOS) and integrate the sensor elements in the readout ASIC. It was immediately recognised that they have several advantages with respect to existing imaging devices in terms of feature-size, integration of functionality, radiation resistance, power consumption, ease of use and low cost. Today, MAPS have overtaken CCDs as the main imaging devices for commercial applications and are now being adapted for x-ray detection, for example in intraoral dental sensors. The demonstration of their excellent performance as particle detectors triggered a world-wide development of MAPS for scientific applications. In the last few years a number of large sensors have been designed and manufactured, including a 12 million pixel device with 5 µm pixels for EUV detection and a 1 ½-D sensor with 32 µm pixels for x-ray detection **[6-429]** (Figure 6.5.5).

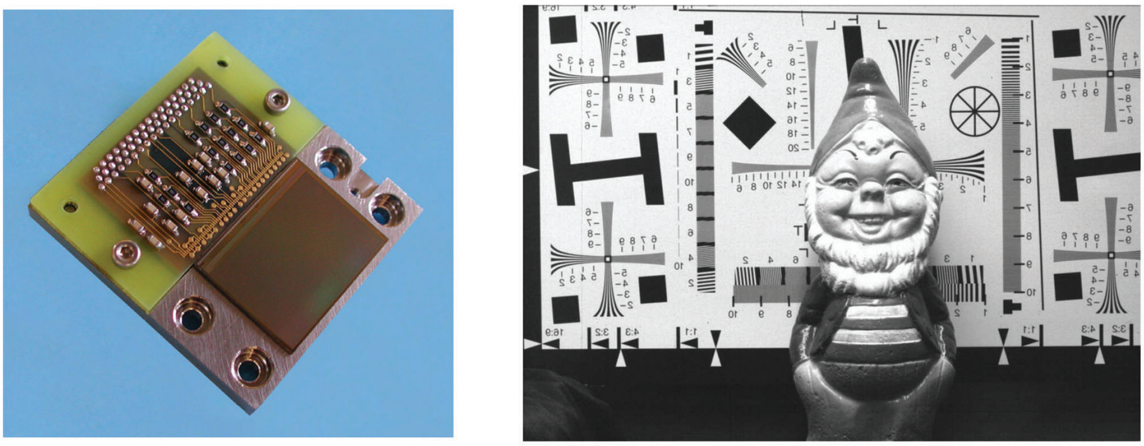

Figure 6.5.5 *Left: Photo of 12M-pixel MAPS mounted on invar block (for cooling). Right: Image taken with this sensor (courtesy of N. Waltham, M. Prydderch).*

For x-ray detection, high efficiency can be achieved by coupling to a scintillator or with a suitable directly deposited high-Z material. Alternatively, a stack of sensors can be arranged to achieve high efficiency together with energy information. High spatial resolution can then be achieved with small pixels and very high time resolution integrated by adopting architectures already developed for high-energy physics experiments: the flexible active pixel sensor (FAPS), capable of frame rates in excess of 10 MHz by storing signals inside the pixel **[6-430]**. Such a sensor with 20-μm pixel and 10 storage cells was already successfully demonstrated and the technology could be scaled up for the needs of XFEL (see Figure 6.5.6). The feasibility of this approach for the XFEL applications, as well as the advantages and disadvantages as compared to other technologies will be evaluated during the third quarter of 2006.

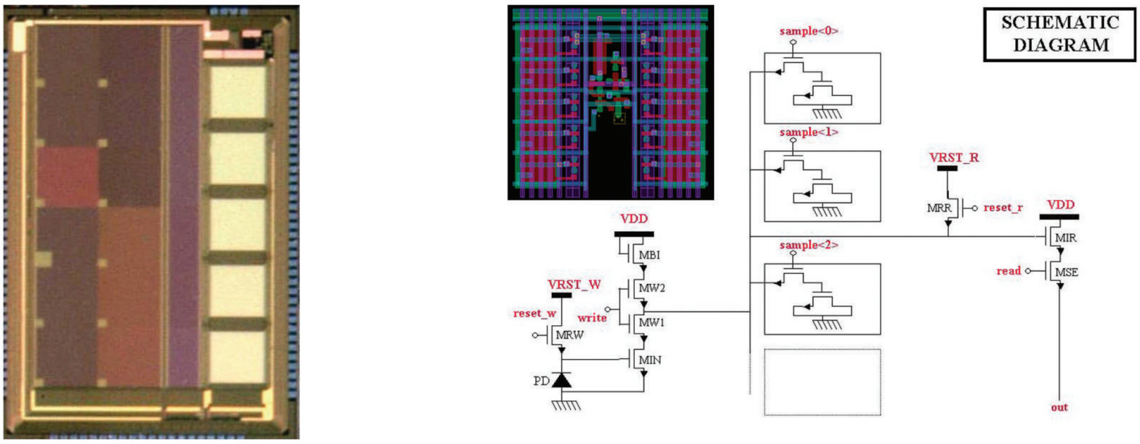

Figure 6.5.6 *Left: Photo of FAPS prototype. Right: schematic of the FAPS pixel (courtesy of R. Turchetta).*

6.5.4.5 R&D of new 2-D system components in Phase 1

The above detectors for day-one operation will be built based around proven technologies and materials to keep risk levels at a manageable level and provide a reliable initial solution. However, to realise the full potential of the XFEL, a step change in sensor performance is required in many areas. This parallel programme of technology development is required to underpin the building activity and to develop ways of breaking through existing performance limits.

For most detector systems Silicon is likely to be the material of choice for the conversion of 5 keV to 15 keV photons. However, this choice raises some immediate concerns:

Efficiency

To be effective above 12 keV it must be used in thick layers (>500 μm) to achieve sufficient stopping power. This leads to parallax errors for tiled surfaces due to uncertainty in conversion depth for abnormal incident photons. This worsens the point spread function and will become severe at high angles.

Radiation damage

Whilst x-rays in this energy range will not cause any bulk damage to Silicon, interface layers on the detector surface and in the ASICs will give rise to problems. Charge build-up at these interfaces will disturb the ASIC transistors and, in the sensor material, will ultimately modulate the bias conditions of the sensor.

Scattering

One of Silicon's great strength is that high position resolution can be achieved by patterning the material with pixels and strips to achieve segmented layouts. However, scattering will occur at the ~0.01% level (for 1 keV photons in Silicon) and the scattered photons will stray from bright spots affecting data quality in low count rate regions.

High signal flux

At high energy densities, fields in Silicon will affect the usual charge collection process: Self-repulsion of the converted charge will broaden the signal image and possibly shield sensor areas, thereby disturbing the local detector bias conditions.

Other sensor materials offer ways of managing some of these issues but challenges exist in making these solutions useable. High-Z materials are one area that should be investigated. This is because high-Z direct conversion semiconductor materials are extremely efficient detectors in this spectral region. For example: 50 μm of CZT stops 98% of 12 keV photons, i.e. more than 10 times better than Silicon. This should deliver low parallax even in small pixel geometries (e.g. $50 \times 50\ \mu m^2$) as well as providing excellent stopping power to protect ASIC electronics behind the detector. In addition, as these materials do not posses oxide interface layers of their own they should be extremely radiation hard in this environment. The potential for thinner layers also minimises the effects of photon scattering as the scattered photons will be efficiently stopped locally. Fields in the device, however, are still likely to be disturbed and this remains a potentially serious problem. In summary, thin layers of materials such as CZT, GaAs, HgI and CdTe have the potential to be efficient, radiation hard detectors matching the performance requirements of the XFEL and high density readout electronics well.

Instrumentation of the sensor material, be it Silicon or high-Z in form, will always require ASICs matched to the detector substrates. These must sense, amplify and process the image data for handling in the DAQ system. Various groups building LHC particle physics detectors have demonstrated that radiation hard ASICs can be built using standard CMOS technology with a feature size of 0.25 µm and lower, provided various layout precautions are taken **[6-431]**. From a technology perspective solutions, therefore, exist. However, each new detector system still requires ASIC development as existing photon counting systems (e.g. Pilatus or Medipix) will not be appropriate because of the pulsed multi-photon structure of the machine. Specific designs suited to the XFEL sensors and tailored to the experiments will have to be developed. In addition, as the form of radiation differs significantly from that studied for particle physics, a qualification of technologies used for exposed environments will also be needed.

The sensor material must then connect via reliable interconnect technology to front-end ASICs that will form the first stage of the DAQ system. Depending on the format and geometry of the sensors, interconnects will either be wire- or bump-bond-based. Again, significant experience exists, particularly in particle physics and SR community. However, new developments enable so-called 3-D stacking or integration to allow stacking of multiple chips on top of each other. If applied, this technology will have to be mastered and adapted for the XFEL detectors.

Data processing in the front-end system raises further concerns as, for example, sensors of 4K×4K pixels, running at 30,000 frames per second with high dynamic range images will produce very large volumes of data. This will have to be processed efficiently and assembled into data sets for offline storage and analysis. Extensive use of fibre-optic systems will ease data transport, however, efficient computing systems will still be required to capture and analyse the experimental data. The bunched nature of the beam structure will necessitate on-detector storage to buffer the data flowing to DAQ.

Synchronising the detector systems to the FEL bunch structure also presents challenges. It is very important to be able to reliably separate the data from each 100 fs pulse so that records can be assembled from each detector system for combined experimental techniques. Systems such as the TTC system, developed at CERN **[6-432]** for the distribution of event clocks, can be used, but detectors that require accurate timing to better than 100 fs will still require local synchronisation. Local sensing of the pulse train, for example, from local beam monitors, will, therefore, be required to lock on to the data correctly. In addition, identifying ‘out-of-time’ events will also be needed to flag error data in the system for discarding.

Finally, because of the large volumes of data involved, data reduction is inevitable for the DAQ system. This means that frames of interest must be rapidly identified and tagged for transmission to off-line storage. The algorithms for achieving this are required as well as the hardware to deliver it. This will lead to complexities as, for example, fluorescence life-time in scintillators (if significant compared to 200 ns) will have to be deconvolved from earlier data frames that might be rejected by the system (and therefore, impossible to reconstruct).

In summary there are several generic development areas which need to be addressed:

- Radiation damage studies of Silicon and high-Z direct conversion semiconductor detectors. This is required to establish the scale of the problem with modern Silicon technologies and define which materials can be used.
- Interconnection and deposition techniques for thin layers of high-Z materials. This is critical for delivering systems matched to the XFEL. Most high-Z materials are used in large volumes in thick blocks for high energy applications; here, the driver is for more efficient, thinner layers.
- The investigation of carrier transport in thin layers of high-Z materials. This will be required to develop accurate mathematical models of detector systems, so that replacements for Silicon systems can be modelled accurately and their relative benefits estimated.
- The investigation of high energy density deposition in materials and subsequent carrier transport, specifically looking at self shielding carrier drift (due to charge cloud repulsion), and diode and ohmic contact performance in high charge collection situations.
- Microelectronics design optimised for fine pixel geometries and integrating architectures. The performance of modern CMOS systems needs to be evaluated in the radiation environments expected at the XFEL.
- Some standardisation of the DAQ system must be defined with a view to understanding how the experiments will synchronise, process and transmit their data to offline storage.

6.5.4.6 Data acquisition, handling and storage

It is important to define clearly and at an early stage what comprises the detector system. Does the detector system includes everything up to the data storage, or only up to the digital output? No matter where the line between “detector” and “instrument control” is drawn, it is important to consider the detector as an integral part of the experiment. Therefore, a close and direct link between the detector builders and the experiment software control systems is important from the very first stages of the project. This is crucially important since the detectors will be capable of producing enormous amounts of data which have to be reduced, stored and ultimately processed. Equally important is the interfacing with the rest of the experiment, since a large fraction of the experiments will be triggered and single-shot measurements. Experience at large scale facilities has shown that a unified approach to instrument control, including detectors, greatly simplifies and improves the operation. This means, where possible, standardised interfaces and protocols.

6.5.4.7 *Preliminary programme for start up of Phase 1*

Table 6.5.1 below indicates a first draft of a timeline to start Phase 1 detector construction and research. This proposed timeline is to be considered as a first initiative to start discussions. Many issues, technical, financial and administrative, have to be clarified to a sufficient degree before actual calls can be issued. But since the first operation of the XFEL is only six years away, it is crucial not to delay the start of detector projects any further.

Step 1: 2-D X-ray Detectors (two-step procedure)	
May-2006	Detailed Requirements
Jun-2006	Launch first call
Sep-2006	Deadline first call
Nov-2006	Evaluation and selection proposals
Q2-2007	Start projects
Step 2: 0-D and 1-D x-ray detectors (one step procedure)	
Q3-2006	Detailed requirements
Q4-2006	Launch call
Q1-2007	Evaluation and selection proposals
Q2-2007	Start projects
Step 3: X-ray streak cameras (one-step procedure)	
Q3-2006	Detailed requirements
Q4-2006	Launch call
Q1-2007	Evaluation and selection proposals
Q2-2007	Start projects
Step 4: Particle detectors (one-step procedure)	
Q4-2006	Detailed requirements
Q1-2007	Launch call
Q2-2007	Evaluation and selection proposals
Q3-2007	Start projects
Step 5: Generic detector research	
Q1-2007	Definition of research areas

Table 6.5.1 *Time line for Phase 1 actvities*

Overall milestones

There are a number of identifiable milestones for the detector projects even at this early stage, mostly set by the progress of the construction of the XFEL machine and availability of the LCLS in the USA.

Q3/2006	Installation of a detector advisory board (DAC)
Q4/2006	Selection of Phase 1 detector projects
Q1/2007	Establishment of XFEL detector group
2009	LCLS becomes available for detector testing
2013	Initial operation of the European XFEL

6.6 Summary of cost and manpower requirements

The capital investment and cost of the personnel necessary to build the photon beamlines and 10 scientific instruments as described in the previous sections of this chapter, are summarised in this section. The basis for the cost estimate is the system layout and the parameters specified here. For an overview about the total project cost, a description of the methodology of the performed estimate for capital investment, the determination of the cost for personnel and the expected uncertainties, see Chapter 10.

Table 6.6.1 gives a summary of the project cost in terms of capital investment and the cost for personnel for the photon beamlines and scientific instruments. The relative distribution of the full cost is shown in Figure 6.6.1. The photon beamlines and scientific instruments contribute about 13% to the overall capital investment and more than 16% to the full project cost. Integrated over the entire construction phase, 779.5 full-time equivalents (FTE) are required for the photon beam system.

	Capital Investment [M€]	**Personnel Cost [M€]**	**Full Cost [M€]**
Photon beamlines	22.41	20.58	42.99
Scientific instruments	73.20	41.12	114.32
Total	95.61	61.70	157.31

Table 6.6.1 *Capital investment, personnel cost and full cost in Million-Euro for the photon beamlines and scientific instruments. Values are given for capital investment, personnel cost and full cost in Million-Euro.*

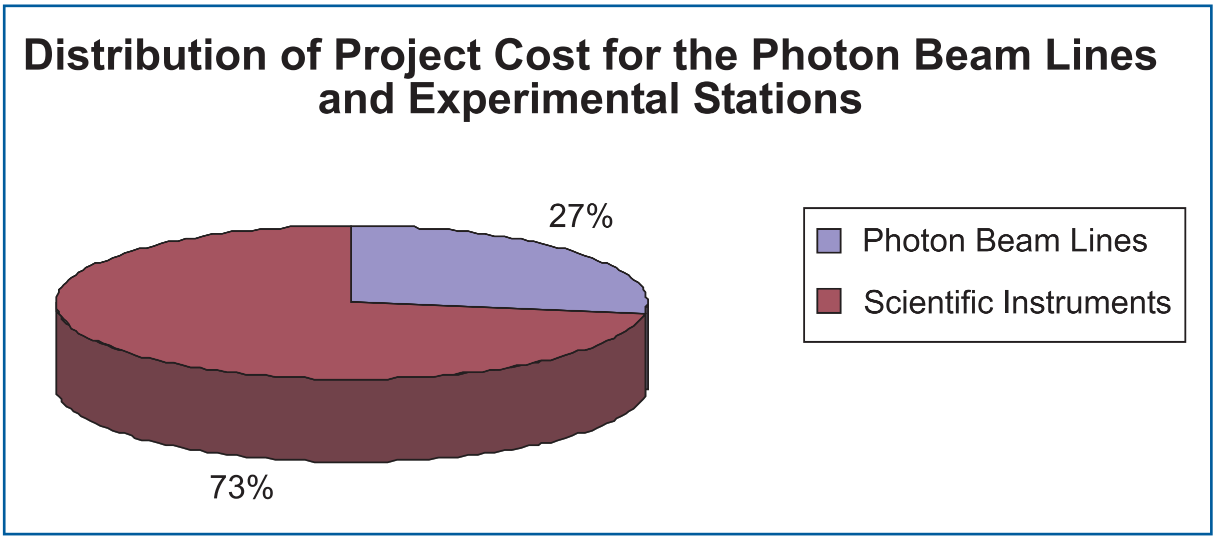

Figure 6.6.1 *Relative distribution of full project cost for the photon beamlines and scientific instruments.*

Photon beamlines and scientific instruments

The cost summarised in Table 6.6.1 and Figure 6.6.1 include the cost and manpower of the following:

Photon beamlines: design, construction, installation and commissioning of the x-ray optics and vacuum systems installed in the photon beamlines; R&D for x-ray optics issues related to the experiment layout; design, construction, installation and commissioning of the photon beam diagnostic systems; R&D for photon diagnostics systems to be used at the scientific instruments;

Scientific instruments: design, construction, installation and commissioning of 10 scientific instruments in the experiments hall; R&D activities in the areas of sample environment and manipulation and optical laser installations; three full pixelated area detector systems; R&D on other detector systems (x-ray streak camera and particle detectors) and for conventional systems installed at the scientific instruments.

References

[6-1] *LCLS-The First Experiments*, Stanford (2000), see also: http://www-ssrl.slac.stanford.edu/lcls/papers/LCLS_experiments_2.pdf

[6-2] TESLA Technical Design Report, eds. F. Richard et al., DESY 2001-011, DESY, Hamburg (2001).

[6-3] M.R. Howells, private communication (2006).

[6-4] M.R. Howells, *Optical designs and tolerances for the 8.3.1 protein crystallography beamline*, ALS technical note, LCBL-538, LBNL, Berkeley, (1999).

[6-5] S. Matsuyama et al., *Diffraction-limited two-dimensional hard-x-ray focusing at the 100 nm level using a Kirkpatrick-Baez mirror arrangement*, Rev. Sci. Instrum. 76 (2005) 083114.

[6-6] http://www-cxro.lbl.gov/

[6-7] J. Arthur et al., *Linac Coherent Light Source (LCLS) – Conceptual Design Report*, SLAC-R-593, SLAC, Stanford (2002).

[6-8] Workshop *Optics for x-ray FEL applications*, DESY, Hamburg, February (2006).

[6-9] G. Grübel, J. Als-Nielsen, A.K. Freund, *The TROIKA beamline at ESRF*, J. de Physique C9 (1994) C9-27.

[6-10] J. Hoszowska, A.K. Freund, E. Boller, J.P.F. Sellschop, G. Level, J. Härtwig, R.C. Burns, M. Rebak, J. Baruchel, *Characterization of synthetic diamond crystals by spatially resolved rocking curve measurements*, J. Phys. D: Appl. Phys. 34 (2001) A47.

[6-11] L. Zhang, A.K. Freund, T. Tschentscher, H. Schulte-Schrepping, *Performance studies of cryogenically cooled monochromator crystals for X-FELs*, SRI 2003 Conference, San Francisco, AIP Conf. Proc. 705 (2004) 639.

[6-12] D. Shastri, P. Zambianchi, D.M. Mills, *Femtosecond x-ray dynamical diffraction by perfect crystals*, SPIE proceedings Vol. 4143 (2000) 69.

[6-13] J.S. Wark, *Femtosecond X-ray diffraction: experiments and limits*, SPIE proceedings Vol. 4143 (2000) 26.

[6-14] W. Graeff, *Short X-ray pulses in a Laue-case crystal*, J. Synchrotron Rad. 9 (2002) 82.

[6-15] R. Follath, in *TESLA Technical Design Report Part V – The Free Electron Laser Laboratory*, G. Materlik, Th. Tschentscher (eds.), DESY 2001-011, DESY, Hamburg (2001) V-309.

Photon beamlines and scientific instruments – References

[6-16] Jarre et al., *Two-Dimensional Hard X-Ray Beam Compression by Combined Focusing and Waveguide Optics*, Phys. Rev. Lett. 94 (2005) 074801.

[6-17] H. Mimura et al., *Hard X-ray diffraction-limited nanofocus with unprecedentedly accurate mirrors*, presented at the XRM2005 Conference, Himeji, Japan (2005).

[6-18] O. Hignette et al., *Focusing below 50 nm using dynamically-bent graded multilayers*, ESRF Highlights 2005, p. 108-109.

[6-19] C.G. Schroer et al., *Hard x-ray nanoprobe based on refractive x-ray lenses*, Appl. Phys. Lett. 87 (2005) 124103.

[6-20] W. Lun, B. Lai, Z. Cai, et al., *Nanometer focusing of hard x-rays by phase zone plates*, Rev. Sci. Instrum. 70 (1999) 2238.

[6-21] B. Nöhammer, C. David, M. Burghammer, C. Riekel, *Coherence-matched micro focusing of hard x-rays*, Applied Physics Letters 86 (2005) 163104.

[6-22] C.G. Schroer and B. Lengeler, *Focusing Hard X Rays to Nanometer Dimensions by Adiabatically Focusing Lenses*, Phys. Rev. Lett. 94 (2005) 054802.

[6-23] B. Nöhammer, J. Hoszowska, A.K. Freund, C. David, *Diamond planar refractive lenses for third- and fourth-generation X-ray sources*, J. Synchrotron Rad. 10 (2003) 168.

[6-24] C.G. Schroer, *Parabolic refractive lenses for the x-ray free-electron laser*, M. Kuhlmann, B. Benner, B. Lengeler, H. Schulte-Schrepping, A.A. Snigirev, I. Snigireva, SPIE proceedings Vol. 5534 (2004) 116.

[6-25] R. Bionta, in *Linac Coherent Light Source (LCLS) – Conceptual Design Report*, J. Arthur et al. (eds.), SLAC-R-593, SLAC, Stanford (2002), pages 9-3 – 9-5.

[6-26] Y.Y. Zhao, E.E. Alp, T.S. Toellner, W. Sturhahn, H. Sinn, D. Shu, *A water cooled compound refracting lens as a white beam collimator*, Rev. Sci. Instr. 73 (2002) 1611.

[6-27] B. Lengeler, *Coherence in X-ray physics*, Naturwissenschaften 88 (2001) 249.

[6-28] H.C. Kang, J. Maser, G. B. Stephenson, C. Liu, R. Conley, A. T. Macrander, S. Vogt, *Nanometer Linear Focusing of Hard X-Rays by a Multilayer Laue Lens*, Phys. Rev. Lett. 96 (2006) 127401.

[6-29] http://www.xradia.com/zpl_pd.htm

[6-30] E. DiFabrizio et al., *Differential Interference Contrast for X-ray Microscopy*, Surf. Rev. Lett. 9 (2002) 243.

[6-31] E. DiFabrizio et al., *Diffractive optical elements for differential interference contrast x-ray microscopy*, Optics Express 11 (2003) 2278.

[6-32] C. David, A. Souvorov, *High-efficiency Bragg–Fresnel lenses with 100 nm outermost zone width*, Rev. Sci. Instr. 70 (1999) 4168.

[6-33] U. Hahn, M. Rüter, *Hochleistungsstrahlverschluss- und Spaltsystem für Synchrotronstrahlung*, Deutsches Patent- und Markenamt, No. DE 101 35 307 C2, München (2001).

[6-34] R. Treusch et al., *Development of photon beam diagnostics for VUV radiation from a SASE FEL*, Nucl. Instr. Meth. A 445 (2000) 456.

[6-35] K. Tiedtke et al., *The SASE FEL at DESY: Photon Beam Diagnostics for the User Facility*, Proceedings SRI2003, San Francisco, AIP Conf. Proc. 705 (2004) 588.

[6-36] R. Treusch, *Photon Diagnostics for the VUV-FEL*, HASYLAB Annual Report 2005, DESY, Hamburg (2006) 159.

[6-37] A. Bytchkov et al., *Development of MCP-based photon diagnostics at the TESLA Test Facility at DESY*, Nucl. Instrum. and Meth. A 528 (2004) 254

[6-38] V. Ayvazyan et al., *Study of the statistical properties of the radiation from a VUV SASE FEL operating in the femtosecond regime*, Nucl. Instr. and Meth. A 507 (2003) 368.

[6-39] M. Wellhöfer, M. Martins, M. Richter, K. Tiedtke et al., *Photoelectron spectroscopy as non-invasive method to monitor SASE-FEL spectra*, in preparation.

[6-40] J. Feldhaus, E. Plönjes-Palm for the VUV-FEL team, *First user experiments at the VUV-FEL*, HASYLAB Annual Report 2005, DESY, Hamburg, (2006) 173.

[6-41] T. Weitkamp, B. Nöhammer, A. Diaz, C. David, E. Ziegler, *X-ray wavefront analysis and optics characterization with a grating interferometer*, Appl. Phys. Lett. 86 (2005) 054101.

[6-42] T. Weitkamp. J. Patommel, C. Schroer, et al., in preparation.

[6-43] L. Le Déroff, P. Salières, and B. Carré, *Beam-quality measurement of a focused high-order harmonic beam*, Opt. Lett. 23 (1998) 1544.

[6-44] D. Yoshitomi, T. Shimizu, T. Sekikawa, S. Watanabe, *Generation and focusing of submilliwatt-average-power 50-nm pulses by the fifth harmonic of a KrF laser*, Opt. Lett 27 (2002) 2170.

[6-45] C. Valentin et al., *Imaging and quality assessment of high-harmonic focal spots*, Opt. Lett. 28 (2003) 1049.

[6-46] H. Mashiko, A. Suda, K. Midorikawa, *Focusing coherent soft-x-ray radiation to a micrometer spot size with an intensity of 10^{14} W/cm^2*, Opt. Lett. 29 (2004) 1927.

[6-47] H. Mashiko, A. Suda and K. Midorikawa, *Focusing multiple high-order harmonics in the extreme-ultraviolet and soft-x-ray regions by a platinum coated ellipsoidal mirror*, Appl. Opt. 45 (2006) 573.

[6-48] A.A. Sorokin et al., *New method based on atomic photoionization for spot-size measurement on focused soft X-ray free-electron laser beams*, submitted for publication.

[6-49] M. Richter, A. Gottwald, U. Kroth, S.V. Bobashev, A.A. Sorokin, L.A. Shmaenok, J. Feldhaus, Ch. Gerth, and K. Tiedtke, Deutsches Patent- und Markenamt, No. 102 44 303.3, München (2002).

[6-50] M. Richter, A. Gottwald, U. Kroth, A.A. Sorokin, S.V. Bobashev, L.A. Shmaenok J. Feldhaus, Ch. Gerth, B. Steeg, K. Tiedtke, R. Treusch, *Measurement of gigawatt radiation pulses from a vacuum ultraviolet free electron laser*, Appl. Phys. Lett. 83 (2003) 2970.

[6-51] R. Klein et al., Synchrotron Radiation News 15 (2002) 23.

[6-52] K. Tiedtke, M. Richter, S. Moeller et al., in preparation.

[6-53] M. Krumrey and G. Ulm, Nucl. Instr. and Meth. A 467-468 (2001) 1175.

[6-54] A. Lindenberg et al., *Atomic-Scale Visualization of Inertial Dynamics*, Science 308 (2005) 392.

[6-55] M. Drescher, publication in preparation.

[6-56] R. Kienberger, to be published.

[6-57] F. Hornsta, *Residual gas ionization profile monitors for the HERA proton machines*, DESY HERA reports 87-25, DESY Hamburg (1987).

[6-58] P. Ilinski, U. Hahn, H. Schulte-Schrepping, K. Tiedtke, M. Sachwitz, *Residual Gas X-ray Beam Position Monitor for PETRA III*, HASYLAB Annual Report 2005, DESY, Hamburg (2006) 151.

[6-59] J.C. Weiskeit, Astrophys. J. 190 (1974) 785.

[6-60] R. Follath, *The versatility of collimated plane grating monochromators*, Nucl. Instr. Meth. A 467-468 (2001) 418.

[6-61] T. Ditmire et al., Nature 386 (1997) 54.

[6-62] Y.L. Shao, T. Ditmire, J.W.G. Tisch, E. Springate, J.P. Marangos, M.H.R. Hutchinson, *Multi-keV Electron Generation in the Interaction of Intense Laser Pulses with Xe Clusters*, Phys Rev Lett 77 (1996) 3343.

[6-63] V. Kumarappan, M. Krishnamurthy, D. Mathur, *Asymmetric emission of high-energy electrons in the two-dimensional hydrodynamic expansion of large xenon clusters irradiated by intense laser fields*, Phys. Rev. A 67 (2003) 043204.

[6-64] E. Springate, S.A. Aseyev, S. Zamith, M.J.J. Vrakking, *Electron kinetic energy measurements from laser irradiation of clusters*, Phys Rev A 68 (2003) 053201.

[6-65] H. Wabnitz et al., Nature 420 (2002) 486.

[6-66] S. Zamith, T. Martchenko, Y. Ni, S.A. Aseyev, H.G. Muller, M.J.J. Vrakking, *Control of the production of highly charged ions in femtosecond-laser cluster fragmentation*, Phys. Rev. A 70 (2002) 011201R.; C. Siedschlag, J.M. Rost, *Surface-plasma resonance in small rare-gas clusters by mixing ir and vuv laser pulses*, Phys. Rev. A 71 (2005) 031401R.

[6-67] P. Tzallas et al., *Direct Observation of Attosecond Light Bunching*, Nature 426 (2003) 267.

[6-68] P. Tzallas et al., *Second-order Autocorrelation Measurements of Attosecond XUV Pulse trains*, J. Mod. Opt. 52 (2005) 321.

[6-69] E. Goulielmakis et al., *A Dispersionless Michelson Interferometer for the Characterization of Attosecond Pulses*, Appl. Phys. B 74 (2002) 197.

[6-70] N.A. Papadogianis et al., *Temporal Characterization of Short-Pulse Third-Harmonic Generation in an Atomic Gas by a transmission Grating Michelson Interferometer*, Opt. Lett. 27 (2002) 1561.

[6-71] P. Emma et al., *Femtosecond and Subfemtosecond X-Ray Pulses from a Self-Amplified Spontaneous-Emission–Based Free-Electron Laser*, Phys. Rev. Lett. 92 (2004) 074801.

[6-72] H. Chapman, K. Nugent, *X-ray Pulse Compression Using Strained Crystals*, Optics Commun. 205 (2002) 351.

[6-73] U. Becker et al., reported at the Workshop on Ultrafast time-Resolved Soft X-ray Science, Berlin, 27-29 April (2005).

[6-74] *Connecting Quarks with the Cosmos: eleven science questions for the new century* National Academies Press (2003).

[6-75] *Frontiers in High energy density Physics - the X-games of contemporary science*, National Academies Press (2003).

[6-76] B. A. Remington, Plasma Phys. Control. Fusion 47 (2005) A191.

[6-77] P. Audebert, J.-P. Geindre, S. Rebibo, J.-C. Gauthier, *Direct observation of the ponderomotive force effects in short-scale-length laser plasmas by frequency-domain interferometry*, Phys. Rev. E 64 (2001) 056412.

[6-78] R. Shepherd et. al., JQSRT 71(2001) 711.

[6-79] M.W.C. Dharma-Wardana, F. Perrot, *Energy relaxation and the quasiequation of state of a dense two-temperature nonequilibrium plasma*, Phys. Rev. E 58 (1998) 3705.

[6-80] D. Riley, N.C. Woolsey, D. McSherry, I. Weaver, A. Djaoui, E. Nardi, *X-Ray Diffraction from a Dense Plasma*, Phys. Rev. Lett. 84 (2000) 1704.

[6-81] J.J. Angulo Gareta, D. Riley, submitted for publication (2006).

[6-82] S. Mazevet, J. Clerouin, V. Recoules, P.M. Anglade, G. Zerah, *Ab-Initio Simulations of the Optical Properties of Warm Dense Gold*, Phys. Rev. Lett. 95, 085002 (2005).

[6-83] M. Tabak et al., Phys. Plasmas 1 (1994) 1626.

[6-84] M. Tatarakis et. al., Nature 415 (2002) 6869.

[6-85] F.B. Rosmej, R.W. Lee, submitted for publication.

[6-86] D. Mihalas, *Stellar Atmospheres*, W. Freeman and Co., San Francisco, (1978).

[6-87] H.R. Griem, *Spectral Line Broadening by Plasmas*, Academic Press, New York (1974).

[6-88] H.R. Griem, *Principles of Plasma Spectroscopy*, Cambridge University Press (1997).

[6-89] J. Lindl, Phys. Plasmas 2 (1995) 3933.

[6-90] C. deMichelis, M. Mattioli, Nuclear Fusion 21 (1981) 677.

[6-91] D. Salzmann, H. Szichman, *Density dependence of the atomic transition probabilities in hot, dense plasmas*, Phys. Rev. A 35 (1987) 807.

[6-92] R.W. Lee et al., J. Opt. Soc. Am. B 20 (2003) 1.

[6-93] F.B. Rosmej et al. , Nucl. Instrum. Methods A 464 (2001) 257.

[6-94] F.B. Rosmej, J. Phys. B.: At. Mol. Opt. Phys. 30 (1997) L819.

[6-95] F.B. Rosmej et al., *Charge-exchange-induced two-electron satellite transitions from autoionizing levels in dense plasmas*, Phys. Rev. E 66 (2002) 056402.

[6-96] R. Loudon, *The Quantum Theory of Light*, Oxford Science Publications (1983).

[6-97] S.J. Gitomer et al., Phys. Fluids 29 (1986) 2679.

[6-98] E. Foord et al., JQSRT 99(2006) 712.

[6-99] T. Ditmire et al., Astrophysical Journal Supplement Series 127 (2000) 299.

[6-100] L.N. Gaier et al., J. Phys. B: At. Mol. Opt. Phys. 37(2004) L57.

[6-101] B.A. Remington et al., Metallurgical and Materials Transactions A-Physical Metallurgy and Materials Science 35A (2004) 2587.

[6-102] D. Kalantar et al., *Direct Observation of the a-e Transition in Shock-Compressed Iron via Nanosecond X-Ray Diffraction*, Phys. Rev. Lett. 95 (2005) 075502.

[6-103] E. Divall, P. Holligan Rutherford-Appleton Laboratory Report RAL-TR-2002-013, (2002) 187.

[6-104] A.J. Langley, W.J. Lester, J.M. Smith, Rutherford-Appleton Laboratory Report RAL-TR-2004-025, (2004) 187.

[6-105] T. Missalla et al., Rev. Sci. Instr. 70 (1999) 1288.

[6-106] D. Neely et al., Rutherford-Appleton Laboratory Report TR-95-025, (1995) 113.

[6-107] G. Chériaux, J-P. Chambaret, Meas. Sci. Technol. 12 (2001) 1769.

[6-108] D. Sayre, *Some implications of a theorem due to Shannon*, Acta Cryst. 5 (1952) 843.

[6-109] J. Miao, P. Charalambous, J. Kirz, D. Sayre, *Extending the methodology of X-ray crystallography to allow imaging of micrometer sized non-crystalline specimens*, Nature 400 (1999) 342.

[6-110] R.H.T. Bates., *Fourier phase problems are uniquely solvable in more than one dimension*, Optik 61 (1982) 247.

[6-111] M.H. Hayes, *The reconstruction of a multidimensional sequence from the phase or magnitude of its Fourier transform*, IEEE Trans. On Acoustics Speech and Signal Processing, 30 (1982) 140.

[6-112] J.R. Fienup, *Phase retrieval algorithms: a comparison*, Appl. Opt. 21 (1982) 2758.

[6-113] R. Henderson, *The potential and limitations of neutrons, electrons and X-rays for atomic resolution microscopy of unstained biological molecules*, Quart. Rev. Biophys. 28 (1995) 171.

[6-114] S. Eisebitt, J. Luning, W.F. Schlotter, M. Lorgen., O. Hellwig, W. Eberhardt, J. Stohr, *Lensless imaging of magnetic nanostructures by X-ray spectro-holography*, Nature 432 (2004) 885.

[6-115] E.L. Saldin, E.A. Schneidmiller, M.V. Yurkov, *Coherence properties of the radiation from X-ray free electron laser*, in press.

[6-116] I.K. Robinson, I.A. Vartanyants, G.J. Williams, M.A. Pfeifer, J.A. Pitney, *Reconstruction of the Shapes of Gold Nanocrystals using Coherent X-ray Diffraction*, Phys. Rev. Lett. 87 (2001) 195505.

[6-117] G.J. Williams, M.A. Pfeifer, I.A. Vartanyants, I.K. Robinson, *Three-Dimensional Imaging of Microstructure in Gold Nanocrystal*, Phys Rev. Lett., 90 (2003) 175501.

[6-118] H.W. Hayden, W.G. Moffat, J. Wulff, *Structure and Properties of Materials III*, Wiley, New York (1965).

[6-119] I.A. Vartanyants, I.K. Robinson, *Partial Coherence Effects on the Reconstruction of the Shape of Small Crystals from Coherent X-ray Diffraction Pattern*, J. Phys.: Condens. Matter 13 (2001) 10593.

[6-120] M.A. Pfeifer, G.J. Williams, I.A Vartanyants, R. Harder, I.K. Robinson, *Three-dimensional mapping of a deformation field inside a nanocrystal*, Nature 422 (2006) 63.

[6-121] I.A. Vartanyants, I.K. Robinson, J.D. Onken, M.A. Pfeifer, G.J. Williams, F. Pfeiffer, H. Metzger, Z. Zhong, G. Bauer, *Coherent x-ray diffraction from quantum dots*, Phys. Rev. B 71 (2005) 245302.

[6-122] I.A Vartanyants, I.K. Robinson, *Imaging of quantum array structures with coherent and partially coherent diffraction*, J. Synchrotron Rad. 10 (2003) 409.

[6-123] J. Miao, T. Ishikawa, B. Johnson, E.H. Anderson, B. Lai, K.O. Hodgson, *High Resolution 3D X-Ray Diffraction Microscopy*, Phys. Rev. Lett. 89 (2002) 088303.

[6-124] H.N. Chapman, A. Barty, S. Marchesini, A. Noy, C. Cui, M.R. Howells, R. Rosen, H. He, J.C.H. Spence, U. Weierstall, T. Beetz, C. Jacobsen, D. Shapiro, *High-resolution ab initio three-dimensional X-ray diffraction microscopy*, J. Opt. Soc. Am. in press (2006).

[6-125] J.E. Trebes et al., Science 238 (1987) 517.

[6-126] R.A. Bartels, et al., Science 297 (2002) 376.

[6-127] M.R. Howells, et al., Science 238 (1987) 514.

[6-128] C. Jacobsen, M. Howells, J. Kirz, S. Rothman, J. Opt. Soc. Am. A7 (1990) 1847.

[6-129] McNulty, J. Kirz, C. Jacobsen, E.H. Anderson, M.R. Howells, D.P. Kern, Science 256 (1992) 1009.

[6-130] S. Lindaas, M.R. Howells, C. Jacobsen, A. Kalinovsky, J. Opt. Soc. Am. A 13 (1996) 1788.

Photon beamlines and scientific instruments – References

[6-131] P. Cloetens et al., Appl. Phys. Lett. 75 (1999) 2912.

[6-132] K.A. Nugent, A.G. Peele, H.N. Chapman, A.P. Mancuso, Phys. Rev. Lett. 91 (2003) 203902.

[6-133] W. Chao, B.D. Harteneck, J.A. Liddle, E.H. Anderson, D.T. Attwood, *Soft X-ray microscopy at a spatial resolution better than 15 nm*, Nature 435 (2005) 1210.

[6-134] H.C. Kang, J. Maser, G.B. Stephenson, C. Liu, R. Conley, A.T. Macrander, S.Vogt, *Nanometer Linear Focusing of Hard X Rays by a Multilayer Laue Lens*, Phys Rev. Lett. 96 (2006) 127401.

[6-135] H.M. Quiney, A.G. Peele, Z. Cai, D. Paterson, K.A. Nugent, Nature Physics 2 (2006) 101.

[6-136] H. He, et al., Appl. Phys. Lett. 85 (2004) 2454.

[6-137] H.J. Freund et al., *Metal Aggregates on Oxide Surfaces: Structure and Adsorption*, Crystal Research and Technology 33 (1998) 977.

[6-138] J.J. Finley et al., *Quantum-confined Stark Shift of Charged Exciton Complexes in Quantum Dots*, Phys. Rev. B 70 (2004) 201308(R).

[6-139] G. Bester et al., Phys.Rev. B 67 (2003) 161306.

[6-140] G.A. Narvaez et al., Phys. Rev. B 72 (2005) 245318.

[6-141] J. Stangl et al., Rev. Mod. Phys. 76 (2004) 725.

[6-142] A. Hesse, J. Stangl et al., Phys.Rev. B 66 (2002) 085321.

[6-143] Th. Wiebach et al., Phys.Rev. B 61 (2000) 5571.

[6-144] J. Stangl et al., Appl.Phys. Lett. 82 (2003) 2251.

[6-145] I. Kegel et al., Phys. Rev. B 63 (2001) 035318

[6-146] T.U. Schülli et al., Phys.Rev.Lett. 90 (2003) 066105.

[6-147] Malachias et al., Phys. Rev. Lett. 91 (2003) 176101.

[6-148] Malachias et al., Phys. Rev. B 72 (2005) 165316.

[6-149] C.G. Schroer et al., Appl.Phys. Lett. 82 (2003) 1485.

[6-150] C.G. Schroer, B. Lengeler, Phys.Rev.Lett. 94 (2005) 054802.

[6-151] Jarre et al., Phys. Rev. Lett. 94 (2005) 074801.

[6-152] C. David et al., Appl. Phys. Lett. 79 (2001) 1088.

[6-153] S. DiFonzo et al., *Non-destructive Determination of local strani with 100nm spatial resolution*, Nature 403 (2000) 638.

[6-154] Jarre et al., Appl. Phys. Lett. 85 (2004) 161.

[6-155] F. Pfeiffer et al., Science 297 (2002) 230.

[6-156] B.C. Larson, W. Yang, G.E. Ice, J.D. Budai, J.Z. Tischler, *Three-dimensional X-ray structural microscopy with submicrometer resolution*, Nature 415 (2002) 887.

[6-157] I.K. Robinson, J.L. Libbert, I.A. Vartanyants, J.A. Pitney, D.M. Smilgies, D.L. Abernathy, G. Grübel, *Coherent X-ray Diffraction Imaging of Silicon Oxide Growth*, Phys. Rev. B, 60 (1999) 9965.

[6-158] G. Rosenfeld et al., Phys. Rev. Lett. 69 (1992) 917.

[6-159] S. Alexander, J.P. McTague, Phys. Rev. Lett. 41 (1978) 702.

[6-160] Y.C. Shen, D.W. Oxtoby, Phys. Rev. Lett. 77 (1996) 3585.

[6-161] W. Klein, Phys. Rev. E 64 (2001) 056110.

[6-162] K. Mecke, private communication.

[6-163] H. Riedel, *Fracture mechanisms*, in Materials Science and Technology, Vol.6, R.W. Cahn, P. Haasen, E.J. Kramer (eds.), VCH, Weinheim (1992).

[6-164] B.C. Stuart et al., Phys. Rev. Lett. 74 (1995) 2248.

[6-165] B.C. Stuart et al., Phys. Rev. B 53 (1996) 1747.

[6-166] B.C. Stuart et al. Optical ablation by high-power short-pulse lasers. J.Opt.Soc. Am B 13 (1996) 459.

[6-167] J. Neev et al., IEEE, J. Selected Topics in Quan. Electron. 2 (1996) 790.

[6-168] M. Feil et al., Appl. Surface Science 127-129(1998)869.

[6-169] M.D. Perry et al., J. Appl. Phys. 85 (1999) 6803.

[6-170] For example, see Proc. 30th Ann.Conf. on Laser Damage in Optical Materials, SPIE proceedings Vol. 3578 (1999).

[6-171] C.W. Siders et al., Science 286 (1999) 1340.

[6-172] M. Rouhi, C&EN, Nov. 15, (1999).

[6-173] A. Plech, V. Kotaidis, M. Lorenc, J. Boneberg, *Femtosecond laser near-field ablation from Gold nanoparticles*, Nature Physics, 2(2006) 44.

[6-174] M.R. Howells et al., *An assessment of the resolution limitation due to radiation damage in x-ray diffraction microscopy*, in press.

[6-175] See e.g. G. Grübel, G.B. Stephenson, in *Proceedings of the 4th Generation Light Source Workshop*, Advanced Photon Source, Argonne National Laboratory, 10/27-29/97, and references therein.

[6-176] S. Brauer et al., Phys. Rev. Lett. 74 (1995) 2010; S.B. Dierker et al., Phys. Rev. Lett. 75 (1995) 449; T. Thurn-Albrecht et al., Phys. Rev. Lett. 77 (1996) 5437; S.G.J. Mochrie et al., Phys. Rev. Lett. 78 (1997) 1275; A. Malik et al., Phys. Rev. Lett. 81 (1998) 5832; A.C. Price et al., Phys. Rev. Lett. 82 (1999) 755; L.B. Lurio et al., Phys. Rev. Lett. 84 (2000) 785; D.O. Riese et al., Phys. Rev. Lett. 85 (2000) 5460; A. Fera et al., Phys. Rev. Lett. 85 (2000) 2316; D. Lumma et al., Phys. Rev. Lett. 86 (2001) 2042; I. Sikharulidze et al., Phys. Rev. Lett. 88 (2002) 115503; D. Pontoni et al., Phys. Rev. Lett. 90 (2003) 188301; H.J. Kim et al. Phys. Rev. Lett. 90 (2003) 068302; A. Madsen et al., Phys. Rev. Lett. 90 (2003) 085701; C. Gutt et al., Phys. Rev. Lett. 91 (2003) 076104; I. Sikharulidze et al., Phys. Rev. Lett. 91 (2003) 165504; A. Madsen et al., Phys. Rev. Lett. 92 (2004) 096104.

[6-177] http://tesla.desy.de/new_pages/TDR_CD/PartV/xfel.pdf); http://tesla.desy.de/new_pages/tdr_update/ supplement.html

[6-178] LCLS "*The First Experiments*", September 2000.

[6-179] L. Cipelletti, L. Ramos, J. Phys.: Condens. Matter 17 (2005) R253.

[6-180] W. Götze, L. Sjogren, Rep.Prog.Phys. 55 (1992) 241.

[6-181] R. Bergman et al., Phys. Rev. B 56 (1997) 11619.

[6-182] M. Grimsditch, M.L. Torell, in *Dynamics of Disordered Materials*, D. Richter et al. (eds.), Springer, Berlin (1989); M. Russina et al., Phys. Rev. Lett. 84 (2000) 3620; U. Buchenau et al., Phys. Rev. Lett. 77 (1996) 4035; C. Masciovecchio et al., Phys. Rev. Lett. 80 (1988) 544.

[6-183] R. Bruning, M. Sutton, Phys, Rev. B 49 (1994) 3124.

[6-184] A.K. Hassan et al., Phys. Rev. B 45 (1992) 12797.

[6-185] D. Engberg et al., Phys. Rev. B 59 (1999) 4053.

[6-186] H. Sinn, J. Phys.: Condens. Matter 13 (2001) 7525.

[6-187] S.K. Sinha et al., Phys. Rev. B 38 (1988) 2297.

[6-188] S. Mora, J. Daillant, Eur.Phys.J. B 27 (2002) 417.

[6-189] J.F. Peters, M.A. de Fries, J. Miguel, O. Toulemonde, J. Goedkoop,ESRF Newslett. 15 (2000) 34; F. Yakhou, A. Letoublon, F. Livet, M. de Boissieu, F. Bley, C. Vettier, ESRF Newslett. 32 (1999) 14; F. Yakhou, A. Létoublon, F. Livet, M. de Boissieu, F. Bley, J. Magnetism Magnetic Materials. 233 (2001) 119; K. Chesnel, M. Belakhovsky, F. Livet, S.P. Collins, G. van der Laan, S.S. Dhesi, J.P. Attane, A. Marty, Phys. Rev. Lett. 66 (2002) 172404.

[6-190] S. Eisebitt, J. Luning, W.F. Schlotter, M. Lorgen., O. Hellwig, W. Eberhardt, J. Stohr, *Lensless imaging of magnetic nanostructures by X-ray spectro-holography*, Nature 432 (2004) 885.

[6-191] A. Malik et al., Phys. Rev. Lett. 81 (1998) 5832.

[6-192] F. Livet et al., Phys. Rev. E 63 (2001) 036108.

[6-193] M. J. Rosker, M. Dantus, A.H. Zewail, J. Chem. Phys. 89 (1988) 6113.

[6-194] A.H. Zewail, J. Phys. Chem. A 104 (2000) 5660.

[6-195] T. Baumert, V. Engel, C. Rottgermann, W.T. Strunz, G. Gerber, Chem. Phys. Lett. 191 (1992) 639.

[6-196] S. Mukamel, *Principles of nonlinear optical spectroscopy*; Oxford University Press, New York (1995).

[6-197] J.-C. Diels, W. Rudolph, *Ultrashort laser pulse phenomena : fundamentals, techniques, and applications on a femtosecond time scale*; Academic Press: San Diego (1996).

[6-198] *Femtochemistry: Ultrafast chemical and physical processes in molecular systems*, Lausanne, M. Chergui (ed.), World Scientific,Singapore (1996).

[6-199] V.P.T. Sundström, R. van Grondelle, *Ultrafast spectroscopy in biology,* in Femtochemistry and femtobiology ultrafast reaction dynamics at atomic-scale resolution, Nobel Symposium 101, V. Sundström (ed.), Imperial College Press, London (1997) 319.

[6-200] *Femtochemistry and femtobiology ultrafast reaction dynamics at atomic-scale resolution*, Nobel Symposium 101, V. Sundström (ed.), Imperial College Press, London (1997).

[6-201] *Femtochemistry and femtobiology ultrafast dynamics in molecular science*, A. Douhal (ed.), World Scientific, New Jersey (2002).

[6-202] G.R. Fleming, T. Joo, M. Cho, A.H. Zewail, V.S. Letokhov, R.A. Marcus, E. Pollak, D.J. Tannor, S. Mukamel, Adv. Chem. Phys. 101 (1997) 141.

[6-203] L. Dhar, J.A. Rogers, K.A. Nelson, Chem. Rev. 94 (1994) 157.

[6-204] M. Chergui, Comptes Rendus de l'Academie des Sciences, Serie IV: Physique Astrophysique 2 (2001) 1453.

[6-205] M. Chergui, *Ultrafast structural dynamics in the condensed phase*, in Investigating extreme physical conditions with advanced optical techniques; B. Di Bartolo, O. Forte (eds.), Kluwer, Dordrecht, Vol. 168 (2005) 497.

[6-206] *Time-resolved electron and x-ray diffraction*, P.M. Rentzepis (ed.), SPIE: Bellingham, Washington (1995).

[6-207] J.R. Helliwell, P.M. Rentzepis, *Time-resolved diffraction*, Clarendon Press, Oxford (1997).

[6-208] K. Sokolowski-Tinten, J. Bialkowski, A. Cavalleri, D. von der Linde, A. Oparin, J. Meyer-ter-Vehn, S.I. Anisimov, Phys. Rev. Lett. 81 (1998) 224.

[6-209] K. Sokolowski-Tinten, D. von der Linde, Phys. Rev. B 61 (2000) 2643.

[6-210] K. Sokolowski-Tinten, W. Ziegler, D. von der Linde, M.P. Siegal, D.L. Overmyer, Appl. Phys. Lett. (2005) 86.

[6-211] L.X. Chen, J Electron Spectrosc. 119 (2001) 161.

[6-212] C. Bressler, M. Chergui, Chem. Rev. 104 (2004) 1781.

[6-213] *TESLA Technical Design Report Part V, The X-ray Free Electron Laser*, G. Materlik, T. Tschentscher (Eds.), DESY report 2001-011, DESY, Hamburg (2001), http://tesla.desy.de/new_pages/0000_TESLA_Project.html

[6-214] L.X. Chen, G. Jennings, T. Liu, D.J. Gosztola, J.P. Hessler, D.V. Scaltrito, G.J. Meyer, J. Am. Chem. Soc. 124 (2002) 10861.

[6-215] L.X. Chen, G.B. Shaw, I. Novozhilova, T. Liu, G. Jennings, K. Attenkofer, G.J. Meyer, P. Coppens, J. Am. Chem. Soc. 125 (2003) 7022.

[6-216] C. Bressler, M. Saes, M. Chergui, R. Abela, P. Pattison, Nucl. Instrum. Meth. A 467 (2001) 1444.

[6-217] M. Saes, C. Bressler, R. Abela, D. Grolimund, S.L. Johnson, P.A. Heimann, M. Chergui, Phys. Rev. Lett. 90 (2003) 047403.

[6-218] M. Saes, C. Bressler, F. van Mourik, W. Gawelda, M. Kaiser, M. Chergui, C. Bressler, D. Grolimund, R. Abela, T.E. Glover, P.A. Heimann, R.W. Schoenlein, S.L. Johnson, A.M. Lindenberg, R.W. Falcone, Rev. Sci. Instrum. 75 (2004) 24.

[6-219] S.L. Johnson, P.A. Heimann, A.M. Lindenberg, H.O. Jeschke, M.E. Garcia, Z. Chang, R.W. Lee, J.J. Rehr, R.W. Falcone, Phys. Rev. Lett. 91 (2003) 157403.

[6-220] M. Chergui, C. Bressler, R. Abela, Synchrotron Radiation News (2004).

[6-221] M. Chergui, S. Mukamel, Chem. Phys. 299 (2004) 155.

[6-222] S.L. Johnson, P.A. Heimann, A.G. MacPhee, A.M. Lindenberg, O.R. Monteiro, Z. Chang, R.W. Lee, R.W. Falcone, Phys. Rev. Lett. 94 (2005) 057407.

[6-223] W. Gawelda, M. Johnson, F.F.M. de Groot, R. Abela, C. Bressler, M. Chergui, J. Am. Chem. Soc. 128 (2006) 5001.

[6-224] M. Benfatto, S. Della Longa, K. Hatada, K. Hayakawa, W. Gawelda, C. Bressler, M. Chergui, submitted for publication.

[6-225] M.P. Hertlein, H. Adaniya, J. Amini, C. Bressler, B. Feinberg, M. Kaiser, N. Neumann, M.H. Prior, A. Belkacem, submitted for publication.

[6-226] U. Buontempo, A. Filipponi, P. Postorino, R. Zaccari, J. Chem. Phys. 108(1998)4131.

[6-227] U. Buontempo, A. DiCicco, A. Filipponi, M. Nardone, P. Postorino, J. Chem. Phys. 107 (1997) 5720.

[6-228] A. Filipponi, P.D. D’Angelo, J. Chem. Phys. 109 (1998) 5356.

[6-229] W. Gawelda, V.T. Pham, M. Kaiser, Y. Zaushytsin, S.L. Johnson, I. Iyas, C. Bressler, M. Chergui, to be published.

[6-230] D. Cubaynes, J.M. Bizau, F.J. Wuilleumier, B. Carré, F. Gounand, Phys. Rev. Lett. 63 (1989) 2460.

[6-231] A.S. Schlachter et al., J. Phys. B.: At. Mol. Opt. 37 (2004) L103.

[6-232] S.W. Scully et al., J. Phys. B.: At. Mol. Opt. 38 (2005) 1967.

[6-233] J. Workman, M. Nantel, A. Maksimchuk, D. Umstadter, Appl. Phys. Lett. 70 (1997) 312.

[6-234] L. Nugent-Glandorf, M. Scheer, D.A. Samuels, A.M. Mulhisen, E.R. Grant, X.M. Yang, V.M. Bierbaum, S.R. Leone, Phys. Rev. Lett. 87 (2001) 193002.

[6-235] L. Nugent-Glandorf, M. Scheer, D.A. Samuels, V.M. Bierbaum, S.R. Leone, J. Chem. Phys. 117 (2002) 6108.

[6-236] H. Lefebvre-Brion, R.W. Field, *Perturbations in the spectra of diatomic molecules*, Academic Press, Orlando (1986).

[6-237] J.T. Hynes, Ann. Rev. Phys. Chem. 36 (1985) 573.

[6-238] P. Barbara, W. Jarzeba, in *Advances in Photochemistry*; John Wiley & Sons, New York, Vol. 15 (1990) 1.

[6-239] R. Jimenez, G.R. Fleming, P.V. Kumar, M. Maroncelli, Nature 369 (1994) 471.

[6-240] M. Maroncelli, J. Mol. Liq. 57 (1993) 1.

[6-241] G.R. Fleming, M.H. Cho, Ann. Rev. Phys. Chem. 47 (1996) 109.

[6-242] N. Nandi, K. Bhattacharyya, B. Bagchi, Chem. Rev. 100 (2000) 2013.

[6-243] P. Larregaray, A. Cavina, M. Chergui, Chem. Phys. 308 (2005) 13.

[6-244] S.K. Pal, A.H. Zewail, Chem. Rev. 104 (2004) 2099.

[6-245] J.P. Bergsma, J.R. Reimers, K.R. Wilson, J.T. Hynes, J. Chem. Phys. 85(1986) 5625.

[6-246] J. Helbing, M. Chergui, J. Chem. Phys. 115 (2001) 6158.

[6-247] J. Helbing, M. Chergui, S. Fernandez-Alberti, J. Echave, N. Halberstadt, J.A. Beswick, Phys. Chem. Chem. Phys. 2 (2000) 4131.

[6-248] N. Winter, I. Chorny, J. Vieceli, I. Benjamin, J. Chem. Phys. 119 (2003) 2127.

[6-249] M.L. Horng, J.A. Gardecki, A. Papazyan, M. Maroncelli, J. Phys. Chem. 99 (1995) 17311.

[6-250] A.L. Harris, J.K. Brown, C.B. Harris, Ann. Rev. Phys. Chem. 39 (1988) 341.

[6-251] V.A. Apkarian, N. Schwentner, Chem. Rev. 99 (1999) 1481.

[6-252] J.M. Tour, Accounts Chem. Res. 33 (2000) 791.

[6-253] R.M. Metzger, Accounts Chem. Res. 32 (1999) 950.

[6-254] M. Gratzel, Nature 414 (2001) 338.

[6-255] S. Yasutomi, T. Morita, Y. Imanishi, S. Kimura, Science 304 (2004) 1944.

[6-256] J.Y. Jiao, G.J. Long, F. Grandjean, A.M. Beatty, T.P. Fehlner, J. Am. Chem. Soc. 125 (2003) 7522.

[6-257] K. Szacilowski, Chem. Eur. J. 10 (2004) 2520.

[6-258] C.G. Pierpont, Coordin. Chem. Rev. 219 (2001) 415.

[6-259] S. Schenkl, F. van Mourik, G. van der Zwan, S. Haacke, M. Chergui, Science 309 (2005) 917.

[6-260] W. Gawelda, C. Bressler, M. Saes, M. Kaiser, A. Tarnovsky, D. Grolimund, S.L. Johnson, R. Abela, M. Chergui, Physica Scripta T115 (2005) 102.

[6-261] N.H. Damrauer, G. Cerullo, A.T. Yeh, T.R. Boussie, C.V. Shank, J.K. McCusker, Science 275 (1997) 54.

[6-262] A.T. Yeh, C.V. Shank, J.K. McCusker, Science 289 (2000) 935.

[6-263] J.A. Weinstein, N.N. Zheligovskaya, M.Y. Mel’nikov, F. Hartl, J. Chem. Soc. Dalton (1998) 2459.

[6-264] J.A. Weinstein et al., Inorg. Chem. 42 (2003) 7077.

[6-265] J. Helbing et al., J. Biophys 87 (2004) 1881.

[6-266] H.Z. Yu, J.S. Baskin, B. Steiger, C.Z. Wan, F.C. Anson, A.H. Zewail, Chem. Phys. Lett. 293 (1998) 1.

Photon beamlines and scientific instruments – References

[6-267] H.Z. Yu, J.S. Baskin, B. Steiger, F.C. Anson, A.H. Zewail, J. Am. Chem. Soc. 121 (1999) 484.

[6-268] H.Z. Yu, J.S. Baskin, A.H. Zewail, J. Phys. Chem. A 106 (2002) 9845.

[6-269] J.S. Baskin, H.Z. Yu, A.H. Zewail, J. Phys. Chem. A 106 (2002) 9837.

[6-270] F. Rosca, A.T.N. Kumar, X. Ye, T. Sjodin, A.A. Demidov, P.M. Champion, J. Phys. Chem. A 104 (2000) 4280.

[6-271] F. Rosca et al., J. Phys. Chem. A 106 (2002) 3540.

[6-272] S.K. Gayen, W.B. Wang, V. Petricevic, R. Dorsinville, R.R. Alfano, Appl. Phys. Lett., 47 (1985) 455.

[6-273] T. Matsuzawa, Y. Aoki, N. Takeuchi, Y. Murayama, J. Electrochem. Soc. 143 (1996) 2670.

[6-274] A.V. Kolobov, P. Fons, A.I. Frenkel, A.L. Ankudinov, J. Tominaga, T. Uruga, Nature Materials 3 (2004) 703.

[6-275] A.V. Kolobov, P. Fons, J. Tominaga, A.L. Ankudinov, S.N. Yannopoulos, K.S. Andrikopoulos, J. Phys. Condensed Mat. 16 (2004) S5103.

[6-276] A.V. Kolobov, P. Fons, J. Tominaga, A.I Frenkel, A.L. Ankudinov, S.N. Yannopoulos, K.S. Andrikopoulos, T. Uruga, Jpn. J. Appl. Phys. 44 (2005) 3345.

[6-277] H.W. Schumacher, C. Chappert, P. Crozat, R.C. Sousa, P.P. Freitas, J. Miltat, H.W. Fassbender, B. Hillebrands, Phys. Rev. Lett. 90 (2003) 017201.

[6-278] H.W. Schumacher, C. Chappert, R.C. Sousa, P.P. Freitas, J. Miltat, Phys. Rev. Lett. 90 (2003) 017204.

[6-279] A.V. Kimel, A. Kirilyuk, P.A. Usachev, R.V. Pisarev, A.M. Balbashov, T. Rasing, Nature 435 (2005) 655.

[6-280] F. Hansteen, A. Kimel, A. Kirilyuk, T. Rasing, Phys. Rev. Lett. 95 (2005) 047402.

[6-281] E. Beaurepaire, J.C. Merle, A. Daunois, J.Y. Bigot, Phys. Rev. Lett. 76 (1996) 4250.

[6-282] F. Sirotti, S. Girlando, P. Prieto, L. Floreano, G. Panaccione, G. Rossi, Phys. Rev. B 61 (2000) R9221.

[6-283] J. Vogel, W. Kuch, J. Camarero, K. Fukumoto, Y. Pennec, S. Pizzini, M. Bonfim, F. Petroff, A. Fontaine, J. Kirschner, Phys. Rev. B 71 (2005) 060404.

Photon beamlines and scientific instruments – References

[6-284] A. Krasyuk, F. Wegelin, S.A. Nepijko, H.J. Elmers, G. Schonhense, M. Bolte, C.M. Schneider, Phys. Rev. Lett. 95 (2005) 207201.

[6-285] J. Raabe, C. Quitmann, C.H. Back, F. Nolting, S. Johnson, C. Buehler, Phys. Rev. Lett. 94 (2005) 217204.

[6-286] C. Bressler, M. Saes, M. Chergui, D. Grolimund, R. Abela, P. Pattison, J. Chem. Phys. 116 (2002) 2955.

[6-287] J.C. Willamson et al., *Clocking transient chemical changes by ultrafast electron diffraction*, Nature 386 (1997) 159.

[6-288] H. Ihee et al., *Direct imaging of transient molecular structures with ultrafast diffraction*, Science 291 (2001) 458.

[6-289] C.-Y. Ruan et al., *Ultrafast diffraction and structural dynamics: The nature of complex molecules far from equilibrium*, Proc. Nat. Acad. Sci. 98 (2001) 7117.

[6-290] M.H. Pirenne, *The diffraction of X-rays and electrons by free molecules*, The University Press, Cambridge (1946).

[6-291] I. Hargittai, M. Hargittai, *Stereochemical Applications of Gas-Phase Electron Diffraction*, VCH Publishers, New York (1988).

[6-292] H. Ihee, B.M. Goodson, R. Srinivasan, V.A. Lobastov, A.H. Zewail, *Ultrafast electron diffraction and structural dynamics: Transient intermediates in the elimination reaction of* $C_2F_4I_2$, J. Phys. Chem. A 106 (2002) 4087.

[6-293] J.C. Williamson, A.H. Zewail, *Ultrafast Electron Diffraction. 4. Molecular Structures and Coherent Dynamics*, J. Phys. Chem. 98 (1994) 2766.

[6-294] J.D. Geiser, P.M. Weber, *Pump-probe diffraction imaging of vibrational wave functions*, J. Chem. Phys. 108 (1998) 8004.

[6-295] T.S. Dibble, L.S. Bartell, *Electron Diffraction Studies of the Kinetics of Phase Changes in Molecular Clusters. 3. Solid-State Phase Transformations in* SeF_6 *and* $(CH_3)_3CCl$, J. Phys. Chem., 96 (1992) 8603.

[6-296] A. Plech et al., *Visualizing chemical reactions in solution by picosecond X-ray diffraction*, Phys. Rev. Lett. 92 (2004) 125506.

[6-297] J. Davidsson et al., *Structural Determination of Transient Isomer of* CH_2I_2 *by Picosecond X-ray Diffraction*, Phys. Rev. Lett. 94 (2005) 245503.

[6-298] S. Bratos, F. Mirloup, R. Vuilleumier, M. Wulff, A. Plech, *X-ray Filming of atomic motions in chemical reactions*, Chem. Phys. 304 (2004) 245.

[6-299] C. Rischel et al., *Femtosecond time-resolved X-ray diffraction from laser-heated organic films*, Nature 390 (1997) 490.

[6-300] A.M. Lindenberg et al., *Atomic-Scale Visualization of Intertial Dynamics*, Science 308 (2005) 392.

[6-301] R.M. Stratt, M. Maroncelli, *Nonreactive Dynamics in Solution: The Emerging Molecular View of Solvation Dynamics and Vibrational Relaxation*, J. Phys. Chem. 100 (1996) 12981.

[6-302] D.P. Millar, K.B. Eisenthal, *Picosecond dynamics of barrier crossing in solution: A study of the conformational change of excited state 1,1'-binaphthyl*, J. Chem. Phys. 83 (1985) 5076.

[6-303] F. Schotte et al., *Watching a protein as it functions with 150-ps time-resolved X-ray crystallography*, Science 300 (2003) 1944.

[6-304] F. Schotte et al., *Picosecond time-resolved X-ray crystallography: probing protein function in real time*, J. Struct. Biol. 147 (2004) 235.

[6-305] R.H. Austin et al., *Dynamics of ligand binding to myoglobin*, Biochemistry 14 (1975) 5355.

[6-306] E. Collet et al., Science 300 (2003) 612.

[6-307] K. Sokolowski-Tinten et al., Nature 422 (2003) 287.

[6-308] M. Chollet et al., Science 307 (2005) 86.

[6-309] E. Collet. M.-H. Lemée-Cailleau, M. Buron, H. Cailleau, S. Ravy, T. Luty, J.F. Bérar, P. Czarnecki, N. Karl, Europhys. Lett. 57 (2002) 67.

[6-310] J. B. Goodenough, Physical Review 100 (1955) 564.

[6-311] Y. Murakami, H. Kawada, H. Kawata, M. Tanaka, T. Arima, Y. Moritomo, Y. Tokura, Phys. Rev. Lett. 80 (1998) 1932.

[6-312] C.W. M. Castleton, M. Altarelli, Phys. Rev. B 62 (2000) 1033.

[6-313] S.B. Wilkins, P.D. Spencer, P.D. Hatton, S.P. Collins, M.D. Roper, D. Prabhakaran, A.T. Boothroyd, Phys. Rev. Lett. 91 (2003) 167205.

[6-314] S. Iwai, M. Ono, A. Maeda, H. Matsuzaki, H. Kishida, H. Okamoto, Y. Tokura, Phys. Rev. Lett. 91 (2003) 057401.

[6-315] A. Cavalleri, M. Rini, H. Chong, S. Formaux, T.E. Glover, P.A. Heimann, J.C. Kieffer, R.W. Schoenlein, Phys. Rev. Lett. 95 (2005) 067405.

[6-316] A. Cavalleri, C. Toth, C.W. Siders, J.A. Squier, F. Raksi, P. Forget, J.C. Kieffer, Phys. Rev. Lett. 87 (2001) 237401.

[6-317] A. Cavalleri, Th. Dekorsy, H. Chong, J.C. Kieffer, R.W. Schoenlein, Phys. Rev. B 70 (2004) 161102(R).

[6-318] A. Plech, V. Kotaidis, M. Lorenc, J. Boneberg, *Femtosecond laser near field ablation from gold nanoparticles*, Nature Physics (2006) 44.

[6-319] R. Neutze, R. Wouts, D. van der Spoel, E. Weckert, J. Hajdu, *Potential for biomolecular imaging with femtoscond X-ray pulses*, Nature 406 (2000) 752.

[6-320] Z. Jurek, G. Oszlanyi, G. Faigel, *Imaging atom-clusters by hard x-ray free electron lasers*, Europhys. Lett. 65 (2004) 491.

[6-321] S.P. Hau-Riege, H. Szoke, H.N. Chapman, A. Szoke, S. Marchesini, A. Noy, H. He, M.R. Howells, U. Weierstall, J.C.H. Spence, *SPEDEN: Reconstructing single particles from their diffraction patterns*, Acta Cryst. A 60 (2004) 294.

[6-322] M. Bergh, N. Timneanu, D. van der Spoel, *A Model for the Dynamics of a Water Cluster in an X-ray Free Electron Laser Beam*, Phys. Rev. E 70 (2004) 051904.

[6-323] R. H. T. Bates, *Fourier phase problems are uniquely solvable in more than one dimension: 1. Underlying theory*, Optik 61 (1982) 247.

[6-324] J.R. Fienup, *Phase retrieval algorithms-a comparison*, Appl. Opt. 21 (1982) 2758.

[6-325] D. Sayre, H.N. Chapman, J. Miao, *On the extendibility of x-ray crystallography to noncrystals*, Acta Cryst. A 54 (1998) 232.

[6-326] J. Miao, P. Charalambous, J. Kirz, D. Sayre, *Extending the methodology of x-ray crystallography to allow imaging of micrometre-sized non-crystalline specimens*, Nature 400 (1999) 342.

[6-327] I.K. Robinson, I.A. Vartanyants, G.J. Williams, M.A. Pfeifer, J.A. Pitney, *Reconstruction of the shapes of gold nanocrystals using coherent x-ray diffraction*, Phys. Rev. Lett. 87 (2001) 195505.

[6-328] S. Marchesini, H.N. Chapman, S.P. Hau-Riege, R.A. London, A. Szöke, *Coherent X-ray diffractive imaging: applications and limitations*, Opt. Express 11 (2003) 2344.

[6-329] S. Marchesini, H. He, H.N. Chapman, S.P. Hau-Riege, A. Noy, M.R. Howells, U. Weierstall, J.C.H. Spence, *X-ray image reconstruction from a diffraction pattern alone*, Phys. Rev. B 68 (2003) 140101.

[6-330] H.N. Chapman, J. Hajdu et al., Ultrafast coherent diffraction imaging with a soft X-ray free-electron laser, submitted for publication.

[6-331] G. Huldt, A. Szöke, J. Hajdu, *Diffraction imaging of single particles and biomolecules*, J. Struct. Biol. 144 (2003) 219.

[6-332] J. Hajdu, E. Weckert, *Life Sciences - Scientific applications of XFEL radiation*, in TESLA, the Superconducting Electron-Positron Linear Collider with an integrated X-ray Laser Laboratory. Technical Design Report., DESY, ISBN 3-935702-00-0, Volume 5 (2001) 150-168.

[6-333] J. Hajdu *Imaging the structure of single particles and biomolecules*, in TESLA XFEL, First stage of the X-Ray Laser Laboratory, P. Audebert et al. (eds.), DESY, Hamburg (2002) 16-22.

[6-334] R. Henderson, *Cryoprotection of protein crystals against radiation-damage in electron and X-ray diffraction*, Proc. R. Soc. 241 (1990) 6.

[6-335] C. Nave, *Radiation damage in protein crystallography*, Radiation Physics and Chemistry 45 (1995) 483.

[6-336] Z. Jurek, G. Faigel, M. Tegze, *Dynamics in a cluster under the influence of intense femtosecond hard x-ray pulses*, Euro. Phys. J. D 29 (2004) 217.

[6-337] S.P. Hau-Riege, R.A. London, A. Szöke, *Dynamics of X-Ray Irradiated Biological Molecules*, Phys. Rev. E 69 (2004) 051906.

[6-338] B. Ziaja, D. van der Spoel, A. Szoke, J. Hajdu, *Auger-electron cascades in diamond and amorphous carbon*, Phys. Rev. B 64 (2001) 214104.

[6-339] B. Ziaja, A. Szoke, D. van der Spoel, J. Hajdu, *Space-time evolution of electron cascades in diamond*, Phys. Rev. B 66 (2002) 024116.

[6-340] B. Ziaja, R.A. London, J. Hajdu, *Unified model of secondary electron cascades in diamond*, J. Appl. Phys. 97 (2005) 064905.

[6-341] B. Ziaja, R.A. London, J. Hajdu, *Ionization by impact electrons in solids: Electron mean free path fitted over a wide energy range*, J. Appl. Phys. 99 (2006) 033514.

[6-342] N. Timneanu, C. Caleman, J. Hajdu, D. van der Spoel, *Auger electron cascades in water and ice*, Chem. Phys. 299 (2004) 277.

[6-343] J. Frank, *Three-Dimensional Electron Microscopy of Macromolecular Assemblies*, Academic Press, San Diego (1996).

[6-344] M. van Heel et al., *Single-particle electron cryo-microscopy: towards atomic resolution*. Quart. Rev. Biophys. 33 (2000) 307.

[6-345] D. Sayre, *X-ray crystallography*, Struct. Chem. 13 (2002) 81.

[6-346] J. Miao, K.O. Hodgson, D. Sayre, A*n approach to three-dimensional structures of biomolecules by using single-molecule diffraction images*, Proc. Natl. Acad. Sci. USA 98 (2001) 6641.

[6-347] J. Miao, T. Ishikawa, B. Johnson, E.H. Anderson, B. Lai, K.O. Hodgson, *High resolution 3D X-ray diffraction microscopy*, Phys. Rev. 89 (2002) 088303.

[6-348] J. Miao, K.O. Hodgson, T. Ishikawa, C.A. Larabell, M.A. LeGros, Y. Nishino, *Imaging whole Escherichia coli bacteria by using single particle x-ray diffraction*, Proc. Natl. Acad. Sci. USA 100 (2003) 110.

[6-349] H.R. Reiss, *Physical basis for strong-field stabilization of atoms against ionization*, Laser Physics 7 (1997) 543.

[6-350] P. Persson, S. Lunell, A. Szoke, B. Ziaja, J. Hajdu, *Shake-up and shake-off excitations with associated electron losses in X-ray studies of proteins*, Protein Science 10 (2001) 2480.

[6-351] I. Andersson, *Large structures at high resolution: spinach ribulose-1, 5-bisphosphate carboxylase/oxygenase at 1.6 Å resolution*, J. Mol. Biol. 259 (1996) 160.

[6-352] S.P. Hau-Riege, R.A. London, G. Huldt, H.N. Chapman, *Pulse requirements for x-ray diffraction imaging of single biological molecules*. Phys. Rev. E 71 (2005) 061919.

[6-353] S.P. Hau-Riege, N. Timneanu, in preparation.

[6-354] D. Starodub et al., *Damped and thermal motion of laser-aligned hydrated macromolecule beams for diffraction*, J. Chem. Phys 123 (2005) 244304.

[6-355] J.J. Larsen, K. Hald, N. Bjerre, H. Stapelfeldt, T. Seidman, *Three Dimensional Alignment of Molecules Using Elliptically Polarized Laser Fields*, Phys. Rev. Lett. 85 (2000) 2470.

[6-356] G. Huldt et al., in preparation.

[6-357] V. Elser, *Reconstruction of an object from its symmetry-averaged diffraction pattern*, http://arxiv.org/pdf/physics/0505174 (2005).

[6-358] C.T. O'Konski, B.H. Zimm, Science 111 (1950) 113.

[6-359] D. Sayre, in Proceedings of the NATO Course, Erice, H. Schenk (ed.), (1990) 353-356.

[6-360] A. Szöke, *Time-resolved holographic diffraction at atomic resolution*, Chem. Phys. Lett. 313 (1999) 777.

[6-361] A. Szöke, *X-ray and electron holography using a local reference beam*, in Short Wavelength Coherent Radiation: Generation and Application, D.T. Attwood, J. Bokor (eds.), AIP Conf. Proc. 147 (1986).

[6-362] A. Szöke, *Holographic methods in X-ray crystallography. 2. Detailed theory and connection to other methods of crystallography*, Acta Cryst. A 49 (1993) 853.

[6-363] M. Tegze, G. Faigel, *Atomic-resolution X-ray holography*, Europhys. Lett. 16 (1991) 41.

[6-364] M. Tegze, G. Faigel, *X-ray holography with atomic resolution*, Nature 380 (1996) 49.

[6-365] A. Szöke, H. Szöke, J.R. Somoza, *Holographic methods in X-ray crystallography 5. Multiple isomorphous replacement, multiple anomalous dispersion and non- crystallographic symmetry*, Acta Cryst. A 53 (1997) 291.

[6-366] H.N. Chapman et al., *High resolution ab initio Three dimensional X-ray Diffraction Microscopy*, J. Opt. Soc. Am. A (2006) 1179.

[6-367] H. Haberland, *Clusters of Atoms and Molecules*, Springer, Berlin (1993).

[6-368] M. Maier-Borst et al., Phys. Rev. A 59 (1999) R3162.

[6-369] H. Wabnitz, et al., Nature 420 (2002) 482.

[6-370] R. Santra, C. Green, Phys. Rev. Lett. 91 (2003) 233401.

[6-371] C. Bostedt et al., to be published.

[6-372] R. Sobierajski et al., in preparation.

[6-373] L. Juha et al., in preparation.

[6-374] K. Sokolowski-Tinten et al., in preparation.

[6-375] H.N. Chapman, K. Nugent, *X-ray Pulse Compression Using Strained Crystals*, Optics Commun. 205 (2002) 351.

[6-376] G. Siuzdak et al., *Mass spectrometry and viral analysis*, Chem. Biol. 3 (1996) 45.

[6-377] M.A. Tito, K. Tars, K. Valegard, J. Hajdu, C.V. Robinson, *Electrospray Time-of-Flight Mass Spectrometry of the Intact MS2 Virus Capsid*, J. Am. Chem. Soc. 122 (2000) 3550.

[6-378] A.A. Rostom, P. Fucini, D.R. Benjamin, R. Juenemann, K.H. Nierhaus, F.U. Hartl, C.M. Dobson, C. V. Robinson, *Detection and selective dissociation of intact ribosomes in a mass spectrometer*, Proc. Natl. Acad. Sci. USA 97 (2000) 5185.

[6-379] B.T. Ruotolo, K. Giles, I. Campuzano, A.M. Sandercock, R.H. Bateman, C.V. Robinson, *Evidence for Macromolecular Protein Rings in the Absence of Bulk Water*, Science 310 (2005) 1658.

[6-380] S.H. Jayasinghe, P.A.M. Eagles, A.N. Qureshi, *Electric field driven jetting: an emerging approach for processing living cells*, Biotechnol. J. 1 (2006) 86.

Photon beamlines and scientific instruments – References

[6-381] Q. Wang et al., *Icosahedral virus particles as addressable nanoscale building blocks*, Angew. Chem. 41 (2002) 459.

[6-382] http://pqs.ebi.ac.uk/pqs-bin/macmol.pl?filename=1ny7

[6-383] A.E. Siegman, *Lasers*, University Science Books (1986).

[6-384] D. Sayre, H.N. Chapman, *X-ray microscopy*, Acta Cryst. A 51 (1995) 237.

[6-385] R. Henderson, *The potential and limitations of neutrons, electrons and X-rays for atomic resolution microscopy of unstained biological molecules*, Quart. Rev. Biophys. 28 (1995) 171.

[6-386] M.R. Howells, in preparation

[6-387] U. Bergman, in *Technical Design Report TESLA Part V – The X-ray Free Electron Laser*, G. Materlik, Th. Tschentscher (eds.), DESY 2001-011, DESY, Hamburg (2001) V-307 ff.

[6-388] R. Gähler, R. Golub, Z. Phys. B 65 (1987) 269.

[6-389] Y.-X. Yan, K.A Nelson, J. Chem. Phys. 87 (1987) 6240.

[6-390] A.A. Rostom et al., *Detection and selective dissociation of intact ribosomes in a mass spectrometer*, Proc. Natl. Acad. Sci. USA 97 (2000) 5185.

[6-391] M.A. Tito et al., *Electrospray Time of Flight Mass Spectrometry of the Intact MS2 Virus Capsid*, J. Am. Chem. Soc. 122 (2000) 3150.

[6-392] S. Brauer et al., Phys. Rev. Lett. 74 (1995) 2010.

[6-393] H.N. Chapman, K. Nugent, *X-ray Pulse Compression Using Strained Crystals*, Opt. Commun. 205 (2002) 351.

[6-394] R. Tatchyn, R. Bionta, *Performance studies of a multilayer-based radiation pulse slicer for Linac Coherent Light Source applications*, SPIE proceedings 4143 (2001) 89.

[6-395] M. Richwin, R. Zaeper, D. Lützenkirchen-Hecht, R. Frahm, *Piezo-QEXAFS: advances in time-resolved X-ray absorption spectroscopy*, J. Synchrotron Rad. 8 (2001) 354.

[6-396] U. Bergman, in Technical Design Report TESLA Part V – The X-ray Free Electron Laser, G. Materlik, Th. Tschentscher (eds.), DESY 2001-011, DESY, Hamburg, (2001) V-307ff.

[6-397] A. Rousse et al., *Non-thermal melting in semiconductors measured at femtosecond resolution*, Nature 410 (2001) 65.

[6-398] A.M. Lindenberg et al., *Atomic-Scale Visualization of Inertial Dynamics*, Science 308 (2005) 392.

[6-399] K. Sokolowski-Tinten et al., *Femtosecond X-ray measurement of coherent lattice vibrations near the Lindemann stability limit*, Nature 422 (2003) 287.

[6-400] F. Schotte et al., *Watching a protein as it functions with 150-ps time-resolved X-ray crystallography*, Science 300 (2003) 1944.

[6-401] T.R. Schibli et al., *Attosecond active synchronization of passively mode-locked lasers by balanced cross correlation*, Opt. Letters. 28 (2003) 947.

[6-402] A.L. Cavalieri et al., *Clocking Femtosecond X-Rays*, Phys. Rev. Lett. 94 (2005) 114801.

[6-403] H. Redlin et al., *Ultrafast-OPCPA burst mode laser synchronized to the VUV-FEL*, to be published.

[6-404] T. Brabec, F. Krausz, *Intense few-cycle laser fields: Frontiers of nonlinear optics*, Rev. Mod. Phys 72 (2000) 545.

[6-405] Kiewiet et al., *Femtosecond synchronization of a 3 GHz RF oscillator to a mode-locked Ti:sapphire laser*, Nucl. Instrum. Methods A 484 (2002) 619.

[6-406] D. Hudson et al., *Modelocked-fiber laser frequency-controlled with an intracavity electro-optic modulator*, Opt. Lett. 30 (2005) 2948.

[6-407] Datasheet for FFS fs fibre laser from Toptica Photonics AG (2006).

[6-408] F. Tauser, F. Adler, A. Leitenstorfer, *Widely tuneable sub-30-fs pulses from a compact erbium-doped fiber source*, Opt. Lett 29 (2004) 516.

[6-409] Datasheet "Alpha10" system by Thales Laser (2006).

[6-410] Kiriyama et al., *Prepulse-free, multi-terawatt, sub-30-fs laser system*, Opt. Express 14 (2006) 438.

[6-411] Datasheet RegA 9050 by Coherent, Inc. (2006).

[6-412] I.N. Ross, P. Matousek, G.H.C. New, K. Osvay, *Analysis and optimization of optical parametric chirped pulse amplification*, J. Opt. Soc. Am. B 19 (2002) 2945.

[6-413] F. Ilday, F. Kärntner, *Cavity-enhanced optical parametric chirped-pulse amplification*, Opt. Lett. 31 (2006) 637.

[6-414] Datasheet "TOPAS" by Quantronix (2006).

[6-415] T. Brixner, G. Gerber, *Quantum control of gas-phase and liquid-phase femtochemistry*, Chem. Phys. Chem. 4 (2003) 418.

[6-416] E.L. Saldin, E.A. Schneidmiller, M.V. Yurkov, *Terawatt-scale sub-10-fs laser technology - key to generation of GW-level attosecond pulses in X-ray free electron laser*, Opt. Comm. 239 (2004) 161.

[6-417] B.W. Adams, *Femtosecond synchronism of x-rays to visible light in an x-ray free-electron laser*, Rev Sci. Inst 76 (2005) 063304.

[6-418] T. Miura et al., *Timing jitter in a kilohertz regenerative amplifier of a femtosecond-pulse Ti : Al2O3 laser*, Opt. Lett. 25 (2000) 1795.

[6-419] P. O'Shea, M. Kimmel, X. Gu, R. Trebino, *Highly simplified device for ultrashort-pulse measurement*, Opt. Lett. 26 (2001) 932.

[6-420] M.M. Shakya et al., Appl. Phys. Lett. 87 (2005) 041103.

[6-421] B. Henke et al., J. Appl. Phys. 52 (1981) 1509.

[6-422] P.A. Jaanimagi, *Fourth-Generation X-Ray Sources and Ultrafast X-Ray Detectors*, SPIE proceedings Vol. 5194 (2004).

[6-423] C. Belzile et al., Rev. Sci. Instr. 73 (2002) 1617.

[6-424] J. Liu, Appl. Phys. Lett. 82 (2003) 3553.

[6-425] Ch. Broennimann et al., J. Synchrotron Rad. 13 (2006) 120.

[6-426] G. Lutz, J. Synchrotron Rad. 13 (2006) 99.

[6-427] E.R. Fossum et al., Proceeding of SPIE 1949 (1993) 256-265.

[6-428] B. Dierickx et al., Proceedings of 1997 IEEE CCD & Advanced Image Sensors Workshop, Brugge, Belgium.

[6-429] A. Fant et al.: presented at PSD7, to be published in NIM A.

[6-430] R. Turchetta, J. Velthuis et al., NIM A 560 (2006) 102-108.

[6-431] G. Anelli et al., Radiation tolerant VLSI circuits in standard deep submicron CMOS technologies for the LHC experiments: Practical design aspects, IEEE Trans. Nucl. Sci. 45 (1999) 1690-1696.

[6-432] B.G. Taylor, TTC Distribution for LHC Detectors, IEEE Trans. Nuclear Science 45 (1998) 821.